ISSN 1349-0087

SPring-8 Research Frontiers

2006

CONTENTS 2006

Note: The principal publication(s) concerning each article is indicated with all author's names in italics in the list of references.

Editor's Note

SPring-8 Research Frontiers 2006 is the ninth issue, covering advances made during two consecutive research terms, the second half of 2005 and the first half of 2006. SPring-8 Research Frontiers describes the remarkable scientific achievements made at SPring-8 in various fields of basic and applied sciences including industrial applications, as well as the developments in the accelerators, beamlines and experimental apparatuses and the present status of the facility. A section on the X-ray free electron laser project, which was started in 2006 at RIKEN, is also included.

Since the publication of the first issue, we have invited specialists from the Proposal Review Committee to serve as the editing coordinators for their respective research fields. However, we have decided to withdraw this editorial procedure to remove this burden. From this issue, the editorial board members give introductory overviews and comment on their respective research fields.

A new article concerning scientific news at SPring-8 is featured, which focuses on the main topics of scientific achievement, strategies for developing the facilities to enhance scientific activities and the future prospects of synchrotron radiation science. This article, titled *A Place in the "X-ray" Sun*, follows the preface written by the director general.

Copies of SPring-8 Research Frontiers will be sent on request. Its full text is also available on the SPring-8 website (http://www.spring8.or.jp/). For the list of publications by the SPring-8 users and staff members, please visit the publications database at https://user.spring8.or.jp/en/pubsch.

We give our appreciation to the many specialists who recommended excellent research results suitable for publication in SPring-8 Research Frontiers. We would also like to express our sincere gratitude to the users and staff members of SPring-8 for contributing their reports to this issue.

Editorial Board

Seishi KIKUTA (Chief Editor)	SPring-8 / JASRI
Shunji GOTO	SPring-8 / JASRI
Tetsuya ISHIKAWA	SPring-8 / RIKEN･JASRI
Jun'ichiro MIZUKI	SPring-8 / JAEA
Haruo OHKUMA	SPring-8 / JASRI
Hiroyoshi SUEMATSU	SPring-8 / RIKEN
Masayo SUZUKI	SPring-8 / JASRI
Masaki TAKATA	SPring-8 / RIKEN･JASRI
Norimasa UMESAKI	SPring-8 / JASRI
Tomoya URUGA	SPring-8 / JASRI
Naoto YAGI	SPring-8 / JASRI
Masaki YAMAMOTO	SPring-8 / RIKEN･JASRI

Preface

SPring-8 celebrates the 10th anniversary of its inauguration in October 2007. Constructed jointly by RIKEN and JAERI (presently JAEA), it has been operated by JASRI which was approved by the Government as the unique designated organization based on a law for SPring-8. JAERI withdrew from the administration of SPring-8 in 2005 along with a new national policy. The above law was revised so that RIKEN is fully responsible for the total operation of SPring-8 except the selection of the users' proposals and the support for the users, which the Government entrusts to JASRI directly. RIKEN entrusts the operation of the system and the machine to JASRI through a bid. The contracts of JASRI with both the Government and RIKEN are of yearly base: thus, from the point of legal view, JASRI cannot be responsible for long-term continuous business of SPring-8, e.g. construction or planning, to which JASRI's potential is most demanded. Practically, JASRI cooperates tightly with RIKEN. Thus, SPring-8 appears to be operated almost unchanged and planning for the future of the facility is in progress in fact.

The Government has started the reorganization of public common facilities for reserch. The above-mentioned revision of the law is regarded as one of transient procedures or attempts. Another target of the Government is the collection of the beam fee, which they have tried for a few years, although we repeatedly explained that the free of charge for non-proprietary use fits a global standard.

In near future, SPring-8 will have new beamlines. In response to our call, six proposals for contract beamlines have been submitted and five of them were approved by the review committee. The construction of XFEL has started and is to be completed in 2010. We have begun the discussion of the total development plan of a new SPring-8 campus which accommodates both the storage ring and XFEL.

Akira Kira
Director General
SPring-8 / JASRI

Scientific Frontiers

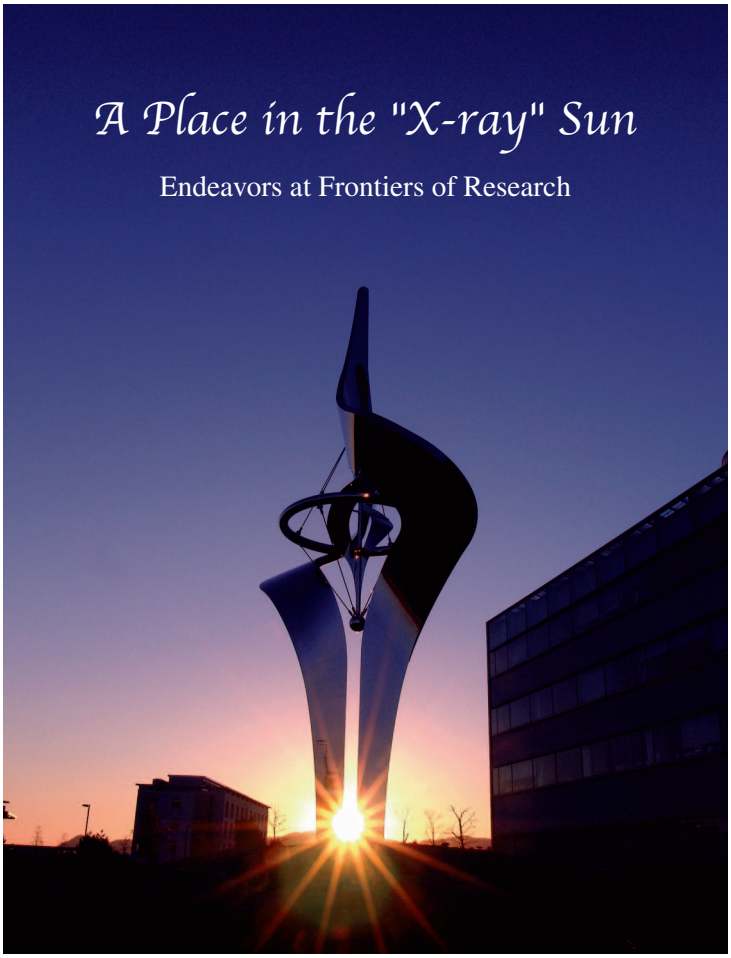

I. Innovations Supporting Activities at SPring-8

Each year, SPring-8 continues to make extensive progress, lead excellent research activities and promote new fields of research, including those presented below.

Top-up Operation has remarkably improved the quality and reliability of science research at SPring-8. One of its biggest contributions is the removal of incident X-ray intensity variations. The monitoring of incident X-ray intensity has not always been completely reliable. In experiments, it has been confirmed that the Top-up Operation eliminates this problem and has enabled great research success such as the findings presented in "The Structural Basis for Fast Phase Change of DVD-RAM" by Shinji Kohara, appearing in Materials Science, Structure. The virtually constant incident X-ray intensity produced by the Top-up Operation precludes the ambiguity resulting from the correction of the time dependence of X-ray intensity and allows for more reliable, precise structure analysis. The time-resolved experiment, one of the most promising techniques for visualizing of the kinetics as well as the dynamics in chemical reaction phenomena, will significantly improve data reliability, particularly in the analysis of the subtle features inherent in chemical reactions. Now, a research group called the "X-ray Pinpoint Structural Measurement Project Group" is attempting a time-resolved experiment on a submicron-scale area in order to reveal the crystal amorphous phase change mechanism in DVD media.

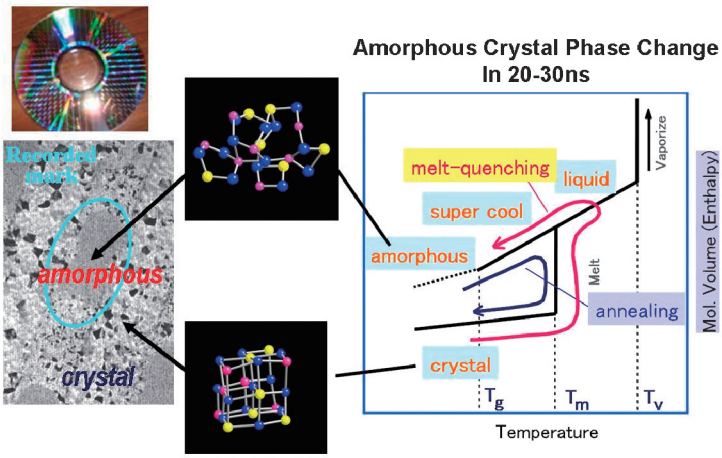

Fig. 1. Challenge of uncovering the ultrafast amorphous crystal phase change mechanism in DVD media.

Long-Term Proposals to allow the continuous use of the beamtime for up to three years is another good example of SPring-8's support of leading-edge scientific activities. This system was implemented to (i) promote research that is expected to generate outstanding results in the field of science and technology, (ii) pave the way for new research areas and methodologies, and (iii) improve industrial-based technology by making the best use of the unique

characteristics of SPring-8.

As listed in Table 1, sixteen proposals have been completed successfully, after progressing rapidly through their challenging objectives in advanced research at SPring-8.

In "The Crystal Structures of a Bacterial Multi-Drug Transporter Reveal a Functionally Rotating Mechanism" by Prof. Satoshi Murakami, a typical achievement of the long-term proposal system is presented. The work described in his proposal (Table 1, [10]) is introduced in the Structural Biology section. In 2002, Prof. Murakami's group published the first report on "The Crystal Structure of Bacterial Multi-Drug Efflux Transporter AcrB" (Fig. 2), which adorned the cover of Nature **419** (2002). In Prof. Murakami's work, "plan-do-check" research on various drugs and experimental conditions was required to reveal the multidrug transport mechanism. The three-year beamtime allowed Prof. Murakami's team to conduct systematic experiments, which eventually led to their great success. Consequently, his long-term proposed experiment resulted in the discovery of a drug export mechanism by adroit three-step functionally rotating. This work was reviewed in the "News & Views" section in Nature **443** (2006) 156. In the section with the heading "The Ins and Outs of Drug Transport," Prof. Shimon Schuldiner (Institute of Life Sciences, Hebrew University) describes the importance of this work: "the structures may prove to be essential tools in tackling the serious problems posed by drug resistance and the diseases caused by mutations in the human versions of these transporters."

In addition, Prof. Makoto Seto's proposal (Table 1, [1]) promoted Prof. Stephen Cramer's proposal (Table 1, [9]) and led to the research "Nuclear Spectroscopy of Nitrogenase and Hydrogenase" by Prof. Cramer *et al.*, which is presented in the Chemical Science section. Dr. Yoshiyuki Tatsumi's proposal (Table 1, [8]) resulted in the research, "Post-Perovskite Phase Transition in Earth's Deep Mantle" by Kei Hirose, as reported in the Earth & Planetary Science section. The long-term proposals have produced distinguished achievements, which are all reported in Research Frontiers.

Table 1. List of Long-Term Proposals

[1] "Study on Local Vibrational Densities of States Using Element and Site Specific Nuclear Resonant Inelastic Scattering and Development of the Measuring Methods" by Prof. Makoto Seto (Kyoto University)

[2] "Studies on Static and Dynamic Structures of Metallic Fluids in the Supercritical Region" by Prof. Kozaburo Tamura (Kyoto University)

[3] "Development of Spectromicroscopy using a Hard X-ray Microbeam" by Prof. Shinjiro Hayakawa (Hiroshima University)

[4] "Development of Experimental Techniques for Charge Density Studies under High Pressure" by Prof. Masaki Takata (Nagoya University/ JASRI)

[5] "Bulk Sensitive Angle Resolved Photoemission Spectroscopy of High T_c Cuprates and Related Materials" by Prof. Shigemasa Suga (Osaka University)

[6] "Study of Electronic and Orbital State in Colossal Magnetoresistance Materials by High Resolution and Magnetic Compton Profile Measurement" by Prof. Akihisa Koizumi (University of Hyogo)

[7] "Investigation on Photoninduced Phenomena by Means of SR X-ray Powder Diffraction under Photoirradiation" by Prof. Yutaka Moritomo (Nagoya University)

[8] "Technical Development for High-Temperature In-Site Observation above 100 GPa and Study of Phase Transitions in the Earth and Planetary Interiors" by Dr. Yoshi-yuki Tatsumi (Japan Agency for Marine-Earth Science and Technology)

[9] "Nuclear Resonance Vibrational Spectroscopy (NRVS) of Hydrogen and Oxygen Activation by Biological Systems" by Prof. Stephen Cramer (University of California)

[10] "X-ray Crystallographic Analysis of Multi-Drug Efflux Transporter Proteins" by Prof. Satoshi Murakami (Osaka University)

[11] "Characterization of Hard X-ray Imaging System on Board Flight Experiment" by Prof. Yasushi Ogasaka (Nagoya University)

[12] "Measurements of SuperRENS Optical Memory Material Properties" by Dr. Paul Fons (National Institute of Advanced Industrial Science and Technology)

[13] "Phase-Contrast Imaging of Lungs" by Prof. Lewis Rob (Monash University)

[14] "Study of Filler Aggregate Structure in Rubber by Time-Resolved Two-Dimensional Ultra Small- and Small-Angle X-ray Scattering" by Prof. Yoshiyuki Amemiya (University of Tokyo)

[15] "Hard X-ray Photoelectron Spectroscopic Accurate Analysis of Next Generation Nano-Scale Devices for Post-Scaling Technology" by Prof. Shigeaki Zaima (Nagoya University)

[16] "Functions and Structure Woven by Coexisting Charge-Ordered Domains: Time- and Space-Resolved X-ray Diffraction from Fluctuating Charge Orders" by Prof. Ichiro Terasaki (Waseda University)

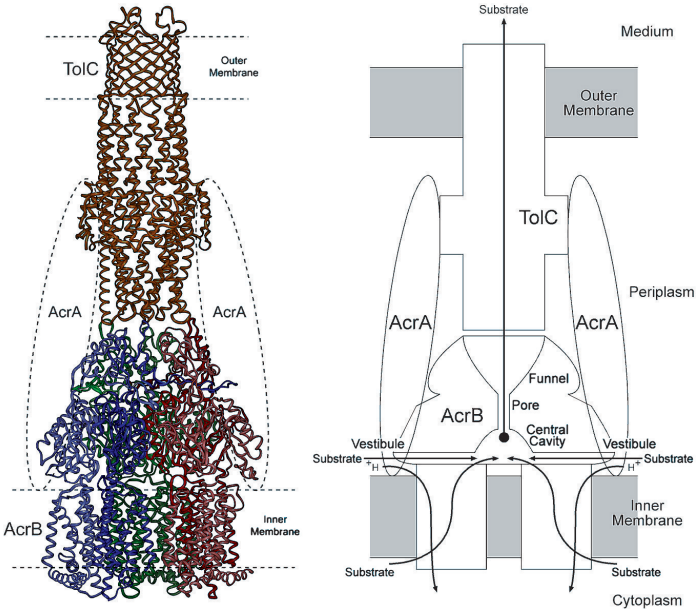

Fig. 2. First report on proposed model of AcrB-AcrA-TolC complex published in 2002 by Satoshi Murakami. Nature **419** (2002) 587.

II. Winds of Change

New Beamline Construction at the 14 currently unutilized ports in the storage ring has been recognized as a top priority. RIKEN has been able to build more than 40 SPring-8 beamlines in a short period of time because of the systematic adoption of standardized components. RIKEN recognizes these beamlines as milestones in the ultimate completion of SPring-8. We, however, will not consider the facility to be complete until all of the currently unused ports are occupied by working beamlines. The unused ports are located in the bending magnet (ports 14B2, 22B2, and 29B2) and the insertion device (ports 03IN, 07IS, 21IN, 28IN, 31IS, 32IN, 33IN, 34IN, 36IN, 43IS, and 48IN).

As the first step towards the completion of SPring-8, Japan Synchrotron Radiation Research Institute (JASRI) is funding the construction of a new beamline at BL14B2. This beamline will allow users to conduct experiments using X-ray absorption fine structure (XAFS) and powder diffraction analyses for industrial applications (Fig. 3).

In order to exploit the full potential of SPring-8, JASRI will continue to make every effort to complete the construction of the beamlines at the vacant ports. Recently, six proposals for the construction of new beamlines were submitted by a specific industry-university complex group, an industry research institute, and a university group. Each plan is appealing and is expected to soon come to fruition. These plans will nurture new research fields at SPring-8 in 2 or 3 years.

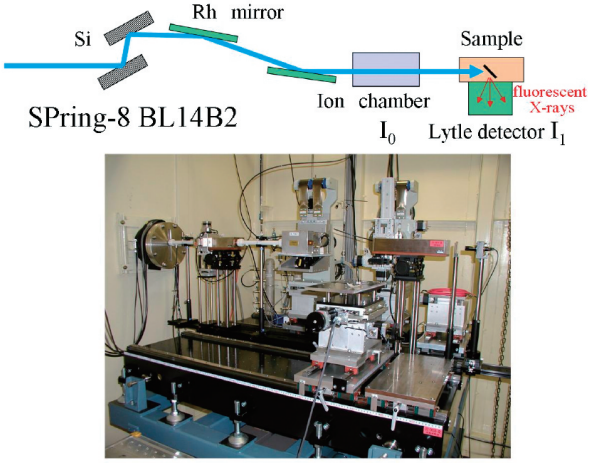

Fig. 3. Experimental hutch of new industrial application beamline BL14B2. The right-hand figure shows one of the EXAFS measurement configurations using the Lytle detector.

Fig. 4. Joint-Project Team, on the day when lasing at 49 nm was achieved.

III. New Horizon

The Launch of the X-ray Free Electron Laser (XFEL) Project was the most exciting news of the year at the SPring-8 campus. On June 20, 2006, the SPring-8 Compact SASE Source (SCSS) reported that the RIKEN-JASRI Joint XFEL Project Team (Fig. 4) at SPring-8 had succeeded in generating laser pulses at 49 nm VUV light at the prototype 250 MeV. The XFEL project was approved to start this year by the Japanese Ministry of Education, Culture, Sports, Science and Technology with a five-year funding plan. The 800-m-long 8 GeV XFEL will be constructed in the south area of the SPring-8 campus, adjacent to the 1 km SPring-8 beamline (Fig. 5). The first phase of the construction plan is to complete the accelerator shield, the linear accelerator, experimental hall, office building, XFEL Beamline 1, and Wide-Range FEL Beamline 1. For more details, please visit the SCSS web site: http://www-xfel.spring8.or.jp [see J. Synchrotron Rad. **13** (2006) 289].

Masaki Takata

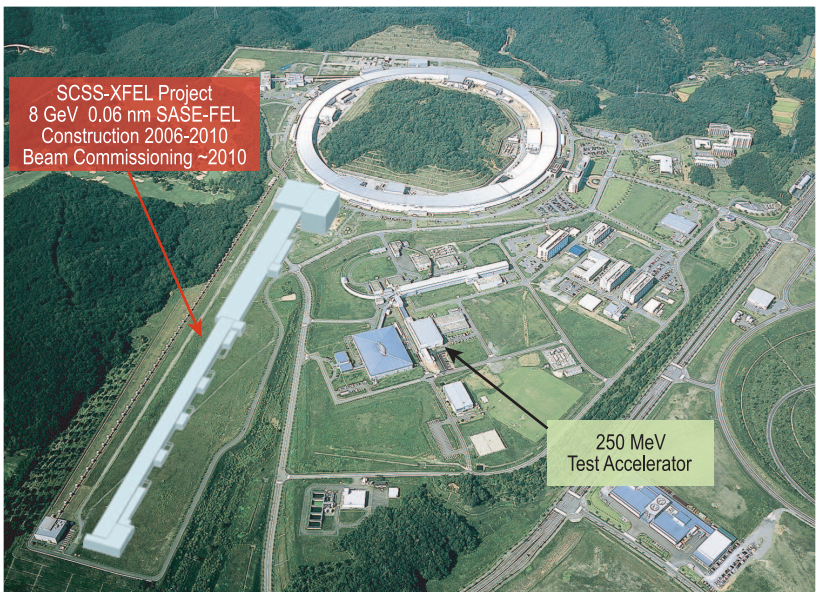

Fig. 5. Building design of 8 GeV XFEL facility.

Life Science
Structural Biology

Proteins are produced according to genetic information coded in the genome and are key molecules in biological systems. In order to understand the nature of biological systems, it is essential to understand the relationship between the structure and function of biological macromolecules, e.g., proteins and nucleic acids. Protein crystallography (PX) and small-angle X-ray scattering (SAXS) are powerful experimental techniques that enable the determination of three-dimensional protein structures and actively performed at SPring-8.

After the completion of the Human Genome Project, structural genomics research projects have been progressing worldwide. At SPring-8, the Protein 3000 project, a Japanese structural genomics project, has been progressing rapidly owing to high-throughput PX beamlines and has been working to elucidate the structure and function of proteins found in various biological systems. The number of determined protein structures using SPring-8 beamlines grows larger every year, and 366 structures were added to the Protein Data Bank (PDB) in 2006. The summary of the Protein 3000 project was described in the last two articles. Furthermore, the number of crucial structural analysis and more detailed structure-function studies are increasing. Herein, selections of remarkable structures determined at SPring-8 are described.

The first three articles are related to the structures of membrane proteins. The drug complex of the AcrB structure revealed a rotating mechanism of drug export from bacterial cells. The Dsb enzyme complex, important in disulfide bond oxidation, showed the utilization of quinine and the DsbA-DsbB transfer of the oxidative state. The membrane binding protease FtsH showed a substrate-translocation mechanism involving open-close motions of subunits driven by ATPase activity.

In studies of nucleotide-protein interaction, many fruitful results were reported. The complex structure of DEAD-box RNA helicase clearly showed the relationship between ATPase activity and the RNA unwinding mechanism. It was found that tRNA modification with pseudouridine is essential for the formation of the H/ACA box ribonucleoprotein particle.

The structure of peptidylarginine deminase 4 revealed that the modification of the N-terminal peptide of histone involves no sequence specific recognition. The firefly luciferase structure revealed the mechanism underlying the yellow-green light of firefly emission and facilitated the engineering of emission wavelength by structure based protein design. The structure of geranylgeranyl pyrophosphate synthase clarified the key residue involved in substrate chain elongation. γ-Glutamyltranspeptidase structures were used to show the reaction mechanism of the enzyme by observing them at a slow reaction speed in crystalline state.

SAXS revealed the dynamical conformational change of multisubunit and/or multidomain orientations. The large molecular complex of an extracellular signaling two-component regulatory system and a fatty acid β-oxidation multienzyme complex were elucidated along with their structural flexibilities in combination using PX results. SAXS measurement of the initially collapsed conformation showing the largest protein size supports the scaling law under various protein conditions. A noncrystalline diffraction study of amiloid fibrils suggested the scales of its aggregated β-structure.

Masaki Yamamoto

Crystal Structures of a Bacterial Multidrug Transporter Reveal a Functionally Rotating Mechanism

The emergence of bacterial multidrug resistance is an increasing problem in the treatment of infectious diseases. The major cause for the multidrug resistance of bacteria is a multidrug efflux transporter, which exports drugs out of the cells. AcrB and its homologues are the major multidrug efflux transporter in gram-negative bacteria, which confer intrinsic drug tolerance and multidrug resistance when they are overproduced. AcrB exports a wide variety of antibiotics, antiseptics, anticancer chemotherapeutics and toxic compounds including anionic, cationic, zwitterionic, and neutral compounds directly out of the cells; these compounds bypass the periplasm and are driven by proton-motive force. AcrB cooperates with a membrane fusion protein AcrA and an outer membrane channel TolC. The X-ray crystal structure of AcrB was first elucidated by our group in 2002 [1]. It is the first structure of not only a multidrug efflux transporter but also a secondary active transporter, driven by proton-motive force [2].

Now, we elucidated the crystal structures of AcrB with and without substrates in the new crystal form [3]. The crystal used in this study has a lower crystallographic symmetry than the crystal used in our previous study. The new crystal structure solved with the new crystal form is asymmetric (Fig. 1). The AcrB-drug complex consists of three asymmetric protomers, each of which has a different conformation corresponding to one of the three functional states of the transport cycle. The three monomers are named as “access” in which the substrate is incorporated (green), “binding” to which the substrate is bound (blue), and “extrusion” by which the substrate is extruded (red).

The bound substrate was found in the periplasmic domain of the “binding” protomer (Fig. 1). In the periplasmic part of each protomer, there is a substrate-binding pocket. In this pocket, there are many aromatic amino acid residues for the binding of hydrophobic substrates by aromatic-aromatic interactions. Different side chains in this pocket form different binding sites to recognize different types of substrate. The mechanism, the multisite binding, for multiple substrate recognition was also found in the soluble multidrug binding transcription factor. The pocket is expanded in the “binding” state and allows substrate binding in this voluminous pocket. The expansion of the binding pocket creates a possible exit between subdomains forming the pocket. However, one functionally important α-helix belonging to the “extrusion” protomer inclines and fills this exit to make the pocket closed (Fig. 1(b): dotted circle) [4].

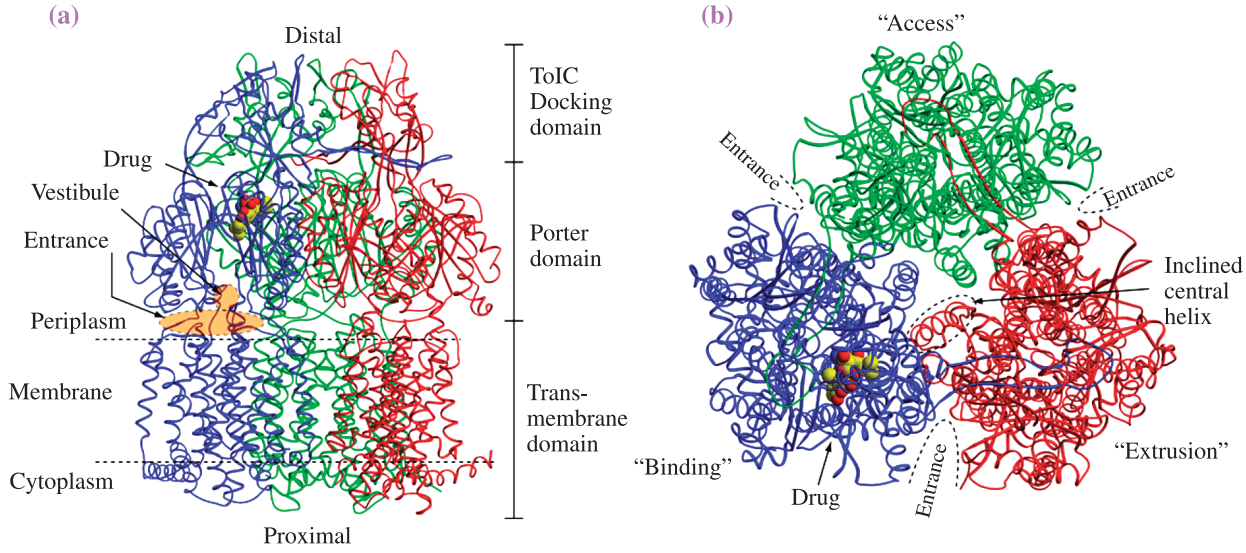

Fig. 1. Structure of the AcrB-drug (minocycline) complex.
Three protomers are individually colored. **(a)**: Ribbon representation viewed from the side parallel to the cytoplasmic membrane plane. The minocycline molecule is shown in CPK representation. The extra-membrane (periplasmic) headpiece is at the top and the transmembrane region is at the bottom. **(b)**: Top view from distal side of the cell.

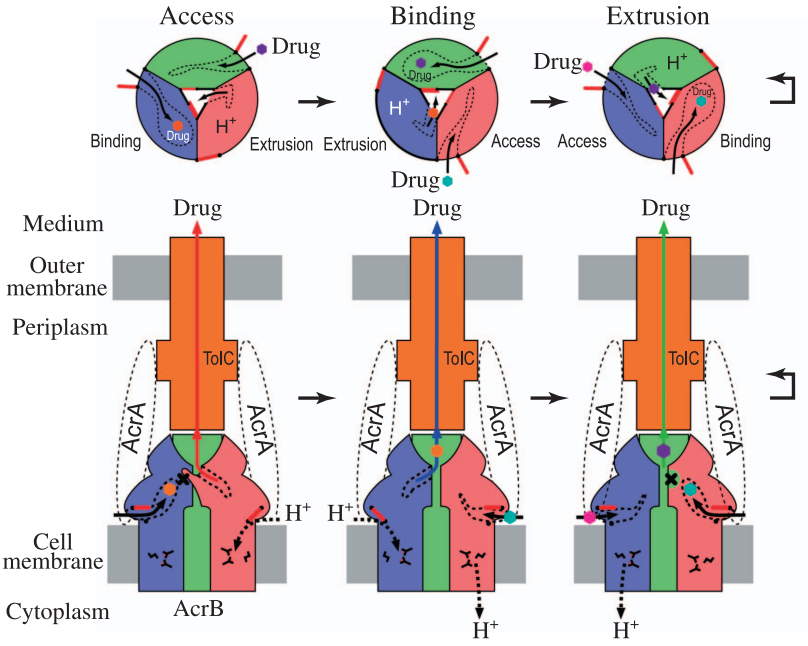

Fig. 2. Schematic illustration of the proposed "functionally rotating ordered multidrug binding change mechanism" mediated by AcrB.
Colors and arrangements in the left panel correspond to those in Fig. 1. **(a)**. The top view from the distal side of the cell. The view from the side parallel to the membrane plane. The entrance and exit within each protomer are depicted as red flaps. The drug binding pocket and translocation pathway are represented as a dotted line. Drugs are illustrated as hexagons.

At the same time, this inclination creates an open space from the shrunk binding pocket in the "extrusion" protomer. Thus, this situation corresponds to just after the extrusion of substrates from the pocket to the exit of the AcrB, which connects to the outer membrane channel, TolC [5]. The remaining protomer "access" also has a shrunken binding pocket, but an open "vestibule" exposed to the periplasmic space. Substrates are incorporated from open vestibule in the "access" state, and bind to the different locations in the voluminous aromatic pocket in the "binding" state. Then, in the "extrusion" state, the vestibule is closed and the exit is opened. At this state, the bound substrate is squeezed out into the TolC channel by shrinking the pocket. All these structural changes are coupled to proton translocation across the membrane (Fig. 2). The protonation in the "extrusion" state and deprotonation in the "access" state of three functionally important charged residues (Asp407, Asp408 and Lys940) in the transmembrane domains would affect the accessibility or influence binding or extrusion of substrate that occurring in the periplasmic domains.

On the basis of the three different conformations and transport states observed for the three protomers of AcrB, we propose that drugs are exported by a three-step functionally rotating mechanism in which drugs undergo ordered binding change (Fig. 2) [3]. Such an ordered binding change mechanism in a trimer is similar in principle to the mechanism of the trimeric F1ATPase, except that AcrB has no central stalk that undergoes mechanical rotation.

The experiments were performed at beamlines **BL41XU** and **BL44XU**.

Satoshi Murakami [a,b]

[a] Institute of Scientific and Industrial Research, Osaka University
[b] PRESTO, CREST, Japan Science and Technology Agency

E-mail: mura@sanken.osaka-u.ac.jp

References

[1] S. Murakami *et al.*: Nature **419** (2002) 587.
[2] S. Murakami and A. Yamaguchi: Curr. Opin. Struct. Biol. **13** (2003) 443.
[3] *S. Murakami, R. Nakashima, E. Yamashita, T. Matsumoto and A. Yamaguchi: Nature **443** (2006) 173.*
[4] S. Murakami *et al.*: J. Biol. Chem. **279** (2004) 3743.
[5] N. Tamura *et al.*: Biochemistry **44** (2005) 11115.

Crystal Structure of the DsbB-DsbA Complex Reveals a Mechanism of Disulfide Bond Generation

Many secretory proteins undergo oxidative folding, in which they acquire intra- or intermolecular disulfide bonds. The periplasmic space of *E. coli* contains a series of Dsb enzymes, which catalyze introduction and isomerization of protein disulfide bonds (Fig. 1). DsbA is the primary disulfide bond donor having the Cys30-Cys33 disulfide at the active site. It is kept in the oxidized and active state by a cytoplasmic membrane protein, DsbB, which transmits electrons from DsbA to either ubiquinone (UQ) or menaquinone, the source of oxidizing power under aerobic or anaerobic conditions, respectively. DsbB has been predicted to have four transmembrane helices and two periplasmic loops. Each of the loops contains one pair of essential cysteines: Cys41-Cys44 and Cys104-Cys130. While the Cys104-Cys130 pair is involved directly in the disulfide exchange with DsbA, the Cys41-Cys44 pair is the target of oxidation by UQ.

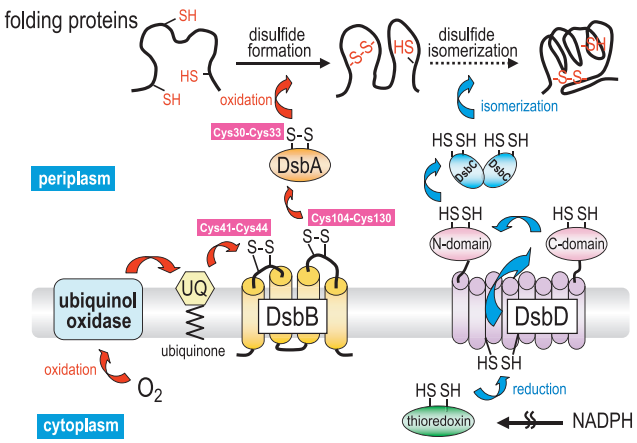

Fig. 1. Dsb enzymes responsible for protein disulfide bond formation in *E. coli*.

To achieve the deep understanding of this disulfide-introducing oxidative system, we determined the crystal structure of the disulfide-linked DsbB-DsbA complex having endogenous UQ, using beamline **BL44XU** [1]. The 3.7 Å resolution structure was complemented with engineered selenomethionine (SeMet) signals to enable structural refinement and consequent illumination of the reaction mechanisms (see [1] for more details). DsbB indeed contains four TM helices with both termini orienting to the cytoplasm (Fig. 2(a)). The four TM segments (TM1-TM4) are arranged into a four-helix bundle configuration. In addition to these TM helices, a short helix with horizontal axis exists in the second periplasmic loop of DsbB. DsbA contains a long and deep hydrophobic groove that presumably captures substrate proteins devoid of tight folding. In the structure of the DsbB-DsbA complex, a Pro100 to Phe106 portion of the second periplasmic loop of DsbB is accommodated in this groove running below the redox active Cys30 residue (Fig. 2(b)).

DsbB in isolation usually contains two intramolecular disulfide bonds, between Cys41 and Cys44 and between Cys104 and Cys130. Strikingly, the residue 130 in the crystal structure of the DsbB-DsbA complex was separated from Cys104 beyond the range (~2 Å) of disulfide bond formation (see Fig. 2(a)). This separation is ascribable to the capture of the Cys104-containing DsbB segment by the deep groove of DsbA. We envisage that such DsbA-induced cysteine relocation should prevent the reverse reaction caused by the backward attack by Cys130 against the Cys30 (DsbA)-Cys104 (DsbB) intermolecular disulfide bond. Moreover, Cys130 has proved to reside very close to the Cys41-Cys44 pair, which must be advantageous for the physiological electron flow from the Cys104-Cys130 pair to the Cys41-Cys44 pair. Thus, we propose that DsbB is designed elegantly to undergo an induced-fit and to gain the ability to oxidize DsbA effectively and

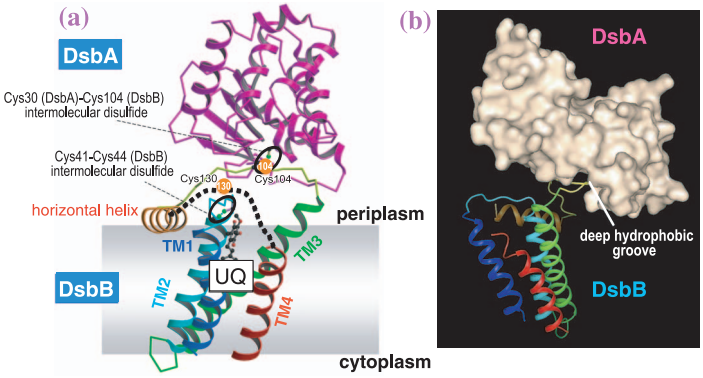

Fig. 2. **(a)** Overall structure of the DsbB(UQ8)-DsbA complex. The segment that connects the horizontal helix and TM4 lacks any electron density and is shown by dotted curve. **(b)** Another view of **(a)** rotated by 90° around a vertical axis.

exclusively even without the aid of UQ [2].

The UQ-binding site on DsbB has not unequivocally been determined in the past. Our crystallographic data indicate the presence of a prominent area of electron density near the N-terminal end of TM2, whose dimension fits that of the quinone ring (Fig. 3(a)). Although the electron density of the isoprenoid chain of UQ was invisible, the disk-like electron density could represent the head group of endogenous UQ8. The difference-Fourier map calculated from the UQ8-bound and the UQ-free crystals demonstrated a strong UQ-specific peak at the position that coincided with the electron-dense area addressed above (Fig. 3(b)). The quinone-binding site we specified here is consistent with the formation of the Cys44-UQ charge transfer complex and its enhancement by Arg48 [3,4], a residue of an implicated quinone-binding role. The area of DsbB having UQ lined up with Cys41, Cys44 and Arg48 can be regarded as the reaction center, where disulfide bonds are generated *de novo* along the chemical scheme shown in Fig. 3(c) [4].

In addition to the disulfide-introducing oxidative pathway, *E. coli* has a disulfide-isomerizing reductive pathway composed of DsbC, DsbD and cytoplasmic thioredoxin (Fig. 1). While DsbC, a disulfide isomerase, resides in the same cellular compartment as DsbA and possesses a thioredoxin fold similar to that of DsbA, it is kept in the reduced state by the action of DsbD. DsbC must not be oxidized by DsbB

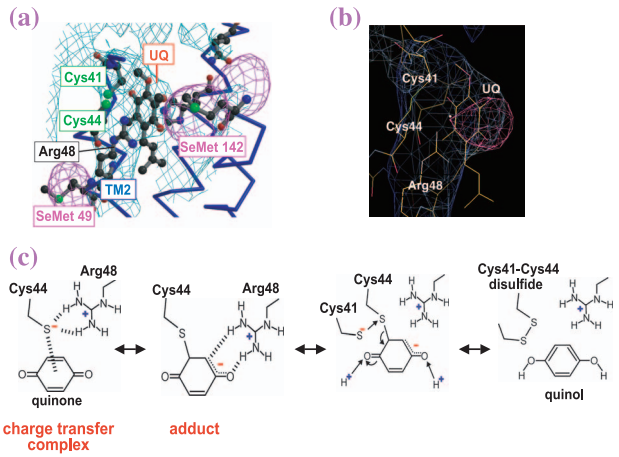

Fig. 3. **(a)** A UQ-binding site on DsbB. **(b)** Difference-Fourier map constructed from UQ8-bound and UQ-free crystals. Electron density that is assigned as representing the UQ8 ring is shown in magenta. **(c)** A chemical scheme for the generation of a disulfide bond conducted by DsbB and UQ.

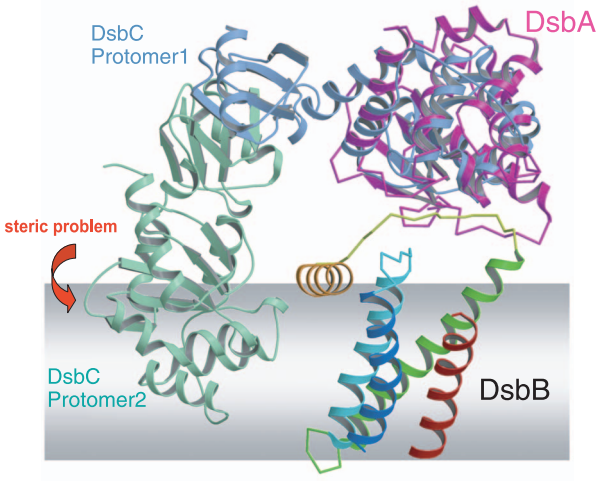

Fig. 4. A hypothetical DsbB-DsbC complex model.

to avoid futile cycles of electron transfer from DsbD to DsbB via DsbC. Unlike DsbA, DsbC exists as a homo-dimer and superimposition of one of its thioredoxin domains on the DsbB-DsbA complex in a way to minimize RMSD resulted in a clash of the other protomer onto the membrane surface (Fig. 4). Thus, DsbC would have a serious steric problem if it were to bind DsbB. This explanation is supported experimentally by the observation that a monomerized mutant of DsbC can function as a DsbB-dependent oxidase in place of DsbA [5]. Our structure provides a basis for the prevention of the crosstalk between the DsbA-DsbB oxidative and the DsbC-DsbD reductive pathways.

Kenji Inaba[a,*] and Koreaki Ito[b,c]

[a] Medical Institute of Bioregulation, Kyushu University
[b] Institute for Virus Research, Kyoto University
[c] CREST, JST

*E-mail: inaba-k@bioreg.kyushu-u.ac.jp

References

[1] *K. Inaba, S. Murakami, M. Suzuki, A. Nakagawa, E. Yamashita, K. Okada and K. Ito: Cell* ***127*** *(2006) 789.*
[2] K. Inaba *et al.*: J. Biol. Chem. **280** (2005) 33035.
[3] K. Inaba *et al.*: J. Biol. Chem. **279** (2004) 6761.
[4] K. Inaba *et al.*: Proc. Natl. Acad. Sci. USA. **103** (2006) 287.
[5] Bader *et al.*: EMBO J. **20** (2001) 1555.

Substrate Translocation Mechanism of Membrane-binding ATP-dependent Protease FtsH

ATP-dependent proteases are involved in various cellular processes including cell division, cell differentiation, signal transduction, and stress response [1]. Among them, FtsH is unique, because it is the only protease that is anchored to the cytoplasmic membrane and the only essential protease for bacterial growth [2]. Some closely related homologues of FtsH have been found in eukaryotic mitochondria and chloroplast [3]. FtsH degrades not only misassembled subunits of membrane protein complexes for their quality control but also some short-lived cytosolic regulatory proteins for cellular regulation [2]. FtsH comprises an N-terminal transmembrane segment and a C-terminal cytosolic region, which consists of AAA$^+$ (ATPases associated with diverse cellular activities) and protease domains [2]. The AAA$^+$ domain is responsible for ATPase activity, and has the conserved Walker-A, Walker-B, and second region of homology (SRH) motifs. The arginine residue at the C-terminus of the SRH motif, the so-called "arginine finger," is crucial for ATP hydrolysis [2].

Recently, we successfully crystallized and determined a soluble region of FtsH (sFtsH) from *T. thermophilus* using the data obtained at **BL38B1** and **BL41XU** beamlines [4]. The hexameric structure (Fig. 1(a)) adopts a flat-cylinder-like shape (135 Å diameter, 65 Å height) bearing a non-crystallographic three-fold rotational symmetry. As shown in the middle panel of Fig. 3(a), the cylinder is divided into two disks. The lower disk (the protease domain) forms the six-fold-symmetric structure (Fig. 1(a), the bottom view). The upper disk is composed of six AAA$^+$ domains, and each AAA$^+$ domain contains ADP. Remarkably, the orientation of the AAA$^+$ domain relative to the protease domain is significantly different between adjacent subunits (Fig. 1(b)). One subunit (orange in Fig. 1(b)) exhibits extensive contacts between AAA$^+$ and protease domains, and thus is designated as a "closed" subunit. In the adjacent subunit designated as an "open" subunit (green in Fig. 3(b)), the AAA$^+$ domain rotates by 31° away from the protease domain. Consequently, the architecture of FtsH is a trimer of dimers.

In the hexameric structure, R313 is the residue corresponding to the arginine finger (Fig. 2(a)). In the closed subunit, the distance between the oxygen atom of the γ-phosphate of the bound ADP and the Nη atom of R313 of the adjacent open subunit (Fig. 2(a), lower) would be close enough for R313 to interact with the oxygen atom of the γ-phosphate of ATP, when bound to the active site. In contrast, the corresponding distance in the open subunit is too far for ATP hydrolysis (Fig. 2(a), upper). Thus, only the ATPase catalytic site in the closed subunit should be active.

Analysis of the primary sequence revealed that FtsH carries a zinc-binding sequence (HEXXH, where X is any residue) within the protease domain. Likewise, the structure around the protease active site shows a significant difference between the two subunits. In the closed form, the AAA$^+$ domain pushes down the lid helix toward the protease domain. As a result, the kinked helix occupies the space for the polypeptide substrate just above the protease catalytic site (Fig. 2(b), lower). On the contrary, in the open form, the lid helix becomes straight and moves away from the active site (Fig. 2(b), upper). Then, the active can accommodate the substrate.

FtsH has an alternative pathway for the polypeptide substrate, a tunnel leading to the protease catalytic site of the open subunit

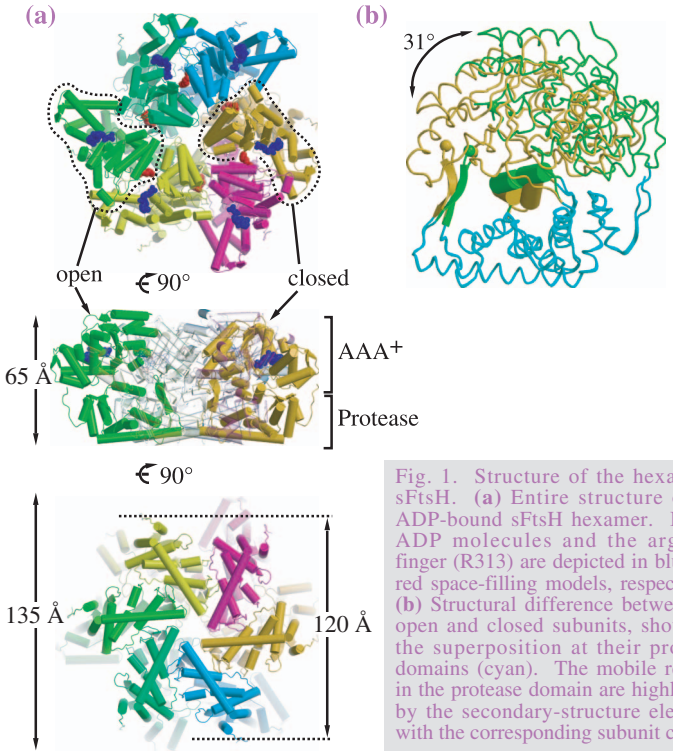

Fig. 1. Structure of the hexameric sFtsH. **(a)** Entire structure of the ADP-bound sFtsH hexamer. Bound ADP molecules and the arginine finger (R313) are depicted in blue and red space-filling models, respectively. **(b)** Structural difference between the open and closed subunits, shown by the superposition at their protease domains (cyan). The mobile regions in the protease domain are highlighted by the secondary-structure elements with the corresponding subunit color.

from the exterior of the molecule via the adjacent closed subunit (Fig. 3(b)). F229 in MFVG motif, which was proposed to be responsible for the substrate binding and translocation [5], is located at the entrance of the tunnel in the closed subunit. On the other hand, F229 in the adjacent open subunit is fully exposed to solvent on the top of the three-fold-symmetric structure.

Combined with the data supporting the ATP-dependent open-close domain arrangements, the present structural features, including the intriguing tunnel and the catalytic environments, allows us to postulate the following model for the ATPase cycle (Fig. 3(a)). (i) The open subunit exchanges its bound ADP with ATP and a closing motion is triggered. (ii) Closing motion accompanies rearrangement of the small subdomain, which leads to the conformational transition of the whole FtsH molecule. (iii) Upon completion of the closing motion, the ATPase catalytic site becomes activated and ATP is hydrolyzed. (iv) The closed subunit can return to the open form without releasing ADP and the whole FtsH structure also returns to the original state. The ATP binding to other open subunits in the same hexamer might help this transition.

The synchronized open-close motions of subunits in FtsH would drive the translocation of a substrate polypeptide to the protease catalytic sites. In accordance with the above ATPase cycle, (i) a substrate polypeptide binds to the MFVG region of the open subunit. (ii) It should be sent into the tunnel leading to the protease catalytic site of the adjacent subunit, (iii) in which it is degraded, and (iv) the MFVG region relieves the grasp on polypeptide and returns to the original position.

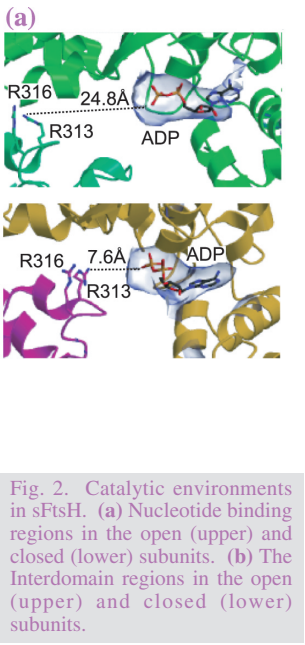

Fig. 2. Catalytic environments in sFtsH. **(a)** Nucleotide binding regions in the open (upper) and closed (lower) subunits. **(b)** The Interdomain regions in the open (upper) and closed (lower) subunits.

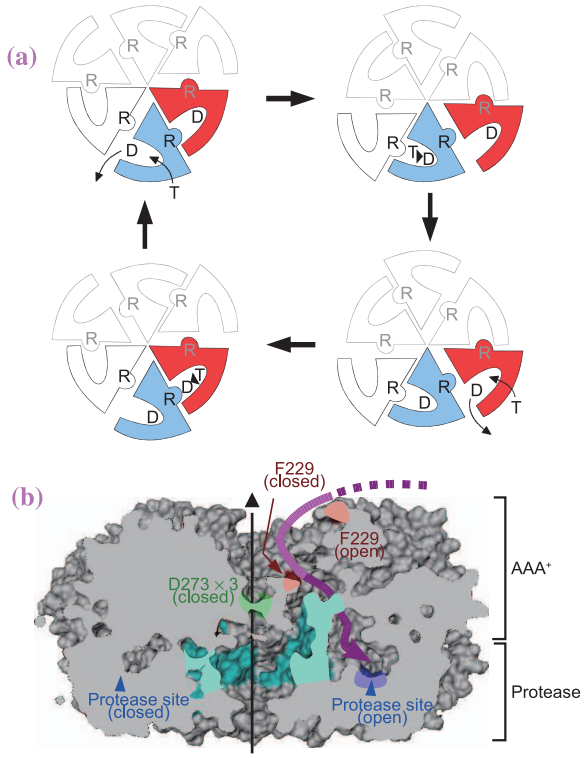

Fig. 3. ATPase cycle and putative polypeptide translocation pathway. **(a)** Schematic diagram of ATPase cycle in the hexameric FtsH. The cycle for the blue subunit is described in the text, where step (i) corresponds to the upper left. T, D, and R represent ATP, ADP, and the arginine finger, respectively. **(b)** A diagram representing a cross section of three-fold-symmetric FtsH, including the three-fold axis (black line) and two protease active sites (blue arrowheads).

Ryoji Suno[a,*], Masasuke Yoshida[a] and Kosuke Morikawa[b]

[a] Chemical Resources Lab., Tokyo Institute of Technology
[b] Institute for Protein Research, Osaka University

*E-mail: suno.r.aa@m.titech.ac.jp

References

[1] P.I. Hanson and S.W. Whiteheart: Nat. Rev. Mol. Cell. Biol. **6** (2005) 519.
[2] K. Ito and Y. Akiyama: Annu. Rev. Microbiol. **59** (2005) 211.
[3] T. Langer: Trends Biochem. Sci. **25** (2000) 247.
[4] *R. Suno, H. Niwa, D. Tsuchiya, X. Zhang, M.Yoshida and K. Morikawa: Mol. Cell* ***22*** *(2006) 575.*
[5] Yamada-Inagawa *et al.*: J. Biol. Chem. **278** (2003) 50182.

Structural Basis for RNA Unwinding Caused by DEAD-box Protein *Drosophila* Vasa

RNA helicases catalyze the alteration of higher-order RNA structures (secondary structure melting, strand separation, and RNA-protein dissociation) coupled with ATP hydrolysis. By doing so, RNA helicases regulate various cellular processes involving RNA. DEAD-box proteins constitute the largest RNA helicase family, and are widely found, from bacteria to humans. They are named after a strictly conserved sequence, Asp-Glu-Ala-Asp (D-E-A-D), and have two RecA-like domains (the N- and C-terminal domains) as a catalytic core.

To elucidate the RNA unwinding mechanism of such proteins, we determined the structure of the core of the *Drosophila* DEAD-box protein Vasa bound to a single-stranded RNA molecule and AMPPNP, an ATP analogue (Fig. 1), at a resolution of 2.2-Å using **BL41XU** beamline [1,2]. AMPPNP strongly interacts with both of the N- and C-terminal domains, thereby bringing them into the closed form. We also identified one water molecule as the putative attacking water for ATP hydrolysis. The water molecule was ideally located for a nucleophilic in-line attack, and interacted with conserved residues (Fig. 2(a)). These results indicate that the present structure is the functional ATP-bound form in the catalytic cycle. The bound RNA runs perpendicular to the cleft and is sharply bent, avoiding a clash with a conserved α-helix (the "wedge" helix) in the N-terminal domain (Fig. 2(b)). Clearly, such a bend would be incompatible with a continuous RNA duplex. The U6 phosphate atom, located at the bending point, is recognized by the conserved residues (Fig. 2(c)). Many of the

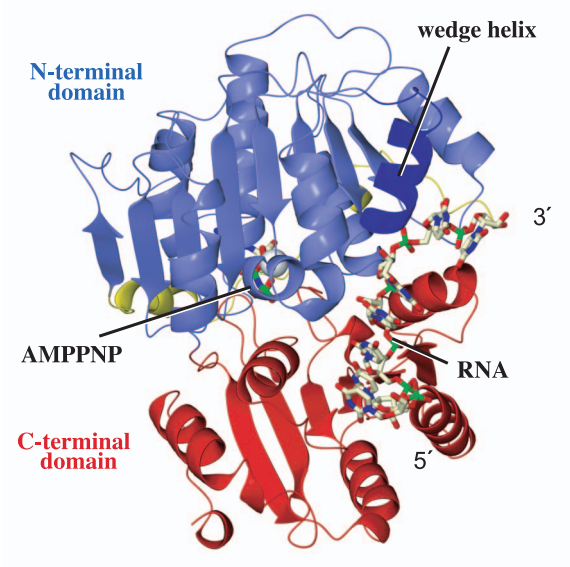

Fig. 1 Overall structure of Vasa•RNA•AMPPNP complex.

conserved residues form an extensive network of interdomain interactions (interactions between the amino- and carboxy-terminal domains) near the RNA and ATP binding sites (Fig. 2(a) and data not shown).

To examine the roles of the conserved residues, we developed mutant proteins and analyzed their RNA binding, ATPase, and RNA unwinding activities (Fig. 3). When RNA-binding residues such as R328, R378, R528 and T546 were mutated, all three of these activities were affected. This is consistent with the fact that Vasa requires RNA for efficient ATPase activity. Interestingly, when residues involved in

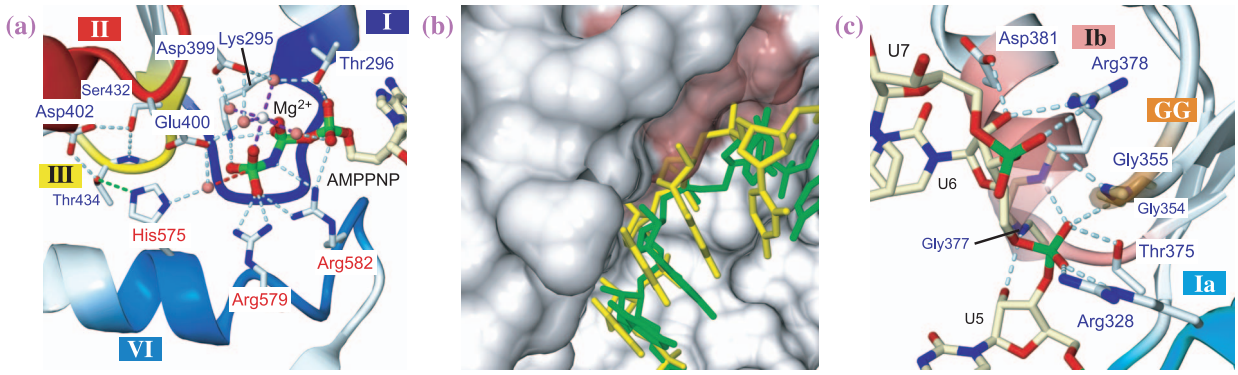

Fig. 2. RNA and ATP bindings. Motifs I, Ia, GG, Ib, II, III, and VI are marked. **(a)** ATPase site. Blue and red characters indicate residues from the N- and C-terminal domains, respectively. Water molecules are shown as pink spheres. Purple and green broken lines indicate coordinated bonds and interdomain interactions, respectively. The red broken line connects the putative attacking water and the γ-phosphorus atom. **(b)** Steric hindrance induced by wedge helix. When a modeled straight RNA (yellow) is superposed on the bound RNA in the present structure (green), it clashes with the wedge helix (pink). **(c)** RNA binding near the bend.

Mutation	Interaction	RNA Xlink (%)	ATPase (%)	unwinding
WT	-	100	100	+++
R328A	RNA	39	25	++
E329A	Inter-domain	150	72	++
Q333A	Inter-domain	47	45	+
R378A	RNA	28	17	+
D381A	RNA	309	118	+++
Q525A	Inter-domain	61	70	-
R528A	RNA	29	7	-
T546A	RNA	52	0	-
R551A	Inter-domain	55	95	+
D554A	ATP / Inter-domain	110	50	-

Fig. 3. Summary of mutational analyses.

interdomain interactions (e.g., E329, Q333, Q525, R551, and D554) were replaced, only RNA unwinding activity was greatly affected without serious decreases in RNA binding or ATPase activities. In other words, the ATPase and RNA unwinding activities are uncoupled in these mutants.

On the basis of these results, we propose a possible mechanism of the unwinding caused by DEAD-box proteins (Fig. 4). The protein can cooperatively bind ATP and the duplex region of substrate RNA. On binding, the protein induces a sharp bend in one strand by providing steric hindrance with the wedge helix. As a result, some base pairs nearby are disrupted and the duplex is destabilized. Then, ATP is hydrolyzed, and the complex dissociates to release the destabilized RNA and recycle the protein. In the uncoupled mutants, the protein can bind two substrates but cannot precisely locate the wedge helix relative to the bound RNA, which results in abortive ATP hydrolysis.

This mechanism is different from those for other helicases, and we propose that this mechanistic difference is correlated with the cellular functions of these proteins. Higher-order RNA structures are fundamental to their functions, and RNA helicases modulate them in a very specific manner. A possible advantage of the present mechanism is that the protein can directly interact with the target regions and minimize the unfavorable modulation near them. This unique mechanism may enable the DEAD-box proteins to be involved in specific, yet ubiquitous, roles in RNA metabolism and regulation.

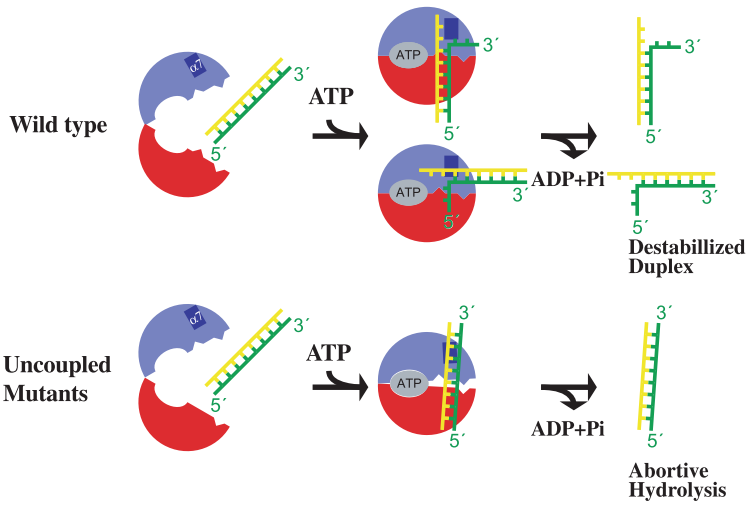

Fig. 4. Proposed mechanisms of RNA unwinding caused by the DEAD-box protein and abortive ATP hydrolysis of the uncoupled mutants.

Toru Sengoku[a,b] and Shigeyuki Yokoyama[a,b,*]

[a] Department of Biophysics and Biochemistry, The University of Tokyo
[b] RIKEN Genomic Sciences Center

*E-mail: yokoyama@biochem.s.u-tokyo.ac.jp

References

[1] T. Sengoku *et al.*: Acta Crystallogr. D Biol. Crystallogr. **60** (2004) 320.
[2] *T. Sengoku, O. Nureki, A. Nakamura, S. Kobayashi and S. Yokoyama: Cell* ***125*** *(2006) 287.*

How RNA Guides Pseudouridine Formation

Pseudouridine is the most frequent type of RNA modification and has been called as the fifth nucleoside. Conversion of uridine to pseudouridine occurs only at the particular sites of substrate RNAs, so pseudouridine synthases must know where to act before catalysis. One type of enzymes comprising single polypeptide relies on specific protein-RNA interaction for substrate selection. In contrast, H/ACA RNA protein complexes (RNPs) are a family of pseudouridine synthases that use guide RNA to recruit suitable substrate RNAs [1]. H/ACA RNPs have a complex structure comprising the pseudouridine catalyst Cbf5/dyskerin and accessory proteins Nop10, Gar1 and L7ae and a distinct H/ACA guide RNA.

H/ACA guide RNAs adopts a consensus structure that minimally includes a single hairpin with a large internal loop, a conserved ACA motif in the 3' tail (Fig. 1(a)) and a K-turn motif in archaeal RNAs. Sequences in the internal loop would form two short duplexes with complementary substrate RNA and thereby specify a central unpaired uridine for modification. There are about 100 human H/ACA RNAs directing pseudouridine formation in ribosomal and splieosomal RNAs. In addition, certain H/ACA RNPs have roles other than modification, like in rRNA processing and telomerase function. Genetic analysis has shown that mutations in dyskerin, a protein component in the complex, could lead to a rare inheritable disease called dyskeratosis congenita.

To understand how Cbf5 protein cooperates with guide RNA and accessory proteins to achieve RNA-guided pseudouridylation, we have determined the crystal structure of an entire H/ACA RNP from archaeal organism *Pyrococcus furiosus* at 2.3 Å resolution by using X-ray light at beamline **BL41XU** [2].

The crystal structure reveals a triangle shaped complex with the catalytic domain of Cbf5 located in the center (Figs. 1(b)). Proteins L7Ae together with Nop10, Gar1 and the PUA domain of Cbf5 extends the catalytic core at three corners, respectively. The RNA hairpin adopts an extended conformation and binds at one side of the active site cleft that divides the catalytic domain into two roughly even parts D1 and D2. The RNA is primarily bound at the upper stem region by L7Ae, Nop10 and Cbf5 and at the lower stem region by the Cbf5 PUA domain. The guide sequences franked by the upper and lower stems are therefore positioned just on the vicinity of the active site cleft, a reasonable place for substrate binding.

The RNP structure shows that accessory proteins L7Ae, Nop10 and the peripheral PUA domain critically coordinate the position of guide RNA in the complex.

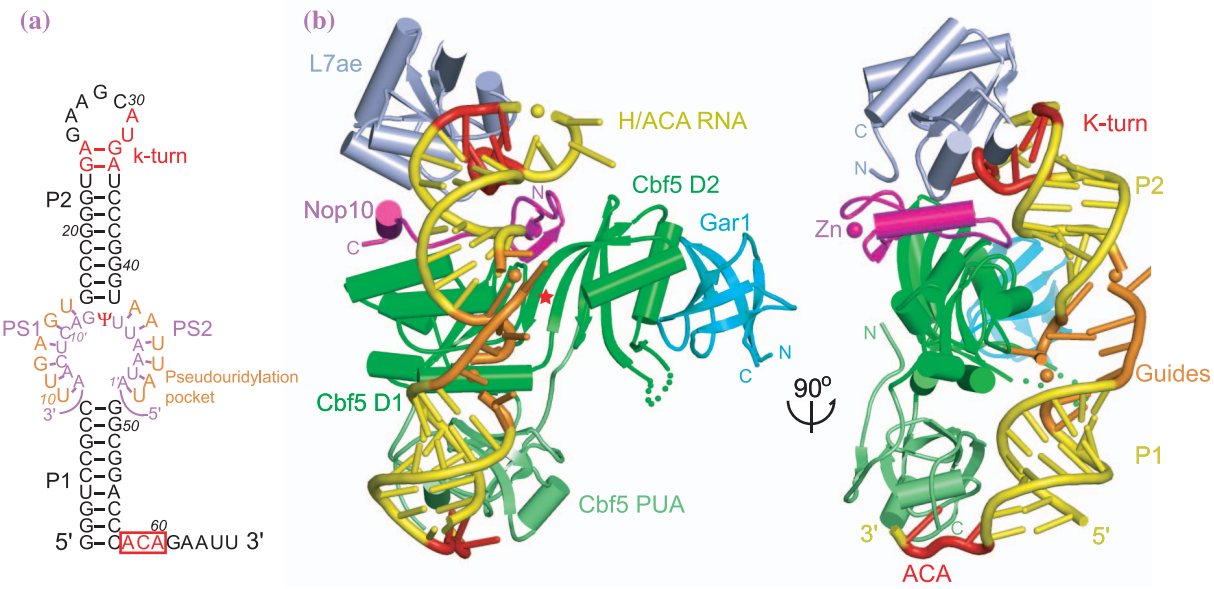

Fig. 1. Structure of H/ACA RNP. **(a)** The H/ACA RNA along with a purple cognate substrate RNA bound in the pseudouridylation pocket. **(b)** Crystal structure of the H/ACA RNP shown in two orthogonal orientations. Dots represent disordered chains. Star denotes the active site of Cbf5. [2]

The binding of the guide RNA depends on its conserved secondary structures and sequence motifs, which allows guide RNA of different sequences to be incorporated into the same protein complex.

Using a previously determined structure of pseudouridine synthase TruB in complex with a substrate hairpin RNA [3], we have built a structural model showing how guide RNA recruits substrate and orients the uridine target in the catalytic site (Fig. 2(a)).

The function of Gar1 is mysterious since it is the only protein that does not bind the guide RNA in the complex. Important clues about its function came from the observation that Gar1 interacts with a partially disordered loop of Cbf5 (Fig. 2(b)). The corresponding loop in stand-alone pseudouridine synthases, which have already had the RNA complex structure determined, interacts extensively with the loaded substrate RNA. The loop of Cbf5 likely assumes a similar role in substrate locking. However, the loop in the substrate-free complex docks against Gar1 and appears too far away from the substrate. Gar1 might control the loop in such an open conformation to aid substrate loading and release.

Guide RNA-mediated substrate recognition allows H/ACA RNP to become a programmable machine: the enzyme is able to recognize different target sites once associated with different guide RNA. Our structure has generated a framework for understanding the mechanism by which H/ACA guide RNA directs pseudouridylation, as well as other functions of H/ACA RNP.

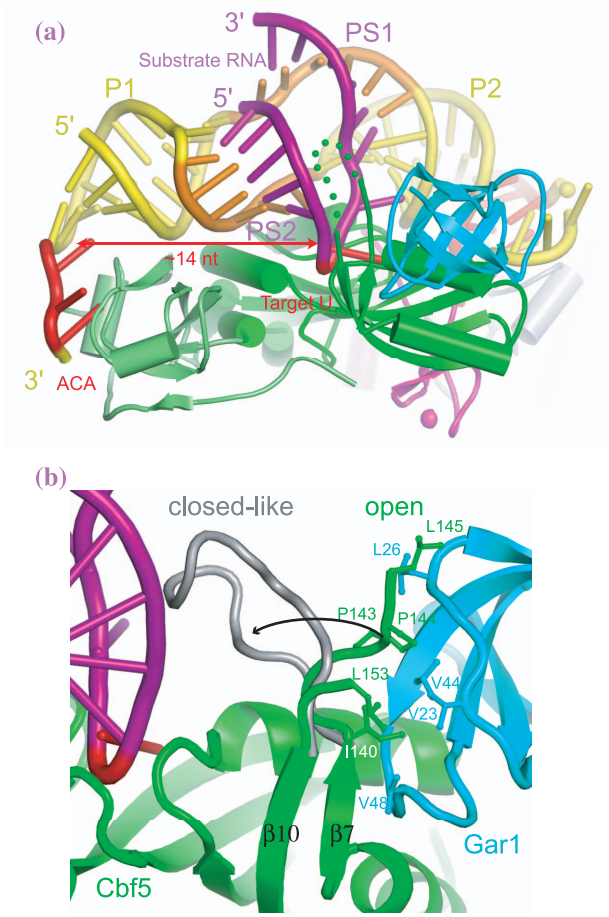

Fig. 2. Proposed mechanism of RNA-guided pseudouridylation **(a)** Structure model of the substrate complex. **(b)** Two states of the putative substrate-binding loop. The possible substrate bound state of the loop is shown in grey. The loop in our structure adopts an open conformation, in which it docks against Gar1 and appears to be unable to bind substrate. [2]

Ling Li and Keqiong Ye*

National Institute of Biological Sciences, China

*E-mail: yekeqiong@nibs.ac.cn

References

[1] U.T. Meier: Chromasoma **114** (2005) 1.
[2] *L. Li and K. Ye: Nature **443** (2006) 302.*
[3] C. Hoang and A.R. Ferre-D'Amare: Cell **107** (2001) 929.

Structural Basis for Histone N-terminal Peptides Recognition by Human Peptidylarginine Deiminase 4

The eukaryotic genome is organized within the nucleosome core particle, which is composed of core histones and their associated DNA. A diverse array of core particle modifications play a fundamental role in specific nucleosome regulation [1]. In these modifications, the Ca^{2+}-dependent citrullination (or deimination) of arginine residues of histone by peptidylarginine deiminase 4 (PAD4) has come into focus as a novel post-translational modification linked to transcriptional regulation in eukaryotes. To date, five types of human PAD, namely, PAD1-PAD4 and PAD6, have been characterized by cDNA cloning [2]. Some of these PADs are also associated with human diseases such as rheumatoid arthritis (RA), in which autoantibodies against proteins citrullinated by PAD are found at early phases of the manifestation of the disease in the majority of RA patients. Furthermore, a significant association was reported to exist between RA and functional variants of the gene encoding PAD4 in the Japanese population [3]. PAD4 is expressed in bloodstream granulocytes, and is the only type of PAD that has a nuclear localization signal and is thus localized in the cell nucleus. In view of this, we previously determined the crystal structures of Ca^{2+}-free PAD4 and a Ca^{2+}-bound inactive mutant with and without a substrate, benzoyl-L-arginine amide, and showed a novel mechanism of the Ca^{2+}-induced activation of the enzyme [4]. Here, we define the structural basis for histone N-terminal peptides recognition by determining the crystal structures of the inactive Ca^{2+}-bound C645A mutant in complexes with three histone N-terminal peptides named peptides H3-1, H3-2, and H4, each consisting of 10 residues that include one target arginine residue for the enzyme [5]. Diffraction data for the Ca^{2+}-bound PAD4 (C645A) in complex with H3-1 and H4 were collected on **BL38B1** at SPring-8 using an ADSC Quantum 4R CCD detector, and those for the complex with peptide H3-2 were collected on NW12 at PF-AR using an ADSC Quantum 210 CCD detector.

The structures of Ca^{2+}-bound PAD4 (C645A) in complexes with the three histones N-terminal peptides are similar to each other. PAD4 has five non-EF-hand Ca^{2+}-binding sites and adopts an elongated fold with two domains (Fig. 1). The N-terminal domain (Met1 to Pro300) is divided into two immunoglobulin-like subdomains. Subdomain 1 has nine β-strands and a nuclear localization signal on the molecular surface in a loop region. The amino acid alterations in functional variants of the enzyme in the Japanese RA population are positioned in subdomain 1, far from the active site in the C-terminal domain, and are unlikely to affect catalytic function directly. Subdomain 2 has ten β-strands, four short α-helices, and three Ca^{2+} ions. The C-terminal domain (Asn301 to Pro663) has a structure of five β β α β modules called an α/β propeller. The active site cleft, in which each histone N-terminal peptide and two Ca^{2+} ions are bound, is found in the α/β propeller structure in the C-terminal domain.

In each histone N-terminal peptide, five successive residues at (N – 2), (N – 1), N, (N + 1), and (N + 2), where N– and N+ define the positions immediately preceding and following the target arginine residue, were unambiguously assigned in $|F_o| - |F_c|$ maps (Fig. 2). The remaining five residues are highly disordered in the three structures. The side chain of the target arginine residue is recognized within the active site cleft in the same manner as that seen for the

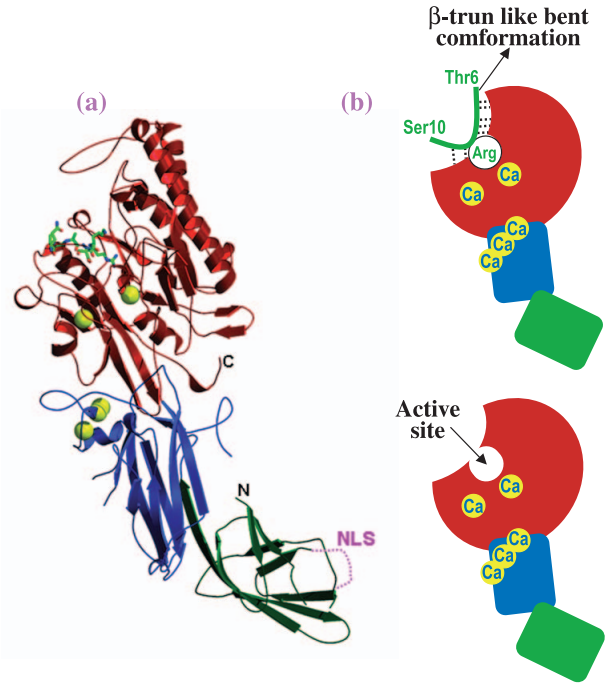

Fig. 1. Structure of Ca^{2+}-bound PAD4 (C645A) in complex with peptide H3-1. **(a)** Ribbon representation of the structure. Ca^{2+} ions and the histone peptide are shown as yellow balls and as a green stick model, respectively. N-terminal subdomains 1 (residues 1-118) and 2 (residues 119-300) and the C-terminal domain (residues 301-663) are colored green, blue, and red, respectively. The nuclear localization signal (NLS) region in subdomain 1 is shown as a dotted line. **(b)** Schematic representations of the structure shown in **(a)** (upper panel). The colors of the N-terminal (subdomains 1 and 2) and C-terminal domains are the same as those of **(a)**. Dotted lines show hydrogen bonds that form a consensus recognition motif at the molecular surface near the active site. For reference, the structure of the Ca^{2+}-bound PAD4 (C645A) is shown in the bottom panel.

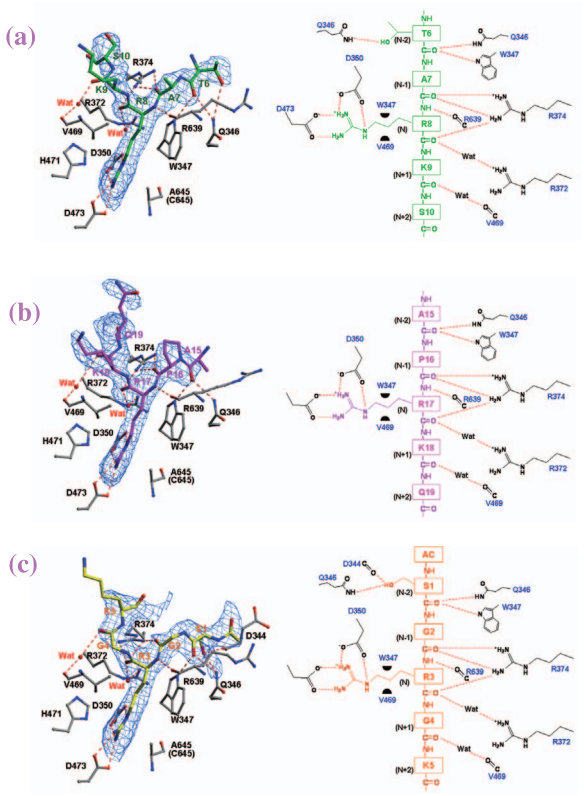

Fig. 2. Structures around active sites of Ca^{2+}-bound PAD4 (C645A) in complex with peptides H3-1, H3-2, and H4. Left, ball-and-stick representation of the structures. The protein moiety is colored grey, and the peptides H3-1 **(a)**, H3-2 **(b)**, and H4 **(c)** are colored green, magenta, yellow, and cyan, respectively. The $|F_o| - |F_c|$ electron densities of the peptides are superimposed, contoured at 2σ. Right, schematic diagrams of the structures on the left. Dotted lines and green half-circles show hydrogen bonds and hydrophobic interactions, respectively.

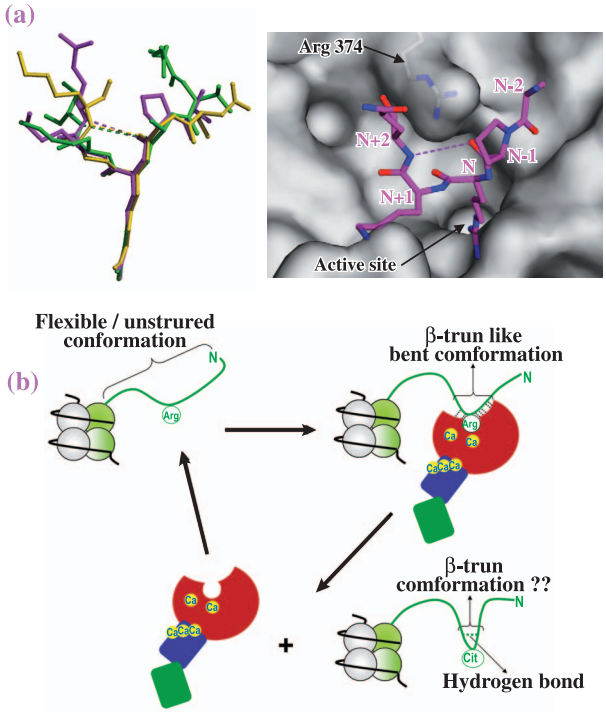

Fig. 3. Histone N-terminal peptide structures. **(a)** Left, structural comparison of PAD4-bound forms. Three peptides, namely H3-1, H3-2, and H4, are shown as ball-and-stick representations colored green, magenta, and yellow, respectively, as in Fig. 2 **(a)**, **(b)**, and **(c)**. Right, top view of the peptide H3-2 structure shown on the left of this figure, together with a molecular surface representation near the active site cleft. The weak intrapeptide interactions between the backbone oxygen at the (N − 1) position and the backbone nitrogen at the (N + 2) position are shown as dotted lines. **(b)** Possible conformational change of N-terminal histone tail in histone citrullination. The N-terminal histone inal tail protruding from the nucleosome core particle is shown as green ribbon.

previously determined BA complex [4]. Peptide recognition at the molecular surface near the active site cleft occurs commonly through backbone atoms of the peptides at the (N – 2), (N – 1), N, and (N + 1) positions (Fig. 2 and Fig. 3). This indicates that PAD4 can target multiple arginine sites in N-terminal histone tails without sequence specificity.

N-terminal histone tails are flexible and protrude from the nucleosome core particle [5]. However, the enzyme induces β-turn-like bent conformations in the histone peptides at the molecular surface near the active site cleft (Fig. 3(a)). It is, therefore, important for target arginine recognition by PAD4 that the local peptide around the target arginine residue takes a highly disordered conformation, because the enzyme recognizes a flexible/unstructured peptide at the molecular surface near the active site cleft and induces a β-turn-like bent conformation (Fig. 3(b)). Most histone-modifying enzymes interact extensively with their peptide ligands and recognize a specific amino acid in a sequence-specific manner. But, this is not the case for PAD4. The enzyme can recognize multiple arginine sites in flexible/unstructured peptides in a non-sequence-specific manner.

Kyouhei Arita, Toshiyuki Shimizu, Hiroshi Hashimoto and Mamoru Sato*

Field of Supramolecular Biology,
Yokohama City University

*E-mail: msato@tsurumi.yokohama-cu.ac.jp

References

[1] S. Khorasanizadeh: Cell **116** (2004) 259.
[2] E.R. Vossenaar *et al.*: BioEssays **25** (2003) 1106.
[3] A. Suzuki *et al.*: Nature Genet. **34** (2003) 395.
[4] K. Arita *et al.*: Nature Struct. Mol. Biol. **11** (2004) 777.
[5] *K. Arita, T. Shimizu, H. Hashimoto, Y. Hidaka, M. Yamada and M. Sato: Proc. Natl. Acad. Sci. USA **103** (2006) 5291.*

Structural Basis of Bioluminescent Color Control in Firefly Luciferase

The firefly emits brilliant yellow-green light. The bioluminescence reaction is carried out by the enzyme firefly luciferase, which catalyzes the oxidative reaction involving firefly luciferin, MgATP and molecular oxygen to yield an excited oxyluciferin. The visible light is emitted during the relaxation of the excited oxyluciferin to the corresponding ground state. The catalytic reaction of luciferase is a two-step reaction (Fig. 1(a)). In the first step, luciferin attacks an ATP molecule and luciferase forms an enzyme-bound luciferyl-AMP intermediate. In the second step, a proton is abstracted from the C-4 carbon of the luciferyl-AMP intermediate and molecular oxygen attacks the position, then an electronically excited oxyluciferin molecule, AMP and CO_2 are produced.

One of the most interesting aspects of the emission in firefly luciferase is the bioluminescence color change induced a luciferase mutation. The color change is caused by a single-amino-acid point mutation in firefly luciferase. In the case of Japanese genji-botaru luciferase, yellow-green light and red colored light are emitted by the wild-type enzyme and the S286N mutant, respectively [1]. We determined the crystal structures of genji-botaru luciferase at the various states in the catalytic reaction to elucidate the color control mechanism of luciferase. We synthesized 5'-*O*-[*N*-(dehydroluciferyl)-sulfamoyl]adenosine (DLSA), which is a luciferyl-AMP intermediate analogue, to determine the crystal structure of the intermediate (Fig. 1(b)).

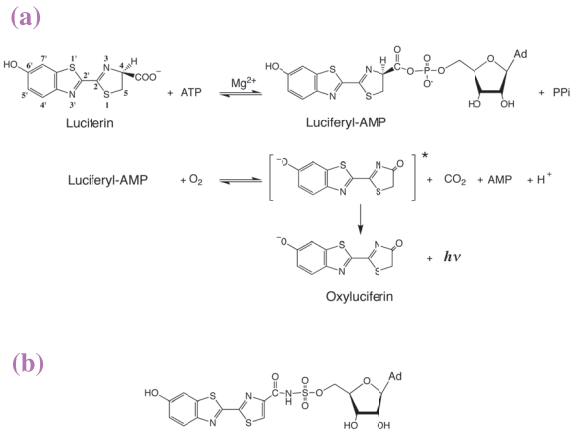

5'-*O*-[*N*-(dehydroluciferyl)-sulfamoyl] adenosine (DLSA)

Fig. 1. **(a)** Bioluminescent reaction catalyzed by luciferase. **(b)** Structure of DLSA, luciferyl-AMP intermediate analogue.

The crystal structure of genji-botaru luciferase complexed with DLSA was determined at a resolution of 1.3 Å using beamline **BL45XU**, PX-station (Fig. 2). The overall structure consists of a large amino-terminal domain and a small carboxyl-terminal domain. DLSA was present in the active site pocket formed by these two domains. We also elucidated the structures of genji-botaru luciferase in complex with Mg-ATP and with in complex AMP/oxyluciferin at 2.3 Å and 1.6 Å, respectively. The conformation of DLSA is similar to that of the oxyluciferin and AMP molecules in the AMP/oxyluciferin complex. The overall structure of the AMP/oxyluciferin complex is almost the same as that of the Mg-ATP complex, but significant differences are observed in the DLSA complex. The Ile288 residue in the DLSA complex is much closer to the DLSA molecule than in the other structures. The movement of Ile288 seems to be involved in the switching of the hydrogen bonding network: Ser286 is hydrogen bonded to Glu313 in the AMP/oxyluciferin complex structure; in contrast, the Ser286 residue of the DLSA complex forms hydrogen bonds with Asn231 and Tyr251 through a water molecule in the DLSA complex (Fig. 3(a)). Due to the movement, three atoms of the side chain of Ile288, which is located in the highly hydrophobic active site, form van der Waals contacts with the DLSA molecule (Fig. 3(c)).

Fig. 2. Crystal structure of wild-type genji-botaru luciferase complexed with DLSA (green).

In addition, we determined the crystal structure of the red-light-emitting S286N mutant luciferase complexed with DLSA at 1.45 Å using beamline **BL44B2**, and compared its structure with those of three types of wild-type crystal. The structure of the S286N mutant complexed with DLSA is similar to the structure of the wild-type enzyme complexed with AMP/oxyluciferin, but not to the structure of wild-type enzyme complexed with DLSA. Note that, the conformational change observed in the wild type was not seen in the S286N mutant. The Ile288 residue of the S286N mutant complexed with DLSA is not close to the DLSA molecule. This might be due to the side chain atoms of Asn286 hydrogen bonding to Glu313 and a water molecule, which seems to prevent Ile288 from shifting (Fig. 3(b)). As a result, only one atom of the side chain of Ile288 forms van der Waals contact in the S286N mutant complexed with DLSA (Fig. 3(c)). Therefore, the structure of the S286N-DLSA complex creates less of a hydrophobic microenvironment than that of the wild-type enzyme-DLSA complex.

The conformation of the DLSA molecule in the wild-type complex is almost same that in the S286N complex. Thus, the difference in both structures is only in the conformational change in luciferase, which controls the hydrophobic microenvironment for the DLSA molecule (Fig. 3(a,b)). We consider that the structure of the DLSA complex indicates the structure just before the light is emitted. Therefore, the difference in the structure of DLSA complex reflects the difference in the energies of the excited state of oxyluciferin. The wild-type luciferase tightly binds the excited state of oxyluciferin in the highly rigid and nonpolar microenvironment created by the hydrophobic side chain of Ile288, minimizing energy loss before emitting yellow-green light. In contrast, the S286N luciferase forms a less rigid microenvironment, which allows some energy loss from the excited state of oxyluciferin due to thermal relaxation. Therefore, the S286N mutant emits the red light low in energy, which is compared with yellow-green light.

To confirm our hypothesis that the degree of the hydrophobicity is related to bioluminescence color, we prepared I288V and I288A mutants and examined the emission colors. As expected, the I288V and I288A mutants emitted orange and red colored light, respectively. Therefore, the amino acid residue at position 288 directly influences the emitted light color and the molecular rigidity of the excited state of oxyluciferin, which is controlled by the transient movement of Ile288, and determines the color control of bioluminescence during the emission reaction.

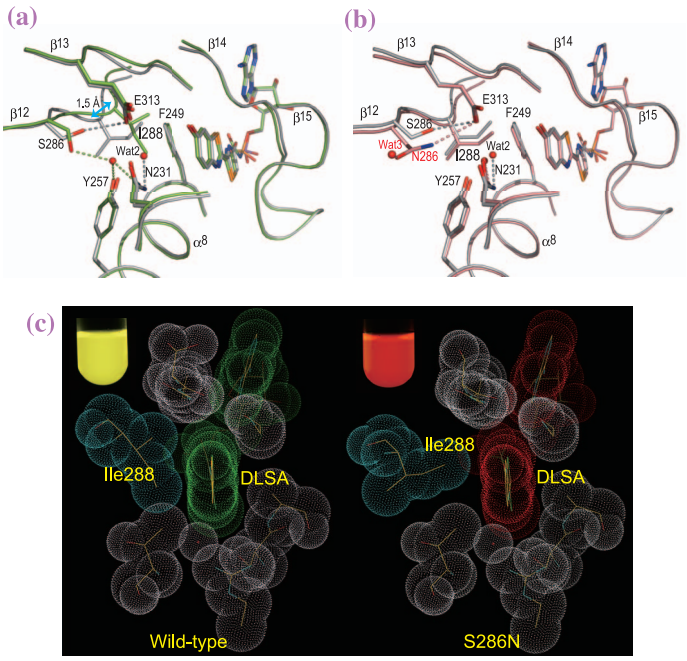

Fig. 3. Comparison of active site in luciferase structures. **(a)** Superposition of wild-type DLSA (green) and wild-type AMP/oxyluciferin (white) complexes. **(b)** Superposition of S286N DLSA (pink) and wild-type AMP/oxyluciferin (white) complexes. **(c)** Comparison of van der Waals interactions in structures of wild-type (left) and S286N (right) luciferases complexed with DLSA. The van der Waals radii of Ile288 (blue), DLSA in wild-type (green) and DLSA in S286N (red).

Toru Nakatsu [a,b]

[a] Graduate School of Pharmaceutical Sciences, Kyoto University
[b] SPring-8/RIKEN

E-mail: nakatsu@pharm.kyoto-u.ac.jp

References

[1] N. Kajiyama and E. Nakano: Protein Eng. **4** (1991) 691.
[2] *T. Nakatsu, S. Ichiyama, J. Hiratake, A. Saldanha, N. Kobashi, K. Sakata and H. Kato: Nature **440** (2006) 372.*

Structure of Geranylgeranyl Pyrophosphate Synthase from *Saccharomyces cerevisiae* — Mechanism of Product Chain Length Determination of *trans*-prenyltransferases

The C_5-isopentenyl pyrophosphate (IPP) serves as the building block for the isoprenoid biosynthesis generating a very broad range of compounds used as hormones (sterol), pigments (carotenoid and chlorophyll), compositions of cell membranes (cholesterol and ergosterol) or cell walls (lipid I, II, and peptidoglycan), and components of signal transduction networks (Ras, Rho, Rap, and Rac) [1]. Condensation of IPP with dimethylallyl pyrophosphate (DMAPP) results in all isoprenoid diphosphates such as C_{15}-farnesyl pyrophosphate (FPP), C_{20}-geranylgeranyl pyrophosphate (GGPP), and longer species such as C_{40}-octaprenyl pyrophosphate (OPP) by *trans*-prenyltransferases forming the *trans* double bond during each IPP condensation reaction (Fig. 1(a)). At the active site, two conserved aspartate-rich motifs called DD*XX*D, where *X* encodes any amino acid, coordinate with Mg^{2+} for substrate binding and the subsequent reaction.

Based on previous study of C_{15}-FPP synthase (FPPs), two bulky amino acid residues at the 4th and 5th position before the first DD*XX*D motif in helix D form a blockage underneath the allylic substrate site to avoid the further elongation of FPP product [2]. However, C_{20}-GGPP synthase (GGPPs) of *S. cerevisiae*, *H. sapiens*, and *S. alba* (mustard) contain small residues at the 4th and 5th position prior the first DD*XX*D motif rather than bulky residues found in other GGPPs (Fig. 1(b)).

To rationalize the mechanism of product chain length determination, the first structure of GGPPs from *S. cerevisiae* has been determined at 1.98-Å resolution at beamline BL17B2 of the National Synchrotron Radiation Research Center (Taiwan) and the Taiwan Contract beamline **BL12B2** at SPring-8 (Japan) [3]. Each subunit is composed of 15 α-helices joined by connecting loops and a central crevice surrounded by α-helices A to I contains two conserved DD*XX*D motifs (helices D and I) at the top for substrate binding with one Mg^{2+} coordinated by Asp^{75}, Asp^{79}, and four water molecules. Helices F and G are involved in the dimer formation, with the major stabilization coming from the helices F (A chain)-F (B chain) and F (A chain)-G (B chain) intersubunit hydrophobic interactions and hydrogen bonding (Fig. 2).

Distinct from other known structures of *trans*-prenyltransferases, the N-termius of helix A and the following loop of *S. cerevisiae* GGPPs protrude from the helix core into the other subunit and contribute to the tight dimer formation proven by truncation mutants.

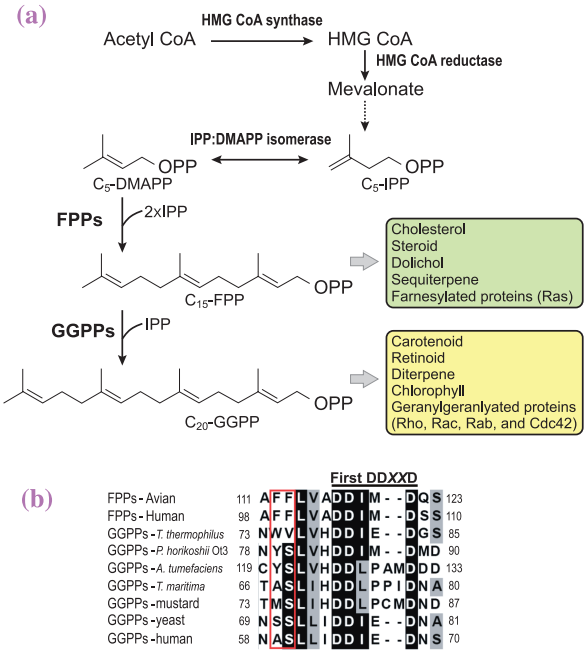

Fig. 1. **(a)** The mevalonate pathway of isoprenoid biosynthesis. **(b)** The partial amino acid sequence alignment of FPPs and GGPPs.

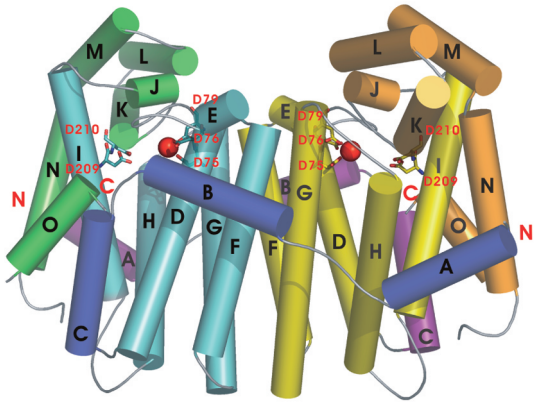

Fig. 2. Structure of *S. cerevisiae* GGPPs. The α-helices shown in cylinder diagrams and colored in blue, cyan, to green and purple, yellow, to orange from N- to C-terminus for the two individual subunits. Two DD*XX*D motifs locating at each active site are shown as sticks and one Mg^{2+} ion is colored in red ball.

Underneath the substrate-binding site, two bulky residues, Tyr[107] (helix F) and His[139] (helix G), occupy the bottom portion of the elongated crevice as a floor to block further chain length elongation of GGPP different from previous studying on FPPs [2] (Fig. 3(a)). Compared to the major product C_{30} synthesized by mutant H139A, the product generated by mutant Y107A is predominantly C_{40}, suggesting the most important role of Tyr[107] in determining the product chain length (Fig. 3(b)).

Based on recently solved GGPPs crystal structures, these enzymes utilize large amino acids from different secondary structural elements to regulate the product chain length. GGPPs from *T. thermophilus*, *P. horikoshii* Ot3, and *A. tumefaciens* use a bulky residue at the 5[th] position before the first DD*XX*D motif and those from yeast, human, mustard, and *T. maritima* utilize two or three large residues in different helices.

In summary, a molecular ruler mechanism controls the chain length of *trans*-prenyltransferases shown in Fig. 4. The essential amino acids for product chain length determination of *trans*-prenyltransferases are Phe[113] for C_{15}-avian FPPs, Trp[74] for C_{20}-*T. thermophilus* GGPPs, Tyr[107] and His[139] for C_{20}-*S. cerevisiae* GGPPs, Leu[164] for C_{30}-*S. solfataricus* HexPPs, and Phe[132] for C_{40}-*T. maritima* OPPs [3-5].

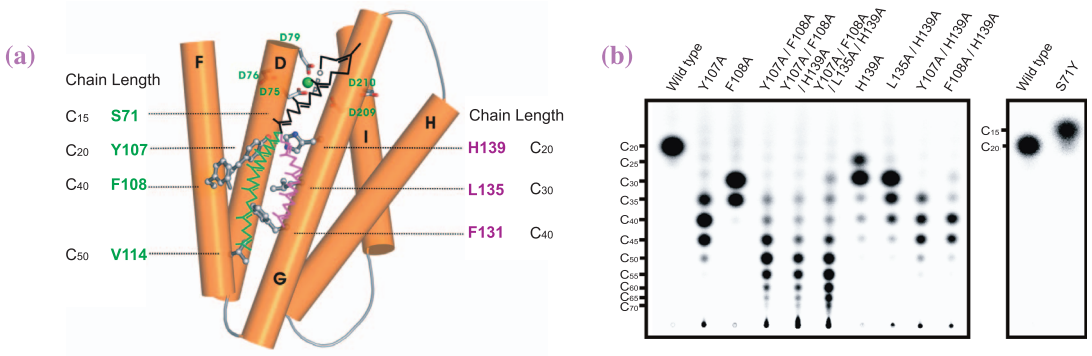

Fig. 3. **(a)** The diagram presents the mechanism of chain length determination of *S. cerevisiae* GGPPs. **(b)** The final products synthesized by wild-type and mutant GGPPs were analyzed through thin-layer chromatography.

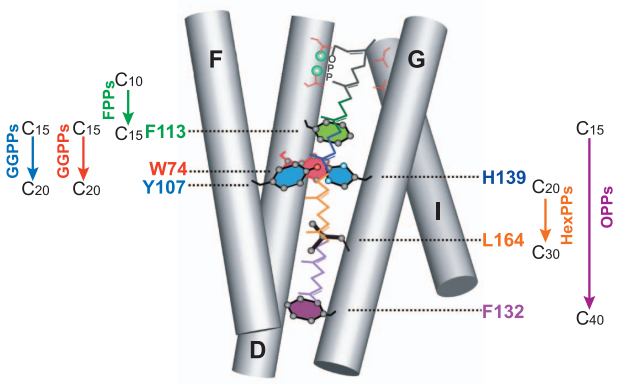

Fig. 4. The molecular ruler mechanism of *trans*-prenyltransferases. The key residues at the bottom of active site for chain length determination are marked.

Tao-Hsin Chang[a,b], Po-Huang Liang[a,b] and Andrew H.-J. Wang[a,b,*]

[a] Institute of Biochemical Sciences, National Taiwan University, Taiwan
[b] Institute of Biological Chemistry, Academia Sinica, Taiwan

*E-mail: ahjwang@gate.sinica.edu.tw

References

[1] P.H. Liang *et al.*: Eur. J. Biochem. **269** (2002) 3339.
[2] L.C. Tarshis *et al.*: Proc. Natl. Acad. Sci. USA **93** (1996) 15018.
[3] *T.H. Chang, R.T. Guo, T.P. Ko, A.H. Wang and P.H. Liang: J. Biol. Chem.* ***281*** *(2006) 14991.*
[4] H.Y. Sun *et al.*: J. Bacteriol. **187** (2005) 8137.
[5] R.T. Guo *et al.*: J. Biol. Chem. **279** (2004) 4903.

Crystal Structures of γ-Glutamyltranspeptidase from *Escherichia coli* and its Reaction Intermediate

γ-Glutamyltranspeptidase (GGT) is an extracellular enzyme that plays a key role in the metabolism of γ-glutamyl compounds including glutathione (GSH) [1]. GGT catalyzes the first step of the degradation of extracellular GSH into constituent amino acids, which are then transported into the cell and used as cysteine and nitrogen sources in *Escherichia coli*, yeast, and mammalian cells [2]. In mammals, GSH/xenobiotic conjugates are cleaved by GGT and these products are metabolized, leading to the excretion of mercapturic acids into the bile and urine. Clinically, GGT is widely used as a marker in blood tests; high level of GGT activity in the blood is indicative of hepatic- and biliary-tract-associated diseases.

GGT is a heterodimer comprising a large (L) subunit and a small (S) subunit generated from a precursor protein by posttranslational processing [3]. GGT catalyzes the hydrolysis of the γ-glutamyl linkage of its substrates to yield glutamate and the transfer of the γ-glutamyl group to other amino acids and peptides (Fig. 1). We determined the crystal structure of *E. coli* GGT, which shares a similar primary structure and enzymatic characteristics with mammalian GGTs, at a resolution of 1.95 Å (R = 20.7%, R_{free} = 23.1%) [4]. Furthermore, we analyzed the course of its enzymatic reaction by X-ray crystallography, in which GGT crystals that were flash-cooled after soaking in GSH solution for various soaking times were used. We also determined the structure of GGT in complex with L-glutamate (GGT-Glu), the product of hydrolysis. All diffraction data were collected at beamline **BL41XU**.

The present analysis first revealed the tertiary structure of GGT; GGT exhibits the stacked αββα fold seen in the members of N-terminal nucleophile hydrolase superfamily (Fig. 2(a)). The β-strands in the L and S subunits form the two central β-sheets, which are flanked by α-helices. Thr-391, the N-terminus of the S subunit generated by posttranslational processing, is the active residue of catalysis. Thr-391 was located in the bottom of the deep groove, from which the pocket for γ-glutamyl moiety binding follows (Fig. 2(b)). The pocket was shielded from the solvent by the surface loop.

A Fourier map for the crystal soaked in the GSH solution for 10 sec showed the density of the γ-glutamyl moiety in the substrate binding pocket (Fig. 3(a)). Remarkably, the Oγ atom of Thr-391 was covalently bonded to the carbonyl carbon of the γ-glutamyl moiety, illustrating that the γ-glutamyl-enzyme intermediate was trapped. This structure represents the state generated by the carbonyl carbon at the γ-position of GSH being attacked by Thr-391 Oγ, which is followed by the release of the Cys-Gly moiety of GSH. Moreover, a water molecule (labeled W2 in Fig. 3(a)) was seen on the carbonyl carbon of the γ-glutamyl-Thr-391-Oγ bond in the intermediate that is to be hydrolyzed. When the GGT crystals were soaked for 1 min or more, the electron density between L-glutamate and Thr-391 was resolved, showing that the hydrolysis of the γ-glutamyl-enzyme intermediate occurred in the crystalline state (Fig. 3(b)). Although the conformation beyond the Cβ in the γ-glutamyl moiety differs from that in glutamate, the binding manner of the α-amino and α-carboxyl groups of the γ-glutamyl moiety was identical to that of L-glutamate.

Extensive site-directed mutagenesis studies of

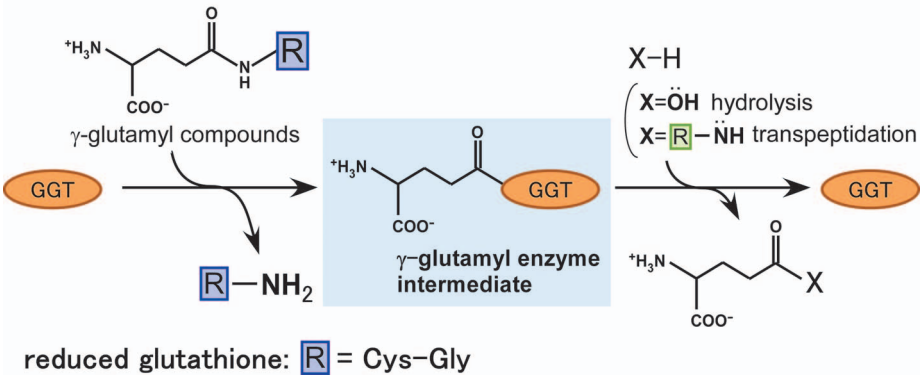

Fig. 1. Reactions catalyzed by GGT.

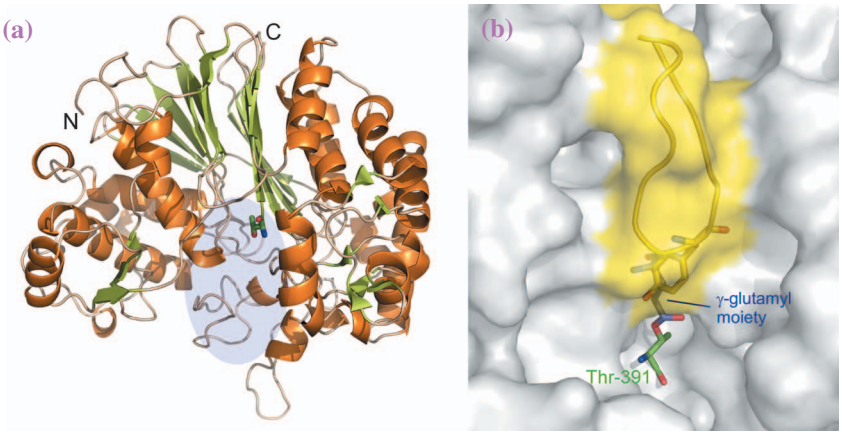

Fig. 2. **(a)** Ribbon drawing of *E. coli* GGT. α-helices are colored brown and β-strands are colored green. The active residue, Thr-391, is shown as a stick model and the substrate binding pocket is shaded. **(b)** Surface drawing around substrate binding pocket. The ribbon (yellow) represents the loop that shields the pocket from solvent.

human GGT identified the residues essential for GGT activity (i.e., Arg-114, Asp-433, Ser-462, and Ser-463 in *E. coli* GGT). These are all involved in the binding of the α-amino and α-carboxyl groups of the substrate. Although the involvement of Glu-108 of human GGT (Glu-115 in *E. coli* GGT) in acceptor binding was shown, Glu-115 is buried inside GGT, where it is hydrogen-bonded to Arg-114, the residue responsible for α-carboxyl-group recognition. These residues are all highly conserved in the GGT amino acid sequences of many species. Future studies on other GGTs including human GGT can be carried out on the basis of the structure of *E. coli* GGT.

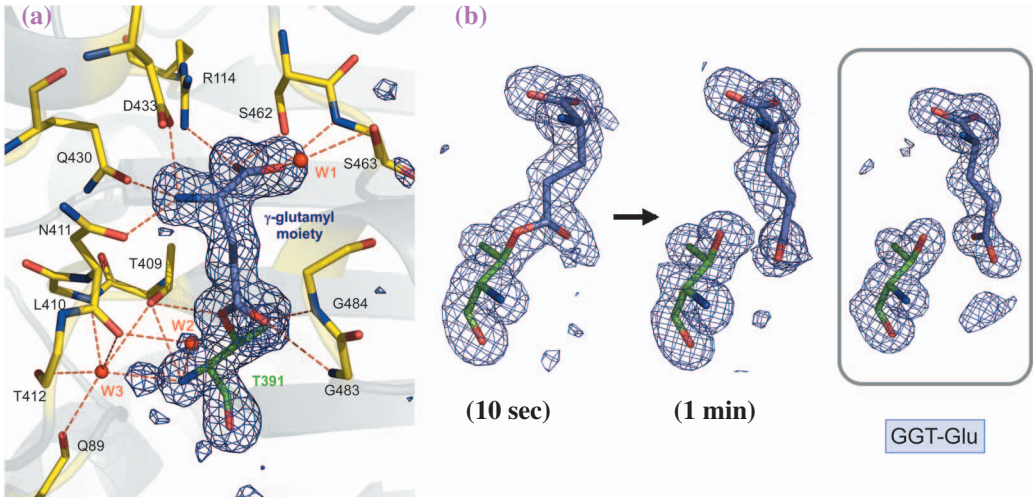

Fig. 3. **(a)** Electron densities of γ-glutamyl moiety and Thr-391 in γ-glutamyl-enzyme intermediate. Ball and stick models are overlaid on the map. **(b)** Hydrolysis of γ-glutamyl-enzyme intermediate. Stick models of γ-glutamyl moiety, L-glutamate and Thr-391 are overlaid on the electron densities. The bond between the γ-glutamyl moiety and Thr-391 in the intermediate was hydrolyzed in 1 min. The map on the right shows the structure of the GGT-Glu complex.

Keiichi Fukuyama* and Toshihiro Okada

Department of Biological Sciences, Osaka University

*E-mail: fukuyama@bio.sci.osaka-u.ac.jp

References

[1] N. Taniguchi and Y. Ikeda: Adv. Enzymol. Relat. Areas Mol. Biol. **72** (1998) 239.
[2] H. Suzuki *et al.*: J. Bacteriol. **175** (1993) 6038.
[3] H. Suzuki and H. Kumagai: J. Biol. Chem. **277** (2002) 43536.
[4] *T. Okada, H. Suzuki, K. Wada, H. Kumagai and K. Fukuyama: Proc. Natl. Acad. Sci. USA **103** (2006) 6471.*

Signaling Pathway in Two-component Regulatory System Revealed by Combination of X-ray Crystallography and Solution Scattering Technique

A sensor histidine kinase (HK) and a cognate response regulator (RR) are protein elements of a two-component regulatory system, which are ubiquitously present in prokaryotes, fungi and plants. The system is involved in cellular signal transduction for homeostasis in response to sudden changes in the environment. HK is a single peptide consisting of three domains, i.e., a sensor, a dimerization/histidine-containing phosphotransfer (DHp), and ATP-binding catalytic (CA) domains from N- to C-termini (Fig. 1). HK functionally acts as a dimer through the interaction of the DHp domain between each subunit. The sensor domain of HK senses an environmental change as an external signal, and then the conformational change induced upon signal receipt would be transmitted to either activate or inactivate the CA domain. The activated CA domain catalyzes the phosphorylation of the special His residue at the DHp domain using ATP. The phospho-group is then transferred to the special Asp in RR, and the resultant phospho-RR can act as a transcriptional factor for promoting the expression of target proteins.

Depending on external signals such as metal ions, amino acids, nitrogen compounds, light, and osmotic pressure among others, the sensor domains display a variety of structures. For example, the oxygen sensor FixL contains a heme iron as an O_2 binding site in the sensor domain, while the ethylene sensor ETR1 has a transmembrane sensor domain containing Cu as an ethylene binding site. On the other hand, the structures of the DHp and CA domains in HK and of RR are essentially the same among a variety of two-component systems. This fact implies that the interdomain or intermolecular signal transduction can be achieved using a similar mechanism. However, there has been no report on the structures of the HK/RR complex, although the structures of each separated domain have been reported for many HKs and RRs in the two-component regulatory system.

The structure of the HK/RR complex of the thermophilic bacterium *Thermotoga martina* was determined by the combination of X-ray crystallography (**BL44B2**) and solution scattering (**BL45XU**) technique [1]. The solution scattering for HK was measured with and without the sensor domain, and in the presence and absence of RR (titration experiment). A comparison of the SAXS parameters thus obtained (Table 1) showed that the sensor domain of HK is located on the molecular edge of the HK dimer giving the longest dimension, and that two molecules of RR can associate with the central portion of the HK dimer with a dissociation constant (K_d) of 8×10^{-11} M^{-2}. On the other hand, an electron density map of the HK/RR complex was obtained at 4.2 Å resolution. On the basis of structural information obtained from the SAXS analysis, the domains of each subunit of HK and RR could be unambiguously assigned, as shown in Fig. 2. To our knowledge, this is the first report on spacial arrangement in the two-component regulatory system.

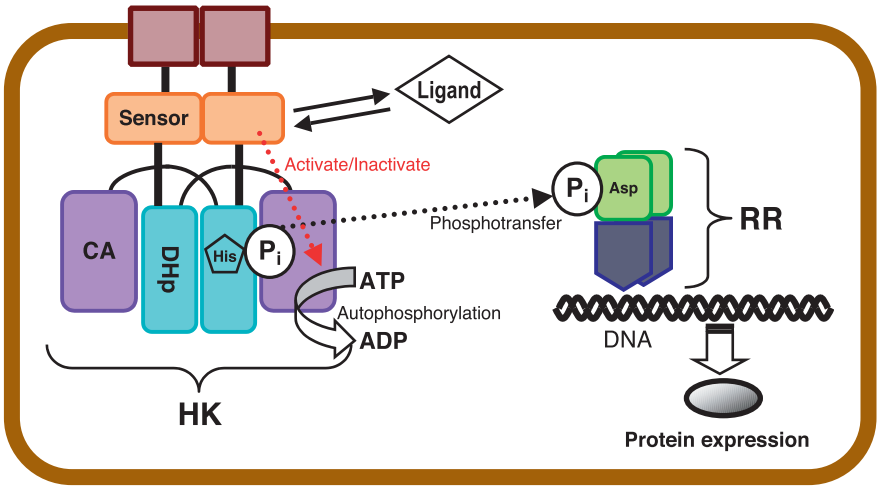

Fig. 1. Schematic drawing of two-component regulatory system.

Table 1. Structural parameters obtained from solution scattering experiments

	M_w(kDa)[(b)]	R_g(Å)[(c)]	D_{max}(Å)[(d)]	Association state
HK/RR	98 (54)	38	105	2:2 Dimer
HK	76 (41)	37	105	Dimer
ΔHK[(a)]	51 (28)	31	88	Dimer
RR	11 (13)	16	42	Monomer

(a) HK without sensor domain.
(b) Molecular mass estimated by the experiments. The values in the parentheses represent theoretical mass of the monomeric protein.
(c) Radii of gyration.
(d) Longest linear distances.

The structure of the HK/RR complex, even at a low resolution, can provide us clues to unveiling interdomain and intermolecular signal transductions in the two-component regulatory system. (i) The sensor domain of one subunit comes in contact with the CA domain of the same subunit, suggesting that the signal could directly transfer from the sensor to the CA domains in the *cis* manner. (ii) In the complex structure, the active site of the CA domain of one subunit is located about 25 Å away from the phosphorylation target His in the DHp domain of another subunit, because His imidazole can be phosphorylated in the *trans* manner. Therefore, in the course of the catalytic reaction, the CA domain would move by 25 Å to directly comes in contact with the DHp domain in the absence of RR [2]. (iii) RR interacts with the HK sensor domain as well as its DHp domain, implying that RR might affect the sensing capability of the sensor domain. These findings significantly support previous experimental results for the oxygen sensor system [3].

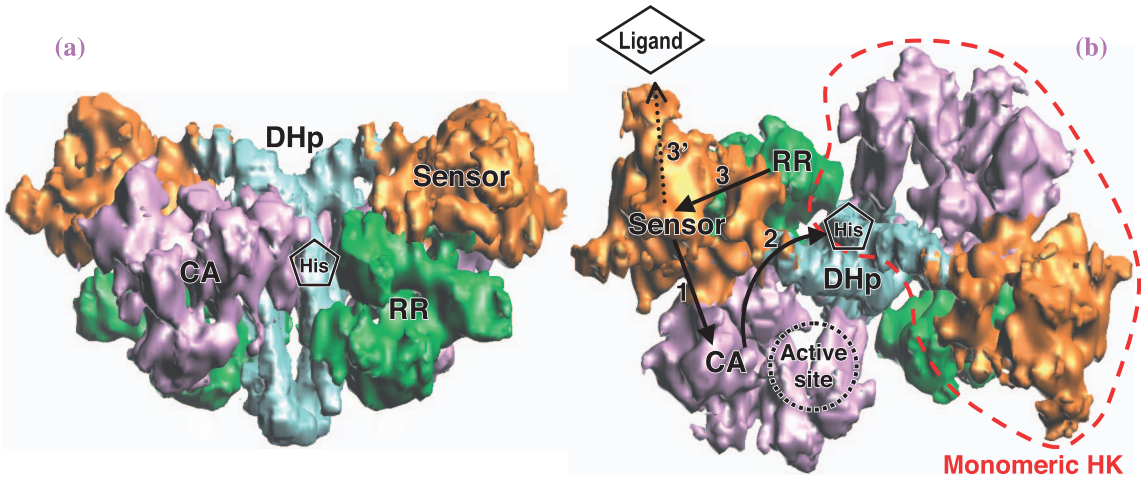

Fig. 2. Electron density map of HK/RR complex and assignment of domains. **(a)** side view and **(b)** top view along dimerization axis. The arrows indicate the pathway of the signal transduction we proposed.

Seiji Yamada, Shuji Akiyama and Yoshitsugu Shiro*

SPring-8 / RIKEN

*E-mail: yshiro@riken.jp

References

[1] *S. Yamada, S. Akiyama, H. Sugimoto, H. Kumita, K. Ito, T. Fujisawa, H. Nakamura, Y. Shiro: J. Mol. Biol.* ***362*** *(2006) 123.*
[2] A. Marina *et al.*: EMBO J. **24** (2005) 4247.
[3] H. Nakamura *et al.*: Proc. Natl. Acad. Sci. USA **101** (2004) 2742.

Quaternary-Structure Change of Fatty Acid β-Oxidation Multienzyme Complex as Revealed by Small-Angle X-ray Scattering Analysis

Fatty acid is a major molecule for biological energy storage. In energy extraction, the molecule is conjugated with coenzyme A (CoA) to form acyl-CoA, which is successively decomposed by β-oxidation (Fig. 1). This metabolic pathway is a cycle of reactions catalyzed by acyl-CoA dehydrogenase (ACD), enoyl-CoA hydratase (ECH), 3-hydroxyacyl-CoA dehydrogenase (HACD), and 3-ketoacyl-CoA thiolase (KACT). Since many organisms possess these enzymes, their reactions are essential to maintain fundamental biological activity. Interestingly, the molecular architecture of β-oxidation enzymes significantly varies among organisms, suggesting that each enzyme is highly optimized for its functional role. In eukaryotic mitochondrion, a multienzyme complex, called the fatty acid β-oxidation multienzyme (FOM) complex, processes acyl-CoA derivatives with a long acyl group. The complex, catalyzing three consecutive reactions by ECH, HACD and KACT, is composed of two polypeptide chains, namely, α and β. The α-subunit exhibits ECH and HACD activities whereas the KACT active site is located in the β-subunit. A homologous multienzyme complex is also found in some prokaryotes, such as *Escherichia coli* and *Pseudomonas fragi*. The remarkable similarity in the amino acid sequence between the mitochondrial and bacterial FOM complexes suggests that they operate using a common catalytic mechanism with a similar protein architecture.

We determined the three-dimensional structures of the FOM complex from *P. fragi* in five crystal forms, among which three forms display distinct quaternary structures [1,2]. These structures revealed that the local environments of the six active sites in the $\alpha_2\beta_2$ heterotetramer are significantly different among the three forms. Thus, quaternary-structure conversion presumably occurs in the consecutive three reactions. However, the crystal packing inevitably restricts all of the structures. To explore the structural event during the chain reaction, the conformation of the complex should be investigated in a solution. Small-angle X-ray scattering (SAXS) with synchrotron radiation is suitable for probing the overall structure of large protein complexes in a solution. Therefore, we analyzed the ligand-induced conformational change of the FOM complex from *P. fragi* by SAXS [2].

The bacterial FOM complex overproduced in *E. coli* was purified to homogeneity. The X-ray scattering intensity of the protein solution was measured with synchrotron radiation at beamline **BL40B2**. We acquired the SAXS data in three different solution conditions: the ligand-free state, the states in the presence of nicotineamideadenine dinucleotide (NAD^+; cofactor for HACD), and of 3-hydroxyhexadecanoyl-CoA (HAC; substrate for HACD).

The conventional SAXS analysis, including the Guinier analysis, indicated that these ligands could induce significant conformational change. However, all of the experimental scattering profiles remarkably deviate from those calculated with known crystal structures. Rigid-body optimization of the structure to the experimental scattering data revealed that the rearrangement of the seven domains in the complex could reasonably account for the discrepancy (Fig. 2). As a result, the structural state for each condition could be estimated (Fig. 3). In the ligand-free state, the FOM complex

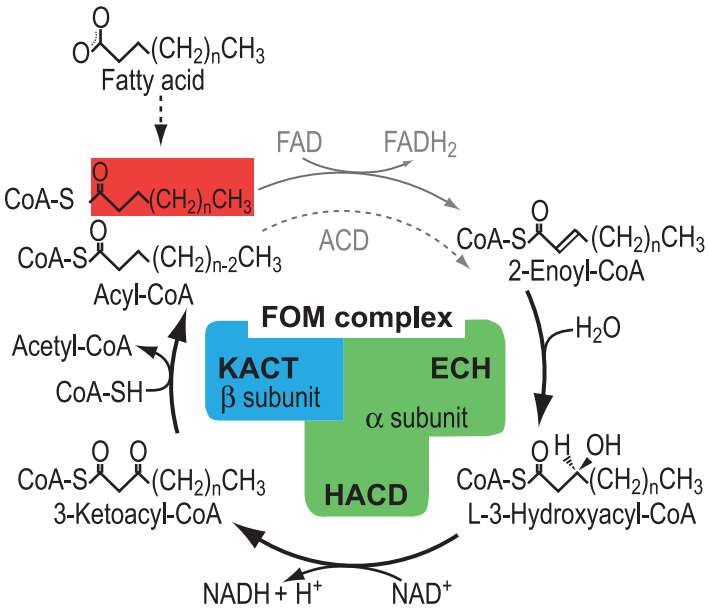

Fig. 1. Fatty acid β-oxidation cycle. The reactions catalyzed by the FOM complex are highlighted. The red box in the acyl-CoA molecule at the beginning of the cycle indicates the acyl group, which comes from the fatty acid molecule. Every cycle of the four reactions shortens the acyl group by two carbon units, which are released as acetyl-CoA.

assumes a flexible architecture, in which the position of the HACD region relative to the remaining ECH/KACT regions fluctuates in a rigid-body manner. The binding of two NAD^+ molecules induces the two-fold-symmetric structure whereas HAC occupies one of the two HACD active sites in the asymmetric heterotetramer. This contention is consistent with the previous crystallographic view that the precedent/following ECH/KACT reactions occur in the symmetric/asymmetric forms, respectively [1]. The ligand-induced conformational change is involved in mechanism of the chain reactions coupled with substrate channeling, which is important for controlling the flux of lipophilic compounds in cellular metabolism [3].

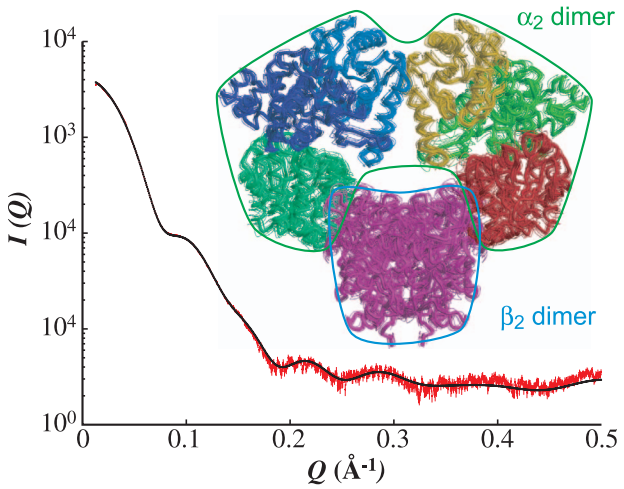

Fig. 2. Rigid-body optimization of atomic structure with experimental scattering data. Only the results for the NAD^+-bound state is shown. The graph represents the experimental scattering intensity with error bars (red). The black line indicates the scattering calculated with the mean structure (thick-tubing model) among the ten optimized structures (thin-tubing model). The structural models are colored to distinguish the seven rigid-body segments for the optimization. The α- and β-subunits are encircled with green and blue lines, respectively.

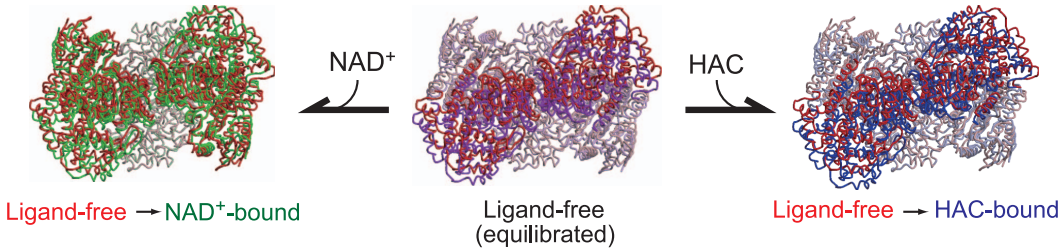

Fig. 3. Ligand-induced conformational change of FOM complex. Each structure is viewed from the top of the molecule drawn in Fig. 2. The HACD region is highlighted with the bright colors. The structures in the NAD^+-bound (green, left) and HAC-bound (blue, right) states were respectively superimposed onto the ligand-free structure (red). We presume that the ligand-free state (middle) is in a structural equilibrium, as represented by the two identical asymmetric models (red and magenta) related by the two-fold axis of the β_2 dimer.

Daisuke Tsuchiya†

Biomolecular Engineering Research Institute

E-mail: dtsuchiy@ttck.keio.ac.jp

† Present address: Institute for Advanced Biosciences, Keio University

References

[1] M. Ishikawa *et al.*: EMBO J. **23** (2004) 2745.
[2] *D. Tsuchiya, N. Shimizu, M. Ishikawa, Y. Suzuki and K. Morikawa: Structure **14** (2006) 237.*
[3] D. Tsuchiya *et al.*: "Functional and Structural Biology on the Lipo-network" (Transworld Research Network, India, 2006), 117.

Scaling Relationship in Initially Collapsed Conformation of Protein Folding

Proteins spontaneously collapse from the extended conformations of the unfolded state to the compact conformation of the native state. Polypeptide collapse is therefore an essential dynamics in protein folding; however, its molecular mechanism is largely unknown due to the scarcity of experimental data on the collapse. We have been investigating the collapse process in protein folding using time-resolved small-angle X-ray scattering (SAXS) analysis [1-3]. Our strategy is unique in that it enables the characterization of transient conformations of proteins with a lifetime shorter than a millisecond. We characterized the folding process of three proteins with different topologies. The characterized dynamics demonstrated a common folding mechanism termed the "collapse and search" mechanism, in which the initial collapse occurring within a millisecond promotes the search for the correct secondary and tertiary structures (Fig. 1). The observation that the folding of the three proteins with different topologies commonly demonstrated the initial and significant collapse suggested that the collapse is caused not by the individual properties of proteins but by the physical properties of proteins. In this research paper, we will give an explanation of the initial collapse on the basis of Flory's theory of polymers [4].

The basic theory of polymer conformations, in which the transition of polymers from an extended coil to a collapsed globule termed the coil-globule transition was developed by Flory [5]. The transition might explain the collapse of proteins; however, no clear evidence for the explanation was presented. According to Flory's theory, a polymer without short-distance interactions has radius of gyration (R_g) described by the scaling law (1):

$$R_g = a N^{\nu} \qquad (1)$$

where N is the number of monomers, a is a parameter and ν is a scaling exponent. At temperatures below the transition temperature (T_θ), the polymer is classified as a globule whose scaling exponent equals 1/3. In contrast, at temperatures above T_θ, the polymer is classified as a coil whose scaling exponent is close to 3/5. Denatured proteins in the presence of denaturants possess a scaling exponent close to 3/5, and are classified as coils. To determine whether the initially collapsed intermediates observed in protein folding are globules, the scaling relationship and the exponent for the intermediates should be examined.

To examine the scaling relationship of collapsed intermediates, it is necessary to investigate proteins with various chain lengths. Thus, we observed the folding process of heme oxygenase (HO), which is the longest protein (263 residues) ever characterized by time-resolved SAXS analysis (Fig. 2). Time-resolved SAXS analysis was performed at beamline **BL45XU**. HO demonstrated a complicated folding mechanism due to a *cis-trans* isomerization of X-proline peptide bonds and oligomer formation. By carefully conducting various double-jump experiments and examining concentration dependencies, we obtained the R_g for the initially collapsed conformation of HO. The R_g values for HO and other proteins in the initially

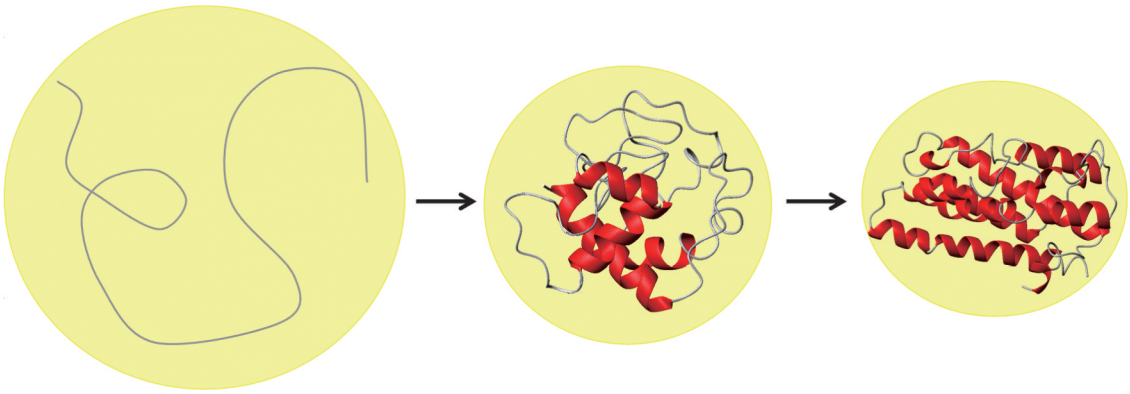

Fig. 1. Collapse and search mechanism of protein folding generally observed for proteins with more than 100 residues. The unfolded protein (left) collapses to the initial intermediate (middle) within a millisecond after initiating the protein folding reaction. The collapsed intermediate searches for the correct secondary and ternary contacts and convert to the native structure (right). The time constant for the native structure formation is in the range of milliseconds to seconds.

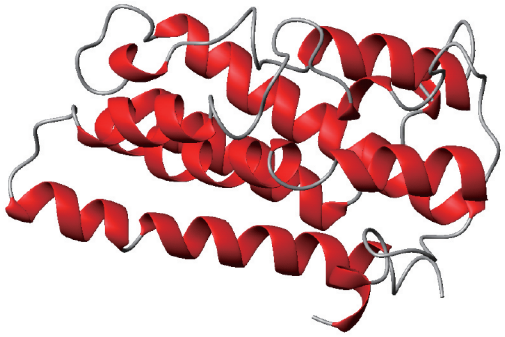

Fig. 2. Folded structure of heme oxygenase.

collapsed conformation were plotted against chain lengths in Fig. 3. The R_g values for the seven proteins are well fitted by the scaling law with $\nu = 0.35 \pm 0.11$, which is close to 1/3 of the predicted value for globules. The observation clearly suggests that the collapsed intermediates correspond to the globules explained by Flory's theory, and that the properties of proteins as polymers likely determine the initial collapse dynamics of protein folding.

The collapse and search mechanism is generally observed for proteins with more than 100 residues. Interestingly, predicting the structure of proteins that are larger than 100 residues is still extremely difficult despite the significant advances in the recent prediction methods. A better understanding of the mechanism of the collapse will give an important insight that will help improve our ability to predict protein structure. Improvements in the time-resolution and quality of SAXS data for the characterization of the chain collapse should reveal rich structural events involved in the process.

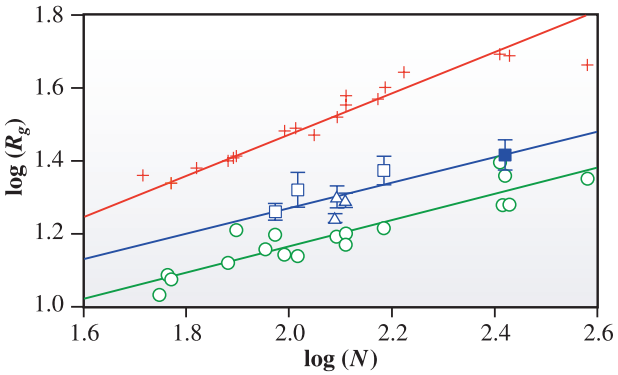

Fig. 3. Relationship between radius of gyration (R_g) and number of amino acid residue (N) for proteins in various conformational states. The blue rectangles and triangles denote the R_g values for the initially collapsed conformation. The filled blue square is the data of HO obtained in this study. The red crosses and green circles are the R_g data of the unfolded and native proteins, respectively.

Satoshi Takahashi[a,b,*] and Tetsuro Fujisawa[c]

[a] Institute for Protein Research, Osaka University
[b] CREST, JST
[c] SPring-8 / RIKEN

*E-mail: st@protein.osaka-u.ac.jp

References

[1] S. Akiyama *et al.*: Proc. Natl. Acad. Sci. USA **99** (2002) 1329.
[2] T. Uzawa *et al.*: Proc. Natl. Acad. Sci. USA **101** (2004) 1171.
[3] T. Kimura *et al.*: Proc. Natl. Acad. Sci. USA **102** (2005) 2748.
[4] *T. Uzawa, T. Kimura, K. Ishimori, I. Morishima, T. Matsui, M. Ikeda-Saito, S. Takahashi, S. Akiyama and T. Fujisawa: J. Mol. Biol. **357** (2006) 997.*
[5] P.J. Flory, Principles of Polymer Chemistry, Cornel University Press, Ithaca, NY (1953).

Microbeam X-ray Diffraction Study on Insulin Spherulites

Insulin is a hormone with a molecular weight of 5.7 kDa, that is composed of two polypeptide chains. In the native state, its secondary structure is primarily α-helical. However, forms a spherical precipitate called spherulite (Fig. 1), which is made of β-amyloid fibrils (Fig. 2), at low pHs and high temperatures (pH 2.0 and 37 - 100 °C). No chemical modification is involved in the assembly of insulin to form spherulite, and insulin retains its three disulfide bridges (two between chains and one within one chain) in spherulite. Amyloids are self-aggregates of insoluble, fibrillar assemblies of protein molecules. Amyloids can be harmful to organisms, causing pathologies such as Alzheimer's disease, Parkinson's disease, Huntington's disease, type II diabetes, and prion diseases. Several nonpathological proteins such as insulin, lysozyme and short peptides self-assemble into amyloid-like fibrils, suggesting that amyloid formation is an inherent property of polypeptide chains. Denatured proteins in amyloid fibers commonly take a cross-β structure even when their native form is α-helical [1].

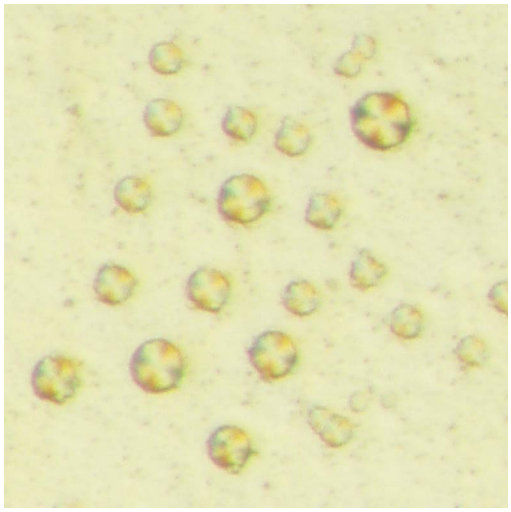

Fig. 1. Bovine insulin spherulites under a polarizing microscope. The diameter of the largest spherulite is about 100 μm.

Although amyloid fibers of various proteins have been studied by X-ray diffraction analysis, the specimens were prepared by orienting fibers by drying and stretching. Thus, the native fully hydrated structure of amyloid fibers has been unknown. We made use of spherulite in which amyloid fibers are naturally oriented. Although each spherulite is only 50-100 μm in diameter, it is possible to investigate regions parts in which fibers are mostly oriented in same direction [2].

The experiment was carried out at beamline **BL40XU** with a 5-μm pinhole. The X-ray energy was 15.0 keV. The X-ray detector was an X-ray image intensifier (V5445P, Hamamatsu Photonics) with a cooled CCD camera (ORCA-II-ER, Hamamatsu Photonics). Small-, medium- and wide-angle diffraction patterns were recorded at different specimen-to-detector distances. Each spherulite was scanned two-dimensionally with 5~20-μm steps.

The small-angle diffraction pattern (Fig. 3) showed a broad oriented peak at a Bragg spacing of 23 nm in the equatorial direction (that is, at right angles to the fibers), which probably corresponds to the distance between the amyloid fibers in spherulite. Since this spacing was constant across the spherulite, the fiber density seems uniform. This supports a model with branching amyloid fibers (Fig. 2, right).

The medium-angle pattern showed broad maxima at Bragg spacings of 3.3 and 1.2 nm. These peaks correspond to the internal structure of an amyloid fiber. A previous electron microscopic study [3] showed that each fiber is composed of about four protofilaments. A helix made of a square arrangement of four cylinders, with a diameter of 2.4 nm and a helical radius of 2.0 nm, can account for the 3.3-nm peak. The 1.2-nm peak probably corresponds to the distance between β-sheets in each protofilament (see below).

The wide-angle pattern showed a meridional (that is, along the fiber axis) arc at a Bragg spacing of 0.48 nm (Fig. 4). This is a peak corresponding to β-sheets that is commonly observed in amyloid fibers, which shows that the hydrogen bonds of the β-sheets are aligned along the axis of the amyloid fibers. No other meridional reflection was observed.

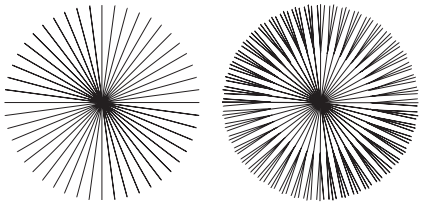

Fig. 2. Arrangement of amyloid fibers in spherulite. The image on the left shows a model without fiber branching, and the image on the right shows a model with fiber branching. Amyloid fibers grow isotropically in three-dimensions from a core whose structure is unknown.

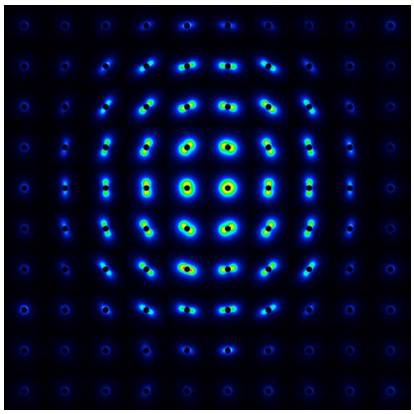

Fig. 3. Galley of small-angle diffraction patterns from an insulin spherulite. A spherulite, located at the center, was scanned with a microbeam with 10-μm steps. Diffraction patterns obtained at each spot were arranged to make this galley. Strong scattering is observed at right angles to the fiber axis. At the center, end-on diffraction from fibers is observed, which is isotropic.

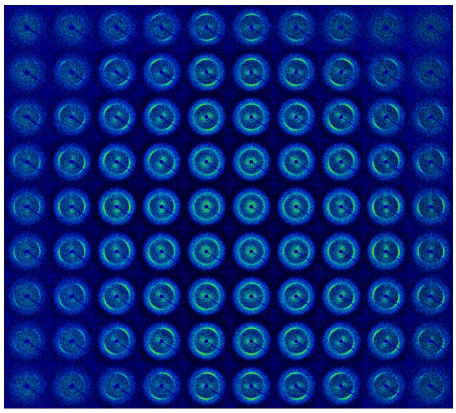

Fig. 4. Galley of wide-angle diffraction patterns from an insulin spherulite. At the peripheries of the spherulite, meridional arcs are observed parallel to the fiber axis.

On the basis of these diffraction patterns and a model of the Aβ peptide of Alzheimer's disease [4], a model of an insulin molecule in the amyloid fiber is proposed (Fig. 5). In this model, the two chains of insulin are aligned side-by-side in a plane perpendicular to the fiber axis. Hydrogen bonds are formed between molecules in neighboring planes making two β-sheets along the fiber axis. The axial separation distance between molecules is 4.8 nm, and the distance between two chains of each molecule within the plane is about 1.2 nm. Since the disulfide bond imposes a strong constraint on the structure, the arrangement of the side chains is mostly deduced.

This is the first study in which an amyloid fiber was investigated in a fully hydrated state. Microbeam X-ray diffraction analysis has advantages over diffraction experiments on dry stretched fiber in that not only can the fibrils be studied in the native state but also the results are not influenced by contaminating materials or other types of aggregate. The structure revealed using this technique will give new insight into amyloid fiber formation and help us understand the mechanism of amyloidosis.

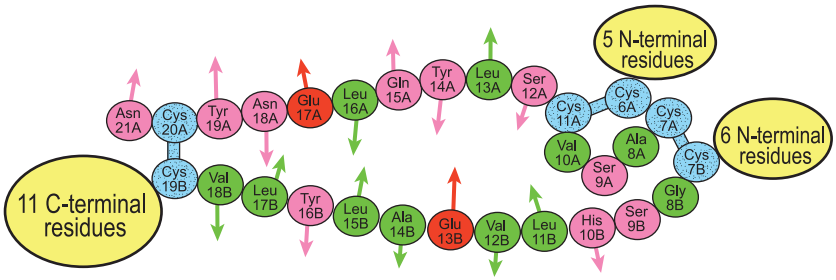

Fig. 5. Structural model of insulin molecule in amyloid fiber. The fiber axis is perpendicular to this drawing. Bovine insulin consists of two chains, namely, A with 21 residues (above) and B with 30 residues (below). There are three disulfide bonds, one within the A chain and two between the chains. The molecule lies in a plane perpendicular to the fiber axis. A portion of the A chain (residues from 12 to 29) and a portion of the B chain (from residues 10 to 18) are connected to the molecules in the planes above and below with hydrogen bonds between the main chains, forming two β-sheets. The arrows indicate the direction of the side chains.

Naoto Yagi

SPring-8 / JASRI

E-mail: yagi@spring8.or.jp

References

[1] M.R.H. Krebs *et al.*: Proc. Natl. Acad. Sci. USA **101** (2004) 14420.
[2] *N. Yagi, N. Ohta, T. Iida and K. Inoue: J. Mol. Biol.* ***362*** *(2006) 327.*
[3] J.L. Jiménez *et al.*: Proc. Natl. Acad. Sci. USA **99** (2002) 9196.
[4] N.-V. Buchete *et al.*: J. Mol. Biol. **353** (2005) 804.

Research Activities from Individual Analysis Program of the National Project on Protein Structural and Functional Analyses (Protein 3000 Project)

A structural genomics project in Japan, the National Project on Protein Structural and Functional Analyses (Protein 3000 Project) funded by MEXT (Ministry of Education, Culture, Sports, Science and Technology, Japan) was established in the fiscal year 2002 and completed in March 2007. This project was comprised of two separate programs. One is focusing on the comprehensive analysis of the fundamental structures of proteins where RSGI (RIKEN Structural Genomics/Proteomics Initiative) takes a leading part. Another program called the "Individual analysis program" involves individual analysis efforts mainly performed by the members of the Japanese university community. In both programs, the structural biology beamlines of the synchrotron radiation facilities played an important role in determining the three-dimensional structures of the target proteins by means of X-ray crystallography. In this report, research activities obtained from the individual analysis program of this project by the use of SPring-8 beamlines are briefly summarized.

The aim of the individual analysis program by the university community is to study both structures and functions of proteins in a selected target field of biological systems. In the individual analysis program, a target of determining more than 500 three-dimensional structures of proteins and their complexes was set as an initial plan. For seven targeting research fields, eight consortiums mainly composed of the university community members were established as presented below:

1) "Development and Differentiation of Organisms and Replication and Repair of DNA" directed by Prof. Masaru Tanokura, the University of Tokyo
2) "Transcription and Translation (Part I)" directed by Prof. Isao Tanaka, Hokkaido University
3) "Transcription and Translation (Part II)" directed by Prof. Yoshifumi Nishimura, Yokohama City University
4) "Posttranslational Modification and Transport"

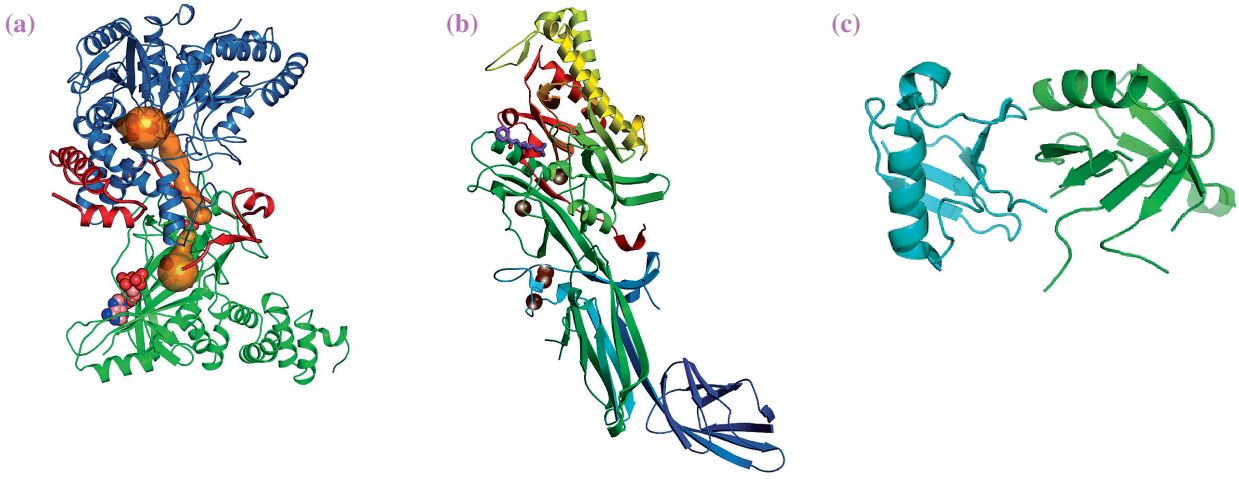

Fig. 1. **(a)** GatCAB (PDB ID: 2F2A) [1]. GatCAB converts Glu-tRNA^{Gln} into Gln-tRNA^{Gln}. In this reaction, initially Glu-tRNA^{Gln} is activated using ATP in GatB (green), and subsequently activated Glu-tRNA^{Gln} is transamidated into Gln-tRNA^{Gln} using ammonia generated by hydrolysis of glutamine in GatA (blue). Two identified reaction centers in GatA and GatB are markedly distant but connected by a long channel (orange), which transfers generated ammonia from GatA to GatB.
(b) Peptidylarginine deiminase 4 (PDB ID: 1WDA) [2]. Peptidylarginine deiminase 4 (PAD4) is a post-translational coregulator that catalyzes the calcium-dependent conversion of specific arginine residues in histone to citrulline. Significant association between rheumatoid arthritis (RA) and functional variants of the gene encoding PAD4 in the Japanese population indicates that human PAD4 is associated with RA and PAD4 inactivators represent potential lead compounds for the treatment of RA.
(c) GLUE-domain of murine EAP45 (PDB ID: 2DX5) [3]. ESCRT-II, a complex that sorts ubiquitinated membrane proteins to lysosomes, localizes to endosomes through interaction between the Eap45 subunit's GLUE domain and phosphatidylinositides. The structure of GLUE domain of mammalian Eap45 complexed with ubiquitin showed that they interact directly, while the corresponding domain of yeast homologue, Vps36, interacts with ubiquitin through inserted Zn-finger.

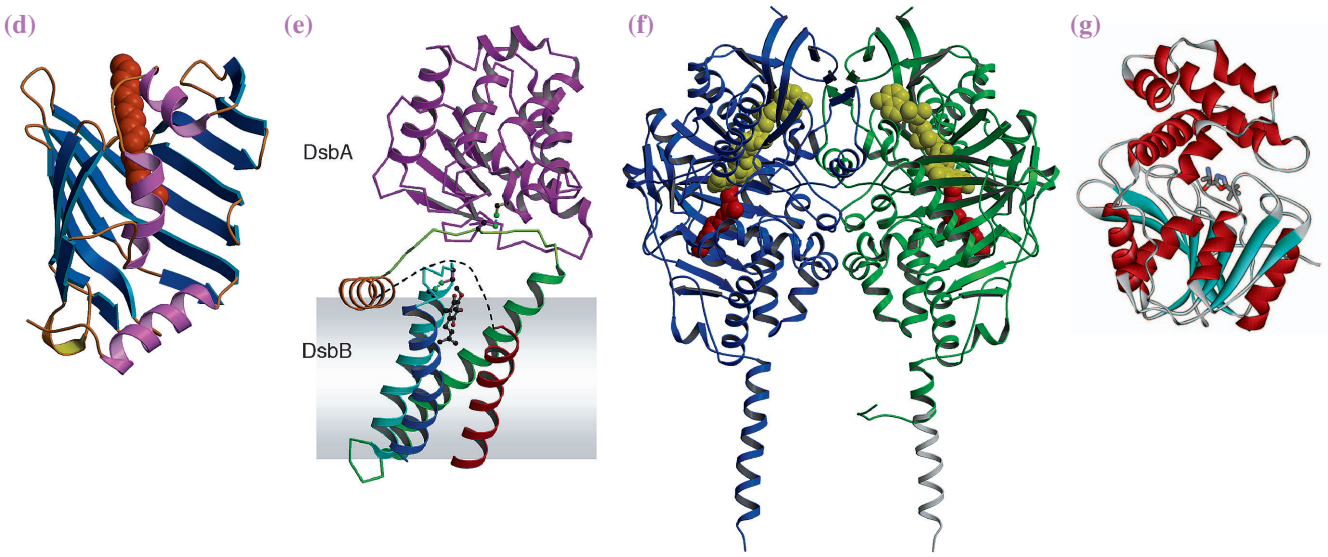

(d) LolB (PDB ID: 1IWN) [4]. The Lol system in Gram negative bacteria exports insoluble outer membrane lipoproteins across the periplasm. LolB is a lipoprotein receptor on the outer membrane. The structure of LolB comprises an antiparallel β-sheet covered by three α-helices. PEGMME used for crystallization is observed in the internal cavity, which might show a plausible binding mode of the lipid moiety of the lipoprotein.
(e) DsbB-DsbA complex (PDB ID: 2HI7) [5]. DsbB generates a disulfide bond in conjunction with ubiquinone, to be relayed by DsbA to client proteins. The crystal structure of a DsbB-DsbA complex reveals the ubiquinone-DsbB reaction center as well as a cysteine relocation mechanism that allows DsbB to oxidize the extremely oxidizing DsbA enzyme.
(f) Monoamine oxidase A (PDB ID: 1O5W) [6]. Monoamine oxidase (MAO), a mitochondrial outer membrane enzyme, catalyzes the degradation of neurotransmitters in the central nervous system and is the target for anti-depression drug design.
(g) Prolyl aminopeptidase (PDB ID: 1X2E) [7]. Prolyl aminopeptidase from *Serratia marcescens* is a pathogenic enzyme causing the collagen degradation of the human skin. The structure predicted the extra space in the active site that can accommodate the acetyloxyproline moiety of collagen. High reactivity toward acetyloxyproline substrate suggested the necessity of acetylation step for efficient degradation of collagen.

directed by Prof. Soichi Wakatsuki, Institute of Materials Structure Science, KEK
5) "Protein Higher-Order Structure Formation" directed by Prof. Kunio Miki, Kyoto University
6) "Intracellular Signal Transduction" directed by Prof. Fuyuhiko Inagaki, Hokkaido University
7) "Brain and Nervous System" directed by Prof. Atsushi Nakagawa, Osaka University
8) "Metabolic Systems" directed by Prof. Seiki Kuramitsu, Osaka University

In the individual analysis program for five years of the project, a total of more than 1,800 protein structures were determined (more than 1,300 structures were deposited with the Protein Data Bank, PDB) by both X-ray crystallography and NMR. The structural biology beamlines of SPring-8 were extensively used by the members of eight consortiums of the individual analysis program. For this purpose, some part of beamtimes is preferentially assigned in the public beamlines such as **BL41XU**, **BL40B2**, and **BL38B1**. Consequently, numbers of crystal structures of the target proteins were determined in this program. Several examples of the protein structures determined by X-ray crystallography using the SPring-8 beamlines are summarized in the Fig. 1(a-g).

Kunio Miki

Graduate School of Science, Kyoto University

E-mail: miki@kuchem.kyoto-u.ac.jp

References

[1] A. Nakamura *et al.*: Science **312** (2006) 1954.
[2] K. Arita *et al.*: Nat. Struct. Mol. Biol. **11** (2004) 777.
[3] S Hirano *et al.*: Nat. Struct. Mol. Biol. **13** (2006) 1031.
[4] K. Takeda *et al.*: EMBO J. **22** (2003) 3199.
[5] K. Inaba *et al.*: Cell **127** (2006) 789.
[6] J. Ma *et al.*: J. Mol. Biol. **338** (2004) 103.
[7] Y. Nakajima *et al.*: J. Bacteriol. **188** (2006) 1599.

Research Activities of the Comprehensive Analysis Program in the National Project on Protein Structural and Functional Analyses (Protein 3000 Project)

RIKEN Structural Genomics/Proteomics Initiative (RSGI) has been serving as a core group to pursue Japan's national project, "the Protein 3000 Project," under the supervision of the MEXT. The comprehensive analysis program, a part of the project, was founded to solve 2,500 important protein structures from bacteria, archaea, and higher eukaryotes. Construction of state-of-the-art facilities, such as high-throughput beamlines at the SPring-8 (Harima) and the large-scale NMR facility (Yokohama), in conjunction with technical developments such as automated and efficient protein production techniques, synergistically facilitates the evolution of structural proteomics.

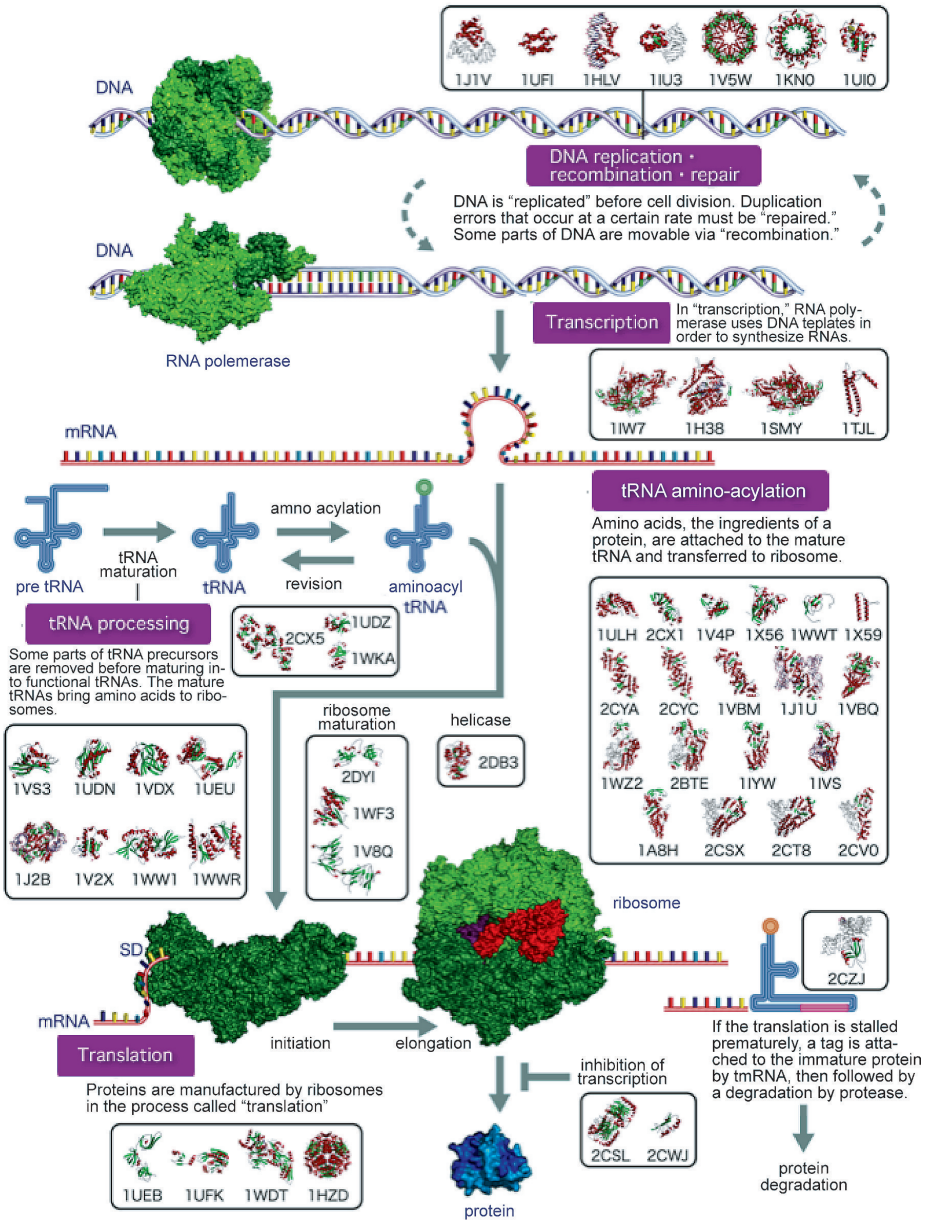

Fig. 1. Comprehensive structural analyses of the DNA replication/repair, transcription, and translation systems. Almost all structures are determined by X-ray crystallography.

Progress Report	Proteins
(1) Plasmids for overexpression	2059
(2) Overproduction in *E. coli*	1450
(3) Purification	944
(4) Crystallization	682
(5) Data collection	460
(6) 3D structure	360
360 + (106) =	466

Fig. 2. Progress of the *Thermus thermophilus* whole-cell project, and the examples of the crystal structures. (data provided by Dr. Seiki Kuramitsu)

For such large-scale structural/functional protein studies, efficient, high-throughput protein production is essential. Flexible and automated protein preparation protocols have been adopted. Proteins that cannot be produced by conventional methods are earmarked for large-scale production by alternative methods. In RSGI, therefore, both cell-based and cell-free systems are adopted. Generally, the structures of large proteins (above 20 kDa) are determined by X-ray crystallography using SPring-8 synchrotron radiation, whereas those of the smaller proteins (below 20 kDa) are determined by NMR spectroscopy using the NMR facility. When NMR spectroscopy or X-ray crystallography alone is not sufficient for the satisfactory structure determination, the two methods can be combined.

RSGI has put enormous effort on the automation and refinement of the system. This innovation have decreased the amount of manual labor, eliminated human error, improved data accuracy and maximized the efficiency and output of each experiment. We now can determine more than 800 protein structures per year. In this 5-year project, we successfully determined 1,333 X-ray structures and 1,342 NMR structures (total 2,675).

Our future challenge would be the technological development so that we can determine more medically-valuable proteins, membrane-spanning proteins, and macromolecular complexes.

Computer-based approaches, such as homology modeling and *in silico* screening, complement experimental approaches. These computer-based approaches are useful tools for the investigation of inter-molecular interactions, and molecular networks (ex. transcription, translation, signaling etc.). The marriage between experimental and computational approaches maximizes our capacity and makes us best prepared for the drug development efforts, for example, against emerging and reemerging infectious diseases. For future research for the drug development, 1-Petaflops computer specialized for molecular dynamics (MDGRAPE-3) has been developed.

Our research system and results will provide a good basis for various areas of life science researches.

Shigeyuki Yokoyama[a,b,c]

[a] Protein Research Group, Genomic Sciences Center, Yokoyama Institute, RIKEN
[b] SPring-8 / RIKEN
[c] Graduate School of Science, The University of Tokyo

E-mail: yokoyama@riken.jp

LIFE SCIENCE
MEDICAL BIOLOGY

This volume of SPring-8 Research Frontiers contains three contributions from different medical fields, which all involves new approaches for advancing medical biology.

The study carried out by Hatta was aimed at clarifying the nature of the lipids in the stratum corneum of the skin. This thin top layer of skin is important in that it not only provides protection to our bodies against various undesirable substances in the environment but also provides a barrier that prevents the evaporation of water. Failures in the protection/barrier mechanism immediately lead to skin diseases and infections. The protection mechanism is also relevant to transdermal drug delivery, which is thought to be an ideal method of drug administration in humans. These functions of the stratum corneum are mainly supported by lipid layers between elongated corneocyte cells. Two parameters characterize the structure of lipid layers: one is the periodicity of the stacking of layers, and the other the lateral packing of lipid chains in the plane of a lipid layer. In the mammalian stratum corneum, two types of lipid with different stacking (lamellar) periodicities have been identified. Moreover, two types of lateral packing, namely, hexagonal and orthorhombic, have been identified at room temperature. However, the correlation between these two parameters was not clear. Hatta and his colleagues used X-ray diffraction and recorded small- and wide-angle data simultaneously. By changing the temperature and making a two-dimensional map of the diffraction data versus temperature, they identified correspondence between the two parameters, that is, a long lamellar periodicity with hexagonal packing and a short periodicity with orthorhombic packing.

Matsumoto's study visualized a network of blood vessels in cortical bone. Adequate blood flow is indispensable to maintain healthy bone. High-resolution X-ray tomography technique was employed to obtain the three-dimensional structure of the network. By making use of the monochromatic nature of X-rays at SPring-8, a quantitative measurement of hydroxyapatite density was possible. The effects of disuse on cortical bone was also studied, and a regression of the vascular network was found.

Torikoshi and his colleagues designed an X-ray collimator for MRT (microbeam radiation therapy) experiments. MRT is a new concept in radiation therapy. It uses finely collimated planar beams which were hypothesized to be just as effective as uniform beams for destroying tumor cells but not as damaging to normal cells. In order to test this hypothesis in experiments on animals and cultured cells, it is necessary to make a collimator for high-energy X-rays (above 100 keV) with tens of slits with a width of 25 microns. Torikoshi *et al.* designed a collimator that was made of alternative stacks of tungsten and polymer sheets. It was manufactured by a company that specializes in making grids commonly used in radiography at hospitals. As a result, it is now possible to conduct studies on MRT at SPring-8, and other groups are also using this collimator.

These three studies are all very different in terms of their techniques and the applications in medical fields, showing the diversity and wide range of medical applications studied at SPring-8.

Naoto Yagi

Hydrophobic and Hydrophilic Domains in Outermost Layer of Skin that Play Important Role in Barrier Function

The outermost layer of skin, stratum corneum (SC), is composed of corneocytes and an intercellular lipid matrix (see Fig. 1). The matrix acts as both the main barrier and as a pathway for substances such as water and drugs to across SC. In mammalian SC, the longitudinal arrangement of lipid molecules, consisting of long and short lamellar structures with repeat distances of about 13 nm and 6 nm, respectively, has been observed by small-angle X-ray diffraction (SAXD) analysis (see Fig. 1). On the other hand, in the lateral arrangement of the lipid molecules, hexagonal and orthorhombic hydrocarbon-chain packings have been observed by wide-angle X-ray diffraction (WAXD) analysis (see Fig. 1). However, the correlation between lamellar structure (long or short) and lateral arrangement (hexagonal or orthorhombic packing) has been unknown. On the basis of results of simultaneous SAXD and WAXD analyses of SC [1], we are now able to show that the long lamellar structure is formed by low-temperature hexagonal hydrocarbon-chain packing and that the short lamellar structure is formed by orthorhombic hydrocarbon-chain packing, as shown in Fig. 1.

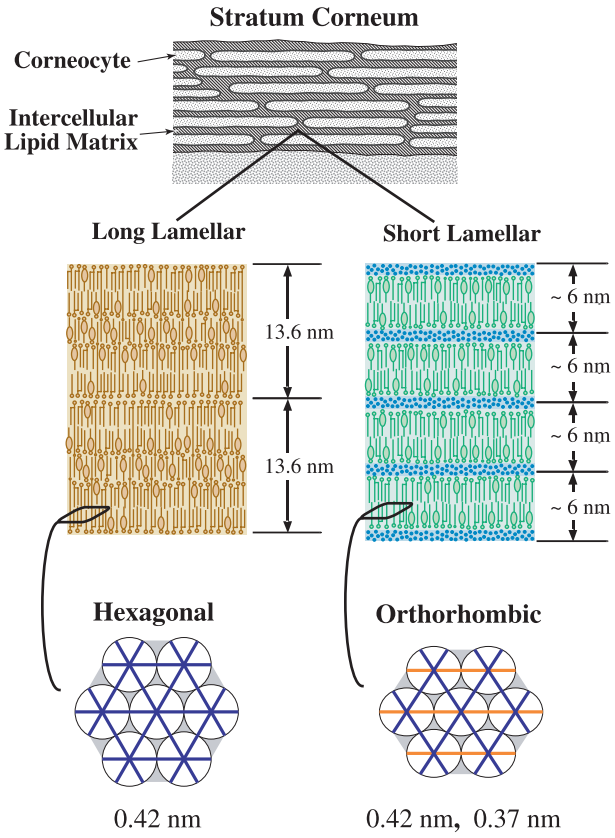

Fig. 1. The top illustration indicates a schematic model of the stratum corneum. The middle illustrations indicate molecular arrangements in the long and short lamellar structures composed of ceramides, fatty acids, cholesterol and water (blue dots represent water molecules). The bottom illustrations indicate the corresponding hydrocarbon-chain packings, that is, the low-temperature hexagonal and orthorhombic hydrocarbon-chain packings.

There were two problems encountered when drawing the above conclusion:

1) At room temperature, in various mammalian SCs there are two states: (i) hexagonal hydrocarbon-chain packing with a lattice constant of 0.42 nm, (ii) orthorhombic hydrocarbon-chain packing with lattice constants of 0.42 nm and 0.37 nm. Because a lattice constant of 0.42 nm is coincidentally common to hexagonal and orthorhombic hydrocarbon-chain packings, the superimposition of the diffraction peaks of WAXD makes detailed data analysis difficult. At present, we only have evidence that when the temperature of SC rises, the orthorhombic state transforms to the high-temperature hexagonal state at 39°C; however, the transition temperature from the low-temperature hexagonal state to a high-temperature state is unknown.
2) Generally, one lamellar structure must be composed of one hydrocarbon chain packing. Thus, it is necessary to clarify whether the lateral packing of the lipid molecules in the long lamellar structure is low-temperature hexagonal or orthorhombic.

To solve the above problems we determined the temperature dependence of SAXD and WAXD in SC [1]. The experiments were carried out at beamline **BL40B2**. All the experiments were performed in a heating scan at a rate of 0.5 K min^{-1}. To elucidate the correlation between lamellar structure and lateral packing, analysis of hairless mouse SCs was performed with special attention given to the structural changes at phase transitions. Data from the SAXD and WAXD analyses of the SCs are plotted against temperature in Figs. 2(a) and 2(b). From results of highly sensitive differential scanning calorimetry (DSC) [2], the transition temperatures of the intercellular lipid matrix in the hairless mouse SCs were 32°C, 39°C, 51°C, 56°C, and 71°C, which are indicated by horizontal lines in Figs. 2(a) and 2(b).

As seen in Fig. 2(b) below 20°C, a narrow ridge at 0.446 nm (S = 2.24 nm^{-1}) appears in the intensity contour; near 32°C, it becomes a broad ridge spread over S = 2.15-2.34 nm^{-1} (note the kinks that appear in the intensity contours). From results of DSC [2], it we found that at 32°C, a phase transition from the low-temperature hexagonal state to the liquid-crystalline state takes place. On the basis of the present results, we propose that (i) the narrow ridge below 32°C, which is a precursor of the broad liquid-crystalline-like ridge, is due to cluster formation in the low-temperature hexagonal state and that (ii) at 32°C, the low-temperature hexagonal state completely transforms into the liquid-crystalline-like state and finally becomes a broad peak near 0.46 nm (S = 2.18 nm^{-1}) for the liquid-crystalline phase near 71°C (see the thick and dotted curve C in Fig. 2(b)).

By comparing the results obtained from simultaneous SAXD and WAXD analyses (in Figs. 2(a) and 2(b)), both the thick curve B, which is a trace of the diffraction peak for the short lamellar structure, and the thick curve D, which is a trace of the diffraction peak for high-temperature hexagonal hydrocarbon-chain packing resulting from orthorhombic hydrocarbon-chain packing, occur in the same temperature range from 51°C to 71°C. On the other hand, the thick curve A, which is a trace of the diffraction peak for the long lamellar structure, corresponds to the thick and dotted curve C, which is a trace of the diffraction peak for liquid-crystalline-like hydrocarbon-chain packing resulting from low-temperature hexagonal hydrocarbon-chain packing, because both curves appear in the same temperature range from 32°C to 56°C. Therefore, we propose two domains in SC, one of which is composed of long lamellar structure, which are hydrophobic in nature [3], with low-temperature hexagonal hydrocarbon-chain packing, and the other is composed of short lamellar structure, which are hydrophilic in nature [3], with orthorhombic hydrocarbon-chain packing.

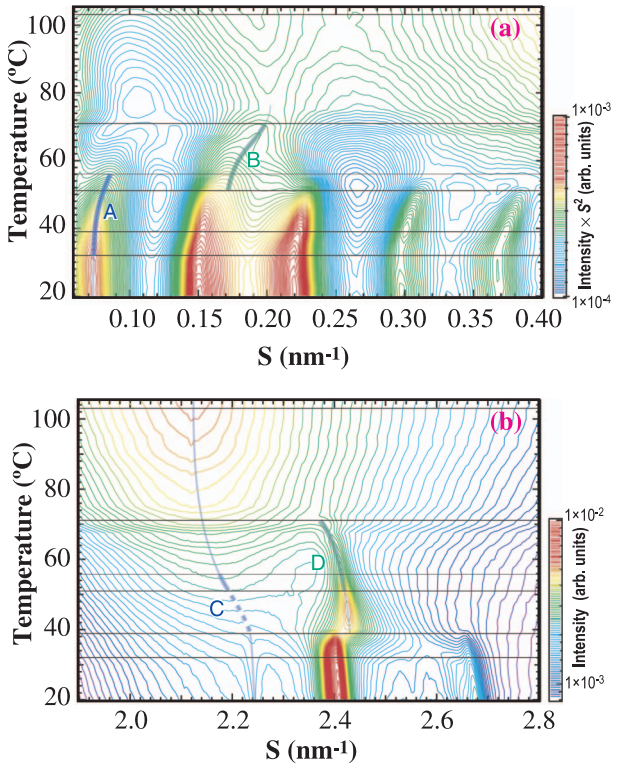

Fig. 2. Results of simultaneous SAXD and WAXD analyses of hairless mouse SCs as a function of temperature. **(a)** Intensity contour of SAXD analysis. **(b)** The intensity contour of WAXD analysis. In **(a)** and **(b)**, the reciprocal spacing is expressed by $S = (2/\lambda)\sin\theta$, where λ is the wavelength of the X-ray beam and 2θ is the scattering angle. High-to-low intensity is shown by a red-to-violet scale.

Ichiro Hatta*, Noboru Ohta and Naoto Yagi

SPring-8 / JASRI

*E-mail: hatta@spring8.or.jp

References

[1] *I. Hatta, N. Ohta, K. Inoue and N. Yagi: Biochim. Biophys. Acta* ***1758*** *(2006) 1830.*
[2] I. Hatta *et al.*: Thermochim. Acta **431** (2005) 94.
[3] N. Ohta *et al.*: Chem. Phys. Lipids **123** (2003) 1.

Fine Structure of Porous Canal Network in Cortical Bone

Blood flow is axiomatically the basis of bone growth, remodeling, and repair because it supplies oxygen, minerals, humoral regulatory factors, bone cell precursors, and other materials requisite for bone integrity [1,2]. In cortical bone, microvessels run through a network of porous canals. Therefore, we can estimate the state of cortical bone perfusion on the basis of the state of the canal network structure. However, despite its importance in bone biology, there have been only a few studies on the canal network structure owing to methodological difficulties. Recently, X-ray CT based on synchrotron radiation (SRCT) has created new opportunities for the 3D analysis of cortical bone microstructures [3,4]. Using monochromatic X-rays with an extremely high intensity enables the removal of beam-hardening artifacts and quantitative imaging with a high signal-to-noise ratio [5], which are beneficial in determining the metric properties of cortical canals such as diameters and volumes.

Figure 1 shows a 2D image of a cortical transverse section in a tibial segment harvested from a 14-week-old male Wistar rat (left) and the section's linear absorption coefficient distribution (right). The image was obtained using 20-keV X-rays and the CT system at beamline **BL20B2**. Reconstruction was carried out using a 2D filtered backward projection algorithm based on radiographic images acquired over an angular range of 0°-180° with 0.5° steps, providing contiguous images composed of 1000 × 1000, 5.83-μm pixels. The use of monochromatic X-rays accurately provided the differentiated peak of the linear absorption coefficient corresponding to pure bone, allowing simple thresholding for the bone segmentation. Laboratory CT lacks this advantage because it uses polychromatic X-rays.

The threshold value was determined to be 5.3 cm^{-1} by comparing binarized SRCT images and the light micrographs of the nondecalcified sliced sample showing the same transverse section. Assuming that the bone X-ray absorption is described as a two-phase mixture (hydroxyapatite and light elements), a linear relationship holds between the linear absorption coefficient (μ_{bone}) and hydroxyapatite density (ρ_{HAp}). To confirm this relationship, a dipotassium hydrogen phosphate (K_2HPO_4) water solution was used as a substitute for hydroxyapatite. The linear regression of the linear absorption coefficient and the concentration of the K_2HPO_4 water solution obtained using 20-keV X-rays provided $\mu_{bone} = 5.45 \cdot \rho_{HAp} + 0.81$ ($r^2 > 0.999$), showing that a threshold value of 5.3 cm^{-1} is equivalent to a hydroxyapatite density of 0.82 g/cm^3.

Disuse or immobilization induces bone atrophy. However, its effect on the canal network structure in cortical bone is poorly understood. In Fig. 2, the volume-rendered 3D display of a pair of tibial diaphyses and close-up views of the boxed regions are shown. These tibiae were harvested from a 14-week-old rat treated by unilateral sciatic neurectomy of the left hindlimbs. Neurectomy-induced disuse leads to canal network regression as well as bone atrophy. The indexes characterizing the canal

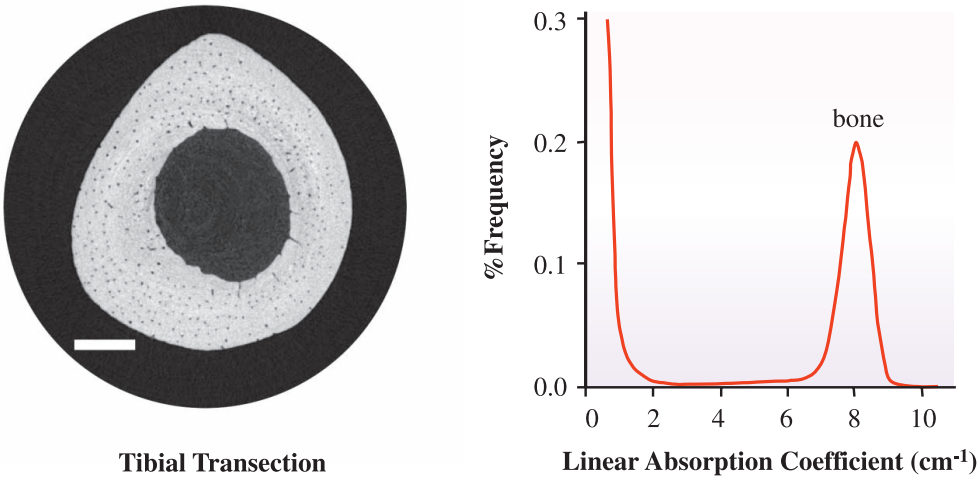

Fig. 1. Reconstructed 2D image of tibial cortical transverse section of rat hindlimb (left) and such section's relative linear absorption coefficient distribution (right). Bar: 200 μm.

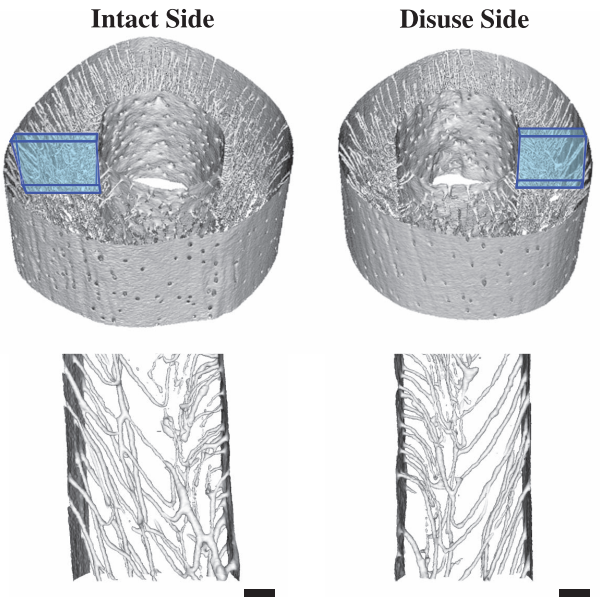

Fig. 2. Image of pair of tibial diaphyses harvested from a rat subjected to unilateral sciatic neurectomy, generated by 3D isosurface rendering of reconstructed 2D images. The boxed regions are enlarged below. Bar: 150 μm. The bone mineral density on the isosurface is 0.82 g/cm^3.

network structure are shown in Fig. 3, indicating that disuse bone atrophy is accompanied by cortical canals, which are decreased in cross-section, sparsely distributed and connected in a tree-like manner. Considering that canals possibly contain capillary vessels structure, this canal network regression could be translated as the regression of the vascular network, leading to a lower perfusion rate, higher flow heterogeneity, and a smaller surface area for oxygen and nutrients needed by cortical bone cells.

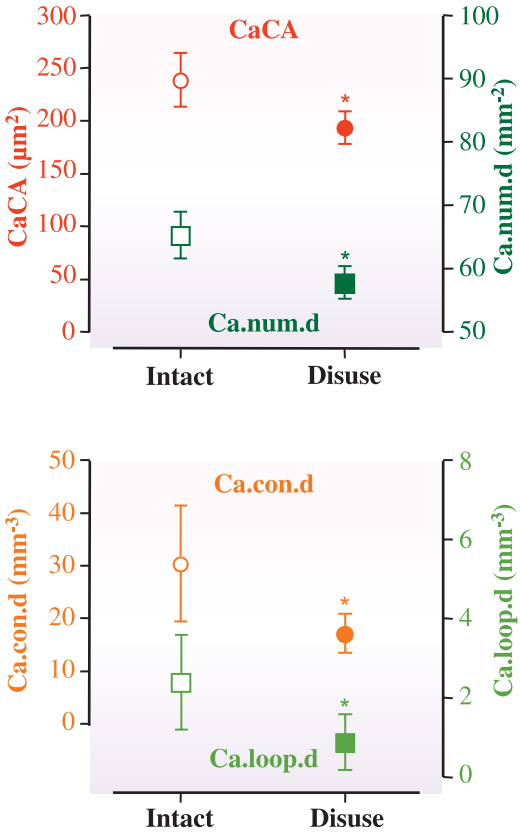

Fig. 3. Plots (mean±SD, n=8) of canal cross-sectional area (CaCA, μm^2), density of canals running longitudinally (Ca.num.d, mm^{-2}), density of canal connections (Ca.con.d, mm^{-3}), and density of canal loops (Ca.loop.d, mm^{-3}). *P<0.05 *vs* intact bone (Wilcoxon matched-pairs signed-rank test).

Takeshi Matsumoto

Bioengineering Division, Osaka University Graduate School of Engineering Science

E-mail: matsu@me.es.osaka-u.ac.jp

References

[1] M. Brookes, W.J. Revell: Blood Supply of Bone: Scientific Aspects, Springer-Verlag, (1998), London, UK.
[2] M.L. Brandi and P. Collin-Osdoby: J. Bone Miner. Res. **21** (2006)183.
[3] F. Peyrin *et al.*: Cell Mol. Biol. **46** (2000)1089.
[4] *T. Matsumoto, M. Yoshino, T. Asano, K. Uesugi, M. Todoh and M. Tanaka: J. Appl. Physiol. **100** (2006) 274.*
[5] U. Bonse and F. Busch: Prog. Biophys. Mol. Biol. **65** (1996)133.

Dose Distribution of Microplanar Beam Array for Microbeam Radiation Therapy

An array of planar synchrotron-generated X-ray beams collimated in a micrometer scale (microplanar beams) has the potential to create a new modality of radiotherapy, as reported by a group of NSLS of Brookheven National Laboratory (BNL), NY, USA in 1992 [1]. In 1995, the BNL group reported the experimental results that necrosis was not observed when irradiating brain tissue with microplanar beams at 312 - 5000 Gy, and no brain damage was observed microscopically when irradiating at 312 - 625 Gy [2]. Furthermore, they found that irradiation with microplanar beams caused growth delay or cell ablation in 9L gliosarcoma implanted in rats with less damage to the contiguous normal tissues [3]. These properties of the microplanar beams are summarized as follows: (a) microplanar beams spare normal tissues such as skin and the central nervous system (CNS), and (b) preferentially damage tumors. However, the mechanism of how normal tissues are spared is still unknown and under discussion.

The techniques of X-ray microplanar beam irradiation were first developed at BNL in the 1990s, and X-ray microplanar beam irradiation has been studied at the European Synchrotron Radiation Facility, Grenoble, France since the mid-1990s. A feasibility study of MRT at SPring-8 was initiated under the collaboration of JASRI, the National Institute of Radiological Sciences and Kitasato University in 2005. The experiments have been carried out at beamline **BL28B2**. We developed multi-slit collimators (MSCs) and evaluated them before beginning the experiments. The final MSC has thirty slits with dimensions of 25 μm height × 30 mm width × 5 mm length in the direction of the beam, which are interspersed with a spacing of 200 μm as shown in Fig. 1. The MSC was assembled by Mitaya Manufacturing Co., Ltd., Kawagoe, Japan. It is composed of an alternate stack of 175-μm-thick tungsten plates and 25-μm-thick polyimide sheets. Less than 0.01% of the photon flux penetrates through the tungsten plate and about 50% of the photon flux penetrates through the polyimide sheets. The polyimide sheets and tungsten plates are in tight contact with each other because they are pressed together with top and bottom brass plates without the use of any materials such as adhesives. The MSC was placed about 44 m downstream from the light source, and biological samples were set at about 1 m downstream from the MSC.

We carried out experiments to reproduce and confirm the sparing effects of microplanar beams on rat's CNS first. In the experiments, a ten-microplanar-beam array with a field size of 2 × 2 mm was irradiated onto rats' heads to penetrate through the cerebellum. The rats were placed prone across the beam direction and exposed to the microplanar beams at 500 - 10,000 Gy. Figure 2 shows a sliced cerebellum extracted from a rat that was irradiated with an

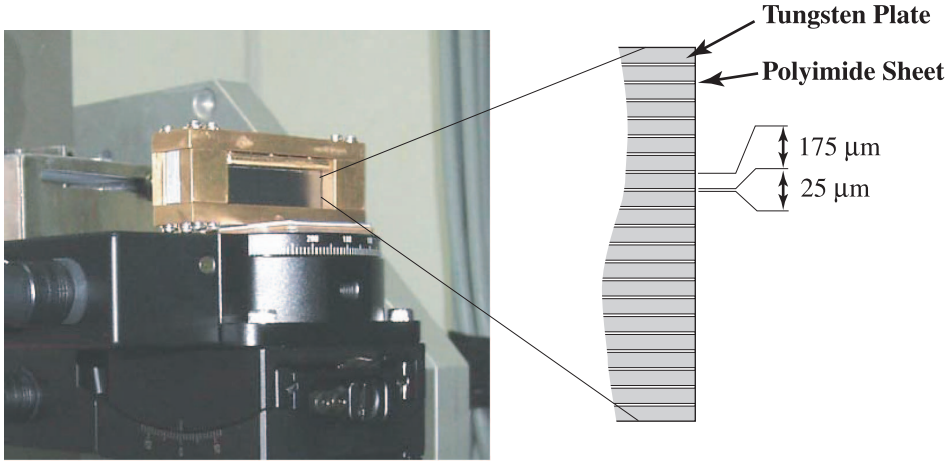

Fig. 1. Multislit collimator (MSC). It is composed of a stack of alternating tungsten plates and polyimide sheets. There are thirty slits 25 μm high, 30 mm wide and 5 mm deep (in beam direction).

entrance dose of about 300 Gy, and euthanized three days after the irradiation. The linear tracks are clearly visible. We also carried out *in vivo* experiments to confirm the tumoricidal effect and the sparing effect for skin as well as *in vitro* experiments to investigate the sparing mechanism from the viewpoint of by-stander effects. In the former experiments, we implanted fibrosarcoma NFs-a into the legs of young mice and irradiated them with microplanar beams at 200 - 1500 Gy. The mice were reared for about one month to observe the tumor growth. The measurement of the subcutaneous tumor sizes showed growth delay in tumors irradiated at various doses.

From a physical point of view, the dose distribution of the microplanar beam array is the most important. The array of microplanar beams has a spatial dose distribution with alternating high-dose areas (peak) and low-dose areas (valley). The valley dose is required to be lower than the tissue tolerance level for a broad beam, otherwise the advantageous response to the microplanar beams is presumably lost. We measured the relative dose distribution of the microplanar beam array physically and biologically. Figure 3 shows a sliced sample from the biological measurements. The valley dose was also measured physically and was preliminarily 0.2 - 0.3% of the peak dose.

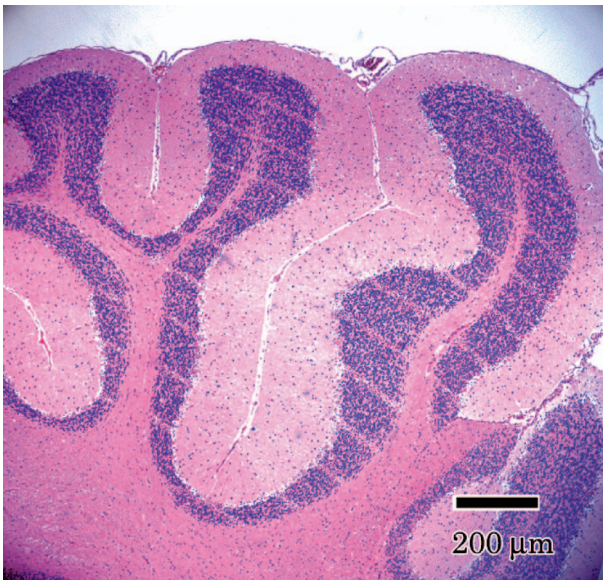

Fig. 2. Linear tracks of apoptotic granular cells developed in X-ray-irradiated stratum granulosum of cerebellum. No obvious changes were seen in the stratum moleculare, (hematoxylin-eosin staining).

Fig. 3. The distribution of DNA lesions induced by irradiation with microplanar beams in a tumor implanted in a leg of a mouse is shown with the relative dose distribution of the microplanar beam, which was measured using a CCD camera. Subcutaneously implanted fibrosarcoma NFs-a in the legs of mice were irradiated at 50 - 500 Gy. The mice were euthanized 0.5 or 5 hours after the irradiation to extract the tumors. The extracted tumors were fixed in ethanol over night, and embedded in paraffin to prepare 10-µm-thick sliced samples. Finally, under a microscope, we observed DNA lesions colorized by the γH2AX antibody, which reacts selectively with double-strand-breaks in DNA. The DNA lesions, which were colored brown, aligned along the beam path. This method enables us to biologically measure not only the width of the microplanar beam that penetrated through the tissue, but also the valley dose relatively.

Masami Torikoshi

National Institute of Radiological Science

E-mail: torikosi@nirs.go.jp

References

[1] D.N. Slatkin *et al.*: Med. Phys. **19** (1992) 1395.
[2] D.N. Slatkin *et al.*: Proc. Natl. Acad. Sci. USA. **92** (1995) 8783.
[3] J.A. Laissue *et al.*: Int. J. Cancer. **78** (1998) 654.

Materials Science
Structure

The Materials Science being developed at SPring-8 has two frontiers, namely, a novel structure determination under unexplored conditions and research on a precise structure-property relationship. The variety of research is increasing following the upgrade of experimental equipments every year. Of particular importance is the progress in data accuracy brought about by a top-up mode operation and a high-pressure experimental technique.

In the present issue, concerning the accurate structure research, the precise Maximum Entropy Method (MEM) charge density study using powder diffraction data: "Accurate structure factors from synchrotron powder diffraction data at SPring-8" by Eiji Nishibori and the three-dimensional amorphous structure research using Reverse Monte Carlo method (RMC): "Structural basis for fast phase change of DVD-RAM" by Shinji Kohara are chosen. Both studies were achieved by advanced data analysis techniques such as MEM and RMC and the excellent findings resulted from reliable data generated by a well-developed experimental machine and a top-up mode operation. In addition, the elaborate work on GaAs surface structure determination using the anomalous dispersion effect, namely, "Element-specific surface X-ray diffraction study of GaAs surfaces" by Masamitsu Takahashi, is also chosen.

This year, various novel structures were discovered under high pressure and reported in specialized journals and press conferences. The present issue deals with four topics, namely, "A Cd-Yb alloy rich in order-disorder transition" by Tetsuo Watanuki, "New helical chain structure for Scandium at 240 GPa" by Yuichi Akahama, "O_8 cluster of the ε phase of solid Oxygen" by Hiroshi Fujihisa and "X-ray-induced dissociation of H_2O and formation of an O_2-H_2 compound at high pressure" by Wendy L. Mao. Among them, the quasicrystal pressure-temperature phase diagram study by T. Watanuki is quite unique and may become a key to unraveling the mystery of the nature of the quasicrystal structure.

Masaki Takata

Accurate Structure Factors from Synchrotron Powder Diffraction Data at SPring-8

The distribution of electron density in materials determines their properties and functions. Many experimental and theoretical studies in materials science such as those using diffraction analysis, spectroscopy and density functional calculations (DFT) have been performed to reveal electron density distributions. An X-ray is a good probe of electrons. The structure factors from X-ray diffraction give information on total electron density distribution including both core and valence electrons. Accurate structure factors are always required in materials science fields, since the structure factors can be used not only for experimental charge density studies but also for evaluating different theoretical calculations.

Recent progress in synchrotron powder X-ray diffraction techniques including the third generation synchrotron X-ray source, detector, measurement system and analytical methods enable us to accurately determine structure factors for charge density studies. Powder diffraction data with high intensity and high angular resolution has now become available. A large Debye-Scherrer camera for studying charge density in detail has been installed at beamline **BL02B2**. The precise charge densities of several kinds of material such as $PbTiO_3$ [1] have been determined from powder diffraction data using the camera. For a proper understanding of the charge densities determined by SPring-8 powder data, quantitative estimation of accuracy of the data is essential. The evaluation of the quantitative accuracy of diffraction data is not an easy task. Benchmark tests need accurate data from both experimental and theoretical sides.

There are accurate structure factors of silicon and diamond that have been measured by various experimental methods, such as the Pendellösung method [2,3]. These data have been widely used for experimental charge density studies. Furthermore, the data have been, widely used for evaluating of the accuracy of theoretical calculations. In this study, we measured accurate powder diffraction data for both silicon and diamond at BL02B2 [4]. The accuracy of the data was estimated by comparing them with both the Pendellösung data and the results of several theoretical calculations.

The synchrotron powder diffraction experiments were carried out at beamline BL02B2. High-energy X-rays, 0.40122(1) Å, were used for reducing the effect of absorption. The higher-angle reflections in powder data have the disadvantage of collecting high counting statistics data because of factors such as the Lorentz factor. To improve the counting statistics of higher-angle-range data, we measured two data sets for one sample at one temperature. To extract accurate structure factors from two powder data sets, the simultaneous analysis of two data sets is most suitable. We developed Rietveld refinement software, which is suited for an accurate structural analysis of multi-powder data. It allows the simultaneous refinement of two different types of statistics for powder diffraction data. The R-factors based on weighted profile, R_{wp}, and the Bragg intensities, R_I, of Rietveld refinements were as small as 2.70% and 1.75% for silicon and 2.93% and 3.74% for diamond. We determined the observed structure factors on the basis of the Rietveld refinements.

The differences between the present structure factors and the previous structure factors determined by Pendellösung method [2,3] were within the standard uncertainty values of the present data. To evaluate the level of agreement between the present powder data and the Pendellösung data, we calculated inter-data-set agreement factors, which are expressed as $\Sigma||F_{powder}| - |F_{Pendellösung}|| / \Sigma |F_{powder}|$. They are 0.5% for silicon and 0.2% for diamond. Considering that these values were obtained by totally different experimental methods, the level of agreement is excellent.

The structure factors of silicon and diamond have been extensively calculated using theoretical calculations. The structure factors are reported as atomic form factors, $f(h\,k\,l)$. The conversion of atomic form factors to structure factors and *vice versa* is very straightforward as long as the thermal parameters are known. To evaluate the level of agreement between the present powder data and the theoretical values obtained by Pere *et al.* [5], we calculated inter-data-set agreement factors, which are expressed as $\Sigma||f_{powder}| - |f_{Theory}|| / \Sigma |f_{powder}|$. The values are within 0.53% for silicon and within 1.6% for diamond.

MEM analysis was carried out to investigate the usefulness of the structure factors determined in this study in revealing electron density distributions. The charge densities determined using theoretical calculations for silicon and diamond have been widely reported by many researchers. Most of charge the densities are reported as deformation maps. To compare the present MEM densities with other

theoretical deformation maps in detail, we have calculated deformation maps from MEM charge densities. MEM deformation maps of silicon and diamonds are shown in Figs. 1(a) and 1(b). The charge density at the bond midpoint for silicon and diamond are 0.22 and 0.42 eÅ^{-3}, respectively. The theoretical value of the valence density for silicon is 0.18 eÅ^{-3} [6] and that for diamond is 0.45 eÅ^{-3} [6]. The values determined in this study are almost identical to those determined using theoretical calculations and are within 0.04 eÅ^{-3}. The results can be regarded as showing that the present MEM charge densities are quantitatively reliable and that such densities can be used to discuss the physical properties of materials.

In this study, we accurately measured structure factors of silicon and diamond by synchrotron X-ray powder diffraction experiments. We evaluated the accuracy of the structure factors by comparing them with the Pendellösung data and the results of theoretical calculations. These results show that the powder diffraction data measured at BL02B2 is highly reliable. Since the data have sufficient accuracy, the present method can be widely used for various materials in powder form.

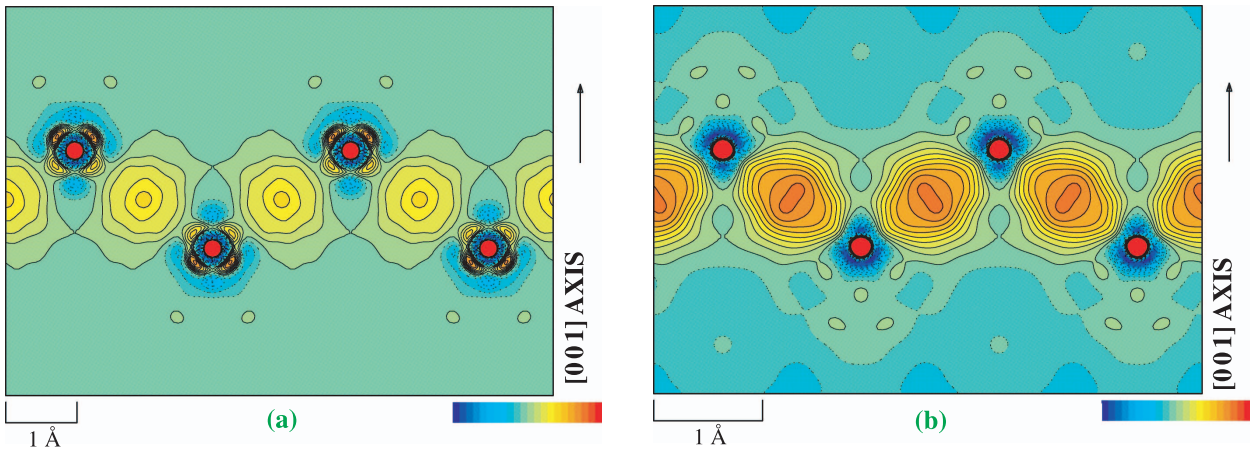

Fig. 1. The deformation charge densities of **(a)** silicon and **(b)** diamond for 110 plane based on MEM analysis. The contour lines are drawn from -0.55 to 0.55 with 0.05 eÅ^{-3} step width for **(a)**, **(b)**.

Eiji Nishibori*, Shinobu Aoyagi and Makoto Sakata

Department of Applied Physics, Nagoya University.

*E-mail: o47271a@cc.nagoya-u.ac.jp

References

[1] Y. Kuroiwa *et al.*: Phys. Rev. Lett. **87** (2001) 217601.
[2] T. Saka and N. Kato: Acta Cryst. A **42** (1986) 469.
[3] T. Takama *et al.*: Acta Cryst. A **46** (1990) 514.
[4] *E. Nishibori, E. Sunaoshi, A. Yoshida, S. Aoyagi, K. Kato, M. Takata, and M. Sakata: Acta Cryst. A* ***63*** *(2007) 43.*
[5] J. Pere *et al.*: J. Phys. Cond. Matt. **11** (1999) 5827.
[6] Z.W. Lu *et al.*: Phys. Rev. B **47** (1993) 9385.

Structural Basis for Fast Phase Change of DVD-RAM

The development of fast phase-change materials in the last century was accomplished as result of the landmark studies on GeTe and Au-Ge-Sn-Te compounds in a single-phase structure by Chen *et al.* [1] and Yamada *et al.* [2], respectively. They reported that these materials show a high phase-stability of the amorphous phase and a very short crystallization time. These approaches led the way to the development of new phase-change rewritable materials and to the discovery, in 1987, of the GeTe-Sb_2Te_3 single-phase material by Yamada *et al.* [3]. The pseudobinary compound 2GeTe-Sb_2Te_3 ($Ge_2Sb_2Te_5$) is one of the well-established mother materials for commercial DVD-RAM (digital versatile disc-random access memory) devices that utilize the crystal-liquid-amorphous (record) and amorphous-crystal (erase) phase change in chalcogenide materials. In order to develop faster phase-change materials, it is necessary to understand the structural origins of the phase change, especially for the 3D structure of the amorphous phase in the amorphous to crystal phase changes. Recently, Kolobov *et al.* investigated the local coordination around the Ge, Sb, and Te atoms in both the crystal and the amorphous phases of $Ge_2Sb_2Te_5$ by means of extended X-ray absorption fine-structure spectroscopy (EXAFS). They ascribed the crystal-amorphous/amorphous-crystal phase change in terms of the umbrella-flip of the Ge atoms from the octahedral site to the tetrahedral site, and concluded that the transformation between the two sites is the reason for the fast optical switching of the DVD-RAM [4]. However, the proposed model based on EXAFS data reveals only the local structure of the amorphous phase; hence, it is necessary to analyze the large-scale 3D structure of the amorphous phase. In this study, we derived the 3D atomic configuration of amorphous $Ge_2Sb_2Te_5$ (a-$Ge_2Sb_2Te_5$, crystallization speed: 20 ns) and amorphous GeTe a-GeTe, crystallization speed: 100 ns) by reverse Monte Carlo (RMC) computer simulation with synchrotron radiation X-ray diffraction data [5].

The high-energy X-ray diffraction experiments were carried out at the SPring-8 high-energy X-ray diffraction beamline **BL04B2** and powder diffraction beamline **BL02B2**. The measured data were analyzed by both Rietveld analysis and RMC simulation.

Figure 1 shows the measured structure factors $S(Q)$. The diffraction patterns of $Ge_2Sb_2Te_5$ and GeTe crystals consist of sharp Bragg reflections, indicating long-range periodicity in the atomic arrangement. On the other hand, the diffraction patterns of $Ge_2Sb_2Te_5$ (953 K) and GeTe (1073 K) liquids show a typical halo pattern peculiar to non-crystalline materials, reflecting the lack of long-range periodicity. These diffraction patterns show a highly disordered state (liquid state) that both $Ge_2Sb_2Te_5$ and GeTe must undergo during a recording process (crystal-amorphous phase change) by a laser-heated melt-quench process.

In order to characterize the short-range structural units, we investigated the bond angle distributions within the first coordination shell of $g_{ij}(r)$. Figure 2 shows the distributions in a-$Ge_2Sb_2Te_5$ and a-GeTe with the typical bond angle distribution, O-Si-O of regular tetrahedron, SiO_4, in amorphous SiO_2. Te-Ge(Sb)-Te and Ge(Sb)-Te-Ge(Sb) in a-$Ge_2Sb_2Te_5$ exhibit a peak at around 90°, which, surprisingly, consists of the angle in the corresponding crystal phase and is different from the typical bond angle, 109.4°, of O-Si-O. Te-Ge-Te in a-GeTe exhibits a

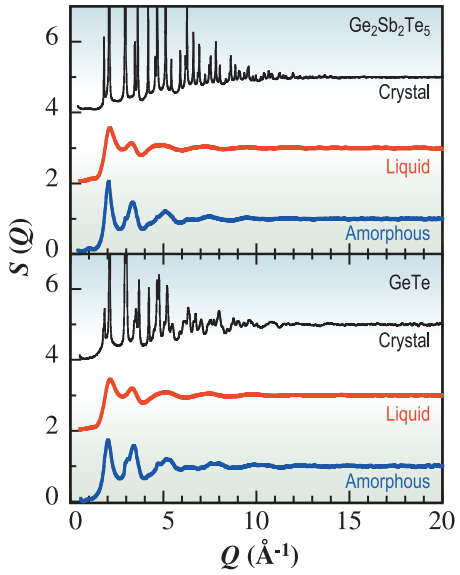

Fig. 1. Total structure factors $S(Q)$ of crystal (300 K), liquid (953 K), and amorphous $Ge_2Sb_2Te_5$ (300 K) and crystal (300 K), liquid (1073 K), and amorphous GeTe.

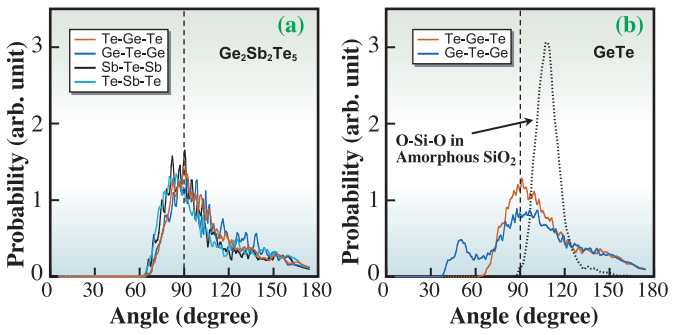

Fig. 2. Bond angle distributions in a-$Ge_2Sb_2Te_5$ and a-GeTe. Dotted lines represent the distribution of O-Si-O of regular tetrahedra in amorphous SiO_2.

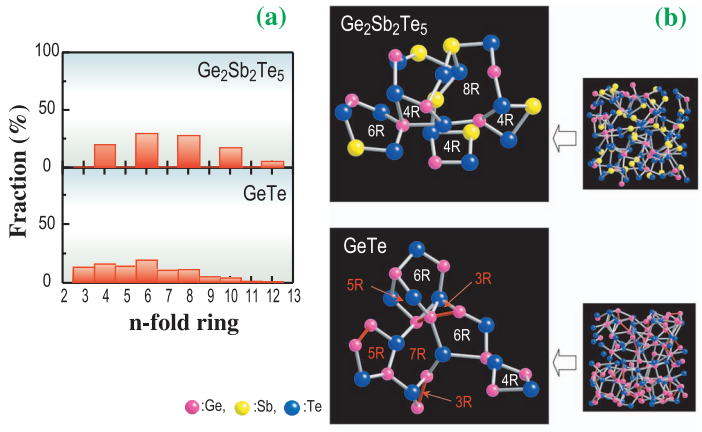

Fig. 3. Ring size distributions in a-$Ge_2Sb_2Te_5$ and a-GeTe **(a)**. The 16 Å × 16 Å × 16 Å atomic configurations and enlarged framework atomic configurations of a-$Ge_2Sb_2Te_5$ and a-GeTe obtained from the RMC snapshot **(b)**.

similar bond angle distribution, but Ge-Te-Ge shows peaks at around 90° and 50° because of the formation of Ge-Ge homopolar bonds. Therefore, it is suggested that a-$Ge_2Sb_2Te_5$ possesses a crystal-like bond angle order, whereas a-GeTe loses such an order upon the formation of Ge-Ge bond. The total coordination number around Ge (Sb) derived from the RMC model is estimated at 3.7 (3.0) for a-$Ge_2Sb_2Te_5$ and 4.1 around the Ge for a-GeTe. Therefore it is suggested that dominant short-range structural units are $GeTe_4$ and $SbTe_3$ for a- $Ge_2Sb_2Te_5$, and $GeTe_4$ and $GeTe_3Ge$ for a-GeTe.

The ring statistics for the amorphous and crystal $Ge_2Sb_2Te_5$ and GeTe were calculated up to the12-fold ring, as shown in Fig. 3(a). It is remarkable that a-$Ge_2Sb_2Te_5$ can be regarded as a "even-numbered ring structure," because the ring statistics is dominated by 4- and 6-fold rings analogous to the crystal phase. On the other hand, we find that a-GeTe has various sizes (both odd- and even-numbered) of rings. These differences in the network of the ring structure are clearly visible in 3D atomic configurations obtained by RMC simulation, as shown in Fig. 3(b).

On the basis of the comparison of the ring statistics, the mechanisms of fast crystal-liquid-amorphous (record) and amorphous-crystal (erase) phase changes in $Ge_2Sb_2Te_5$ are proposed, as shown by the schematic presentation in Fig. 4. In the crystal-liquid phase-change process (stage I), the atomic configuration in the crystal phase is disarranged by laser heating and melted in liquid, where there is no significant structural difference between $Ge_2Sb_2Te_5$ and GeTe (see also Fig. 1). However, in the liquid-amorphous phase-change process (stage II), only even-numbered rings are constructed in a-$Ge_2Sb_2Te_5$. In the amorphous-crystal phase-change process (stage III), a-$Ge_2Sb_2Te_5$ transforms to the crystal phase via the transformation of only the large even-numbered (8, 10, 12-fold) rings into the crystal structure (4- and 6-fold rings). On the other hand, a-GeTe exhibits various sizes (both odd- and even-numbered) of rings in stage II. Therefore, the recombination of the various-size rings is required in stage III. Thus the construction of odd-numbered rings in a-GeTe disturbs the fast crystallization of the amorphous phase, and it is worth mentioning that the addition of Sb_2Te_3 to GeTe can effectively prevent the formation of Ge-Ge bonds in a-$Ge_2Sb_2Te_5$.

In conclusion, we found that the ring statistics of amorphous $Ge_2Sb_2Te_5$ is dominated by 4- and 6-fold rings analogous to the crystal phase, by means of RMC analysis. We believe such unusual ring statistics of amorphous $Ge_2Sb_2Te_5$ to be the key in the fast crystallization speed of the material.

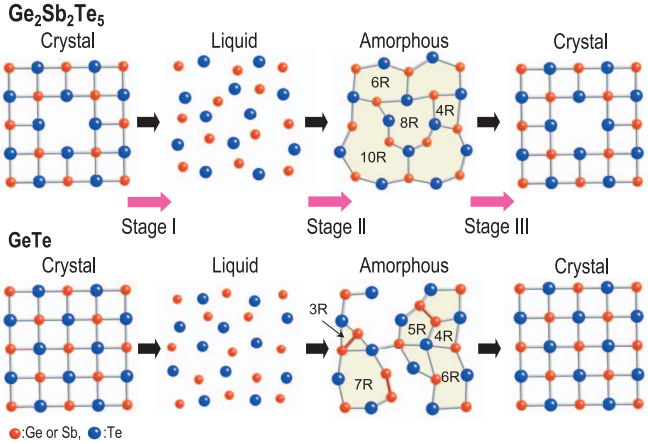

Fig. 4. Schematic presentation of possible ring size transformation in crystal-liquid-amorphous phase change (record) and amorphous-crystal phase change (erase) in $Ge_2Sb_2Te_5$ and GeTe. Stages I and II: recording process, stage III: erasing process.

S. Kohara[a,d], N. Yamada[b,d] and M. Takata[c,a,d,*]

[a] SPring-8 / JASRI
[b] Matsushita Electric Industrial Co., Ltd.
[c] SPring-8 / RIKEN
[d] CREST, JST

*E-mail: takatama@spring8.or.jp

References

[1] M. Chen *et al.*: Appl. Phys. Lett. **49** (1986) 502.
[2] N. Yamada *et al.*: Proc. SPIE **695** (1986) 79.
[3] N. Yamada *et al.*: Jpn. J. Appl. Phys. **26** (1987) 61.
[4] A.V. Kolobov *et al.*: Nature Materials **3** (2004) 703.
[5] *S. Kohara, K. Kato, S. Kimura, H. Tanaka, T. Usuki, K. Suzuya, H. Tanaka, Y. Moritomo, T. Matsunaga, N. Yamada, Y. Tanaka, H. Suematsu, and M. Takata: Appl. Phys. Lett.* ***89*** *(2006) 201910.*

Element-specific Surface X-ray Diffraction Study of GaAs Surfaces

Gallium arsenide is a semiconductor showing excellent performance in optoelectronic and high-frequency devices. It plays a critical role in today's highly networked society, being used in cell phones, satellite communication and laser diodes. For these applications, atomically controlled device structures are grown by molecular-beam epitaxy (MBE) and metal-organic chemical vapor deposition (MOCVD). A detailed understanding of surface structures under growth conditions is an important basis for these techniques.

Atomic arrangements on a semiconductor surface often differ from those of the ideal bulk structure. Firstly, atoms are displaced from the bulk positions to reduce the number of dangling bonds at the surface. The resultant surface reconstruction involves several atomic layers that are below the surface. Secondly, through the exchange of atoms between the substrate and the environment, chemical compositions are allowed to deviate from that in bulk in the case of compound semiconductors. This flexibility in stoichiometry results in a number of variations of surface reconstructions. For the full determination of a surface reconstruction, therefore, both the positions and the species of surface atoms need to be determined. Although electron diffraction analysis, which is most widely used for surface structure analysis, is capable of completing this task in principle, it is very difficult to differentiate atoms with similar atomic numbers such as Ga and As. Scanning tunneling microscopy cannot differentiate atomic species either. Element-specific techniques, such as ion scattering, photoemission spectroscopy and the analysis of X-ray fluorescence excited by electrons, have trouble distinguishing the signals from the surface and the substrate.

Figure 1 shows the GaAs(001)-c(4×4) structure investigated in the present work. This surface was used as a template for the growth of InAs quantum dots or dilute magnetic semiconductors and thus has been attracting much interest recently. Because this surface was observed under As-rich conditions, it was initially considered that all the atoms in the topmost layer were As atoms [2]. Later on, however, a new structure model in which half of the top-layer atoms are considered to be Ga atoms was proposed [3]. Experimentally, the claim of the presence of Ga was based on the presence of an asymmetric structure with respect to the [1 -1 0] axis accompanied by the buckling of surface dimers. However, asymmetric dimers are widely observed structures even for single-element semiconductors, such as Si(001) and Ge(001). Direct evidence of Ga-As heterodimer formation was not available at the time. Thus, we applied element-specific surface X-ray diffraction analysis of GaAs(001)-c(4×4) for surface structure determination that specified atomic species [1].

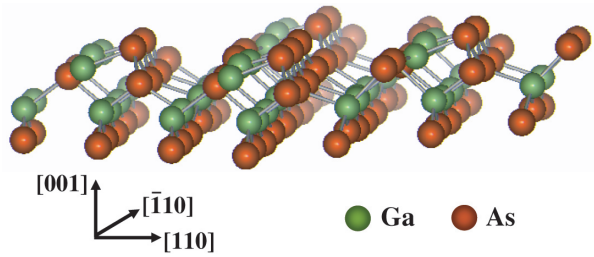

Fig. 1. Ball-and-stick model of GaAs(001)-c(4×4).

For surface studies under crystal growth conditions, we have developed an X-ray diffractometer integrated with an MBE chamber at beamline **BL11XU** [4]. The intense X-rays of SPring-8 have speeded up the measurements of surface X-ray diffraction, which is weaker than the diffraction from bulk crystals by several orders of magnitude. Moreover, the wide spectrum of SPring-8 X-rays has enabled the determination of the species of surface atoms as well as their coordinates.

Our analysis was carried out in two steps. The first step was determining atomic positions by conventional surface X-ray diffraction measurements at an X-ray energy of 10 keV. By combining in-plane and out-of-plane measurements, we determined the three-dimensional coordinates of the atoms up to the sixth layer from the surface. As shown in Fig. 2, the simulation based on the asymmetric-dimer model fits the measurements better than the symmetric-dimer model. The experimentally determined coordinates showed very good agreement with those obtained using a first-principles calculation [5]. Still, it was unclear whether the dimers are As-As homodimers or Ga-As heterodimers. Even when both atoms in the surface dimer were assumed to be As, a similarly result was obtained because the atomic numbers of Ga and As are very close, 31 and 33, respectively. Thus, up until this stage, we had just confirmed the formation of asymmetric dimers rather than that of heterodimers. To resolve this uncertainty, we

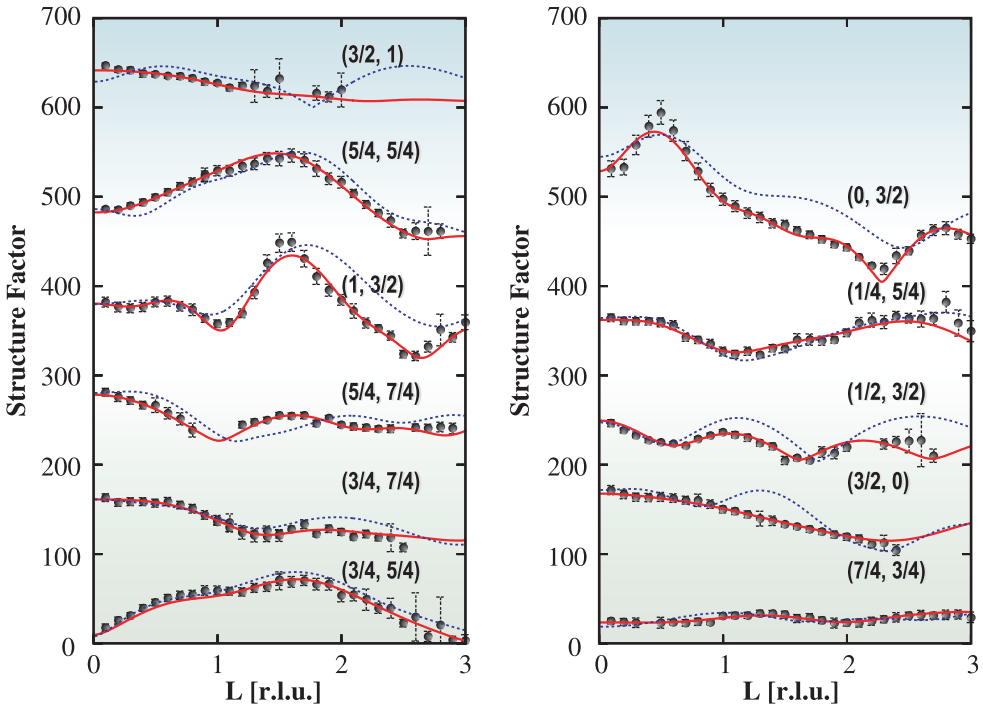

Fig. 2. Comparison of measured (filled black circles) and simulated (red and blue lines) fractional-order rods. The simulation based on the asymmetric dimer model (solid red lines) give better fitting than the symmetric dimer model (dashed blue lines).

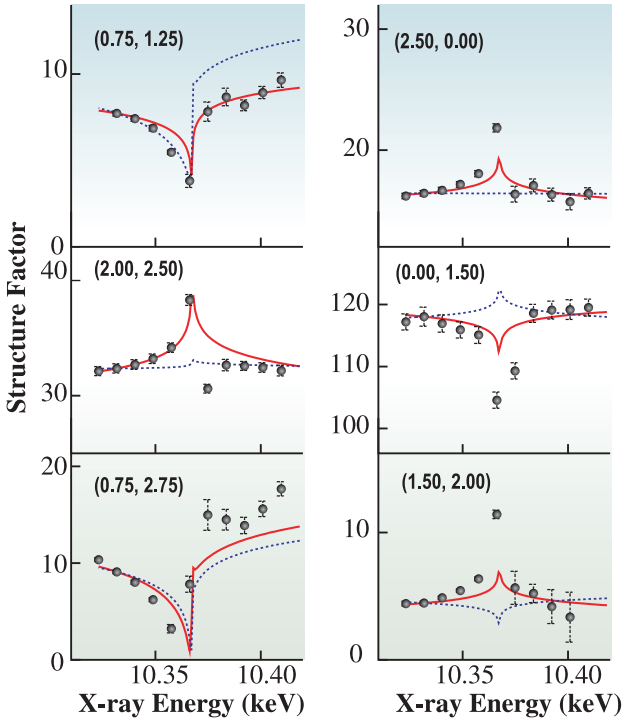

Fig. 3. X-ray energy dispersion of the structure factors. The circles are observed structure factors. The red and blue lines represent the results from calculations when Ga-As and As-As dimers are assumed, respectively.

measured the variation in X-ray diffraction intensity as a function of X-ray energy. As shown in Fig. 3, the experimental results (filled circles) agree better with the model in which the topmost layer consists of both gallium and arsenic (red lines) than the counterpart in which only arsenic is present on the surface (blue lines).

In summary, we have investigated the structure of GaAs(001)-c(4×4) by element-specific surface X-ray diffraction analysis. The formation of Ga-As surface dimers in this surface has been confirmed using the anomalous scattering of X-rays. This study has provided direct experimental evidence of the presence of Ga-As dimers in GaAs(001)-c(4×4).

Masamitu Takahasi

SPring-8 / JAEA

E-mail: mtaka@spring8.or.jp

References

[1] *M. Takahasi and J. Mizuki: Phys. Rev. Lett.* ***96*** *(2006) 055506.*
[2] M. Sauvage-Simkin *et al.*: Phys. Rev. Lett. **62** (1989) 563.
[3] A. Otake , J. *et al.*: Phys. Rev. Lett. **89** (2002) 206102.
[4] M. Takahasi *et al.*: Jpn. J. Appl. Phys. **41** (2002) 6247.
[5] *M. Takahasi, P. Kratzer, E. Penev and J. Mizuki: Surf. Sci.* ***600*** *(2006) 4099.*

Cd-Yb Alloy Rich in Order-disorder Transitions — Clue to Understanding of Nature of Quasicrystalline Icosahedral Lattice —

Unlike ordinary metal crystals with translational periodic lattices, quasicrystals have icosahedral lattice components that pile up to form successively larger icosahedral units and eventually fill three-dimensional space without translational periodicity. The structural nature of quasicrystals has attracted considerable interest, particularly interest in the phase transition phenomena on the icosahedral quasi-periodic lattice. In contrast to the numerous reports on the structural phase transitions of metal crystals, very few studies have been reported on quasicrystals. The structural nature of quasicrystals is still unknown.

A Cd-Yb alloy is an advantageous system for studying order-disorder phase transition phenomena. $Cd_{5.7}Yb$ forms an icosahedral quasicrystal that consists of the icosahedral atomic clusters of four successive shells with an icosahedral quasiperiodic arrangement (Fig. 1(a)) [1]. The Cd_4 tetrahedral atomic unit in the innermost part of the cluster is orientationally disordered at ambient pressure and temperature [2]. Order-disorder transitions are hence expected to occur as a result of the pressure and/or temperature tuning of the orientational state of the Cd_4 tetrahedra.

When the atomic composition changes slightly to Cd_6Yb, Cd-Yb alloy forms a crystalline approximant of the quasicrystal [1]. The approximant consists of the same atomic clusters as the quasicrystal but they pack in a body-centered cubic (bcc) configuration showing translational symmetry (Fig. 1(b)) [2]. The major relationships between the neighboring clusters in the quasicrystal appear again in the approximant. Because of these structural similarities, studying the approximant will provide a clue to help us understand the quasicrystal, which has more complex structure.

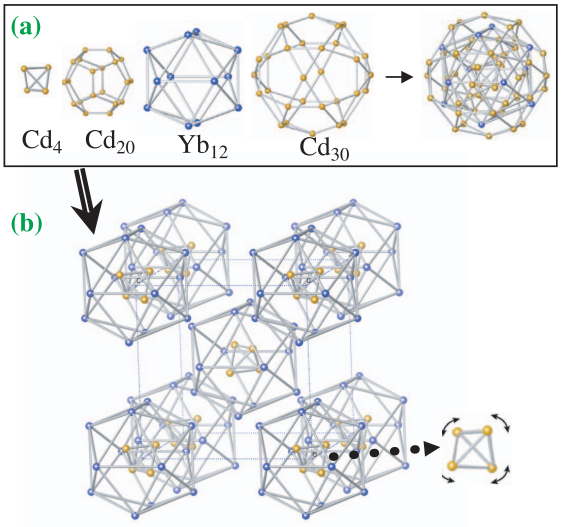

Fig. 1. Successive shells of the atomic cluster in Cd-Yb quasicrystal and its crystalline approximant (**a**). The structure of the approximant (Cd_6Yb) is described as a bcc packing of the cluster (**b**). The innermost shell of the Cd_4 tetrahedron is orientationally disordered at ambient pressure and temperature.

We investigated the structure of the Cd-Yb approximant under high pressure and low temperature, and revealed the rich behavior in order-disorder phase transitions [3]. The Cd_4 tetrahedra exhibit various types of orientational order that sensitively depend on pressure and temperature.

Single-crystal synchrotron X-ray diffraction experiments at pressures up to 5.2 GPa and temperatures down to 10 K were performed at beamline **BL22XU** [4]. Figure 2 shows oscillation photos acquired in isobar processes at ambient pressure, 2.7 GPa and 5.2 GPa. At room temperature, the crystal maintained a bcc structure with the orientational disorder of the Cd_4 tetrahedra continuing up to 5.2 GPa (Fig. 2(a)). However, a different behavior was observed for the bcc phase upon cooling at each pressure. At ambient pressure, superlattice spots due to the orientational order appear at 110 K (phase I) (Fig. 2(b)) as previously reported [5]. At 2.7 GPa, the bcc phase sequentially transforms into ordered phases II and III at 245 K and 135 K, respectively, as indicated by the superlattice series and the following additional weak ones (Figs. 2(c) and 2(d)). At 5.2 GPa, the bcc phase showed another sequential transition to phase IV at 225 K and to phase V at 145 K (Figs. 2(e) and 2(f)). The ordered structures of these phases differ from each other as shown by the superlattice patterns.

Figure 3(a) shows an outline of the phase diagram. Four ordered phases were newly found along with the known phase I. Besides the well-defined phases, slight modifications (III', IV') seem to appear. The main ordering structure of phases II and III are characterized by the <111> propagation direction of ordering, which is shown in Fig. 3(b), and that of phases I, IV, and V of the [110] propagation is shown in Fig. 3(c). The propagation direction mainly depends on pressure. It alternates from [110] to <111> at about 1.0 GPa and again to [110] in the

range of 3.5-4.3 GPa. The two-step transitions of bcc-II-III and bcc-IV-V can be interpreted as the sequential ordering of the Cd_4 tetrahedron. Primary ordering is followed by fine ordering without alteration of the main ordering structure. The high degree of symmetry of the local structure of this material is considered to allow the Cd_4 tetrahedra to take various orientational states.

Information of an correlations between the neighboring Cd_4 tetrahedra was obtained from the analysis of the temperature variation of the superlattice intensity. Two types of interaction, namely, short- and long-range interactions exist, which are presumably attributed to the atomic packing effect and the electron-lattice interaction through itinerant electrons, respectively. In addition to the highly symmetric structure of this material, the coexistence of the two different types of interaction is considered to be responsible for the complicated phase behavior.

Since the Cd-Yb quasicrystal has a higher degree symmetry than the crystalline approximant and two different interactions exist in the quasicrystal as well, the present results lead to the expectation that there is richer behavior in the quasicrystal. In addition, we expect that further structural study of the Cd-Yb quasicrystal compared with the approximant at the corresponding *P-T* region will help us clarify the essential nature of the icosahedral quasiperiodic lattice.

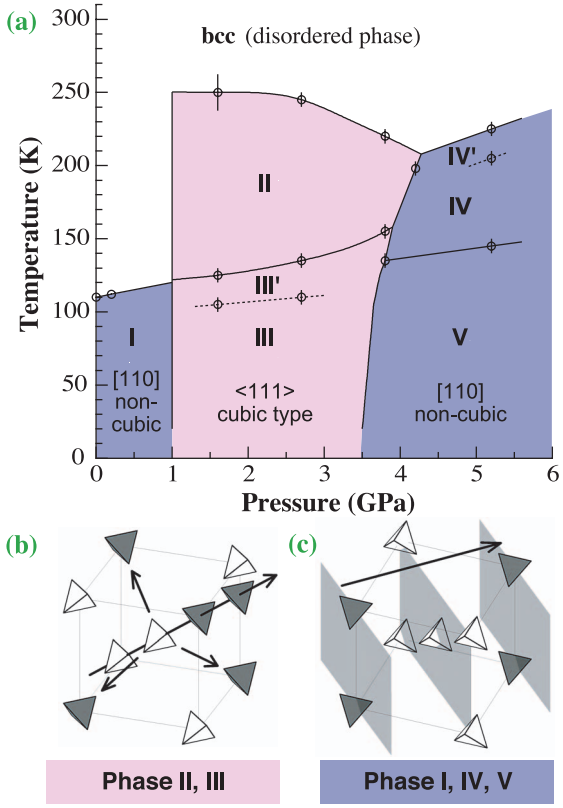

Fig. 3. Phase diagram outline of the Cd-Yb crystalline approximant **(a)**. Illustration of main ordering structure of the Cd_4 tedrahedra in phases II and III **(b)**, and in phases I, IV, and V **(c)**. The two orientations are represented by white and gray tetrahedra. Arrows represent the propagation direction of ordering along the <111> directions in **(b)** and the [110] direction in **(c)**.

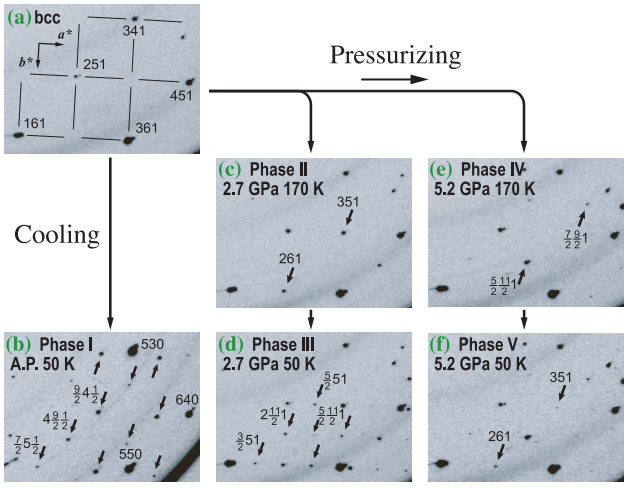

Fig. 2. X-ray oscillation photos of a Cd-Yb crystalline approximant at high pressure and low temperature. Arrows indicate representative superlattice spots that appear owing to the orientational ordering of the Cd_4 tetrahedra by cooling in the isobar process.

Tetsu Watanuki

SPring-8 / JAEA

E-mail: wata@spring8.or.jp

References

[1] A. P. Tsai *et al.*: Nature **408** (2000) 537.
[2] H. Takakura *et al.*: Nat. Materials **6** (2007) 58.
[3] *T. Watanuki, A. Machida, T. Ikeda, K. Aoki, H. Kaneko, T. Shobu, T. J. Sato and A. P. Tsai: Phys. Rev. Lett.* ***96*** *(2006) 105702.*
[4] T. Watanuki *et al.*: Philos. Mag. **87** (2007) 2905.
[5] R. Tamura *et al.*: Jpn. J. Appl. Phys. **41** (2002) L524.

New Helical Chain Structure for Scandium at 240 GPa [1]

Studies of the 3*d* transition metals at high-pressure have attracted attention for a variety of reasons, such as the interest in structural phase transitions induced by electronic transitions, their natural magnetic character and because they are major components of the Earth's core. At present, these metals are considered to exhibit a systematic structure sequence of pressure-induced phase transitions due to electron transfer from the s-band to the d-band under pressure (the so-called *s-d* transition): hcp - bcc - hcp - fcc [2].

However, our recent X-ray study of titanium (Ti) revealed that its structural sequence is different from the canonical sequence, that is, the hcp phase, with increasing pressure, transforms to the ω phase with a host-guest structure, and furthermore, rather anisotropic structures consisting of zigzag chains (see Fig. 1) occur in the high-pressure phases above 100 GPa [3]. Why does such an anisotropic structure occur under high pressure? We hypothesize that the large radius of the 3*d* electron orbital of Ti may be a key in the reason behind the structural stability.

Scandium (Sc) is the first member of the 3*d* transition elements and neighbors Ti. Its 3*d* electron orbital has a larger radius than that of Ti. In order to test our hypothesis, the structure of Sc was investigated under high pressure. In this work, X-ray diffraction experiments of Sc were carried out over a wide range of pressures, up to 300 GPa using a monochromatic synchrotron radiation source on beamline **BL10XU**.

From our experiments, four structural phase transitions were found. Each high-pressure phase was assigned in order of pressure to Sc-II, III, IV and V, respectively. The first transition from hcp (Sc-I) to Sc-II was observed at 23 GPa. The structure of Sc-II has been explained as a tetragonal lattice comprising a host lattice and a guest lattice [4]. The other three phase transitions occurred at pressures of 104, 140 and 240 GPa, respectively. The profiles of Sc-III, IV and V consist of a large number of diffraction lines and suggest that the structures of these phases are not Braves lattices, but are complicated structures. Namely, these structures do not follow the predicted sequence.

The transition to Sc-V was sharp and almost complete at 244 GPa. This high-pressure phase was stable up to 300 GPa. The diffraction profile of Sc-V shown in Fig. 2 is completely indexed on the basis of the 6 screw hexagonal lattice with this S.G or its enantiomorph. The relative intensities were well explained by this structure with six Sc atoms in the 6*a* Wyckoff positions with 0.461 and with an *R* factor of R_{wp} = 25%. The structure of Sc-V shown in Fig. 3 consists of infinite 6 screw chains parallel to the *c* axis. The Sc atoms have two nearest-neighbor atoms with an intra-chain distance of 2.05 Å. The nearest-

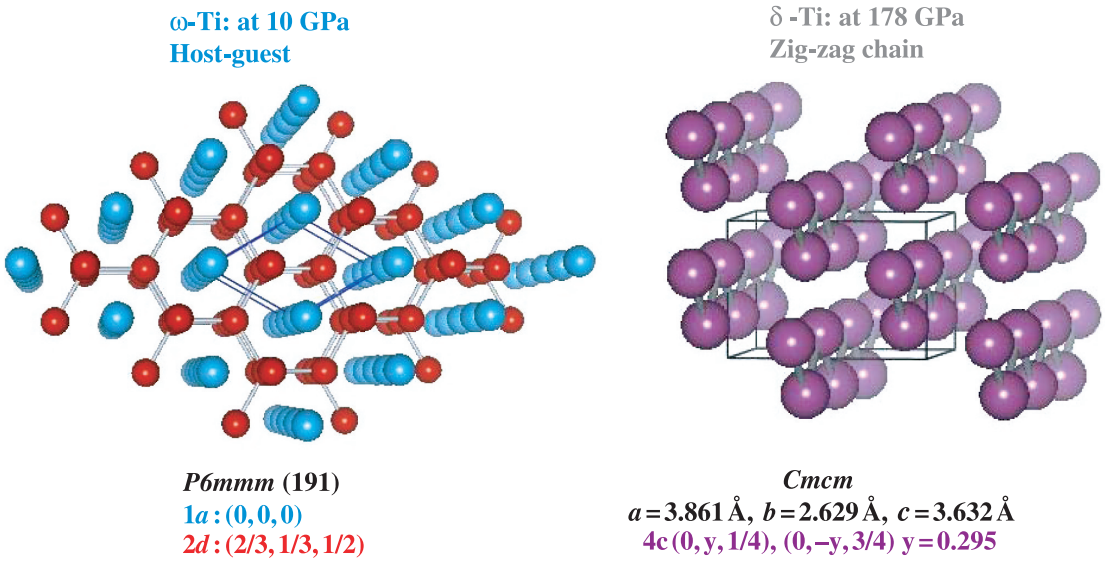

Fig. 1. Structures of high-pressure phases of titanium (Ti) metal: ω-Ti at 10 GPa and δ-Ti at 178 GPa.

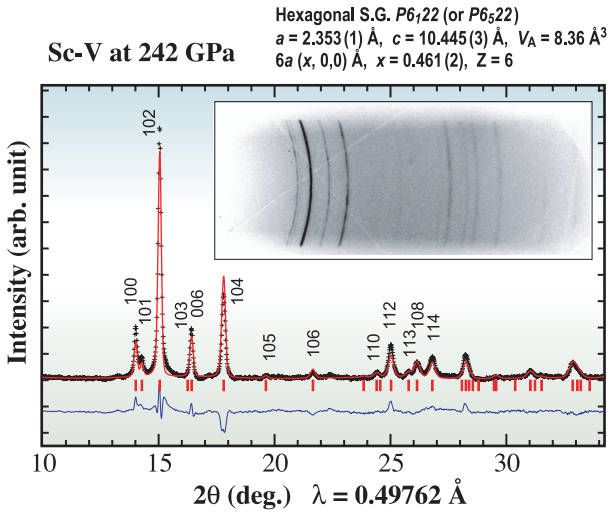

Fig. 2. Powder diffraction profile of the highest pressure phase of Sc, Sc-V, at 242 GPa, together with the diffraction image. The profile is completely indexed on the basis of the hexagonal $P6_122$ or $P6_522$ lattice. The solid red line represents the Rietveld fit.

neighbor distance between chains is 2.155 Å, which is 5% longer than in the intra-chain distance.

On the basis of the above results, an anisotropic chain-like structure also occurs in Sc. The nearest-neighbor distance between Sc atoms is 2.05 Å. Considering the radius of 1.24 Å of the 3*d* electron state of the Sc atom, as quoted by Harrison [5], the atomic distance means that the 3*d* orbitals of an Sc atom overlap with those of the neighbor atoms in the chain (Table 1). This suggests that the $3d_{zz}$-orbital localized near the inner core is hybridized with the 4*s*-orbital, and directional covalent bonding between the hybridized orbitals results in the anisotropic chain-like structure. In conclusion, the present observation provides not only evidence supporting our hypothesis but also a new viewpoint for understanding the structural stability of the transition metals under extremely high pressures, that is, the importance of interactions among the 3*d* orbitals of nearest-neighbor atoms.

Table 1. Radius of 3*d* orbital: r_d (Å) by W.A. Harrison [5].

Sc	Ti	V	Cr	Mn	Fe	Co	Ni
1.24	1.08	0.98	0.90	0.86	0.80	0.76	0.71

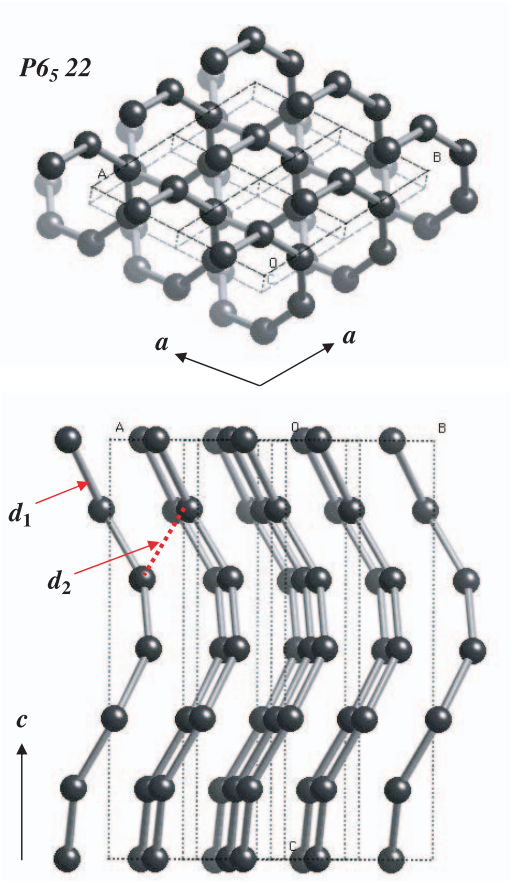

Fig. 3. Structure of the Sc-V phase at 242 GPa on the basis of the $P6_122$ lattice. The structure consists of infinite 6_1 chains parallel to the *c* axis. The intra-chain and inter-chain distances, d_1 and d_2 are 2.051 Å and 2.155 Å, respectively.

Yuichi Akahama[a,*], Hiroshi Fujihisa[b] and Haruki Kawamura[a]

[a] Graduate School of Material Science, University of Hyogo
[b] Research Institute of Instrumentation Frontier, AIST

*E-mail: akahama@sci.u-hyogo.ac.jp

References

[1] *Y. Akahama, H. Fujihisa and H. Kawamura: Phys. Rev. Lett.* ***94*** *(2005) 195503.*
[2] J. C. Duthie and D. G. Pettifor: Phys. Rev. Lett. **38** (1977) 564.
[3] Y. Akahama *et al.*: Phys. Rev. Lett. **87** (2001) 275503.
[4] H. Fujihisa *et al.*: Phys. Rev. B **72** (2005) 132103.
[5] W.A. Harrison: in Electronic Structure and the Properties of Solid: The Physics of the Chemical Bond (W.H. Freeman and Company, 1980).

O_8 Cluster in the ε Phase of Solid Oxygen

The investigation of the molecular dissociation and metallization of molecular solids has been a long-term problem in solid-state physics and earth and planetary sciences. The investigation of the pressure-induced metallization and molecular dissociation processes of the simplest diatomic molecules, such as H_2, N_2, O_2, F_2, Cl_2, Br_2, and I_2, has, for a long time, attracted much attention. It is known that oxygen solidifies into a state called the β-phase at room temperature and 6 GPa, and with further increase of pressure, the β-phase undergoes phase transitions to the δ-phase at 9 GPa and the ε-phase at 10 GPa (Fig. 1). Because of the enhancement of in molecular interactions, the pink color of the β-phase changes orange (δ-phase) and red (ε-phase), and further to black with increasing pressure. Akahama *et al*. found that a ζ-phase appears at 96 GPa when ε-phase oxygen is further pressured (Fig. 1) [1]. The ε-phase, which has a metallic luster, is known to exhibit superconductivity at low temperature [2]. Oxygen molecules are one of the very few molecules having magnetic moments, and have attracted attention from the viewpoint of the relationship between the molecular magnetization and crystal structures, electronic structures, and superconductivity. Until now, as possible models of the ε-phase structure, the O_4 model of a pair of O_2 molecules (estimated from optical measurements) and the chain model, in which the O_2 molecules are one-dimensionally connected (theoretical prediction) have been proposed. However, the diffraction patterns calculated from these models are not consistent with the experimental one, and thus these models have been in doubt. We have attempted powder X-ray diffraction experiments and structural analyses of the ε-phase [3].

The oxygen ε-phase was prepared as follows. First, oxygen gas and a diamond-anvil high-pressure cell (DAC) were cooled with liquid nitrogen, and thus the oxygen was liquidized. The liquid oxygen was enclosed in the sample chamber of the DAC (60 μm in diameter and 30 μm in thickness), and pressurized to solidify it. The solidified oxygen can maintain the solid state under continued applied pressure even at room temperature. Then, X-ray diffraction patterns of the solidified oxygen powder were obtained using beamline **BL10XU**.

The analytical procedure for determining the structure from the powder diffraction patterns was as follows. First, we assumed that the crystal structure of the oxygen ε-phase belongs to the lowest symmetry space group, *P1*, and constructed an initial model by the simulated annealing method. Secondly,

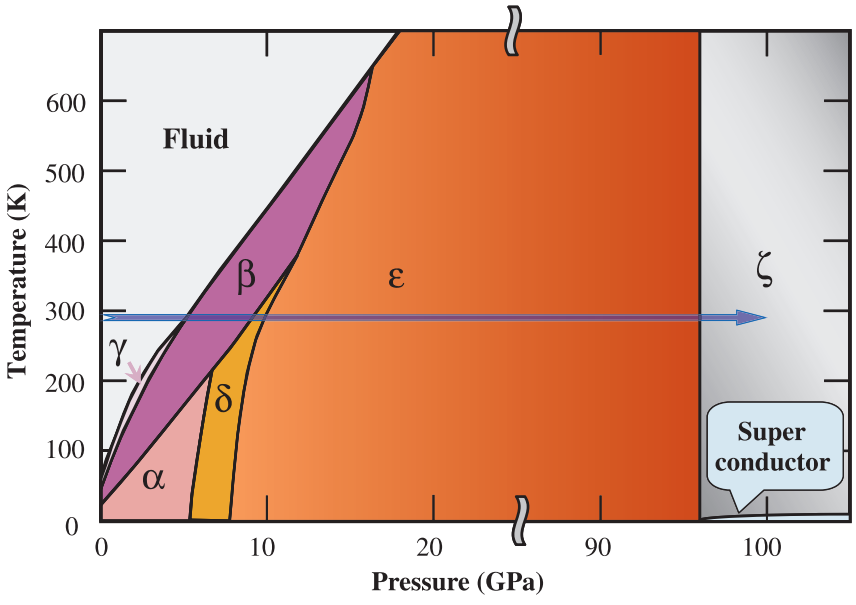

Fig.1. Pressure-temperature phase diagram of oxygen.

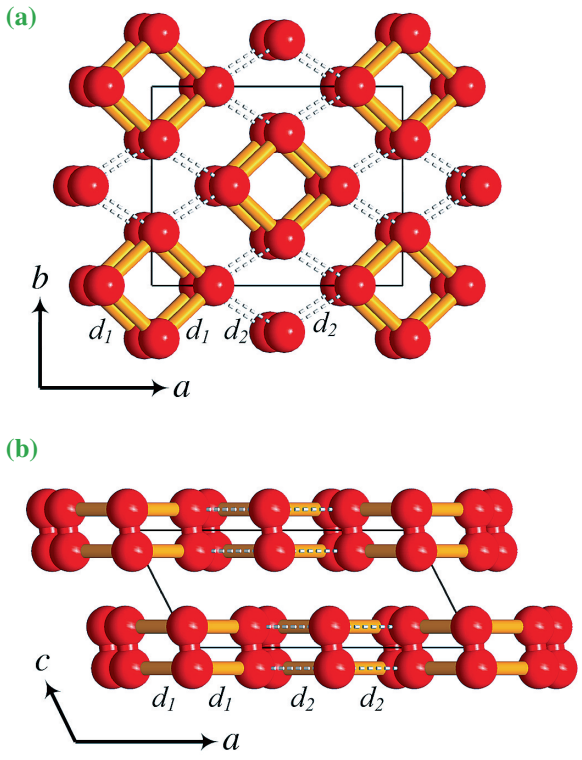

Fig. 2. Crystal structure of oxygen ε-phase formed at 11 GPa. **(a)** Projected figure to the *ab* plane, **(b)** Projected figure to the *ac* plane. The intramolecular bond length of the oxygen molecule was fixed at 1.20 Å. The intracluster bond length of the O_8 cluster (orange bar line d_1) is 2.34 Å, and the intercluster distance (dotted line d_2) is 2.66 Å.

considering the features of the structure, the symmetry was gradually raised from *P1* to $P\bar{1}$, *C2*, and *C2/m*. Lastly, after making the structure more precise using the Rietveld analysis, the structure obtained showed an O_8 cluster in which four oxygen molecules take a boxlike arrangement (Fig. 2). Thus, we have found that the structure of the ε-phase is based on an O_8 cluster, but is different from the O_4 model estimated from optical measurements or from the chain model predicted theoretically. Furthermore, we have confirmed that this structure is formed under pressure up to 96 GPa.

The boxlike cluster is a unique conformation that was first discovered for oxygen (Fig. 3), and has never been reported experimentally or theoretically for any other diatomic molecules. The formation mechanism of the O_8 cluster found in this work is not yet clear, and we hypothesize that the charge transfer between oxygen molecules or the magnetic moment of oxygen molecules plays a significant role in the formation. Hereafter, based on the structure of the ε-phase, we plan to determine the structure of the oxygen ζ-phase formed under pressures above 96 GPa, which exhibits metallization and superconductivity. If successful, the results will provide significant information for the clarification of the mechanisms of metallization and superconductivity of oxygen. Also, because of the discovery of the new diatomic-molecule conformation in our work, we expect that structural analyses of hydrogen and other elements will be accelerated.

Two weeks after the publication of our study [3], a British group reported the crystal structure of the ε-phase determined by single crystal X-ray diffraction [4]. This independent study revealed the same O_8 structure and was immediately reviewed [5].

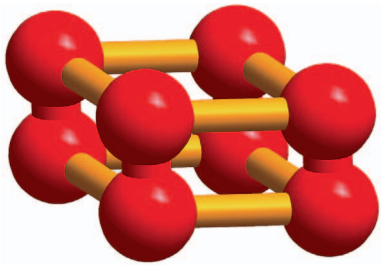

Fig. 3. Structure of the O_8 cluster found in the solid oxygen ε-phase.

Hiroshi Fujihisa [a,*], Yuichi Akahama [b] and Yasuo Ohishi [c]

[a] Research Institute of Instrumentation Frontier, AIST
[b] Graduate School of Material Science, University of Hyogo
[c] SPring-8 / JASRI

*E-mail: hiroshi.fujihisa@aist.go.jp

References

[1] Y. Akahama *et al.*: Phys. Rev. Lett. **74** (1995) 4690.
[2] K. Shimizu *et al.*: Nature **393** (1998) 767.
[3] *H. Fujihisa, Y. Akahama, H. Kawamura, Y. Ohishi, O. Shimomura, H. Yamawaki, M. Sakashita, Y. Gotoh, S. Takeya and K. Honda: Phys. Rev. Lett. **97** (2006) 085503.*
[4] L.F. Lundegaard *et al.*: Nature **443** (2006) 201.
[5] B. Militzer and R.J. Hemley: Nature **443** (2006) 150.

X-RAY-INDUCED DISSOCIATION OF H_2O AND FORMATION OF AN O_2-H_2 COMPOUND AT HIGH PRESSURE

The high-pressure behavior of H_2O is a subject of fundamental importance in physics, chemistry, and planetary sciences. H_2O has a very rich phase diagram – at least ten stable phases of ice and more than five additional metastable forms of crystalline and amorphous ice – and exhibits a wide range of unusual phenomena, such as symmetric hydrogen bonding, multi-site disordering, multiple critical points, etc. Although at ambient pressure X-rays are known to produce metastable free radicals in molecular systems or induce stable reactions by overcoming kinetic energy barriers, documented examples of X-ray induced transitions at high pressure are extremely rare.

We observed unexpected radiation chemistry in the 'simple' H_2O system at high pressure. Beginning with an H_2O sample contained in a diamond anvil cell at high pressure, we found that exposure to moderately high energy (~10 keV) X-rays resulted in cleaving of the H_2O molecules, formation of O-O and H-H bonds, and conversion of the O and H framework in ice VII into a new molecular compound of O_2 and H_2. X-ray diffraction, X-ray Raman spectroscopy (XRS), and optical Raman spectroscopy were used to establish that this new crystalline solid differs from previously known phases.

For oxygen bonded with hydrogen in H_2O, the oxygen *K*-edge in XRS spectra were dominated by a cluster of peaks around 540 eV as shown in dense water below 0.9 GPa, ice VI between 1 and 2 GPa, and ice VII just above 2 GPa (Fig. 1). At pressures above 2.5 GPa, however, X-radiation induced dramatic, irreversible changes in the XRS spectra. A distinctive, sharp peak at 530 eV characteristic of O-O bonding in O_2 grew with time and reached a plateau after approximately six hours of exposure to the incident X-ray beam, with the plateau intensity increasing with increasing pressure (Fig. 1). Visually, the sample changed from colorless to light brown after the conversion (Fig. 2).

Optical Raman spectroscopy measurements of the H_2O sample after XRS irradiation showed intense, characteristic H_2 and O_2 vibrons and a diminished H_2O signal, demonstrating the dissociation of H_2O molecules and the recombination into O_2 and H_2 molecules. The resultant O_2 and H_2 molecules do not exist in the known high pressure phases of hexagonal close-packed H_2 and ε-O_2, but form a new compound consisting of both molecular O_2 and H_2. X-ray diffraction studies of this new H_2-O_2 compound indicate that the new material is a well-crystallized solid. Its diffraction pattern shows some similarity to ε-O_2, but the new compound has a number of additional peaks, a more complicated crystal structure, and possibly lower symmetry than ε-O_2.

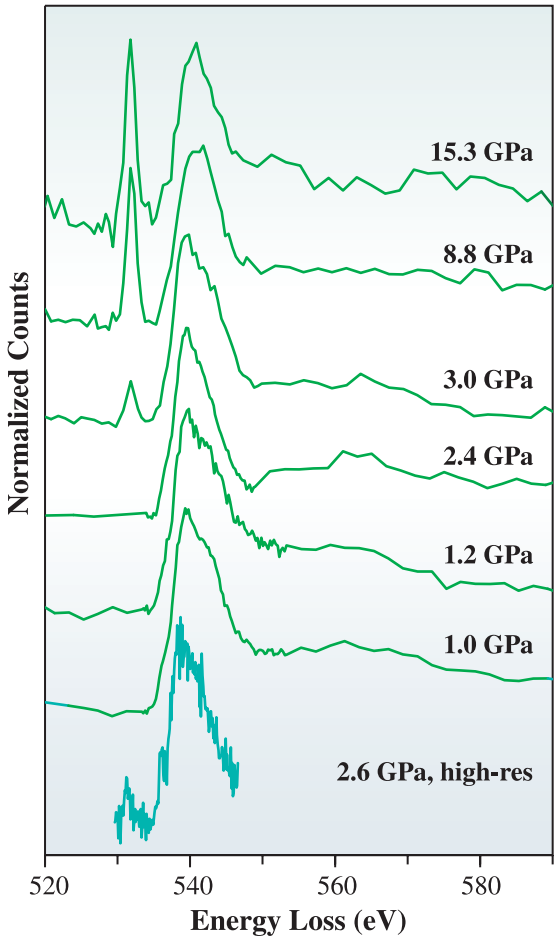

Fig. 1. XRS patterns of H_2O sample at high pressure after irradiation [1]. Bottom spectra at 2.6 GPa was measured at beamline **BL12XU**, SPring-8 using 9.886 keV X-radiation with high energy resolution (300 meV). All other spectra were measured with 9.687 keV X-radiation at beamline 13-IDC, Advanced Photon Source with 1 eV resolution.

Once synthesized and kept at high pressure, the new phase is extremely stable with respect to laser exposure, further x-radiation, and long shelf-time up to at least 200 days. Bubbles of a O_2-H_2 gaseous mixture (identified by ORS) were released from the solid when the pressure was reduced below 1 GPa. When these bubbles were compressed to high pressures and irradiated with X-rays again, they reformed the new compound (Fig. 2). Formation of this material has thus been approached from both directions: starting with H_2O and with an O_2-H_2 mixture. Heated in a diamond-anvil cell, the new phase is stable up to 700 K at 15 GPa. At higher temperature, this material reverts to ice VII before melting. While the pressure at which this phenomena occurs at ambient temperature is quite high (i.e. 2.6 GPa), it is feasible that low temperature could metastably quench this new compound to more modest pressures. This material opens new possibilities for studying molecular interactions in the O_2-H_2 system in particular and molecular hydrogen containing systems in general, and may open the door to exciting new directions in radiation chemistry research.

Wendy Mao †

Lujan Neutron Scattering Center,
Los Alamos National Laboratory, USA

E-mail: wmao@pangea.stanford.edu

† Present Address:
Geological & Environmental Sciences, Stanford Univ. and
Photon Science, Stanford Linear Accelerator Center

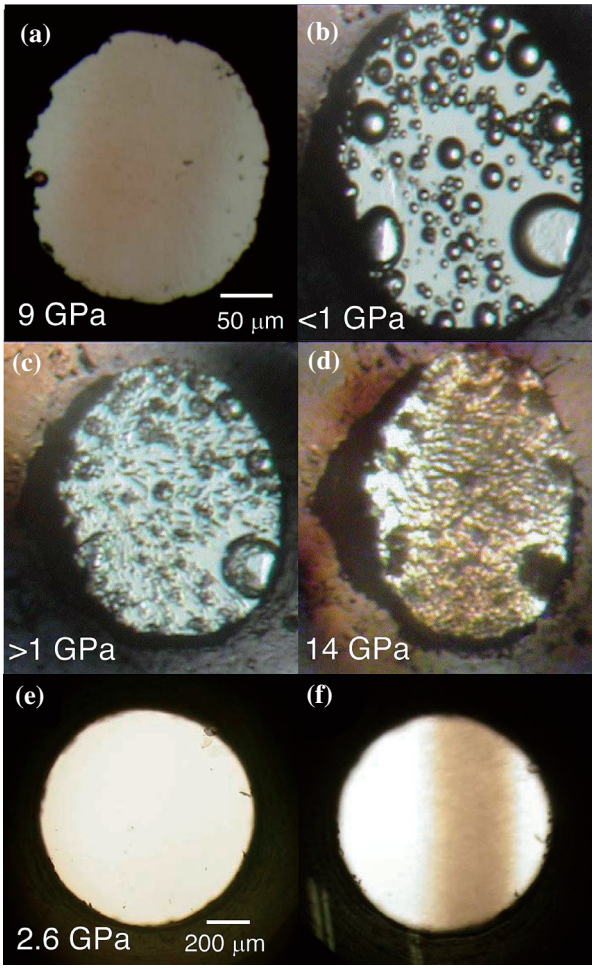

Fig. 2. Photomicrographs of two diamond anvil samples [1]. Top four panels were taken at beamline 13-IDC. **(a)** After XRS measurement at 8.8 GPa. The light brown streak through the middle of sample shows the portion irradiated by the X-ray beam. A small ruby ball on left edge of gasket was used for pressure calibration. **(b)** After release of pressure to below 1 GPa, bubbles of O_2 and H_2 formed. **(c)** Bubbles collapsed upon increase of pressure as the H_2 and O_2 were incorporated into the crystalline sample. **(d)** Sample after XRS measurement at 15.3 GPa. Bottom two panels were taken at BL12XU. **(e)** Before and **(f)** after X-ray exposure at 2.6 GPa.

References

[1] *W.L. Mao, H-k. Mao, Y. Meng, P.J. Eng, M.Y. Hu, P. Chow, Y.Q. Cai, J. Shu and R. Hemley: Science* ***314*** *(2006) 636.*

Materials Science
Electronic & Magnetic Properties

Materials science focused on electronic and magnetic properties continues to play one of the major roles at SPring-8. This chapter is organized into four parts: (1) inelastic X-ray scattering for investigating dynamical dielectric functions and particle-hole pair excitations in energy and momentum space, (2) fermiology using Compton scattering and angle resolved photoelectron spectroscopy (ARPES) methods applied to strongly correlated and heavy-electron systems, (3) excitation of atoms and molecules for studying decay processes, and (4) studies on magnetic and dielectric materials geared towards to device applications.

Recent progress and development on synchrotron X-ray sources like SPring-8 have encouraged the realization of sophisticated inelastic X-ray scattering and spectroscopic experiments, which have become powerful tools to investigate momentum- and energy-dependent charge and lattice dynamics, and electronic structures. This year, three inelastic X-ray scattering studies are highlighted. One is a non-resonant inelastic X-ray scattering on MgB_2, which was a recently discovered superconductor with a relatively simple crystal structure unlike high-T_C cuprates, to investigate dynamically screened electron-electron and electron-ion interactions. This work has led to the discovery of an interesting momentum dependence of single particle excitation. The second is a resonant inelastic X-ray scattering (RIXS) work on the charge-transfer Mott insulator $LaCuO_4$ with polarization and incident X-ray energy dependences to elucidate not only the nature of particle-hole excitations, but also the RIXS process and cross section. The third is a magnetic Compton scattering on the Perovskite manganites to examine the type of orbital nature in the valence band, which is a central issue in understanding the physical properties of this system. Since SPring-8 has a Compton dedicated beamline, this kind of experimental activity is quite high. Compton experiments can reveal the fermiology of electronic states. Here, we present two studies of ARPES, which is another method for fermiology, on strongly correlated electron and heavy electron systems. Since both works have been carried out with the use of soft X-rays, it can be said that the results are bulk-sensitive; in other words, the results are intrinsic. Then the results can be compared with directly sophisticate theoretical calculations. This opens up new possibilities of comparing theoretical and experimental results quantitatively.

What happens when an electron from an inner-shell orbital localized at a particular atomic site is ionized? The answer is well known in an isolated atom such that the ionized atom undergoes Auger decay. However, it is not so simple if other atoms exist in the vicinity of the excited atom. Morishita *et al.* have identified the interatomic Coulombic decay process, which was proposed theoretically, in the Ar dimer by an electron-ion coincidence technique. Another work on atoms and molecules is gas-phase soft X-ray electron spectroscopy for accurate determination of the vibrational fine structure in molecular core-level photoemission. A new finding, that is, a violation of the Franck-Condon principle, has been discovered experimentally on CH_4. Next, we show studies on magnetism. One is the diffraction work on a frustrated magnetic system under a very high pulsed magnetic field up to 40 T, in which it was found that the stepwise lattice contractions associated with multistep magnetization change in $CuFeO_2$. We show two works oriented to device applications and also related to nanotechnologies. X-ray magnetic circular dichroism (XMCD) is inherently an element specific and orbital selective experimental technique that has greatly contributed to our understanding of electronic structures/properties related to magnetism. XMCD combined with photoelectron emission microscopy (PEEM) has been applied to study the magnetic anisotropy and domain structure of the half-metallic ferromagnetic oxide $(LaSr)MnO_3$, which has been studied extensively for spintronic device applications. Another magnetic material, Mn-Ir/Co-Fe, which is one of the candidates for realizing high-density magnetic storage devices, has been studied to investigate the effect of Mn spins on giant exchange anisotropy by MCD. The last work in this chapter focuses on the effect of the size of dielectric materials on dielectric constant, which has been a topic of long-standing interest, and problems for device applications. Funakubo *et al.* have discovered size-effect-free materials with high dielectric constants in form of a film.

Please enjoy our showcase of studies on Materials Science.

Jun'ichiro Mizuki

Low-Energy Charge-Density Excitations in MgB_2: Striking Interplay between Single-Particle and Collective Behavior for Large Momenta

Magnesium diboride (MgB_2), discovered in 2001 as a superconductor with a high critical temperature (T_c) of nearly 40 K [1], has been subjected to intense theoretical and experimental studies worldwide. MgB_2 is now widely accepted as a phonon-mediated conventional superconductor based on the anisotropic Eliashberg formalism. The strong electron-phonon coupling between the 2D σ bands and the in-plane vibration of the B layers dominates the superconducting properties and is largely responsible for the unusually high T_c.

Within this phonon-mediated picture of superconductivity, dynamically screened electron-electron, and electron-ion interactions play an important role. Detailed knowledge of the dielectric screening and the associated crystal potential, local-field, and exchange-correlation effects should provide further insight into the dynamical property and hence the superconducting behavior of the material. Using state-of-the-art high-resolution nonresonant inelastic X-ray scattering (NIXS) experiments performed on the Taiwan Inelastic X-ray Scattering beamline **BL12XU**, we discover that the charge response of MgB_2 is truly remarkable [2]. Indeed, as is shown in Fig. 1, a long-lived, low-energy collective excitation in MgB_2 is found to exist not only for small momentum transfer (q) as previously predicted [3], but it actually extends to higher Brillouin zones (BZ's) along the c* axis, displaying a consinelike, periodic energy dispersion with q. Experimentally, the energy dispersion can be described entirely by a simple cosine function: $\omega = \omega_0 - 2\gamma\cos(qc)$, with ω_0 = 3.55 eV, γ = 0.49 eV, and c = 0.352 nm, the lattice constant of MgB_2 along the c* axis. The enhanced scattering cross section at high q and the negligible multiple-scattering effects of the X-ray measurements play a decisive role for the clean observation of this excitation over a large momentum range.

In order to understand the physics behind the data presented in Fig. 1, we have calculated the dynamical structure factor S(q, ω) based on *ab initio* time-dependent density-functional theory (TDDFT), including fully the crystal local-field effects (CLFE). The details can be found in Ref. [2]. The calculated S(q, ω) is compared with the experiment in Fig. 2. The energy dispersion of the collective excitation (dashed curve) can be seen to agree almost perfectly with experiment throughout the four BZ's investigated. Based on the mathematical analysis of the formalism used in the calculation [2], the significance of the

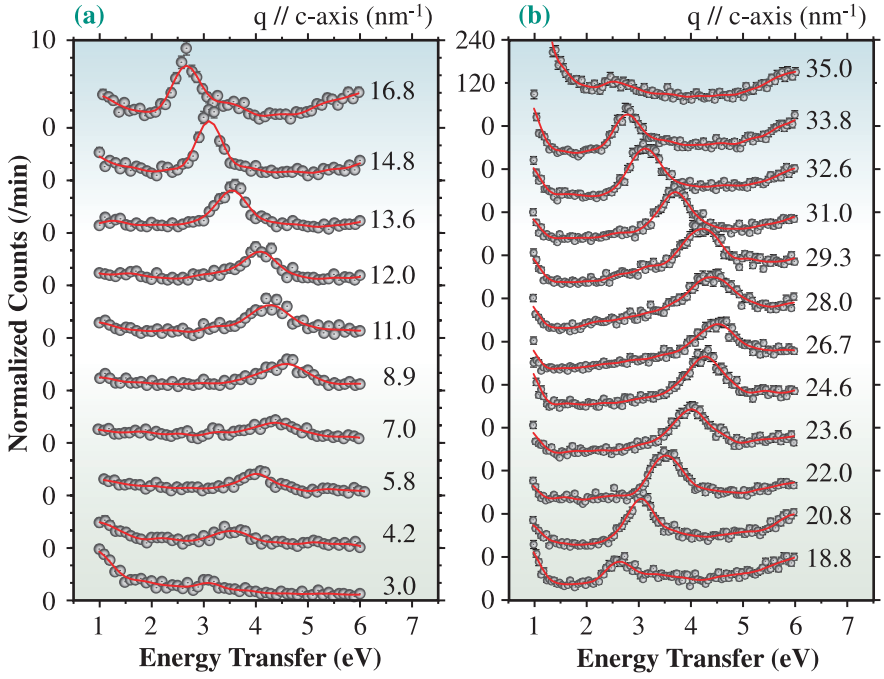

Fig. 1. NIXS spectra at various momentum transfers along the c* axis. The total energy resolution was 65 meV for **(a)** and 250 meV for **(b)**.

agreement is traced back to the fact that the dynamical response represented by S(q, ω) for q's in higher BZ's contains essentially the contribution of two terms: The first term corresponds to the response appropriate for homogeneous media and gives rise to charge fluctuations involving incoherent electron-hole pairs. The second term introduces all the CLFE in the form of a coupling function (*F*), which formally feeds the small-q charge response into charge fluctuations for large q's [2]. It should be noted that the coupling function is *material dependent*, whose actual strength determines whether such excitation can be realized in S(q, ω).

Indeed, in Fig. 3, the contribution to the S(q, ω) of MgB_2 from the first and second terms are shown for q = 32.7 nm^{-1} in the fourth BZ along the c* axis. Clearly, within the energy region of the excitation, the first term amounts only to a weak background, while the second term features a sharp peak, which is typical of the collective excitation for the reduced q (= 2.9 nm^{-1}) in the first BZ. The strength of *F* as shown in the inset of Fig. 3 is ~60 times larger in MgB_2 compared to simple metals and covalent semiconductors. Therefore, in MgB_2 *F* feeds the small-q physics into the charge fluctuation for large q's, and the collective excitation can be viewed as acting – via *F* – as a source driving the collective charge fluctuation generated in a NIXS event for large q's. It is important to notice that this process is intrinsically periodic [2].

In conclusion, the electron-hole degrees of freedom in MgB_2 lead to a novel charge response in which long-lived, collective charge-density fluctuations can be excited in a NIXS event involving large momenta. The mechanism behind the observed periodic excitation is the strong coupling between the single-particle and collective excitation channels, mediated by large CLFE due to charge inhomogeneity normal to the Mg and B layers. The impact of the CLFE on the charge response of MgB_2 rivals their importance in materials involving confined geometries such as carbon nanotubes and superlattices. Ultimately, the nature of the measured charge excitations stems from the layered electronic structure of MgB_2 and the delocalized nature of the orbitals involved in the screening. Analogous physics should be at play in other layered compounds of current interest.

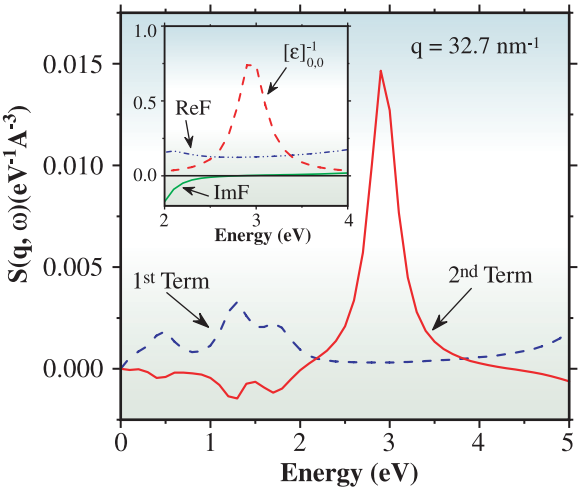

Fig. 3. Contributions from the first and second terms to S(q, ω) of MgB_2 at q = 32.7 nm^{-1} along the c* axis. The inset shows the real and imaginary parts of the coupling function (*F*) and the charge response (ε^{-1}) for q = 2.9 nm^{-1}. See Ref. [2] for further details.

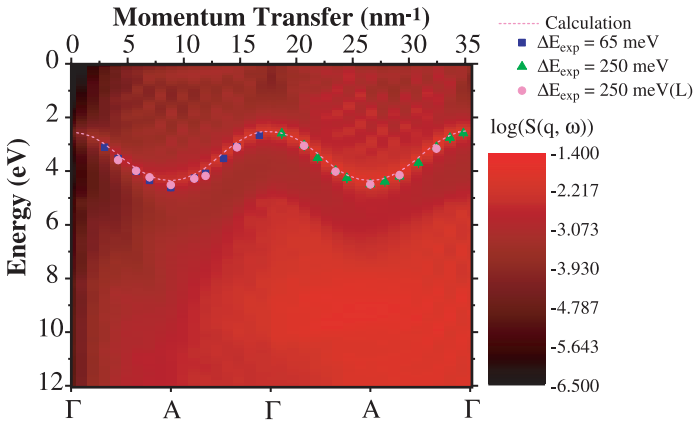

Fig. 2. Theoretical S(q, ω) in false color log scale as a function of energy and momentum transfer showing the cosine energy dispersion of the low-energy collective excitation. Filled symbols (■▲●) marks the energy positions obtained from the NIXS spectra.

Y.Q. Cai[a,*] and A.G. Eguiluz[b,c]

[a] National Synchrotron Radiation Research Center, Taiwan
[b] Department of Physics, The University of Tennessee, USA
[c] Materials Science and Technology Division, Oak Ridge National Laboratory, USA

*E-mail: cai@nsrrc.org.tw

References

[1] J. Nagamatsu *et al.*: Nature **410** (2001) 63.
[2] *Y.Q. Cai, P.C. Chow, O.D. Restrepo, Y. Takano, K. Togano, H. Kito, H. Ishii, C.C. Chen, K.S. Liang, C.T. Chen, S. Tsuda, S. Shin, C.C. Kao, W. Ku, and A.G. Eguiluz: Phys. Rev. Lett.* ***97*** *(2006) 176402.*
[3] W. Ku *et al.*: Phys. Rev. Lett. **88** (2002) 057001.

Incident Energy and Polarization Dependent RIXS Study of La_2CuO_4

Resonant Inelastic X-ray scattering (RIXS) is a novel technique used widely [1-5] to probe the valence structure of many classes of materials. When momentum selectivity is used in Cu *K* edge RIXS, one can follow the dispersion of particle-hole pair excitations. The nature of particle-hole excitations in charge-transfer insulators is of high interest to the field of high-temperature superconductivity.

La_2CuO_4 is an archetypal two-dimensional (2D) charge-transfer insulator. Strong Coulomb repulsion favors localization of carriers, and is responsible for insulating behavior. Meanwhile a small hopping integral prefers an antiferromagnetic state at temperatures below about T_N~320 K.

In comparison to non-resonant inelastic X-ray scattering, the RIXS process is poorly understood. Recent work [5] has emphasized the role of the incident photon energy to preferentially enhance particular excitations in the high-T_c superconductor $HgBa_2CuO_{4+d}$, but very little work has been reported on the polarization dependence of the momentum-selective RIXS cross section. With that in mind, in an international collaborative effort involving measurements at the Advanced Photon Source and SPring-8, we present a systematic study of the incident polarization and incident energy dependence of the RIXS cross section at the Cu *K* edge of La_2CuO_4.

Figure 1 shows the incident energy-dependent effect clearly in the context of La_2CuO_4 at a momentum transfer corresponding to the Brillouin zone center. Here we can identify clearly three peaks

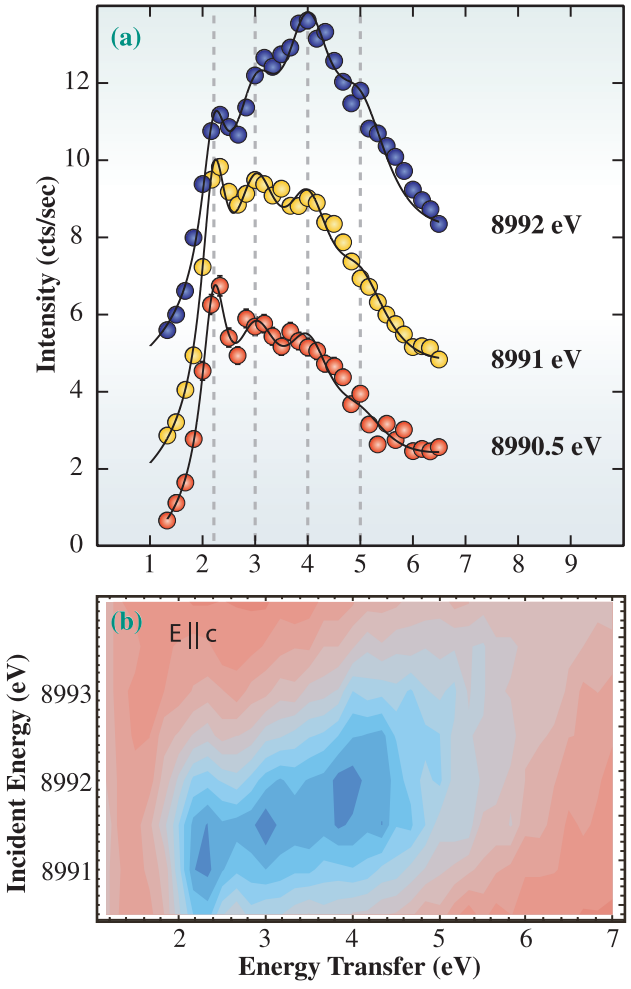

Fig. 1. **(a)** Three scans showing the incident energy dependent effect on the RIXS cross section of La_2CuO_4. **(b)** A contour plot constructed from seven such linescans. Features are clearly discernible at 2.25, 3.0, and 4.0 eV.

at 2.25, 3.0, and 4.0 eV, in contrast to previous studies on this system which could only resolve one [4] or two [2] features in this spectral range. We have extended this result to finite momentum and catalogued the appearance of features at select momentum transfers points throughout the 2D Brillouin zone of the CuO_2 plane. A similar analysis serves to identify a multiplet of weakly dispersive features.

Figure 2 summarizes the results of our analysis of the incident energy and momentum dependent RIXS spectra. Striking similarities and differences are present in the dispersive behavior of the particle-hole excitations. For example, a distinct softening of the 2.25 eV feature occurs when the polarization is chosen to lie in the CuO_2 plane. This effect is most likely either a result of the symmetry of the excitations involved or a resonance enhancement effect. This phenomenology indicates that, like the incident energy, the polarization degree of freedom is an important parameter of the RIXS process.

The appearance of multiple features in the 1-7 eV region of this charge-transfer insulator reveals the complexity of the energy structure in transition metal oxides. Positive identification Positive identification of the features eludes researchers at the moment, but theoretical modeling is likely to benefit our understanding of these excitations.

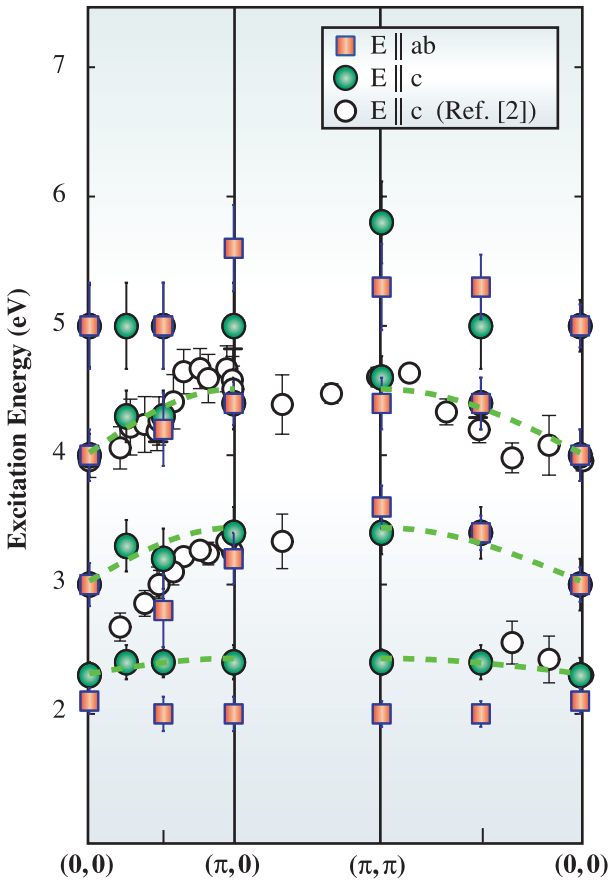

Fig. 2. Dispersion of identifiable features across the 2D Brillouin zone. This figure also shows the polarization dependence.

Jason N. Hancock[a,*], Guillaume Chabot-Couture[b] and Martin Greven[a,b]

[a] Stanford Synchrotron Radiation Laboratory, USA
[b] Department of Applied Physics, Stanford University, USA

*E-mail: jhancock@stanford.edu

References

[1] *L. Lu, J.N. Hancock, G. Chabot-Couture, K. Ishii, O.P. Vajk, G. Yu, J. Mizuki, D. Casa, T. Gog and M. Greven: Phys. Rev. B* ***74*** *(2006) 224509.*
[2] Y.J. Kim *et al.*: Phys. Rev. Lett. **89** (2002) 177003.
[3] M.Z. Hasan *et al.*: Science **288** (2000) 1811.
[4] P. Abbamonte *et al.*: Phys Rev. Lett. **83** (1999) 860.
[5] L. Lu *et al.*: Phys. Rev. Lett. **95** (2005) 217003.

Coexistence of Localized and Itinerant e_g Electrons in a Bilayer Manganite

Perovskite manganites are intriguing materials as a subject of research because of a variety of physical properties, such as metal-insulator transition, colossal magnetoresistance effect, charge ordering, and orbital ordering. In these systems, the Mn-3*d* electronic state, which is split into the e_g and t_{2g} orbitals in the crystal field of MnO_6 octahedron, is responsible for the physical properties. Thus far, the ferromagnetic metal (FM) state below T_c has been explained on the basis of the double exchange mechanism in which the spin degree of freedom is taken into account. Recent studies on manganites have opened our eyes anew to the importance of the orbital degree of freedom as well as charge and spin ones. In this study, two-dimensional spin momentum density (2D-SMD) has been reconstructed from directional magnetic Compton profiles (MCPs) measured in a bilayer manganite and has been examined from the viewpoints of the momentum wave functions derived from both molecular orbital and band calculations in order to verify the localized and/or itinerant characteristics of the Mn-3d electronic state [1].

MCP, $J_{mag}(p_z)$, is defined as

$$J_{mag}(p_z) = \iint (\Sigma|\chi_{i\uparrow}(\mathbf{p})|^2 - \Sigma|\chi_{j\downarrow}(\mathbf{p})|^2)\, dp_x dp_y, \quad (1)$$

where p_z is an electron momentum component along the scattering vector of X-rays, and $\chi_{i\uparrow(\downarrow)}(\mathbf{p})$ is a momentum wave function of the *i*-th electron with an up spin (down spin) in the initial state. As shown by eq. (1), $J_{mag}(p_z)$ is represented as the double integral of the difference in momentum density, $|\chi_i(\mathbf{p})|^2$, between the majority and minority spin states with respect to p_x and p_y. Thus, the integrated intensity of $J_{mag}(p_z)$ is proportional to the amount of spin magnetic moments in a ferromagnetic sample, and the shape of $J_{mag}(p_z)$ depends on both the orbitals occupied by magnetic electrons and observation directions when we measure MCP in a single crystal. These features enable us to evaluate the occupation number with respect to each orbital on the basis of the fact that the spins in Mn-3*d* orbitals induce the magnetization of manganite system. When we measure a number of MCPs in different directions, SMD can be reconstructed from them. This approach reveals the Mn-3*d* electronic state visually.

The sample used is a single crystal of $La_{2-2x}Sr_{1+2x}Mn_2O_7$ with x = 0.35. The Brillouin zone shows almost a two-dimensional nature because of a structural feature, that is, MnO_2 bilayers alternate with $(La,Sr)_2O_2$ blocking layers along the *c* axis. According to the magnetic phase diagram determined by neutron-diffraction measurement, the present sample shows an in-plane ferromagnetic structure below

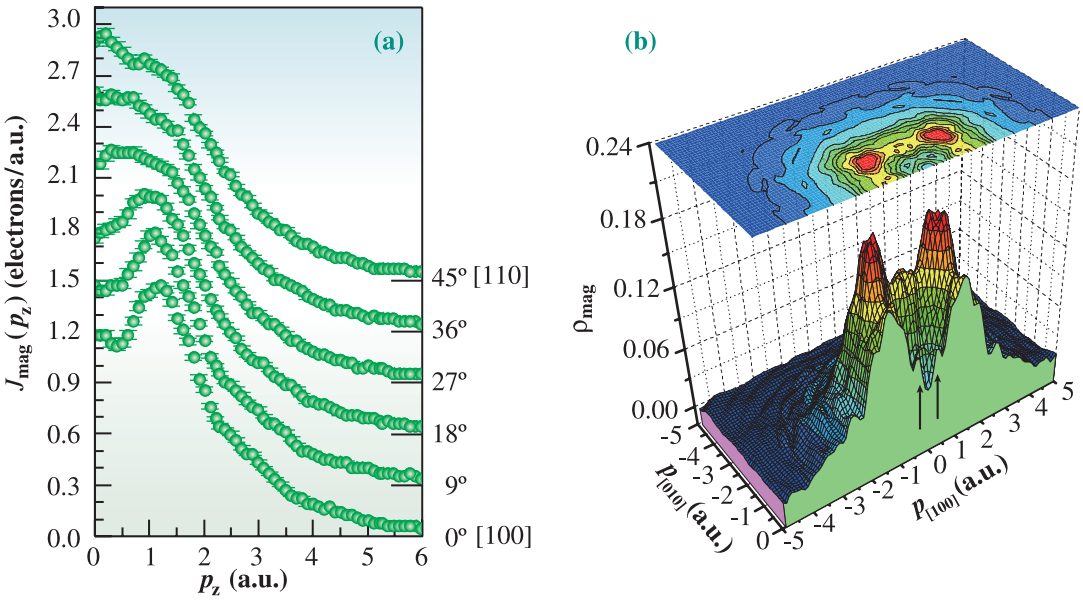

Fig. 1. MCPs and 2D-SMD. **(a)** Directional MCP's measured between the [100] and [110] axes at intervals of 9°. **(b)** 2D-SMD projected on (100) plane, which was obtained by the expansion of the measured area according to structural symmetry.

T_c (≈ 125 K) [2]. MCP measurement was performed at beamline **BL08W**. An external magnetic field of ±2.5 T was alternately applied to the sample at 10 K. The magnetic effect was obtained using the difference between the two Compton profiles measured in the opposite field directions.

Figure 1(a) shows the MCPs measured between the [100] and [110] axes at 9° intervals. The orbital structure, which consists of the t_{2g} and e_g orbitals, is clearly reflected in the change in MCP depending on observation direction. The 2D-SMD, which is the projection of the spin momentum density of Mn-3*d* orbitals on the (001) plane, was reconstructed from the directional MCPs by using the direct Fourier-transform method as shown in Fig. 1(b) [3]. In order to evaluate orbital occupancy, we derived the 2D-SMDs of the $x^2 - y^2$, $3z^2 - r^2$ and t_{2g} orbitals from the result of a molecular orbital calculation for $(MnO_6)^{8-}$ cluster [4], and fitted them to the experimental 2D-SMD. The occupation numbers obtained are 0.39, 0.23 and 3.03 for the $x^2 - y^2$, $3z^2 - r^2$ and t_{2g} orbitals, respectively, indicating the dominance of the $x^2 - y^2$ orbital in the e_g state. We also derived the theoretical 2D-SMD from the result of a local spin density approximation band calculation and compared it with the experimental 2D-SMD. The theoretical 2D-SMD externally appears to reproduce the experimental one. Then, the Lock-Crisp-West (LCW) folding method [5], which transforms the momentum density to an occupation-number density (OND) in the first Brillouin zone, was applied to both the 2D-SMDs. The obtained result is shown in Fig. 2. The upper and lower left panels indicate the 2D-ONDs derived from the experimental and theoretical 2D-SMDs, respectively. In the figure, t_{2g}-like bands basically draw a flat structure because of full occupancy, emphasizing on e_g-like bands. The electron pocket around the Γ point, the zonal distribution along the $k_{[100]}$ and $k_{[010]}$ axes, and hole pockets around corners are consistent between the two 2D-ONDs, while the dense areas around both ends of the axes cannot be explained only by the present band calculation. The discrepancy would be understood by considering the contribution of a molecular orbital, because the small but sharp peaks denoted by arrows in Fig. 1(b) well reflect a hybridization effect between the $x^2 - y^2$ and O-2*p* orbitals. Then, we tentatively obtained the 2D-OND of the $x^2 - y^2$ orbital, although the LCW method ought to be basically applied to the momentum density described by the Bloch state. The result shown in the lower right panel of Fig. 2 well explains the dense areas in the experimental 2D-OND. This is considered an indicator of the coexistence of localized and band like e_g electrons in the FM state below T_c.

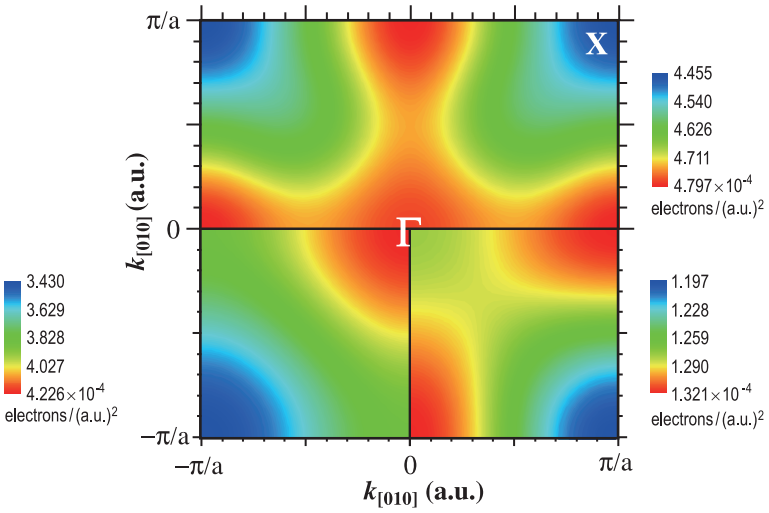

Fig. 2. 2D-OND derived from experimental 2D-SMD (upper), band calculation (lower left) and $x^2 - y^2$ orbital (lower right).

Akihisa Koizumi

Graduate School of Material Science, University of Hyogo

E-mail: akihisa@sci.u-hyogo.ac.jp

References

[1] *A. Koizumi, T. Nagao, N. Sakai, K. Hirota and Y. Murakami: Phys. Rev. B* ***74*** *(2006) 012408.*
[2] M. Kubota *et al.*: J. Phys. Soc. Jpn. **69** (2000) 1606.
[3] Y. Tanaka *et al.*: J. Phys. Chem. Solids **61** (2000) 365.
[4] A. Koizumi *et al.*: Phys. Rev. Lett. **86** (2001) 5589.
[5] D. G. Lock *et al.*: J. Phys. F: Met. Phys. **3** (1973) 561.

Electronic Structure of Heavy Fermion Superconductors

The discovery of superconductivity in heavy fermion (HF) compounds has stimulated the studies of this class of materials [1]. Recently, a "high-T_C" superconductivity of T_C = 18 K was discovered in $PuCoGa_5$ [2], indicating that there remains an unexplored class of exotic superconductors in HF compounds. In these compounds, the superconductivity coexists or competes with magnetic ordering, and this is the most characteristic feature of HF superconductors. It has been proposed that these properties originated from the dual character of *f* electrons, i.e., their localized and delocalized characters [3]. However, their detailed electronic structures have not been studied yet, and the nature of *f* electrons as well as the mechanism of the superconductivity originating from such electrons are not well understood. To reveal the electronic structures of HF superconductors, we have performed angle resolved photoemission specroscopy (ARPES) experiments for typical HF superconductors, namely. UPd_2Al_3 and $CeIrIn_5$. UPd_2Al_3 shows an antiferromagnetic transition at T_N = 14 K, and undergoes a transition into the superconducting state at T_C = 2 K. $CeIrIn_5$ is a HF superconductor with T_C = 0.4 K. Although it does not show the magnetic ordering, $CeRh_{1-x}Ir_xIn_5$ exhibits both superconductivity and antiferromagnetic (AF) ordering in $0.3 < x < 0.6$ [4], suggesting that the ground state of $CeIrIn_5$ is very close to the magnetic ordering state. The Fermi surfaces of both compounds, at low temperatures were investigated by dHvA experiments, and they were well explained by the band structure calculations [5,6]. Therefore, it is considered that *f*-electrons have strong itinerant character in these compounds. Photoemission experiments were mainly performed at SPring-8 beamline **BL23SU**. 4*d*-4*f* resonant ARPES experiment for $CeIrIn_5$ was performed at Hiroshima Synchrotron Radiation Research Center (HiSOR) BL-1.

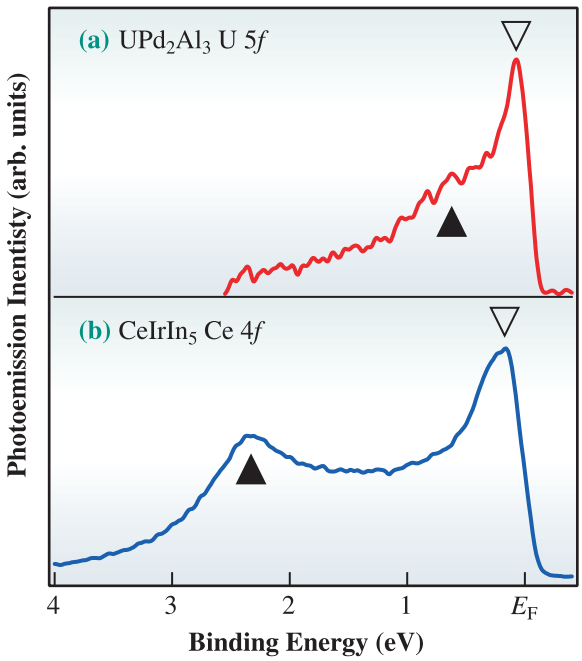

Fig. 1. **(a)** U 5*f* spectrum of UPd_2Al_3 and **(b)** Ce 4*f* spectrum of $CeIrIn_5$.

Figure 1 shows the *f*-derived angle-integrated photoemission (AIPES) spectra of UPd_2Al_3 and $CeIrIn_5$. The U 5*f* spectrum of UPd_2Al_3 was obtained by subtracting the photoemission spectra measured at $h\nu$ = 400 eV and $h\nu$ = 800 eV, and the Ce 4*f* spectrum of $CeIrIn_5$ was obtained using 3*d*-4*f* resonant photoemission ($h\nu$ = 881.2 eV). Both spectra have two pronounced components as indicated by the triangles in the figure. One is located around E_F, and the other is located on the deeper binding energy side. The relative intensities and the positions of this broad satellite differ markedly between UPd_2Al_3 and $CeIrIn_5$. These satellites originate from the electron correlation effects, which cannot be taken into account by band structure calculations. The Ce 4*f* spectrum of $CeIrIn_5$ is essentially understood within the framework of the single impurity model, suggesting that Ce 4*f* electrons in this compound are dominated by the localized character. On the other hand, the U 5*f* spectrum of UPd_2Al_3 is dominated by the strong quasi-particle peak located near E_F, and the intensity of the correlated feature is much weaker than that of CeIrIn5.

Figure 2 shows ARPES spectra of UPd_2Al_3 measured for A-H-L direction at $h\nu$ = 465 eV and ARPES spectra of $CeIrIn_5$ measured for Γ-X direction at $h\nu$ = 122 eV. For both directions of Brillouin zone, Fermi surfaces with large contribution from *f* states are expected in band structure calculations. In these spectra, the contribution from U 5*f* states or Ce 4*f* states is dominant. For UPd_2Al_3, some dispersive bands were clearly observed in the ARPES spectra, suggesting that the U 5*f* states have strong itinerant character. On the other hand, the ARPES spectra of $CeIrIn_5$ have the double peak structure arising from the spin-orbit interaction. In contrast to the case of

UPd_2Al_3, their momentum dependence is very small, suggesting that the 4*f* electrons are dominated by the localized character. A detailed analysis of ARPES spectra suggests that the peak near E_F has a small energy dispersion of ~30 meV [7], and that this might be the origin of the observed itinerant nature of Ce 4*f* states in this compound. Therefore, we have observed the very different natures of *f* electrons in UPd_2Al_3 and $CeIrIn_5$. For UPd_2Al_3, although a correlated feature exists, the itinerant nature dominates the spectra. Meanwhile, for $CeIrIn_5$, the localized nature dominates the spectra, and the contribution from itinerant states is very small. The present results bring us a step closer to understanding the of dual natures of *f* electrons in HF superconductors [8].

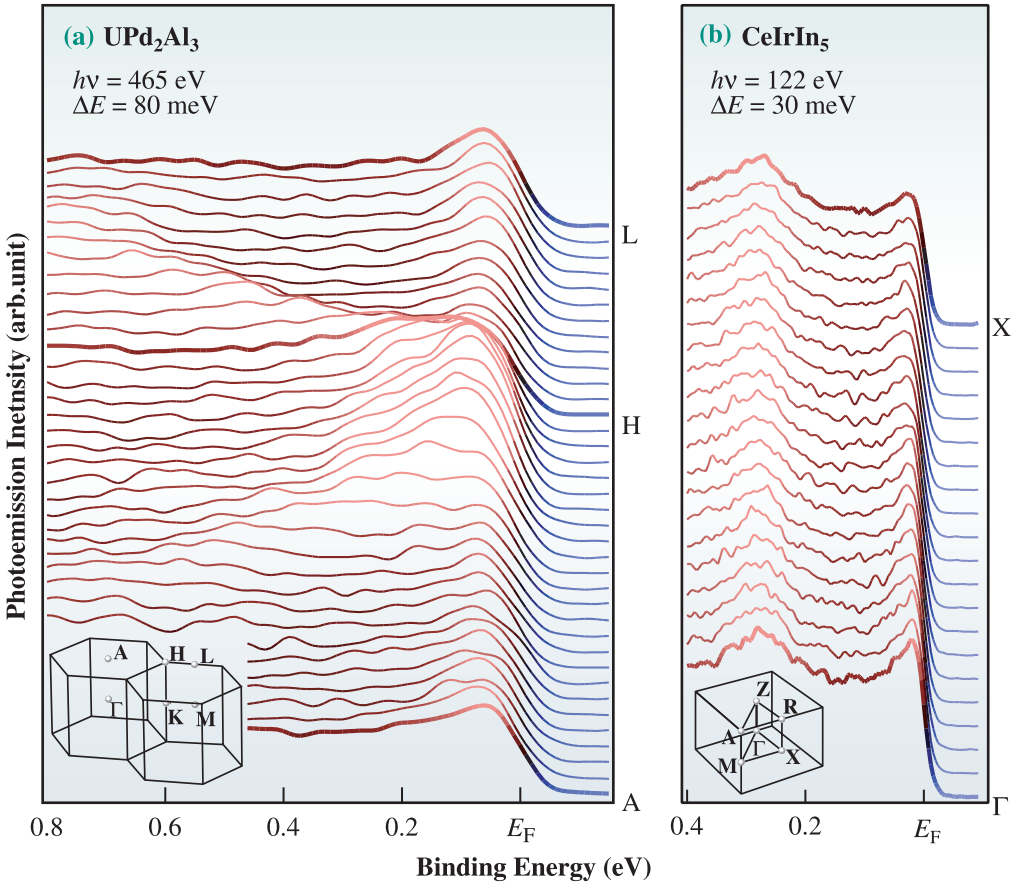

Fig. 2. **(a)** ARPES spectra of UPd_2Al_3 measured at $h\nu$= 465 eV and **(b)** ARPES spectra of $CeIrIn_5$ measured at $h\nu$= 122 eV.

Shin-ichi Fujimori

SPring-8 / JAEA

E-mail: fujimori@spring8.or.jp

References

[1] W. Assumes *et al.*: Phys. Rev. Lett. **52** (1984) 130.
[2] J.L. Sarrao *et al.*: Nature **420** (2002) 297.
[3] N.K. Sato *et al.*: Nature **410** (2001) 340.
[4] P.G. Pagliuso *et al.*: Phys. Rev. B **64** (2001) 100503(R).
[5] Y. Inada *et al.*: J. Phys. Soc. Jpn. **68** (1999) 3643.
[6] Y. Haga *et al.*: Phys. Rev. B **63** (2001) 060503(R).
[7] *S.I. Fujimori, A. Fujimori, K. Shimada, T. Narimura, K. Kobayashi, H. Namatame, M. Taniguchi, H. Harima, H. Shishido, S. Ikeda, D. Aoki, Y. Tokiwa, Y. Haga and Y. Ónuki: Phys. Rev. B* ***73*** *(2006) 224517.*
[8] *S.I. Fujimori, Y. Saitoh, T. Okane, H. Yamagami, A. Fujimori, K. Shimada, H. Namatame, M. Taniguchi, H. Shishido, D. Aoki, S. Ikeda, Y. Haga, E. Yamamoto, and Y. Ónuki: Physica C - in press.*

Electronic Structure of $LaNiO_3$ Thin Films Studied by Soft X-ray Angle Resolved Photoemission Spectroscopy

Perovskite nickel oxides $RNiO_3$ (R: rare earth) are well known to show interesting behaviors such as metal-insulator transitions, spin and orbital ordering, etc. $LaNiO_3$ (LNO), which is the reference material of the series, exhibits Pauli paramagnetic metal behavior at any temperature (T); however, while the other members (e.g., R = Pr, Nd, Sm) show T-dependent phase transitions [1]. The specific heat and susceptibility data, as well as T^2 dependence of resistivity of LNO suggest that this compound is well described as a strongly correlated system. An enhanced effective mass ($m^* \sim 10m_b$) is also well established. Although growing a single crystal of $RNiO_3$ is very difficult, single crystalline epitaxial thin films have been successfully synthesized for device applications.

Angle-resolved photoemission spectroscopy (ARPES) is one of the most powerful methods to directly investigate the momentum-resolved electronic structures of solids. However, ARPES measurements carried out using vacuum ultraviolet (VUV) photons strongly depends on the surface condition owing to very low photoelectron mean free paths. Recent progress in instrumentation for high-resolution soft X-ray (SX) ARPES has made it possible to perform *in situ* ARPES measurements to reveal the bulk electronic structure of compounds.

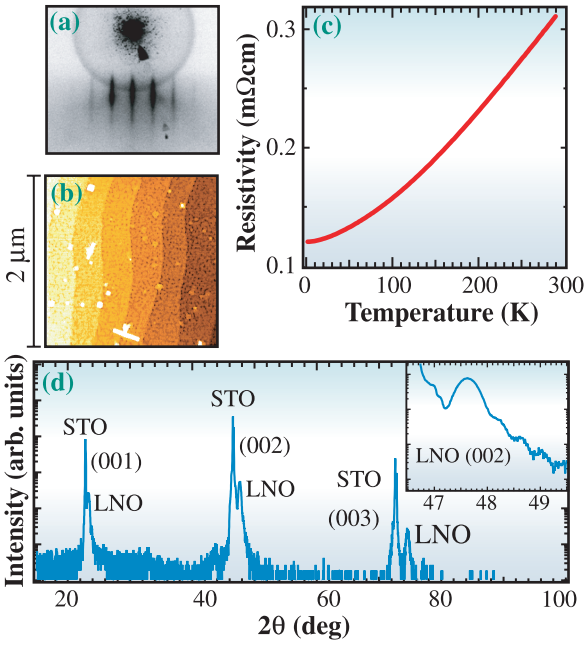

Fig. 1. **(a)** RHEED pattern, **(b)** AFM image, **(c)** temperature dependence of resistivity, and **(d)** XRD pattern (Inset: expansion graph in the vicinity of the (002) Bragg peak) of LNO films grown on STO (001) substrates.

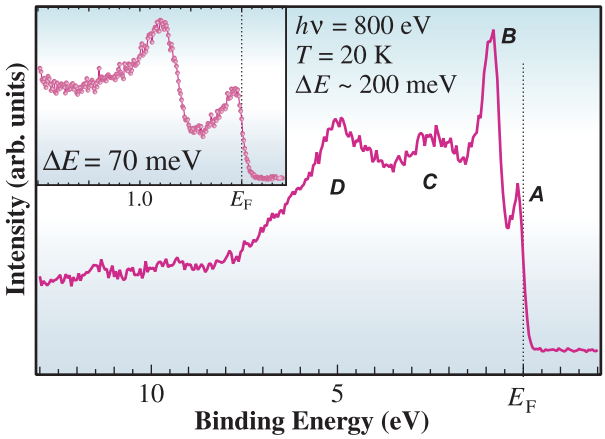

Fig. 2. *In situ* valence band photoemission spectrum of LNO films. The inset shows high-resolution ($\Delta E \sim 70$ meV) photoemission spectrum of near-E_F region.

The fabrication of LNO thin films and SX-photoemission measurements were carried out using a high-resolution synchrotron radiation PES system combined with a pulse laser deposition chamber at beamline **BL17SU** [2]. The LNO films were grown on $SrTiO_3$ single-crystal substrates. A sintered stoichiometric LNO pellet was used as an ablation target. A Nd YAG laser was used in its frequency-tripled mode (λ = 355 nm) at a repetition rate of 1 Hz. The STO substrates were annealed at 900 °C at an oxygen pressure of 1×10^{-4} Pa before deposition. The substrate temperature was set to 650 °C and the oxygen pressure was 10 Pa during the deposition. The LNO films were subsequently annealed at 400 °C for 30 minutes at the atmospheric pressure of oxygen to remove vacancies. After cooling the sample to below 100 °C and evacuating the growth chamber, the surface morphology and crystallinity of the fabricated LNO films were checked by an *in situ* observation of reflection high-energy electron diffraction (RHEED) patterns. The sharp streak pattern shown in Fig. 1(a) indicates a high-quality and smooth film. After PES measurements, the samples were characterized *ex-situ* in terms of surface morphology by atomic force microscopy (AFM), electrical resistivity by 4-probe method, and crystal structure by X-ray diffraction (XRD) analysis [Fig. 1(b,c,d)] [3].

The *in situ* angle-integrated PES spectra of the fabricated LNO thin films are shown in Fig 2. The features labeled A and B are Ni 3*d* e_g and t_{2g} states,

respectively, which were not resolved clearly in previous PES spectra of polycrystalline LNO. The higher binding energy features labeled C and D are attributed to the O 2*p* dominant states [3].

We also performed photon-energy dependent SX-ARPES measurements of the LNO films to probe the 3-dimensional Fermi surfaces (FSs) of LNO. The FSs obtained from a band structure calculation [4] and the region probed in the Brillouin zone (BZ) are shown in Fig. 3(a), respectively. Figure 3(b) (top panel) shows FS mapping in the k_x-k_z plane obtained by changing the photon energies from $h\nu$ = 570 to 700 eV. We can clearly observe the electron FS located around the Γ-point, as predicted by the band structure calculation. After thus determining the k_z dispersions and the center of the electron FS surface accurately, we then measured tilt angle dependence using a photon energy of 630 eV. As shown in Fig. 3(b) (bottom panel), in addition to the electron FS, the edge of the hole like FS located around the R-point in the BZ was observed. Figure 3(c) shows band maps for two cuts marked in Fig. 3(b). In cut1, the experimentally determined band dispersion results in the formation of the electron FS, while in cut2, the bands forming the hole like FS are unambiguously identified. These bands and FSs are responsible for the strongly correlated properties of LNO.

The successful mapping of 3-dimensional FSs using *in situ* SX-ARPES measurements of LNO thin films thus opens up exciting possibilities for studying the momentum-resolved electronic structure of 3-dimensional highly correlated materials undergoing phase transitions.

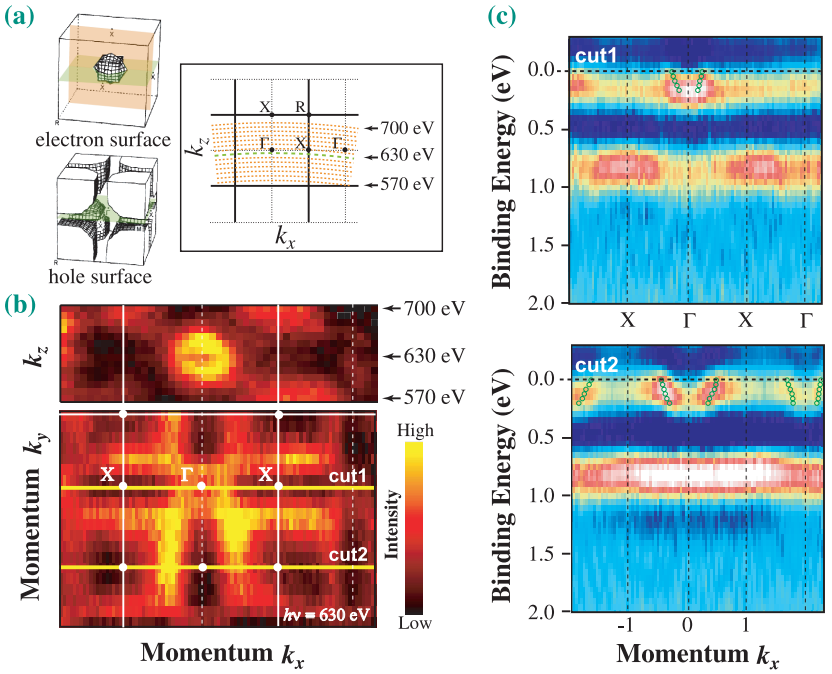

Fig. 3 **(a)** Fermi surface (cubic notation) of LNO obtained from a band structure calculation [4] and the momentum region probed by SX-ARPES of this study. **(b)** Fermi surface mapping obtained by SX-ARPES. **(c)** Second-derivative intensity maps for two cuts marked in **(b)**.

Shik Shin

SPring-8 / RIKEN

E-mail: sshin@spring8.or.jp

References

[1] J.B. Torrance *et al.*: Phys. Rev. B **45** (1992) 8209.
[2] K. Horiba *et al.*: J. Electron Spectrosc. Relat. Phenom. **144-147** (2005) 1027.
[3] *K. Horiba, R. Eguchi, M. Taguchi, A. Chainani, A. Kikkawa, Y. Senba, H. Ohashi and S. Shin: cond-mat/0606192.*
[4] N. Hamada *et al.*: J. Phys. Chem. Solids **54** (1993) 1157.

Interatomic Coulombic Decay from Auger Final States in Argon Dimer

It is well known that an isolated atom in an inner-shell excited state decays through a cascade of radiative and/or Auger transitions. As a result, photons and electrons are emitted at specific energies to the atom. Many analytical methods, such as electron spectroscopy, are based on this fact and used nowadays as key techniques in many studies including those at SPring-8. Then, what will happen when other atoms exist in the vicinity of the excited atom? Generally, it is considered that the neighboring atoms merely distort or shift the energy spectrum. However, recent theoretical [1] and experimental [2-4] studies demonstrated that the excited atom can decay through a new mechanism called interatomic Coulombic decay (ICD). In the ICD, the excited atom can decay through the transfer of its excitation energy to the neighboring atom and an ICD electron is emitted. Although we report here a result for the argon dimer in Auger final states as a simplified example, the ICD can be expected to occur after Auger decay in any systems including biomolecules in water. It is worth noting that DNA is damaged not only by primary energetic radiations (X-, γ- and β-rays) but also, perhaps more efficiently, by an electron at energy lower than 20 eV [5] and that the energy of the ICD electron is generally low (<10 eV).

Experiments were carried out at the soft X-ray photochemistry beamline **BL27SU** with an operation mode of 6/42 filling + 25 bunch. Argon dimers were produced through the expansion of cooled argon gas (130 K and 1.3 bar) via an aperture of 50 μm diameter [4]. The dimers produced were irradiated using monochromatized soft X-rays at 257 eV, i.e., about 10 eV above the 2*p* ionization threshold of the atomic argon. The electrons and ions produced were accelerated toward position-sensitive detectors, which are installed face to face. We measured the time-of-flights (TOFs) and detection positions of all charged particles (except energetic Auger electrons) in coincidence, and determined the 3-dimensional momenta of all charged particles emitted upon ionization and subsequent fragmentation. Each detector can detect up to six electrons/ions for one ionization event.

Figure 1 shows the TOF spectrum derived with the ion-ion coincidence mode. The x and y coordinates correspond to the TOFs of the first and second ions. Two curved lines show the (A):Ar^++Ar^+ and (B):Ar^++Ar^{2+} coincidences because the Ar^+ and Ar^{2+} ions with zero kinetic energy result in the TOFs of 5.1 and 3.5 μs, respectively. In fact, the atomic ions have large initial kinetic energies owing to a mutual Coulombic repulsion and the dimer has a random orientation with respect to the spectrometer axis. As a result, the coincidence TOF spectra have significantly broad distributions, as shown in Fig. 1.

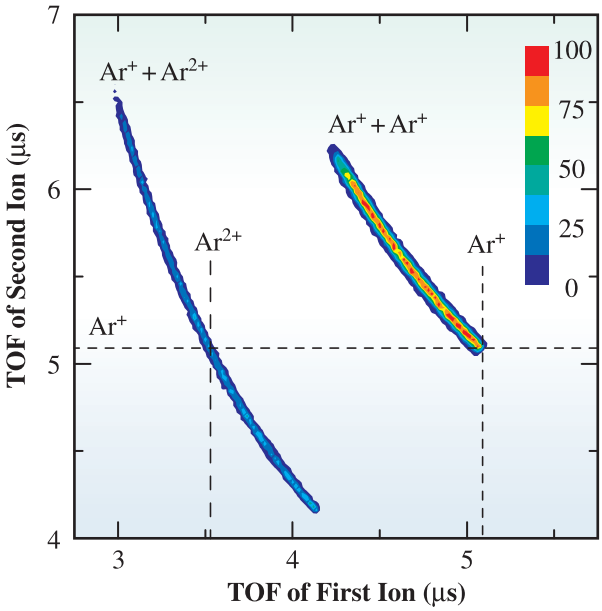

Fig. 1. Time-of-flights (TOFs) of ions from argon dimers. The dashed lines show the TOFs of ions with zero kinetic energy.

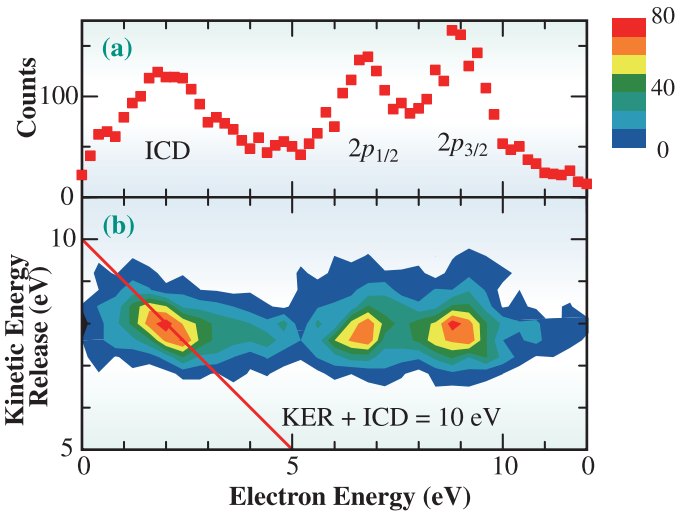

Fig. 2. **(a)** Electron spectrum of argon dimers. **(b)** Correlation between electron energy and kinetic energy release by fragment argon ions.

By limiting the gate on Ar^{+}+Ar^{2+} coincidence signals, we determined events in which the dimer dissociates into an Ar^{+}+Ar^{2+} ion pair and obtained the electron energy spectrum (see Fig. 2(a)). The two peaks at 6.5 and 8.7 eV correspond to photoelectrons from the Ar2$p_{1/2}$ and 2$p_{3/2}$ inner shells, and the peak at 2 eV originates from the ICD electrons, as described below. Figure 2(b) shows the correlation between the electron energy and the kinetic energy release (KER) by the Ar^{+}+Ar^{2+} pair. The photoelectron peaks have almost no correlation with the KER, while the ICD peak tilts with a slope of -1, suggesting that the sum of the ICD electron energy and KER is constant (~10 eV). It was also confirmed that the ICD electron energy is independent of the photon energy, while the two photoelectron peaks shift according to the photon energy.

Figure 3 shows the energy levels relevant to ICD emission. Most of the $2p^{-1}$ states in the photoionized dimer decay to $nl^{-1}nl'^{-1}$ states (n = 3) via conventional Auger transitions, forming Ar^{2+}+Ar Auger final states, i.e., the dimer consisting of a doubly charged ion and a neutral atom. These Auger final states cannot decay further through electron emission if the atomic Ar^{2+} ion is isolated because the triple ionization threshold (84.13 eV) is above these states. However, the decay becomes possible if an ICD electron can be emitted from the neighboring Ar atom. If we consider the ionization of the outermost electron from an Ar atom (15.76 eV), the sum of the Ar^{2+} and Ar^{+} energies at the dissociation limit are about 10 eV below $Ar^{2+}(3p^{-3}3d)$ Auger final states. The Coulombic repulsion energy between Ar^{2+} and Ar^{+} is about 8 eV at a nuclear distance of 3.8 Å (i.e., the equilibrium bond distance of a neutral dimer). Thus, the $Ar^{2+}(3p^{-3}3d)$+Ar of the Auger final states and $Ar^{2+}(3p^{-2})$ + $Ar^{+}(3p^{-1})$ at distances ~3.8 Å provide an energy of ~2 eV to the ICD electron emitted from the neighboring Ar atom.

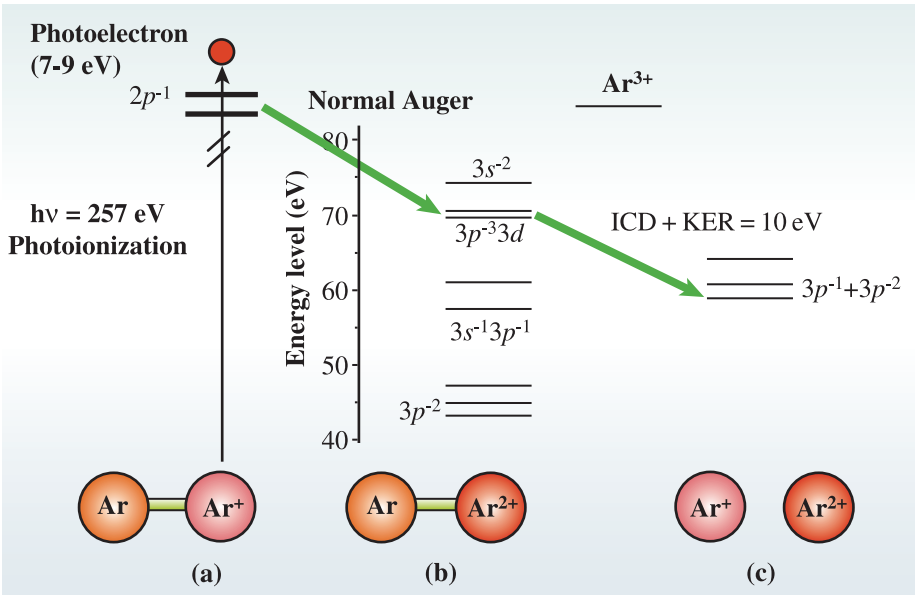

Fig. 3. Energy levels relevant to ICD electron emission.

Y. Morishita[a,*], N. Saito[a], I.H. Suzuki[a] and K. Ueda[b]

[a] National Institute of Advanced Industrial Science and Technology (AIST)
[b] Institute of Multidisciplinary Research for Advanced Materials, Tohoku University

*E-mail: aist-morishita@aist.go.jp

References

[1] L.S. Cederbaum *et al.*: Phys. Rev. Lett. **79** (1997) 4778.
[2] T. Jahnke *et al.*: Phys. Rev. Lett. **93** (2004)163401.
[3] *Y. Morishita, X.-J. Liu, N. Saito, T. Lischke, M. Kato, G. Prümper, M. Oura, H. Yamaoka, Y. Tamenori, I.H. Suzuki, and K. Ueda: Phys Rev. Lett.* ***96*** *(2006) 243402.*
[4] X.-J. Liu *et al.*: J. Phys. B: At. Mol. Phys. **40** (2007) F1 and references therein.
[5] B. Boudaïffa *et al.*: Science **287** (2000)1658.

Recoil Effects in High-energy Molecular Core-level Photoemission

One of the main historical challenges and goals of gas-phase soft X-ray electron spectroscopy has been accurate determination of the vibrational fine structure in molecular core-level photoemission [1]. Reliable values of vibrational constants and intensity ratios are a prerequisite for determining quantities of fundamental physical and chemical significance, such as ionization energies and chemical shifts. Core-level photoelectron spectra are an excellent source for this information. It has been customary to assume that well above the core-ionization threshold, the vibrational structure of the photoelectron spectrum is entirely determined by the well-known Franck-Condon principle. We have demonstrated experimentally, on the example of methane, that this in not the case and that, in fact, a violation of the Franck-Condon principle takes place due to the photoelectron recoil effect.

Methane (CH_4) is a tetrahedral molecule, which has four normal vibrational modes – symmetric and asymmetric stretch of the C-H bonds and two bending modes. When a carbon 1*s* electron is removed by photoemission, the molecular potential changes and the nuclear geometry will change towards its new equilibrium. As the adjustment – shortening of the C-H bonds – is centrally symmetric, the motion is the same as in the symmetric stretch vibrational mode. The result is the excitation of a symmetric stretch vibrational progression, observed in the C 1*s* photoelectron spectrum of CH_4 (Fig. 1), and theoretically described by the Franck-Condon factors. In our experiment [2], performed at beamline **BL27SU**, the photoelectron spectra were recorded using a high-resolution Scienta SES-2002 analyzer.

As required by the momentum conservation law, the departing photoelectron with a certain energy and momentum gives the molecule a ***recoil momentum*** of equal magnitude. The key question is, how is this momentum shared between the nuclei of the molecule? If the molecule would receive the momentum as a rigid body, a *translational* recoil would take place, and we would only observe a small energy loss in the electron spectrum. However, one has to take into account that: (i) core-level photoemission is very well localized to a single atom, the *emitter* and, (ii) the time-scale for ejecting the electron from the molecule is much shorter than the molecular vibrational period. These conditions mean that the recoil momentum is first received solely by the *emitter* atom and is later distributed to the whole molecule through the molecular bonds. The energy and momentum conservation determines the momentum given to each atom (neglecting the quantum effects for now). The end result is that we have both *translational* and *vibrational* recoil, i.e., the recoil momentum can also induce molecular vibrations.

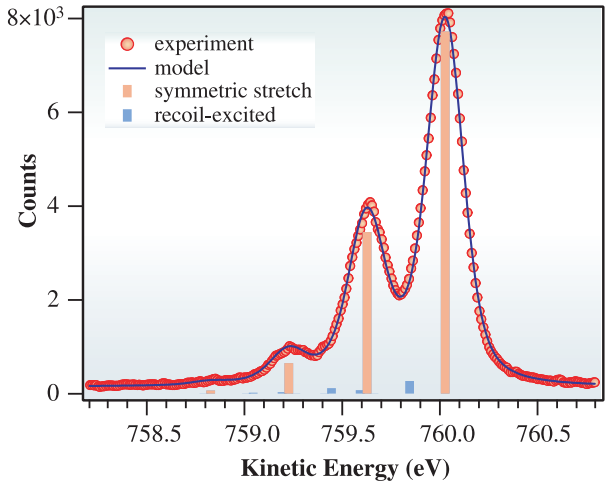

Fig. 1. Carbon 1*s* photoelectron spectrum of methane, excited with 1050 eV photons, and its vibrational structure [2].

The effects of recoil in C 1*s* photoemission from methane are shown in Fig. 2. Initially, the carbon atom gets a momentum away from the center of the

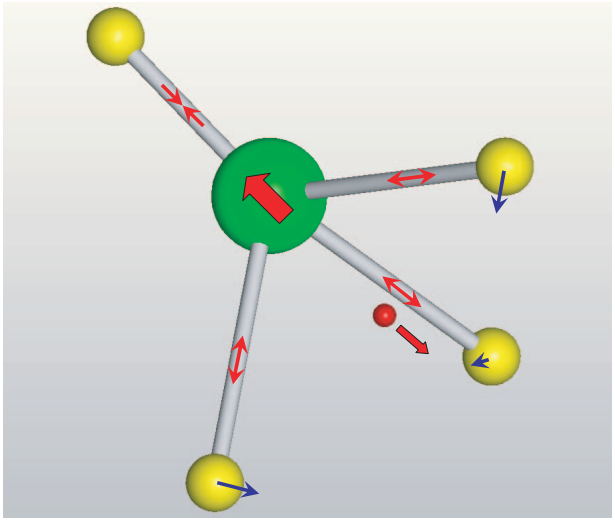

Fig. 2. Recoil excitation of the asymmetric stretch (red arrows) and bending (blue arrows) vibrational modes in a methane molecule, following C 1*s* photoemission.

molecule – a molecular-frame motion that corresponds to a combination of two vibrational modes: the asymmetric stretch and one bending mode. Thus, these two modes can become excited by recoil and the excitation probability increases with the photoelectron (and photon) energy: the higher above the threshold, the stronger the effect becomes. Note that these are *different* modes than the symmetric stretch excited on the basis of the Franck-Condon principle.

Quantum mechanically, the recoil vibrational excitations are quantized, with the average energy given by the classical model. The theory of recoil excitations can be handled conveniently in the momentum space, where one arrives at expressions much akin to the familiar Franck-Condon integrals in the coordinate space. Based on the recoil momentum, molecular symmetry and vibrational wavefunctions in the momentum space, we predicted the recoil-induced changes in the photoelectron spectrum. A new vibrational structure starts to appear (see Fig. 1), although it is still weak at these electron energies. However, this allowed us to solve the puzzle of apparent long-range photon energy dependency in the vibrational brancing ratios of the dominant symmetric stretch progression (Fig. 3). It turned out that the symmetric stretch structure itself does not change, but a new structure, albeit yet unresolved, starts to appear. If the spectrum is still analyzed as if due to a single vibrational mode, then the intensity ratios become distorted by the underlying recoil excitations.

Recent studies [3] have shown that recoil effects play a role also in the core-level photoemission from solids. Future studies using harder X-rays would make the recoil effects much more pronounced, providing access to the vibrational modes that are otherwise hidden, or would even dissociate the molecules.

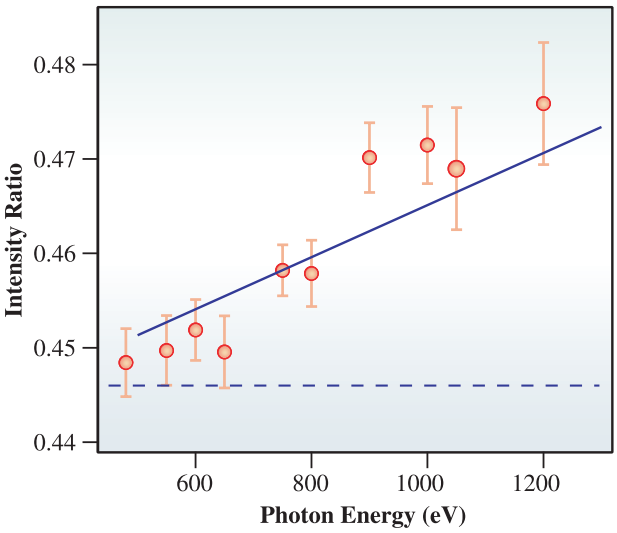

Fig. 3. Conventional analysis of the C 1*s* photoelectron spectrum using only the symmetric stretch progression. Experimental intensity ratio of the v = 1 and v = 0 peaks shows a rising trend, which is explained by taking into account the distortion by the underlying recoil excitations (blue line).

Edwin Kukk[a,*] and Kiyoshi Ueda[b]

[a] Department of Physics, University of Turku, Finland
[b] Institute of Multidisciplinary Research for Advanced Materials, Tohoku University

*E-mail: edwin.kukk@utu.fi

References

[1] K. Siegbahn: Electron spectroscopy for atoms, molecules and condensed matter: In G. Ekspong, editor, Nobel Lectures in Physics 1981-1990, World Scientific, 1993.
[2] *E. Kukk, K. Ueda, U. Hergenhahn, X.-J. Liu, G. Prümper, H. Yoshida, Y. Tamenori, C. Makochekanwa, T. Tanaka, M. Kitajima and H. Tanaka: Phys Rev. Lett.* ***95*** *(2005) 133001.*
[3] T. Fujikawa *et al.*: J. Electron Spectrosc. Relat. Phenem. **151** (2006) 170; Y. Takata *et al.*: Phys. Rev. B **75** (2007) 233404.

Field-induced Lattice Staircase in a Frustrated Antiferromagnet $CuFeO_2$

Let us consider three spins placed on the vertices of a triangle with a nearest neighbor antiferromagnetic interaction, *J*, which is a system depicted in Fig. 1(a). Two of the three spins form a state of lowest energy when their moments are aligned anti-parallel with each other, but the third one cannot find a stable alignment. This triangular coordination is called "geometrical spin frustration." Although theory predicts that the 2D Ising triangular lattice antiferromagnet (TLA) does not exhibit magnetic order at any finite temperature, real materials with the triangular lattice structure often achieve a magnetic ordering by distorting the lattice symmetry, as illustrated in Fig. 1(b).

$CuFeO_2$ is an archetype TLA. It has the delafossite structure (space group $R\bar{3}m$ at room temperature, displayed in Fig. 1(c). The magnetic structure in zero field is the collinear four-sublattice (4SL) ↑↑↓↓ structure below 11 K [see Fig. 3(b)] [1]. This ground state is realized by distorting the lattice as described above [2,3].

We have performed synchrotron X-ray Bragg diffraction measurements under very high magnetic fields at beamline **BL19LXU**, using a single crystal of $CuFeO_2$ [4]. A pulsed field magnet, up to 40 T, has been developed in collaboration with the ISSP, University of Tokyo and KYOKYGEN, Osaka University [5].

Figure 2 shows the results obtained from our measurements. The lattice constant b_{orth} [with orthorhombic notation shown in Fig. 3(a)] is seen to exhibit stepwise changes with increasing magnetic field in coincidence with multistep magnetization changes. We see that lattice changes scale nicely with magnetization changes.

We discuss the origin of the stepwise changes in the lattice constant *b*. The nearest neighbor exchange interaction in the basal plane of $CuFeO_2$ is a sum of the direct exchange interaction, which is assumed to be ferromagnetic, and the 90° antiferromagnetic superexchange interaction through an O^{2-} ion [1]. The experimental evidence that the b_{orth} axis elongates at low temperature in zero field [2], implies that the direct exchange interaction diminishes and the antiferromagnetic interaction dominates. In the 4SL phase [see Fig. 3(b)], all spins connected by the nearest neighbor J'_1 bonds along the b_{orth} axis are antiferromagnetically aligned; in other words, the spin arrangement in the J'_1 row is ↑↓↑↓. As shown in Fig. 3(c), in the five-sublattice phase ($13 \leq H \leq 20$ T), one of the five bonds along the J'_1 row in the unit cell accommodates two parallel spins at the ends and costs excess energy. In order to lower this excess in the exchange energy, b_{orth} axis contracts to resume the ferromagnetic direct exchange interaction. Similarly, in the three-sublattice phase ($20 \leq H \leq 34$ T)

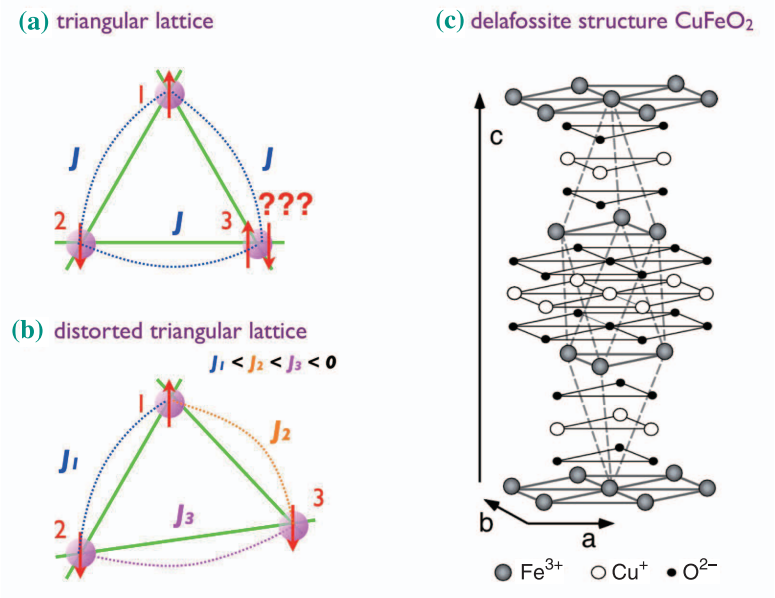

Fig. 1. Three spins placed at the vertices of **(a)** a triangle and **(b)** a distorted triangle resulting in difference in the exchange interactions. **(c)** Delafossite crystal structure of $CuFeO_2$.

[see Fig. 3(d)], one of the three bonds along the J'_1 row in the unit cell accommodates two parallel spins at the ends, so that an additional lattice contraction along the b_{orth} is needed. In these field-induced lattice changes, we expect that a uniform distortion will occur rather than a local distortion at the "wrong" bonds. This explains qualitatively the stepwise lattice contractions in b_{orth} associated with the multistep magnetization changes in $CuFeO_2$.

Our unique apparatus, combining strong magnetic field and synchrotron X-rays, opens a new field in materials science research. Many interesting phenomena are expected to occur in magnetic materials as well as superconductors at high magnetic fields. The duration of the pulsed magnetic field is 5 - 25 milli-seconds and consequently, we need strong X-rays to obtain reliable data. BL19LXU is best suited for this purpose, since the World's strongest high energy X-rays are available at this beamline.

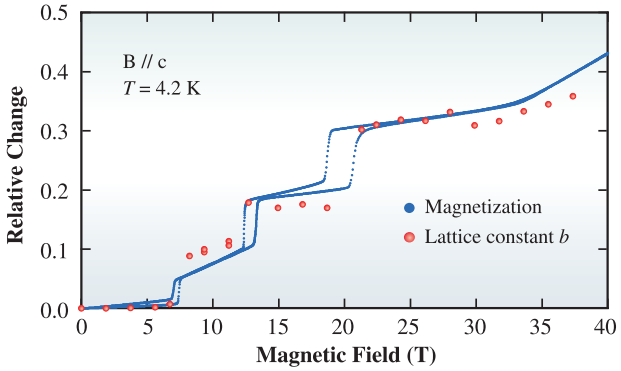

Fig. 2. Magnetic field dependence of the relative changes of the magnetization normalized with the saturation moment 5 μB of Fe^{3+} (blue circles) and the fractional change of the lattice constant (red circles), $\alpha[b_{orth}(B = 0\ T) - b_{orth}(B)] / b_{orth}(B = 0\ T)$, where α is a numerical factor. The measurements were done at $T = 4.2$ K.

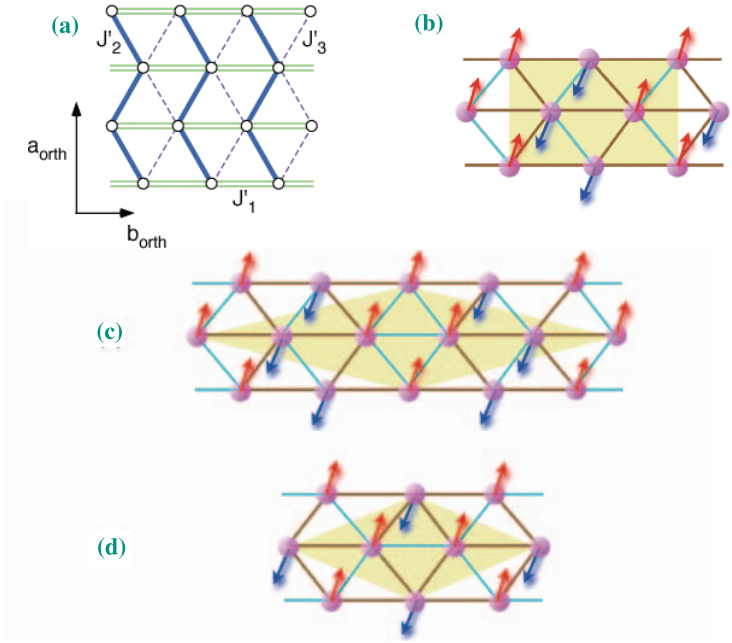

Fig. 3. **(a)** The exchange interaction paths in the basal plane. The spin structures in the basal plane of **(b)** the four-sublattice ↑↑↓↓ state, **(c)** the five-sublattice ↑↑↑↓↓ state and **(d)** the three-sublattice ↑↑↓ state. Blue and brown bonds denote ferromagnetic and antiferromagnetic arrangements, respectively. The magnetic unit cells in the respective phases are marked with yellow.

Noriki Terada[a,b,*], Yasuo Narumi[c] and Koichi Katsumata[a]

[a] SPring-8 / RIKEN
[b] National Institute for Materials Science
[c] ISSP, The University of Tokyo

*E-mail: TERADA.Noriki@nims.go.jp

References

[1] M. Mekata *et al.*: J. Phys. Soc. Jpn. **62** (1993) 4474.
[2] N. Terada *et al.*: J. Phys. Soc. Jpn. **75** (2006) 023602.
[3] N. Terada *et al.*: J. Phys. Soc. Jpn. **75** (2006) 113702.
[4] *N. Terada, Y. Narumi, K. Katsumata, U. Staub, K. Kindo, M. Hagiwara, Y. Tanaka, A. Kikkawa, H. Toyokawa, T. Fukui, R. Kanmuri, T. Ishikawa and H. Kitamura: Phys. Rev. B* ***74*** *(2006) 180404(R).*
[5] Y. Narumi *et al.*: J. Synchrotron Rad. **13** (2006) 271.

Direct Observation of Step-induced Magnetic Domain Formation in Manganite Films

There has been a great deal of interest recently in a spin tunnel junction employing half-metallic ferromagnets as electrodes because of their potential applications to future spintronic devices. The half-metallic ferromagnetic oxide $La_{0.6}Sr_{0.4}MnO_3$ (LSMO) is one of the most promising materials for spintronic devices owing to full spin polarization of its conduction carriers and high Curie temperature of 350 K [1]. However, in spite of intensive studies, a high performance device has not been realized. To improve the performance of an LSMO-based spintronic device, it is indispensable to obtain the information on the magnetic anisotropy and domain structure of LSMO films.

Photoelectron emission microscopy (PEEM) combined with X-ray magnetic circular dichroism (XMCD) is a powerful technique for studying this issue. Since XMCD provides information on the magnetization vector projected in the incident direction of a synchrotron radiation (SR) beam, it is possible to obtain all the three independent components of the magnetization vector by rotating the sample. The mapping of the magnetization distribution with a high spatial resolution enables us to observe the magnetic domain structures in ferromagnteic materials (Fig. 1). To determine the complex magnetic domain structure of LSMO films, we have performed the direct XMCD-PEEM observation of the in-plane magnetic domain structure of LSMO films epitaxially grown on stepped $SrTiO_3$ (STO) substrates [2]. XMCD-PEEM experiments were carried out using Elmitec PEEMSPECTOR at the soft-X-ray undulator beamline **BL25SU** [3].

Figures 2(a) and 2(b) show the magnetic domain images of LSMO films obtained at the azimuthal angles of 0° and 90° between the incident SR beam direction and the [100] direction, respectively. The bright and dark parts in the images correspond to magnetic domains with magnetization vectors parallel and antiparallel to the incident SR beam, respectively. The elongated magnetic domains along the [100] direction can be clearly observed in Fig. 2(a), where the incident SR beam is parallel to the [100] direction. The existence of “stripe” domains is clearly indicative of the uniaxial magnetic anisotropy of LSMO thin films. The uniaxial magnetic anisotropy may be induced by the step structure along the [100] direction on the surface of LSMO films (see the inset in Fig. 2(a)),

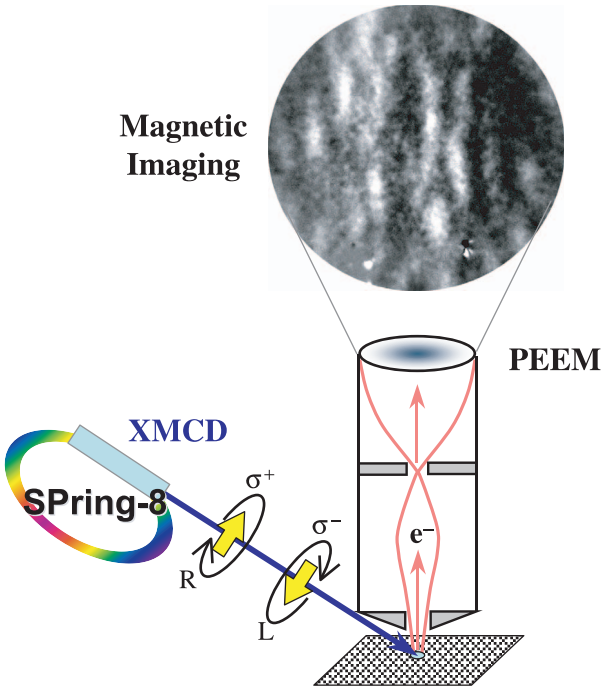

Fig. 1. Schematic illustration of XMCD-PEEM observation.

since the [100] and [010] directions are crystallographically equivalent in the case of LSMO films grown on STO substrates.

The uniaxial nature was further confirmed by measuring the azimuthal angle dependence of domain contrast in XMCD-PEEM images. As expected, the contrast between the stripe domains disappears completely when the direction of the SR beam is perpendicular to the step direction, as shown in Fig. 2(b). Instead, we can see a weak bubble-like contrast in Fig. 2(b), which suggests the existence of additional magnetization components perpendicular to the step direction. Such magnetic domain formation strongly suggests the presence of an additional magnetic anisotropy, namely, a biaxial magneto-crystalline anisotropy, with the easy axis along the [110] direction in LSMO films grown on STO substrates [4].

The direct observation of the magnetic domain structure by XMCD-PEEM suggests that the competition between two magnetic anisotropies, namely, the step-induced uniaxial magnetic and biaxial magnetocrystalline anisotropies, plays an important role in defining the magnetic properties of LSMO films and also provides the possibility of controlling the magnetic domain structure of LSMO films by the competition between the two magnetic anisotropies with different symmetries. Moreover, the present study demonstrates the usefulness and reliability of XMCD-PEEM for studying the magnetic anisotropy and domain structure of magnetic materials. We hope that this study promotes further XMCD-PEEM works on various types of magnetic materials for spintronic devices at SPring-8 in the near future.

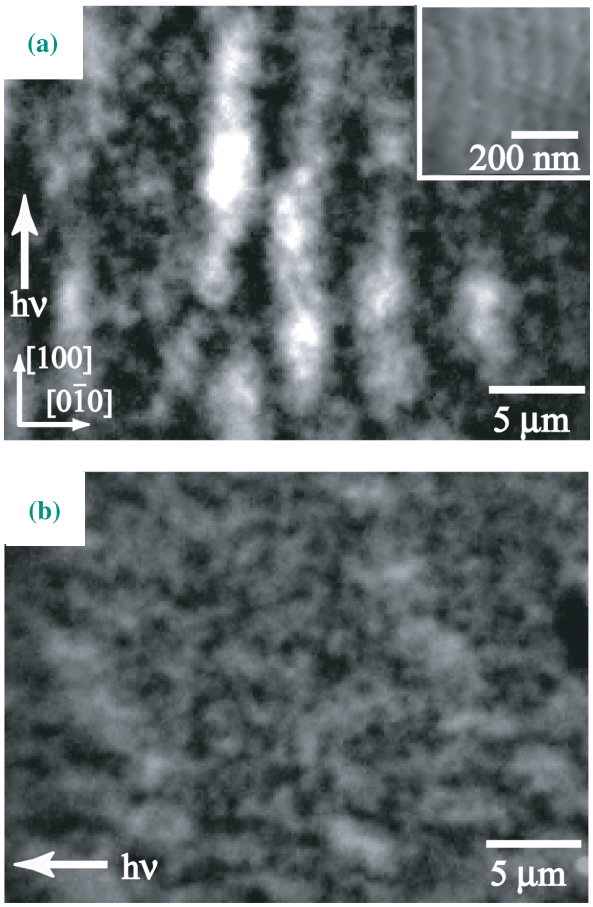

Fig. 2. Magnetic images of ferromagnetic LSMO film obtained at photon energy corresponding to Mn L_3-edge. The incident direction of the synchrotron radiation beam was parallel to the **(a)** [100] and **(b)** [010] directions. The atomic step direction is aligned with the [100] direction, as shown in the atomic force microscopic image in the inset.

Hiroshi Kumigashira*, Toshiyuki Taniuchi and Masaharu Oshima

Department of Applied Chemistry,
The University of Tokyo

*E-mail: kumigashira@sr.t.u-tokyo.ac.jp

References

[1] H. Yamada *et al.*: Science **305** (2004) 646.
[2] H. Kumigashira *et al.*: Appl. Phys. Lett. **82** (2003) 3430.
[3] *T. Taniuchi, H. Kumigashira, M. Oshima, T. Wakita, T. Yokoya, M. Kubota, K. Ono, H. Akinaga, M. Lippmaa, M. Kawasaki, H. Koinuma: Appl. Phys. Lett. **89** (2006) 112505.*
[4] M. Mathews *et al.*: Appl. Phys. Lett. **87** (2005) 242507.

Microscopic Origin and Role of Uncompensated Antiferromagnetic Spins in Mn-Ir Based Exchange Biased Bilayers

The exchange bias of ferromagnetic (FM) / antiferromagnetic (AFM) bilayers, characterized by a horizontally shifted magnetization hysteresis loop, is an indispensable physical phenomenon for the realization of high-density magnetic storage devices, such as hard disk drives (HDDs) and magnetic random access memories (MRAMs). A strong exchange biasing property is required to achieve a high storage density. While the microscopic mechanism of the exchange bias has been the subject of extensive studies for the last 50 years, it is not yet completely understood. The information required to clarify the mechanism is the asymmetry of a spin structure in a bilayer system, which is obviously required to provide exchange anisotropy, against the reversal of a practical external magnetic field. As the only candidate that mediates the spin motion from the FM layer to the AFM layer during the magnetic field reversal, uncompensated AFM spins might play a key role in the magnetization of the AFM layer and likely be a clue for investigating the asymmetric spin structure formed in the AFM layer. X-ray magnetic circular dichroism (XMCD) in a *transmission mode* is a powerful tool for detecting the uncompensated AFM spins at the buried interface because of its element selectivity and excellent sensitivity. We thus investigated the microscopic origin [1] and role of the exchange anisotropy [2] of the uncompensated AFM spins by XMCD spectroscopy at beamline **BL25SU** for Mn-Ir based exchange biased bilayers, which are widely used for the application of HDDs and MRAMs nowadays.

The AFM layer thickness (d_{AF}) dependences of (a) X-ray absorption spectra (XAS) and (b) XMCD spectra at Mn $L_{2,3}$-edges were measured for $Mn_{73}Ir_{27}$ / $Co_{70}Fe_{30}$ bilayers. The X-ray beam was incident on the sample surface at an angle of 30°. A magnetic field of +14 kOe was applied along the axis rising 20° from the sample surface. As d_{AF} increases, the resonant absorption magnitude at the respective L-edge naturally increases (Fig. 1(a)), depending on the effective volume of Mn absorption. On the other hand, the XMCD magnitude at the respective resonant peak does not markedly change (Fig. 1(b)), indicating that uncompensated Mn moments resulting in an XMCD signal do not exist homogeneously in the entire Mn-Ir layer. From an inverse-proportion of the normalized XMCD magnitude by resonant absorption against d_{AF} (not shown), it was confirmed that the uncompensated Mn moments are localized at the interface of less than a few monolayers between the FM and AFM layers. The FM layer material greatly affects the uncompensated Mn moments and changes the sign and magnitude of the XMCD signal. Furthermore, no MCD signal is observed on the spectrum, when the FM layer is detached from the Mn-Ir layer. We thus

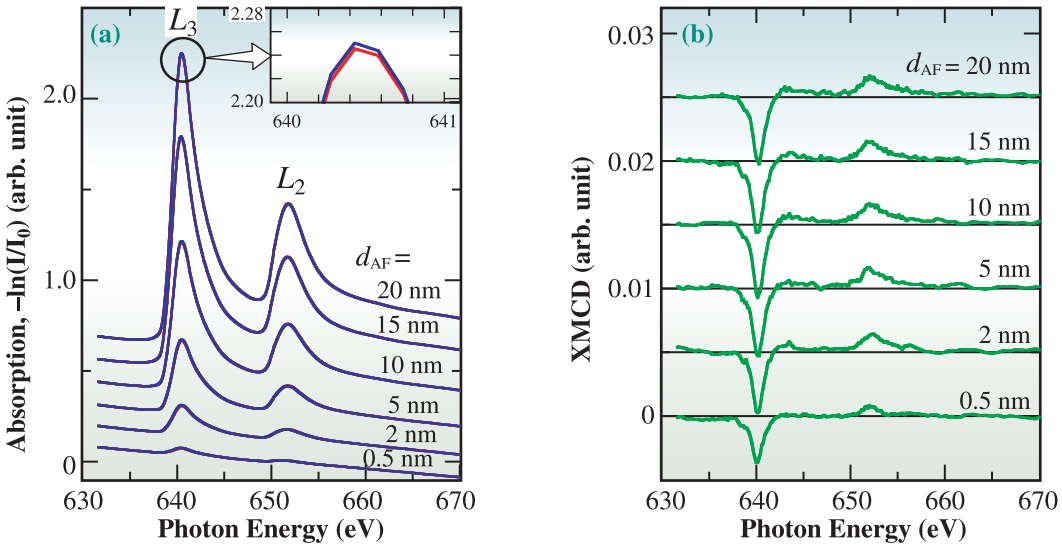

Fig. 1. **(a)** XAS and **(b)** XMCD spectra at Mn $L_{2,3}$-edges in Mn-Ir(d_{AF})/$Co_{70}Fe_{30}$(2.5 nm) bilayers. The spectra are vertically shifted to be distinguished from each other. Thin horizontal lines accompanied by the XMCD spectra indicate base (XMCD = 0) lines.

conclude that the uncompensated AFM spins are induced exactly at the interface through the exchange interaction between the FM and AFM layers, as illustrated in Fig. 2.

To clarify the role of uncompensated AFM spins in exchange anisotropy, the magnetization of the AFM spin was also studied. If the uncompensated AFM spins provide the asymmetric spin structure against the field reversal and dominate the exchange bias strength by themselves, a certain part of such spins should be irreversible and should result in the vertical offset of their ESMH corresponding to the exchange biasing strength. Figure 3 shows the Mn- and Co-ESMH loops of the $Mn_{73}Ir_{27}$ / $Co_{70}Fe_{30}$ bilayers, with different exchange biasing strengths (J_K). Different J_K values of (a) 0.55 erg/cm^2 and (b) 1.18 erg/cm^2 were achieved by changing the chemical ordering of the Mn-Ir layer [3]. For the accurate determination of the vertical offset of the ESMH, both the parallel and antiparallel configurations were examined. However, we cannot observe any vertical offsets of the Mn-ESMH in both bilayers, which is different from the case in a previous study [4]. That is, all the uncompensated AFM components follow the rotation of FM moments and only mediate the spin motion from the FM layer to the AFM layer in Mn-Ir based exchange biased bilayers.

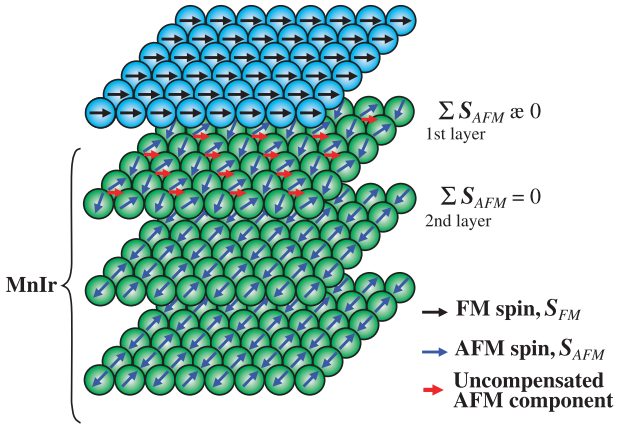

Fig. 2. Schematic illustration of uncompensated AFM moments induced at the interface.

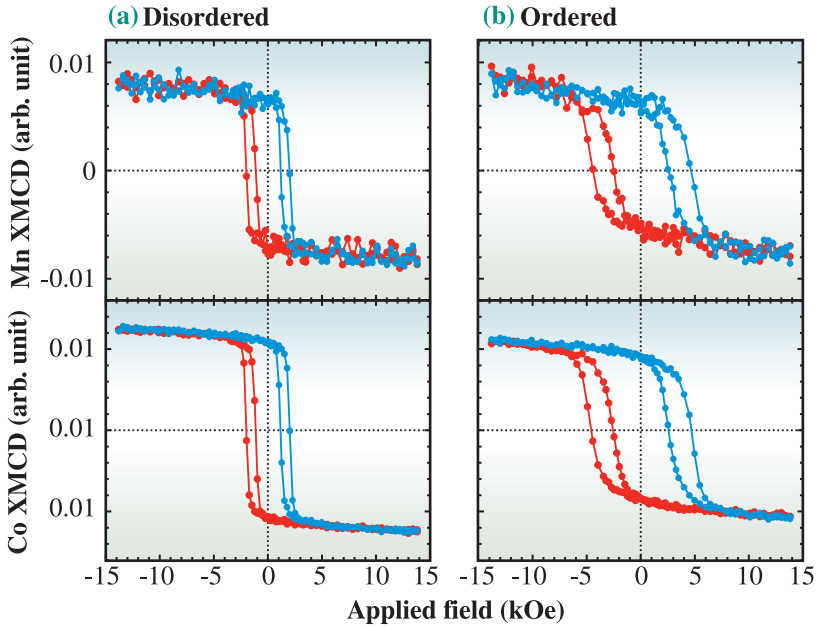

Fig. 3. Mn and Co ESMH loops of **(a)** disordered and **(b)** ordered Mn-Ir/Co-Fe bilayers. The hysteresis loops were obtained in the exchange bias direction either parallel (red) or antiparallel (blue) to the incident X-ray wave vector.

M. Tsunoda[a,*], T. Nakamura[b] and C. Mitsumata[c]

[a] Department of Electronic Engineering, Tohoku University
[b] SPring-8 / JASRI
[c] Advanced Electronics Research Laboratory, Hitachi Metals Ltd.

*E-mail: tsunoda@ecei.tohoku.ac.jp

References

[1] *M. Tsunoda, S. Yoshitaki, Y. Ashizawa, C. Mitsumata, T. Nakamura, H. Osawa, T. Hirono, D.Y. Kim and M. Takahashi: J. Appl. Phys.* ***101*** *(2007) 09E510.*
[2] *M. Tsunoda, T. Nakamura, M. Naka, S. Yoshitaki, C. Mitsumata and M. Takahashi: Appl. Phys. Lett.* ***89*** *(2006) 172501.*
[3] K. Imakita *et al.*: Appl. Phys. Lett. **85** (2004) 3812.
[4] H. Ohldag *et al.*: Phys. Rev. Lett. **91** (2003) 017203.

Thickness-degradation-free Dielectric Thin Films

The thin-film dielectric is one of the most important components of current electronic devices and the heart of these devices is the parallel plate capacitor where a thin film of dielectrics is sandwiched by a pair of electrodes. For the realization of high-density and high-performance devices, it is necessary to make higher-density capacitors by the utilization and scaling down of thin films of novel dielectric materials having a high relative dielectric constant above 200. Leading candidates for these materials are simple perovskite-structured oxides, schematically drawn in Fig. 1(a), as typified by $SrTiO_3$ and $(Ba,Sr)TiO_3$ [1,2]. However, a marked drop of the dielectric constant with the decrease in film thickness, widely known as the "size effect," is frequently reported to be serious especially for these high-dielectric-constant materials [1,2]. In this article, we propose thin films of *c*-axis-oriented bismuth layer-structured dielectrics (BLDs) as novel candidates for size-effect-free materials to overcome these problems (refer to the detail in [3]).

BLDs have a natural superlattice structure along the *c*-axis consisting of two kinds of 2-dimensional nanolayers, i.e., $(Bi_2O_2)^{2+}$ and a pseudoperovskite block generally described as $(A_{m-1}B_mO_{3m+1})^{2-}$, where *m* is the number of BO_6 octahedra in pseudoperovskite blocks as schematically shown in Figs. 1(b) and 1(c). BLDs with an even *m*-number show no ferroelectricity along the *c*-axis because of the mutual counterbalance of their polarity due to a mirror plane in the pseudoperovskite layer. Therefore, *c*-axis-oriented BLD films with an even *m*-number act as paraelectrics.

c-axis-oriented epitaxial $SrBi_4Ti_4O_{15}$ and $CaBi_4Ti_4O_{15}$ films with various thicknesses were grown at 700 °C by metalorganic chemical vapor deposition (MOCVD). $(001)_c$-oriented epitaxial $SrRuO_3$ films having an atomically flat surface grown on $(001)SrTiO_3$ single crystals by MOCVD were used as substrates.

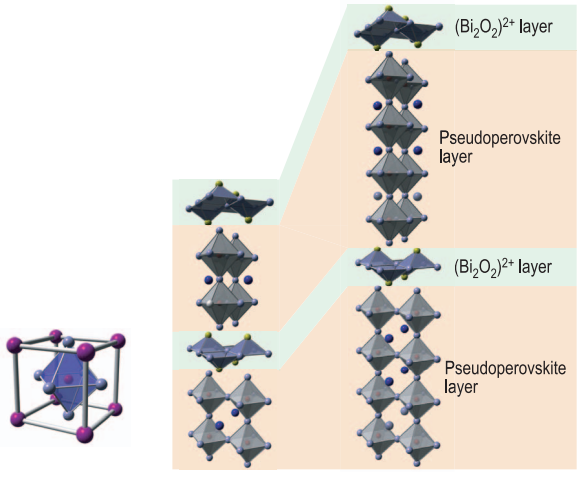

Fig. 1. Schematic diagrams of crystal structure. **(a)** simple perovskite structure, **(b)** $SrBi_2Ta_2O_9$ (*m*=2), and **(c)** $SrBi_4Ti_4O_{15}$ (*m*=4).

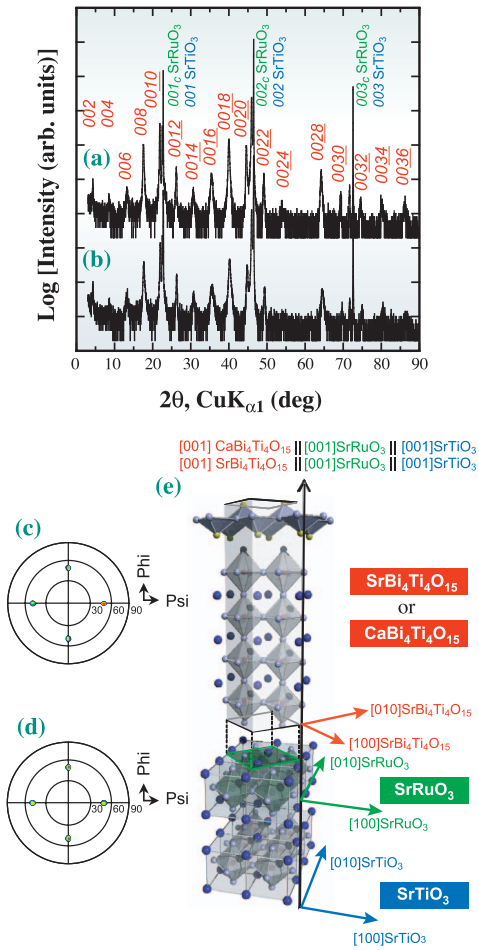

Fig. 2. ((**a**) and (**b**)) X-ray diffraction patterns and ((**c**) and (**d**)) X-ray pole figure measurement of *c*-axis-oriented epitaxial. ((**a**) and (**c**)) $SrBi_4Ti_4O_{15}$ and ((**b**) and (**d**)) $CaBi_4Ti_4O_{15}$ films grown on $(100)_cSrRuO_3//(100)SrTiO_3$ substrates. The fixed 2θ angle corresponds to *119* diffractions of each phase. **(e)** Schematic diagrams indicating the epitaxial relationship between $SrBi_4Ti_4O_{15}$, $SrRuO_3$ and $SrTiO_3$.

The constituent phase and orientation of the films were identified by conventional X-ray diffraction (XRD) analysis using a high-resolution four-circle diffractometer and Cu-$K_{\alpha1}$ radiation. The crystal structure was examined in detail by XRD analysis using synchrotron radiation at beamline **BL13XU** [4] with a wavelength of 0.99 Å.

Figure 2 shows the typical XRD patterns of 98 nm- and 85 nm-thick (a) $SrBi_4Ti_4O_{15}$ and (b) $CaBi_4Ti_4O_{15}$ films grown on $(001)_cSrRuO_3//(001)SrTiO_3$ substrates, respectively. Only the $00\underline{2}l$ (l = integer number) peaks of each BLD phase were observed. Epitaxial growth of these films was confirmed by X-ray pole figure measurement as can be seen in Figs. 2(c) and 2(d), i.e., $(001)SrBi_4Ti_4O_{15}$ or $CaBi_4Ti_4O_{15}//(001)_cSrRuO_3//(001)SrTiO_3$ [see Fig. 2(e)].

Figure 3(a) shows the film thickness dependences of surface-normal and in-plane lattice parameters, and the unit

cell volume of epitaxial $SrBi_4Ti_4O_{15}$ films, where each value indicates the change normalized by those of the 154 nm-thick film. The in-plane lattice parameter gradually increased with film thickness scaling, indicating the increase in in-plane residual strain. Hence, the maximum misfit strain was induced when the in-plane lattice of $SrBi_4Ti_4O_{15}$ was fully clamped by that of the $SrRuO_3$ interlayer without any misfit dislocations, and then the misfit strain exponentially decreased, as seen in Fig. 3(a), with the increase in film thickness and the release of the clamping of the in-plane $SrBi_4Ti_4O_{15}$ lattice through the induction of the misfit dislocations. Here, the residual strain change between thinnest and thickest $SrBi_4Ti_4O_{15}$ films was 56%, which corresponds to a 10% decrease in dielectric constant according to a report on the mechanical bending of $(Ba_{0.7}Sr_{0.5})TiO_3$ films [5]. On the other hand, the surface-normal lattice parameter decreased with the increase in the in-plane one to maintain unit cell volume. However, surprisingly, unit cell volume increased with the decrease in film thickness as shown in Fig. 3(b). Figure 3(c) shows the room temperature relative dielectric constant as a function of the film thickness of *c*-axis-oriented epitaxial $SrBi_4Ti_4O_{15}$ and $CaBi_4Ti_4O_{15}$ films, where those of $SrBi_2Ta_2O_9$ films and the reported data for $(Ba_{0.5},Sr_{0.5})TiO_3$ films (dotted line) are also shown for comparison. $SrBi_4Ti_4O_{15}$ films did not show any degradation in dielectric constant with the decrease in film thickness down to 17 nm, corresponding to about 4 unit cells (c = 4.040 nm), indicating the size-effect-free dielectric characteristics. This result clearly indicates that in-plane stress applied to *c*-axis-oriented $SrBi_4Ti_4O_{15}$ films hardly affects their dielectric characteristics. Moreover, the relative dielectric constants of $SrBi_4Ti_4O_{15}$ and $CaBi_4Ti_4O_{15}$ films were almost 200 for both films irrespective of the type of cation in pseudoperovskite blocks. Furthermore, these values were around 4 times larger than that of $SrBi_2Ta_2O_9$ films with an *m*-number of 2, suggesting that the dielectric constant of BLDs was mainly determined by *m*-number.

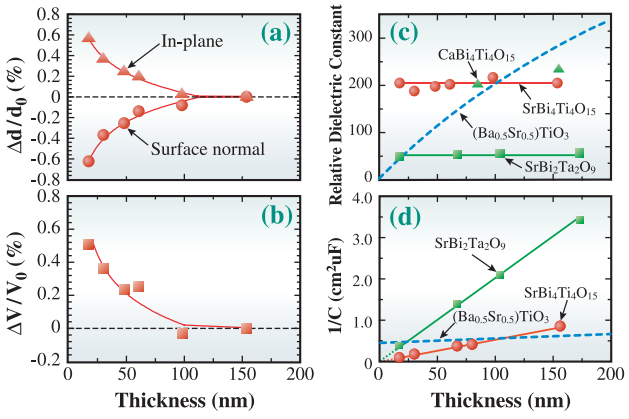

Fig. 3. Thickness dependences of **(a)** surface-normal and in-plane lattice parameters, and **(b)** unit cell volume of $SrBi_4Ti_4O_{15}$ films. Thickness dependences of **(c)** relative dielectric constants of $SrBi_4Ti_4O_{15}$ and $CaBi_4Ti_4O_{15}$ films together with those of $SrBi_2Ta_2O_9$ films. **(d)** Reciprocal capacitance as a function of thickness of $SrBi_4Ti_4O_{15}$ films.

The marked drop of dielectric constant with the decrease in film thickness as in $(Ba_{0.5},Sr_{0.5})TiO_3$ films shown in Fig. 3(c) is generally explained by the dead layer model. Figure 3(d) plots the thickness dependence of the reciprocal capacitance of $SrBi_4Ti_4O_{15}$ films, where data for $SrBi_2Ta_2O_9$ and $(Ba_{0.5},Sr_{0.5})TiO_3$ films (dotted line) are also shown for comparison. For $(Ba_{0.5},Sr_{0.5})TiO_3$ films, the thickness dependence of the reciprocal capacitance showing a linear relationship did not cross the zero point. This indicates that that the data for these $(Ba_{0.5},Sr_{0.5})TiO_3$ films were followed by the dead layer model, suggesting the existence of the dead layer having a low dielectric constant between these $(Ba_{0.5},Sr_{0.5})TiO_3$ films and electrodes. On the other hand, data for $SrBi_4Ti_4O_{15}$ and $SrBi_2Ta_2O_9$ films cross the zero point as shown in Fig. 3(d), followed by the simple single capacitor model.

The results of the present study suggest that the film-thickness-independent dielectric characteristics are the common features for the BLD with even an *m*-number. This result indicates that a natural superlattice structure parallel to the direction of the applied electric field is the key for realizing size-effect-free characteristics and in-plane orientation does not affect it.

In summary, *c*-axis-oriented $SrBi_4Ti_4O_{15}$ and $CaBi_4Ti_4O_{15}$ films with various thicknesses were epitaxially grown on $(100)_c SrRuO_3//(100)SrTiO_3$ substrates by MOCVD. The relative dielectric constant of these films kept a constant value of 200 irrespective of the film thickness down to 17 nm, indicating size-effect-free dielectric characteristics. These dielectric characteristics were considered to be brought about the dielectric constant being extremely insensitive dielectric constant to the residual strain in the films induced by exogenetic stresses, such as thermal, misfit and electrostrictive ones. The dead-layer-free interface was also a critical factor especially for size-effect-free dielectric characteristics. These characteristics are very attractive for high-density capacitor applications.

Hiroshi Funakubo[a,b,*] and Osami Sakata[c]

[a] Department of Innovative and Engineered Materials, Tokyo Institute of Technology
[b] PRESTO, Japan Science and Technology Agency (JST)
[c] SPring-8 / JASRI

*E-mail: funakubo.h.aa@m.titech.ac.jp

References

[1] C.S. Hwang *et al.*: Jpn. J. Appl. Phys. **34** (1995) 5178.
[2] L.J. Sinnamon *et al.*: Appl. Phys. Lett. **78** (2001) 1724.
[3] *K. Takahashi, M. Suzuki, T. Kojima, T. Watanabe, Y. Sakashita, K. Kato, O. Sakata, K. Sumitani and H. Funakubo: Appl. Phys. Lett.* ***89*** *(2006) 082901.*
[4] O. Sakata *et al.*: Surf. Rev. Lett. **10** (2003) 543.
[5] T. Shaw *et al.*: Appl. Phys. Lett. **75** (1999) 2129.

Chemical Science

The recent beamline upgradings are accelerating an expansion of chemical science research field subject to SPring-8. In concert, the fruitful researches were carried out at the beamlines of powder diffraction, small angle scattering (SAXS) and nuclear spectroscopy, while the pilot applications of SAXS/WAXD and grazing incidence SAXS(GISAXS) measurements are making substantial progress from the viewpoint of effective utilization of potential abilities of beamlines. The research object also has wide variety in feature such as polymer morphology, thin film, catalysis, gas absorption, protein molecule reaction and etc.

In the present issue, ten topics have bee chosen. The first three studies, "Study on structural change of Pd nanoparticles with hydrogen absorption/desorption process" by Hirokazu Kobayashi, Hiroshi Kitagawa *et al.*, "Guest-induced instant and reversible crystal-to-crystal transformation of 1,4-bis(ferrocenylethynyl) anthraquinone" by Hiroshi Nishihara *et al.* and "Observation of gas adsorption process on porous coordination polymer by X-ray diffraction" by Yoshiki Kubota *et al.*, describe the *in situ* observations of molecular absorption on nanoporous coordination polymers by powder diffraction. This has recently been one of the most active research subjects at BL02B2.

Polymer science is also an area of recent active research that is producing attractive results due to the upgrading of SAXS beamline BL40B2. "First direct observation of nano-nucleation by small angle scattering on polymers" by Kiyoda Okada, Masamichi Hikosaka *et al*. is the first significant approach to obtaining a fundamental understanding of the nucleation process in polymerization. "Structural model of a poly(vinyl-alcohol) film uniaxially stretched in water" by Tsukasa Miyazaki *et al*. reveals the molecular orientation behavior in a uniaxially stretched polymer film for the first time. This result is a very important industrial application developed at SPring-8 relevant to the dichromatic performance of the polarizer used for liquid crystal displays (LCD). In "Characterization and degradation behavior of segmented poly(urethaneurea)s with lysine-based diisocyanate" by Atsushi Takahara *et al*. a nano-level polymer structure is also revealed by performing a accurate SAXS experiment. The development of advanced experimental techniques for polymer structure analysis, GISAXS and SAXS/WAXD, are discussed in "*In situ* investigation of annealing effect on higher-order structure of polyethylene thin films by synchrotron grazing-incidence small-angle and wide-angle X-ray scattering" by Sono Sasaki *et al*. and "Structural transition of poly[(R)-3-hydroxybutyrate] single crystals on heating as revealed by SAXS and WAXD" by Masahiro Fujita, Tadahisa Iwata *et al.*, respectively. "Synchrotron radiation research for the progress of self-regenerative function to Rh-, and Pt-perovskite catalysts" by Hirohisa Tanaka and Yasuo Nishihata discusses the industrial utilization of research at SPring-8, which may contribute to economic growth. Finally, "Nuclear spectroscopy of nitrogenase and hydrogenase" by Stephen P. Cramer *et al.* outlines a promising application of nuclear resonant spectroscopy to bioscience.

Masaki Takata

Study on Structural Change of Pd Nanoparticles with Hydrogen Absorption/Desorption Process

Hydrogen is the cleanest vector of energy, and holds promise for solving the current pollution problem by its use in zero-emission vehicles. To utilize hydrogen as a clean energy source, the development of an effective, safe and stable storage medium is required. Hydrogen-storage alloys can store hydrogen above room temperature because chemical interactions between the alloy and the hydrogen are sufficiently strong for hydrogen accumulation at the ambient temperature. Therefore hydrogen-storage alloys have been studied extensively as a hydrogen-storage medium for many years. However, there has been little research on the dynamics of the structural change following hydrogen absorption/desorption, although it is important for the development of practical hydrogen-storage alloys.

As a new type of hydrogen storage alloy, we have investigated mono-dispersed metal nanoparticles. It is well known that metal nanoparticles exhibit characteristic properties based on the quantum-size effect. Since the hydrogen-storage properties of metals are strongly related to their electronic states, novel hydrogen-storage properties are expected in metal nanoparticles. We have studied the hydrogen-storage properties of Pd nanoparticles, and they are different from those of bulk Pd [1].

In this study, we carried out *in situ* XRD measurements to investigate the dynamics of the structural change of Pd nanoparticles with hydrogen pressure. Poly(*N*-vinyl-2-pyrrolidone) (PVP)-protected Pd nanoparticles were prepared by stepwise growth [2].

A transmission electron microscopy (TEM) image of the prepared PVP-protected Pd nanoparticles is shown in Fig. 1, indicating that an almost constant size of particles was obtained. As shown in the inset, the obtained size distribution of particles is narrow, and this

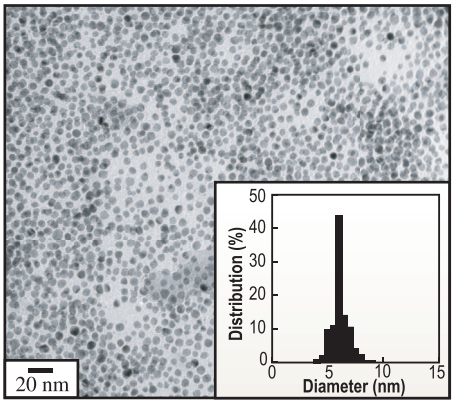

Fig. 1. TEM image of Pd nanoparticles.

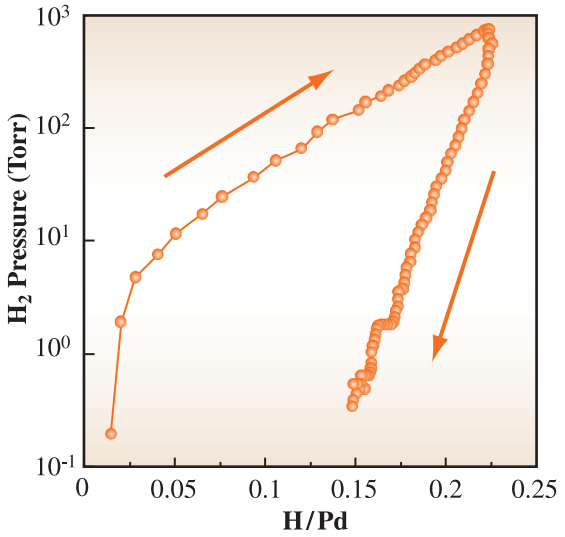

Fig. 2. PC isotherm of Pd nanoparticles at 303 K. The isotherm was measured according the directions of arrows.

indicates that mono-dispersed nanoparticles were synthesized. The mean diameter of the Pd nanoparticles was 6.1 ± 0.8 nm.

The hydrogen absorption/desorption behavior up to 760 Torr hydrogen pressure was investigated by measurement of the hydrogen pressure-composition (PC) isotherm using an automatic PC isotherm apparatus (Suzuki Shokan Co., Ltd.). The hydrogen PC isotherm at 303 K observed for the Pd nanoparticles is shown in Fig. 2. The hydrogen composition (H/Pd) increases with hydrogen pressure, which shows that Pd nanoparticles absorb hydrogen. The ratio of H/Pd at 760 Torr was 0.22. In the desorption process, the total amount of H/Pd decreases with hydrogen decompression, and it is 0.15 at 0 Torr, i.e., the amount did not return to zero under vacuum.

The structure of the Pd nanoparticles was investigated by X-ray powder diffraction method using synchrotron radiation with 51.148 pm wavelength at beamline **BL02B2**. The X-ray diffraction patterns of the sample sealed in a glass capillary were measured in situ under controlled hydrogen pressure in the range 0-760 Torr [3]. Figure 3 shows the *in situ* X-ray diffraction (XRD) patterns of the Pd nanoparticles upon the processes of absorption and desorption of hydrogen. Under vacuum (0 Torr), Pd nanoparticles showed the diffraction pattern from a face centered cubic (fcc) lattice, as for bulk Pd. With increasing hydrogen pressure, diffraction peaks of the Pd nanoparticles shifted continuously to the lower-angle side, indicating that

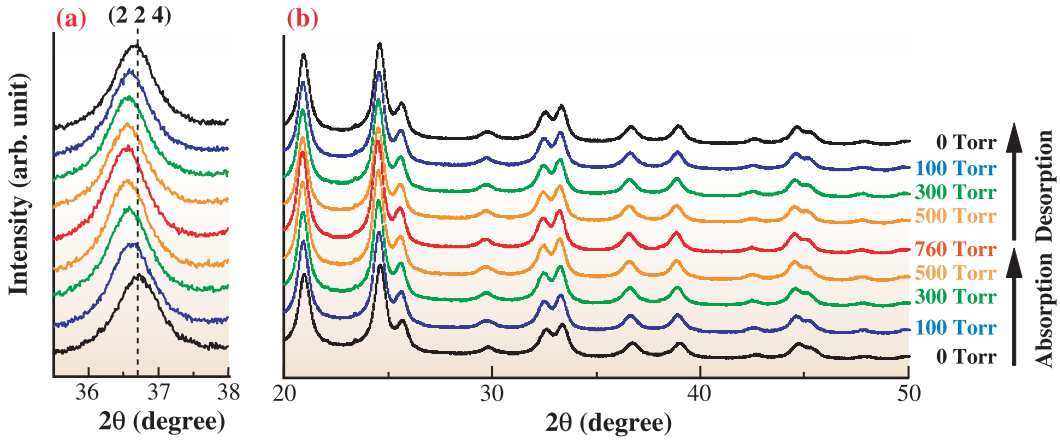

Fig. 3. *In situ* synchrotron XRD patterns for Pd nanoparticle during hydrogen absorption/desorption at 303 K.

hydrogen atoms enter the inside of the Pd lattice and expand it. With decreasing hydrogen pressure, the diffraction peaks of the Pd nanoparticles were shifted continuously to the higher-angle side.

The lattice constant under various hydrogen pressures was estimated by Le Bail fitting to the diffraction patterns, shown in Fig. 4. It can be seen that the lattice constant increases with hydrogen pressure. The lattice constant under a hydrogen pressure of 760 Torr is larger by 0.018 Å than the constant under vacuum, and the extent of lattice expansion for the Pd nanoparticles is smaller than that for the Pd bulk. The lattice constant decreases with hydrogen decompression, and the lattice constant at 0 Torr is larger by 0.006 Å than that of pristine sample, indicating that the lattice constant does not completely revert to the same position as in the pristine sample. Additionally, it should be noted that the lattice constant shows a hysteresis in the course of hydrogen absorption/desorption as observed in the PC isotherm, i.e., the lattice constant during the desorption process is larger than that during the absorption process. The behavior of the hydrogen-pressure dependence of the lattice constant is very similar to that of the PC isotherm, demonstrating that the hydrogen-storage behavior of Pd nanoparticles is correlated with the volumetric change of the Pd nanoparticles. From this result, the incomplete return of the PC isotherm in during desorption process suggests that some of the hydrogen atoms remain as a hydride (Pd-H) in the Pd lattice. Generally, for hydrogen storage alloys, hydrogen absorption/desorption is a first-order phase transition. For example, bulk Pd absorbs hydrogen at 20 Torr and completely desorbs it at 8 Torr at 303 K. Therefore, the existence of hydrogen atoms partially remaining in the Pd lattice under vacuum strongly implies that there exist absorption sites in the Pd nanoparticle with different stability from those of the bulk.

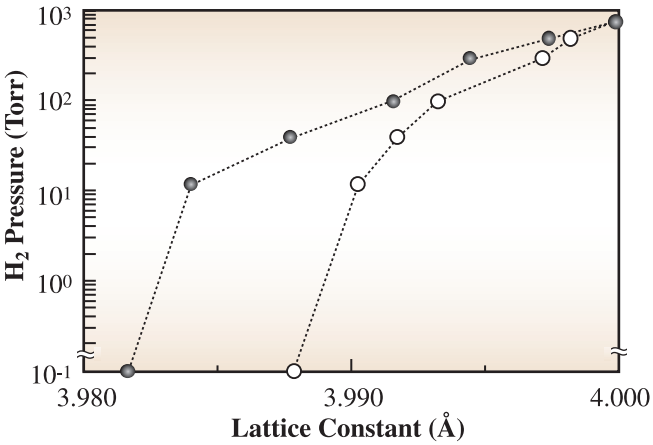

Fig. 4. Hydrogen pressure dependence of lattice constant of Pd nanoparticles (closed circles: absorption, open circles: desorption) obtained by fitting of XRD patterns.

Hirokazu Kobayashi [a,*], Miho Yamauchi [a], Hiroshi Kitagawa [a,b] and Masaki Takata [c]

[a] Department of Chemistry, Kyushu University
[b] CREST, JST
[c] SPring-8 / RIKEN·JASRI

*E-mail: h.k1016scc@mbox.nc.kyushu-u.ac.jp

References

[1] M. Yamauchi and H. Kitagawa: Synth. Met. **153** (2005) 353.
[2] W. Yuan *et al.*: J. Phys. Chem. B **101** (1997) 5301.
[3] *Y. Kubota, M. Takata, R. Matsuda, R. Kitaura, S. Kitagawa, K. Kato, M. Sakata and T.C. Kobayashi: Angew. Chem. Int. Ed.* ***44*** *(2005) 920.*

Guest-Induced Instant and Reversible Crystal-to-Crystal Transformation of 1,4-bis(ferrocenylethynyl)anthraquinone

For decades, much attention has been focused on crystallization from a mixture of electron donor (D) and acceptor (A) molecules, forming D- and/or A-stacked column structures that exhibit unique physical properties such as ferromagnetism, strong visible-NIR light absorption, and high electronic conductivity. The tendency toward DA stacking in a crystal indicates that D-A conjugated molecules can form a network structure, which may manifest interesting physical properties. We are interested in the properties of a new D-A conjugated system [1-3] of ferrocenylethynylanthraquinones (FcAq's), from two viewpoints: the protonation-induced intramolecular electron transfer reaction causing valence tautomers, and the construction of D-A stacked nanoporous network structures, which have attracted much recent attention due to their high potential for applications such as selective gas adsorption, heterogeneous catalysts, and molecular recognition. In the present study, we have found that a new T-shaped FcAq compound, 1,4-bis(ferrocenylethynyl) anthraquinone (1,4-Fc_2Aq), gives a facile single crystal formation in the presence of guest solvent molecules, and undergoes an instant and reversible crystal-to-crystal transformation by heating and guest vapor treatment [4].

The crystal structures of 1,4-Fc_2Aq's obtained from various solvents were confirmed by single-crystal X-ray diffraction analysis. Most of the structures show the inclusion of the solvent as the guest molecule. The crystal structure of α-1,4-Fc_2Aq·CH_2Cl_2 along the *b* axis is shown in Fig. 1(a) as an example. The crystal was obtained by recrystallization from dichloromethane-hexane at 263 K; under such conditions, a large (25 × 1 × 1 mm^3) crystal was grown within a week. α-1,4-Fc_2Aq·CH_2Cl_2 has subnanopores with dimensions of 5.7 Å × 3.5 Å along the *b* axis, in which dichloromethane as guest molecules are contained with a 1,4-Fc_2Aq to dichloromethane mole ratio of 1:1. An infinite one-dimensional columnar structure is formed along the *b* axis by an alternating arrangement of π-conjugated spacers and π-π stacking interactions between Fc (D) and Aq (A) moieties (Fig. 2(b)). The Aq and Cp planes lean about 45 degrees to the *b* axis. The two kinds of complex columns are almost perpendicular to each other and are arranged alternately to construct the porous framework. Crystals with the formula 1,4-Fc_2Aq·X (X = guest molecule) were formed in various solvents. Their crystal structures are similar to the structure of α-1,4-Fc_2Aq·CH_2Cl_2, but the size of the subnanopores changes according to the size of the guest molecules included.

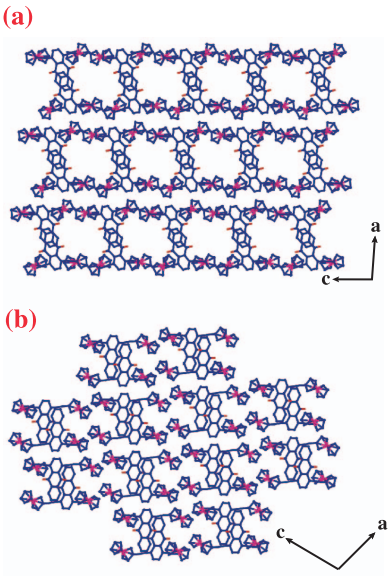

Fig. 1. Crystal structure of α -1,4-Fc_2Aq·CH_2Cl_2 along the *b* axis (**a**) and that of solvent-free 1,4-Fc_2Aq along the *b* axis (**b**). Hydrogen atoms and disordered guest molecules (CH_2Cl_2) are omitted for clarity.

The recrystallization of 1,4-Fc_2Aq from *o*-dichlorobenzene-hexane at 293 K produced crystals without pores and solvent molecules, the structure of which is shown in Fig. 2(b). In the solvent-free form, a columnar structure is maintained (Fig. 2), whereas the syn conformation of the ferrocenes in 1,4-Fc_2Aq allows for the formation of pairs of adjacent molecules in the crystal, and the pattern of the stacking arrangement changes from D-A to D-A-A compared with that of the porous 1,4-Fc_2Aq·X.

Thermal desorption of the guest molecules in 1,4-Fc_2Aq·X was examined by thermal gravimetric analysis (TGA). The TG curve indicated the desorption of guest molecules at T_{de} = 346-380 K without chemical decomposition. To clarify the crystal structure after the desorption of guest molecules, the synchrotron XRPD of a sample prepared by heating 1,4-Fc_2Aq·THF at 420 K under vacuum was measured, and the cell parameters of the sample were determined by the Rietveld method. The XRPD-derived cell parameters were consistent with those of solvent-free 1,4-Fc_2Aq. Thus, it is confirmed that guest desorption causes crystal-to-crystal transformation from 1,4-Fc_2Aq·X to solvent-free 1,4-Fc_2Aq.

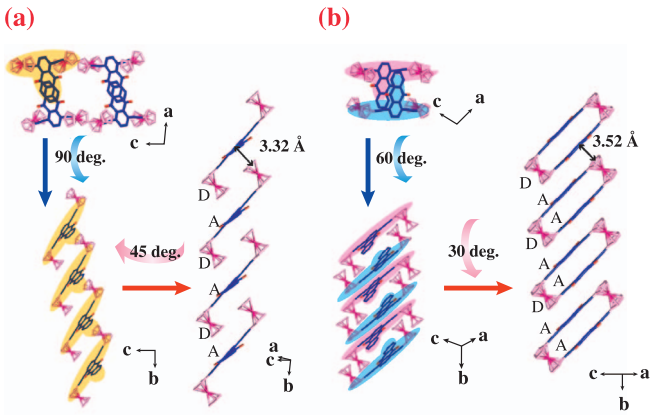

Fig. 2. One-dimensional columnar structure of 1,4-Fc_2Aq·X (**a**) and that of solvent-free 1,4-Fc_2Aq (**b**).

The reversibility of the crystal-to-crystal transformation by guest desorption and adsorption of 1,4-Fc_2Aq were studied by variable-temperature XRPD (VT-XRPD) at beamline **BL02B2**. For this measurement, we prepared a vacuum-sealed cell, shown in Fig. 3(a). After the tube stood for 3 hours at room temperature, the XRPD pattern completely changed from that of solvent-free 1,4-Fc_2Aq to that of 1,4-Fc_2Aq·THF (Fig. 3(b), from i to ii). Then, THF was frozen at 90 K and the sample was heated from 300 K to 420 K, followed by maintenance of the temperature of the sample capillary, T_s, at 300 K and increasing the temperature of the THF capillary, T_g, from 90 K to 400 K. XRPD patterns were measured at every 50 K, and the X-ray exposure time was 5 min for every measurement. By heating the 1,4-Fc_2Aq·THF sample, THF molecules were released and the XRPD patterns of solvent-free 1,4-Fc_2Aq emerged. At 400 K, patterns corresponded perfectly with the pattern of solvent-free 1,4-Fc_2Aq (Fig. 3(b), iii). When the capillary was filled with THF vapor by increasing T_g, THF molecules were adsorbed on the host, and XRPD patterns arising from 1,4-Fc_2Aq·THF were observed (Fig. 3(b), iv-vii). When T_s and T_g were kept at 300 K, guest adsorption was completed within 5 min. These results indicate a rapid and reversible crystal-to-crystal transformation between 1,4-Fc_2Aq·THF and solvent-free 1,4-Fc_2Aq. In view of the conformational change required, this fast transformation is particularly remarkable. These features are derived from the crystal structure flexibility caused by the D-A interaction, which is weaker than other chemical bonds, and from the higher stability of 1,4-Fc_2Aq·THF compared with solvent-free 1,4-Fc_2Aq.

In conclusion, a D-A conjugated compound, 1,4-Fc_2Aq, was newly synthesized. Crystals of 1,4-Fc_2Aq have either a solvent-incorporated porous structure or a solvent-free nonporous one, which can be reversed instantly by the desorption and absorption of guest molecules, causing the alternation of the D-A arrangement in a one-dimensional columnar structure.

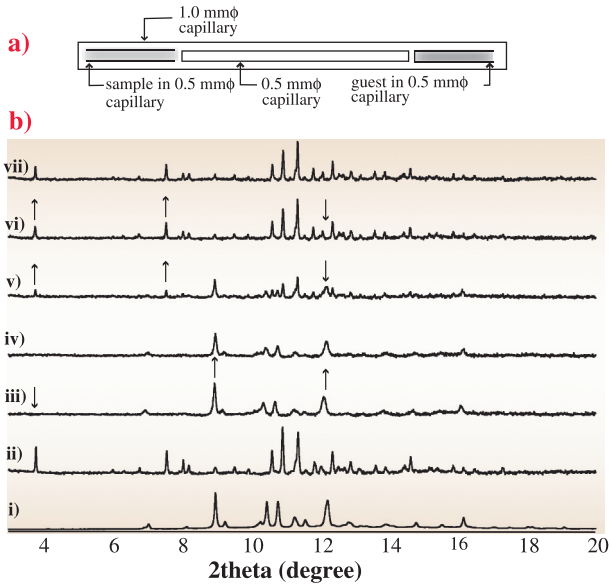

Fig. 3. **(a)** Illustration of capillary used in VT-XRPD experiment. **(b)** XRPD pattern of solvent-free 1,4-Fc_2Aq (i) and results of VT-XRPD measurement (ii-vii). The temperatures of the sample (T_s) and guest (T_g) are (ii) T_s = 350 K, T_g = 90 K, (iii) T_s = 400 K, T_g = 90 K, (iv) T_s = 300 K, T_g = 200 K, (v) T_s = 300 K, T_g = 300 K, (vi) T_s = 300 K, T_g 350 K, and (vii) T_s = 300 K, T_g = 400 K, respectively.

Mio Kondo[a], Hiroshi Nishihara[a,*] and Eiji Nishibori[b]

[a] Department of Chemistry, The University of Tokyo
[b] Department of Applied Physics, Nagoya University

*E-mail: nisihara@chem.s.u-tokyo.ac.jp

References

[1] M. Murata *et al.*: Chem Lett. (2000) 1328.
[2] M. Murata *et al.*: J. Am. Chem. Soc. **123** (2001) 12903.
[3] M. Kondo *et al.*: Angew. Chem. Int. Ed. – in press.
[4] *M. Kondo, M. Murata, H. Nishihara, E. Nishibori, S. Aoyagi, M. Yoshida, Y. Kinoshita and M. Sakata, Angew. Chem. Int. Ed.* ***118*** *(2006) 5587.*

Observation of Gas Adsorption Process on Porous Coordination Polymer by X-ray Diffraction

Metal-organic microporous materials (MOMMs) [1] have attracted the attention of scientists for a number of reasons including the creation of nanometer-sized spaces and the discovery of novel phenomena as well as commercial interests such as their application in gas separation, gas storage and heterogeneous catalysis. Recent activities in crystal engineering have provided several examples of MOMMs that have rigid open frameworks, and therefore have the potential to be functionally related to zeolites. MOMMs often have a much more dynamic framework than is generally believed, and the characteristic of metal-organic species. The structural rearrangement of the host framework responding to guest molecules proceeds from the "open" phase to the "close" phase. MOMMs could also be used as a unique class of materials, with unique characteristic unlike rigid porous materials. Although the sorption profiles of MOMMs with saturated amounts of guest molecules have been well characterized so far [2,3], their intermediate profiles are still unknown. It is important to determine how guest molecules are recognized, and finally confined by nanopores. An in-depth understanding of the intermediate state provides us with a feasible design for a porous framework, which changes its structure into one well suited for the desired guest molecules and results in an efficient accommodation system. Therefore, fundamental structural information on not only the host framework but also the guest molecules is required throughout adsorption phenomena. X-ray diffraction is one of the most powerful methods that can directly provide structural information for adsorbed molecules. Herein, we report the structure analysis of an intermediate phase during gas adsorption in the nanochannels of a MOMM using *in situ* synchrotron powder diffraction at beamline **BL02B2** [4].

In our previous work [3], we reported acetylene gas adsorption on CPL-1 (coordination polymer 1 with pillared-layer structure: $Cu_2(pzdc)_2(pyz)$, where pzdc is pyrazine-2,3-dicarboxylate and pyz is pyrazine). From accurate structural analysis, acetylene molecules were found to be trapped by the non-coordinated oxygen atoms of carboxylate forming double hydrogen bonds. The *in situ* powder diffraction patterns of gas adsorption between the anhydrous hollow phase (phase I) and the saturated adsorbed phase (phase S) revealed another phase mixed with the saturated phase. In an acetylene adsorption isotherm, a step is recognized at about 0.7 molecules per unit pore during a steep rise at a low pressure region. These data suggest the existence of an intermediate phase (phase M) of adsorption. By carefully adjusting both the temperature and the gas pressure, we succeeded in obtaining phase M as a single phase at a pressure of 150 kPa at 360 K. A structure analysis was carried out using the MEM (maximum entropy method)/Rietveld method [5]. Figure 1 shows the crystal structures of phases M and S. Acetylene molecules are located at the center of the nanochannel with one molecular site per unit pore. The refined occupancy factor of the acetylene molecule in phase M was 0.70(2) and shows very good agreement with the step position in the adsorption isotherm. In phase M, the molecular axis of acetylene is perpendicular to the nanochannel direction and is on the line connecting the two oxygen (O1) atoms of carboxylate bonded to a Cu ion. This orientation is different from that in phase S in which the molecular axis is on the line connecting the non-coordinated oxygen (O2) atoms of carboxylate. The interatomic distance between the hydrogen atom of acetylene and the neighboring O1 atom is 2.57 Å, while the distance to the O2 atom is 2.64 Å. These values are approximately equal to the sum of the van der Waals radii of hydrogen (1.2 Å) and oxygen (1.4 Å), 2.6 Å. Figure 2 shows the section MEM charge densities containing the molecular axis of acetylene. In phase M, few electron densities were observed

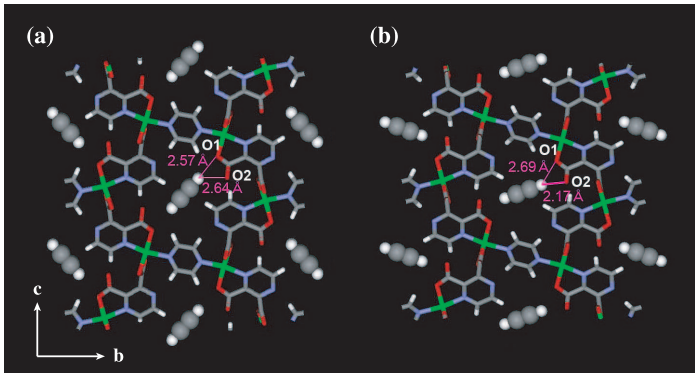

Fig. 1. Crystal structures of CPL-1 with adsorption of acetylene viewed in nanochannel directions. **(a)** intermediate adsorbed phase M and **(b)** saturated adsorbed phase S. These figures show around one unit pore. Acetylene molecules are shown as balls. Other atoms are connected by lines. Acetylene molecules occupy the sites with a probability of 0.7 in **(a)**.

between the adsorbed acetylene molecules and the O1 atoms on the pore wall. In phase S, the acetylene molecules were trapped by hydrogen bonds between the acetylene molecules and the O2 atoms. From these results, the interaction of acetylene molecules with the oxygen atom site is much weaker in phase M than in phase S.

Figure 3 shows the acetylene adsorption isotherm and crystal structures of phases I, M and S. By acetylene adsorption, the pillar-ligands, i.e., the pyrazine-rings, slightly rotated and the crystal lattice sheared in the direction of the *a*-axis, indicating a flexible transformation for efficient guest accommodation in phase M. Subsequently, phase M changes to phase S with a slight rotation of acetylene molecules and then hydrogen bonds are formed with two non-coordinated oxygen atoms. With this change, there is now sufficient space for the pyrazine ring to rotate. The shearing of the lattice also occurs again to permit more efficient guest accommodation. In the change from phases M to S, unit cell volume decreases, where the lattice parameter *c* contracts with the change of the orientation of the acetylene molecule forming double hydrogen bonds with two oxygen atoms on the pore wall. However, the rotation of the pillar-ligand creates a space without changing pore volume significantly. At the same time, the change in the size and shape of the nanochannel causes more acetylene load to reach the saturation of adsorption.

Using X-ray structure analysis, we have succeeded in visualizing the rearrangement of guest molecules and the transformation of the framework during adsorption. These findings will contribute to the development of novel functional MOMMs responsive to guest molecules. More structural studies on gas adsorption process should be promoted to attain an in-depth understanding of adsorption phenomena.

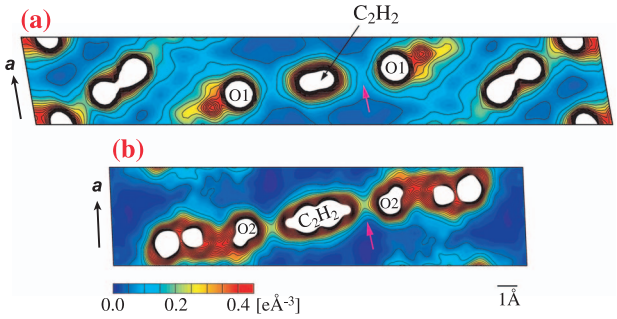

Fig. 2. Section MEM charge densities of CPL-1 with adsorption of acetylene containing molecular axis of acetylene and *a*-axis. **(a)** intermediate adsorbed phase M and **(b)** saturated adsorbed phase S. Contour lines are drawn from 0.00 to 1.00 eÅ^{-3} with intervals of 0.05 eÅ^{-3}. Higher density regions are omitted in the figure.

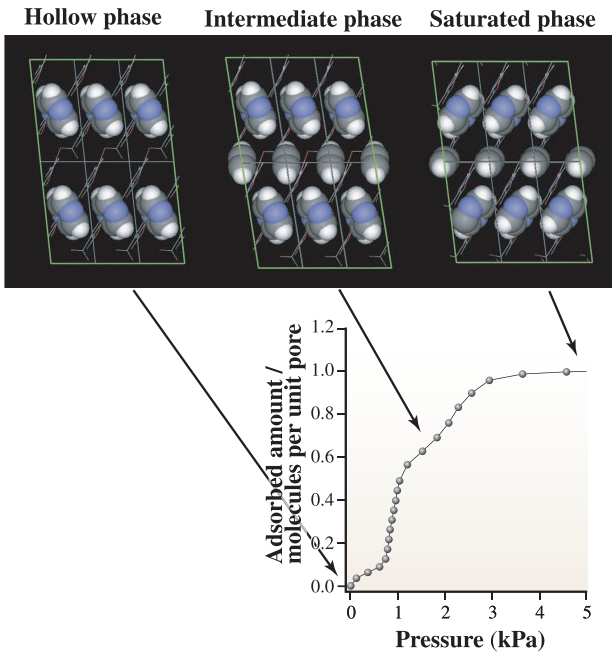

Fig. 3. Acetylene adsorption isotherm and crystal structures of CPL-1 with adsorption of acetylene corresponding to the amount of adsorbed gas. These figures are viewed from the side of the nanochannels. Pillar-molecules (pyrazine) and adsorbed acetylene molecules are shown by the space filling model. Other molecules are shown by connecting lines.

Yoshiki Kubota[a,*], Masaki Takata[b] and Susumu Kitagawa[c]

[a] Department of Physical Science, Osaka Prefecture University
[b] SPring-8 / RIKEN
[c] Department of Synthetic Chemistry and Biological Chemistry, Kyoto University

*E-mail: kubotay@p.s.osakafu-u.ac.jp

References

[1] S. Kitagawa *et al.*: Angew. Chem. Int. Ed. **43** (2004)2334.
[2] R. Kitaura *et al.*: Science **298** (2002) 2358.
[3] R. Matsuda *et al.*: Nature **436** (2002) 238.
[4] *Y. Kubota, M. Takata, R. Matsuda, R. Kitaura, S. Kitagawa, T. C. Kobayashi: Angew. Chem. Int. Ed. **45** (2006) 4932.*
[5] M. Takata *et al.*: Z. Kristallogr. **216** (2001) 71.

First Direct Observation of Nano-Nucleation by Small Angle X-ray Scattering on Polymers

Crystallization from the melt (or gas) is an important phenomena in any material, and it significantly determines the structure and physical properties of the material. The initial stage of crystallization has been assumed to be nucleation in classical nucleation theory (CNT) since the 1930s [1], but it could not be confirmed experimentally for a long time due to technical difficulties. To solve the nucleation mechanism is important in understanding the structure and physical properties of any material, and also results in interesting applications for industry.

Although nuclei of nm order which we will refer to as nanonuclei have been previously generated, the number density of nuclei in the melt was too small to be detected by small angle X-ray scattering (SAXS) [2], where the nuclei include 2-10^6 atoms, particles or repeating units. Hence, alternative experimental nucleation studies have been performed on macroscopic crystals (macrocrystals) using optical microscope (OM) or a bubble chamber. Recently, simulation studies have been also carried out on colloid systems. However these studies cannot presume the direct observation of nano-nucleation, because macrocrystals and colloids are considerably different from the real image of nanonucleus. Therefore a long-standing and important unsolved problem is the observation of nano-nucleation and the determination of the size distribution $f(N,t)$ of nanonuclei under isothermal melt-crystallization, where N is the number of atom, particle or repeating unit (hereafter, referred to as particles) in a nucleus and t is crystallization time. $f(N,t)$ should clarify the real image of nano-nucleation, i.e., how the number

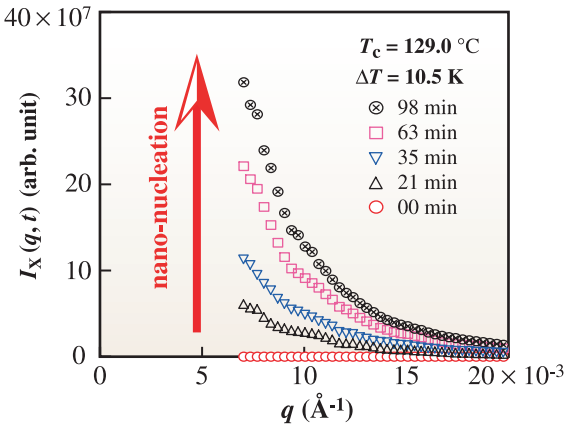

Fig. 1. Plots of $I_X(q,t)$ against q as a parameter of t at T_c = 129.0 °C. $I_X(q,t)$ increased with the increase of t, which is the direct evidence of nano-nucleation.

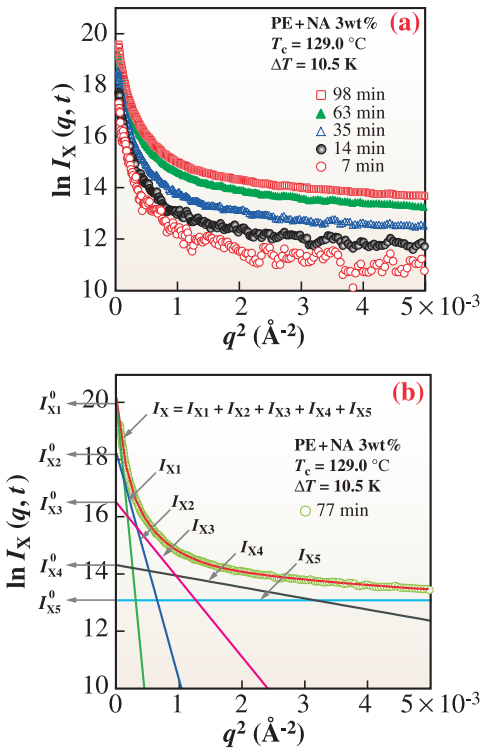

Fig. 2. Plots of ln $I_X(q,t)$ against q^2. **(a)** ln $I_X(q,t)$ against q^2 as a parameter of t. **(b)** Typical result obtained from "extended Guinier plot method". ln $I_X(q,t)$ was separated by five straight lines (I_{X1}, I_{X2},... I_{X5}). $f(N,t)$ and N were obtained from the vertical intercept and slope of the straight lines, respectively, where j indicates the different nuclei of size N_j.

and N of nanonuclei increase with t. To overcome the above difficulties, we added a nucleating agent (NA) to a polymer, by which the scattering intensity (I_x) from nanonuclei increased by as much as a factor of 10^4. We succeeded in detecting I_x for polyethylene (PE) in 2003 for the first time, as discussed in Ref. [3]. Since polymers are long chainlike molecules, their topological character is added to the fundamental nucleation mechanism. The NA is a crystalline material that accelerates nucleation and has been widely used in industry. An advantage of observing nucleation in polymers is the existence of an effective NA. Here, we report that we succeeded in observing $f(N,t)$ and in clarifying the real image of nano-nucleation using PE by SAXS [4].

We used PE (NIST, SRM1483a, M_n = 32×10^3, M_w / M_n = 1.1), where M_n and M_w are the number-average molecular weight and the weight-average molecular weight, respectively, and M_w / M_n is the index of dispersion. Sodium 2,2'-methylene-bis- (4,6-di-t-

butylphenylene) phosphate (ADEKA Corp., NA-11SF) was used as a NA. The sample was melted at 160°C for 5 min within a thin evacuated glass capillary (ϕ1 mm) and then isothermally crystallized at its crystallization temperature (T_c = 129.0°C). The SAXS experiment was carried out at beamline **BL40B2**. The range of the scattering vector (q) was (7×10^{-3} – 2×10^{-2}) Å^{-1} and the wavelength (λ) was 1.5 Å.

Figure 1 shows plots of excess scattering intensity $I_x(q,t)$ against q as a parameter of t, where $I_x(q,t)$ indicates the net increase in I_x counted from I_x at t = 0. $I_x(q,t)$ increased with increasing of t. Therefore nano-nucleation was confirmed, because this increase in $I_x(q,t)$ should result from nano-nucleation.

Plots of ln $I_x(q,t)$ against q^2 as a parameter of t are shown in Fig. 2(a). We applied the extended Guinier plot method for q^2 = (0.05×10^{-3} – 1.50×10^{-2}) Å^{-2} [5]. Figure 2(b) shows part of the typical result of obtained from the extended Guinier plot method for t = 77 min. ln $I_x(q,t)$ was separated by five straight lines I_{xj} for each t, where j = 1, 2, ..., 5. The $f(N,t)$ and N of the nanonuclei were obtained from the vertical intercept and slope of the straight lines, respectively.

Figure 3 shows log $f(N,t)$ against log N as a parameter of t. $f(N,t)$ increased with increasing t at a fixed N and stopped increasing after 10^2 min. The increase in $f(N,t)$ and the stop of the increase correspond to the induction and steady periods, respectively. $f(N,t)$ decreased with increasing N for any t. From this result, we can clarify two points as follows. One is that the nanonucleus exhibits considerable fluctuation with respect to the shape and/or size, i.e., it can take all possible shapes, has a large entropy and should be generated and disappear

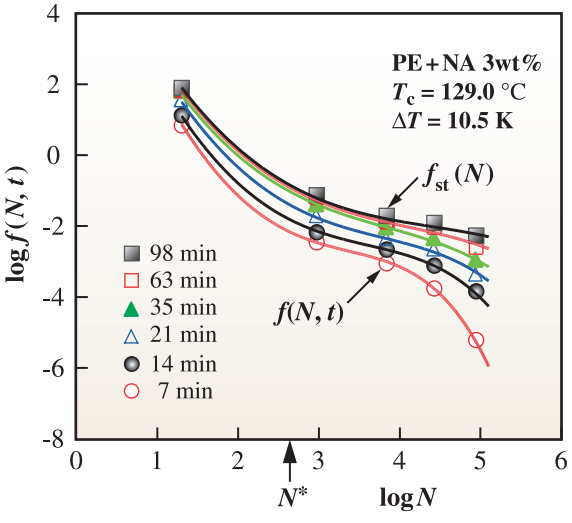

Fig. 3. Plots of log $f(N,t)$ against log N as a parameter of t. N^* indicates N of the critical nucleus, when it is in an activated state because of free energy of nucleation. $f_{st}(N)$ is $f(N,t)$ in the steady state.

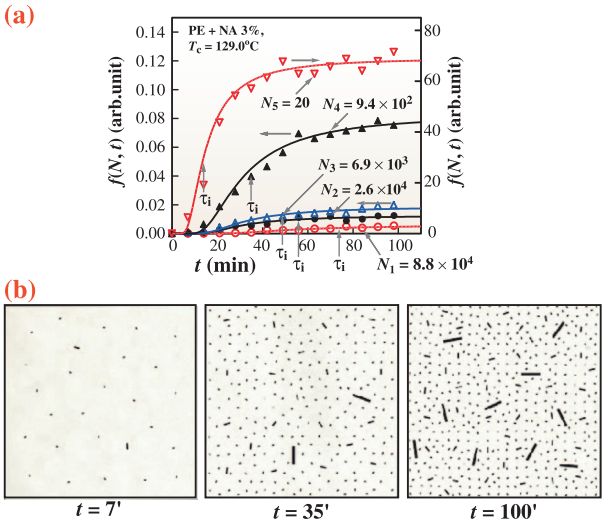

Fig. 4. **(a)** Time evolution of $f(N,t)$ as a parameter of N. The right axis indicates $f(N,t)$ for N_5 and the left axis indicates that of the other N_i. Induction times (τ_i) were shown. **(b)** Illustration of real image of nano-nucleation.

frequently. The other is that only a small fraction of nanonuclei can survive and develop to macrocrystals.

The time evolution of $f(N,t)$ as a parameter of N is shown in Fig. 4(a). $f(N,t)$ for smaller N increased significantly faster and saturated with the increase of t. $f(N,t)$ for larger N increased much more slowly and saturated with the increase of t. We clarified the real image of nano-nucleation for the first time in Fig. 4(b). At first, smaller nanonuclei are generated up to t = 7 min. Many nanonuclei are generated and some of them grow into larger nuclei up to t = 35 min. Many more and larger nanonuclei are generated and grow up to t ≅ 100 min.

Kiyoka Okada [a], Kaori Watanabe [b] and Masamichi Hikosaka [c,*]

[a] Collaborative Research Center, Hiroshima University
[b] Japan Science and Technology Agency (JST)
[c] Graduate School of Integrated Arts and Sciences, Hiroshima University

* E-mail: hikosaka@hiroshima-u.ac.jp

References

[1] V.R. Becker and W. Döring: Ann. Phys. **24** (1935) 719.
[2] Y.A. Akpalu and E.J. Amis: J. Chem. Phys. **111** (1999) 8686.
[3] M. Hikosaka *et al.*: J. Macromol. Sci. Phys. B **42** (2003) 847.
[4] *K. Okada, K. Watanabe, I. Wataoka, A. Toda, S. Sasaki, K. Inoue, M. Hikosaka: Polymer **48** (2007) 382.*
[5] M.H. Jellinek and I. Fankuchen: Ind. Eng. Chem. **37** (1945) 158.

Structural Model of a Poly(vinyl-alcohol) Film Uniaxially Stretched in Water

Recently, liquid crystal displays (LCD) have been widely used in various industrial applications, such as televisions and the monitors in cellular phones. Poly(vinyl alcohol) (PVA) has been promising as a substrate for the polarizers used in LCD, because it possesses a high ability of PVA-iodine complex formation in the film microstructure. When PVA films are soaked in a KI/I_2 aqueous solution, adsorbed polyiodine ions are one-dimensionally aligned along the PVA chains, which are oriented by film drawing, resulting in the formation of PVA-iodine complexes, which show excellent dichromatic performance. It was suggested that PVA-iodine complexes are formed in amorphous regions in PVA films when the films are soaked in KI/I_2 aqueous solution with a relatively low iodine concentration [1,2]. Therefore, it is very important to investigate the orientation of the molecular chains in the film microstructure, particularly in the amorphous regions, because the high dichromatic performance of the polarizers is attributed to the PVA-iodine complexes with a high degree of orientation in amorphous regions.

To elucidate the development of the orientation in PVA molecular chains in the amorphous regions with the strain, we investigated the structural changes in PVA films during uniaxial deformation in water without molecular chain relaxation by simultaneous measurements of small-angle X-ray scattering (SAXS) and the tensile stress-strain (S-S) relationship. Simultaneous SAXS and S-S were performed at beamline **BL40B2** with our newly developed stretch machine with a water bath, which can be jacked up and down so as to enclose and disclose the film sample to examine a film sample in water, as schematically shown in Fig. 1. The experimental setup at BL40B2 is shown in Fig. 2. This stretch machine allows a film sample to be stretched laterally to receive X-ray radiation at the same position of the sample during deformation. A typical stretching speed and data acquisition time of a two-dimensional scattering pattern obtained using a CCD detector system with an image intensifier are 5 mm/min and 15 s, respectively.

PVA films with a degree of polymerization of 2400 were used in this study. The thickness of the films is 0.075 mm. In a previous work, we studied the swelling behavior of the film with water. It was concluded that only amorphous regions in the film are swollen in water, while the crystalline domains do not absorb water.

A S-S curve and typical two-dimensional (2D) SAXS patterns obtained simultaneously during uniaxial deformation in water at 298 K are shown in Fig. 3 [3]. We examined the longitudinal and transversal 1D scattering slices of 2D patterns, which describe the actual microstructural parameters in the film, and the mechanical transition is shown in the S-S curve.

Consequently, we determined the microstructure changes associated with the film stretching, as follows [3]. Below the strain of 70%, the crystalline lamellae are oriented in the direction perpendicular to the stretching direction, and the intervening amorphous regions swollen with water are elastically deformed in proportion to the macroscopic film deformation. Beyond the strain of 70%, the molecular chains in the

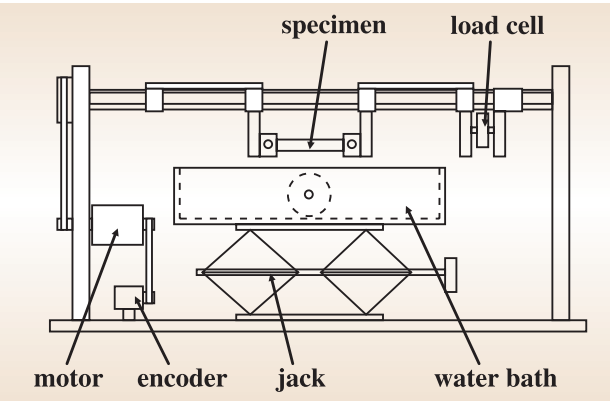

Fig. 1. Schematic drawing of the newly developed stretch machine for *in situ* SAXS measurements during uniaxial deformation of PVA films in water.

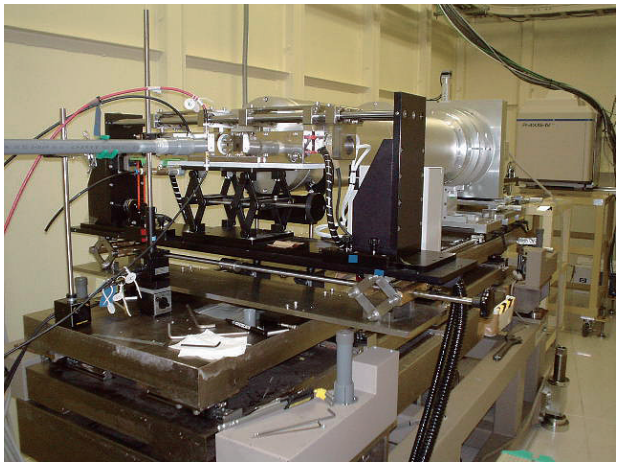

Fig. 2. Experimental setup at BL40B2.

intermediate amorphous region are relaxed owing to lamellar breakup. Above 180% strain, the structural transition of the lamellar structure to a microfibrillar structure takes place, as suggested by the appearance of the transversal streak scattering shown in Fig. 3 and the mechanical transition at the strain of 180%. Moreover, the interfibrillar interaction of the adjacent microfibrils decreases with the film deformation by the pulling-out of the tie chains, which penetrate the adjacent microfibrils, leading to the further stress relaxation of most of the microfibrils. Finally, a network with long-range connectivity composed of the relaxed microfibrils and the interfibrillar extended amorphous chains exists prior to the breaking of film break.

It is thought that these interfibrillar amorphous chains play an important role in the structure the highly oriented PVA-iodine complexes in the film microstructure. That is to say, it is suggested that highly oriented PVA-iodine complexes, which contribute to the high dichromatic performance of polarizers, are formed in these interfibrillar extended amorphous regions.

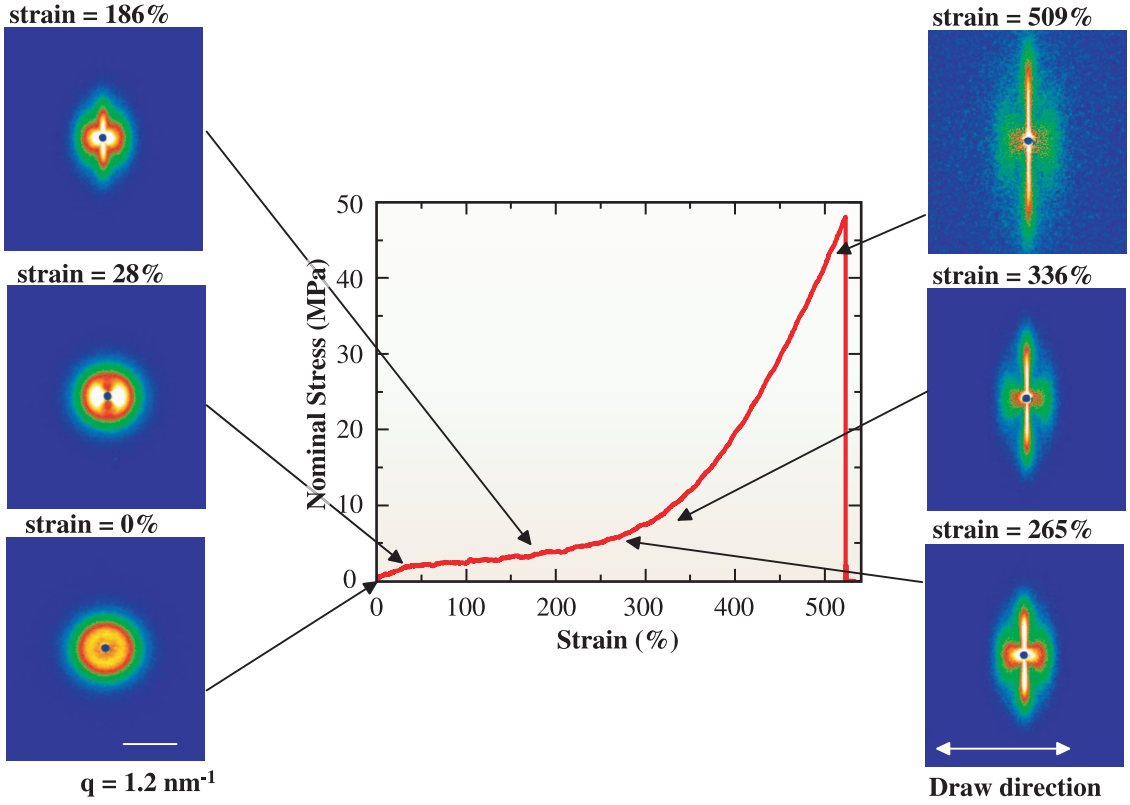

Fig. 3. Stress-strain curve and typical 2D patterns collected during uniaxial deformation in water at 298 K. Each pattern was obtained in 15 s from the point indicated by each arrow.

Tsukasa Miyazaki

Core Technology Center, Nitto Denko Corporation

E-mail: tsukasa_miyazaki@gg.nitto.co.jp

References

[1] K. Miyasaka: Adv. Polym. Sci. **108** (1993) 91.
[2] T. Miyazaki *et al.*: Polymer **46** (2005) 7436.
[3] *T. Miyazaki, A. Hoshiko, M. Akasaka, T. Shintani and S. Sakurai: Macromolecules **39** (2006) 2921.*

Characterization and Degradation Behavior of Segmented Poly(urethaneurea)s with Lysine-Based Diisocyanate

Various environmentally friendly biodegradable polymers have been developed. However, the majority of these polymers are typically hard and brittle plastics, and few biodegradable elastomeric polymers have been synthesized so far. The recent development of diisocyanates based on lysine has removed an obstacle to the synthesis of polyurethane elastomers, which are expected to yield non-toxic degradation products. If the lysine-based diisocyanate component in SPUU were liberated by hydrolysis of the urethane bonds of the polymer during degradation, the products would be lysine derivatives, which are essentially non-toxic products. In this study, segmented poly(urethaneurea)s (SPUU) were synthesized from lysine-based diisocyanate. To evaluate the molecular aggregation states of soft and hard segments, wide-angle X-ray diffraction (WAXD), and small-angle X-ray scattering (SAXS) were performed. The degradation behavior was investigated by a biochemical oxygen demand (BOD) test.

SPUU were synthesized via a standard two-step prepolymer method. LDI (lysine-based diisocyanate: LDI) was reacted with polycaprolactone diol (PCL) as a prepolymer reaction for 180 min at 358 K. Then, 1,4-butanediamine (BDA) was added to the prepolymer and allowed to react for 1 h in DMF. The soft segment consisted of PCL and LDI, whereas the hard segment consisted of LDI and BDA. Sample names were designated as PCL (PCL M_n) (PCL fraction)LDI-BDA. The obtained polymers were multi-block copolymers of hard and soft segments.

SPUU films were characterized by differential scanning calorimetry (DSC), wide-angle X-ray diffraction (WAXD) using a laboratory X-ray source, and small-angle X-ray scattering (SAXS) at beamline **BL40B2**. Degradation studies were performed by a BOD test in an activated sludge according to JIS K 6950, using activated sludge taken from a sewage plant in Meito-ku, Nagoya.

Differences in state of molecular aggregation of SPUU were confirmed by DSC. Crystal melting of PCL in the soft segments was observed between temperatures of 283 K and 320 K. The crystallinity of PCL decreased with a decrease in PCL content. This crystal melting of PCL did not occur in the case of PCL(1250)(71)LDI-BDA. Decreasing PCL content over 71 wt%, a baseline shift corresponding to the glass transition temperature (T_g) of the hard segments was observed between temperatures of 370 K and 380 K.

The crystallinity of the soft and hard segments was investigated by WAXD measurements. SPUU containing long soft segments showed PCL crystalline diffraction peaks at q = 15.1 (d = 0.41 nm), 15.6 nm (d = 0.40 nm), and 16.8 nm (d = 0.38 nm) corresponding to the orthorhombic (110), (111), and (200) planes, respectively. In this SPUU, these peaks became weak with a decrease in PCL content, and disappeared for PCL(1250)(71)LDI-BDA.

The phase structure of SPUU was characterized

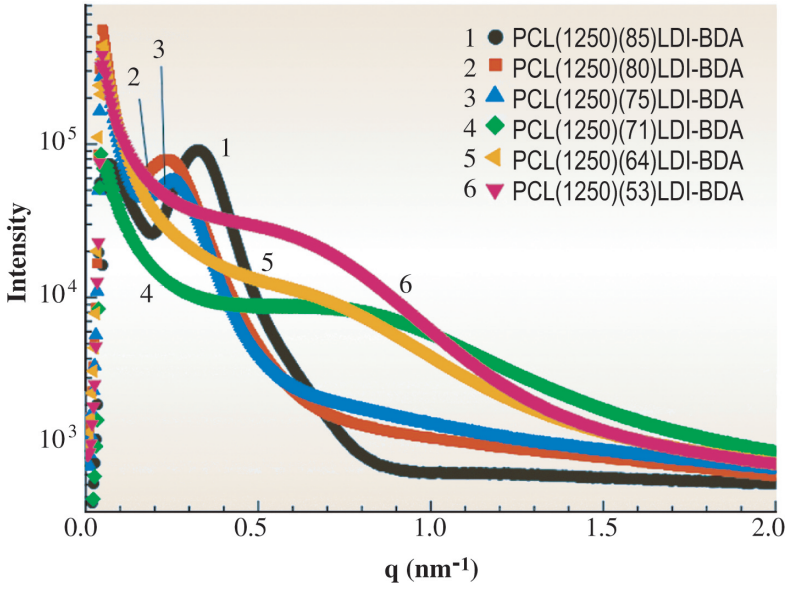

Fig. 1. The dependence of corrected intensity on scattering vector, q for PCL(1250)(X)LDI-BDA.

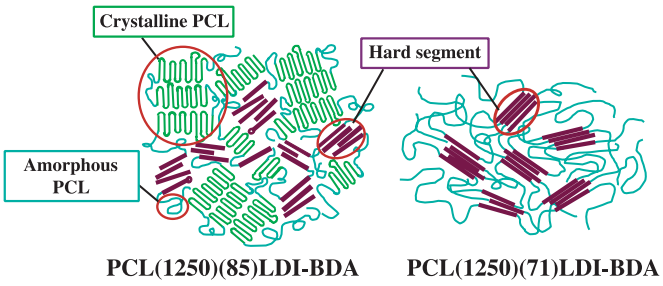

Fig. 2. The structure model of PCL(1250)(X)LDI-BDA.

by synchrotron SAXS measurements. SAXS was measured at BL40B2. Figure 1 shows the dependence of the corrected intensity on the scattering vector, q of SPUU. Here q is defined as $4\pi \sin\theta/\lambda$. The large peak observed at q = *ca.* 0.23-0.33 nm^{-1} (L = 27.3-19.6 nm) is attributed to the long period between the PCL crystallites. Even for PCL(1250)(85)LDI-BDA without the hard segment component, the long period was clearly observed. The intensity of this peak decreased with an increase in the hard segment content and disappeared for PCL(1250)(71)LDI-BDA. Also, this peak disappeared above the melting temperature of PCL. However, a scattering peak corresponding to the distance between the hard segment domains was observed in PCL(1250)(71)LDI-BDA. The structure model of PCL(1250)(X)LDI-BDA based on the above-mentioned characterization is depicted in Fig. 2. In the case of a high PCL fraction, PCL formed a stacked and folded lamellar crystal between hard segment domains. Since the PCL formed a lamellar crystal, PCL(1250)(X)LDI-BDA with X > 75 formed a three-phase structure consisting of the glassy hard segment, amorphous PCL and a crystalline PCL phase. On the other hand, in the case of PCL(1250)(X)LDI-BDA with X = < 71, a two-phase structure consisting of the hard and soft segments appeared due to the loss of crystallinity of PCL in the soft segment phase.

To investigate the biodegradability of SPUU, a BOD degradation test was carried out. The BOD degradation rate of SPUU was increased with increasing PCL content (Fig. 3). SPUU with a high PCL content (above 71 wt%) showed the high degradability in the activated sludge. On the other hand, SPUU with a low PCL content (64 wt% and 53 wt%) showed low degradability. This indicated that the ester linkages of PCL were degraded easily by microorganisms.

Biodegradable segmented poly(urethaneurea)s (SPUU) were successfully synthesized from lysine-based diisocyanete (LDI), with polycaprolactone diol (PCL) and 1,4-butanediamine (BDA) constituting the hard segments. Thermal analysis by DSC and structural analysis by SAXS and WAXD measurements revealed that the relative ratio of PCL to BDA segments in SPUU changed the crystallinity of the PCL segment and the microphase separation structure consisting of soft and hard segments.

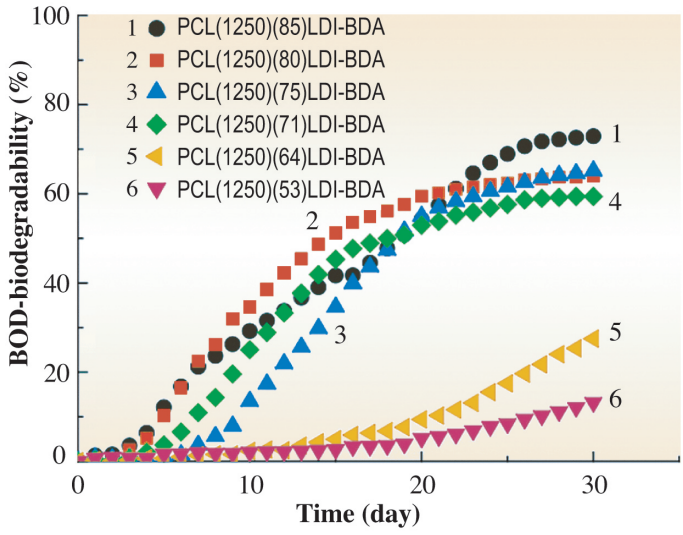

Fig. 3. The BOD degradation behaviors of PCL(1250)(X)LDI-BDA.

Atsushi Takahara[a,*], Michiko Hadano[a] and Sono Sasaki[b]

[a] Institute for Materials Chemistry and Engineering, Kyushu University
[b] SPring8 / JASRI

*E-mail: takahara@cstf.kyushu-u.ac.jp

References

[1] A. Takahara *et al.*: Macromol. Symp. **224** (2005) 207.
[2] *M. Hadano, T. Yamaguchi, H. Otsuka, K. Aoi, S. Sasaki and A. Takahara: J. Soc. Rubber Ind.* ***79*** *(2006) 219 (in Japanese).*

In situ Investigation of Annealing Effect on Higher-order Structure of Polyethylene Thin Films by Synchrotron Grazing-incidence Small-angle and Wide-angle X-ray Scattering

Polymer thin films have been used for parts of components of displays, as the insulation layer of semiconductors and as materials to coat papers for printing. To satisfy the physical properties of the thin films as materials, it is important to control their higher-order structures at nano-to-meso scales. In general, crystalline polymers form a higher-order structure consisting of crystalline and amorphous regions. The surface and local morphologies of thin films are generally investigated by microscopic observation. However, the essential structural property of the thin films is still under discussion. The grazing-incidence small-angle X-ray scattering (GISAXS) method has recently attracted considerable attention as a powerful tool for the meso-scale structural analysis of the thin films of polymers, for example, microphase-separated block copolymers and nanoporous polymers [1,2]. In this study, the annealing effect on the lamellar stacking structure of polyethylene thin films prepared on Si wafers has been investigated at molecular and lamellar scales by synchrotron GISWAXS measurements [3].

The sample used in this study was additive free high-density polyethylene (HDPE, melt index = 14) supplied from Mitsui Chemicals, Inc., as a typical example of crystalline polymers. Thin films with a thickness of ca. 400 nm were prepared onto the native oxide covered Si (110) surface of wafers with a 0.1 wt% *p*-xylene solution of HDPE under a N_2 atmosphere by a dip-coating method [4]. The obtained films were isothermally crystallized from the melt at 373 K for 24 h under a N_2 atmosphere.

In general, scattering from an organic thin film is relatively weak in intensity. Therefore, utilizing high brilliance and highly parallel synchrotron X-rays as incident beams is effective in detecting GISWAXS from HDPE thin films. To investigate the molecular and meso-scale order structure of the films, synchrotron GISWAXS measurements were carried out using an imaging intensifier (II), a charge coupled device (CCD) detector and imaging plate (IP) detectors at beamline **BL40B2**. Figure 1 shows the experimental geometry of the GISWAXS measurements. The components of the scattering vector, **q**, parallel and perpendicular to the sample surface were defined as $\mathbf{q}_y = (2\pi/\lambda)\sin(2\theta_f)\cos(\alpha_f)$ and $\mathbf{q}_z = (2\pi/\lambda)(\sin(\alpha_i) + \sin(\alpha_f))$, respectively, for reflected scattering. Here, α_i is the incident angle of the X-ray beams, α_f is the exit angle, λ is the wavelength of the incident X-ray beams and $2\theta_f$ is the angle between the scattered beam and the plane of incidence. The subscripts s and w in Fig. 1 indicate the GISAXS and the grazing-incidence wide-angle X-ray scattering (GIWAXS) geometries, respectively. The nano-scale order structure such as the chain-packing distance and chain orientation in the crystal region can be evaluated for the films by two-dimensional GIWAXS measurements. On the other hand, the meso-scale order structure such as lamellar stacking distance and lamellar orientation can be investigated for the films on the basis of the two-dimensional GISAXS data. The λ of the incident X-rays was 0.15 nm and the sample-to-detector distances were *ca.* 100 mm for GIWAXS and *ca.* 2177 mm for GISAXS. A 2000 mm-long vacuum path was utilized between the sample cell and the detector for GISAXS measurements. The data collection time was 10 s per GISAXS pattern with the II + CCD detector and 300 s per GIWAXS or GISAXS pattern with the IP detector.

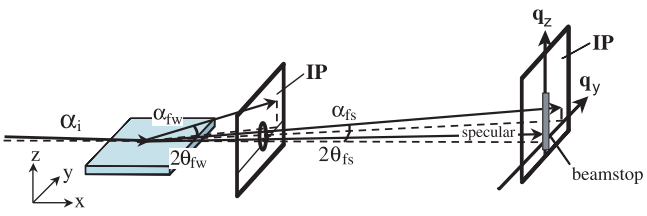

Fig. 1. Schematic geometry of GISWAXS measurements.

In situ GISWAXS measurements were carried out for the films at the annealing temperatures, *Ta*, of 378 K, 383 K, 388 K and 393 K in a stepwise annealing process from 300 K to 453 K. The film on the silicon wafer was placed on the heater stage of a low-vacuum sample cell, and the sample temperature was accurately monitored and controlled with ultra-thin and wide K-type thermocouples and a program temperature controller. At each *Ta*, GISWAXS from the film was measured for 300 s after annealing for 600 s. The heating rate was *ca.* 10 deg/min and the temperature fluctuation of the film at each *Ta* was ± 0.5 deg. The detectable **q**-ranges of GIWAXS and GISAXS in these experiments were *ca.* 21 nm^{-1} ~ 4.2 nm^{-1} and 1.3 nm^{-1} ~ 4.2 × 10^{-2} nm^{-1}, respectively.

Figures 2(a) ~ 2(f) show GISWAXS patterns measured at α_i = 0.13 deg for a melt-crystallized HDPE thin film in the initial state at 300 K, in the stepwise annealed state at 378 K, 383 K, 388 K and 393 K, and in the melt state at 453 K, respectively. As shown in the GIWAXS pattern in Fig. 2(a), the (110) and (200) reflections of oriented HDPE orthorhombic

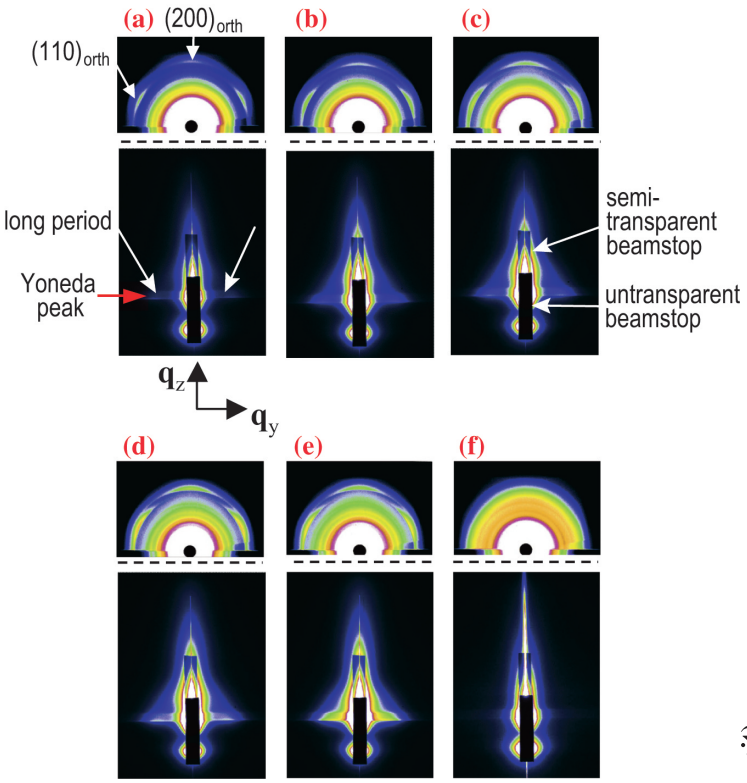

Fig. 2. GISWAXS patterns measured at α_i = 0.13 deg for a melt-crystallized HDPE thin film in the initial state at 300 K **(a)**, in the stepwise annealed state at 378 K **(b)**, 383 K **(c)**, 388 K **(d)** and 393 K **(e)**, and in the melt state at 453 K **(f)**. The upper and lower images at each temperature are the GIWAXS and GISAXS patterns, resp1ectively.

crystals were measured in the out-of-plane direction for the initial thin film. These reflections were azimuthally broad peaks and the maximum intensity of the (200) reflection was on the $\mathbf{q}_z$ axis. It was revealed that the a axis of the orthorhombic unit cell was oriented in the perpendicular direction to the film surface. In other words, the chain axis (the *c* axis) was oriented parallel to the film surface. The reflection peaks for the annealed thin films were almost the same in $\mathbf{q}_y$ and $\mathbf{q}_z$ as those for the initial thin film. The relative intensity of these reflections increased with an increase in annealing temperature, as shown in the GIWAXS patterns of Figs. 2(b) - 2(e). This implied that the degree of crystallinity was increased by annealing.

On the other hand, scattering peaks were detected only in the in-plane direction near a Yoneda peak in the GISAXS pattern in Fig. 2(a), which means that crystalline lamellae were stacked parallel to the film surface. The $\mathbf{q}_y$ of these peaks relates to the long period, the average distance between stacked crystalline lamellae. The Yoneda peak arises in the in-plane direction due to the interference of the incident and scattered waves [5]. By stepwise annealing, these scattering peaks slightly shifted to a lower $\mathbf{q}_y$ range in the in-plane direction and increased in relative intensity with an increase in *Ta*. Figure 3 shows the in-plane intensity profiles of the *in situ* GISAXS patterns at α_{fs} = 0.13 nm^{-1} along the Yoneda peak in Figs. 2(a) - 2(e). It clearly indicated that the shoulder peak gradually shifted from $\mathbf{q}_y$ = *ca.* 0.25 nm^{-1} to *ca.* 0.20 nm^{-1} with increasing sample temperatures from 300 K to 393 K. The GISAXS data suggested that crystalline lamellae were stacked with large disordering parallel to the film surface, and the long period became longer from *ca.* 25 nm to *ca.* 32 nm by annealing. These results suggest that the synchrotron GISWAXS experimental technique can be applied to the kinetic study of the higher-order structure of polymer thin films.

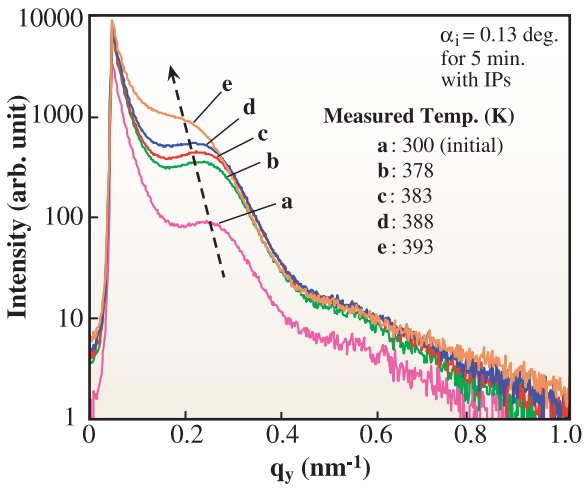

Fig. 3. In-plane intensity profiles of the *in situ* GISAXS patterns in Figs. 2**(a)** – 2**(e)** measured for the HDPE thin film in a stepwise annealing process from 300 K.

Sono Sasaki[a,*], Hiroshi Okuda[b] and Masaki Takata[a,c]

[a] SPring-8 / JASRI
[b] International Innovation Center, Kyoto University
[c] SPring-8 / RIKEN

*E-mail: sono@spring8.or.jp.

References

[1] C. Tang *et al.*: J. Am. Chem. Soc. **127** (2005) 6918.
[2] B. Lee *et al.*: Nature Mater. **4** (2005) 147.
[3] S. Sasaki, H. Masunaga, H. Tajiri, K. Inoue, H. Okuda, H. Noma, K. Honda, A. Takahara, and M. Takata: J. Appl. Crystallog. (SAS2006 Proc.) - to be published.
[4] H. Yakabe *et al.*: Polym. Bull. **53** (2005) 213-222.
[5] Y. Yoneda: Phys. Rev. **131** (1963) 2010.

Structural Transition of Poly[(*R*)-3-hydroxybutyrate] Single Crystals on Heating as Revealed by SAXS and WAXD

Poly[(*R*)-3-hydroxybutyrate] (P(3HB)) is a biodegradable thermoplastic material, produced from renewable carbon sources by bacteria as intercellular carbon and energy reserves. P(3HB) has thus attracted much attention as a material to solve problems concerning energy resources and disposal of solid waste. Enzymatic degradation of P(3HB) material by extracellular P(3HB) depolymerase occurs first at amorphous regions and subsequently at the crystalline regions. Accordingly, the crystalline regions in the material play an important role in the regulation of the biodegradability as well as the physical properties. For wide applications of P(3HB) the physical properties of the material should be improved more.

Annealing is a treatment method to improve the physical properties as a result of the change in morphology of crystalline regions and removing a residual stress, etc., by heating. Polymer crystals, which are lamellar crystals with folded chains, can reorganize into more stable state, thickened crystals, by heating below their equilibrium melting temperature. The evidences provided from the annealing experiments of polymer crystals have contributed to the development the high-performance polymer materials, although the molecular mechanism of the crystal thickening during annealing has been still an object of argument. In P(3HB), there is a few works on the annealing behavior and the thickening mechanism at a molecular level is still unclear. Here, the real-time annealing experiments of P(3HB) crystal by synchrotron radiation small-angle X-ray scattering (SAXS) and wide-angle X-ray diffraction (WAXD) are reported [1,2].

The number-average molecular weight and polydispersity of P(3HB) used here are 15,000 and 1.6. Single crystals of P(3HB) were grown isothermally in its dilute solution at desired crystallization temperatures (T_c). The sedimented single crystal mats were obtained by a filtration after the suspension was cooled down to room temperature, and then dried under vacuum. The single crystal mats were set in the sample holder, and heated from room temperature to around 180 °C at a heating rate of 10 °C / min. Real-time SAXS and WAXD measurements were carried out at **BL45XU** beamline. Thermal properties of the single crystal mats were evaluated by differential scanning calorimetry (DSC).

Figure 1(a) shows two-dimensional (2D) SAXS patterns of the sedimented mats of P(3HB) single crystals grown at 60 °C. These images were taken at elevated temperatures. The meridian corresponds to the lamellar stacking direction in the sedimented mats. On the meridian, scattering peak from the stacking period of original crystals is clearly recognized as indicated with the yellow arrowheads. The lamellar thickness was estimated as 4.0 nm. The original peak shifted little on heating up to 120 °C. A new scattering peak at a lower angle was observed at an annealing temperature (T_a), as indicated with the red arrowheads in Fig. 1(a). Figure 1(b) shows the corresponding circular-averaged 1D profiles. It was found that the crystals exhibit discontinuous increase in thickness during the transition, and the population of reorganized crystals increases while that of original ones decrease with temperature. The similar behavior was also observed in the single crystals grown at other crystallization temperatures. The onset of the transition was found to depend on the crystallization temperature. Namely, the transition occurs at higher temperatures with the increase of the original lamellar thickness.

The changes in lamellar thickness against T_a for

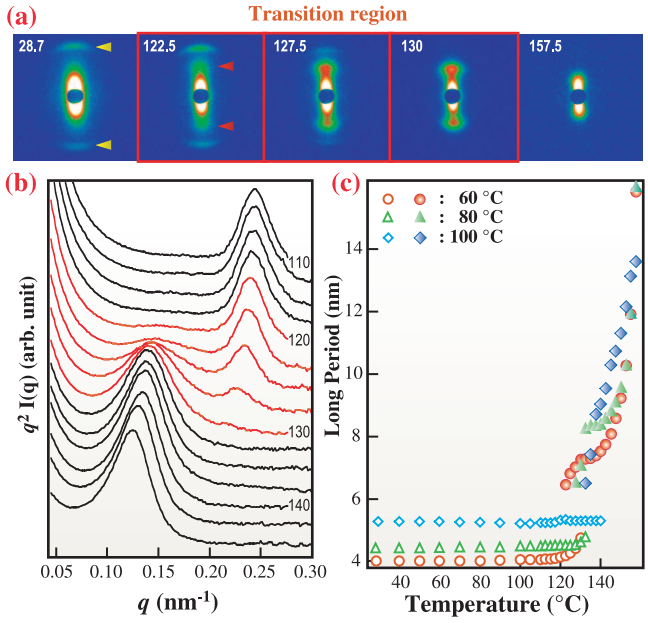

Fig. 1. 2D SAXS patterns (**a**) and integrated 1D profiles (**b**) of P(3HB) single crystals grown at 60 °C. In (**b**), the red lines correspond to the profiles in the transition region. (**c**) Long period plotted against annealing temperature. Open and filled symbols represent long periods of original and reorganized crystals, respectively.

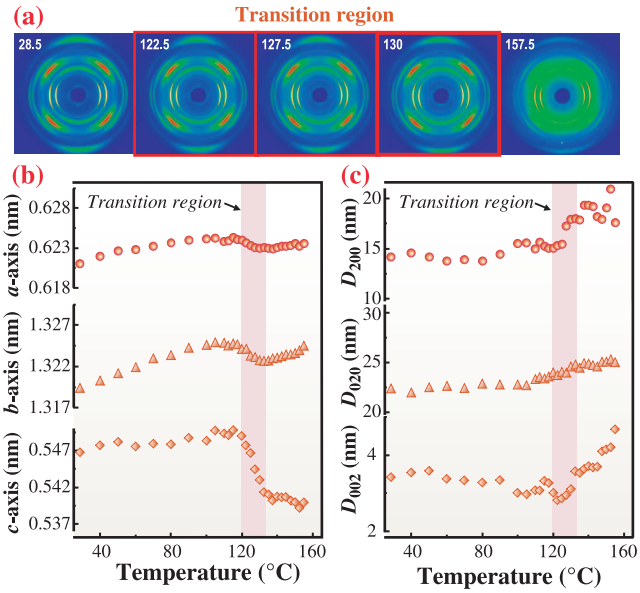

Fig. 2. **(a)** 2D WAXD patterns of P(3HB) single crystals grown at 60 °C. **(b)** Lattice dimension plotted against annealing temperature for T_c = 60 °C. **(c)** Crystallite size plotted against annealing temperature for T_c = 60 °C.

the single crystals grown at 60, 80, and 100 °C are shown in Fig. 1(c). This figure clearly demonstrates a discontinuous lamellar thickening and the coexistence of the two populations with different lamellar thicknesses. After the discontinuous increase, the remaining peak shifted to lower angles, and finally diminished due to complete melting.

The representative 2D WAXD patterns are shown in Fig. 2(a). Well-resolved fiber diffraction patterns of P(3HB) crystal were obtained. From the 2D WAXD patterns, temperature dependence of lattice dimensions (*a*-, *b*-, and *c*-axes), apparent crystallite size (D_{200}, D_{020} and D_{002}), which were estimated from the peak positions and widths, are shown in Fig. 2(b) and 2(c). The crystal lattice, i.e., intermolecular distance, expanded gradually with temperature, and the lattice dimensions turn to contract at the onset of lamellar thickening. This fact means that the chains registered in the original crystal are released and then rearranged. The D_{002}, which corresponds to crystalline core thickness, also started to increase in response to lamellar thickening, indicating that the discontinuous increase is accompanied by not only the formation of amorphous layer between crystals but also the real thickening of crystal

As shown in Fig. 3, the crystallinity first decreased and then recovered during the thickening process. On the other hand, the lamellar thickening was accompanied by endo- and exothermic signals in DSC. Therefore, the discontinuous lamellar thickening of P(3HB) single crystal is caused by

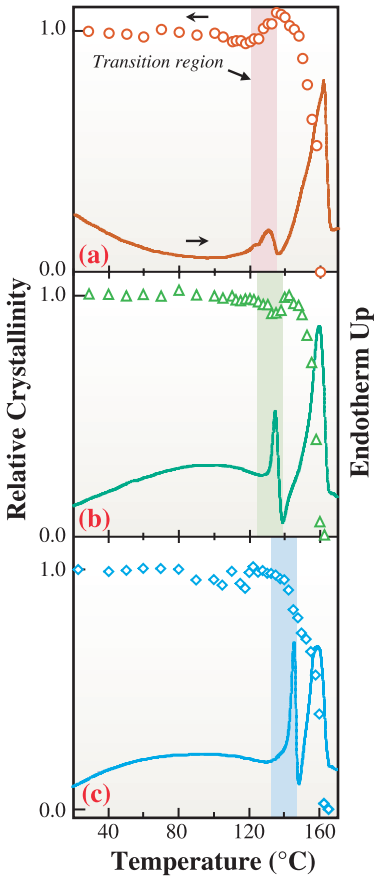

Fig. 3. Crystallinity plotted against annealing temperature and DSC curve; **(a)** Tc = 60 °C, **(b)** 80 °C, and **(c)** 100 °C.

melting and recrystallization. The degree of recovery in crystallinity fell with increasing in the original lamellar. This is because the crystallization rate becomes slower with increasing in the temperature region where the transition occurs. We have considered that the discontinuous lamellar thickening is cooperative process with the adjacent crystals along the stacking direction. The chains released from the lattice mutually diffuse, leading to a thicker crystal, into the space in which the adjacent crystal existed [2].

Mashiro Fujita[a,*], Tadahisa Iwata[b] and Kazuki Ito[c]

[a] Bioengineering Laboratory, RIKEN Wako Institute
[b] Graduate School of Agricultural and Life Sciences, The University of Tokyo
[c] SPring-8 / RIKEN

*E-mail: mfujita@riken.jp

References

[1] M. Fujita *et al.*: Macromol. Rapid Commun. **26** (2005) 678.
[2] *T. Sawayanagi, T. Tanaka, T. Iwata, H. Abe, Y. Doi, K. Ito, T. Fujisawa, and M. Fujita: Macromolecules* ***39*** *(2006) 2201.*

Synchrotron Radiation Research for Progress of Self-regenerative Function to Rh-, and Pt-perovskite Catalysts

It is inevitable that the demand for precious metals, namely Pd, Rh, and Pt, for use as automotive catalysts has increased, in the absence of technological innovation, owing to the global strengthening of emission controls and to the increase in the number of automobiles particularly in China and India. Automotive catalysts deteriorate as a result of a decrease in the active surface area of precious metals induced by grain growth in high-temperature exhaust gas. To compensate for this deterioration, conventional catalysts are loaded with an excess amount of precious metals, which however leads to over-consumption and supply problems. A self-regenerative "intelligent catalyst," which suppresses the grain growth of Pd, was developed in 2002 and has been industrialized since then. This new technology is based on the reversible change of Pd with perovskite oxides between a solid solution and metallic nanoparticles under an inherent redox environment of exhaust gases during vehicle use [1,2]. Very recently, we have succeeded in realizing the self-regeneration function of an intelligent catalyst for Rh and Pt by utilizing synchrotron radiation research performed at beamlines **BL14B1** and **BL01B1** [3].

Figure 1 shows the powder X-ray diffraction pattern in the limited range of momentum transfer, Q, for $CaTi_{0.95}Rh_{0.05}O_3$ after oxidation. Two Bragg reflections from the sample are assigned to the pseudocubic cell of the ABO_3 perovskite structure. The structure factor for the (100) reflection can be expressed approximately as $F(100) \propto |f_A - f_B - f_O|$, where f_A, f_B, and f_O are the atomic scattering factors for the A-site, B-site, and oxygen atoms, respectively. The inset represents the energy dependence of the reflection intensity near the Rh *K*-edge (23.220 keV). The dip of the intensity at the edge energy clearly indicates that Rh occupies the B-site of the $CaTiO_3$-type perovskite structure, since $|f_{Ca}|$ is always smaller than $|f_{Ti}|$ in this energy range.

The self-regeneration function is analyzed by XAFS. The XAFS profile of $CaTi_{0.95}Rh_{0.05}O_3$ samples after oxidation (O), reduction (OR), and reoxidation (ORO) at 800 °C for 1 hour in each step are shown in Fig. 2. The edge shift towards lower energies for the OR sample indicates that a greater proportion of Rh is in the metallic state. The edge position for the O and ORO samples is slightly higher than that of the trivalent Rh seen in Rh_2O_3, implying an unusually higher valence state of Rh. The calculated radial structure function clearly shows a reversible change in the local structure around Rh. The first peak for the oxidized and re-oxidized samples corresponds to the 6 oxygen atoms of a RhO_6 octahedron. For the

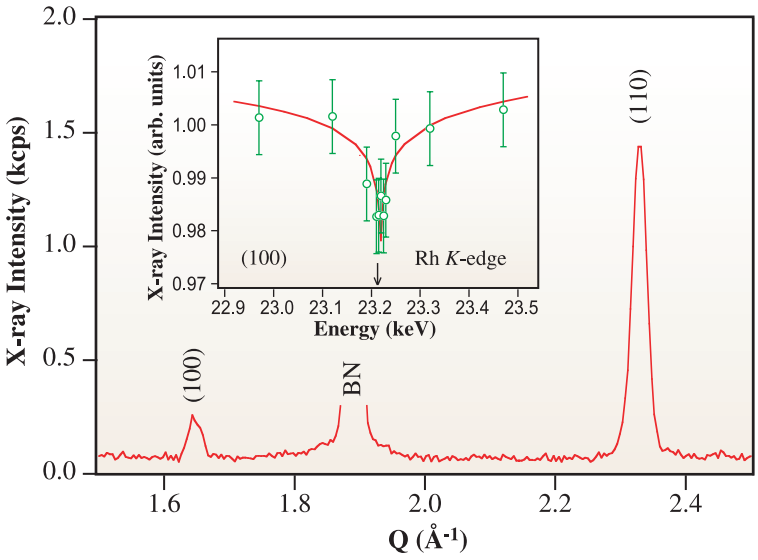

Fig. 1. X-ray powder diffraction patterns of $CaTi_{0.95}Rh_{0.05}O_3$ around Bragg reflections (100) and (110) for pseudocubic cell of perovskite structure. The oxidized sample contained BN as a binder. The inset gives the energy dependence of the (100) reflection intensity near the Rh *K*-edge.

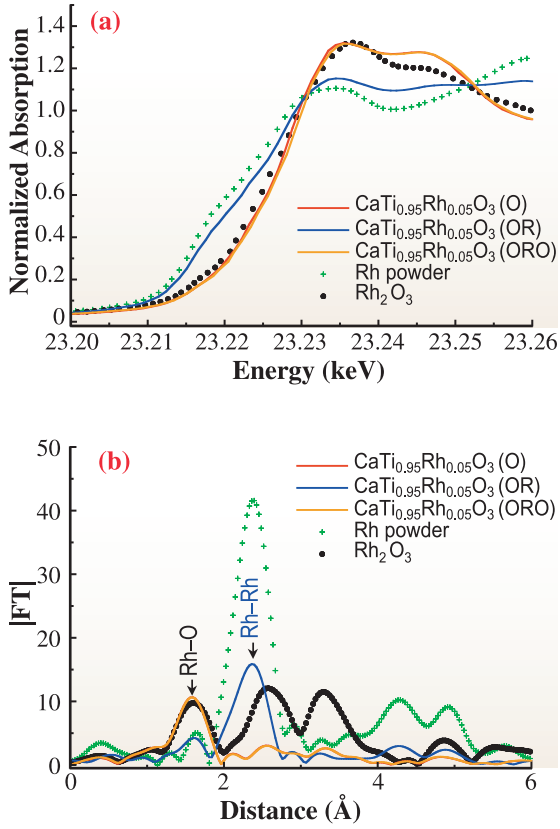

Fig. 2. **(a)** XANES profile near the Rh *K*-edge for $CaTi_{0.95}Rh_{0.05}O_3$ after oxidization (O), reduction (OR), and re-oxidization (ORO), together with Rh_2O_3 and Rh powders as reference materials. **(b)** The radial structure function around Rh calculated as magnitude of the Fourier transform of k^3-weighted EXAFS oscillations.

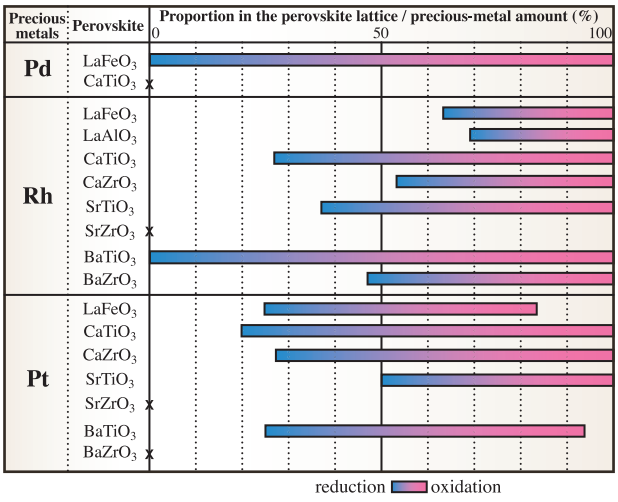

Fig. 3. Comparison of solid solution of precious metal for various perovskites. A longer bar indicates better self-regeneration performance. X indicates that the precious metal forms no solid solution with perovskite.

reduced sample, the coordination number of the oxygen atoms decreases and the Rh-Rh bond appears due to the formation of metallic clusters or nanoparticles. At the same time, the perovskite oxide releases oxygen and retains its electro-neutrality.

We have successfully realized the self-regeneration function for Pt in the same way as that for Pd and Rh. The proportion of precious metal present in the perovskite lattice as a solid solution was estimated from the coordination number of the first nearest neighbor with oxygen (Pd-O, Rh-O, or Pt-O bonds) and is given for various combinations in Fig. 3. In a reductive atmosphere, precious metals emerge from oxides to form metallic nanoparticles that demonstrate a higher catalytic activity. Perovskite oxides should maintain a stable structure so that they can capture and release precious metals at high temperatures under a redox environment.

We have demonstrated that a precious-metal-containing perovskite catalyst can behave as an intelligent catalyst, which regenerates itself to maintain a high catalytic activity even in a harsh redox environment at high temperatures. Such technology is expected as a solution to precious-metal reduction. A DXAFS experiment is now in progress to investigate the real time-dependent behavior of precious metals.

Hirohisa Tanaka[a,*] and Yasuo Nishihata[b]

[a] Daihatsu Motor Co., Ltd.
[b] SPring-8 / JAEA

*E-mail: hirohisa_tanaka@mail.daihatsu.co.jp

References

[1] Y. Nishihata *et al.*: Nature **418** (2002) 164.
[2] Y. Nishihata and H. Tanaka: SPring-8 Research Frontiers, 2001B/2002A, p. 75.
[3] *H. Tanaka, M. Taniguchi, M. Uenishi, N. Kajita, I. Tan, Y. Nishihata, J. Mizuki, K. Narita, M. Kimura, K. Kaneko: Angew. Chem. Int. Ed.* ***45*** *(2006) 5998.*

Nuclear Spectroscopy of Nitrogenase and Hydrogenase

In nature, the reduction of dinitrogen to ammonia ($N_2 \rightarrow 2NH_3$), and the reversible oxidation of H_2 to protons and electrons ($2H^+ + 2e^- \rightleftarrows H_2$), rely on two critical enzymes – respectively nitrogenase (N_2ase), and hydrogenase (H_2ase). N_2 fixation is the key step in the nitrogen cycle, and the biological process is responsible for about half of the protein available for human consumption. The other half is produced using natural gas in fertilizer factories by the Haber-Bosch process – an activity that corresponds to ~2% of world energy production. The H_2 used in the synthetic process is derived from natural gas, and the production of ammonia currently consumes about 5% of global natural gas consumption. H_2 processing is crucial for the metabolism of many anaerobic organisms, and knowledge about the mechanism of H_2 evolution may prove critical for a future 'H_2 economy'. Bacteria are able to catalyze the reversible oxidation of H_2 using cheap and abundant Fe, while the best synthetic catalysts rely on precious Pt group metals. In summary, a better understanding of N_2ases and H_2ases may have an impact on our use of fossil fuels and our ability to transition to a more sustainable energy economy.

In nature, at least three different forms of each enzyme have evolved – what they have in common is the use of Fe at the active site, either with or without the assistance of a second metal (Mo, V, Ni). As illustrated in Fig. 1, X-ray crystallography has provided detailed atomic level structures for the electron transfer chains and active sites of these enzymes. However, so far it has been difficult to capture key enzyme intermediates in the crystalline state, and important questions remain about both structure and mechanism. For this reason, we have turned to a spectroscopic technique – Nuclear Resonance Vibrational Spectroscopy (NRVS).

The NRVS experiment involves scanning an extremely monochromatic X-ray beam through a

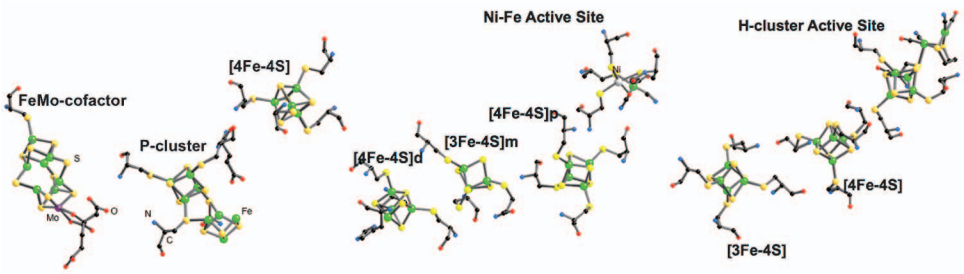

Fig. 1. The electron transfer chains and active sites for (left to right): *A. vinelandii* Mo N_2ase, *D. vulgaris* [NiFe] H_2ase, and *C. pasteurianum* [FeFe] H_2ase.

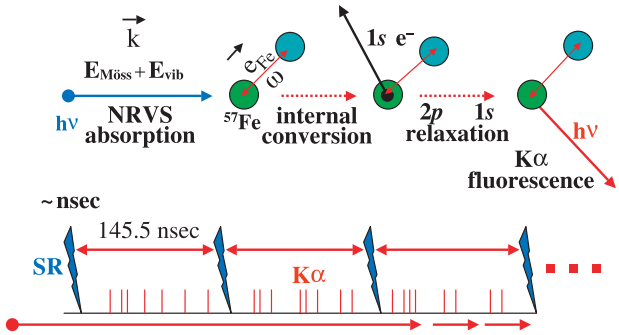

Fig. 2. Schematic illustration of the NRVS measurement. Left to right: monochromatic photons from SPring-8 beamline BL09XU excite an ^{57}Fe nucleus and a vibration with frequency ω. The excited ^{57}Fe nucleus relaxes by internal conversion with a lifetime of ~100 ns by expelling a 1*s* electron. The subsequent Kα radiation is measured between synchrotron pulses (bottom) by an avalanche photodiode detector.

nuclear resonance. Apart from the 'zero phonon' (recoil-free) Mössbauer resonance, there are additional transitions that correspond to nuclear excitation plus excitation or de-excitation of vibrational modes. A time-gated APD detector allows separation of these nuclear events from the almost instantaneous scattering and X-ray fluorescence (Fig. 2). NRVS offers a less restrictive selection rule than infrared or resonance Raman spectroscopy – the only requirement for intensity is motion of the resonant nucleus (in our case ^{57}Fe) along the direction of the incident X-ray beam in a given normal mode. The bottom line is that the intensity for a particular normal mode is proportional to the fraction of kinetic energy due to ^{57}Fe in that mode. The benefit of NRVS for characterization of Fe in N_2ase and N_2ase should be clear – we only observe normal modes associated with motion of the Fe atoms.

The partial vibrational density of states (PVDOS) that can be measured by NRVS covers a frequency range from ~10 cm^{-1} to nearly 1000 cm^{-1}, as illustrated in Fig. 3 for the electron transfer protein rubredoxin [1,2], the FeMo cofactor of *A. vinelandii* N_2ase [3], and the mononuclear H_2ase from *M. marburgensis* called Hmd [4]. A wide variety of normal modes occur over these two orders of magnitude. At the low end are modes that involve large regions of polypeptide chain, as shown in Fig. 4, while at

the high end are the stiffest modes (such as Fe-CO bends) or those involving the lightest atoms, such as Fe-H and Fe-D stretches (not shown). In between are Fe-S stretching modes and cluster breathing modes that involve S-Fe-S and Fe-S-Fe bending.

We have used normal mode calculations, based on empirical force fields as well as based on DFT calculations, to interpret Fe metalloprotein NRVS. For example, by combining the CHARMM force field for peptide motion with our own empirical Fe-S force constants, we have modeled the entire spectrum for rubredoxin [2]. The lowest frequency mode is illustrated in Fig. 4. Also shown are the totally symmetric 'breathing' mode at 200 cm^{-1} for the FeMo cofactor [3], and the highest frequency mode, which is mostly Fe-C-O bending in nature, for the mononuclear Hmd H_2ase [4].

What have we learned from NRVS so far, and what does this technique promise for the future? With N_2ase, we have seen how the cluster dynamics are dominated by the presence of interstitial atom 'X'. For Hmd H_2ase, we have seen the importance of CO ligands in the Fe dynamics and obtained new data regarding the cysteine and tentative water ligands. Longer term, NRVS could allow characterization of bound substrates such as N_2 and H-, which is critical for understanding the catalytic mechanisms. But, if NRVS is to achieve its full potential, we will eventually need another order of magnitude in flux, as well as better monochromators and detectors. With such improvements, NRVS will become an extraordinarily powerful probe of Fe enzyme biochemistry.

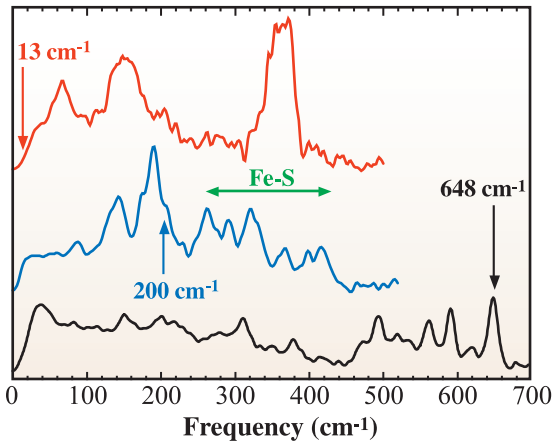

Fig. 3. Representative ^{57}Fe metalloprotein NRVS spectra. Top to bottom: **(a)** rubredoxin, **(b)** Hmd H_2ase, and **(c)** the isolated FeMo cofactor from N_2ase.

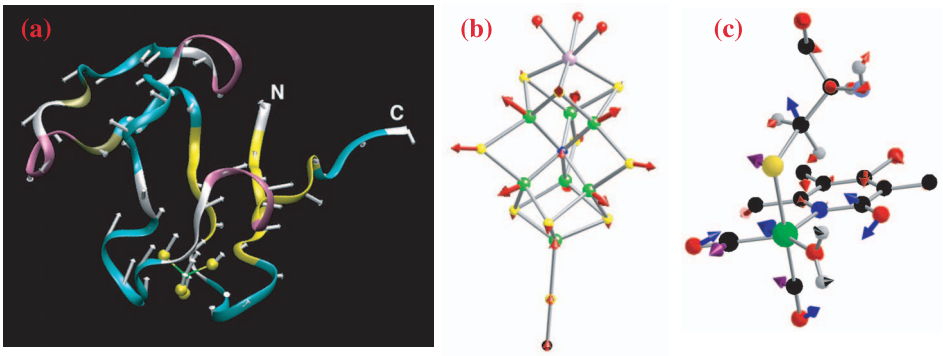

Fig. 4. Atomic motion in representative ^{57}Fe metalloprotein normal modes. Color code: S – yellow, Fe - green, C – black, O – red, and N – blue. Left to right: **(a)** the lowest frequency mode at 13 cm^{-1} for rubredoxin, **(b)** the totally symmetric mode at 200 cm^{-1} for the N_2ase FeMo cofactor, and **(c)** highest frequency mode at 648 cm^{-1} for the mononuclear Fe site in Hmd H_2ase. In the latter case, the motion of Fe and CO groups has been modified for clarity.

Stephen P. Cramer [a,b,*], Yuming Xiao [b] and Yisong Guo [b]

[a] Physical Biosciences Division, Lawrence Berkeley National Lab., USA
[b] Department of Applied Science, UC Davis, USA

*E-mail: spjcramer@ucdavis.edu

References

[1] Y. Xiao *et al.*: J. Am. Chem. Soc. **127** (2005) 14596.
[2] *M.-L. Tan, A.R. Bizzarri, Y. Xiao, S. Cannistraro, T. Ichiye, C. Manzoni, G. Cerullo, M.W.W. Adams, J.F.E. Jenney, S.P. Cramer: J. Inorg. Biochem.* ***101*** *(2006) 375.*
[3] *Y. Xiao, K. Fischer, M.C. Smith, W. Newton, D.A. Case, S.J. George, H. Wang, W. Sturhahn, E.E. Alp, J. Zhao, Y. Yoda, S.P. Cramer: J. Am. Chem. Soc.* ***128*** *(2006) 7608.*
[4] *Y. Guo, H. Wang, Y. Xiao, S. Vogt, R.K. Thauer, S. Shima, T. Rauchfuss, P. Volkers, E. Alp, W. Sturhahn, Y. Yoda, S.P. Cramer: J. Am. Chem. Soc.* ***129*** *(2007) - in preparation.*

Earth & Planetary Science

From the solar system to Earth's interior, SPring-8 research covers various experimental techniques. The present issue selected four topics. The first topic, "Composition, mineralogy and three-dimensional structures of particles derived from short period comet Wild II" by Tomoaki Nakamura is the research using X-ray fluorescence and diffraction analysis as well as microtomography of precious samples brought to Earth by the "STARDUST" project during NASA's comet sample return mission. Many scientists are involved in this project and the present result is one of the most important ones. They have found a wide range of compositions and structures in the comet Wild II particles that were collected and brought to Earth by NASA's Stardust spacecraft. The present findings suggested the existence of high temperature events in the early solar system, which can make us say "Stardust Findings Suggest Comets More Complex Than Thought."

The other three topics are related to the structure and physical properties of deep Earth materials. The X-ray absorption experiment under high pressure using a single crystal diamond capsule was carried out for "Anomalous compression of basaltic magma: implications for pressure-induced structural change in silicate melt" by Satoru Urakawa *et al*. The migration of silicate melt in the mantle is controlled by a density relationship with the surrounding solids. This study demonstrates the compressibility changes brought about by structural change in the melt under high pressure. For the structure-property research on large-volume samples at high pressure, the elaborate work, "High-pressure generation to simulate the earth's deep interior" by Tange *et al*., was carried out using the large-volume press. They succeeded in generating an extremely high pressure exceeding 70 GPa using the multi-anvil apparatus with sintered diamond cubes. One of the most powerful tools for a high-pressure and high-temperature X-ray diffraction experiment is the laser-heated diamond-anvil cell (LHDAC). The research, "Post-perovskite phase transition in Earth's deep mantle" by Kei Hirose accurately determined the $MgSiO_3$ post-perovskite phase transition boundary using multiple pressure standards. The result shall provide a more accurate understanding of the origin of the seismic boundary near the bottom of the mantle. Earth & Planetary Sciences are endless sources of interest for SPring-8.

Masaki Takata

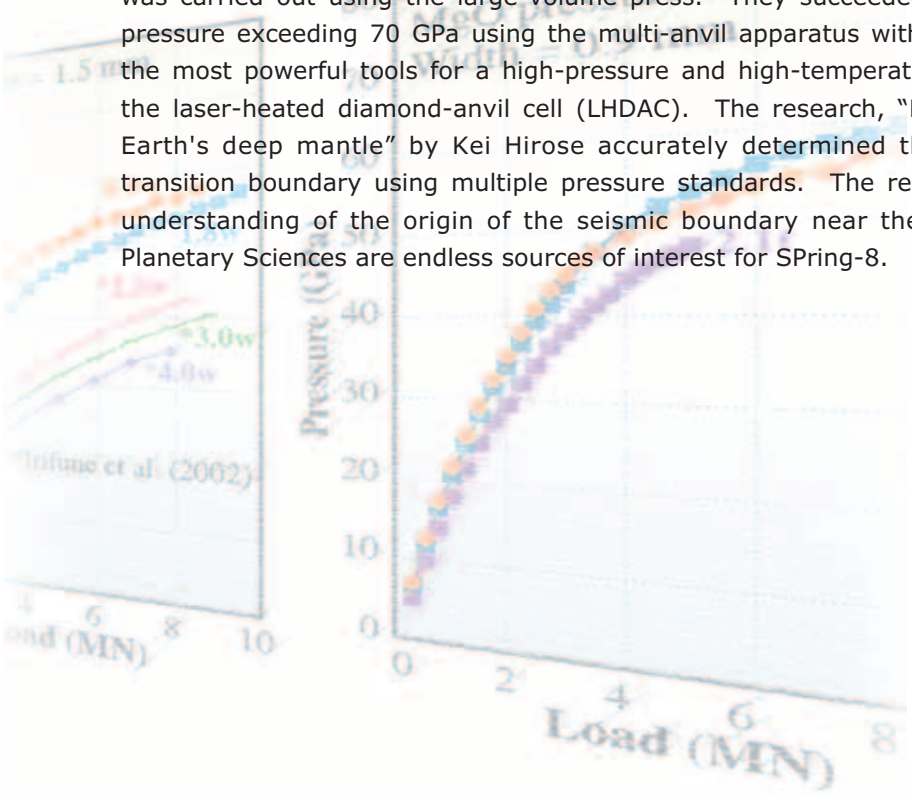

Composition, Mineralogy, and Three-dimensional Structures of Particles Derived from Short-period Comet Wild 2

More than 10000 small rock particles have been successfully recovered from the comet Wild 2 [1]. The Stardust spacecraft arrived at a position 200 km from the comet in 2004, collected numerous particles swept from the comet, and then returned to Earth in 2006. The silica aerogel collectors, which are superlight materials with a density of approximately 10 mg/cc onboard the spacecraft, have captured the cometary particles that traversed at 6 km/s against the collectors. As part of the preliminary examinations that were conducted by the international organization, we performed compositional, mineralogical, and morphological characterizations of the cometary particles using synchrotron radiation. The ultra-high photon density of the SPring-8 X-ray beam enabled us to detect very minor elements and minerals in the Stardust cometary particles.

Elemental abundance: X-ray fluorescence analysis was performed at beamline **BL47XU** using monochromated X-ray with an energy of 15 keV. The elemental abundance was obtained from both particles and tracks that are carrot-shaped holes in which the cometary particles decelerated (Fig. 1), because we need to determine the composition of a particle prior to its entry into the aerogel. Figure 2 shows the elemental abundance obtained from a large track that contains four particles [2]. The abundances of major elements such as S, Ca, Cr, Mn, Fe, and Ni are close to the solar abundance, but the abundance of minor elements is higher than the solar abundance. We analyzed four tracks and individual tracks show different compositional features. However, when we summarized all of the data from more than 20 tracks obtained by an international team [3], the elemental abundance of the cometary particles is close to the solar abundance including both major and minor elements. This demonstrates that the cometary particles are very pristine “raw materials” that formed our solar system.

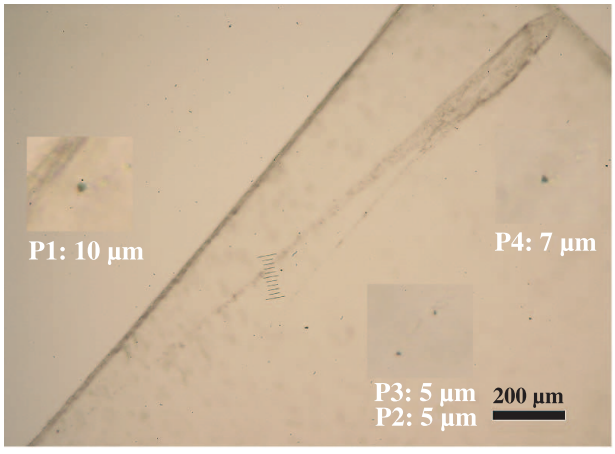

Fig. 1. A piece of aerogel with tracks and particles. A large particle came in from the upper right, broke into four pieces (P1 to P4), and stopped at the ends of the tracks. Evaporated materials are distributed along the tracks.

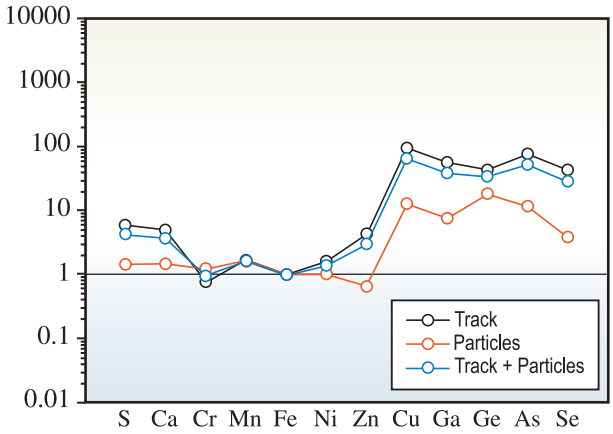

Fig. 2. Elemental abundance of tracks and particles (sum of P1 to P4) shown in Fig. 1. The abundance is normalized to Fe and solar abundance.

Mineralogy and structures of cometary particles: individual particles are obtained from the aerogels and exposed to X-ray for diffraction and tomography. X-ray diffraction analysis on more than 30 particles was carried out at beamline **BL37XU** at SPring-8 and 3A and 9C at KEK, while microtomography on 4 particles was performed at beamline **BL47XU**. Figure 3 shows the X-ray diffraction pattern and three-dimensional structures of a cometary particle [4]. The particles consist of anhydrous silicates such as olivine and pyroxene (Fig. 3(a)). No hydrous phases have been

detected so far. This suggests that solid materials in the comet Wild 2 are not hydrated despite of the presence of water ice. The internal structure of the particle (Figs. 3(b) and 3(c)) is similar to that of igneous rocks with poikilitic texture: olivine occurs within low-Ca pyroxene without pore spaces between them. This suggests that the particle was once melted before incorporation into the comet in the early solar system. Melting during capture in the aerogel is not possible, because the periphery of the particle was not melted with the surrounding aerogel. The presence of this kind of particles suggests that high temperature (>1550 °C) events occurred in the early solar system and the particle that were melted during the events were incorporated into a region of the outer solar system where comets have formed.

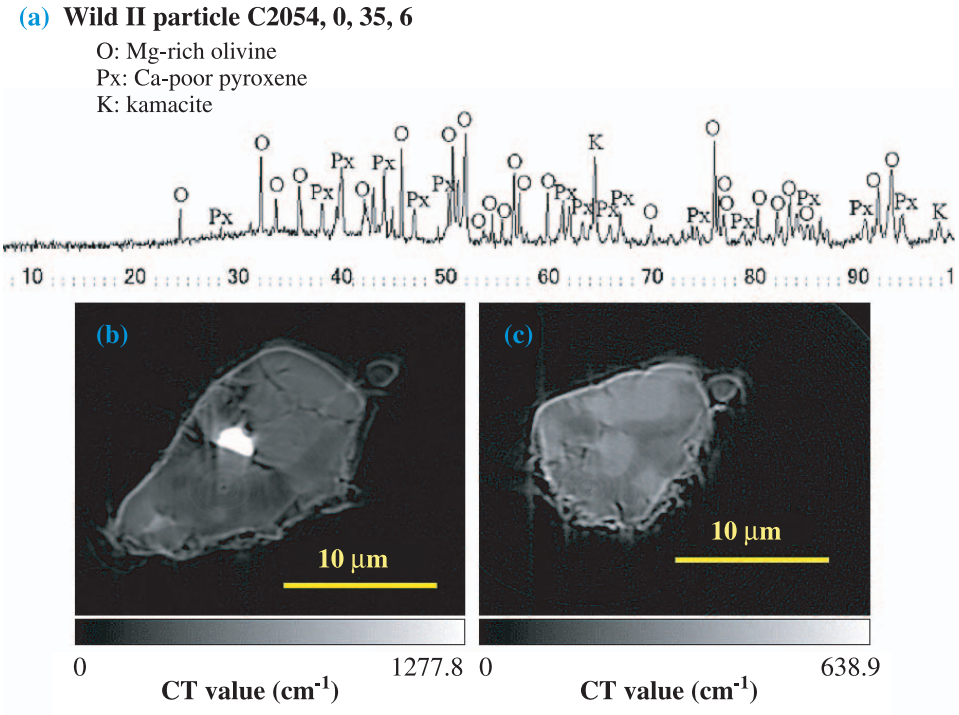

Fig. 3. X-ray diffraction pattern **(a)** and micro tomography images **(b)** and **(c)** of a cometary particle. In **(b)** and **(c)**, olivine grains (light grey) occur within Ca-poor pyroxene (dark grey).

Tomoki Nakamura[a,*] and Akira Tsuchiyama[b]

[a] Department of Earth and Planetary Science, Kyushu University
[b] Department of Earth and Space Science, Osaka University

*E-mail: tomoki@geo.kyushu-u.ac.jp

References

[1] D. Brownlee *et al.*: Science **314** (2006) 1711.
[2] *A. Tsuchiyama, T. Nakamura, T. Okazaki, K. Uesugi, T. Nakano, T. Akaki, Y. Iida, K. Jogo and Y. Suzuki: submitted to Meteoritics and Planetary Science (2007).*
[3] G.F. Flynn *et al.*: Science **314** (2006) 1731.
[4] *T. Nakamura, A. Tsuchiyama, T. Akaki, K. Uesugi, T. Nakano, A. Takeuchi, Y. Suzuki and T. Noguchi: submitted to Meteoritics and Planetary Science (2007).*

Anomalous Compression of Basaltic Magma: Implications to Pressure-induced Structural Change in Silicate Melt

The transportation of magmas, which are generated by the partial melting of deep-seated mantle rocks, in the planetary interior is driven by buoyant force. The relative density between magmas and surrounding rocks controls whether magma ascends to the surface or remains in the deep interior. Density also controls the gravitational separation of crystals from the deep magma ocean in the earliest Earth, which could generate chemical stratification of the Earth's interior. Magmas are normally less dense than coexisting crystals at atmospheric pressure, but they are more compressible than crystals (Fig. 1). More than two decades of experimental studies have shown that the density of magmas can be higher than that of coexisting crystals at high pressure (e.g., Ref. [1]). Density crossover could have notable effects not only on the chemical stratification in the early Earth but also on recent volcanic activities.

Experimental studies on the compressibility of magmas have been carried out by static compression sink/float experiments, in which the flotation or settling of crystal in the magma is recognized from a quenched sample, yielding the density of magma at a fixed pressure. The equation of state for magma evaluated from one or two density data is, however, highly ambiguous. The structural change of magma with pressure also makes it difficult to represent the compression property of magma by a single equation of state. An alternative technique is expected to solve this problem. The X-ray absorption method [2,3] is advantageous because it can measure directly the density of magma at the desired pressure and can yield an accurate equation of state for magma. We have studied the density of the basaltic magma, which is the most abundant magma on Earth and other Earth-like planets such as Mars and the Moon, at high pressure using X-ray absorption method.

X-ray absorption experiments were carried out using the large-volume high-pressure apparatus SMAP-1 installed at beamline **BL22XU**, where a highly brilliant monochromatic X-ray is available (Fig. 2). The basaltic magma was confined in the single-crystal diamond capsule that is X-ray transparent rather than in silicate, the hardest material, which is uniformly deformed under pressure and is chemically inert with magma. The absorption of X-ray from the basaltic magma was measured up to 4.6 GPa and 1900 K, and the density was calculated from the Lambert-Beer law, $I/I_0 = \exp(-\mu\rho t)$.

X-ray absorption measurements provide the density of basaltic magma along its melting curve. Density data are normalized to 1673 K to draw an isothermal compression curve, which shows that the density of basaltic magma rapidly increases with pressure (Fig. 3). Fitting the Birch-Murnaghan equation of state to density data yields an anomalous

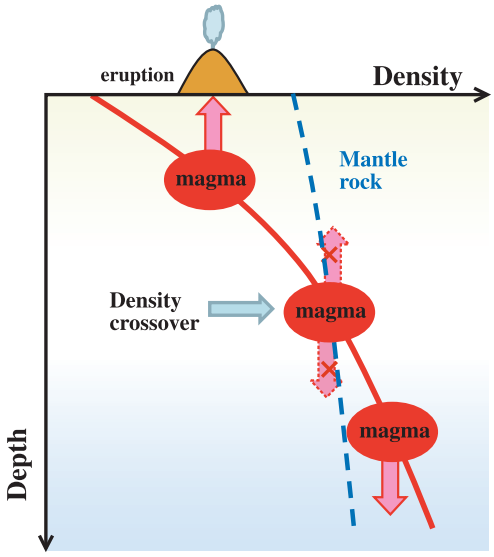

Fig. 1. Density profiles of magma and mantle rock as a function of depth. Transport of magma within the mantle is controlled by its density. Pressure corresponding to density crossover determines the critical depth at which magma can ascend.

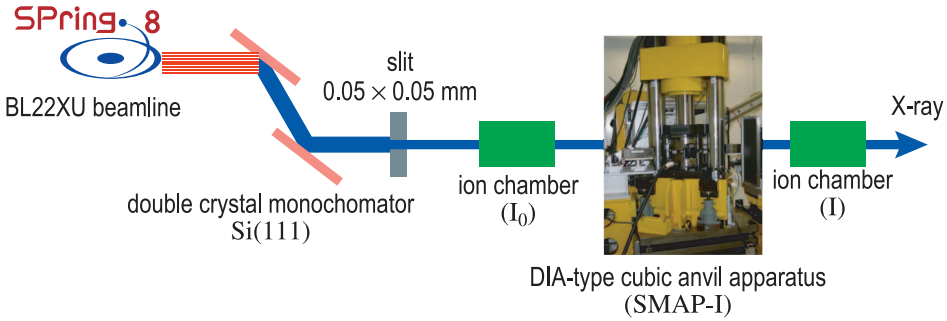

Fig. 2. Experimental setup for X-ray absorption measurements of magma at high-pressure and high-temperature at BL22XU.

negative pressure derivative of the bulk modulus of the basaltic magma (Birch-Murnaghan equation of state is a constitutive equation that provides a mathematical relationship between pressure, temperature and volume). This means that the basaltic magma becomes more compressible at higher pressure, in contrast to the normal crystalline solid. This result strongly indicates that the structure of basaltic magma changes with increasing pressure, including the shrinkage of networks of SiO_4 and AlO_4 tetrahedra and the increase in the coordination number of aluminum ions. Although Agee [1] predicted the equation of state for the basaltic magma on the basis of his sink/float experiments as shown in Fig. 3, his analysis cannot explain the complex compression behavior of basaltic magma. A linear extrapolation of our data, if correct, may shift the pressure of density crossover toward a pressure lower than that of the previous estimation. Compared with the density of olivine, which is the crystalline phase coexisting with basaltic magma in the mantle, the density of the basaltic magma would exceed that of olivine at approximately 7 GPa, which is lower than the pressure of density crossover predicted by Agee [1] by 1 GPa. The basaltic magma could not ascend from a position deeper than 200 km in the Earth's interior.

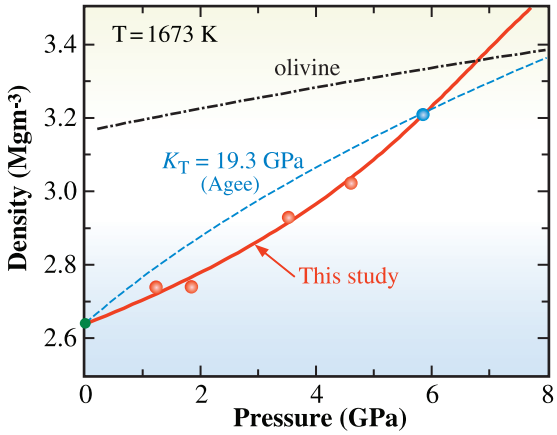

Fig. 3. Pressure *vs.* density diagram showing the compression curves of basaltic magma and coexisting olivine crystal. The red curve with density data is for basaltic magma determined in this study. The densities of basaltic magma are normalized to 1673 K. The blue dashed line is the calculated compression curve fitted to the density data at 5.8 GPa obtained by Agee [1].

Satoru Urakawa[a,*], Tatsuya Sakamaki[b] and Eiji Ohtani[b]

[a] The Graduate School of Natural Science and Technology, Okayama University
[b] The Graduate School of Science, Tohoku University

*E-mail: urakawa@cc.okayama-u.ac.jp

References

[1] C.B. Agee: Physics of the Earth and Planetary Interiors **107** (1998) 63.
[2] Y. Katayama *et al.*: J. Synchrotron Rad. **5** (1998) 1023.
[3] E. Ohtani *et al.*: High-Pressure Technology for Geophysical Applications, ed. by J. Chen *et al.*, Elsevier, Amsterdam, 2005.
[4] T. Sakamaki, S. Urakawa, A. Suzuki, E. Ohtani and Y. Katayama - in preparation.

Higher-pressure Generation to Simulate the Earth's Deep Interior

Astronauts have collected rocks on the Moon, while some specimens from asteroids have been obtained by unmanned spacecraft. However, mankind has not yet reached even the surface of the Earth's mantle, which only lies at a 30 km depth under our feet. Therefore, we cannot obtain rock samples from the Earth's deep interior directly. There are several approaches to investigate and study such an inaccessible location from which no direct rock samples can be obtained. One of the most important approaches is seismology. Seismic observation enables us to obtain a CT scan of the Earth's interior in terms of the seismic wave velocity and density. However, to understand the chemistry and mineral composition of the Earth's interior and discuss its dynamics and evolution, it is necessary for us to have a fundamental knowledge about the Earth building materials. High-pressure and high-temperature experiments reproduce the deep Earth's condition and synthesize the Earth's building materials in a laboratory built on the Earth's surface. In the investigation of the Earth's interior, high-pressure experimental devices play a role as a "sub-ground research ship," similar to a spacecraft in space exploration. Thus, samples synthesized by high-pressure and high-temperature experiments are equivalent to the Moon rocks returned to the Earth by astronauts.

The Kawai-type multi-anvil apparatus (KMA; Fig. 1) is one of the most popular experimental devices to reproduce the deep Earth's conditions. KMA was originally developed in Japan and is now widely used throughout the world; it is a sophisticated system using 6-8 type double-staged multi-anvils to generate the quasi-hydrostatic pressure in a large volume. This large compressed volume is an important feature of KMA; it enables us to build a resistance furnace, which produces uniform high-temperature conditions and provides a great advantage in simulating the Earth's interior and in sample synthesis. Because of these features, KMA has played important roles in high-pressure Earth science, particularly in understanding the 660 km seismic discontinuity (e.g., Ref. [1]). Although the KMA can accurately reproduce the Earth's interior, the generated pressure has been limited to <30 GPa by the mechanical strength of the tungsten carbide (WC) second-stage anvils. In other words, the Earth simulator "KMA" had been stagnant just below the 660 km discontinuity (i.e., top of the lower mantle) for a long time. However, recently, with the use of the sintered diamond (SD) as the material for second-stage anvils, the pressure limits of experiments using KMA has considerably increased to more than 60 GPa (e.g., Ref. [2]).

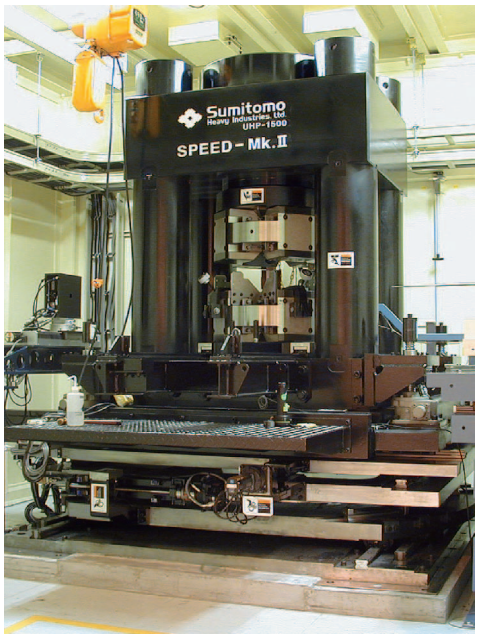

Fig. 1. Kawai-type apparatus called "SPEED-Mk.II", which is installed at BL04B1.

Here, we briefly report on the technical developments related to high-pressure generation using KMA with SD anvils. High-pressure experiments were conducted at beamline **BL04B1** using a KMA called "SPEED-Mk.II". The 14.0 mm SD cubes with truncated edge lengths of 1.5 mm were used as second-stage anvils. Uniaxial oil pressure was concentrated to the pressure media placed into the center of second-stage SD anvils through six first-stage WC anvils. Semi-sintered MgO (+ 5 wt% Cr_2O_3) or Al_2O_3 was used for pressure media, and pyrophyllite heated at 700°C for 30 minutes was also used as a gasket. The generated pressure was measured using Au internal standard, which was placed into the center of the pressure media, and the EOS (Tsuchiya, 2003). A schematic illustration of the cell assembly is shown in Fig. 2. We systematically varied the volume of the pressure media and gaskets to determine the optimum setting in terms of thickness and width of the gaskets.

As a result of a series of experiments, we observed changes in the efficiency and limitations of high-

pressure generation with varied cell assemblies. Figure 3 shows the results of high-pressure generation as a function of press load for each experimental condition. At first, the pressure generating efficiency increases with decreasing gaskets width because smaller gaskets consume less press load. Secondly, the pressure generation limits also change with gasket thickness, and the effect is significant above 40 GPa. In addition, we successfully used an Al_2O_3 pressure media, and the pressure limit increased to ~10 GPa at 8 MN in comparison with that using MgO at each optimum setting. Al_2O_3 with larger bulk modulus than that of MgO would enable this expansion.

High-pressure generation techniques using SD anvils in KMA have been further developed to reach 70 GPa (i.e., at a depth of 1660 km in the Earth). The new experimental method maintains the original advantages of KMA and is characterized by excellent stability at high pressure and high temperature with a large sample volume. This improved sub-ground ship will clarify the nature of the ocean in the Earth's lower mantle.

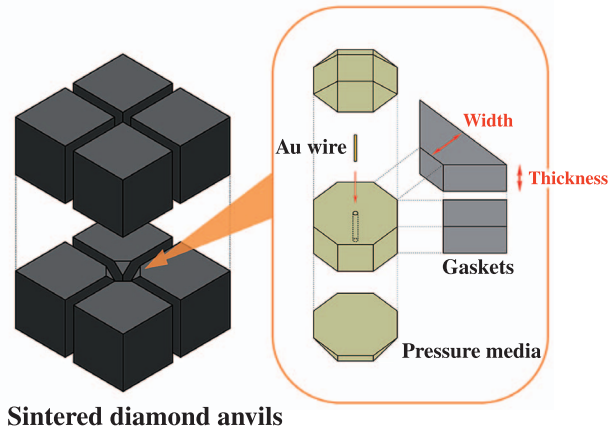

Fig. 2. Schematic of second-stage SD anvils, pressure media and gaskets. Pressure media are totally surrounded by the two types of gasket. The Kawai-cell composed by eight anvils including pressure media is loaded into a large volume press (Fig. 1). High-pressure cell assembly is optimized in terms of width and thickness of the trapezoidal gasket. Au pressure standard was placed into the center of the pressure media.

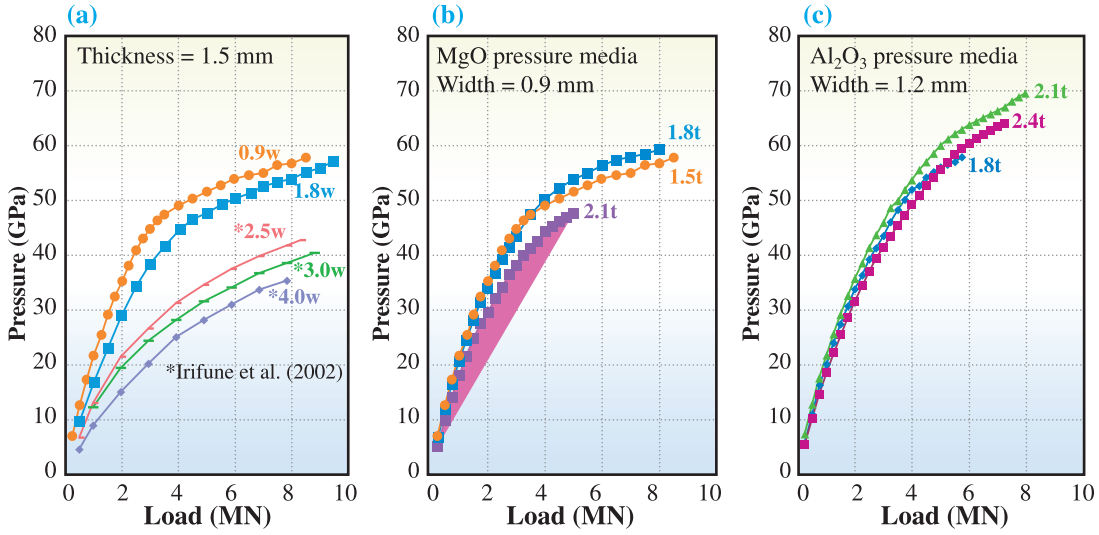

Fig. 3. High-pressure generation curves using 14 mm SD anvils with 1.5 mm of truncated edge. Errors of measured pressure were similar to each symbol. In each curve, the indexed value indicates the width (w) or thickness (t) of the gasket used. **(a)** Pressure *vs* press load for various gasket widths using MgO pressure media. Pressure generating efficiency increases with decreasing gasket width. **(b)** Optimization of gasket thickness using MgO pressure media. Pressure generation reached a plateau at ~50 GPa. **(c)** Optimization using Al_2O_3 pressure media. The use of Al_2O_3 pressure media broke the plateau observed in the case of MgO pressure media.

Yoshinori Tange* and Tetsuo Irifune

Geodynamics Research Center, Ehime University

*E-mail: tan@sci.ehime-u.ac.jp

References

[1] E. Ito and E. Takahashi: J. Geophys. Res. **94** (1989) 10637.
[2] E. Ito *et al.*: Advances in High-Pressure Technology for Geophysical Applications, (eds. J. Chen, Y. Wang, T.S. Duffy, G. Shen and L.F. Dobrzhinetskaya) (Elsevier 2005) 451.
[3] T. Irifune *et al.*: Phys. Chem. Minerals **29** (2002) 645.

Post-perovskite Phase Transition in Earth's Deep Mantle

The recent discovery of the post-perovskite phase suggests that $MgSiO_3$-rich perovskite, a predominant mineral in the Earth's lower mantle, undergoes a phase transformation near the bottom of the mantle, called the D" layer [1] (Fig. 1). The first publication on the $MgSiO_3$ post-perovskite phase transition [2] showed that it occurs at approximately 125 GPa and 2500 K, corresponding to a 2700 km depth in the mantle, using Pt as pressure standard. This closely matches the general depth at which the D" seismic-wave velocity discontinuity is observed (2600 to 2700 km depth), suggesting that this seismic boundary is a phase transformation origin. However, recently there has been an extensive debate on the accuracy of the *P-V-T* equation of state (pressure scale) of the internal pressure standard used in these high-pressure experiments. Moreover, the effects of chemical impurities such as FeO and Al_2O_3 found in the Earth's mantle need to be examined.

We have experimentally determined the post-perovskite phase transition in $MgSiO_3$ using multiple pressure standards of Pt, Au, and MgO [2,3]. The high-pressure and high-temperature conditions were generated in a laser-heated diamond-anvil cell (LHDAC). They were compressed with Re gasket and beveled diamond anvils with 200-μm culet. Heating was carried out using the TEM_{01}-mode Nd:YLF laser or a multi-mode Nd:YAG laser for 2 to 41 min. Angle-dispersive X-ray diffraction spectra were collected on the CCD detector and imaging plate (IP) at beamline **BL10XU**. The results of two separate sets of experiments on $MgSiO_3$ based on the Au pressure marker are shown in Fig. 2. The stabilities of perovskite and post-perovskite phases were determined by the changes in relative X-ray intensities. The coexistence was judged by the significant growth of both the phases with similar intensities. These results indicate that post-perovskite phase transition occurs at 113 GPa and 2400 K with a positive Clapeyron slope of +4.7±0.5 MPa/K. However, the results strongly depend on the pressure scale. All experimental data on the post-perovskite phase transition in $MgSiO_3$ are shown in Fig. 3 [2-4], which demonstrates that the transition pressure changes by as much as 15 GPa depending on the pressure standard and its *P-V-T* equation of state.

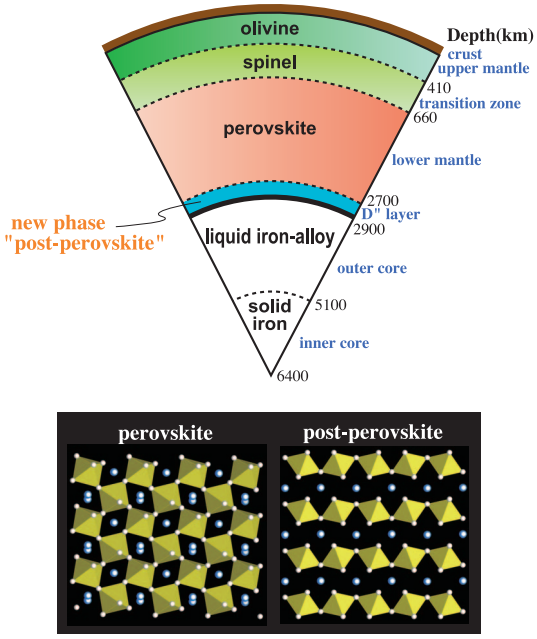

Fig. 1. **(a)** Schematic illustration of the Earth's interior. The main constituent mineral changes between layers; olivine in the upper mantle, spinel phase in the transition zone, perovskite phase in the lower mantle, and post-perovskite phase in D" layer. **(b)** Crystal structures of perovskite and post-perovskite. The yellow octahedra and white balls represent SiO_6 polyhedra, and the blue balls indicate Mg ions in both images.

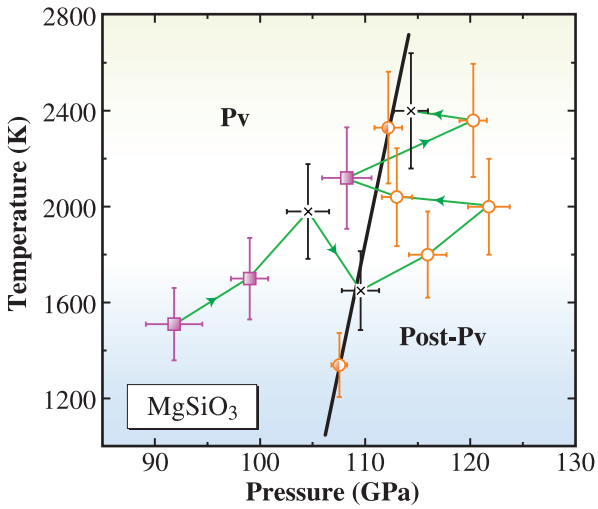

Fig. 2. Phase diagram of $MgSiO_3$ based on the Au pressure scale. Solid squares, perovskite; open circles, post-perovskite; half-filled circles, coexistence of perovskite and post-perovskite. Crosses show that the pattern did not change at these conditions. The sequential change in the *P-T* conditions in the first run is illustrated by arrows.

The MgO pressure scale may be the most practical at this moment, because it has been extensively studied and is least controversial, although the absolute pressure scale over 100 GPa is not available. Indeed, the post-spinel transformation boundary in Mg_2SiO_4 based on MgO pressure scale matches the depth of the 660-km seismic discontinuity [5]. Our results also indicate that the pressure of post-perovskite phase transition (119 GPa at the realistic mantle temperature of 2400 K) derived from the MgO scale is consistent with the location of the D" seismic discontinuity at around 2600 km depth in the Earth's mantle. Note that the MgO scale predicts a significantly large Clapeyron slope for this boundary (+11.5 MPa/K). Such a large Clapeyron slope suggests that the post-perovskite phase transformation will promote extensive upwelling of high-temperature plumes from the hot core-mantle boundary region.

In addition, all of our data on $MgSiO_3$, $(Mg_{0.9}Fe_{0.1})_2SiO_4$, natural pyrolitic mantle (KLB-1 peridotite), and basaltic oceanic crust (MORB) compositions are plotted together in Fig. 4 [3]. Only Au was used as pressure the standard for these experiments, because Pt and MgO readily react with the iron-bearing samples. These results indicate that the stabilities of perovskite and post-perovskite phases in these natural compositions are consistent with the phase transition boundary in pure $MgSiO_3$. The compositional variations from pure $MgSiO_3$ to natural mantle and crust materials have little effect on the post-perovskite phase transition.

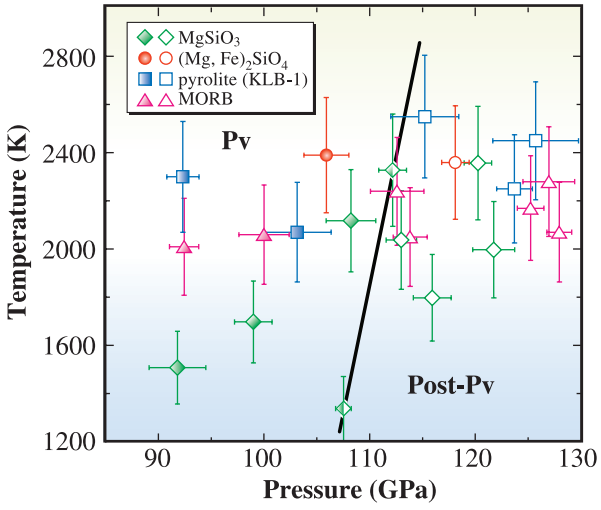

Fig. 4. Stabilities of perovskite (solid symbols) and post-perovskite (open), based on the Au pressure scale. All of these data are consistent with the phase transition boundary in pure $MgSiO_3$, as shown by the bold line.

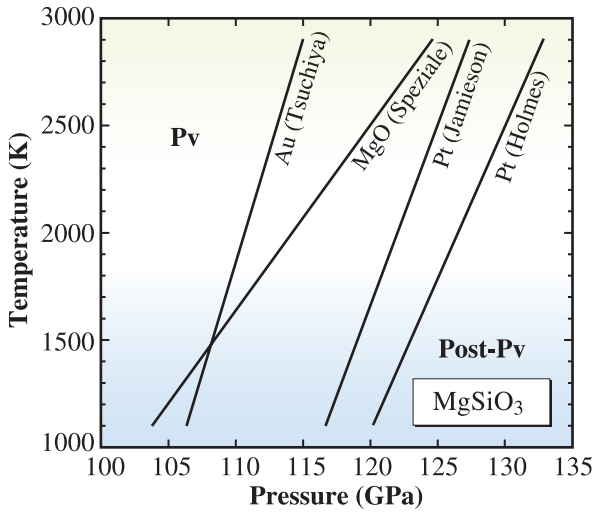

Fig. 3. Post-perovskite phase transition boundary in $MgSiO_3$ based on the Pt-scale [2,4] and the Au and MgO pressure scales [3]. The location and the Clapeyron slope are strongly dependent on the internal pressure standard and its *P-V-T* equation of state.

Kei Hirose [a,b]

[a] Department of Earth and Planetary Sciences, Tokyo Institute of Technology
[b] Institute for Research on Earth Evolution, Japan Agency for Marine-Earth Science and Technology

E-mail: kei@geo.titech.ac.jp

References

[1] K. Hirose: Rev. Geophys. **44** (2006) RG3001.
[2] M. Murakami *et al.*: Science **304** (2004) 855.
[3] *K. Hirose, R. Sinmyo, N. Sata and Y. Ohishi: Geophys. Res. Lett. **33** (2006) L01310.*
[4] S. Ono and A.R. Oganov: Earth Planet. Sci. Lett. **236** (2005) 914.
[5] Y. Fei *et al.*: J. Geophys. Res. **109** (2004) B02305.

Environmental Science

Environmental science involves various research fields. The topics selected in this section mostly relate to health hazards and environmental destruction. Actual environmental samples are often very dilute, small in quantity, or spatially or chemically inhomogeneous, so analyses using high-brilliance synchrotron radiation (SR) X-rays are indispensable to study such samples. Moreover, new techniques are being developed that further enhance the study of environmental samples.

In the first topic, Hokura *et al.* show the 2-dimensional cellular distribution of cadmium in hyperaccumulating plant tissues by high-energy μ-X-ray fluorescence imaging. This is a powerful technique that can be used to obtain information on the distribution and chemical state of heavy elements. Hokura *et al.* showed that the distribution of cadmium positively correlates with that of zinc.

The second topic concerns the treatment of soil contaminated by organic arsenic compounds. Harada *et al*. have determined the effectiveness of heat treatment as a step in the detoxification of soil contaminated with organic arsenic compounds. They successfully revealed the heat treatment changes chemical state of arsenic compounds from the organic state to the inorganic pentavalent state using XANES analysis.

The third topic concerns the removal of NO_x emissions from diesel engines in vehicles. Shimizu studied the dynamical structure changes of high performance Ag/Al_2O_3 catalysts during de-NO_x catalysis by *in situ* Quick XAFS analysis and discovered the reductive aggregation and oxidative redispersion of Ag species, which are crucial steps in efficient catalysis.

Mitsunobu *et al.* developed a new method combining a column reactor with a time-resolved Quick XAFS technique. This method is a very simple and a direct tool to determine chemical state and local structure during a chemical reaction at solid-water interfaces. They applied it to the oxidation of As(III) induced by amorphous manganese oxide (δ-MnO_2), natural strong oxidizer, which is an important reaction for toxicology and geochemistry, and directly measured the rate constant of As(III) oxidation.

The last topic concerns the detection of asbestos used in conventional building materials, which is now a most pressing health hazard. Recently, the legal standard for the regulation of asbestos was reduced from 1.0 to 0.1 wt%, which exceeds the detection limits of conventional laboratory analysis methods. Kato *et al*. developed an SR X-ray powder diffraction method using surface diffractometry optimized for the detection of crystalline asbestos, and achieved a detection limit of up to 0.02 mg (0.02 wt%) of asbestos.

Tomoya Uruga

Study of Mechanisms for Transportation and Storage of Heavy Metals in Cadmium Hyperaccumulator Plant Using High-energy μ-XRF Analysis

Specific types of plant can grow in contaminated soils and absorb a large amount of heavy elements [1]. *Arabidopsis halleri* is known as a cadmium and zinc hyperaccumulator [2,3], and it can accumulate more than 10000 mg·kg^{-1} cadmium and zinc in its shoot [2]. This characteristic makes it highly suitable for phytoremediation, a soft method in which plants are used to clean up heavy metal-polluted environments [1]. However, the cellular distribution of cadmium and the mechanisms of cadmium transportation and accumulation in the plant have not yet been elucidated. The two-dimensional (2D) analysis of trace cadmium in plant tissues is a key method used to investigate such accumulation mechanism. Recent studies using scanning electron microscopy (SEM) with energy dispersive X-ray spectrometry (EDS) documented the cellular distribution of zinc in the tissues of *A. halleri* [2]. In its leaves, zinc was mostly sequestered in the base of trichomes and in mesophyll cells [2]. Trichomes are epidermal hairs present at the surface of the leaves of *A. halleri*, and their functions are thought to be the exudation of various molecules or the storage of substances such as metals. However, conventional SEM-EDS mapping is not suitable for the analysis of cadmium due to the low sensitivity of the electron beam excitation for heavy elements. Furthermore, the detection of the Cd L-line is also difficult because the line overlaps with the K-line peak of potassium, which is an essential element for plants.

In this study, we have developed an in vivo micro-X-ray fluorescence (μ-XRF) imaging technique utilizing high-energy synchrotron radiation (SR) to determine the distribution of cadmium and zinc in the tissues and cells of hyperaccumulator plants and to investigate their physiology and mechanism of accumulating cadmium [4].

Plant samples of *A. halleri* ssp. *gemmifera* [3] were collected around an abandoned mine site in Hyogo prefecture. The leaves of the plant were subjected to nondestructive analysis without any sample preparation. Some samples were cut with a vertical slicer, and thin sections were sealed in a Mylar® plastic bag together with a small piece of moist unwoven paper to prevent the sample from drying out.

2D μ-XRF imaging was carried out at beamline **BL37XU**. An X-ray beam from an undulator was monochromatized by a Si(111) double-crystal monochromator to 37 keV to effectively excite the K-lines of cadmium and to minimize the overlap of the K-line peak with the Compton scattering peak. The X-ray beam was focused with an FZP to a beam size of *ca.* 3 × 3 μm^2. The FZP was produced by the sputtered-slice manufacturing method [5]. A Si(Li) solid-state detector was placed in an appropriate position. Samples were placed on the x-y stepper motorized stage, which was step scanned to obtain a 2D image. The step size was set to 3 μm. The integrated XRF intensity of each line, e.g., Cd Kα, was calculated from the spectrum and normalized by that of the incident beam I_0, which was measured using an ionization chamber, and then an elemental map of the measured area was calculated.

Before the microbeam analysis, the elemental distribution at the plant organ level was investigated using a non-focused beam at BL37XU. The X-ray beam was adjusted using horizontal and vertical slits, allowing us to obtain a beam size of 50 × 50 μm^2. The other experimental conditions, including the excitation energy, were almost the same as those used for μ-XRF imaging.

Elemental maps of Cd, Zn, Rb, and Sr are presented in Fig. 1, in which the normalized X-ray fluorescence intensities are scaled to red (maximum) and blue (minimum). Each image indicates the relative distribution of the specific element; thus, the concentration scale varies for each image. The distribution of cadmium in the leaves has been very clearly revealed by the *in vivo* monitoring of the Cd Kα line for the first time. These images can be

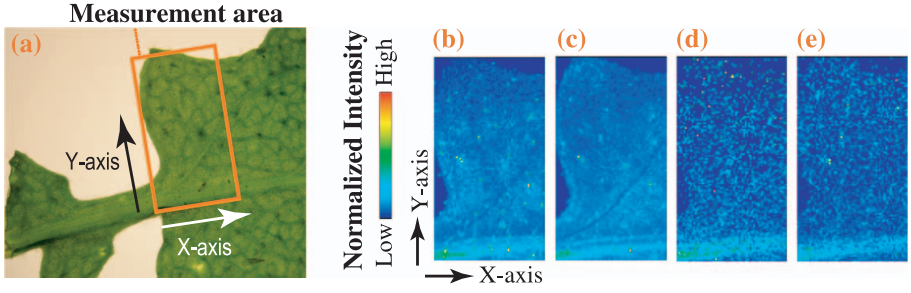

Fig. 1. XRF imaging of leaf of *A. halleri* ssp. *gemmifera*. **(a)** Image of leaf, and distribution of **(b)** Cd, **(c)** Zn, **(d)** Rb, and **(e)** Sr. X-ray beam size, 50 × 50 μm^2; scan step, 50 μm; measurement time, 1 s/pixel; image size, 66 × 132 pixels.

directly used to correlate the distribution of various elements with plant tissue structure. As can be seen in Figs. 1(b) and 1(c), cadmium and zinc show a wide distribution in mesophyll tissues and the main vein of leaves. The distribution of cadmium was found to positively correlate with that of zinc. Both elements preferentially accumulated in specific tissues on the leaf, namely, the trichomes, which are epidermal hairs present on the surface of the plant leaves.

μ-XRF imaging was carried out on trichomes prepared from the leaves. The elemental distributions of cadmium, zinc, strontium, and calcium are presented in Fig. 2 together with photographs taken under an optical microscope and an SEM. The 2D cellular distribution of cadmium in the trichomes was first observed by *in vivo* μ-XRF imaging. It was found that both cadmium and zinc accumulated to a high degree in the base of the bifurcation area of the trichomes, whereas strontium and calcium were mostly distributed throughout the entire upper part of the trichomes. These distributions of cadmium and zinc showed striking subcellular compartmentation.

The distribution areas of cadmium and zinc accumulated inside the trichomes were found to shrink gradually as the result of slow drying. This finding supported the notion that the compartmentation of cadmium and zinc occurs in the vacuole of the trichomes because 80-90% of the vacuole of a living cell is composed of water. The compartmentation of cadmium and zinc was considered to play an important role in the accumulation process of the elements; consequently, a detailed *in vivo* analysis should be carried out in the future.

In conclusion, we have for the first time succeeded in determining the 2D cellular distribution of cadmium in hyperaccumulating plant tissue using a high-energy X-ray microbeam. Data were obtained using a living sample. The cellular distribution of cadmium was found to correlate positively with that of zinc. Because both zinc and cadmium belong to Group 12 in the periodic table, this finding may suggest that the accumulation of these elements proceeds via similar transportation pathways in the plants. These results will provide important information for a better understanding of the mechanism of cadmium hyperaccumulation by plants.

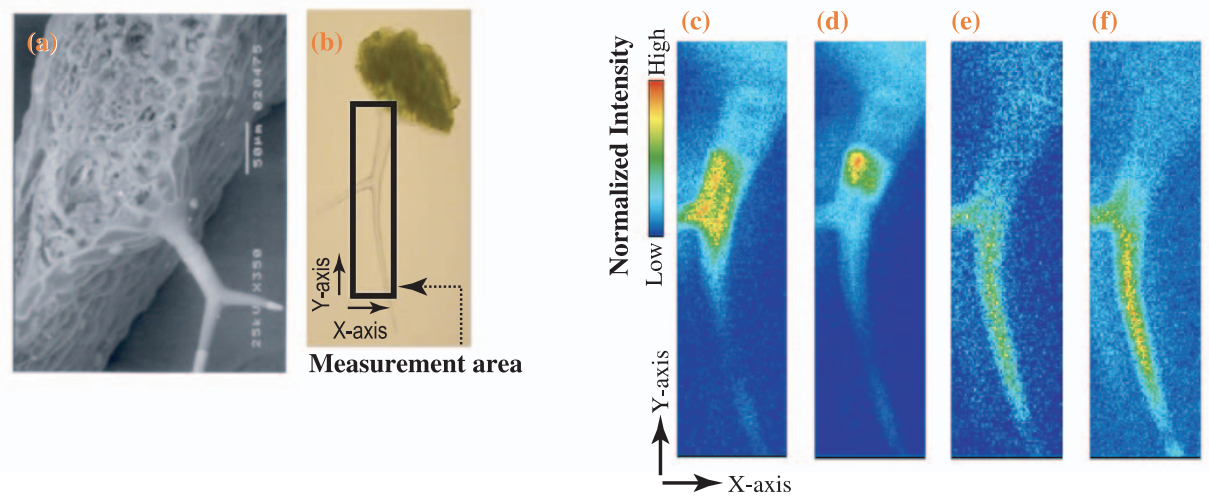

Fig. 2. Micro-XRF imaging of trichome taken from leaf. **(a)** SEM image, **(b)** image of trichome, and distribution of **(c)** Cd, **(d)** Zn, **(e)** Sr, **(f)** Ca. X-ray beam size, 3 × 3 μm^2; scan step, 3 μm; measurement time, 0.5 s/pixel; image size, 59 × 226 pixels.

Akiko Hokura[a], Nobuyuki Kitajima[a,b], Yasuko Terada[c] and Izumi Nakai[a,*]

[a] Dept. of Applied Chemistry, Tokyo University of Science
[b] Fujita Co.
[c] SPring-8 / JASRI

*E-mail: inakai@rs.kagu.tus.ac.jp

References

[1] I. Raskin and B.D. Ensley: Phytoremediation of Toxic Metals: Using Plants to Clean Up the Environment, John Wiley & Sons, Inc. (1999).
[2] H. Küpper *et al.*: Planta **212** (2000) 75.
[3] H. Kubota *et al.*: Int. J. Phytoremediation **5** (2003) 197.
[4] *A. Hokura, R. Onuma, N. Kitajima, Y. Terada, H. Saito, T. Abe, S. Yoshida and I. Nakai: Chem. Lett.* ***35*** *(2006) 1246.*
[5] M. Awaji *et al.*: Rev. Sci. Inst. **74** (2003) 4948.

Thermal Treatment of Soil Contaminated by Organic Arsenic Compounds

In traditional cases, environmental pollution due to arsenic derived from geological sources has caused ground water contamination by the dissolution of arsenic ions from the vein of ore. As a results of this pollution, people who use the contaminated water for daily purposes suffer from chronic poisoning symptoms. In most of these cases, the original cause of the pollution is the leaching of 'inorganic' arsenic pollutants into the ground water [1]. However, in Kamisu city (Ibaragi Prefecture, Japan), there was an extremely rare case of ground water contamination caused by 'organic' arsenic substances in 2005. From the results of a detailed study, diphenylarsenic acid (DPAA) and phenylarsonic acid (PAA), i.e., organic substances with phenyl radicals, were detected in the ground water of Kamisu city. After more extensive surveying and excavation of the soil in the suspected area, about 100 tons of concrete-like agglomerate and 2000 tons of contaminated soil containing about 1500 mg/kg organic arsenic acids were discovered in the earth at a depth of 4 meters, and they were concluded to be the source of pollution. From the date marked on beverage cans found in the agglomerate, it seems that the organic arsenic acids had been poured into the soil with cement in the 1990s. Because organic substances with phenyl radicals are not present in nature, there was a speculation that the DPAA and PAA found originated from the Imperial Japanese Army. In general, for inorganic arsenic, the toxicity of trivalent arsenic is higher than that of pentavalent arsenic, and the toxicity of organic arsenicals with methyl radicals is much lower than those of inorganic substances. However, the toxicity of organic arsenicals with phenyl radicals is not known [2].

We have confirmed heat treatment as a detoxification process that has been applicable to this unprecedented pollution caused by DPAA and PAA. In this study, we examined the change in the chemical state of organic arsenic compounds in artificially contaminated soil before and after heat treatment by XAFS.

Uncontaminated soil was collected in Ibaraki, Japan. The soil was dried at room temperature and filtered through a 425-μm-opening sieve, and the fine fraction was collected as a substrate. About 500 g of the substrate was mixed with 100 ml of methanol (or ethanol), which disolved DPAA or PAA. And then, the artificially contaminated soil was dried at room temperature again. In addition, artificially contaminated cement was also prepared by the above-described method. The total arsenic concentration in these soils and cement were about 2000 mg/kg. The samples were heated at 850°C in a tubular furnace for 30 min under air. XANES analysis was performed on 6 samples and 8 standard compounds at beamline **BL01B1** in the transmission and fluorescence modes.

Figure 1 shows a comparison of the XANES spectra of all the samples and standard compounds. The white-line positions of the heat-treated samples are close to those of pentavalent arsenicals. However, an obvious difference in the shape of the spectra in the vicinity of 11870 eV, i.e., right before the absorption edge, can be seen between the organic and inorganic compounds (except for As and As_2O_3). To clarify these points, Fig. 2 shows a schematic of the white-line energy positions in terms of relative energy for the samples and standard compounds. White-line peak positions were obtained from the point

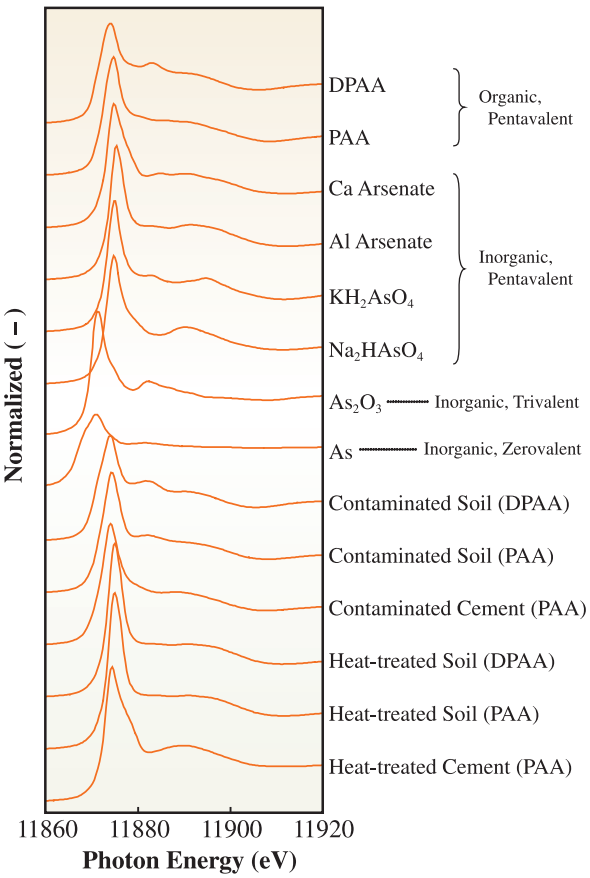

Fig. 1. Normalized As-*K* XANES spectra of organic and inorganic arsenic samples.

at which the first derivative gives the top of the peak in part of the near-edge. Looking at the energy positions of the absorption edge of the inorganic arsenicals and heat-treated samples, were higher than those of organic arsenicals, it is clear that the chemical state of arsenic in the soil and cement have been changed from the organic state to the inorganic state. This tiny but visible difference in the energy positions of the absorption edge between organic and inorganic arsenicals is attributed to the change in the electron state of arsenic atoms induced by the loss of phenyl radicals during heat treatment [3].

Table 1 shows the result of spectrum fit analysis applied to the XANES spectra. By superimposing each sample spectrum on each standard spectrum, the similarity of each combination is evaluated using 'R' values, which were calculated using the following equation [4].

$$\text{residual } R \text{ value} = \frac{\Sigma(\text{XANE}_{measd} - \text{XANES}_{calcd})^2}{\Sigma(\text{XANE}_{measd})^2}$$

All of the R value ranges obtained are represented by one of four kinds of symbol in the table. Similarly to the result of energy position analysis, the result of the curve fitting analysis indicates that the organic arsenic had been changed to inorganic arsenic by heat treatment. Furthermore, the arsenic chemical compounds in the heat-treated soil and cement are proximate to aluminum arsenate and calcium arsenate, respectively. This observation agrees with the fact that As_2O_5 reacts with major components of soil and cement such as Al_2O_3 and CaO, respectively, and becomes an insoluble arsenate compound when it is generated by the thermal decomposition of DPAA or PAA in soil or cement [5].

Table 1. Similarities of organic and inorganic arsenic samples with standard compounds.

	Standard Compounds						Samples				
	DPAA	PAA	Ca Arsenate	Al Arsenate	KH_2AsO_4	Na_2HAsO_4	Contaminated Soil (DPAA)	Contaminated Soil (PAA)	Contaminated Cement (DPAA)	Heat-treated Soil (DPAA)	Heat-treated Soil (PAA)
Contaminated Soil (DPAA)	○	○					-	-	-	-	-
Contaminated Soil (PAA)	△	○					△	-	-	-	-
Contaminated Cement (DPAA)	△	◎					△	◎	-	-	-
Heat-treated Soil (DPAA)				○	△					-	-
Heat-treated Soil (PAA)				○						◎	-
Heat-treated Cement (PAA)			○			△					

*Notation
- : Not calculated,
◎ : 0<R≦0.06, ○ : 0.06<R≦0.09, △ : 0.09<R≦0.12, blank : R>0.12

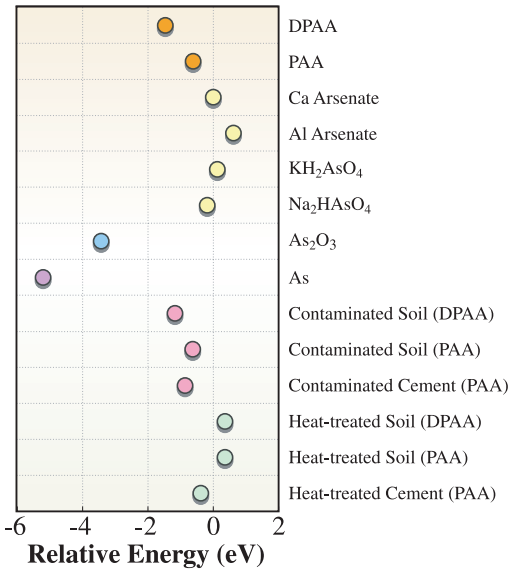

Fig. 2. Relative white-line peak positions obtained from point at which first derivative gives top of peak in vicinity of edge.

As discussed above, strong evidence of the effectiveness of heat treatment applied to the detoxification of organic arsenic contamination has been successfully obtained through experiments performed using XAFS analysis in SPring-8. Analysis using synchrotron radiation, which makes chemical form analysis intended for low-concentration elements in bulk samples possible, is expected to grow in application in the environmental field.

Hiroki Harada[a,*], Shuji Hamano[a] and Masaki Takaoka[b]

[a] Hitachi Zosen Corporation
[b] Department of Urban & Environmental Engineering, Kyoto University

*E-mail: h_harada@hitachizosen.co.jp

References

[1] S. Bang *et al.*: Chemosphere **60** (2005) 389.
[2] Web site of Ministry of the Environment, Government of Japan: http://www.env.go.jp/
[3] P. Smith *et al.*: Environ. Sci. Technol. **39** (2005) 248.
[4] *M. Takaoka, A. Shiono, K. Nishimura, T. Yamamoto, T. Uruga, K. Oshita, T. Matsumoto and H. Harada: Environ. Sci. Technol. 39 (2005) 5878.*
[5] K. Toriyama *et al.*: Symposium on Combustion **41** (2003) 409 (in Japanese).

Reductive Aggregation and Oxidative Redispersion of Silver Species as a Crucial Step in De-NO_x Catalysis

Nitrogen oxides (NO_x: NO and NO_2) are major air pollutants that cause photochemical smog formation and acid rain. The emission of various nitrogen oxides into our atmosphere occurs on a massive scale. Worldwide, over 30 million tons of NO_x are vented into the earth's atmosphere each year. On the other hand, the demand for diesel engines in vehicles, which is the one of the major sources of NO_x emissions, is expected to increase because of the strong efforts to reduce CO_2 emissions. However, the full worldwide expansion of such engines is hindered by the difficulties in effective NO_x and particulate removal. Three major catalytic techniques are widely proposed and used for the removal of NO_x emissions from lean-burn and diesel-operated vehicles: NO_x storage, urea-selective catalytic reduction (SCR), and HC-SCR. Among these techniques, HC-SCR is the most efficient and simplest method, because small quantities of unburnt fuel in diesel engine exhaust streams can be used to reduce the pollutant NO_x to N_2. Numerous catalysts have been tried and tested for HC-SCR. It is now well established that silver supported on alumina (Ag/Al_2O_3) is one of the most active and selective catalysts for HC-SCR. However, the temperature window for NO_x reduction is narrow and they are not sufficiently active in the low temperature region (150-300 °C), which is typical of diesel engines. Until recently, these drawbacks have prevented the commercialization of Ag/Al_2O_3 catalysts for HC-SCR. However, the recent discovery that the addition of a small amount of hydrogen to the feed of the HC-SCR can dramatically improve the performance of Ag/Al_2O_3 catalysts has stimulated interest in HC-SCR for practical use [1]. Recent attention has been focused on the mechanistic causes of the hydrogen effect, even though a comprehensive explanation of the hydrogen effect has yet to be obtained. We performed detailed mechanistic studies, including the identification of surface intermediates and their dynamic changes [1-3].

A typical example of the H_2-promoted HC-SCR catalysis of Ag/Al_2O_3 is shown in Fig. 1. The addition of 0.5% H_2 into a $NO+C_3H_8+O_2$ gas mixture boosted the NO conversion rate at temperatures lower than 400 °C. Interestingly, the promotion effect of H_2 on NO conversion is reversible. The NO conversion rate decreased after the removal of H_2. This reversible change in NO conversion rate is in agreement with the time-dependence of the intensity of the band (350 nm) assignable to the $Ag_n^{\delta+}$ cluster. This finding suggests that the formation of the $Ag_n^{\delta+}$ cluster is essential for the "hydrogen effect."

The structure of the $Ag_n^{\delta+}$ cluster was analyzed by *in situ* EXAFS at 573 K (Ag *K*-edge Quick XAFS

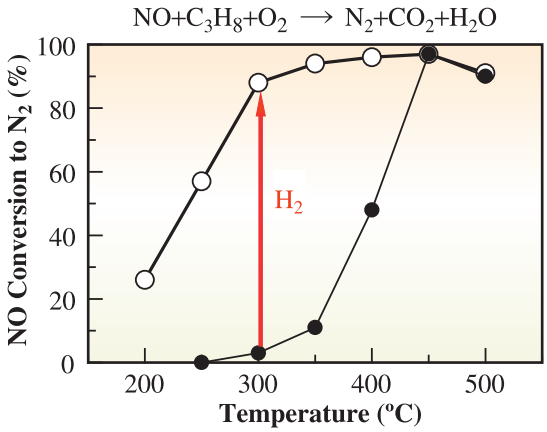

Fig. 1. Effect of H_2 addition on NO conversion in HC-SCR using Ag/Al_2O_3.

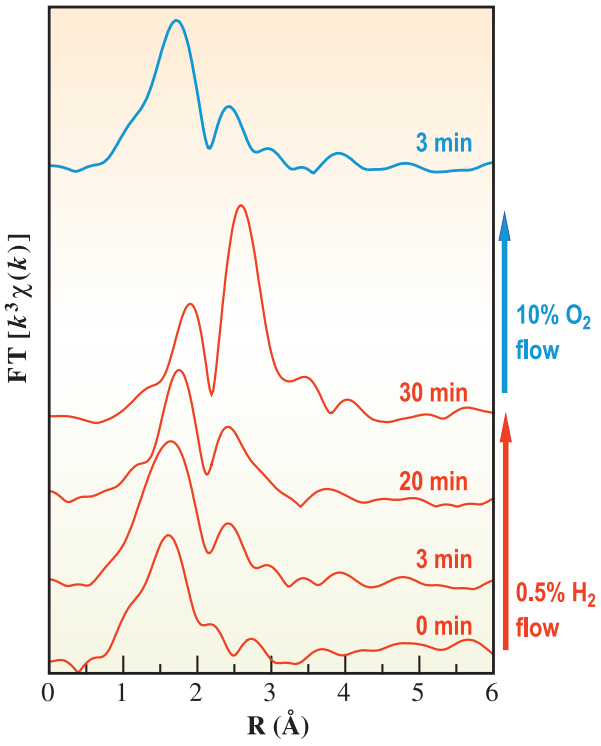

Fig. 2. Fourier transforms of Ag *K*-edge *in situ* EXAFS spectra measured at 573 K.

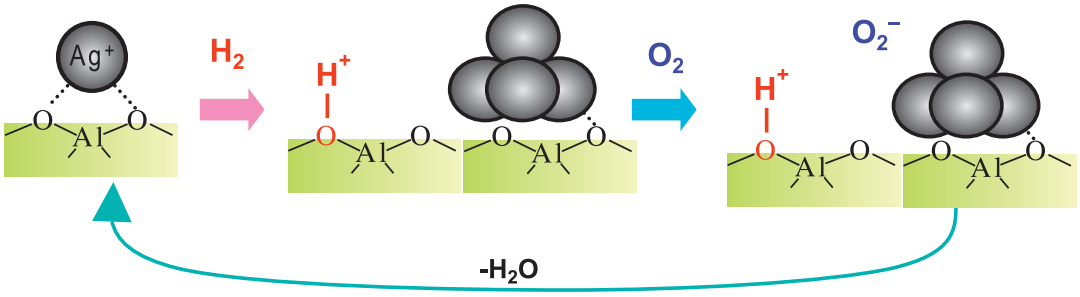

Fig. 3. Changes in structure of Ag species in Ag/Al_2O_3 upon H_2 reduction and subsequent O_2 oxidation.

measurements performed in the transmission mode at beamline **BL01B1**) [2]. A wafer form of Ag/Al_2O_3 was placed in a quartz *in situ* cell [4] under a gas flow. Before the reaction, the Ag/Al_2O_3 wafer shows only a large Ag-O contribution, indicating that Ag^+ ions are highly dispersed on the alumina surface. Results shown in Fig. 2 show that the reduction of Ag^+ ions by 0.5% H_2 results in their aggregation to yield silver clusters. Finally, an Ag-Ag shell having a coordination number of 3.2 and a bond distance of 2.83 Å was observed. These values are smaller than those for bulk Ag metal particles (12 Ag atoms at 2.89 Å), and we assign the Ag-Ag contribution to the Ag_4^{2+} cluster. The cluster is redispersed to Ag+ ions upon reoxidation at 573 K. When the flowing gas was switched from H_2 to O_2, the coordination number for the Ag-Ag shell decreased, whereas that for the Ag-O shell increased. Taking into account the FTIR result that the acidic protons formed by the H_2 reduction of Ag/Al_2O_3 are consumed in the reoxidation reaction with O_2 and the ESR result showing the formation of O_2^- (superoxide) radicals under a similar condition, the catalytic cycle in Fig. 3 is presented [2].

Combined with kinetic results [3], the total mechanism of the hydrogen effect is shown in Fig. 4. The reaction consists of the following steps: (1) The H_2 dissociation on the Ag site, (2) the spillover of H atoms to form protons, (3) the aggregation of isolated silver to form reduced $Ag_n^{\delta+}$, (4) the reduction of O_2 with $Ag_n^{\delta+}$ and H^+ to yield O_2^- and H_2O, (5) the partial oxidation of hydrocarbons by O_2^- to yield an acetate intermediate, and (6) the oxidation of NO to the NO_2 intermediate. This conclusion provides, for the first time, an explanation of H_2-promoted HC-SCR on the molecular level, which will be useful for the rational design of more efficient catalysts. The present results improve our ability to tailor the structure and catalytic behavior of silver clusters by controlling the reactant gas composition.

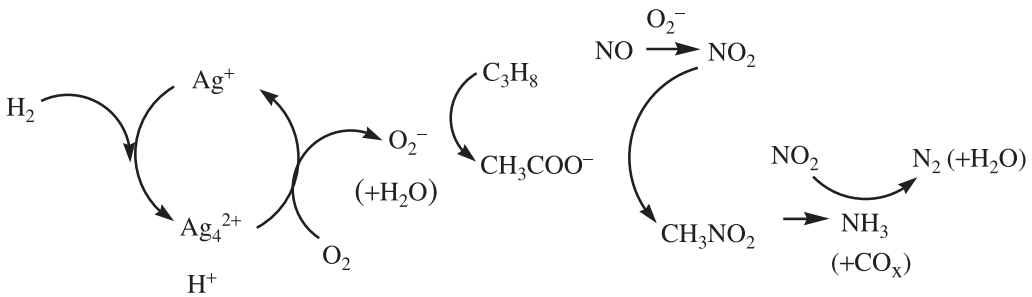

Fig. 4. Proposed mechanism of H_2 promoted HC-SCR.

Ken-ichi Shimizu

Department of Applied Chemistry, Nagoya University

E-mail: kshimizu@apchem.nagoya-u.ac.jp

References

[1] K. Shimizu and A. Satsuma: Phys. Chem. Chem. Phys. **8** (2006) 2677.
[2] *K. Shimizu, M. Tsuzuki, K. Kato, S. Yokota, K. Okumura and A. Satsuma: J. Phys. Chem. C* ***111*** *(2007) 950.*
[3] K. Shimizu *et al.*: J. Catal. **239** (2006) 402.
[4] K. Okumura *et al.*: J. Phys. Chem. B **109** (2005) 12380.

New Method to Observe Chemical Reactions at the Solid-water Interface by QXAFS Combined with a Column Reactor

Recently, the environmental and human health impacts of elevated concentrations of arsenic (As) in groundwater have received increased attention because of its toxicity [1]. The predominant forms of As in the environment are as inorganic arsenate (As(V)) and arsenite (As(III)). Unlike the arsenate anions, $H_2AsO_4^-$ and $HAsO_4^{2-}$, the dominant As(III) species up to pH 8 is the nonionic H_3AsO_3, which does not adsorb onto mineral surface as strongly as As(V) [2-4]. The As(III) species is substantially more toxic than As(V). Therefore, it is important for the geochemistry and toxicology of As to determine its oxidation state. In natural systems, amorphous manganese oxide (δ-MnO_2) can be the strong oxidizer and sorbent for various trace elements including As. Considering the fate of As in the environment, the oxidation of As(III) by Mn oxide is an important reaction. Although details about the chemical mechanism of As(III) by amorphous Mn oxide have been reported, more information is needed for the kinetics of the oxidation of As(III) to As(V).

In this study, to observe the kinetics and dynamics in the oxidation process of As(III) by Mn oxide, we applied a new method that combines a column reactor with the time-resolved measurement of As species at the solid-water interface using quick XAFS (QXAFS) technique [5], which can measure XAFS spectra within shorter time than the conventional measurement by step scan of monochromator of the incident X-ray. In particular, a short time scale detection is required for the observation of As oxidation by Mn oxide, since the oxidation of As(III) by Mn oxide is quite rapid. The application of this method allows us to gain better understanding of the various reaction processes at the solid-water interface.

A small disposable polystyrene column with an inner diameter of 10 mm was used as the reactor to investigate the oxidation of As(III) with Mn oxide (Fig. 1). Arsenite solution was introduced into a column reactor with the outflow port closed. Using a peristaltic pump connected to the outlet of the column, the As(III) solution started to flow into the δ-MnO_2 layer, initiating the oxidation reaction.

Quick XAFS measurements at As-*K*-edge, performed at beamline **BL01B1**, were carried out in fluorescense mode using a Lytle detector. The Si(111) monochromator was moved continuously from 9.63° (11.836 keV) to 9.00° (12.638 keV) in 1 min. The measurements were conducted at 27 ± 2°C under ambient air condition.

In the As(III)/ δ-MnO_2 system, the absorption edge of As shifted to higher energy with time (Fig. 2), showing the rapid oxidation of As(III) by δ-MnO_2. Figure 3(a) shows the As(III) and As(V) ratio obtained by the simulation of XANES spectra during the oxidation reaction of As(III). Arsenic(III) was rapidly oxidized by δ-MnO_2, and about 50% of the original As(III) added was oxidized to As(V) within 20 min (Fig. 3(a)). The net stoichiometry of the oxidation of As(III)

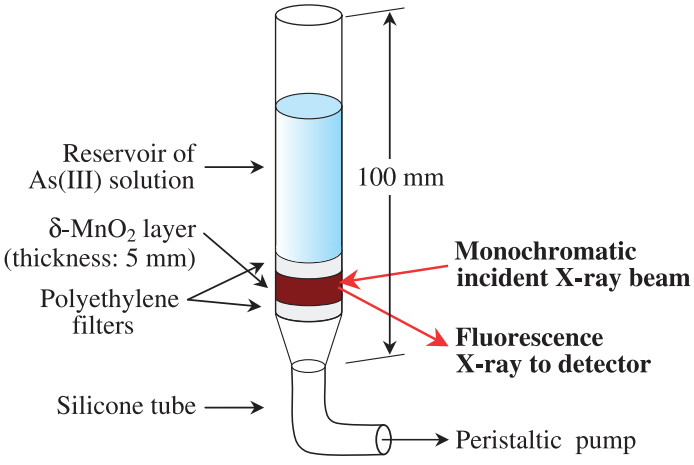

Fig. 1. Schematic figure of the column reactor.

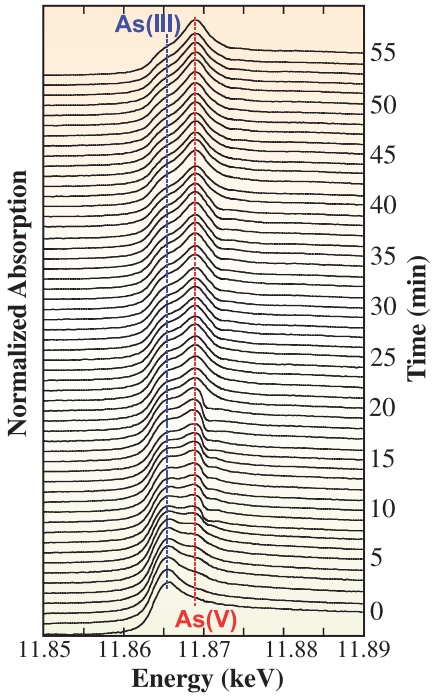

Fig. 2. Arsenic *K*-edge XANES spectra of As(III)/δ-MnO_2 system.

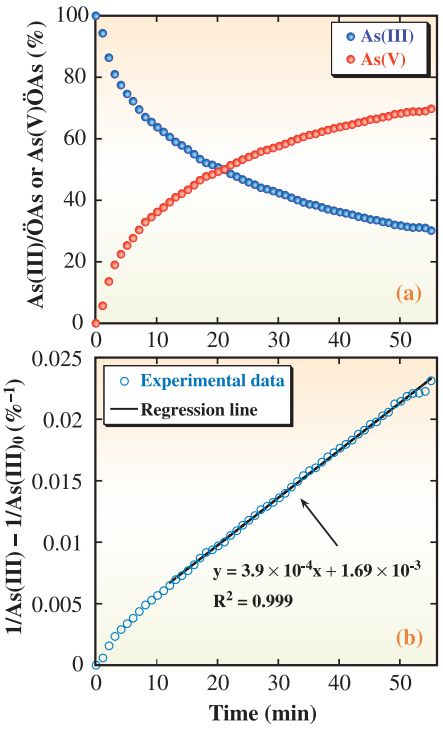

Fig. 3. **(a)** Decrease of As(III) and formation of As(V) during the oxidation of As(III) by δ-MnO_2. **(b)** Relationship between elapsed time and 1/As(III) – 1/As(III)$_0$ (As(III): percentage of As(III) fraction; As(III)$_0$ = 100%).

by δ-MnO_2 can be written as

$$MnO_2 + H_3AsO_3 + 2H^+ = Mn^{2+} + H_3AsO_4 + H_2O.$$

The decrease of As(III) in this study follows a second order reaction kinetic, as shown by the linear relation in the time dependence of 1/As(III) 1/As(III)0 (As(III): the percentage of As(III) fraction; As(III)0: initial As(III)) in Fig. 3(b).

The rate constant (k') value based on the second order reaction is 3.9×10^{-4}%$^{-1}$ min^{-1} at pH 7.1, which was obtained by the least-squares fitting of the plot (Fig. 3(b)). Several data points before 12 min are not on the regression line. Although the reason is not clear at present for the discrepancy, it is possible that the As(III) oxidation was induced by the incident X-ray beam at the initial time range.

The validity of our k' value is discussed by comparison with other reports. Our k' value is within the range from 2.9×10^{-5} to 2.6×10^{-3} %$^{-1}$min^{-1} reported in previous researches, showing that the present k' value may be valid considering other reported data.

In many previous works, however, the oxidation rate is determined indirectly by measuring concentrations of As(III) and As(V) dissolved in the aqueous phase. The rate constant obtained by such a method includes the sorption/desorption processes of As(III) and As(V). Since the sorption coefficient of As(III) and As(V) are different, the k' value obtained by the method may include some ambiguities. On the other hand, the k' value obtained in our system reflects only the oxidation of As(III) by δ-MnO_2 at the solid-water interface. This point is a highlight of the method based on the observation of the oxidation kinetics using QXAFS and the column reactor.

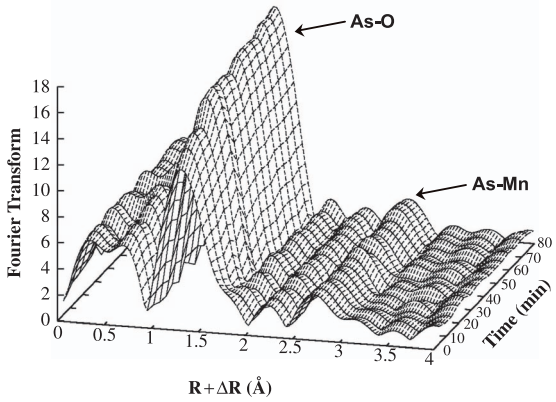

Fig. 4. Radial structure functions (phase shift is uncorrected) for As during the oxidation of As(III) by δ-MnO_2.

Time-resolved Fourier Transform of the $k^3\chi(k)$ EXAFS for As(III)/δ-MnO_2 system is presented in Fig. 4. The first shell due to As-O shell shifts slightly to shorter distance with time due to the bond length of As(V)-O that is smaller than that of As(III)-O. The magnitude of the As-O shell in Fig. 4 increases with time. Although the variation of EXAFS spectra in Fig. 4 is simply due to the increase of the As(V)/As(III) ratio with time, the present results show that the method can be applied not only to the kinetic study but also to the characterization of local structure of As at the solid-water interface during reaction by EXAFS analysis. Moreover, since this method is very simple, we can apply it to various elements and reaction systems at the solid-water interface.

Satoshi Mitsunobu[a,*], Yoshio Takahashi[a] and Tomoya Uruga[b]

[a] Department of Earth and Planetary Systems Science, Hiroshima University
[b] SPring-8 / JASRI

*E-mail: mitsunobu@hiroshima-u.ac.jp

References

[1] P. Bhattacharya *et al.*: Int. J. Water Res. Manage. **13** (1997) 79.
[2] Y. Takahashi *et al.*: Environ. Sci. Technol. **38** (2004) 1038.
[3] S. Mitsunobu *et al.*: Environ. Sci. Technol. **40** (2006) 7270.
[4] B. A. Manning and S. Goldberg: Environ. Sci. Technol. **31** (1997) 2005.
[5] *S. Mitsunobu, Y. Takahashi and T. Uruga: Anal. Chem. 78 (2006) 7040.*

Detection of Very Small Amount of Asbestos by Synchrotron X-ray Powder Diffraction

Asbestos is well recognized as a health hazard and is highly regulated. An estimated 1.3 million employees in construction and general industry have faced significant asbestos exposure on the job. Heaviest exposures occur in the construction industry, particularly during the removal of asbestos in renovation or demolition. Employees are also likely to be exposed during the manufacture of asbestos products (such as textiles, friction products, insulation, and other building materials) and while carrying out repair work on automotive brakes and clutches.

In Japan, asbestos products are defined as products that include asbestos at more than 1.0 weight %. In view of the present situation, laws regarding asbestos regulation have been revised recently. In particular, the standard concentration of asbestos was reduced from 1.0 to 0.1 weight %. Thus far, phase contrast microscopy and laboratory X-ray diffraction have been used together for qualitative and quantitative analyses, respectively. However, the detection limit of asbestos by laboratory X-ray diffraction is considered to be in the range of 0.5-1.0 weight %. That is to say, laboratory X-ray diffraction is insufficient as a quantitative analysis method for the revised standards.

Here, we improved the detection limit for the amount of asbestos by synchrotron X-ray powder diffraction. Samples spray painted with asbestos that was filtered through filter paper after being concentrated were used for the analyses. The samples for analytical use took the form of films (Fig. 1). Accordingly, surface diffractometry using a 2-dimensional detector was optimized as illustrated in Fig. 2. The experiment was carried out at the powder diffraction beamline **BL02B2**. We selected chrysotile (chemical formula: $Mg_3(Si_2O_5)(OH)_4$) from three types of asbestos as the sample for analytical use, because this is most difficult to detect by diffraction owing its poor crystallinity and because it is the only asbestos licensed to be manufactured.

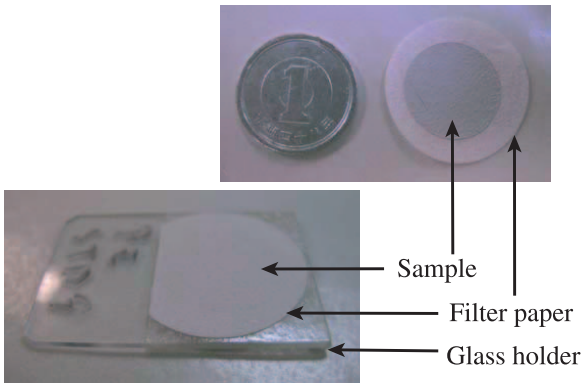

Fig. 1. Asbestos sample on filter paper.

First, we measured samples with three different concentrations of asbestos (0.1, 0.3 and 0.7 weight %) to evaluate the potential of synchrotron X-ray surface diffractometry for quantitative analysis. The arrows in Fig. 3 shows 002 peaks diffracted from each sample. By using a 2-dimensional detector, namely an imaging plate (IP), a whole powder pattern can be collected in 1 minute. The integrated intensity of the 002 reflection is proportional to the concentration of asbestos. The result shows that the synchrotron X-ray has a sufficient ability to detect 0.1 weight % asbestos. To determine the detection limit for the amount of

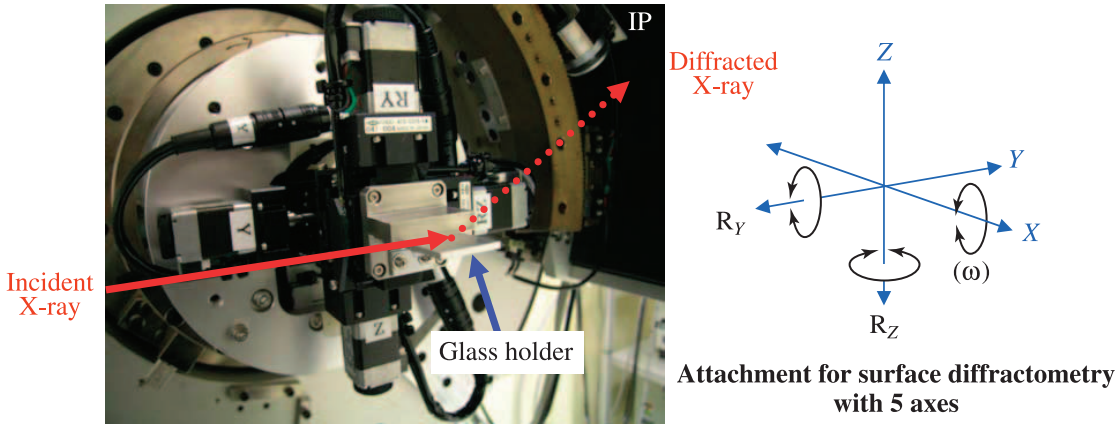

Fig. 2. Surface diffractometry using a 2-dimensional detector for analytical use.

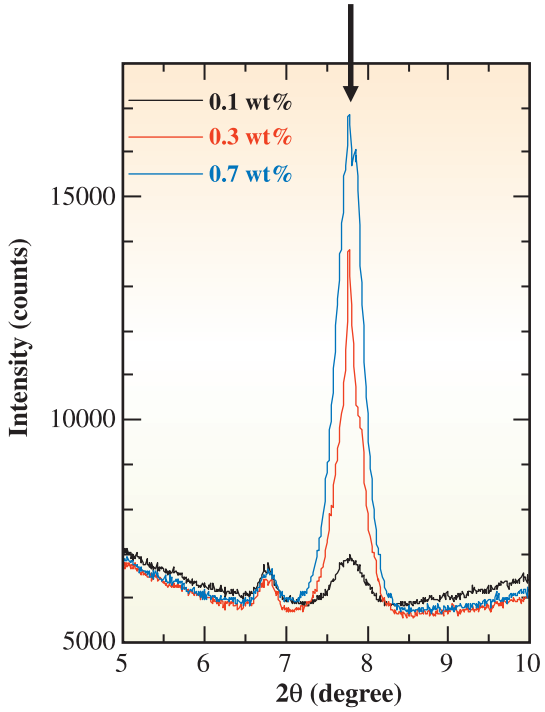

Fig. 3. Diffracted peaks from analytical samples with Chrysotile.

asbestos, we measured 0.02 mg of chrysotile, which corresponds to 0.02 weight %. As a result, an X-ray exposure time of only 5 seconds enabled us to detect asbestos as shown in the left-hand side of Fig. 4. The 1 minute data in the right-hand side of Fig. 4 showed adequate counting statistics for quantitative analysis. Thus, we have demonstrated the potential of synchrotron X-ray powder diffraction in the fields of not only advanced materials science but also routine analytical research [1-5].

On the other hand, additional time was required for sample exchange, sample position alignment and IP exchange/readout, which takes more than ten times as long as the measurement. This point prevented us from promoting the analytical research using synchrotron radiation. To overcome this bottleneck, we are now developing an auto sample exchanger, an image recognition system and an X-ray detector to achieve a high-throughput of synchrotron X-ray powder diffraction [6]. I believe that this system should contribute to materials science research as well as analytical research.

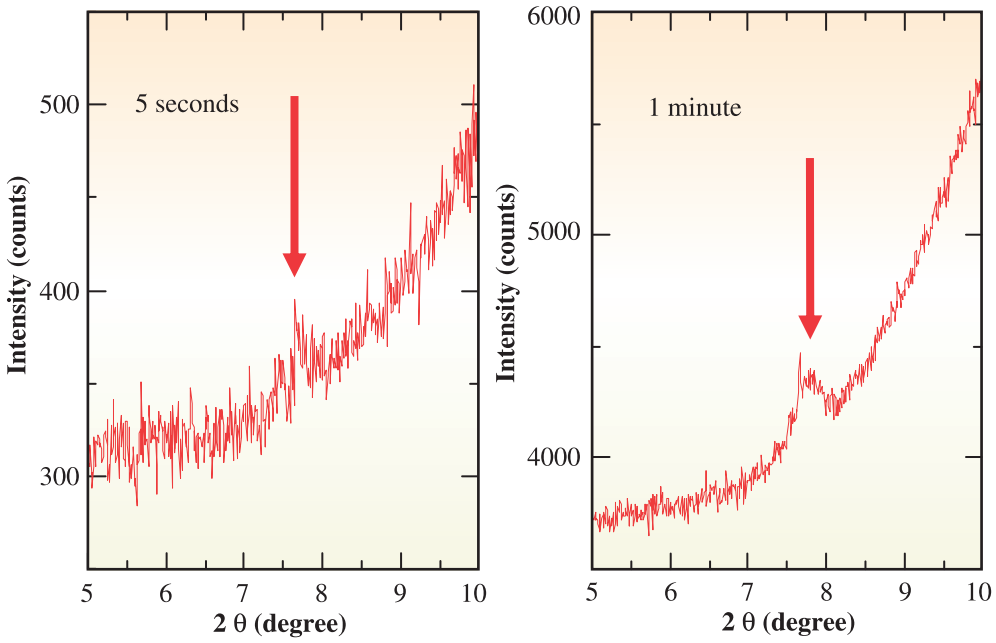

Fig. 4. Diffracted peaks from 0.02mg (0.02 wt%) of Chrysotile.

Kenichi Kato

SPring-8 / RIKEN

E-mail: katok@spring8.or.jp

References

[1] Mainichi Newspaper (front page), 1 April 2006.
[2] Asahi Newspaper (third page), 1 April 2006.
[3] Nikkeisangyo Newspaper (8th page), 4 April 2006.
[4] Nikkankogyo Newspaper (27th page), 4 April 2006.
[5] Kankyo Newspaper (front page), 19 April 2006.
[6] *K. Kato, M. Takata and T. Ishikawa: J. Soc. Instrument and Control Engineers* ***46*** *(2007) – in press.*

Industrial Applications

Since it found that there was a strong need for synchrotron radiation utilization research among researchers in the industry, JASRI has adopted various systems such as the coordination, the trial use and Large-Scale Advanced Scientific Facilities Strategic Utilization Proposal systems, which have been used continuously. After the introduction of the national project entitled the Large-Scale Advanced Scientific Facilities Strategic Utilization Program, the number of industrial applications has increased significantly.

Twelve experiments representative of the outstanding work carried out in the field of Industrial Applications in 2005B and 2006A are introduced here. Although the majority expert users had previously belonged to electronics, many researchers from other industrial fields, such as those involving nondestructive evaluation, fuel cells, hydrogen storage materials, polymers and cosmetics, are now joining SPring-8.

The very interesting experiments discussed in this section were performed using the following nine different beamlines, that is, three experiments were accomplished using the Surface and Interface Structures beamline BL13XU, two experiments were carried out using the Engineering Science Research beamline BL19B2, and the remaining eight experiments were performed using the Industrial Consortium beamline BL16XU, the Medical Imaging beamline BL20B2, the Hyogo beamline BL24XU, the Soft X-ray Spectroscopy beamline BL25SU, the White Beam X-ray Diffraction beamline BL28B2, the High Flux beamline BL40XU, and the Infrared Materials Science beamline BL43IR.

In the electronics field, which still supplies the majority of users, next-generation gate dielectric films, magnetic recording films, hard disk drives (HDD) and multilayer ceramics capacitors (MLCDCs) have been studied mainly by XRD, XMCD and IR. As examples of such studies, the strain observation in Si substrates used in LSI technologies indicated that the Si substrates with local strain have good crystal quality with very small strain, while strained Si substrates such as Bulk, SGOI and SSOI have large strain, but very poor crystal qualities.

Time-resolved studies of the electrochemical oxidation occurring in fuel cells and crystal structure analysis of unusual rare earth-Mg-Ni-based hydrogen alloys were introduced in the field of energy devices.

Studies on nondestructive evaluation using imaging techniques are valuable in the industry. In this section, a technique of three-dimensionally imaging crystal defects in single crystal CaF_2 materials for observing optics and fatigue cracks in structural components will be introduced.

One of the industries that are directly related to people's lives is cosmetics. The development of hair care products is of special interest to the cosmetics industry. XRD analysis of single-hair fibers will prove to be a very useful tool for determining the characteristics of hair.

It can be declared with confidence that the excellent research presented in this section provides good models for materials researchers and analytical scientists.

Norimasa Umesaki

Evaluation of phase separation of Hf-silicate films by In-Plane SAXS

High-k films (ex. HfSiO) have been investigated as next-generation gate dielectric films to serve as an alternative to SiO_2 for the reduction of direct leakage current. Amorphous HfSiO is needed to improve device characteristics. HfSiON containing N will be used, because HfSiON is amorphous and stable after high temperature annealing (1000 °C). However, there is a concern about the generation of small HfO_2 phase separation and crystallization after annealing because of the increase in the dispersion of device characteristics [1]. Thus, a high sensitive evaluation method is required to determine the state of the film accurately.

As methods for the evaluation of crystallization and phase separation of thin films, there are TEM, XRD and small angle X-ray scattering (SAXS). It is difficult to determine the boundary of the HfO_2/SiO_2 accurately from the TEM image. Although XRD (ex. GIXD) is useful for the evaluation of crystallization of very thin films (~1 nm), the evaluation of phase separation (not crystalline) cannot be carried out by XRD. SAXS is expected to provide a quantitative analysis (ex. average diameter and distribution) of the phase separation. We have already ensured that In-Plane SAXS using conventional laboratory equipment could be used for the quantitative analysis of phase separation of thick HfSiON (more than 10 nm). However, it was difficult to analyze thin films (less than 5 nm) using conventional laboratory equipment.

To evaluate very thin HfSiON films (3 nm) by In-Plane SAXS, we used the synchrotron radiation X-ray at beamline **BL13XU**.

Several HfSiO films (3 nm, Hf/(Hf+Si) = 50%) were deposited by MOCVD on Si (100) surface treated with dilute HF. After nitridation, some samples were annealed at 1000 °C in N_2. The measurement was performed using XRD goniometer (ATX-GSOR). The energy of the X-ray was 11.919 keV (1.04 Å). The sample was set in a He atmosphere to reduce the air scattering. Incident X-ray grazed the sample at a critical angle, and the detector was scanned in-plane parallel to the sample surface (Fig. 1).

Figure 2 shows In-Plane SAXS results and estimated HfO_2 particle diameter. The peak at 1 degree of HfSiO (w/o N) is considered scattering from the uniformly crystallized HfO_2. The average diameter of the HfO_2 particle is approximately 3.5 nm (at Hf/(Hf+Si) = 50%). The intensity of the scattering of the HfSiON (w/ N) decreases clearly with the increase in the N concentration, and correspondingly, the average diameter decreases to less than 1 nm. However, the distribution of the HfO_2 particle is disarranged and a small part of the HfO_2 particle grew until several nm. The distribution of as-depo. (w/o N) is the widest and the average diameter is about 1.7 nm. By including N, the HfO_2 particle is destroyed and this suppresses the regrowth of the HfO_2 particle. This is why the Hf-N bond, as shown in the XPS data, is formed.

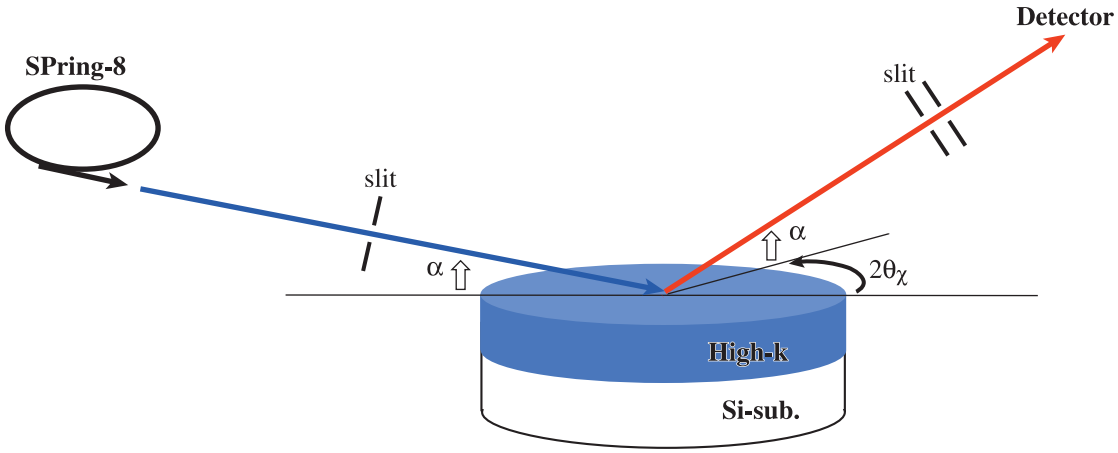

Fig. 1. Schematic of the experimental arrangement setup of In-Plane SAXS (BL13XU).

These samples were evaluated by TEM to observe the HfO_2 phase separation and the crystallization directly, TEM is widely used to determine the diameter of particles (Fig. 3). However, the boundary between the HfO_2/SiO_2 in as-depo. and samples with high N content is not clear and it is impossible to determine the average diameter of the HfO_2 particles accurately from the TEM image. Moreover, using conventional laboratory equipment, it is difficult to detect this very small change, even with thick films (more than 10 nm). Only by using synchrotron radiation will it be possible to evaluate small changes of even less than 1 nm.

These new information about HfSiON films will help in the detailed understanding of electric characteristics and these experimental data can be used for process refinement.

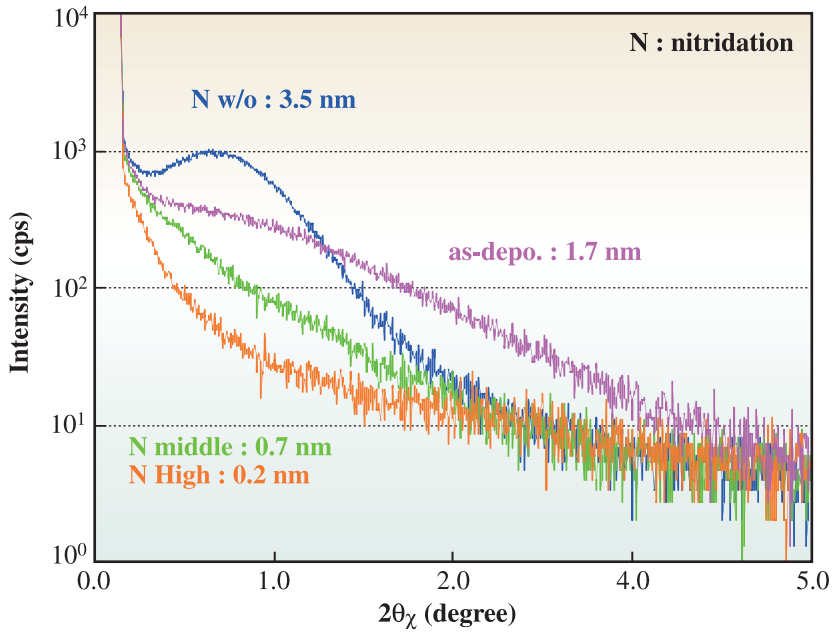

Fig. 2. In-Plane SAXS result and HfO_2 particle diameter (Hf/(Hf+Si) = 50%).

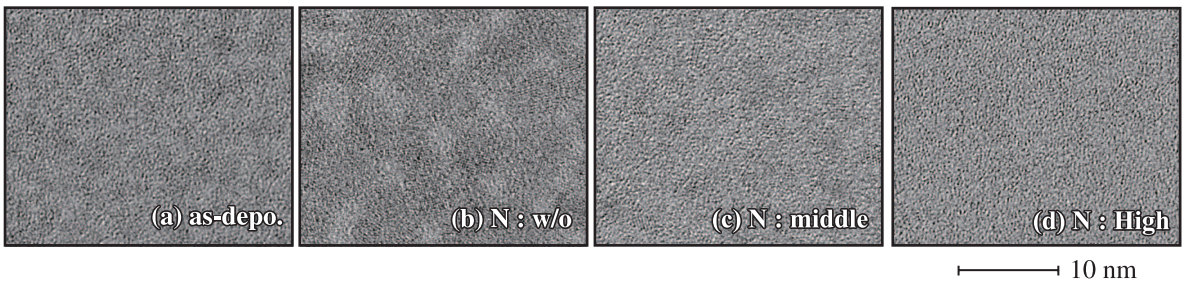

Fig. 3. TEM image (N: nitridation). **(a)** as-depo, **(b)** N:w/o, **(c)** N:middle, **(d)** N:High.

Nobutaka Satou* and Mamoru Takahashi

Physical Analysis Group II, Toshiba Nanoanalysis Corp.

*E-mail: nobutaka.satou@nanoanalysis.co.jp

Reference

[1] M. Koyama *et al.*: IEDM2002, p. 849

Evaluation of Global and Local Strain Induced for Carrier Mobility Enhancement in Si Substrates

In state-of-the-art LSI technologies, strain management in Si is recognized as one of the most important technologies for achieving high-performance operation. This is because carrier mobility can be enhanced by introducing the appropriate strain in the channel region of MOSFETs [1]. Two techniques are proposed for strain introduction. One is "local strain," in which the strain is introduced only in a desired region during LSI fabrication. The other is "global strain," which means using a wafer with strained-Si film as a starting material. We consider that quantitative evaluations of amount and uniformity of local and global strains in Si substrates are essential to develop these new techniques. The strain in Si has been characterized by Raman spectroscopy, X-ray diffraction, electron diffraction, and other methods. However, it has been difficult to obtain a detailed profile of the strain in the ultra-thin strained-Si film using traditional evaluation techniques. In this study, we evaluated the local strain induced by SiN deposition on Si substrates and the global strain in so-called strained Si substrates using in-plane X-ray diffraction (XRD) techniques at beamline **BL13XU**.

The structures of the strained Si substrates (global strain) are shown in Fig. 1(a-c). The thickness of the strained-Si film for Bulk substrate was 17.5 nm with 20% Ge concentration in an underlying relaxed SiGe layer (Fig1(a)). SiGe-on-insulator (SGOI) substrate had approximate thickness of 17, 70, and 200 nm for strained-Si, SiGe, and buried oxide (BOX) film, respectively (Fig1(b)). The Ge concentration was also 20%. The Si-on-insulator (SSOI) substrate had a structure with 17 nm strained-Si film directly on the 200 nm BOX layer (Fig1(c)). For the local strain, SiN capping layers with 0 (reference), 20, 40, 60, and 80 nm thicknesses were deposited on Si or SOI (Si-on-isulator) substrates by low-pressure chemical vapor deposition (LP-CVD) for introducing the strain at the Si_3N_4/Si interface. The SOI film thicknesses were 30, 50, and 100 nm. To obtain the depth profile of strain in the near-surface region, we adopted grazing incidence X-ray diffraction using a synchrotron X-ray with approximately 0.1 nm wavelength. If the incident angle the of X-ray to the sample surface is less than the critical angle (0.14°) for total reflection, the X-ray wave field in the sample becomes evanescent and is limited to the top of surface (less than 10 nm) [2]. The X-ray penetration depth varies according to X-ray incident angle. If there is a depth profile of the lattice parameter, the scattering angle of the in-plane diffraction should vary depending on the incident angle.

The result of the in-plane XRD for the Bulk substrate is shown in Fig. 2. The peak position corresponded to $2\theta_\chi$ of the scattering angle, reflecting the lattice distance of the (400) plane perpendicular to the sample surface. Each peak consists of many components, probably reflecting the domain structure in the observation area. However, the peak shape did not change with the change in the incident angle. This indicates that the domain structure was uniform in the depth direction. On the contrary, it is apparent that the peak shifted toward a smaller angle ($2\theta_\chi$) as the X-ray incident angle (ω) increased from 0.12 to 0.15°. This peak shift implies that the lattice distance expanded toward the depth direction. However, different strain depth profiles were observed at different areas in the same substrate. The disordering

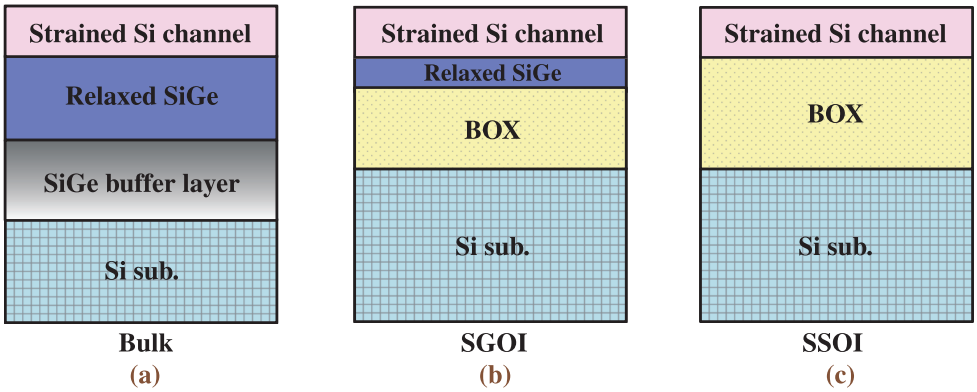

Fig. 1. Structures of strained Si substrates, **(a)** Bulk, **(b)** SGOI, and **(c)** SSOI. The film thickness of each layer in the strained Si substrates is shown.

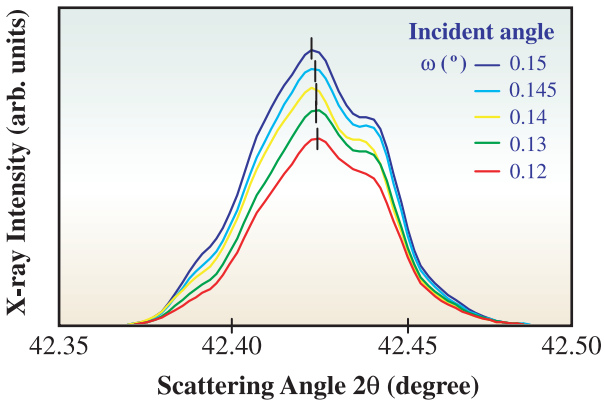

Fig. 2. Results of in-plane XRD of Bulk strained Si substrate with changing incident X-ray angle.

of strain depth profiles could come from the crystalline defects. We consider that it is necessary to measure the strain precisely in the channel depth of MOSFETs and to design the device parameters based on the measurement, since the largest lattice deformation 0.012% toward depth, and disordering of strain depth profiles were observed, as described above.

As for the sample of local strain, the peak positions of the X-ray diffraction profiles for the Si substrate with Si_3N_4 cap of 80 nm thickness are shown in Fig. 3. The diffraction angle shifted toward the smaller angle with decreasing X-ray incident angle (decreasing X-ray penetration depth). Therefore, we concluded that the local strain was concentrated at the Si_3N_4/Si interface. We also evaluated the strain by UV-Raman spectroscopy [3]. There is a strong correlation in observed strains between UV-Raman spectroscopy and in-plane XRD. However, these are not matched each other. We consider that was because the penetration depth of the XRD measurement with synchrotron radiation was set to be shallower than that of the UV-Raman spectroscopy measurement.

Table 1. Summary of Δd/d and FWHM for each substrate with local or global strain.

Strain	Δd/d (%)	FWHM (°)
Local strain	0.014	0.004
Global strain	0.81	0.04
Cz-Si	____	0.004

Table 1 summarizes the Δd/d (%) and full-width-at-half-maximum (FWHM) for each substrate. The FWHM of the strained Si substrate (global strain) was larger than that of the Si substrate with Si_3N_4 cap of 80 nm thickness (local strain), which was almost the same as that of Cz-Si. Strained Si substrates (global strain) had a large strain of approximately 0.81% (tensile). However, the strain of SiN-capped Si (local strain) was only 0.014% (compressive). Therefore, we can conclude that the Si substrates with local strain had good crystal quality with very small strain, while the strained Si substrates such as Bulk, SGOI and SSOI had a large strain, but the crystal qualities were very poor.

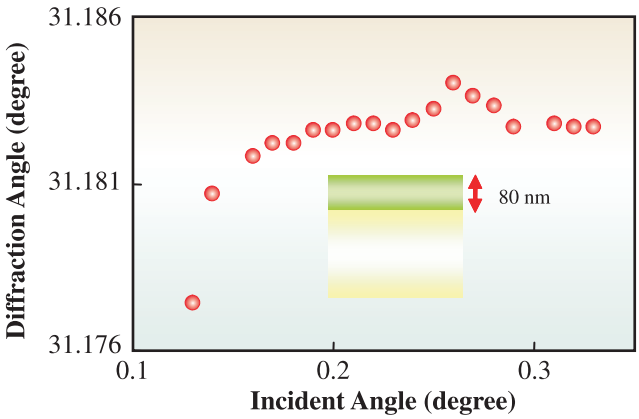

Fig. 3. Depth strain profile of local strain at Si_3N_4 interface by (440) in-plane XRD.

Atsushi Ogura

School of Science and Technology, Meiji University

E-mail: a_ogura@isc.meiji.ac.jp

References

[1] S. Takagi *et al.*: J. Appl. Phys. **80** (1996) 1567.
[2] G.H. Vineayard: Phys. Rev. B**26** (1982) 4146.
[3] *A. Ogura, K. Yamasaki, D. Kosemura, S. Tanaka, I. Chiba, and R. Shimidzu: Jpn. J. Appl. Phys.* ***45*** *(2006) 3007.*

Interfacial Magnetic Structure of Mn between Ferromagnetic/Antiferromagnetic Bilayers in Magnetic Sensor Heads

Higher recording density hard disk drives (HDD) are indispensable devices for our information-oriented society. Since the annual growth rate of the recording density of HDD is over 40%, many researchers have focused on the development of advanced HDD with a recording density of 1 Tb/in^2. Issues regarding their development are 1) high sensitivity and nanomachining of magnetic sensor heads, and 2) high resolution in recording media.

Recently, with the decrease in track size in sensor heads, instability of exchange coupling between ferromagnetic (FM) / antiferromagnetic (AFM) bilayers comes to the surface, that is, magnetization in the FM layer, which is pinned by the AFM layer, has rotated or flipped through the nanomachining process. Therefore, a higher robustness of exchange coupling is indispensable to realizing high recording density HDD. To improve the robustness, it is necessary to understand the mechanism of exchange coupling and control the magnetic structure at the FM / AFM interface by optimizing parameters such as materials, orientation, grain size and so on (see Fig. 1).

X-ray magnetic circular dichroism (XMCD) and element specific magnetic hysteresis (ESMH) analyses are powerful techniques for investigating the interface magnetic structure. Ohldag *et al.* reported the existence of pinned interfacial AFM spins (Mpin), as determined from observing the vertical offset of hysteresis loops of uncompensated AFM spins (Mn) [1]. Up to now, the exchange coupling energy J, calculated for ideal interface is higher by orders of magnitude than the observed one, J_k, for nonideal interface such as polycrystalline bilayers. They estimated a small Mpin fraction, ρ, of 4% for uncompensated Mn spins and explained that $J_k \sim \rho J$. This idea is reasonable, but a mechanism that stabilizes Mpin at the interface is unclear. We, therefore, verified the existence of Mpin by measuring the Mn hysteresis loops for FM (CoFe) / AFM (MnPt) bilayers by XMCD and ESMH analyses. The samples were glass(sub.)/ underlayer/ MnPt(15)/ CoFe(2)/ Cu(1)/ Ru(2). The numbers in parentheses are the nominal thicknesses in nanometers. J_k was 0.1 ~ 0.3 erg/cm^2 obtained by controlling the MnPt orientation. X-ray absorption spectra were measured by the total electron yield (TEY) method, which has high sensitivity to the interfacial region. We used left and right elliptically polarized X-rays from a twin helical undulator at beamline **BL25SU**. The X-rays were incident at a grazing angle of 30° from the exchange bias direction on the sample surface. Magnetic fields were applied using an electromagnet along the axis

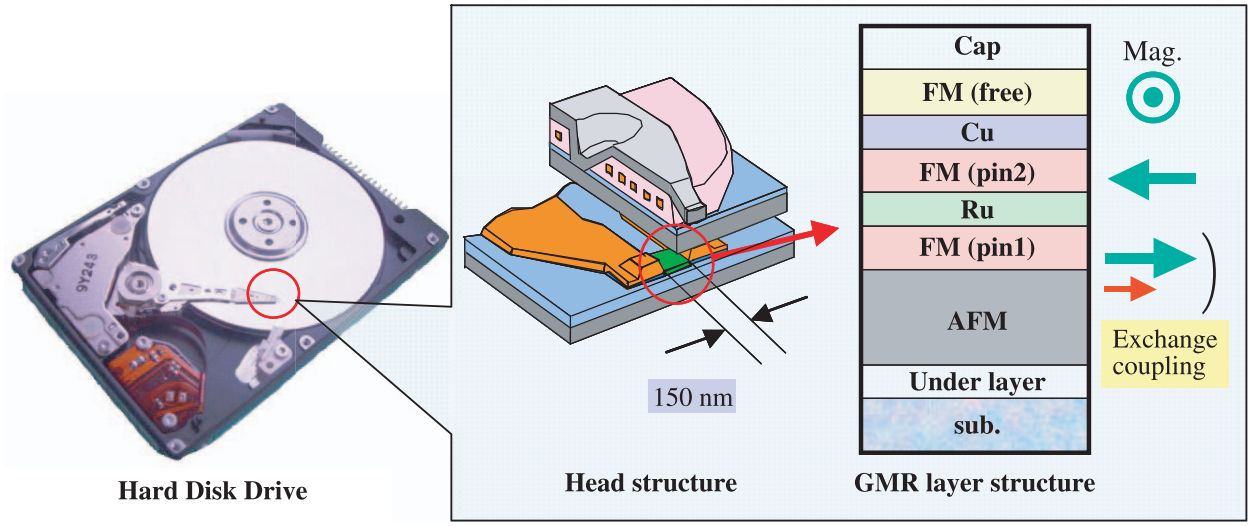

Fig. 1. Schematic drawing of hard disk drive, head structure and giant magneto resistance (GMR) layer structure. AFM means antiferromagnetic layer; FM, ferromagnetic layer; Cap, capping layer and Mag., magnetization. It is necessary to understand the mechanism of exchange coupling and control the magnetic structure at the FM / AFM interface to realize high recording density HDD.

raised 20° from the sample surface. To realize a near antiparallel configuration of the exchange bias direction to the incident X-rays, two divided MnPt samples were set by the antiparallel configuration for the TEY method. We performed the following to measure at a higher S/N ratio: 1) adjustment of slit size under the monochromator and undulator gap, and 2) maintaining a low noise around the sample and output signal processing.

Figure 2 shows the Mn and Co ESMH loops for the FM (CoFe) / AFM (MnPt) bilayers samples. The red and blue lines show the parallel and antiparallel configurations between the exchange bias direction and the incident X-rays, respectively. Co ESMH loops exhibited the typical exchange bias phenomenon, i.e. a horizontal loop shift. We could observe the Mn ESMH loops, which mean the induced ferromagnetic component (uncompensated spins) through the exchange coupling at the FM / AFM interface. The Mn ESMH loops also exhibited a horizontal shift, corresponding well with that of the respective Co loops. If the Mpin of Mn exists, the Mn ESMH loops will vertically shift. However, no vertical offsets of the Mn ESMH loops were observed for all samples, meaning no existence of Mpin. These results indicate that the insignificant uncompensated Mn spin was pinned at the interface to induce exchange coupling on the FM layer (CoFe) [2].

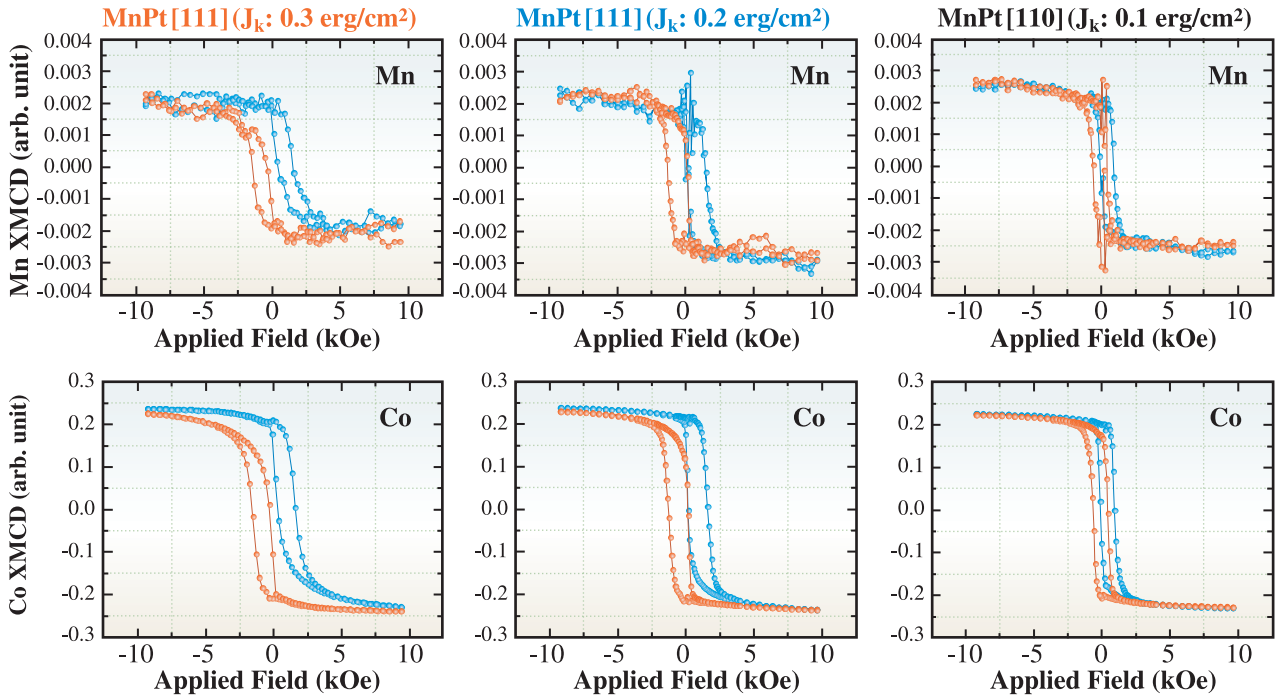

Fig. 2. Mn and Co ESMH loops for FM (CoFe) / AFM (MnPt) bilayers samples. The hysteresis loops were acquired with the exchange bias direction either parallel (red lines) or antiparallel (blue lines) to incident X-rays. No vertical offsets of Mn ESMH loops were observed.

Tatsumi Hirano[a,*], Tetsuya Nakamura[b] and Hitoshi Osawa[b]

[a] Hitachi Research Lab., Hitachi Ltd.
[b] SPring-8 / JASRI

*E-mail: tatsumi.hirano.nm@hitachi.com

References

[1] H. Ohldag *et al.*: Phys. Rev. Lett. **91** (2003) 17203.
[2] M. Tsunoda *et al.*: Appl. Phys. Lett. **89** (2006) 172501.

Real-Time Monitoring of an Electrochemical Reaction Inside a Fuel Cell: A time-resolved Hard X-ray Diffraction Study

Fuel cells that convert the chemical energy of fuel, such as hydrogen or methanol, directly into electricity can offer clean and highly efficient energy conversion systems in the near future. Owing to recent extensive studies, the basic performance of such fuel cells are now about to reach pratical levels. For example, car manufacturers are showing prototypes of hydrogen fuel cell cars, and electronic companies are looking at a new battery market for portable electronics by replacing Li-ion batteries with longer-lasting direct methanol fuel cells.

There are, however, still several hurdles to be overcome before such fuel cells can be truly commercialized. One such technological hurdle is the improvement of the durability and reliability of fuel cells, particularly electrocatalysts that promote electrochemical reactions in the fuel cells. During long-term operation, the power of fuel cells gradually decreases due to the oxidative degradation of platinum catalysts. Since the platinum catalysts' surface is exposed to extremely severe chemical conditions, i.e., in a strong acid or under high electrochemical potential, platinum catalysts dissolve into the electrolyte causing considerable reduction in the fuel cell performance. Consequently, the development of innovative electrocatalysts with high corrosion protection performance is one of the main research interests in this research field.

To obtain information for designing better electrocatalysts, there is a great interest in the direct monitoring of the oxidative degradation behaviors of platinum catalysts in a real operating condition. A hard X-ray diffraction method using with the high penetration ability of high-energy X-rays through components of fuel cells such as electrolyte and electrode materials is one of the suitable experimental techniques for such purpose. Here, we present the results of time-resolved hard X-ray diffraction studies on the electrochemical oxidation process of platinum electrocatalysts, which shows how platinum oxides are formed on the catalyst surface and how such oxides affect the properties of nanoparticles [1].

Time-resolved *in situ* X-ray diffraction (XRD) measurements were performed in the transmission geometry at beamline **BL16XU**. The photon energy used was 30 keV. Diffraction profiles were collected using a CCD camera in every 0.5 s. Carbon supported platinum nanoparticles (*ca.* 3 nm, 50 wt%-Pt loading) were spread onto a carbon electrode. This electrode was placed in an electrochemical cell with 0.5 mol dm^{-3} H_2SO_4 electrolytes, and the potential of the electrode was controlled by an electrochemical analyzer.

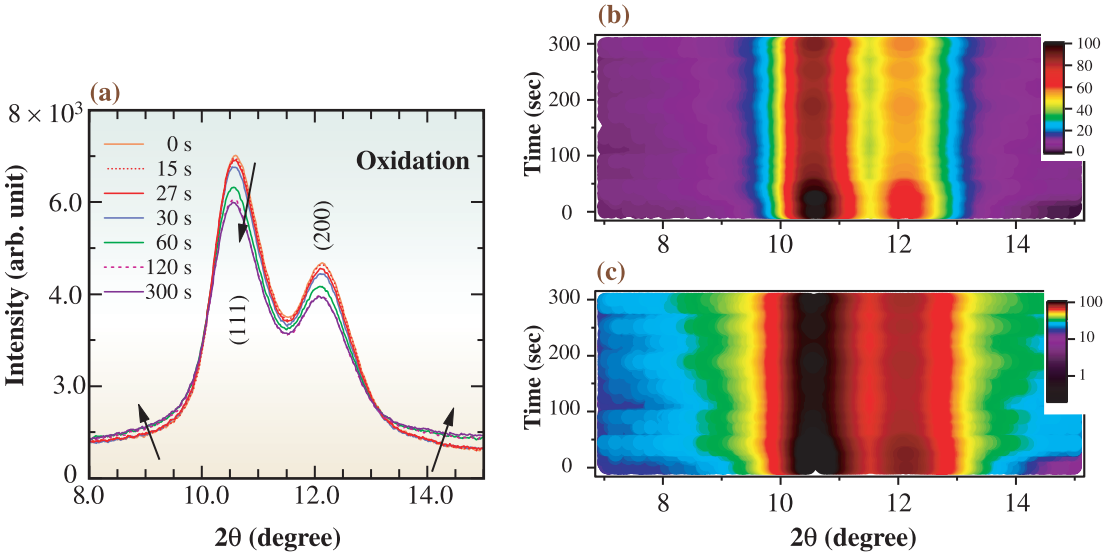

Fig. 1. **(a)** Time variation of *in situ* X-ray diffraction profiles of platinum nanoparticles upon oxidation at 1.4 V (*vs* RHE). XRD intensity maps with respect to 2-theta and time, in normal scale **(b)** and in log scale **(c)**. Diffractions from platinum and platinum oxides are highlighted respectively.

Figure 1(a) shows the evolution of the X-ray diffraction profiles in the first oxidation process at 1.4V *vs*. RHE (Reversible Hydrogen Electrode). Upon oxidation, the intensities of platinum (111) and (200) diffraction peaks gradually decreased; simultaneously, the background intensity, which is attributed to the diffuse scattering from the amorphous-like PtO_x, increased. This indicates that the surface of platinum nanoparticles was gradually oxidized into amorphous-like platinum oxides. The fraction of oxides is 40%, as estimated by the diffraction peak area loss, corresponding to the monolayer of the particles' surface. (The detailed structure of surface oxides is similar to that of β-PtO_2 as determined by our DXAFS (dispersive X-ray absorption fine structure) measurements performed at beamline **BL28B2** [2]). Interestingly, during the first 15 s, (111) and (220) diffraction intensities did not significantly change. OH adsorption and/or atomic O adsorption, which do not cause significant surface reconstruction, would occur at this stage.

We show the XRD intensity map with respect to both 2θ and time in Figs. 1(b) and 1(c). The time variation of surface oxide formation is more clear in these figures. In addition to the diffraction intensity change, we also observed clear peak shifts to the lower diffraction angle. This suggests that the core parts of the platinum nanoparticles are expanded when the nanoparticles' surfaces are covered with their oxides (Fig. 2). This result is somewhat surprising, since such lattice expansion is not observed at the bulk surface. This lattice expansion observed only at the nanoparticles' surface could be one reason why nanoscaled catalysts show the accelerated oxidative degradation phenomenon.

Observed surface oxides and structural change in the core part of nanoparticles should be closely related with corrosion phenomena of platinum catalysts. Currently, on the basis of the above results, the development of the catalyst with higher corrosion protection performance is under the way.

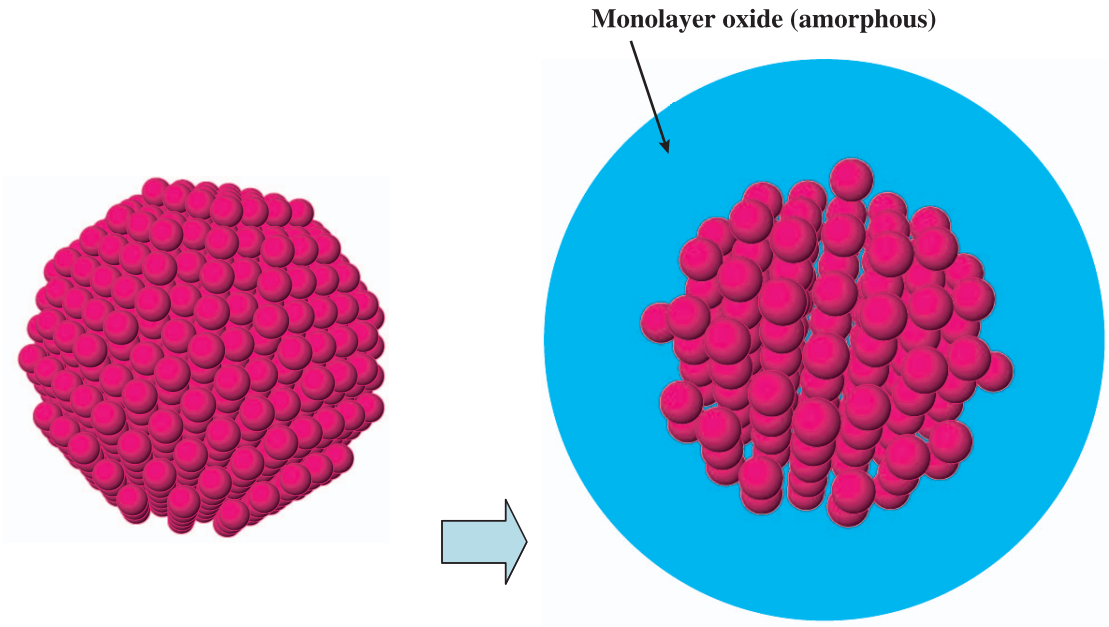

Fig. 2. Schematic drawing of surface oxidation process of platinum nanoparticles at 1.4 V.

Hideto Imai* and Koichi Izumi

Fundamental and Environmental Research Laboratories,
NEC Corporation

*E-mail: h-imai@ce.jp.nec.com

References

[1] *H. Imai, K. Izumi, M. Matsumoto, Y. Kubo, K. Kato and Y. Imai - to be published.*
[2] H. Imai, K. Izumi, and Y. Kubo: Electrochemistry **74** (2006) 883.

Crystal Structure Analysis of La-Mg-Ni-based Hydrogen Storage Alloys

The rare earth-Mg-Ni-based alloy is a promising hydrogen storage material for fuel cells and nickel metal hydride batteries because its hydrogen storage capacity is higher than that of conventional $MmNi_5$-based (Mm: mischmetal) alloys. In 1997, Kadir and Sakai *et al.* reported on $REMg_2Ni_9$ (RE: rare earths) alloys [1]. Subsequently, various alloys with a hydrogen storage capacity of 1-2 wt.% have been reported [2]. The hydrogen storage property of these alloys is dependent on their composition and crystal structure. However, there are few studies on the relationship between them. This is attributable to the complexity of the crystal structure of the alloys. Concerning this alloy system, there have been reports on many kinds of long-period one-dimensional superstructures, in which AB_5 units ($CaCu_5$-type structure) and A_2B_4 unit (Laves structure) are rhombohedrally or hexagonally stacked with a ratio of *n*:1 along the *c*-axis direction [3]. Most of the rare earth-Mg-Ni-based alloys have multi-phase structures consisting of more than one kind of superstructure.

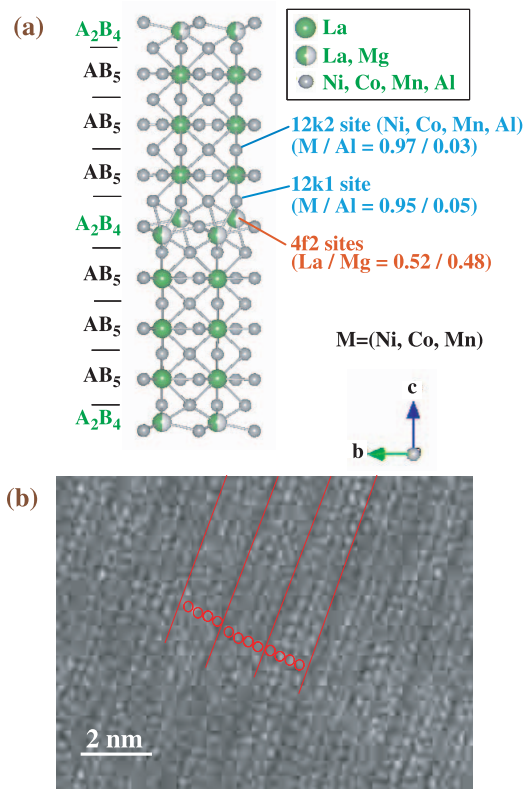

Fig. 1. **(a)** Crystal structure viewing [1 0 0] direction and **(b)** TEM image of 5:19H (Pr_5Co_{19}-type) phase of $La_{0.8}Mg_{0.2}Ni_{3.4-x}Co_{0.3}(MnAl)_x$ alloy.

Therefore, it is difficult to refine the crystal structure using conventional XRD pattern with characteristic X-ray radiations. On the other hand, in synchrotron XRD measurement, the effect of the preferred orientation is suppressed, and the diffraction pattern with high resolution and high intensity is obtained even by a short-time measurement. In this work, the effect of the partial substitution of Ni with Mn and Al on the crystal structure and hydrogen storage property was studied for La-Mg-Ni-based alloys using synchrotron XRD measurements.

$La_{0.8}Mg_{0.2}Ni_{3.4-x}Co_{0.3}(MnAl)_x$ ($0 \leq x \leq 0.4$) alloys were prepared by induction melting. The XRD samples were prepared by sealing the alloy powder with an average particle size of about 20 μm into Lindeman glass capillary with an inner diameter of 0.3 μm. Synchrotron XRD measurements were carried out using a large-diameter Debye-Scherrer camera with an imaging plate at beamline **BL19B2** (wavelength 0.7 Å).

Five kinds of stacking-structured phases, rhombohedral Gd_2Co_7-type (hereinafter 2:7R), hexagonal Ce_2Ni_7-type (2:7H), hexagonal Pr_5Co_{19}-type (5:19H), rhombohedral Ce_5Co_{19}-type (5:19R), and rhombohedral La_5MgNi_{24}-type (1:4R) phases were identified from the XRD patterns. There were also peaks assignable to $CaCu_5$-type phase (AB_5 phase) and C15*b*-$AuBe_5$-type phase (AB_2 phase). Figure 1(a) shows projections onto the (1 -2 0) plane of 5:19H phase. The 5:19 phase was confirmed also by HRTEM observation (Fig. 1(b)).

By means of Rietveld analysis (software: RIETAN-2000 [4]), the abundances of each phase were determined, and the site occupancy and lattice parameters of the phases were refined. Figure 2 shows the Rietveld refinement pattern with synchrotron XRD pattern for $La_{0.8}Mg_{0.2}Ni_{3.25}Co_{0.3}(MnAl)_{0.15}$ alloy, and Fig. 3 shows the relationship between Mn and Al amounts and phase abundance in the $La_{0.8}Mg_{0.2}Ni_{3.4-x}Co_{0.3}(MnAl)_x$ alloys. With the increase in Mn and Al amounts from $x = 0$ to $x = 0.2$, the mass fraction of 2:7H phase decreased, and those of 5:19R, 5:19H, and 1:4R phases increased. For the alloys with $x = 0.15$ and 0.2, 5:19H and 1:4R phases were dominant, respectively. Further substitution to $x > 0.2$ decreased the mass fraction of the stacking-structured phases and increased those of the AB_5 and AB_2 phases. The alloy with $x = 0.4$ contained no stacking-structured phases. In 5:19H and 1:4R phases, Mg occupies the

La sites of A_2B_4 units, and Al occupies the Ni sites between AB_5 units or those between A_2B_4 and AB_5 units (Fig. 1). The stabilization of these phases at a narrow composition range could be related to the preferential occupation of Mg and Al in particular sites.

Hydrogen absorption-desorption characteristics were evaluated by measuring pressure-composition-temperature (P-C-T) curves using a Sievert type apparatus at 80 °C. The hydrogen storage capacity of the alloys with x = 0-0.2 was 1.3 wt.%, which was 1.2 times as high as those of the conventional alloys. The alloy with x = 0.4 showed a lower capacity of 1.1 wt.%. Results of the Rietveld analysis and P-C-T measurements suggest that the capacity decreased with the increasing mass fraction of AB_5 phase, and that stacking-structured phases have a larger capacity than AB_5 phase.

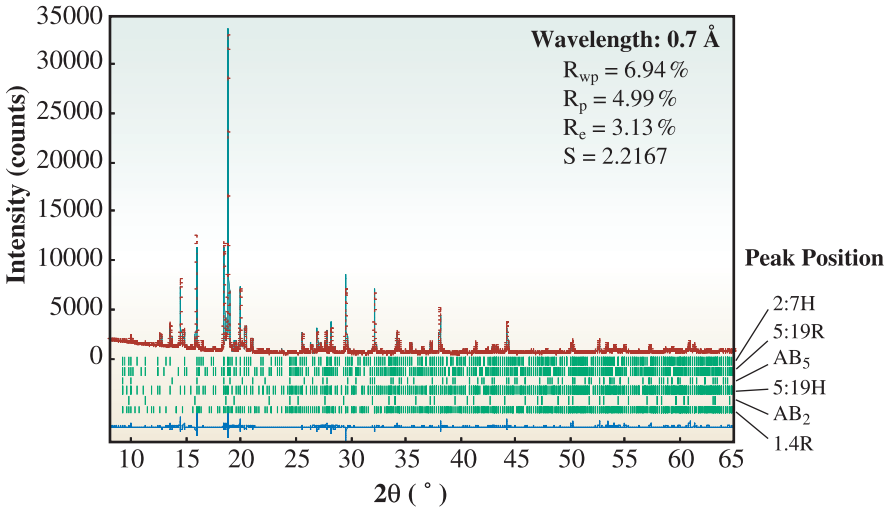

Fig. 2. Rietveld refinement pattern with synchrotron XRD pattern for $La_{0.8}Mg_{0.2}Ni_{3.25}$ $Co_{0.3}(MnAl)_{0.15}$ alloy.

Synchrotron X-ray diffraction measurements and Rietveld analysis elucidated the effect of the partial substitution of Ni with Mn and Al on the crystal structure and hydrogen storage capacity of the La-Mg-Ni-based alloys. This suggests that it is possible to develop a promising electrode alloy with superior discharge capacity and cycle life by further optimizing the alloy composition together with crystal structure analysis.

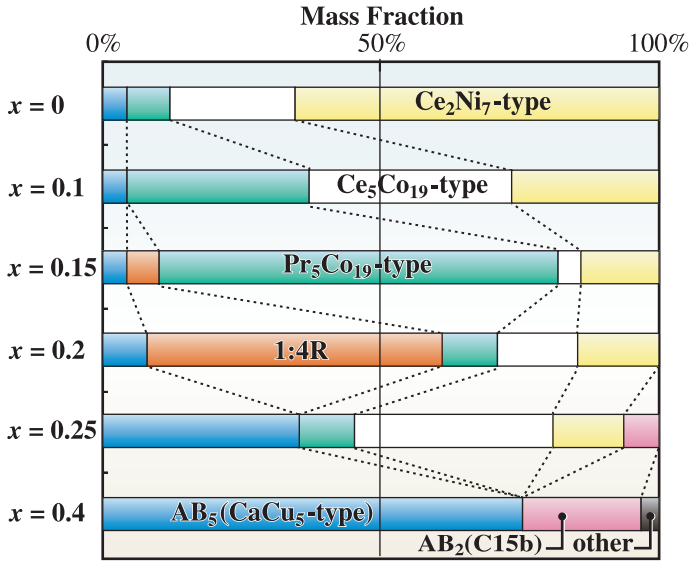

Fig. 3. Phase abundance of $La_{0.8}Mg_{0.2}$ $Ni_{3.4-x}$ $Co_{0.3}(MnAl)_x$ ($0 \le x \le 0.4$) alloys obtained by Rietveld refinement.

Masaharu Watada* and Tetsuya Ozaki

GS Yuasa Corporation

*E-mail: masaharu.watada@jp.gs-yuasa.com

References

[1] K. Kadir *et al.*: J. Alloys Compds. **257** (1997) 115.
[2] T. Kohno *et al.*: J. Alloys Compds. **311** (2000) L5.
[3] H. Hayakawa *et al.*: Mater. Trans. **46** (2005) 1393.
[4] F. Izumi and T. Ikeda: Mater. Sci. Forum **321-324** (2000) 198.

Evaluation of Local Homogeneity Fluctuation of Sinter of Small Chip MLCCs by Mid-infrared Spectroscopy

Multilayer ceramic capacitors (MLCCs) are composed of several hundreds of alternately stacked dielectric layers and internal electrode layers, as shown in Fig. 1. Conventional mass-production processes for MLCCs require a high-temperature sintering of about 1300°C to obtain a dense body, and those processes consume much energy. To preserve the earth's environment, some investigations were proposed to decrease sintering temperature, but the extent to which the temperature has been decreased is still not enough. Densification properties during the sintering of dielectrics and electrodes are quite different, because dielectrics are made of ceramics and electrodes are made of metal. The analysis of the fluctuation of the local homogeneity of small-chip MLCCs after sintering is very important to obtain a high reliability. However, the sintering process and resultant local homogeneity fluctuation of low temperature sintered MLCCs were not sufficiently analyzed yet.

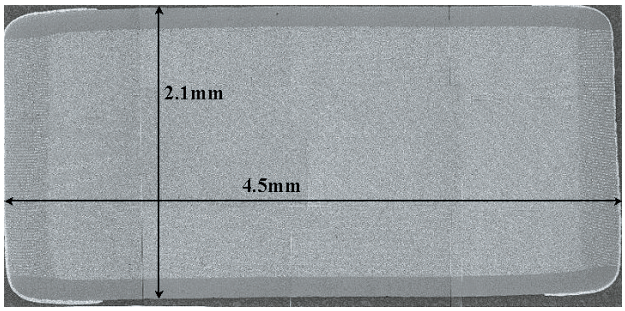

Fig. 1. Cross sectional view of mass production product of MLCC. Right and left terminals are terminal electrodes, and bright lines of inside are internal electrodes.

Absorption bands of some dielectric ceramics appear at the mid-infrared region [1,2], and some of their peaks change owing to changes in the homogeneity of ceramics. Therefore, it is possible to evaluate the homogeneity of ceramics by mid-infrared spectroscopy. A conventional infrared spectrometer cannot obtained a spectrum from a small sample with a satisfactory signal-to-noise ratio because of the low brilliance of a conventional light source. However, it is possible to obtain a satisfactory mid-infrared spectrum from small samples using a microfocus spectrometer combined with synchrotron radiation as a high brilliance light source at beamline **BL43IR**. The purpose of this study is to analyze the local homogeneity fluctuation of low temperature sintered MLCCs using BL43IR beamline of SPring-8 with a microfocus apparatus.

The MLCCs sample were prepared by the conventional green-sheet method. $BaTiO_3$ powder was mixed with 3.08 wt% Li-B-O glass powder to prepare the low sintering temperature material. A green sheet was prepared by the conventional coating method from the mixture of mixed powder, an organic binder, and a solvent. The thickness of the prepared green sheet was about 13 μm. The Ni internal electrode was printed at one of the surfaces of the green sheet. One hundred green sheets were stacked and pressed, and then cut to a certain size to obtain individual green chips. The obtained green chips were sintered in the temperature range from 650°C to 750°C at a weak reduced atmosphere. The microstructure of the polished cross section of sintered samples was observed with FE-SEM (Hitachi, S-4000). Mid-infrared (MIR) spectra were observed in the range from 400 to 6000 cm^{-1} with an infrared spectrometer (Bruker IFS120HRX)

The microstructure of the samples sintered at various temperatures was superimposed on Figs. 2-4. The number of pores decreased with increasing sintering temperature. However, no significant

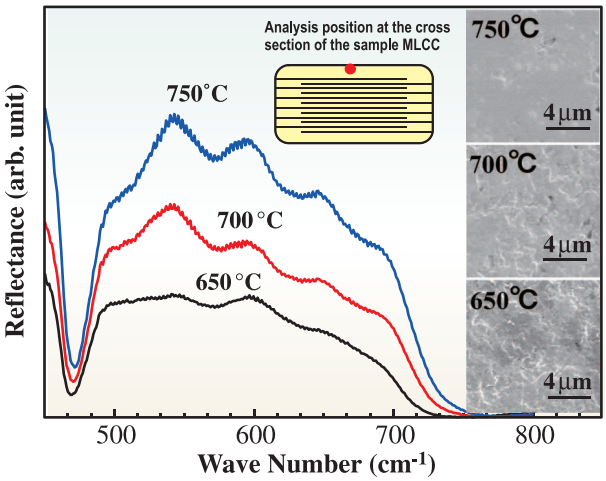

Fig. 2. MIR spectra and microstructures obtained from the center-region of the polished samples sintered at various temperatures. A superimposed picture showed an analysis position.

difference between the cover-region (Fig. 2) and center-region (Fig. 3) of the samples sintered at the same temperatures was observed in the SEM images. The Ti-O vibration peaks on IR spectra obtained from the center-region and cover-region of the samples sintered at various temperatures are shown in Fig. 2 and Fig. 3, respectively. The vibrational structure of peaks can be observed in the range from 450 to 750 cm^{-1} on the obtained spectra. The relative intensity of low-wave-number side of the peak was decreased with increasing sintering temperature. The physical meanings of these vibrational structures have not been sufficiently understood yet, but it was observed that the degree of the symmetry of the peak shape increased with increasing sintering temperature. Therefore, it is possible to evaluate the degree of sintering using the degree of symmetry of the Ti-O peak on IR spectra. The IR spectra obtained from center- and cover-regions of the 700°C sintered sample are shown in Fig. 4. The low degree of symmetry and low resolution of the vibrational structure in the spectrum obtained from the center-region shows a relatively low degree of sintering. In

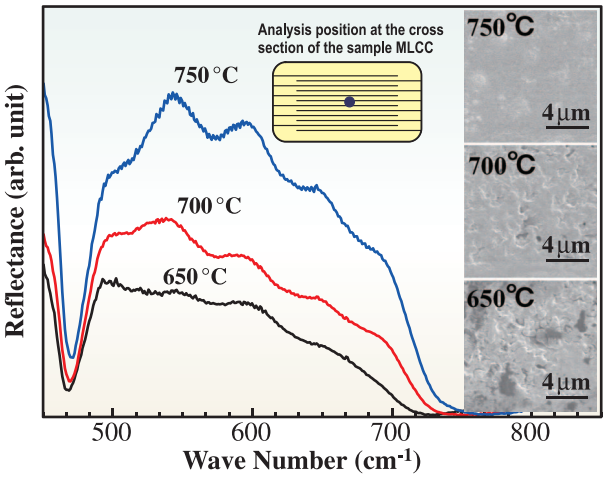

Fig. 3. MIR spectra and microstructures obtained from the cover-region of the polished samples sintered at various temperatures. A superimposed picture showed an analysis position.

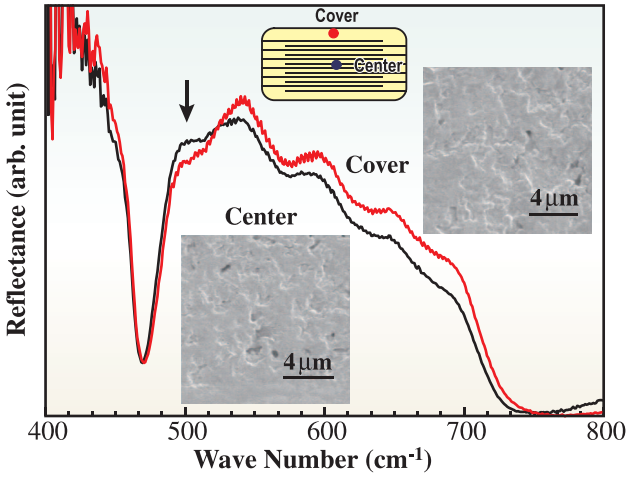

Fig. 4. Comparison between the spectra and microstructures obtained from center- and cover-region respectively of the sample sintered at 700°C. A superimposed picture showed an analysis position.

the sintering process, a grain growth process follows a densification process. The densification process contains the densification of powder compacts and homogenization of individual grains. The microstructure of compressed powder changes during the densification process, but barely changes during the homogenization of individual grains. Therefore, it may be understood by the lower symmetry of the Ti-O peak obtained from center-region than those of cover-region that the homogenization of center-region of the samples was delayed cover-region. The densification of the Ni internal electrode proceeds at a temperature lower than that of ceramics during sintering. And those dense internal electrodes retarded the densification of ceramics at the center-region since the dense electrodes could not shrink further.

Koichiro Tsuzuku[a,*], Tomoya Hagiwara[a], Shunsuke Takeoka[a] and Yuka Ikemoto[b]

[a] Tinker Group, R&D Lab., Taiyo Yuden Co., Ltd.
[b] SPring-8 / JASRI

*E-mail: ktuzuku@jty.yuden.co.jp

Nondestructive Three-dimensional Observation of Crystal Defects in Single Crystal CaF_2 by Step-scanning White X-ray Section Topography

When we use single-crystalline materials for optics, it is important to understand the relationship between crystal defects and optical properties. A single crystal of calcium fluoride (CaF_2) is an attractive material for ultraviolet (UV) optics because of its high transparency to ultraviolet light and optical isotropy. The CaF_2 crystal has been used for the lenses of a deep UV optical lithography system. Large single crystals of CaF_2 are grown by the Bridgman-Stockbarger method and several types of crystal defects have occurred under the crystal growth process. We have found that the crystal defects within the lenses could cause serious problems in the performance of the deep UV image formation due to the extremely small inhomogeneity of the optical properties. Therefore, a technique for visualizing crystal defects deep within a single crystal is important.

X-ray topography is a valuable technique for investigating the crystal defects nondestructively. An in-house X-ray topography system is useful for observing defects near the surface of a crystal, but it is not practical for the defects deep within a thick crystal due to X-ray extinction by absorption. Data concerning crystal defects as well as defect at the surface are very important because the inhomogeneity of optical properties such as refractive index or birefringence emerges as an integrated value along the optical axis.

There are several reports of X-ray topography using high-energy and high-brilliance synchrotron radiation. Ludwig [1] demonstrated the visualization of three-dimensional distribution images of crystal defects that were reconstructed from a series of images that were recorded by tomographic acquisition using the monochromated synchrotron radiation. This technique is effective in measuring a nearly perfect single crystal, but it is not useful to observe an imperfect crystal, which has subgrain structures. Since the Bragg conditions for monochromatic X-rays on subgrains are different from each other, only a subgrain can be observed for an exposure.

We have developed the technique of step-scanning white X-ray section topography for the measurement of the three-dimensional distribution of subgrains and other crystal defects within bulky single crystal CaF_2. Using white X-rays enables the measurement of not only a perfect single crystal but also an imperfect single crystal for an exposure. Figure 1 shows the setup of the step-scanning white X-ray section topography system at beamline **BL28B2**. The white X-rays from the light source were shaped as a sheet-like beam of size between 10 mm and 30 mm (horizontal) × 0.1 mm (vertical) in accordance with the size of samples by the slits.

The single crystals of CaF_2 were grown along the (1 1 1) orientation. The samples were cut into cylinders from the ingots. The sizes of the samples were between 30 mm and 60 mm in diameter and between 30 mm and 50 mm in thickness. The sample was set on the goniometer composed of several stages.

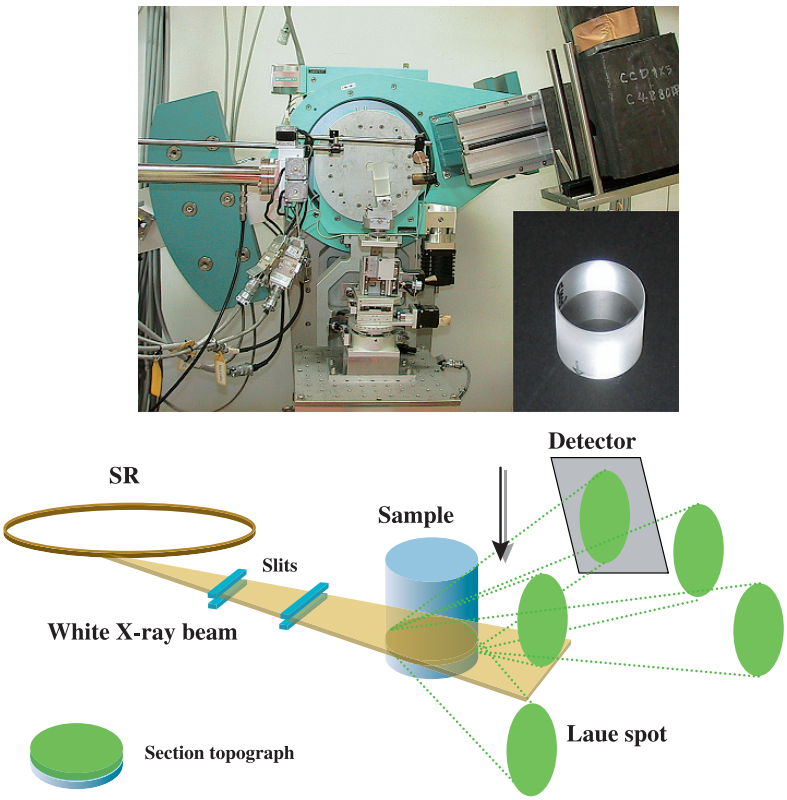

Fig. 1. Photographs of experimental setup and procedure of the step-scanning white beam X-ray section topography. The sample in the photograph was 30 mm in diameter and 30 mm in thickness.

Section topographs of the samples were recorded using a CMOS flat-panel detector or a CCD detector combined with a scintillator and a relay lens system. All cross-sections of the sample were recorded by repeating the exposure and translation of the sample along the horizontal and perpendicular directions to the top face of the sample. The exposure time of a section topograph was between 1 s and 15 s. Details of the experimental condition have been reported elsewhere [2].

Figure 2 shows an example of the section topographs corresponding to the cross section of the sample, which was 30 mm in diameter and 30 mm in thickness. It was clearly observed that the sample was composed of many subgrains. The subgrain boundaries were recognized as overlapping or separation of the images of the subgrains. Variations in the intensity of the subgrain images corresponded to crystal defects such as dislocations.

Figure 3 shows three-dimensional images reconstructed from the section topographs. Figure 3(a) is expressed by three horizontal planes, two vertical planes and a surface model of a subgrain shown as a yellow surface of the sample which was 30 mm in diameter and 30 mm in thickness. Figure 3(b) was expressed as a part of the sample which was 60 mm in diameter and 50 mm in thickness. It was easy to recognize the network structure of subgrains within the crystal. Furthermore, the width of the grain boundaries shown in Fig. 3(a) was thicker than that shown in Fig. 3(b). This indicates that the tilt angle between subgrains in Fig. 3(a) is larger than that in Fig. 3(b).

We have successfully visualized the three-dimensional distribution of the crystal defects of single crystal CaF_2. The step-scanning white X-ray section topography is a very useful and simple technique for analyzing the three-dimensional distribution of crystal defects within large single crystals.

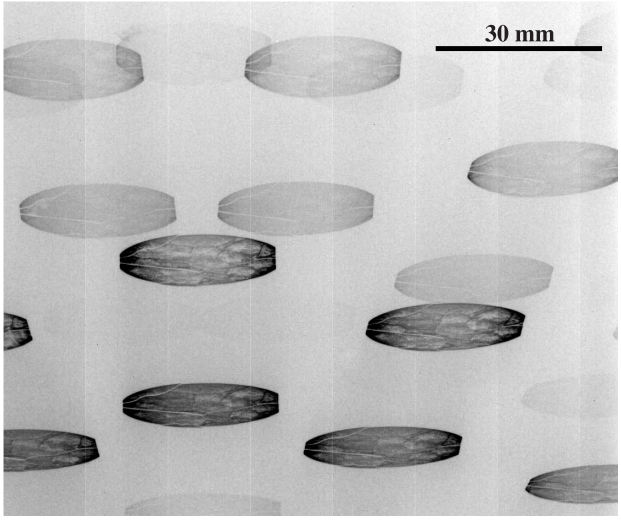

Fig. 2. Typical section topographs of the sample.

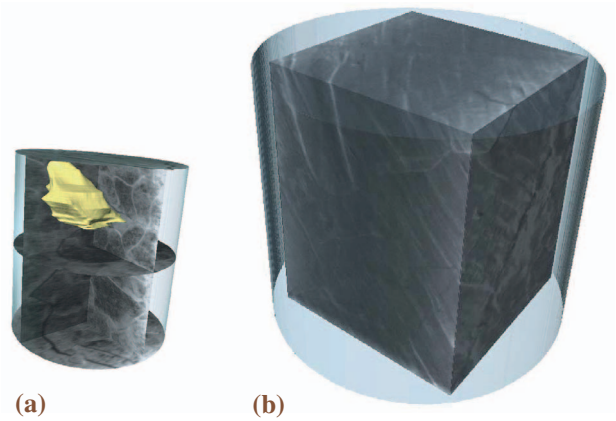

Fig. 3. Three-dimensional reconstructed image from section topographs. **(a)** 30 mm diameter and 30 mm thickness. **(b)** 60 mm diameter and 50 mm thickness.

Taihei Mukaide

Canon Research Center, CANON Inc.

E-mail: mukaide.taihei@canon.co.jp

References

[1] W. Ludwig *et al.*: J. Appl. Cryst. **34** (2001) 602.
[2] *T. Mukaide, K. Kajiwara, T. Noma and K. Takada: J. Synchrotron Rad.* ***13*** *(2006) 484.*

Structural Study on One-dimensionally Aligned Polyfluorene Thin Films for Application of Polarized Organic Light-emitting Diode

Organic light-emitting diodes (OLEDs) are expected to become the next generation of light sources because of its many advantages such as high efficiency, low power consumption and flexibility. In particular, the possibilities in the field of displays are enormous, and so many researchers are progressively developing OLED displays to generate multicolored light with high efficiency. In addition, the processes for depositing organic materials can lead to the production of large light-emitting areas on flexible substrates at very low cost.

Considerable progress in the field of polymer light-emitting diodes (PLEDs), a kind of OLED in which the materials are composed of emissive polymers, has been made since the report of Burroughes *et al.* [1]. Conventional PLEDs, which are composed of the emissive layer and carrier transport layers with a thickness of about 100 nm sandwiched between the anodes of transparent indium tin oxide (ITO) and the cathodes of metals, are emitting non-polarized light. Figure 1 shows the device configuration of polarized PLEDs. As shown in Fig. 1, PLEDs consisting of an aligned emissive polymer are expected to exhibit polarized emission, because the intrinsic characteristic of conjugated polymers originates from the electrons delocalized along the polymer backbone (main chain). The development of polarized PLEDs is important for their application to liquid crystal display (LCD) backlights: if a polarized light source is employed as a backlight, the LCDs power efficiency could be markedly improved since the light loss through a polarizer placed in the LCD is approximately zero. Namely, polarized PLEDs are the most advanced devices for next-generation display systems.

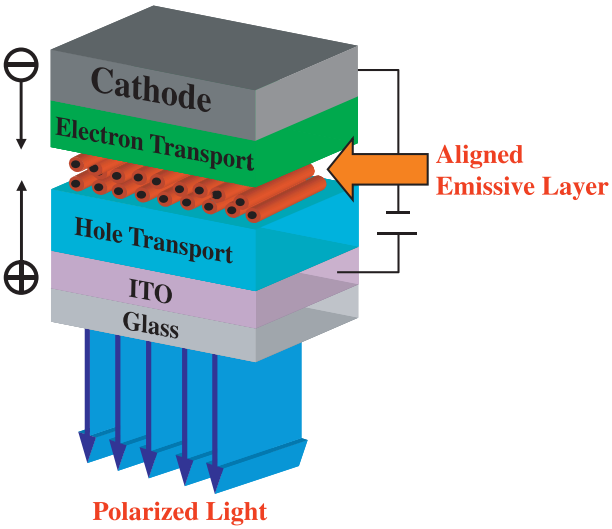

Fig. 1. Device configuration of polarized PLEDs.

According to recent reports [2], polarized PLEDs composed of aligned liquid crystal (LC) emissive polymers on a rubbed alignment layer have been generally developed. One very attractive class of such LC polymers is polyfluorene (PF) because of the following reasons. PF has emerged as an attractive material for PLEDs and can be well aligned on a rubbed polyimide layer via the thermotropic LC state. Once suitable LC polymers have been identified, the main issue to be addressed is the choice of alignment layer. Usually, the alignment layer is positioned between an electrode and an active emitting layer, which causes some problems in terms of device performance. In addition, standard polyimide is a good electrical insulator, leading to poor device performance when it is used for the alignment layer.

Here, we introduce our original technique of "friction transfer." It offers a way for the direct preparation of an aligned polymer thin film without an underlying alignment layer, thus avoiding the disadvantages of the alignment technique described above. When some kind of polymers are squeezed and drawn against a clean surface of metal or glass, the highly aligned polymer film remains on the surface [3]. We have already applied the friction transfer technique to the preparation of aligned thin films of various conjugated polymers. Recently, we have succeeded in preparing highly aligned thin films of thermotropic LC polymer, poly(9,9-dioctylfluorene) (PFO) by this technique (Fig. 2), and found that subsequent thermal treatments of the friction-transferred PFO films are specifically effective for the improvement of molecular alignments and surface morphology [4].

In this study, we have examined the fine structure of the film plane of a friction-transferred PFO thin film by grazing incidence X-ray diffraction (GIXD), beamline **BL13XU**. It clarified the fine structure of aligned polymer thin films, thus leading to improved device performance.

As shown in Fig. 3, the orthogonal (ϕ = 0°) diffraction pattern of the thin film shows the series of long-period peaks, corresponding to 0k0 (k = 2, 4, 6, 8, 10). These peaks are associated with the crystallographic direction along the alkyl side chains. On the other hand, the parallel (ϕ = 90°) diffraction

pattern shows no 0*k*0 peaks. This indicates that the *b*-axis is orthogonal to the friction direction. Instead of 0*k*0 reflections, the series of the 00*l* reflection appeared. The *c*-axis of PFO is parallel to the friction direction. Moreover, we observed that changes in the scattering intensity at the fixed scattering angle 2θ indicate the distribution of arrangement of the reflecting plane to the friction direction. The half-width of the distribution of the PFO parallel 008 reflection was estimated to be 2.94°. This result shows that the polymer chains are well-ordered in the friction direction. To quantitatively estimate a molecular orientation of polymers, we introduce an aligned fraction factor f_{20} for uniaxial oriented polymer thin films. The aligned fraction calculated from the X-ray diffraction data is described below:

$$f_{20} = (3 \langle \cos^2\theta \rangle - 1) / 2$$

Here, θ indicates an angle between a polymer chain and *c*-axis of unit cell. The fraction of the *c*-axis in thin films is 0.999, which is extremely large (a fraction at perfect alignment is 1.0 by definition). Almost perfect alignments are accomplished in the PFO thin film.

In conclusion, we have succeeded in preparing almost perfect alignments of polymer in PFO thin films by a friction transfer combined with thermal treatment. Already, we have reported the performance of polarized PLEDs prepared by friction transfer [5]. Aiming to develop high performance and stable polarized PLEDs, we are going to confirm the relationship between the aligned structure and the device performances.

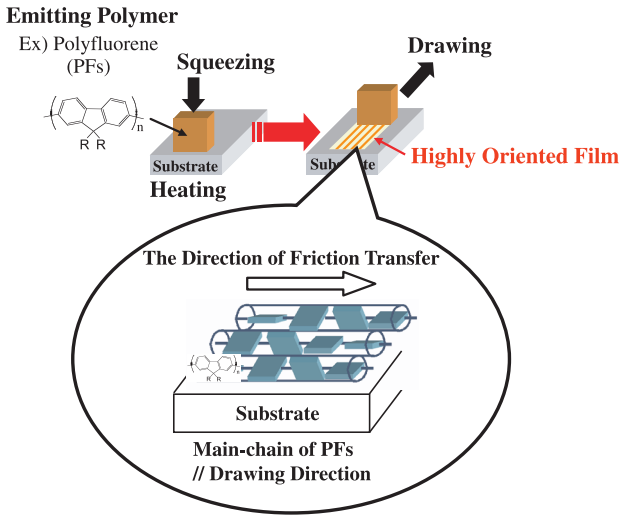

Fig. 2. Schematic illustrations of the friction transfer technique and the aligned polymer structure in PFO thin films.

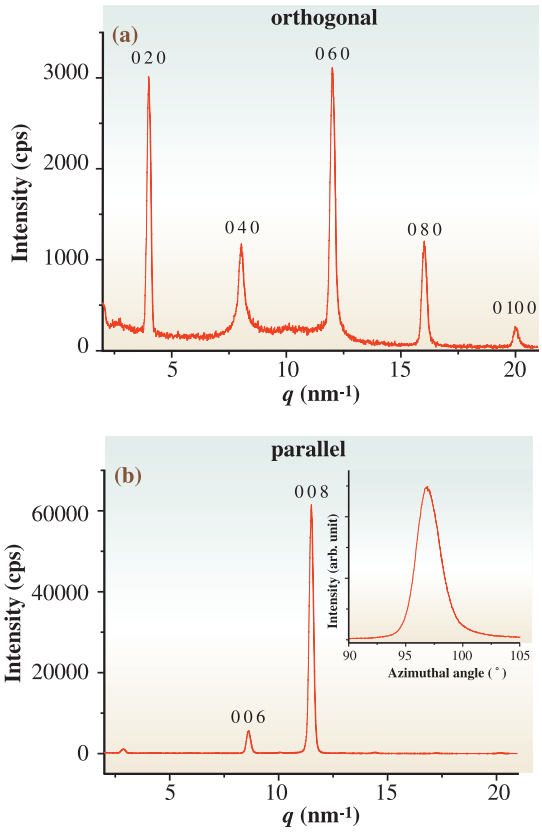

Fig. 3. In-plane GIXD profiles of PFO thin films with scattering vectors **(a)** orthogonal to the friction direction and **(b)** parallel. The inset shows the rocking scan of 008.

Yuji Yoshida[a,*], Masahiro Misaki[a] and Katsuya Fujisawa[b]

[a] Photonics Research Institute, National Institute of Advanced Industrial Science and Technology (AIST)
[b] Kuraray Co., Ltd.

*E-mail: yuji.yoshida@aist.go.jp

References

[1] J. H. Burroughes *et al.*: Nature **347** (1990) 539.
[2] S.W. Culligan *et al.*: Adv. Mater. **15** (2003) 1176.
[3] J.C. Wittmann and P. Smith: Nature **352** (1991) 414.
[4] M. Misaki *et al.*: Macromolecules **37** (2004) 6926.
[5] *M. Misaki, Y. Ueda, S. Nagamatsu, M. Chikamatsu, Y. Yoshida, N. Tanigaki and K. Yase: Appl. Phys. Lett.* ***87*** *(2005) 243503.*

Deformation Behavior of Isotactic Polypropylene Spherulite during Hot Drawing Investigated by Simultaneous Microbeam SAXS-WAXS and POM Measurement

The clarification of the deformation mechanism of hierarchical structures of crystalline polymers during drawing, particularly the identification of the sequence of stress focusing in the polymer structure, is one of the most important issues in the polymer processing field, because it can greatly help in the design of materials with improved mechanical properties. However, the hierarchical structure of crystalline polymers generally has a spatial inhomogeneity and they are non-uniformly deformed under force fields such as drawing [1]. Furthermore, a plate-like crystalline structure, which is called the lamella structure, inside of a polymer spherulite sometimes has very complex morphologies such as twisting [2] and cross-hatched structures [3].

To obtain detailed information on the deformation behavior of the hierarchical structure in such complex polymer systems, a combinatorial approach of microbeam small- and wide-angle X-ray scattering (μSAXS-WAXS) simultaneous measurement is used, in which a unique method provides us the structural information in a wide-scale hierarchy at a local region. We applied μSAXS-WAXS to the observation of the deformation behavior of an isotactic polypropylene (iPP) spherulite during hot drawing [4].

iPP is one of the most intensively investigated crystalline polymers because of its wide applications to commodities such as automobile parts, packaging film, and plastic containers. Film products of iPP are usually processed through hot drawing. Moreover, iPP forms a cross-hatched structure in a spherulite, which is formed by an epitaxial growth of the lamella structure called the daughter lamella from a face of an already grown lamella called the parent lamella. In this study, we focused on the observation of the deformation behavior of cross-hatched structures in an iPP spherulite during hot drawing.

An iPP sample was prepared using polymerizing propene with a polymerization catalyst. A synthesized iPP sample with a melting temperature of 160°C was melted at 230°C and then isothermally crystallized at 130°C for several hours, and we finally obtained very large iPP spherulites of 300 μm diameter.

μSAXS-WAXS was performed at beamline **BL40XU**, which is a high-flux beamline equipped with a helical undulator upstream of the beamline. We generated a microbeam of about 5 μm diameter by merely inserting a micro-pinhole of 2 μm diameter combined with a large guard pinhole of 100 μm diameter with an interval of about 5 cm between them upstream of the sample position. As for the detector, we used a CCD detector coupled with an image intensifier for SAXS data acquisition and a flatpanel detector for WAXS data. The use of a two-dimensional detector for both SAXS and WAXS is essential for microbeam experiments because a crystal structure at a local area of spherulite has a high anisotropy. To track the deformation of a targeted spherulite during hot drawing, we designed a special uni-axial stretching machine that functions in sample position adjustment through microscopy observation, which is independent of the uni-axial stretching process itself.

In Fig. 1, sets of polarized optical microscopy (POM)-μSAXS-WAXS data simultaneously acquired before and after hot drawing are shown. We irradiated the red dot region of a microphotograph with an X-ray microbeam and obtained μSAXS-WAXS data. μSAXS data before drawing clearly showed a four-leaf clover pattern originating from a cross-hatched structure, while only two disordered spots were observed for the μSAXS data after drawing. There are large differences in μWAXS data between before and after drawing.

From μSAXS data during hot drawing, we calculated the positions of the peak and its FWHM for both the parent and daughter lamellae, and obtained

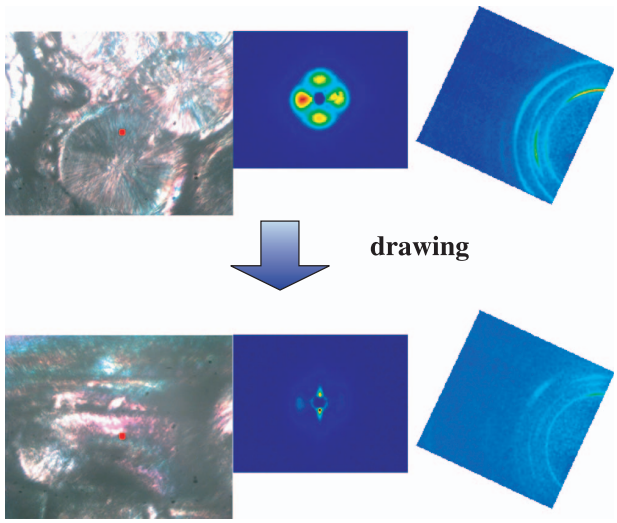

Fig. 1. POM, μSAXS and μWAXS patterns simultaneously acquired before and after hot drawing of polypropylene spherulite.

information on the relationship between the changes in the long period and the disordering of the lamellar long period. From μWAXS data, we calculated FWHM of WAXS peak and the azimuthal distribution of each diffraction peak, and estimated ordered crystal size and crystal orientation.

On the basis of these analyses, we clearly identified the sequence of stress focusing inside the cross-hatched structure during hot drawing and constructed its detailed deformation model as shown in Fig. 2. Initially, the long period simply increases, while no disordering of the stacking structure occurs, which indicates that the stretching of the amorphous region between lamellar crystals occurs before the disordering of the stacking structure (see Fig. 2(b)). Next, the disordering of the lamellar stacking structure and the decrease in the ordered crystal size of the parent lamella start, while no decrease in the crystal size of the daughter lamella occurs (Fig. 2(c) and 2(b')). Interestingly, the ordered crystal size of the daughter lamella is initially smaller than that of the parent lamella and is unchanged during the drawing until a drastic rearrangement starts. Finally, the rearrangement of crystal orientation drastically occurs through tilting, sliding and rotation processes (see Fig. 2(c) and 2(c')).

As shown above, μSAXS-WAXS is a very powerful probe for identifying the sequence of stress focusing during hot drawing and is greatly useful for various polymer systems with interesting morphologies such as the twisting structure and the interpenetrating spherulite structure.

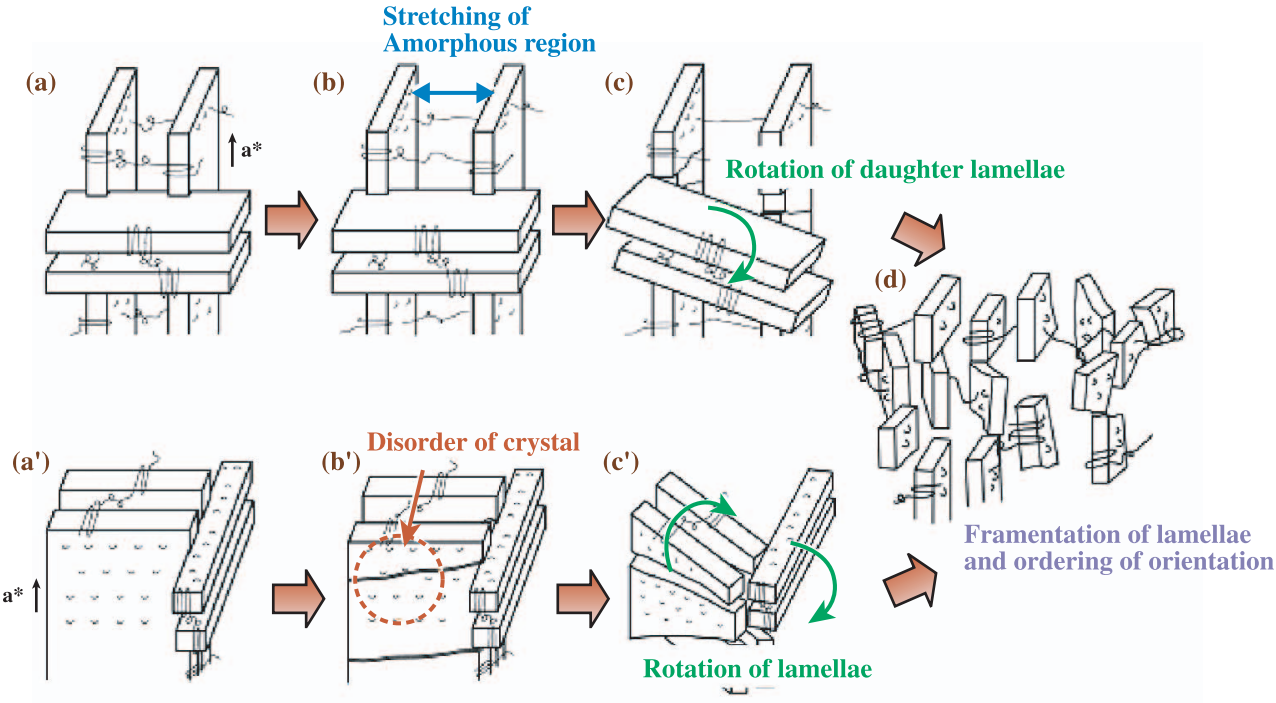

Fig. 2. Detailed deformation model of lamella structure constructed from μSAXS-WAXS results.

Yoshinobu Nozue[a,*], Yuya Shinohara[b] and Yoshiyuki Amemiya[b]

[a] Sumitomo Chemical Co., Ltd., Petrochemicals Research Laboratory
[b] Graduate School of Frontier Sciences, The University of Tokyo

*E-mail: nozue@sc.sumitomo-chem.co.jp

References

[1] K. Shimamura *et al.*: Nihon Rheology Gakkai-shi **7** (1979) 42 (in Japanese).
[2] Y. Fujiwara: J. Appl. Polym. Sci. **4** (1960) 10.
[3] H.D. Keith and F.J. Padden: J. Appl. Phys. **44** (1973) 1217.
[4] *Y. Nozue, Y. Shinohara, Y. Ogawa, T. Sakurai, H. Hori, T. Kasahara, N. Yamaguchi, N. Yagi, Y. Amemiya: Macromolecules* ***40*** *(2007) 2036.*

Application of Wide Angle X-ray Diffraction to Hair Conditioners

Consumer products from diapers to laundry detergents to cosmetics to toothpastes are all indispensable for maintaining our health and comfort in daily life. These commodities are consistently expected by consumers to be better than previous products, and therefore relentlessly developed by manufactures towards superior performance. A high-tech trend of consumer products requires top-notch methodologies to analyze and evaluate product performance, structure, and composition. The needs for unique and powerful analytical and evaluation tools lead us to the application of synchrotron radiation-sourced techniques in order to utilize excellent features of SR's, e.g., super brilliance and directionality. These features are favorable for microscopic understanding and elucidation of product efficacies and performance, specifically, of beauty care products based on the interaction of ingredients with the skin and hair at the molecular level. This article reports two examples of the application of an SR-sourced X-ray analytical technique to the development of hair conditioners.

X-ray diffraction (XRD) analysis of single hair fibers was carried out to evaluate hair conditioning products, which were supposed to affect the internal structure and mechanical response of hair fibers. The human hair shaft is composed of keratin protein, which has the basic structure of three α-helices wrapped around one another to form a protofibril, then the assemblance of eleven protofibrils to form a microfibril. Bundles of these microfibrils pass through and around hair cells. XRD data were collected at Hutch A of beamline **BL24XU** (Hyogo ID), using a monochromatic (15 keV, 0.08266 nm) and collimated incident beam (80 × 80 μm^2). An IP Laue camera (camera length at 500 mm) was used with a sample holder, in which a single hair fiber is oriented perpendicular to the incident beam. SR-XRD of single hair fibers shows diffraction patterns of hard α-keratin, which have two major characteristic features in the wide angle X-ray diffraction (WAXD) region [1]: (1) a broad equatorial spot centered at 0.97 nm, corresponding to the mean distance, or spacing, between α-helical axes, and (2) a fine meridian arc at 0.517 nm, which is related to the projection of the α-helix pitch along the coiled-coil axis, above a broader arc around 0.5 nm of less ordered coiled coils.

First, changes in the XRD pattern of hair fibers after a chemical treatment indicate the microscopic effect of the treatment on the hair structure. We observed changes in the WAXD pattern of identical single fibers of Asian virgin hair over sequential bleaching and conditioning on site to eliminate variations among fibers. We found that the degree of crystallinity across the hair fiber axis could be an illustrative parameter to describe the mechanism underlying the repair of damaged hair using hair conditioning products. Three key findings follow: (1) The degree of crystallinity across the hair axis was increased by 28±6% at 95% confidence level by the

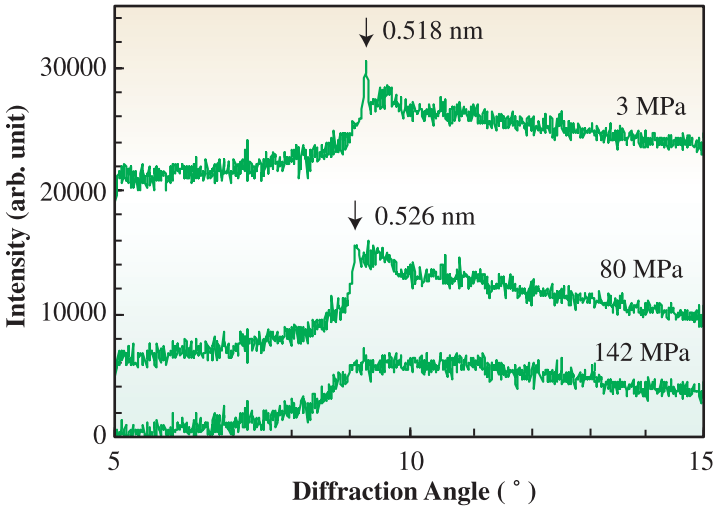

Fig. 1. Shift of diffraction peak of helical pitch after stress application. Sample: human hair treated with dilute hydrochloric acid at pH = 4.5.

bleaching condition we applied in the series of XRD studies. (2) Treatment with an aqueous solution of key ingredients of a candidate conditioning formulation (T-1, hereafter) demonstrated a consistent decrease in diffraction intensity after the treatment. The intensity change *versus* bleaching was calculated at 13±5% at 95% confidence level. (3) The ratio of diffraction intensity changes over treatment *versus* bleaching, i.e., $(I_B\text{-}I_T)/(I_B\text{-}I_V)$, where I_V, I_B, and I_T are intensities of the "spacing" diffraction of virgin, bleached, and treated hair fibers, respectively, was chosen as a measure of the "recovery" of crystallinity, and was defined as "recovery rate" in this study. Thus, we concluded that the T-1 solution recovered the crystallinity, which was increased by the bleaching, at 68±43% back to the virgin state at 95% confidence level.

Second, the XRD pattern of human hair under mechanical stress provides us with information on the microscopic deformation of the constituent keratin protein. The pitch elongation of α-keratin contributes 50% of the macroscopic strain [2]. Bundles of healthy hair fibers of an Asian female were damaged by a standard damaging treatment, shampooed, and then treated with a conditioning formulation (T-2, hereafter), while a control sample was prepared by treating with water after the shampooing. Mechanical stress was applied by hanging weights down on a sample. The stretching speed of α-keratin was measured at about 1%/h. The helical pitch of the α-keratin molecule for each stress was determined from the diffraction pattern (Fig. 1). Thus, a stress-strain, or crystal deformation, curve of the α-keratin pitch of the hair sample was obtained, as shown in Fig. 2, in which the stress-crystal deformation data points were collected from three hair fibers taken from an identical hair bundle. The longitudinal crystal modulus of elasticity, or spring constant, of α-keratin in the hair fibers was calculated as a slope in the Hookean region of the stress-crystal deformation curve. A duplicate measurement confirmed that the crystal modulus of elasticity of α-keratin in hair fibers treated with the T-2 formulation was 5.1 GPa *versus* 6.5 GPa of the control. The spring constants demonstrated that the T-2 formulation softened the damaged hair fibers.

We could develop and launch successfully the following two hair care products on the basis of the above-mentioned two research outcomes, respectively: a conditioner with hair breakage defense efficacy launched in September 2004 (the former), and a conditioner for unruly or naturally wavy hair launched in April 2007 (the latter).

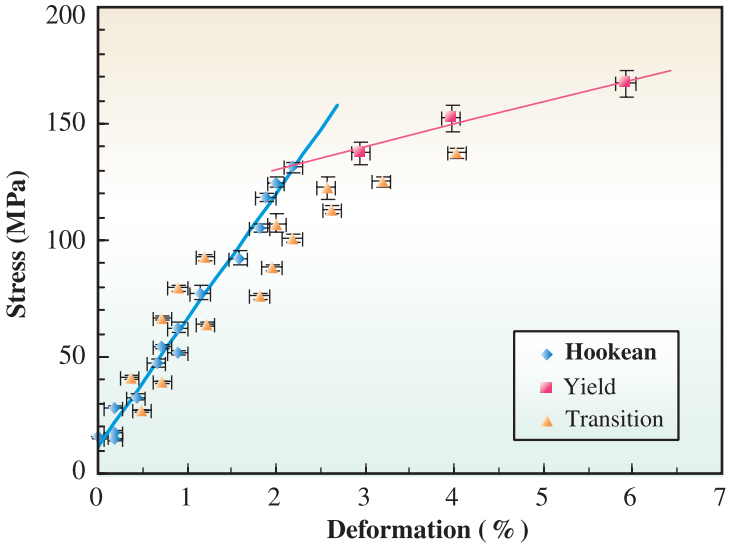

Fig. 2. Stress-crystal deformation curve of α-keratin in hair fibers. Sample: human hair damaged, shampooed, then conditioned with T-2 formulation.

Norimichi Sano

Analytical, Research & Development,
Procter & Gamble Japan K.K.

E-mail: sano.n.2@pg.com

References

[1] F. Briki *et al.*: Cellular and Molecular Biology **46** (2000) 1005.
[2] L. Kreplak *et al.*: Biopolymer **58** (2001) 526.

Three-dimensional Imaging of Fatigue Cracks by Microtomography with Refractive Contrast Effect

Fatigue is a major cause of failure in structural components in many industrial fields. To suppress the undesirable failure and prolong the service life of products, the exploration of durable materials and process technologies is carried out, together with the development of testing procedures. X-ray computed tomography (CT) developed for medical diagnosis currently plays a key role in the nondestructive evaluation of materials. It utilizes X-ray attenuation passing through materials and offers three-dimensional (3D) information on the internal structure. Synchrotron radiation can feature another characteristic of the interaction between X-ray and materials, i.e., phase shift, as a sensitive index. It is well known that the effect of the phase shift appears as a refractive contrast on projection images, which remarkably enhances the edge of an object by setting a detector apart from the object.

The purpose of this study is to demonstrate the applicability of X-ray CT with the refractive contrast to the imaging of minute fatigue cracks in macroscopic engineering materials. Although the cracks are tiny in the initial stage and difficult to image using the conventional X-ray CT or fluoroscopy, 3D images, however, are successfully reconstructed by the micro-CT (μCT) technique with highly parallelized brilliant X-ray of SPring-8. In addition to this purpose, the effect of laser peening, an emerging surface processing technology, which is to retard fatigue crack growth, was examined by μCT [1].

Fatigue test samples were prepared from a cast aluminum alloy, JIS AC4CH [2]. A small drill hole of

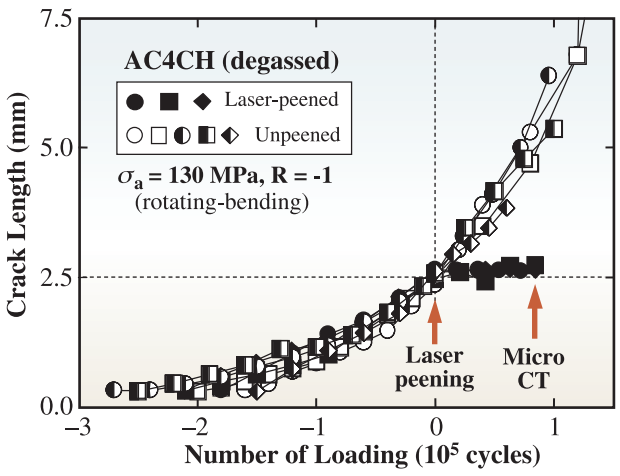

Fig. 1. Fatigue crack growth behavior.

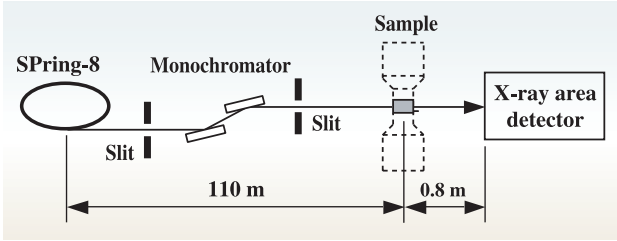

Fig. 2. Experimental setup of μCT imaging.

0.3 mm diameter was made at the center of each sample to initiate a fatigue crack from the drill hole. A precrack with a length of 2.5 mm was introduced on the surface of every sample by rotating-bending fatigue loading. Laser peening was applied to some of the precracked samples to impart compressive residual stress on the surface [1]. All samples were then further subjected to fatigue loading of 1×10^5 cycles. Figure 1 shows the propagation behavior of the surface cracks on the unpeened reference and laser-peened samples. Each curve was shifted in a manner where the number of fatigue cycles at the crack length of 2.5 mm became the origin of the horizontal axis. Here, the crack length was measured on the surface with an optical microscope. The cracks rapidly propagated on the unpeened samples. In contrast, on the laser-peened samples, the cracks remained unpropagated during the additional 10^5 cycles.

Imaging experiments with refractive contrast effect were performed at beamline **BL19B2**. The setup is schematically shown in Fig. 2 [1]. The X-ray energy was adjusted to 28 keV with a Si double-crystal monochromator. The distance between a bending magnet (X-ray source) and the sample was about 110 m. The area detector (cooled CCD camera) was set 0.8 m behind the sample to obtain a refractive contract effect, after the preliminary experiments in which the detector position was varied. Projection data of 1024 × 1024 was recorded every 0.5° from 0° to 180°. The effective pixel size of the detector was about 6 μm, considering the optical magnification of a relay lens after a converter. Slice images were reconstructed by a standard algorithm of filtered-back projection.

Reconstructed slice images at the elevation of the drill holes are shown in Fig. 3. The drill hole is distorted around the surface of the laser-peened sample, which suggests that a fairly large plastic deformation was induced on the surface by laser

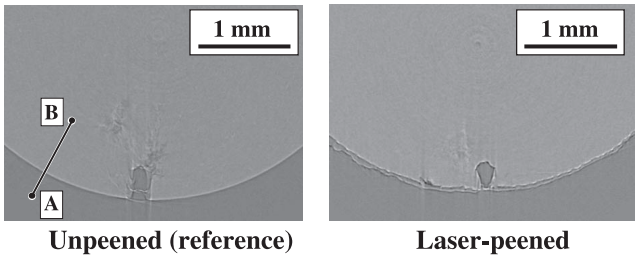

Fig. 3. Reconstructed slice images.

peening. The contrast in the images probably due to crack opening was observed near the drill hole inside the samples. The borders between the objects and surrounding air are enhanced with a pair of fine stripes in black and white. The attenuation coefficient along the line AB in the reference sample is shown in Fig. 4. Edge enhancement by refractive contrast is evident at the border of the object in the reconstructed images.

Three-dimensional images of fatigue cracks were made by extracting the crack image in each slice and then stacking them sequentially. Figure 5 shows the crack images in the unpeened reference and the laser-peened samples [1]. The shadows depicted in white might correspond to the opening of the fatigue cracks. The upper images are those viewed from the direction of the sample axis, while the lower images are those viewed from the direction perpendicular to the axis. The initial drill holes can be identified at the center of the shadows. These images well agree with the surface observation by optical microscopy and suggest that the crack growth is impeded in the case of the laser-peened sample not only on the surface direction but also toward the inside, which could not be realized without the highly parallelized brilliant

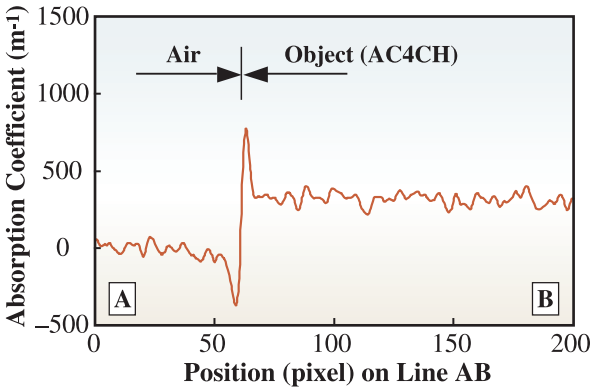

Fig. 4. Attenuation coefficient along line AB in Fig. 3.

X-ray of SPring-8. Further evaluation should be performed, taking into account the refractive contrast effect on the reconstructed images quantitatively.

The edge enhancement of the objects due to refractive contrast was observed in the images reconstructed by X-ray μCT with the highly collimated brilliant X-ray of SPring-8, which enabled us to visualize fatigue cracks nondestructively in an engineering material, AC4CH cast aluminum alloy. The effect of laser peening, which is to retard the propagation of precracks toward the inside as well as on the surface direction, was confirmed by μCT imaging. The results agree well with the precise observation on the surface using an optical microscope. By using the μCT technique in SPring-8, the nondestructive observation of crack growth is feasible in parallel with the measurement of residual stress redistribution. This provides indispensable information for optimizing residual stress distribution and process parameters, considering actual loading conditions.

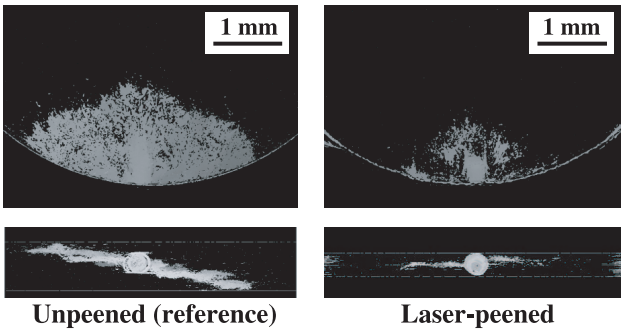

Fig. 5. Three-dimensional images of fatigue cracks.

Yuji Sano[a,*] and Kiyotaka Masaki[b,†]

[a] Toshiba Corporation
[b] The University of Elecro-communications

*E-mail: yuji.sano@toshiba.co.jp

† Present address: Okinawa National College of Technology

References

[1] *Y. Sano, N. Mukai, M. Yoda, T. Uehara, I. Chida and M. Obata: SPIE* ***6343*** *(2006) 634324.*
[2] K. Masaki *et al.*: to be publishd in Mater. Sci. Eng. A.

Where do Crystals Start to Grow and How is the Microstructure Evolved? — Solidification of Zn-Al Alloys for Improving Zn-coated Steel Sheets —

Steel sheets coated with Zn-based alloys such as Zn-Al and Zn-Al-Mg, have been widely used for various applications because of their excellent corrosion resistance. In the hot-dip coating process, a steel sheet is dipped in a molten Zn bath for certain duration and is then pulled from the bath. The molten layer on the steel sheet solidifies, producing the coating layer. The hot-dip process for Zn coating is a type of solidification process.

Uniformity of the solidified structure in the coating layer is an important issue in improving the quality of products. Despite this importance from the industrial viewpoint, the solidification phenomenon in a molten Zn layer is still not well understood. It is valuable to clarify how the microstructure of Zn-Al alloys is evolved during solidification.

SPring-8, a third generation synchrotron radiation facility, enables us to use monochromatized hard X-rays, which are advantageous for observing microstructure evolution *in situ*. Using synchrotron radiation, we performed time-resolved X-ray imaging to observe crystal growth and solidification of Sn-based and Al-based alloys [1-4]. In this project, an experimental technique was developed for observing the solidification of Zn-Al alloys *in situ*.

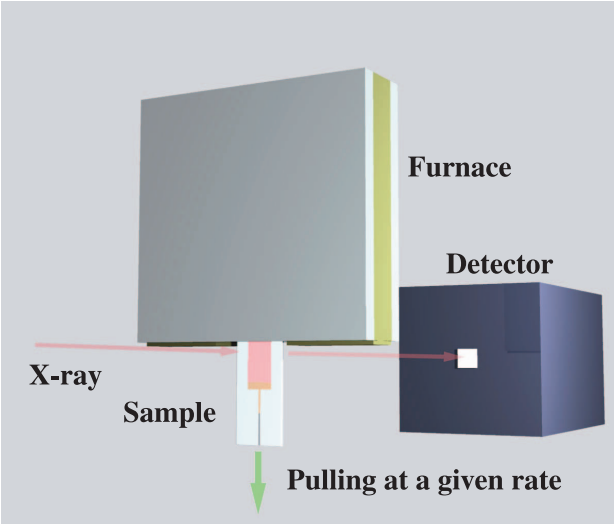

Fig. 1. Set-up of time-resolved X-ray imaging for solidification of metallic alloys. The alloy specimen was melted in the furnace and was pulled down at a given rate. Solidification occurred from the bottom to the top. The X-ray beam passing the specimen was detected using the image detector.

The experiments were performed at beamline **BL20B2**. The setup of the observation system is shown in Fig. 1. An image detector consisting of an X-ray direct-sensing pickup tube "SATICON" was used (pixel size: 4 or 10 μm/pixel, 1024 pixels × 1024 pixels; depth: 10-bit resolution; frame rate: 32 fps max). A sample-to-detector distance was 2.5-3.0 m, which gave rise to the phase contrast along with the absorption contrast. The specimen was melted in the furnace and was pulled down at a given rate.

Figure 2 shows the sequence of transmission images (1 fps and 10 μm/pixel) for the solidification of the Zn-10mass%Al alloy at a pulling rate of 10 μm/s. Dendrites of the primary Al-rich phase were clearly observed by the absorption contrast, and the eutectic interface of the Al-rich and the Zn-rich phases was also detected by the phase contrast (arrow a). Nucleation ahead of the growing Al-rich dendrite and fragmentation of the Al-rich dendrites (arrows b and c) occurred during the unidirectional solidification. The

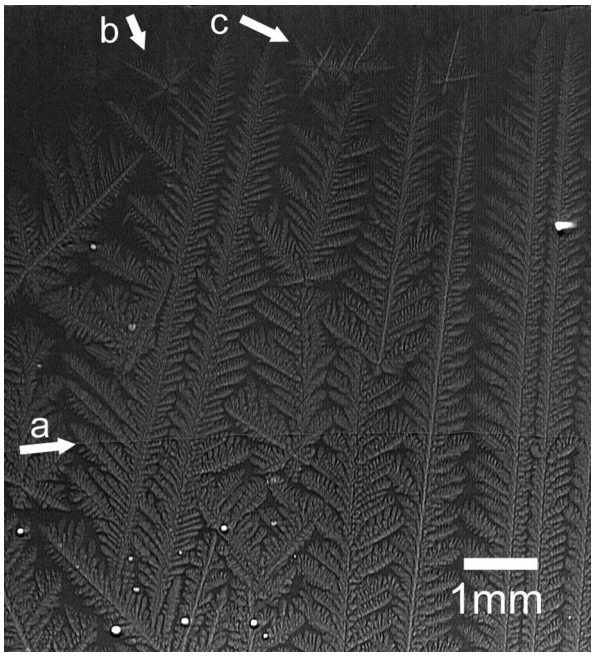

Fig. 2. Development of Al-rich dendrites (gray) in Zn-10mass%Al alloy. The pulling rate was 10 μm/s in the vertical direction. The interface of eutectic solidification (Al-rich and Zn-rich phases) was realized by the phase contrast **a**. Fragmentation (**b** and **c**) and nucleation ahead of the dendrite tips resulted in the formation of equiaxed grains.

observation showed that the grain size of the Al-rich phase was determined by the frequency of both nucleation and fragmentation.

Time-resolved imaging (16 fps and 4 μm/pixel) was also performed for the solidification of the Zn-10mass%Al alloy at a higher cooling rate of about 5 K/s. Figure 3(a) shows a transmission image obtained after the nucleation of the Al-rich phase in the Zn-Al alloy was realized. Development of the Al-rich dendrites is also shown in Fig. 3(b). As shown in Fig. 3(c), the crystals (envelope size, 10 - 20 μm; width of the branches, several μm) formed just after nucleation can be detected using the present setup.

The frequency of nucleation in the Zn-Al alloy on the steel sheet was higher that that in the Zn-Al alloy without the steel sheet. The increase in nucleation frequency suggests the presence of preferred nucleation sites on the steel sheet. The *in situ* observation at a high frame rate (32 fps max) and a high spatial resolution (10 μm) enables the determination of where the crystals start to grow and how the microstructure is evolved, and provides valuable information for improving the microstructure control of Zn-coated steel products.

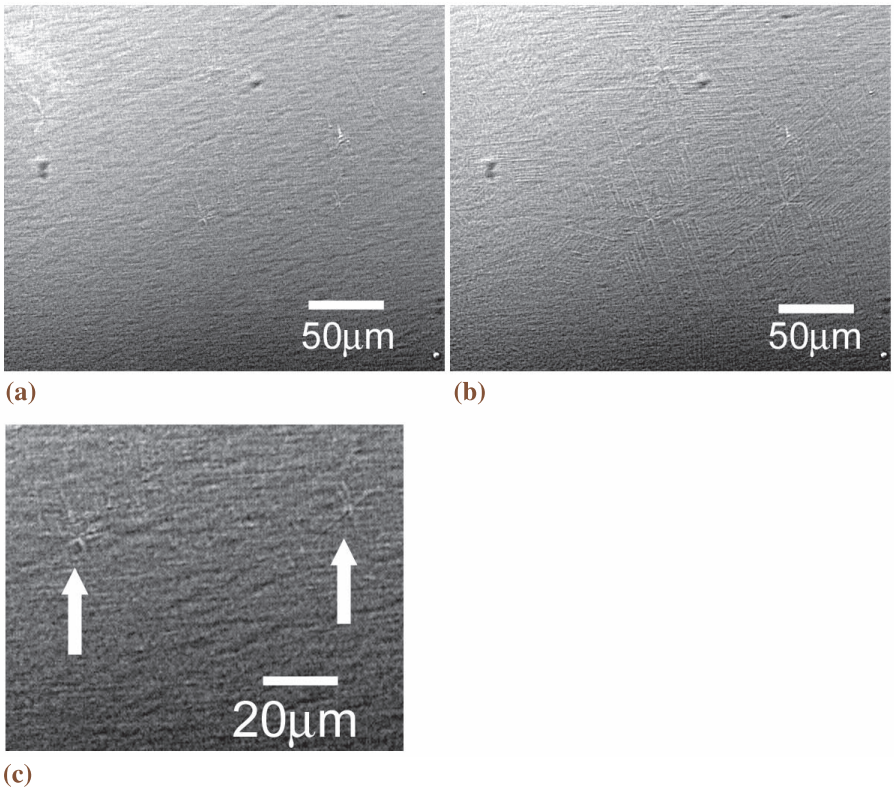

Fig. 3. Observation of solidification in Zn-10mass%Al alloy. **(a)** After nucleation of the Al-rich phase occurred, **(b)** development of Al-rich dendrites, and **(c)** close-up view of the crystals after the nucleation. The present setup enabled to observe where the crystals nucleated and how they grew during the cooling procedure. The in situ observation provides valuable information for controlling the microstructure of Zn-coated steel products.

Hideyuki Yasuda [a,*] and Hiroshi Harada [b]

[a] Department of Adaptive Machine Systems, Osaka University
[b] Hirohata R&D Laboratory, Nippon Steel Corporation

*E-mail: yasuda@ams.eng.osaka-u.ac.jp

References

[1] R.H. Mathiesen *et al.*: Phys. Rev. Lett. **83** (1999) 5062.
[2] R.H. Mathiesen *et al.*: Metall. Mater. Trans. B **33** (2002) 613.
[3] H. Yasuda *et al.*: J. Crystal Growth **262** (2004) 645.
[4] B. Li *et al.*: Phys. Rev. E **70** (2004) 062602.

Instrumentation & Methodology

Although nine years have passed since the inauguration of SPring-8 in 1997, the development of new instrumentations and methodology continues. One reason for this is the request for more user-friendly instrumentations by many new users in the synchrotron radiation. With more experience of users and facility members, more improved instrumentations to the source performance have been developed, or the adaptability of existing techniques has been enhanced. In addition, perpetual improvement of the source has increased its brilliance more than 1000 times since 1997. The progress with the light source naturally resulted in parallel progress with the users' instrumentations and new methodologies. The availability of much greater photons in a much smaller localized region in the sample facilitates photon-hungry measurements such as inelastic scattering with a small cross-section. With the development of ultra-fast X-ray detectors, time-resolved diffraction measurement with pico-second resolution became feasible and nuclear phenomena related to the electron excitation were clearly demonstrated. Now many users enjoy the heart of the third generation source, distinguished by its extremely high brilliance and very small source size, but some users require higher performance than the third generation source is capable of delivering. This demand will be a strong driving force for new generation light sources, such as X-ray Free Electron Lasers (XFELs).

Eight interesting articles are selected for the "Instrumentation & Methodology" chapter of this volume. Dr. Go Ueno and his coauthors present the mail-in system and beamline automation developed for protein structure analysis. This is an expanding field that many researchers who are not yet familiar with the synchrotron radiation business want to break into. Recently, it has become a common view that most protein structures can be solved once a single, high quality crystal is obtained. One question naturally raised is whether or not the powder diffraction technique is useful for protein crystallography. Dr. Toshihiko Oka partially addresses this question by using powder diffractometry to determine the structure of the purple membrane. The availability of much greater numbers of photons has expanded the capabilities of spectroscopy. Two new methodologies, having been difficult to realize because of the small signal level, are introduced: one is hard-X-ray excited photoelectrons as reported by Dr. Yasutaka Takata and Prof. Yosuke Kayanuma; the other is resonant inelastic X-rays as reported by Dr. Atsushi Higashiya and his coauthors. The increased number of photons has enabled research into ultrafast phenomena. Dr. Yoshihito Tanaka and Dr. Yujiro Hayashi report their studies of pico-second time-resolved diffraction on laser-induced lattice deformation in semiconductor crystals. Prof. Shunji Kishimoto reports very convincing Nuclear Excitation by Electron Transition (NEET) data as a result of the improvement of the detector system for NEET measurement. FY 2006 was a great year for novel undulator development using the low temperature technique, as reported by Dr. Takashi Tanaka. In conjunction with another milestone project in 2006, Dr. Makina Yabashi presents a single-shot characterization technology for X-ray pulses to be used for the XFEL.

We hope we will have excellent development in instrumentation and methodology in the following years as well.

Tetsuya Ishikawa

Mail-in Data Collection and Beamline Automation at SPring-8 Structural Biology Beamlines

The structural genomics projects progressing worldwide, including Protein 3000 project by MEXT of Japan, are aiming at accumulating the information on a significant number of three-dimensional protein structures and functions based on genetic sequencing analyses [1]. Such cyclopedic projects are supposed to drive the biological research to associate protein structures with their functions. Furthermore, those efforts are anticipated to originate new approaches to drug discovery based on genomics. In order to deal with a vast variety of protein crystals in the structural genomics project, development of a high-throughput beamline for protein crystallography was indispensable. RIKEN Structural Genomics Beamlines I & II (**BL26B1** & **BL26B2**) [2] have been constructed to address the requirement of rapid diffraction data collection for numbers of protein crystals. The demand of the more efficient use of the beam-time led to technical development of a beamline automation system.

The schematic diagram of device and control system of the RIKEN Structural Genomics Beamlines is shown in Fig. 1(a). The light source and optics adopted are the standard design for bending magnet beamlines at SPring-8 [3]. The beamline accommodates MAD (Multi-wavelength Anomalous Diffraction) experiments with heavy atoms typically used for protein structure determination. Equipments in the end station are designed for users to conduct the automatic operation without entering the experimental hutch. A sample auto-changer robot SPACE (SPring-8 Precise Automatic Cryo-sample Exchanger) [4] is installed to automate the sample handling procedure without human error. A goniometer head can be positioned by a remote translation stage for sample centering. Other devices are also mounted on the remote-controllable alignment stages, including two types of area detectors; a mosaic CCD (Charged Coupled Device) and a large IP (Imaging Plate), which are remotely switchable.

The control system of the beamline was developed based on the client and server architecture, on which each device is controlled by distributed server program. BSS (Beamline Scheduling Software) [5] is a graphical user interface (GUI) controlling entire beamline *via* the network. The BSS provides the whole utilities for users to operate the beamline, such as exchanging samples, collecting diffraction images, XAFS (X-ray Absorption Fine Structure) measurement, and so on. In particular, the most outstanding feature of the BSS is the scheduling function of successive data collections for multiple sample crystals, which makes the unattended beamline operation possible for a long term (Fig. 1(b)).

The SPACE handles the specially designed sample pin and tray, originally developed at SPring-8 (Fig. 2). The sample pin is equipped with screw threads to be attached to the goniometer, which ensures the high positional reproducibility (< 10μm) of protein crystals. Once the first centering is manually done at the beamline, the centering can be automatically reproduced on the second mounting, or later. This is the most outstanding feature of the SPACE, which makes the unattended beamline operation possible over a long period of time.

Samples and data management system covering laboratory and beamline, i.e. mail-in system, is supported by a networked database D-Cha (Database for Crystallography with Home-lab. Arrangement) (Fig. 3). The D-Cha manages the massive sample information by tray identification number, and provides the GUI to edit the experimental schedule of each tray *via* a web browser. Prior to experiments, users send sample trays to beamline with dry shipper *via* home delivery service. The individual crystal information and experimental schedule are uploaded to D-Cha from users laboratory. At the beamline, the experimental schedule is extracted from D-Cha, and registered to BSS. The SPACE installed at the

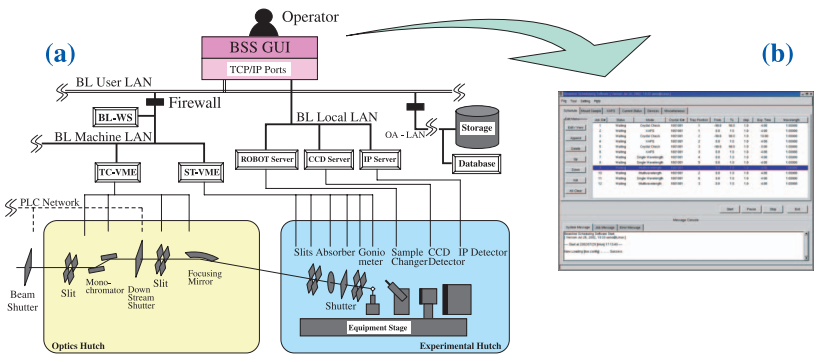

Fig. 1. **(a)** Schematic diagram of device and control system of RIKEN Structural Genomics Beamlines. **(b)** BSS main window. Schedule list of successive data collection is shown.

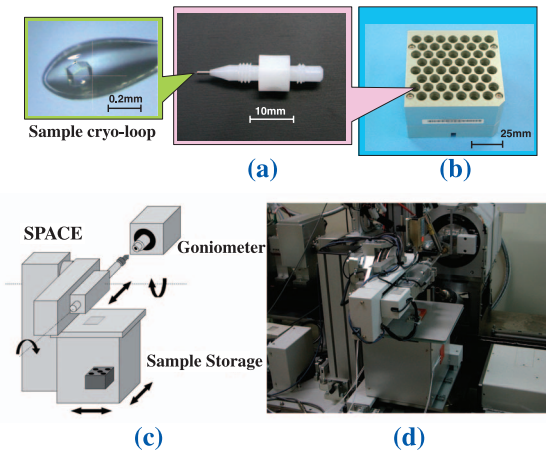

Fig. 2. **(a)** Sample pin. **(b)** Sample tray. A tray can store fifty-one samples at once. **(c)** Schematic view and **(d)** photograph of SPACE.

beamline sequentially changes the crystals according to the experimental schedule. The acquired data is uploaded to D-Cha, and the diffraction images can be browsed or downloaded by users *via* the Internet. Users need not to visit the beamline to obtain the diffraction data.

At the beamline, all crystals in the tray are successively mounted on the gonoimeter to collect the screening data, which is used to evaluate the crystal quality. Beamline operators assure the centering of each crystal at first. The diffraction data and the record of the goniometer translation are registered to D-Cha. Since the screening data for a crystal can be obtained within ten minutes, the screening experiment for a sample tray finishes within daytime. Users qualify the crystals referring diffraction image browser of D-Cha, and make the data collection schedule for selected crystals. By following the screening process, users can definitely select the best crystal to collect the data set, and also can make an efficient experimental schedule. A full-automatic overnight data collection is conducted according to the registered schedule. Samples are automatically mounted and centered utilizing the record of the goniometer translation, taking advantage of the screw-type sample pin with SPACE.

BL26B2 has been continuously operated with the automation system since 2003. In 2006, more than twenty-five crystals a day have been constantly delivered and screened, and eight data sets in daily average have been constantly collected. Examples of newly determined three-dimensional protein structures based on diffraction data collected at BL26B2 are shown in Fig. 4. Presently, technical developments such as BSS and SPACE are similarly implemented to other structural biology beamlines at SPring-8, providing users a common look and feel at all beamlines.

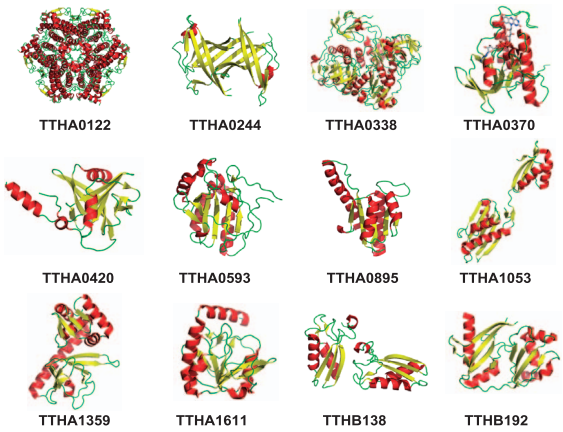

Fig. 4. Protein structures newly determined by diffraction data collected at BL26B2, SPring-8. All structures have been deposited into PDB. Provided by Akio Ebihara and Seiki Kuramitsu at SR System Biology Research Group, RIKEN SPring-8 Center.

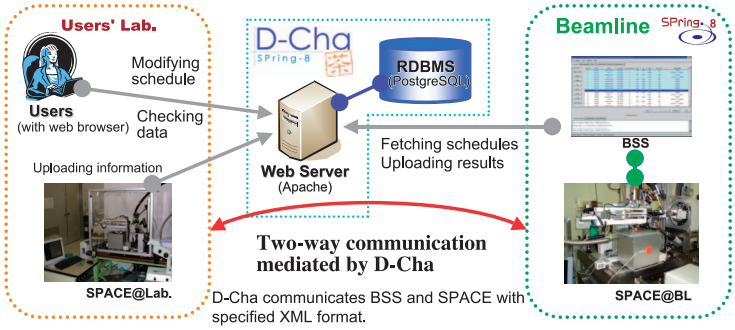

Fig. 3. Networked database D-Cha developed for mail-in data collection at SPring-8.

Go Ueno[a,*], Nobuo Okazaki[b] and Kazuya Hasegawa[b]

[a] SPring-8 / RIKEN
[b] SPring-8 / JASRI

*E-mail: ueno@spring8.or.jp

References

[1] D. Baker and A. Sali: Science **294** (2001) 93.
[2] *G. Ueno, H. Kanda, R. Hirose, K. Ida, T. Kumasaka and M. Yamamoto: J. Struct. Funct. Genomics 7 (2006) 15.*
[3] S. Goto *et al.*: J. Synchrotron Rad. **5** (1998) 1202.
[4] G. Ueno *et al.*: J. Appl. Cryst. **37** (2004) 867.
[5] G. Ueno *et al.*: J. Synchrotron Rad. **12** (2005) 380.

High-resolution powder diffraction from purple membrane

To understand the actions of proteins in living cells, knowledge in their structures and dynamics in their natural environment is required. X-ray diffraction can be used to study biological membranes and filamentous materials under physiological conditions. Acquiring high-resolution diffraction data of the samples of protein assemblies requires a small X-ray beam and a detector system with a high spatial resolution and a wide dynamic range. X-ray beams provided by third-generation synchrotron facilities have small diameters and low angular divergences. Imaging plate (IP) detectors with spatial resolution of about 100 μm and dynamic range of 10^5 are suitable for recording their diffraction patterns because stacked biological membranes and oriented sols of filamentous assemblies of proteins have long-range ordered structures and display wide-ranging intensity resolutions.

A Guinier camera was developed for powder diffraction experiments of microcrystalline materials with large unit cells [1] (Fig. 1). The camera has a maximum specimen-to-detector distance of 1000 m with the highest angular resolution of 0.024° when using a blue IP of 100 μm spatial resolution. The high angular resolution lends itself to X-ray diffractometry of biological membranes and/or sols of filamentous biological materials because many diffraction peaks at high angles could be too close to each other to be separated with low-resolution detectors.

Powder X-ray diffraction was applied to structural analysis of Purple Membrane (PM), which is a two-dimensional crystalline array of bacteriorhodopsin acting as a light-driven proton pump in *Halobacterium salinarium*. X-ray diffraction images of oriented films of PMs showed clear peaks up to a resolution of 7.0 Å. It was, however, difficult to separate diffraction peaks and to evaluate intensities beyond the resolution because diffraction peaks overlapped considerably. Thus, X-ray diffraction studies of PM on the structural changes during proton pumping have been limited to low resolution even in recent years.

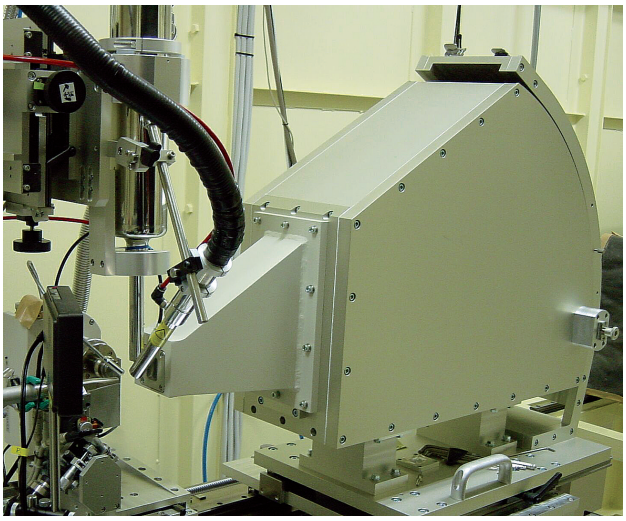

Fig. 1. Photograph of the Guinier camera.

Oriented films of PMs were measured with the Guinier camera [2]. Figure 2 shows a one-dimensional diffraction profile of the PM film reduced from the diffraction patterns on two IPs. The intensities of diffraction peaks decrease gradually with increasing S, but peaks are visible beyond 0.40 $Å^{-1}$ (2.5 Å resolution). The lattice constant of PM at around 110 K was calculated to be 61.0 Å from the positions of 47 sharp diffraction peaks located between 0.03 and 0.32 $Å^{-1}$. The expected positions of diffraction peaks from a hexagonal lattice correspond exactly to the observed peak positions in the diffraction profile (Fig. 2). As a result, 52 diffraction intensities of 55 expected reflections from (1 0) to (11 3) are integrated using the profile fitting method. An electron density map of BR projected normal to the membrane plane was calculated at a resolution of 4.2 Å (Fig. 3). The map clearly indicates electron density of seven transmembrane α-helices and its trimer structure. When the map is compared with those in previous studies obtained at a resolution of 7.0 Å, it displays characteristics to be observed in a projection map calculated at a resolution of around 3.5 Å by electron. Firstly, the four helices (A, E, F and G) located at the outer rim of the BR monomer have projection densities lower than the three helices (B, C and D) in the inner part. This characteristic comes from the tilting of the four helices from the membrane normal as demonstrated in a crystal structure of BR. Secondly, small but significant density peaks are visible in the map. In particular, a small peak is identified between helices C, D, E and F. Such a peak is invisible in the maps obtained at 7.0 Å. When referring to the crystal structure, the small peak plausibly corresponds to the electron densities of the β-ionone group of the chromophore retinal and the side chain of Trp189 adjoining the chromophore.

In powder diffraction studies, as the diffraction angle becomes larger, the number of peaks increases

and peaks become wider and weaker. As a result, it is difficult to distinguish each diffraction peak separately at a high diffraction angle. Owing to the high angular resolution of the large Guinier camera, observed peaks became sharp up to a high resolution (Fig. 2) and peak widths became less than half of that obtained in an earlier experiment. As a result, intensities were evaluated up to a spacing of 4.2 Å. The present experimental data for PM suggest the possibility of X-ray diffraction experiments for structural studies of intact biological membranes and macromolecule assemblies.

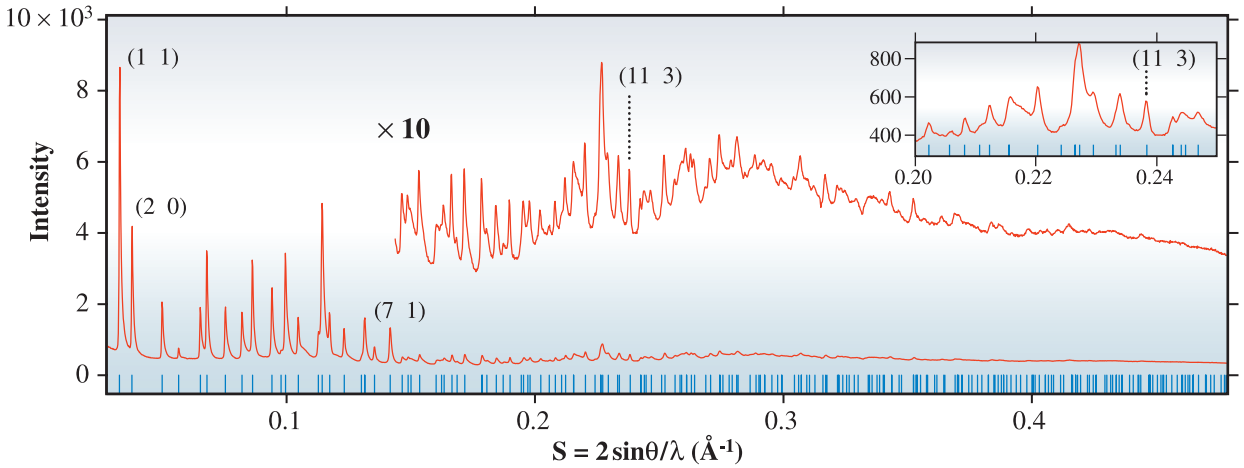

Fig. 2. X-ray diffraction profile of PM. Bars below the diffraction profile are the expected positions of diffraction peaks from a hexagonal lattice of a plane group *p3*. The inset shows the magnified profile.

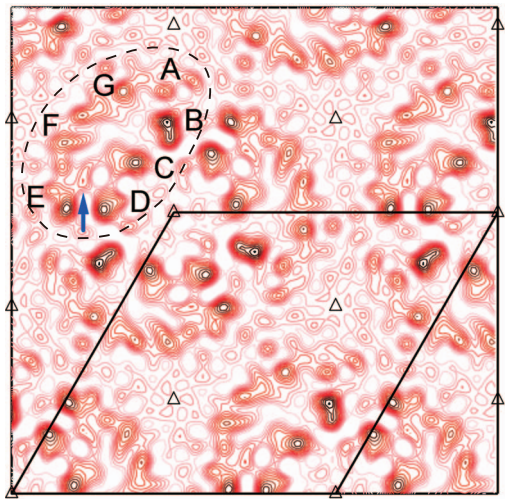

Fig. 3. Electron density map of PM projected onto a membrane plane. The dashed line shows the border of one BR monomer. An arrow indicates a small peak between helices C, D, E and F.

Toshihiko Oka

Faculty of Science and Technology, Keio University

E-mail: oka@phys.keio.ac.jp

References

[1] K. Miura *et al.*: AIP Conf. Proc. **705** (2004), 989.
[2] *T. Oka, K. Miura, K. Inoue, T. Ueki and N. Yagi: J. Synchrotron Rad.* ***13*** *(2006) 281.*

Photoelectrons Kicks Back: Recoil Effects in Photoelectron Spectroscopy

Photoelectron spectroscopy is widely used for the study of electronic structure of solids. The binding energy E_B of the electron in the sample is determined from the following equation:

$$E_B = h\nu - E_{kin} - \varphi,$$

where E_{kin} is the measured electron kinetic energy, $h\nu$ is the photon energy for excitation, and φ is the work function. This procedure, however, overlooked recoil effects, i.e., the momentum (or energy) imparted to the emitting atom by the outgoing electron. This is simply because the recoil effect is not easily measurable in vacuum ultraviolet (VUV) and soft X-ray (SX) photoelectron spectra.

In the last few years, hard X-ray (HX) photoelectron spectroscopy with the excitation energy of 6-8 keV has been realized using high brilliance synchrotron radiation [1-3], resulting in useful studies on semiconductors and correlated materials. The achieved high energy resolution (ΔE < 80 meV) enables us to investigate recoil effects in a solid.

In this study, we successfully observed the recoil effects in the C 1*s* core level photoelectron spectra of highly oriented pyrolytic graphite (HOPG). HX photoelectron spectra at the excitation energies of 5950 and 7940 eV were measured at the undulator beamline **BL29XU**. Details of the apparatus including X-ray optics are described in Refs. [2,3]. SX spectra at the excitation energy of 340, 870 eV were measured at the undulator beamline **BL17SU**. The total instrumental energy resolution (ΔE) for the SX and HX spectra were determined as 100 meV and 120 meV by fitting the Fermi-edge profiles of Au measured at 20 K.

C 1*s* core level spectra of HOPG measured at room temperature with SX excitation (340 and 870 eV) and HX excitation (5950 and 7940eV) are shown in Fig. 1(a). The spectra are obtained effectively in normal emission geometry. The peak position of the spectrum obtained with $h\nu$ = 870 eV shifts to lower binding energy in comparison with that of $h\nu$ = 340 eV spectrum. This shift is due to the difference in the probing depth of photoelectrons between these excitation energies. With increase of the kinetic energy, the probing depth of a photoelectron becomes larger. The spectra of $h\nu$ = 340 and $h\nu$ = 870 eV are dominated by the surface and bulk components, respectively. With increase of the excitation energy, i.e., the kinetic energy of the C 1*s* photoelectron, the peak position shifts to the higher binding energy side. It is also obvious that asymmetric broadening becomes much wider for the higher energy photoelectrons, while the total instrumental energy resolution for these spectra is almost the same.

For the possible origin of these spectral changes, the effect of associated elementary excitation such as plasmons is discarded, since the peak position itself shifts, depending on the kinetic energy. The asymmetric line shape of the C 1*s* core level spectra obtained with soft X-ray excitation has been discussed in relation with semimetallic character of graphite, and can be fitted by the Doniach-Sunjic function [5]. This possibility can also be excluded for the same reason. Thus, we are led to a picture based on recoil effects for explaining the observed peak shift and broadening, which depends on the kinetic energy of the photoelectron.

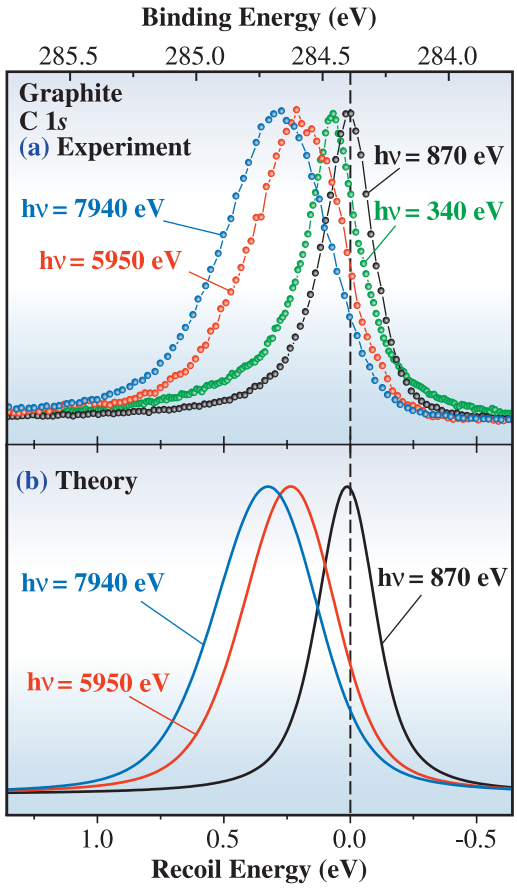

Fig. 1. **(a)** Photon energy dependence of C 1*s* core level spectra of graphite. The soft X-ray ($h\nu$ = 340 and 870 eV) and hard X-ray ($h\nu$ = 5950 and 7940 eV) are measured at the emission angle of 90° and 85° relative to the sample surface. **(b)** Theoretically obtained spectra taking into account the recoil effect in a Debye model with $\hbar\omega_b$ = 75 meV.

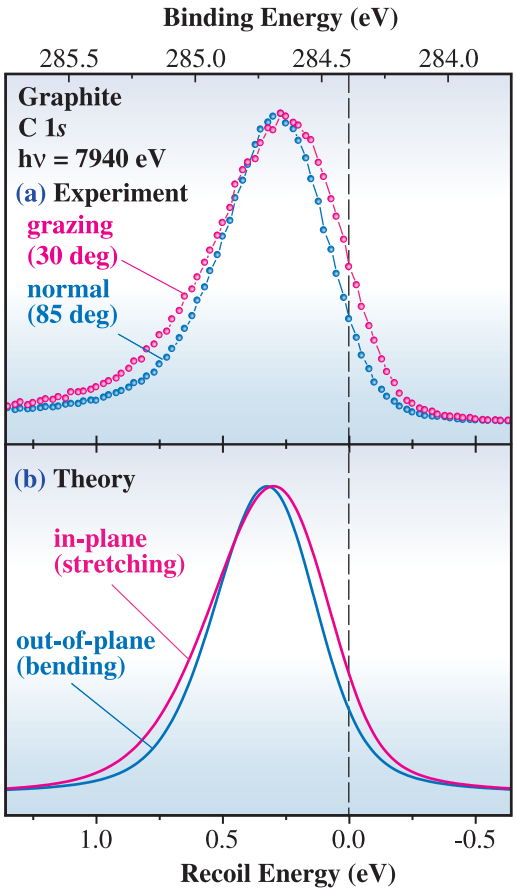

Fig. 2. **(a)** C 1*s* core level spectra of graphite measured at the photon energy of 7940 eV at the emission angles of 85° (normal) and 30° (grazing) relative to the sample surface. **(b)** Theoretically obtained spectra with the Debye energies $\hbar\omega_b$ = 75 meV and $\hbar\omega_s$ = 150 meV for the bending and stretching modes, respectively.

For an atom with mass M in free space, the recoil energy δE is simply estimated from the momentum conservation as $\delta E = (m/M)E_{kin}$, where m is the electron mass. For a carbon atom with the mass ratio m/M = 1/22000, δE becomes as large as 0.36 eV for E_{kin} = 8 keV. In the solid, this recoil energy is absorbed by the phonon bath, resulting in the excitation of phonons. The zero-phonon transition corresponds to the event in which the recoil energy is transferred to the center of mass motion of the total crystal. This is essentially the same as the Mössbauer effect in the γ-ray emission from nuclei embedded in crystals.

Based on these considerations, a full quantum calculation with adiabatic approximation and an anisotropic Debye model for graphite was carried out. Details are described in Ref. [4]. The theoretical spectra of the C 1*s* normal emission photoelectrons of graphite are plotted as a function of the recoil energy in Fig. 1(b). The lifetime broadening (full width at half maximum) is taken to be 160 meV as is known for graphite [5]. The spectra are then convoluted with a Gaussian function corresponding to the experimental resolution of 120 meV. Theoretical spectra reproduce the experimental spectra fairly well without any adjustable parameters. Note that, at 870 eV excitation, the peak shift is quite small, but phonon excitations cause the asymmetric broadening.

Figure 2 (a) shows the experimental C 1*s* core level spectra of HOPG measured with 7940 eV excitation at the emission angle of 85° (the same as that in Fig. 1(a)) and 30° relative to the sample surface. The peak slightly shifts to lower binding energy and becomes broader for the grazing emission spectrum. Theoretical spectra are shown in Fig. 2(b). The theoretical spectra reproduce well the observed emission angle dependence. The larger spectral width in the grazing angle emission, relative to the normal one, is attributed essentially to the large Debye cut-off frequency for the stretching mode, which is roughly twice that for the bending mode.

The experimental and theoretical results confirm the recoil effects of photoelectrons in solids, making it an important aspect of high-energy photoelectron spectroscopy. We are investigating recoil effects in valence band photoelectron spectra. Such studies using high energy photoelectron spectroscopy will give us new insights on the dynamics of chemical bonding.

Yasutaka Takata[a,*] and Yosuke Kayanuma[b]

[a] SPring-8 / RIKEN
[b] Graduate School of Engineering, Osaka Prefecture University

*E-mail: takatay@spring8.or.jp

References

[1] K. Kobayashi *et al.*: Appl. Phys. Lett. **83** (2003) 1005.
[2] Y. Takata *et al.*: Nucl. Instrum. Meth. A **547** (2005) 50.
[3] T. Ishikawa *et al.*: Nucl. Instrum. Meth. A **547** (2005) 42.
[4] *Y. Takata, Y. Kayanuma, M. Yabashi, K. Tamasaku, Y. Nishino, D. Miwa, Y. Harada, K. Horiba, S. Shin, S. Tanaka, E. Ikenaga, K. Kobayashi, Y. Senba, H. Ohashi and T. Ishikawa: Phys. Rev. B* ***75*** *(2007) 233404, cond-mat/ 0609241.*
[5] T. Balasubramanian *et al.*: Phys. Rev. B **64** (2001) 205420.

Application of Resonant Inelastic X-ray Scattering (RIXS) Method to Materials Physics

Resonant inelastic X-ray scattering (RIXS) is a promising tool to probe the momentum dependence of low-energy excitations in solids [1,2]. A schematic process of RIXS for Cu 1*s*-4*p* excitation is illustrated in Fig. 1, in which the labels (I), (II), and (III) stands for the respective step of the RIXS process. The incident light excites the Cu 1*s* electron to the Cu 4*p* states in step (I). In the step (II) of the de-excitation, the Cu 3*d* electron is excited across the Fermi level (red circle). When the Cu 4*p* electron relaxes into the Cu 1*s* state with the Cu 3*d* excitation, the corresponding energy is emitted in the form of photons (step (III)). The emitted energy is smaller than the excitation energy by the amount of the energy loss for the Cu 3*d* excitation as explained above. Namely, RIXS measurements probe second-order optical processes.

In RIXS, an electron is excited from the occupied core state to the unoccupied state, and the energy ($h\nu$-dependence) and momentum (Δk-dependence) differences between the occupied and unoccupied states are probed. In general, the excitation of valence electrons in inelastic X-ray scattering is too weak to be distinguished from other excitation processes with good statistics. Therefore, resonance enhancement near the core excitation threshold is utilized in RIXS. As a great advantage for studying the momentum dependence of the electronic energies, RIXS is much more bulk sensitive than photoemission and is applicable to insulators. Another advantage of RIXS measurement is the freedom to change the photon energy near the core absorption threshold to select different intermediate states [2].

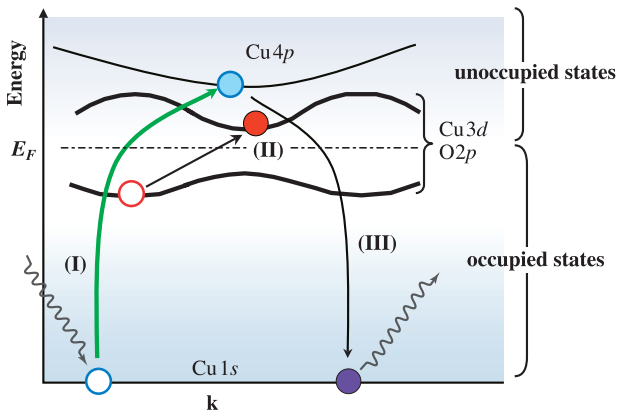

Fig. 1. Schematic picture of inelastic resonant X-ray scattering for Cu 1*s* - 4*p* absorption [3].

The experiment was carried out in the third hutch of beamline **BL19LXU** [4]. Figure 2 shows the experimental setup designed for RIXS in the Cu 1*s* absorption region around 9 keV. In this figure, all the components shown in the top view are set on a single optical bench with a size of 1 m × 2 m. The linearly polarized undulator radiation was tuned to a proper monochromatic energy using two Si (111) crystals. It was further monochromatized by two channel-cut Si (220) crystals, with the energy resolution of 360 meV full width at half maximum (FWHM). Then, the light was focused by a bimorph mirror with a focusing length of about 1 m. The horizontal focus size was smaller than 100 μm on the sample. The monochromatic light was incident onto the polished surface of the sample, which was kept in an evacuated chamber with polyimid windows (shown in Fig. 2, photo 1). Horizontally scattered radiation was analyzed by a setup constructed on an arm rotating around the sample position. The angle of the arm determines the scattering vector and therefore the momentum transferred to the excited electron. The energy of the scattered radiation was analyzed by a spherically bent Si (553) crystal (shown in Fig. 2, photo 2), which was mounted on a biaxial goniometer enabling both energy analysis and adjustment of the tilting angle. The diameter of the Rowland circle was 1 m. The analyzed light was focused on a NaI scintillation detector. The size of the slit in front of the detector was set to 0.4 mm. The slit and the detector were put on the same plate, which is moved

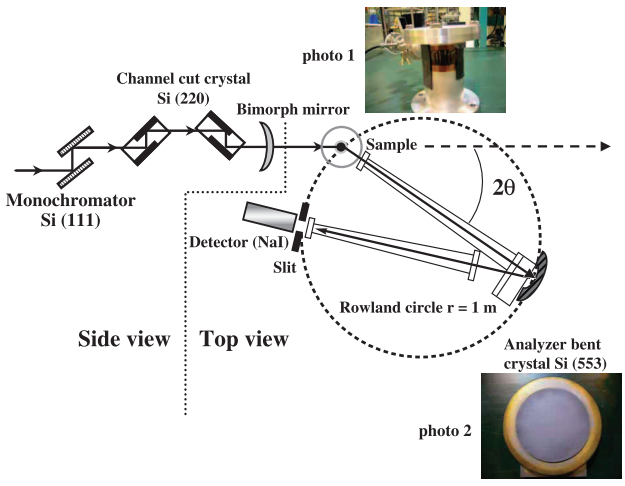

Fig. 2. Schematic picture of our experimental setup at BL19LXU (photo 1). Sample chamber with polyimid windows (photo 2). Spherically bent Si (553) crystal.

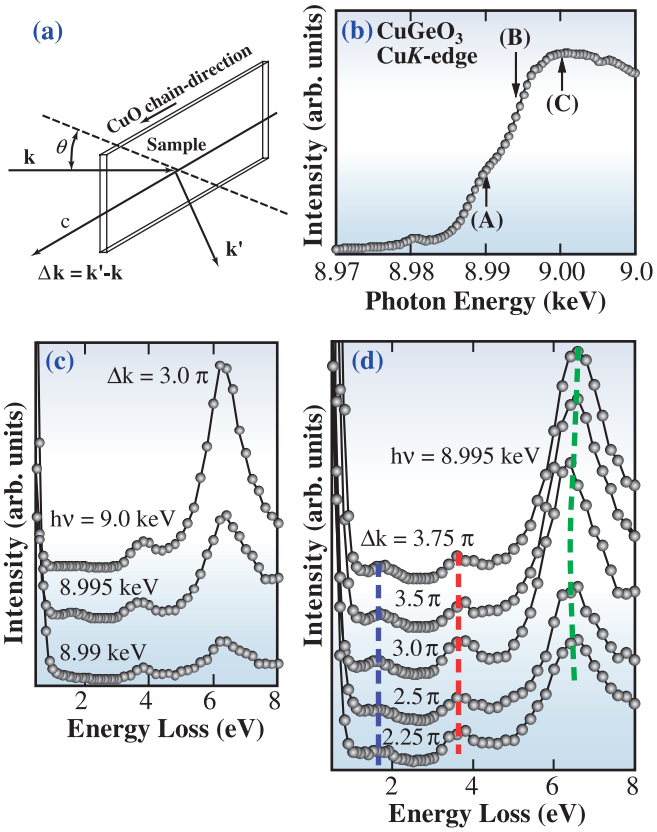

Fig. 3. **(a)** Schematic diagram for explaining RIXS in the transmission mode **(b)** Cu 1*s* - 4*p* absorption spectrum in $CuGeO_3$ **(c)** $h\nu$-dependence of RIXS spectra at $\Delta k = 3.0\pi$. **(d)** Δk-dependence of RIXS spectra at $h\nu = 8.995$ keV.

horizontally so that the slit followed the Roland circle. The total energy resolution, determined from the width (FWHM) of the quasi-elastic scattering peak, was about 440 meV. Most parts of the optical path from the sample position to the detector were evacuated using of polyimid windows to minimize the loss due to the scattering by air.

As an example of application, we show the RIXS spectra of $CuGeO_3$. This sample is one-dimensional insulator and has a single chain with the edge-sharing CuO_2 plaquettes configuration. For a thin film $CuGeO_3$ sample, the chain axis is oriented by Laue diffraction measurement, where the naturally grown surface was used for measurement. The measurement has been performed at room temperature in the transmission mode as shown in Fig. 3(a). The Δk measurement for single chain direction has been performed by changing both 2θ and θ angles as shown in Fig. 2 and Fig. 3(a).

Figure 3(b) shows the Cu 1*s*-4*p* XAS spectrum measured by means of the fluorescence yield. The labels in XAS indicate the incident photon energies used for RIXS measurement shown in Figs. 3(c) and 3(d). In Fig. 3(b), the Cu 1*s*-3*d* quadrupole peak is located at $h\nu = 8.98$ keV. The label (A) corresponds mainly to the Cu 1*s*-4*p*π transition, whereas the Cu 1*s*-4*p*σ absorption is dominant in the regions of label (B) and (C). Figure 3(c) shows the $h\nu$-dependence of the RIXS spectra at $\Delta k = 3.0\pi$. In Fig. 3(c), each spectrum reflects the difference in the intermediate states. These spectra have some characteristic features. For example, the spectrum at $h\nu = 8.995$ keV shows a low-energy loss peak around 1.6 eV. To investigate the character in detail, we performed the measurement of Δk-dependence for RIXS spectrum at $h\nu = 8.995$ keV as shown in Fig. 3(d). Figure 3(d) shows three dispersions around 1.6 eV (blue dashed line), 3.5 eV (red dashed line), and 6.5 eV (green dashed line). To clarify the origins of these features, we compare our result with the theoretical calculation. As a result, the features around 3.5 eV and 6.5 eV correspond to the excitation states from the Zhang-Rice singlet made of the Cu 3*d* hole coupled with the O 2*p* hole and the bonding state between Cu 3*d* and O 2*p* states to the upper Hubbard band, respectively. The feature around 1.6 eV is described as the *d*-*d* transition on the same Cu site [5].

RIXS measurement can thus provide bulk information of not only occupied states but also unoccupied states with the momentum dependence. Therefore, this method is a very powerful tool for materials science.

Atsushi Higashiya [a,*], Shigemasa Suga [b] and Tetsuya Ishikawa [a]

[a] SPring-8 / RIKEN
[b] Graduate School of Engineering Science, Osaka University

*E-mail: codbelo@spring8.or.jp

References

[1] M.Z. Hasan *et al.*: Science **288** (2000) 1811.
[2] A. Higashiya *et al.*: Solid State Communications **130** (2004) 7.
[3] K. Tsutsui *et al.*: Phys. Rev. Lett. **91** (2003) 117001.
[4] M. Yabashi *et al.*: Phys. Rev. Lett. **87** (2001)140801.
[5] *S. Suga, S. Imada, A. Higashiya, A. Shigemoto, S. Kasai, M. Sing, H. Fujiwara, A. Sekiyama, A. Yamasaki, C. Kim, T. Nomura, J. Igarashi, M. Yabashi and T. Ishikawa: Phys. Rev. B* ***72*** *(2005) 081101(R).*

Picosecond X-ray Stroboscopy Probing Crystal Lattice Deformation Induced by Pulsed Laser Irradiation

When the surface of a semiconductor crystal is irradiated by a femtosecond pulsed laser, the crystal lattice close to the surface is transiently deformed. The deformation propagates as a wavepacket toward the backside of the crystal, and is reflected and then comes back to the surface. This phenomenon is called acoustic pulse echoes, the technique of which has, for example, been anticipated as a tool for investigating the underlying structures in materials such as thin layers and defects, similar to sonar which can detect underwater objects. The optically induced acoustic pulse has been detected mainly by optical pump-probe methods with picosecond time resolution, which give integrated effects of deformation such as slope and displacement of the surface. However, the transient lattice strain in the material had not been directly observed by X-ray diffraction.

The pulsed nature of the synchrotron radiation (SR) and the synchronization technique between SR pulse and ultrashort laser pulse can take snapshots of X-ray diffraction profiles of crystal lattice motion with 40 ps resolution. The 27-m-long undulator beamline **BL19LXU** is equipped with a femtosecond pulsed laser system synchronized with the SR pulse timing. The time evolution of X-ray diffraction intensity can be obtained by changing the delay between the laser and X-ray SR pulses. The high repetition rate of the SR envisaged as a quasi-continuous wave is also useful for surveying the wide time range profile of target phenomenon using the multichannel scaling (MCS) technique. The use of both the multichannel scaling and the pump-probe technique offers the efficient time-resolved experiments such as pulsed echo observation, requiring picosecond time-resolution at large delay time.

Transient lattice strain produced by ultrashort laser pulse light generally includes inclination of lattice planes (i.e. shear strain) as well as dilation and contraction (i.e. longitudinal strain). The strain with both longitudinal and shear components cannot be quantitatively analyzed from the rocking curve measurement using a monochromatic and parallel incident X-ray beam. In the triple crystal diffractometry (TCD), the Bragg diffracted beam from the sample is angularly resolved by an analyzer crystal, so that the distribution of diffracted intensity in a reciprocal space is measured with high momentum resolution. The centroid shift of the diffracted intensity distribution in the direction parallel to the reciprocal lattice vector represents the longitudinal strain; the

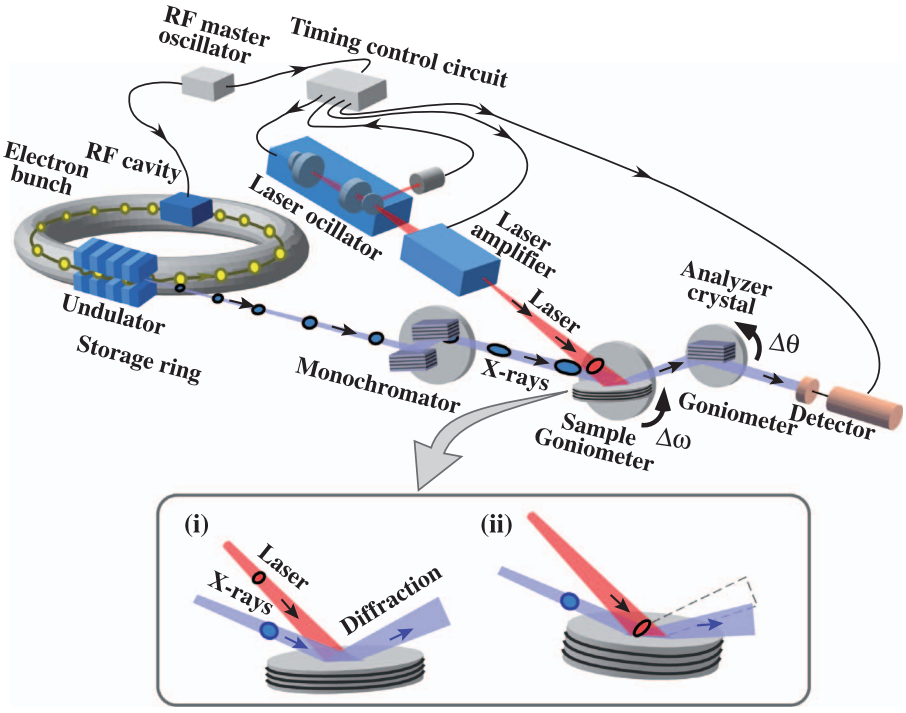

Fig. 1. Schematic illustration of experimental setup for picosecond time-resolved triple crystal diffraction.

shift in the perpendicular direction corresponds to the shear strain.

The intense synchrotron radiation produced at the beamline has enabled us to combine the time-resolved technique and the TCD [1]. The time-resolved TCD (TR-TCD) has been applied to the detection of acoustic pulse echoes that are generated in silicon and gallium arsenide semiconductor plates by femtosecond laser irradiation (Fig. 1) [2]. In Fig. 2, the obtained time-dependent longitudinal strain component for the pulse echoes showed that the polarity of the strain pulse was dependent on the optically induced initial stress, and that the bipolar pulse waveform was gradually deformed and broadened in the course of propagation. The pulse duration broadening was consistent with a boundary roughness for an unpolished plate (Fig. 3). This implies that the method can provide a new non-contact method to probe the roughness of optically inaccessible internal boundaries in materials.

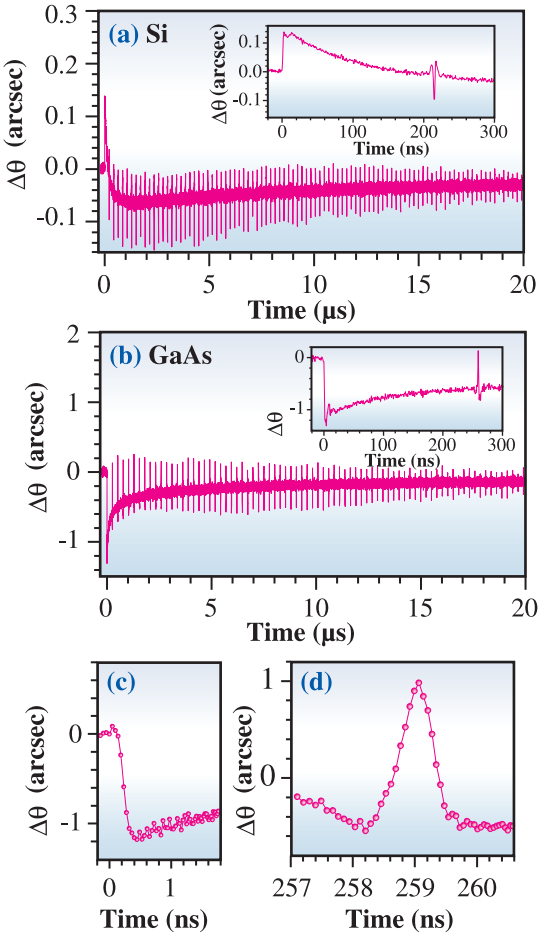

Fig. 2. Acoustic echoes for Si **(a)** and GaAs (**(b)**, **(c)** and **(d)**) wafers observed by multichannel scaling (**(a)** and **(b)**) and pump-probe technique(**(c)** and **(d)**).

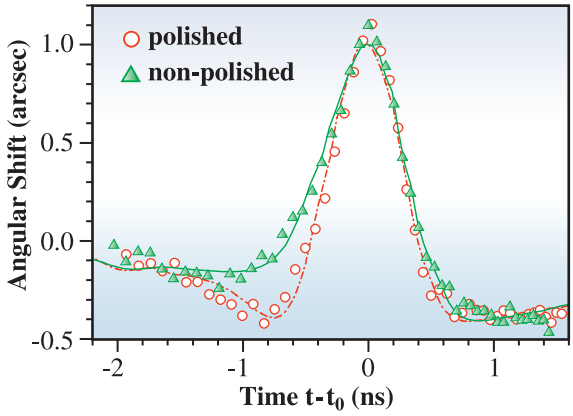

Fig. 3. Angular shift of the time-resolved X-ray diffraction profile of 1st echo pulse dependent on the back surface roughness.

Yoshihito Tanaka[a,*] and Yujiro Hayashi[a,b]

[a] SPring-8 / RIKEN
[b] Hokkaido University

*E-mail: yotanaka@riken.jp

References

[1] Y. Hayashi *et al.*: J. Synchrotron Rad. **12** (2005) 685.
[2] *Y. Hayashi, Y. Tanaka, T. Kirimura, N. Tsukuda, E. Kuramoto and T. Ishikawa: Phys. Rev. Lett.* ***96*** *(2006) 115505.*

Nuclear Excitation by Electron Transition on ^{197}Au around the *K*-absorption Edge

Nuclear excitation by electron transition (NEET) on ^{197}Au occurs in the *K*-shell ionization between the $K \rightarrow M_1$-hole atomic transition ($1S_{1/2}$: 80.725keV → $3S_{1/2}$: 3.425 keV) and the $3/2^+ \rightarrow 1/2^+$ nuclear transition (0 → 77.351 keV), with a very small probability of less than 10^{-7} to the ionization. We succeeded in observing the first NEET signal on ^{197}Au at beamline **BL09XU** in 1999 [1]. Figure 1 shows a schematic view of NEET of ^{197}Au. The incident X-rays of 80.989 keV were then used to ionize the gold atoms above the K-absorption edge. In 2001, we observed the NEET events around the *K*-edge by sweeping the energy of the incident photons. In contrast to the existing model [2-4], assuming that NEET on 197Au could have occurred even below the *K*-edge due to a finite *K*-shell width, the actual NEET events appeared to start increasing above the *K*-edge with a fine structure existing at higher energies. However, we had a statistic problem because of the low efficiency of the single Si avalanche diode (Si-AD) detector.

We tried again the same measurements in 2004 after improving the detector efficiency by replacing the single Si-AD by a couple of Si-AD arrays. Radiation just emitted from excited nuclei, especially the *L*-internal conversion electron (maximum energy: 63 keV), was mainly detected by the detector. The efficiency of the Si-AD arrays was about 4.3-times higher than that of the single Si-AD. In the addition to the measurements at nuclear resonance, we observed the NEET events as a function of the incident-photon energy (E) around the *K*-edge. The results were recently reported in Ref. [5]. Figure 2 shows the numbers of the NEET events, N_{ne}. The solid curve was given by connecting the averages of five neighboring points. Here, ΔE_K in the horizontal axis was defined by $E - E_K$; E_K was the *K*-edge energy. The *K*-edge was set by fitting the derivative of the measured *K*-absorption, $d\mu/dE$ with the Lorentz form, shown as the closed circles and the dashed curve in Fig. 3. The FWHM of the *K*-edge, W_K, was 58 ± 3 eV. The open circles in Fig. 3 indicate the derivative of the NEET events around the leading part in Fig. 2, dN_{ne}/dE; the solid curve is its fitted Lorentz form. The NEET edge at E_{NEET} was determined by the peak and was located at ΔE_K = +(40 ± 2) eV. The FWHM of the peak W_{NEET} was 14 ± 9 eV which was less than one third of W_K.

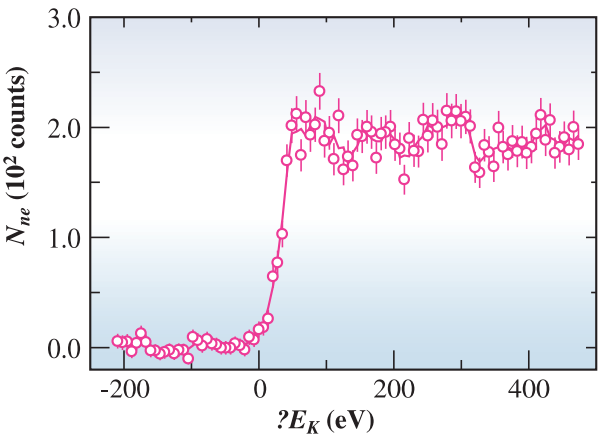

Fig. 2. Number of NEET events as a function of ΔE_K (where ΔE_K = 0 eV means the *K*-absorption edge).

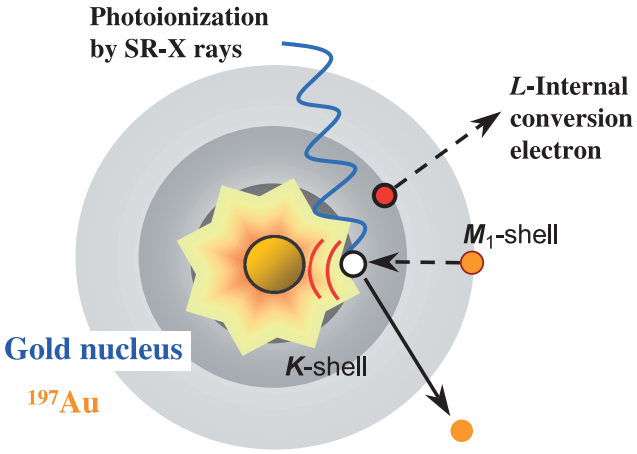

Fig. 1. Schematic view of NEET on ^{197}Au.

Why was the NEET edge ΔE_K higher than E_K and why was W_{NEET} narrower than W_K? Our understanding is as follows. From the energy conservation rule between the initial and the final states, NEET just occurs when the energy of the *K*-hole state (E_{Kh}) is the same as the sum of the nuclear transition energy (E_N) and the M_1-hole state energy (E_{M1h}). Using the reference values, E_{NEET} (=E_{Kh}) is given by ΔE_K = +51 eV, which is near, but different from the observed value of +40 eV. This may suggest that the absolute values of E_N and E_K should be revised. By adopting an M_1-level width of 14.3 eV (FWHM), a beam width of 3.5 eV (FWHM), and neglecting the very narrow width of the nuclear level, the observed W_{NEET} should be less than the sum of these widths, 18 eV, since an energy width in the

NEET transition depends on the widths of the initial and final states. Our result of 14 ± 9 eV includes the expected value. Moreover, a fine structure of the NEET events is seen at $E > E_{NEET}$ in Fig. 2. If energy conservation is strictly maintained involving the energy of an ejected photoelectron from the *K* shell, this feature may be explained by a common mechanism with the modulation of extended X-ray absorption fine structure (EXAFS). The EXAFS modulation means a variation of the photoabsorption rate, or an interference effect produced by the outgoing photoelectron scattered from near neighboring atoms. The scattering process of the photoelectron in NEET should also affect the atomic transition rate. At $E > E_{NEET}$, the excess energy of $\varepsilon_{NEET} = E - E_{NEET}$ $(= E - (E_N + E_{M1}))$ is transferred to an outgoing photoelectron emitted in NEET. Since the kinetic energy, ε_{ph}, of the normal photoelectron emitted from the *K*-shell without NEET, satisfies $E - E_K$, ε_{NEET} should be ΔE_{NA} $(=E_N - (E_K - E_{M1}))$ lower than ε_{ph} at the same *E*. We will precisely confirm these prospects by experiments in the near future.

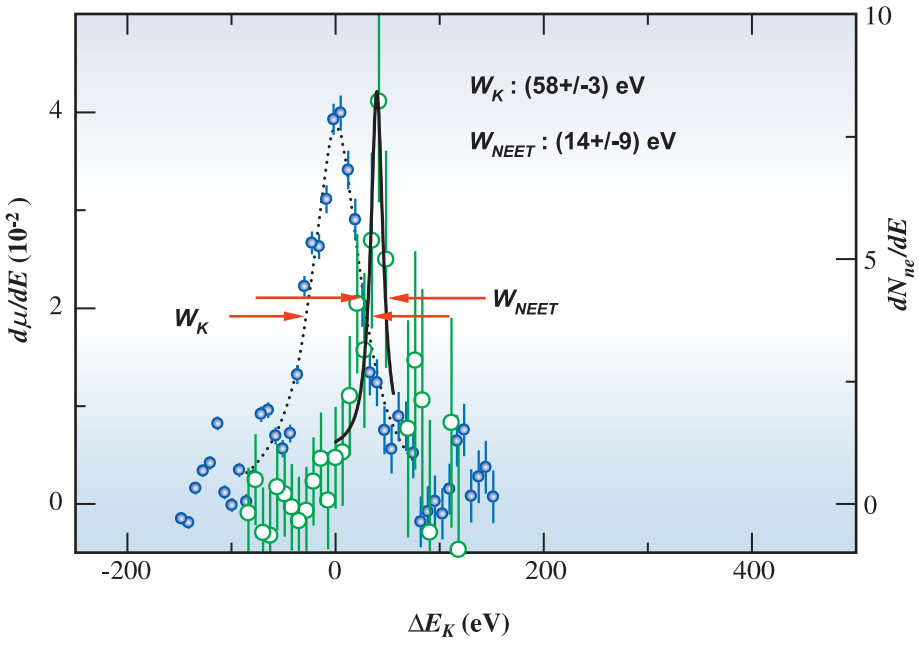

Fig. 3. Derivative of the *K*-absorption curve (closed circles) and its Lorentz fitting (dotted curve); the peak was set to $\Delta E_K = 0$ eV. The derivative of the NEET events, dN_{ne}/dE, is also plotted by the open circles; the solid curve is its Lorentz fitting. The arrows indicate the FWHM of the NEET edge, W_{NEET}, and that of the *K*-edge, W_K.

Shunji Kishimoto

Institute of Materials Structure Science,
High Energy Accelerator Research Organization

E-mail: syunji.kishimoto@kek.jp

References

[1] S. Kishimoto *et al.*: Phys. Rev. Lett. **85** (2000) 1831.
[2] M. Morita: Prog. Theor. Phys. **49** (1973) 1574.
[3] E.V. Tkalya: Nucl. Phys. A **539** (1992) 209.
[4] M.R. Harston: Nucl. Phys. A **690** (2001) 447.
[5] *S. Kishimoto, Y. Yoda, Y. Kobayashi, S. Kitao, R. Haruki, R. Masuda and M. Seto: Phys. Rev. C* ***74*** *(2006) 031301(R).*

Reinforcement of High T_c Superconducting Bulk Rings for Short-Period Undulators

In most undulators, permanent magnets (PMs) are adopted to generate a strong magnetic field with a periodic length around several centimeters. The magnetic performance of PM materials such as NdFeB has been improved yearly. However, it should be noted that there is a theoretical limit to the remanence of NdFeB, i.e., 1.6 T. To break the limit, undulators based on superconducting magnets exploiting low-T_c superconducting wires have been under development for decades; however, we still have several technical challenges to be overcome for a routine operation of such superconducting undulators (SCUs), especially the thermal budget problem. The operation of SCUs at around liquid helium temperature under the condition where the electron beam and synchrotron radiation are passing nearby can easily lead to quench due to the heat load from them [1].

Instead of low-T_c superconductors, we have proposed the application of high-T_c superconducting (HTS) bulk magnets for the future development of short-period undulators [2], in which ring-shaped HTS bulk magnets (bulk rings) are mounted on the PMs of conventional undulators to enhance the magnetic field. To realize this concept, we have a lot of technical challenges to be overcome as well as the conventional SCUs. What is most important is to improve the mechanical property of the bulk rings, which can be easily damaged due to electromagnetic stress during the magnetization process. In fact, the bulk ring samples used in the proof-of-principle experiments were found to be broken after several trials [3], implying that they should be reinforced by some means. We have tested two procedures to reinforce the HTS bulk ring: resin impregnation and iron ribbing.

The resin impregnation is usually applied to HTS bulk samples to improve the mechanical properties [4]. In this method, the bulk sample is immersed in molten resin and the resin penetrates into the bulk sample through microcracks having openings on the surface. The voids connected to these cracks are also filled with resin, which drastically improves the mechanical properties of the HTS bulk samples. In addition to the resin impregnation, a pole piece made from high-permeability material such as permendur can be inserted and glued to the bulk ring as a rib (iron ribbing). It is worth noting that the pole piece also works as a flux concentrator to achieve stronger magnetic field. It is effective to use the resin impregnation to glue the pole piece and bulk ring. A problem in this scheme is the difference in thermal expansion coefficient. A simple calculation shows that the difference in contraction between the permendur and YBaCuO, a typical HTS material, is around several microns when the temperature is reduced from 300 K to 100 K, which may damage the glue function of the resin impregnation.

To investigate the effects of the reinforcement methods described above, we prepared four bulk ring

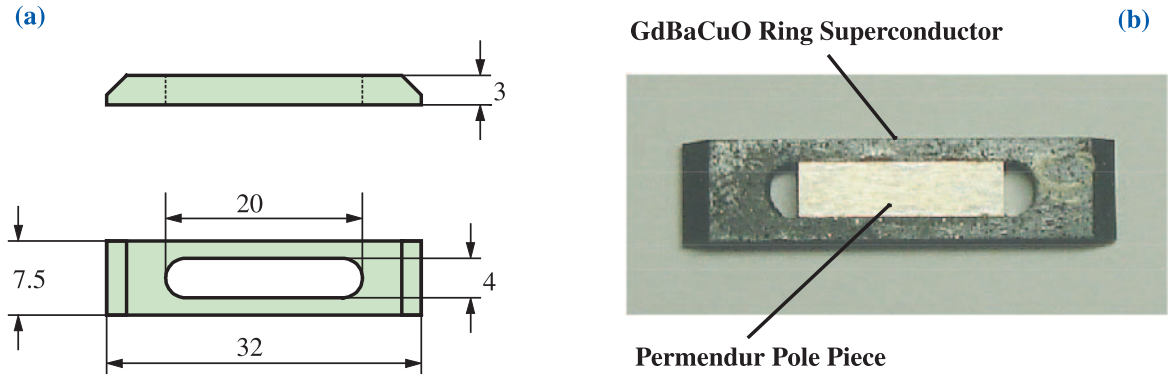

Fig. 1. **(a)** Overall dimensions of the ring HTSC sample prepared for the experiments to check the reinforcement method. **(b)** Photograph of sample C, in which a pole piece made of permendur is inserted.

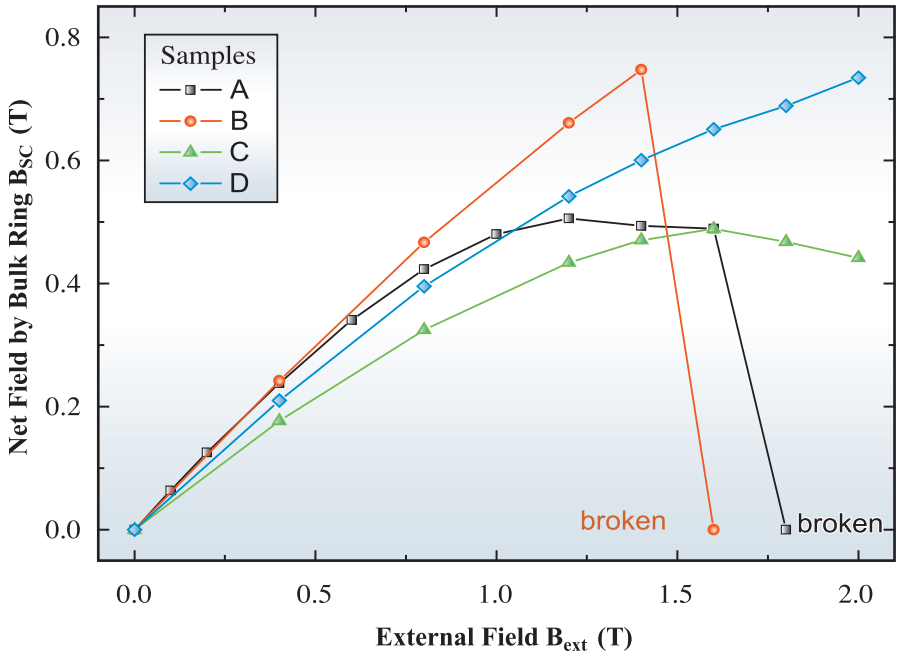

Fig. 2. Summary of the experiments to investigate the reinforcement method. Samples A and B were broken at the external fields of 1.8 T and 1.6 T, respectively, while samples C and D survived even after application of 2.0 T, the strongest field that can be applied by the electromagnet used in the experiment.

samples (A, B, C and D) made of GdBaCuO that were reinforced with several different methods, and carried out experiments to check the mechanical property of these samples. Figure 1(a) shows the overall dimensions of the sample. After machining, three samples (B, C and D) were immersed in epoxy resin for impregnation, where a pole piece made from permendur was inserted into samples C and D. Thus, samples C and D have the same structure. No treatment was made for sample A. Figure 1(b) shows a photograph of the sample C.

To investigate the effect of reinforcement, the samples were cooled to a temperature of 25 K and exposed to an external magnetic field up to 2 T, and the magnetic field at the center of the sample was measured by a Hall probe. Figure 2 shows the results of the experiments, where the net magnetic field B_{sc} generated by the bulk ring is plotted as a function of the external field B_{ext}. Samples A and B were broken after B_{ext} reached 1.8 T and 1.6 T, respectively, which means that resin impregnation alone is not enough to reinforce the bulk ring for undulators. On the other hand, samples C and D survived even after applying 2 T, which is close to the expected peak field of the undulators with HTS bulk rings with a magnetic period around 1 cm. Thus, we can conclude that the iron ribbing combined with resin impregnation significantly reinforces the bulk ring and improves its mechanical properties.

Takashi Tanaka

SPring-8 / RIKEN

E-mail: ztanaka@spring8.or.jp

References

[1] T. Tanaka: Physica C - in press.
[2] T. Tanaka, T. Hara, H. Kitamura, R. Tsuru, T. Bizen, X. Marechal and T. Seike: Phys. Rev. ST-AB **7** (2004) 090704.
[3] *T. Tanaka, T. Hara, R. Tsuru, D. Iwaki, T. Bizen, X. Marechal, T. Seike and K. Kitamura: Supercond. Sci. Technol.* ***19*** *(2006) S438.*
[4] M. Tomita and M. Murakami: Nature **421** (2003) 517.

Single-shot High-resolution Spectrometry for X-ray Free-electron Laser

X-ray free-electron laser (XFEL) can generate ultrahigh-brilliant femtosecond X-rays with full spatial coherence. New schemes for conditioning and diagnosing the X-ray properties should be developed both for accelerator operation and for user experiments. In particular, the single-shot measurement of the X-ray spectrum is important. The single-shot scheme is essential with the presence of the intrinsic fluctuation of the self-amplified spontaneous emission (SASE) lasing process, which starts from random noises. A high-resolution measurement that resolves a microstructure of the energy spectrum enables the evaluation of a femtosecond pulse width, which is difficult to measure using a conventional time-domain method. Other notable applications are (i) the high-resolution measurement of the acceleration energy of the electron beam and (ii) the precise adjustment of the magnetic strengths of the undulator segments for the efficient amplification of radiation.

Single-shot high-resolution spectrometry can be performed for visible and ultraviolet light using an optical grating. In the X-ray region, however, a resolution better than $\Delta E/E$ = 1 eV/10 keV = 10^{-4} has been not realized due to limitation in the availability of optical components. We have developed a new instrument by combining a focusing mirror and a perfect crystal of silicon [1]. With the mirror, the incident parallel X-rays (with a divergence of θ_D < 1 μrad) are focused into a small spot and succeedingly diverged (θ_D = 2.3 mrad). The photon energy of the divergent beam is analyzed with a diffraction of the silicon crystal according to Bragg's law. Since the incident angle on the analyzer crystal varies with the position, the photon energy of the diffracted beam also has a positional dependence. The spatial profile of the diffracted beam, which represents the energy spectrum of the incident X-rays, is measured with an X-ray camera (Fig. 1).

The quality of the X-ray mirror is crucial. Conventional X-ray mirrors which have large figure errors inevitably produce random intensity modulations called speckles. The speckle prevents one from obtaining a spectrum with good accuracy. In the present study, a state-of-the-art mirror with an extremely smooth surface [2], which has been developed in collaboration with Osaka University, was utilized. This mirror is fabricated with a special polishing method called EEM (Elastic Emission

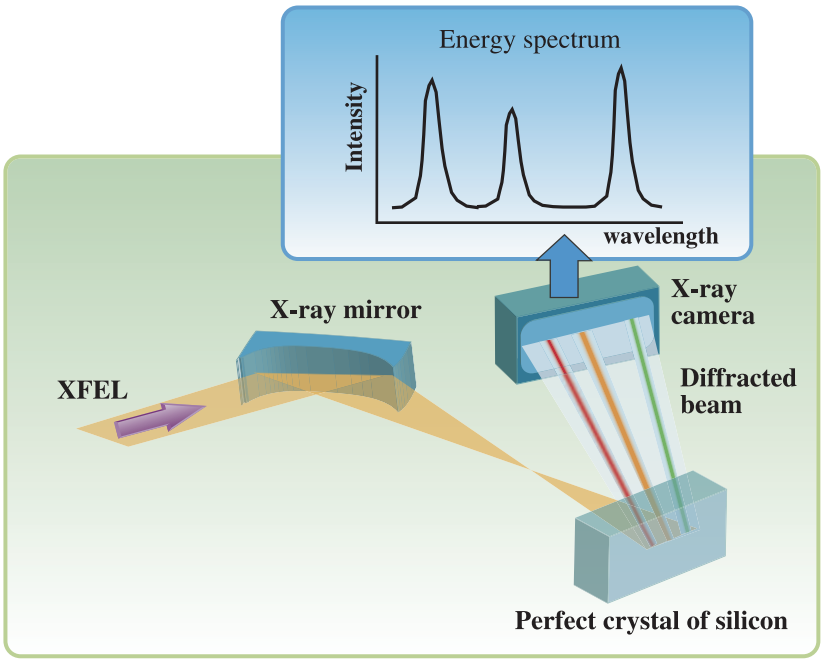

Fig. 1. Principle of spectrometer. The incident beam, which is focused and diverged by the X-ray mirror, is diffracted by the perfect crystal of silicon. The spatial profile of the diffracted beam is recorded using the X-ray camera.

Machining) [3] and a precision metrology technique called MSI (Microstitching Interferometry) [4].

An experiment was performed at the 1-km beamline (**BL29XU**) using the parallel X-ray beam with a photon energy of 10 keV. A monochromator was optionally used to select a narrow bandpath from the incident beam. Silicon 555 diffraction was employed for analyzing the spectrum, where the theoretical resolution is 14.5 meV with a total energy range of 3.5 eV. The profile of the diffracted beam was measured with the X-ray camera (Fig. 2). The beam position linearly depended on the photon energy of the incident monochromatic beam, as designed. From the width of the profile, the energy bandwidth of the optical system was evaluated to be 13.1 ± 1.9 meV (Fig. 3).

The achieved resolution and the uniformity of the intensity distribution of the optical system enable the evaluation of an X-ray pulse width in the range of sub-femtosecond to several picoseconds by choosing an appropriate diffracting plane. This method can contribute to a number of applications related to the FEL short pulse, such as ultrafast diffraction, to resolve atomic/molecular dynamics and high-power experiments for generating nonlinear optical phenomena.

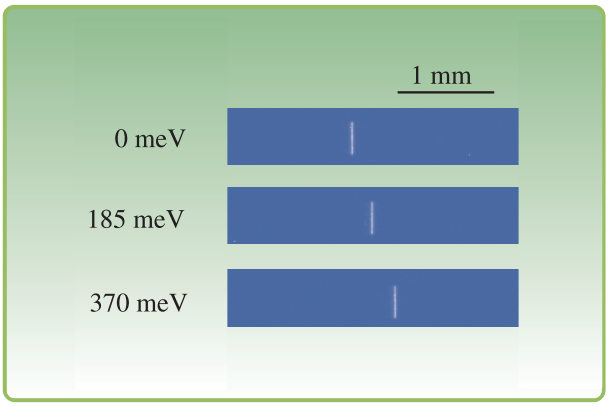

Fig. 2. Profile of diffracted beam. The position of the diffracted beam is shifted as the incident photon energy changes. The numbers on the left indicate deviations of the incident photon energy.

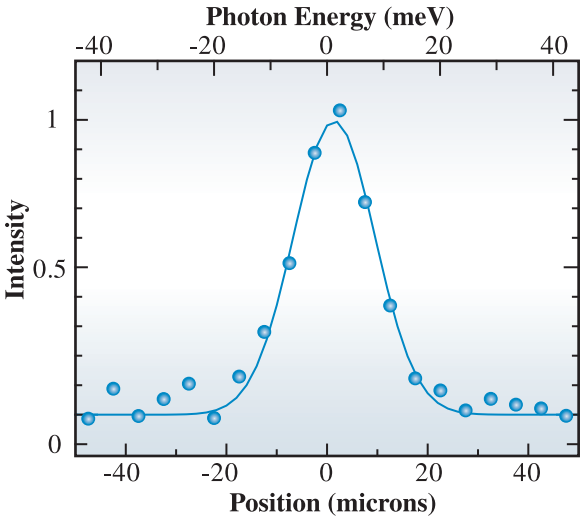

Fig. 3. Energy resolution. Measurement result of energy resolution using monochromatic X-rays as incident beam. A resolution of 13.1 meV was obtained by subtracting the energy spread of the incident beam.

Makina Yabashi[a,*], Kazuto Yamauchi[b] and Tetsuya Ishikawa[a,c]

[a] SPring-8 / JASRI
[b] Department of Precision Science & Technology, Osaka University
[c] SPring-8 / RIKEN

*E-mail: yabashi@spring8.or.jp

References

[1] *M. Yabashi, J.B. Hastings, M.S. Zolotorev, H. Mimura, H. Yumoto, S. Matsuyama, K. Yamauchi and Tetsuya Ishikawa: Phys. Rev. Lett.* ***97*** *(2006) 084802.*
[2] H. Mimura *et al.*: J. Synchrotron Rad. **11** (2004) 343.
[3] Y. Mori *et al.*: Proc. SPIE-Int. Soc. Opt. Eng. **4501** (2001) 30.
[4] K. Yamauchi *et al.*: Rev. Sci. Instrum. **74** (2003) 2894.

Nuclear Physics

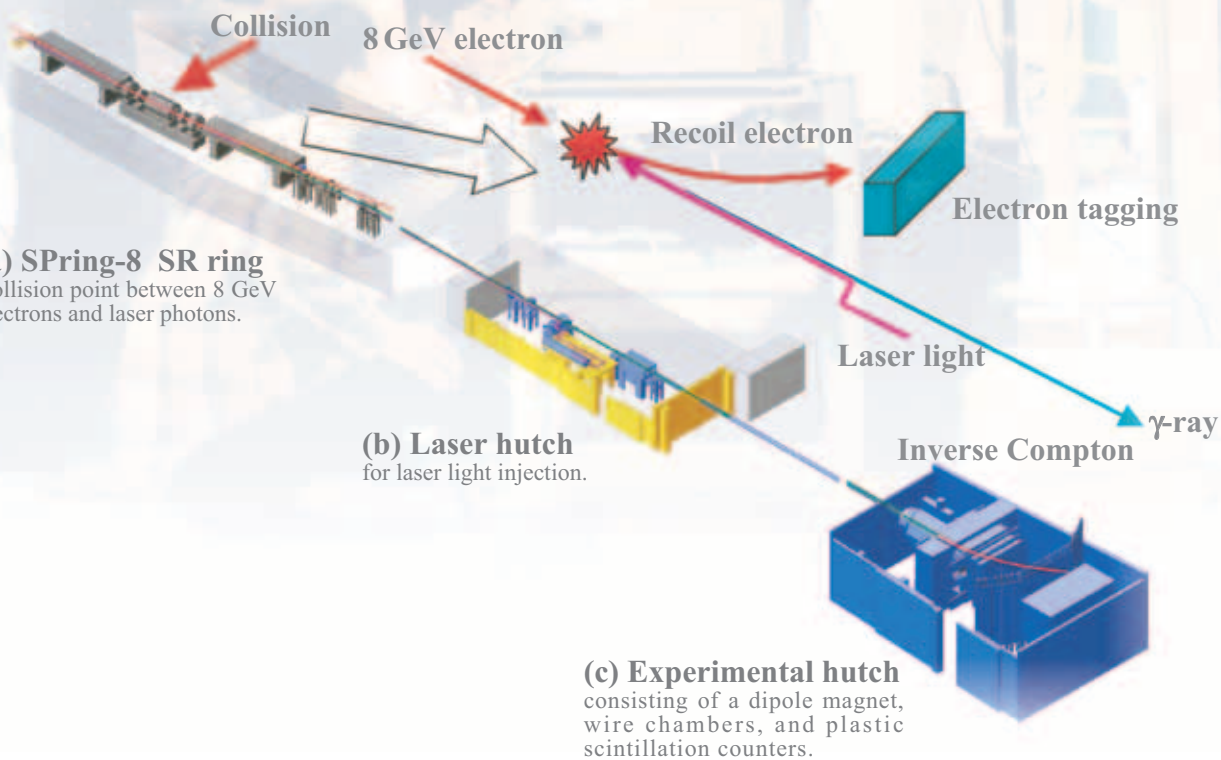

K^+ Meson Photoproduction Off Neutron at BL33LEP

A nucleon is composed of three quarks. For example, a proton is composed of two up (u) quarks and one down (d) quark. A neutron is composed of one u quark and two d quarks. There are additionally four other types of quarks, that is, charm (c), strange (s), top (t), and bottom (b), which are produced by high-energy collisions. All the quarks discovered so far are listed in Table 1. On the other hand, an anti-nucleon is composed of three anti-quarks. There are six types of anti-quarks, namely, $\bar{u}$, $\bar{d}$, $\bar{c}$, $\bar{s}$, $\bar{t}$, and $\bar{b}$, in total.

Table 1. Discovered quarks

Charge \ Generation	1	2	3
+2/3e	u	c	t
−1/3e	d	s	b

We have constructed beamline **BL33LEP** to study the meson production reactions using a linearly polarized high-energy photon beam. The photon beam is produced by the backward Compton scattering of an ultraviolet Ar laser from 8 GeV electrons. The energy range of tagged photons is from 1.5 to 2.4 GeV, and the photon polarization is typically 90% at 2.4 GeV. When the photons strike liquid hydrogen (LH_2) and deuterium (LD_2) targets, mesons are produced. We can see the s quark and $\bar{s}$ anti-quark pair production in this energy range. We studied the production mechanism of the K^+ meson, which is composed of a u quark and an $\bar{s}$ anti-quark. In the reaction, a hyperon, which is composed of three quarks including one s quark, is also produced.

The production mechanism of the K^+ meson is important for understanding the role of nucleon resonances. Experimental information on excited nucleons and excited Δ resonances has been obtained primarily in studies of π meson production. Constituent quark models predict more nucleon resonances than have been observed experimentally. This is mysterious and these unobserved nucleon resonances are called “missing resonances.” Quark model studies suggest that these resonances can couple to s quark channels, such as $K^+\Lambda$, $K^+\Sigma^0$, and $K^+\Sigma^-$, which have not been well studied.

Theoretically, K^+ meson photoproduction is

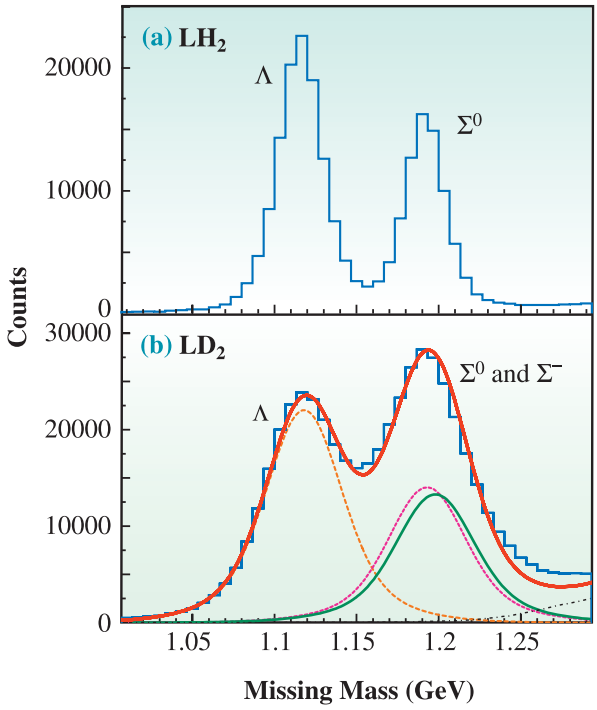

Fig. 1. Missing mass spectra obtained for K^+ photoproduction off **(a)** LH_2 and **(b)** LD_2 targets. Produced hyperons are identified.

described in terms of particle exchanges, such as nucleon, excited nucleon, and Δ resonance in the s channel, hyperon and excited hyperon in the u channel, and K meson and excited K meson in the t channel. The photon beam asymmetry has a unique feature; At a small |t| and at high energies, its value is +1 or -1 if the excited K meson or K meson is exchanged, respectively.

Recently, we have studied K^+ photoproduction off proton and found evidence of a nucleon resonance at the center of a mass energy (W) of about 1.95 GeV. The experimental data were limited to $K^+\Lambda$ and $K^+\Sigma^0$ productions off the proton. No experimental result has yet been published for K^+ photoproduction off a neutron. We obtained data on the $\gamma n \rightarrow K^+\Sigma^-$ reaction for the first time [1].

Figure 1 shows the missing mass spectra for the $p(\gamma,K^+)X(LH_2)$ and $N(\gamma,K^+)X(LD_2)$ reactions. The contribution from $K^+\Sigma^-$ production was obtained from the yield difference between the LH_2 and LD_2 data. Figure 2 shows photon beam asymmetry. It is interesting that the asymmetry for the $K^+\Sigma^-$ differs largely from that for the $K^+\Sigma^0$. The reaction mechanism differs between the two productions. The small asymmetry for $K^+\Sigma^0$ may imply the existence of nucleon resonances in this energy range.

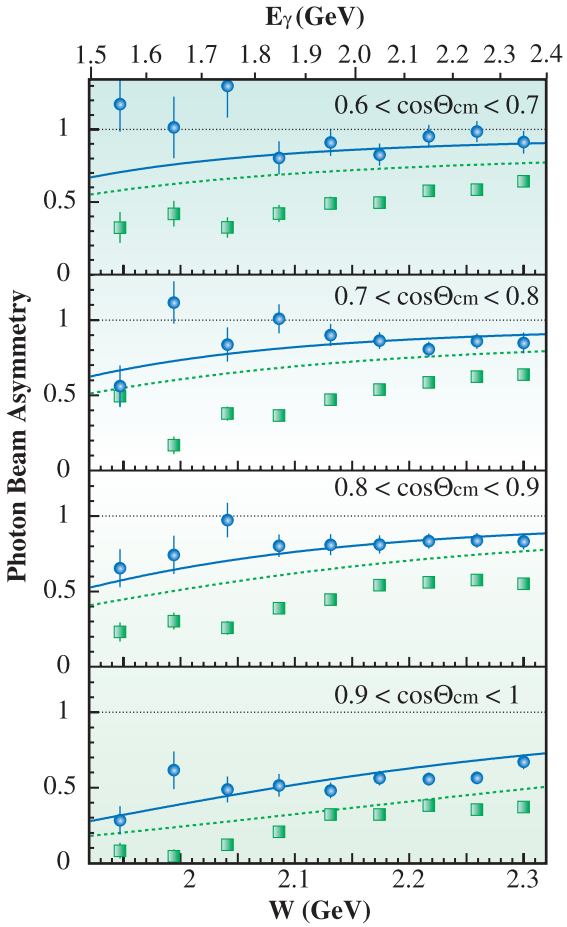

Fig. 2. Photon beam asymmetry for $\gamma n \rightarrow K^+\Sigma^-$ (circles) and $\gamma p \rightarrow K^+\Sigma^0$ (squares). The solid and dashed curves are the Regge model calculations for $K^+\Sigma^-$ and $K^+\Sigma^0$, respectively.

Hideki Kohri for the LEPS Collaboration

Research Center for Nuclear Physics (RCNP),
Osaka University

E-mail: kohri@rcnp.osaka-u.ac.jp

References

[1] *H. Kohri, D.S. Ahn, J.K. Ahn, H. Akimune, Y. Asano, W.C. Chang, S. Daté, H. Ejiri, S. Fukui, H. Fujimura, M. Fujiwara, S. Hasegawa, K. Hicks, T. Hotta, K. Imai, T. Ishikawa, T. Iwata, H. Kawai, Z.Y. Kim, K. Kino, N. Kumagai, S. Makino, T. Mart, T. Matsuda, T. Matsumura, N. Matsuoka, T. Mibe, M. Miyabe, Y. Miyachi, M. Morita, N. Muramatsu, T. Nakano, M. Niiyama, M. Nomachi, Y. Ohashi, H. Ohkuma, T. Ooba, D.S. Oshuev, C. Rangacharyulu, A. Sakaguchi, T. Sasaki, P.M. Shagin, Y. Shiino, A. Shimizu, H. Shimizu, Y. Sugaya, M. Sumihama, Y. Toi, H. Toyokawa, A. Wakai, C.W. Wang, S.C. Wang, K. Yonehara, T. Yorita, M. Yoshimura, M. Yosoi and R.G.T. Zegers: Phys. Rev. Lett.* ***97*** *(2006) 082003.*

Search for Pentaquark Baryon Associated with Photoproduction of Λ(1520) from Liquid Deuterium Target

The LEPS collaboration reported the first evidence of the Θ^+ in a reaction $\gamma C \rightarrow \Theta^+ K^- X$ from a plastic counter [1]. A narrow peak of a baryon resonance was observed at 1.54±0.01 GeV/c^2 in the K^- missing mass spectrum from a neutron by applying a correction to get rid of the Fermi motion effect. This peak was identified as a pentaquark state ($uudd\bar{s}$ = Θ^+) because its strangeness quantum number was +1. Positive observations of this resonance were followed by other experiments, namely, DIANA, CLAS, SAPHIR, bubble chamber experiments, HERMES, ZEUS, COSY-TOF, and SVD-2. On the other hand, many high-energy experiments including BaBar, Belle, HERA-B, SPHINX, HyperCP, CDF, and FOCUS have reported null results. Some of them have set upper limits for the production ratio of Θ^+ to Λ(1520) below a few %. Since the statistical significances in a series of positive observations were not high enough, further confirmation with high statistics data continued in the above experiments. Recently, some of new results have appeared as listed in Ref. [2]. While SVD-2 and DIANA showed positive confirmations, CLAS did not support the earlier observation in a reaction $\gamma d \rightarrow \Theta^+ K^- p$ with 30 times more data. The upper limit for the total cross section was set to 0.3 nb at the 95% confidence level.

The LEPS collaboration has also collected further data with a liquid deuterium target, which includes neutrons. A photon beam was produced at **BL33LEP** by the backward Compton scattering of an Ar laser (7 W, ~351 nm) from 8-GeV electrons in SPring-8. The maximum photon energy reached 2.4 GeV, and photons with an energy higher than 1.5 GeV were tagged by detecting recoil electrons. The liquid hydrogen (LH_2) or deuterium (LD_2) target was exposed to the photon beam at an intensity of ~10^6 /sec. Integrated numbers of tagged photons reached ~3×10^{12} for the LH_2 runs and ~4.5×10^{12} for the LD_2 runs in the years 2002 - 2003. The LH_2 data was collected for calibrations and background studies. Charged particles produced in photoreactions were detected using a forward spectrometer, which consisted of a silicon vertex detector, three drift chambers and a dipole magnet (0.7 Tesla). Particle identification was done by measuring the time-of-flight at a plastic scintillator wall 4 m downstream of the target.

Two charged particles were detected at the forward spectrometer in the LD_2 runs. In the case in which K^+ and K^- were detected as performed in Ref. [1], the Θ^+ was searched for in the K^- missing mass spectrum from a neutron with a correction for Fermi motion. In addition to this detection mode, K^- and a proton were detected so that the Θ^+ was identified in their missing mass from a deuteron without any effect due to Fermi motion. In the present study, the reaction $\gamma d \rightarrow \Theta^+ \Lambda(1520) \rightarrow \Theta^+ K^- p$ was examined in the forward acceptance not as done by the CLAS experiment. The left panel of Fig. 1 shows the $K^- p$ invariant mass distribution. The quasi-free production of $K^+\Lambda(1520)$ is seen above the spectra from non-resonant K^+K^-p and ϕp photoproductions. The right

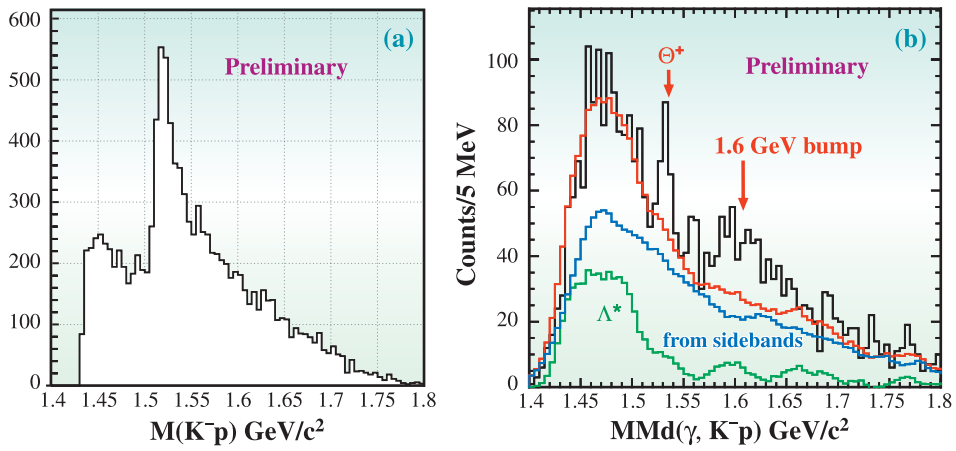

Fig. 1. $K^- p$ invariant mass distribution in LD_2 data and $K^- p$ missing mass spectrum after selecting Λ(1520) production. Background estimates based on side-bands in the real data are overlayed.

panel of Fig. 1 shows the missing mass spectrum of K^-p from a deuteron after requiring that the invariant mass corresponds to the $\Lambda(1520)$ mass (1.50 to 1.54 GeV/c^2). A peak structure was observed at 1.53 GeV/c^2, which corresponds to the Θ^+ signal. MC-based and real-data-based methods, which were complementary to each other, were adopted for reliable estimates of the background spectrum. These methods gave statistical significances of 4-5σ in the missing mass region of 1.520 - 1.545 GeV/c^2. The width of the cut to select $\Lambda(1520)$ production was varied as shown in Fig. 2. The S/N ratio of the peak structure increased with the narrower cut while it dropped with the wider cuts. The peak height was maintained while varying the width. This dependence shows that the peak structure is associated with $\Lambda(1520)$ production. Differential cross sections are being measured in order to compare them with the upper limits from other experiments.

Data collection with a higher intensity photon beam is desired to confirm the existence of the Θ^+ with higher statistics. Currently, additional data is being collected with a beam that is produced by injecting two solid state lasers (8 W, 355 nm) into SPring-8 simultaneously, as shown in Fig. 3. Interference between the two lasers was avoided using 80-MHz quasi-CW lasers. The photon beam intensity has reached 2 × 10^6 /sec. Five to ten times higher statistics is aimed at using the new data. We also

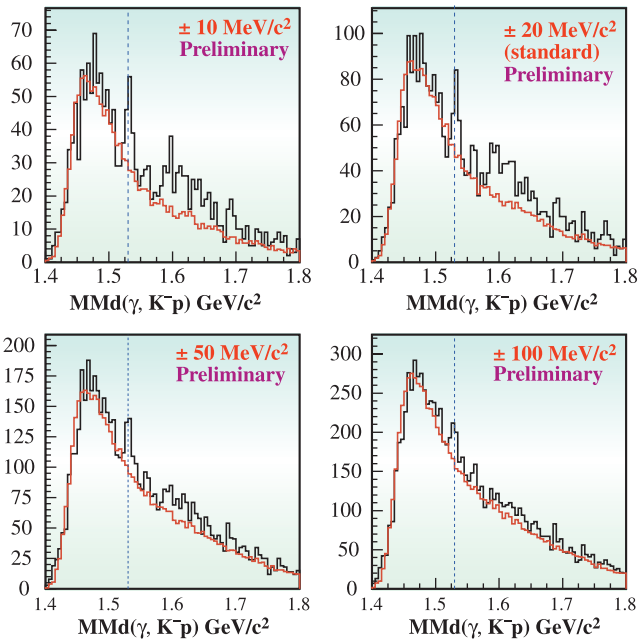

Fig. 2. K^-p missing mass distributions in LD_2 data. The condition to select the $\Lambda(1520)$ photoproduction was varied from ±10 MeV/c^2 to ±100 MeV/c^2. Background spectra from the MC simulations are overlayed.

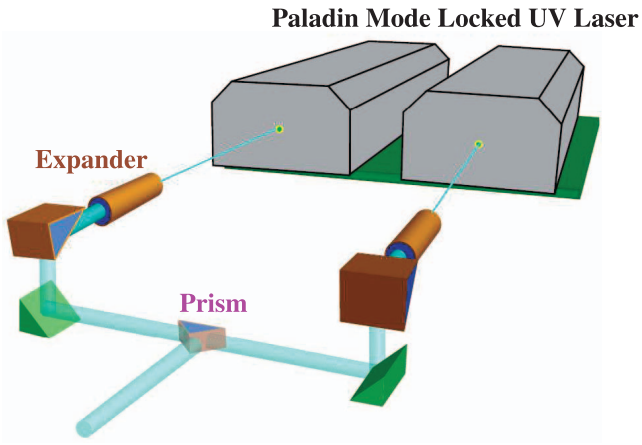

Fig. 3. A schematic view of two lasers injected into SPring-8. Two beam axes were merged at a knife-edge prism after adjusting laser focuses with expanders and mirrors.

plan to cover acceptance regions other than the forward direction. While the final state of the present analysis is similar to that of the CLAS experiment, the acceptance coverage of the K^-p detection is not overlapped. A new time projection chamber has been constructed in order to surround the target, and it is expected to cover both LEPS and CLAS acceptance regions. As a near future project, the construction of a new beamline to produce a higher intensity photon beam has been proposed at BL31ID. We aim to obtain an intensity of ~10^7 /sec by injecting 4 sets of higher power lasers with beam shaping to match the electron beam shape. A good divergence of the electron beam in the straight section will result in better resolution for tagger energy measurement and a well-collimated photon beam to place a large detector system far from the storage ring. High statistics data collection and systematic studies of the Θ^+ photoproduction are expected.

Norihito Muramatsu for the LEPS Collaboration

Research Center for Nuclear Physics (RCNP),
Osaka University

E-mail: mura@rcnp.osaka-u.ac.jp

References

[1] T. Nakano *et al.* [LEPS Collaboration]: Phys. Rev. Lett. **91** (2003) 012002.
[2] A. Aleev *et al.* [SVD Collaboration]: hep-ex/0509033; M. Battaglieri *et al.* [CLAS Collaboration]: Phys. Rev. Lett. **96** (2006) 042001; B. McKinnon *et al.* [CLAS Collaboration]: Phys. Rev. Lett. **96** (2006) 212001; V.V. Barmin *et al.* [DIANA Collaboration]: hep-ex/0603017.

Accelerators & Beamlines Frontiers

Beam Performance

Developments and Upgrades of Storage Ring

Improvement of Top-up Operation

Development of the Bunch current monitor [1]

The bunch current measurement is necessary for equalizing the bunch current of the filling pattern. At present, users demand that the non-uniformity of the bunch current should be less than 10%. To achieve this requirement, we developed the bunch current measurement system. We measured the waveform composed of 2436 RF buckets from a button pickup electrode using a 20 Gs/s oscilloscope. The bunch current is calculated from the minimum peak of the waveform for each bucket. Because the sampling rate (50 ps/point) is not sufficient to obtain the minimum pulse signal (width of approximately 300 ps), we interpolate the measured points and obtain accuracy of less than 1% compared with the measured value of DCCT for the filling pattern of a single bunch. It required about 27 seconds to measure entire bunch current. It is sufficient for top-up injection with a 1-minute interval, but if we reduce the measurement time further, we can stabilize the total beam current more precisely. We therefore improved the performance of the bunch current measurement system. We found that we could reduce the calculation time by utilizing the CPU of a Microsoft Windows computer interfaced with the oscilloscope instead of sending a large volume of data to the workstation. By using this scheme, the measurement time is reduced from 27 seconds to 10 seconds. We also implement function to measure the synchronous phase angle for each bunch, which is vital for time-resolving experiments. Figure 1 shows an example of the measured bunch currents and phase angles.

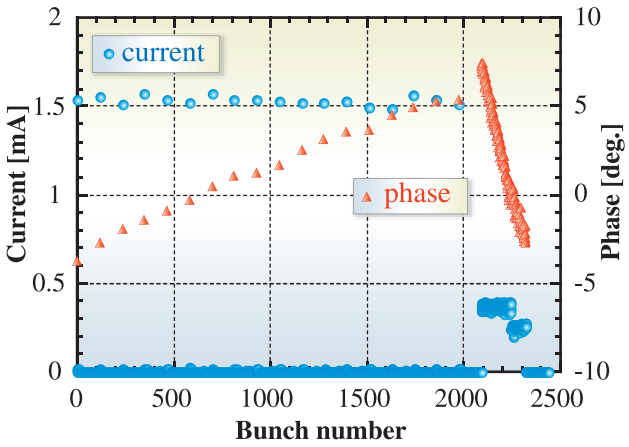

Fig. 1. An example of the measured bunch currents and phase angle in the case of filling mode of a 2/21-partially filled multi-bunch with 18-isolated bunches.

Suppression of Stored Beam Oscillation

Although the total stored current is made constant with high accuracy, the stored beam oscillation generated by the injection bump can cause fluctuations in the photon intensity at the experimental station. At present, the tilt of the bump magnet field is the main source of the vertical oscillation of the stored beam at the beam injection. The SPring-8 storage ring has four pulse bump magnets for beam injection. These magnets were made of 0.1-mm-thick laminated silicon steel of C-type configuration. If the fields of the bump magnets have a tilt against the direction perpendicular to the horizontal plane, the stored beam is kicked by the field and begins to oscillate in the vertical direction. The oscillation lasts until it decays out, thus, it may disturb the experiment that is sensitive to the photon intensity variation although the decay time is in tens of msec. To suppress the oscillation of the stored beam as much as possible, it is necessary to measure precisely the field directions of bump magnets. Using a search coil, we measured the horizontal magnetic field B_x. Then, the tilt angle of the magnetic field is measured by searching the angle at the minimum output voltage from the search coil. The tilt angle of the search coil was calibrated by a dipole magnet of H-type configuration, which has a precise mechanical relation between a pole face and a reference plane for alignment. Because the time evolution of the bump is very fast, we tried to measure the effect of the Eddy current. We measured the frequency dependence of the tilt angle of the magnetic field of the spare bump magnet, as shown in Fig. 2. We will continue to measure the tilt angle for all bump magnets. Based on the results, we will align the

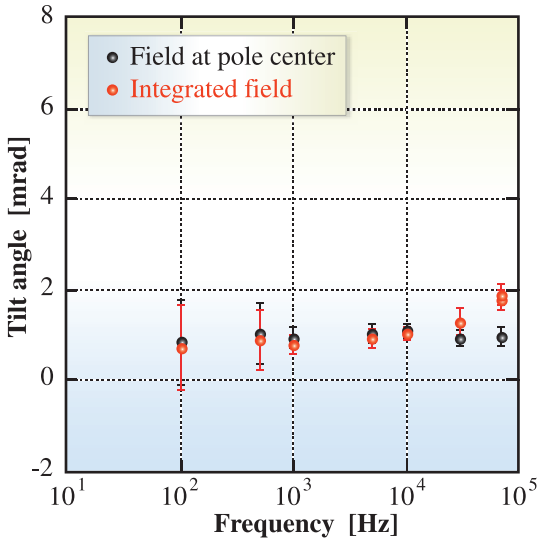

Fig. 2. Frequency dependence of the tilt angle for the bump magnet. Black points indicate the angle of the center of the magnet. Red points indicate the angle of the integrated field along the design orbit.

bump magnets. In addition, we will design the tilt control system for the bump magnets, which is used at a beam-based alignment to suppress the vertical oscillation.

Installation of Counter-Sextupole Magnets in Long Straight Sections

In the summer shutdown of 2000, we had locally removed and rearranged quadrupole and sextupole magnets to realize magnet-free long straight sections [2]. At that time, three unit cells were converted to the matching section, as shown in Fig. 3. The betatron phase advance in this section was set at $2\pi n$, where n is an integer (n=2 in the horizontal direction and n=1 in the vertical direction). Then, if no sextupole magnets are excited in the matching section, this part becomes "transparent," i.e., the electrons at the exit will have the same position and angle as they had at the entrance, and the periodicity of the ring can be kept high even after introducing long straight sections into the ring. This betatron phase matching is effective for obtaining large dynamic apertures and, hence, for realizing beam injection with high efficiency.

Such a phase condition, however, holds only for electrons with a design momentum. Because the beam is focused horizontally in the arc section by strong quadrupole magnets, the effect of chromatic aberration over the matching section is non-negligible. If the local chromaticity is uncorrected, off-momentum electrons receive a different focusing force from on-momentum ones, and betatron phase-slip occurs. As a result, the momentum acceptance of the ring becomes narrow and the Touschek beam lifetime becomes short. To correct the local chromaticity and enlarge the momentum acceptance, we have to excite sextupole magnets in the matching section. This, however, cause a harmful effect on the betatron phase matching and

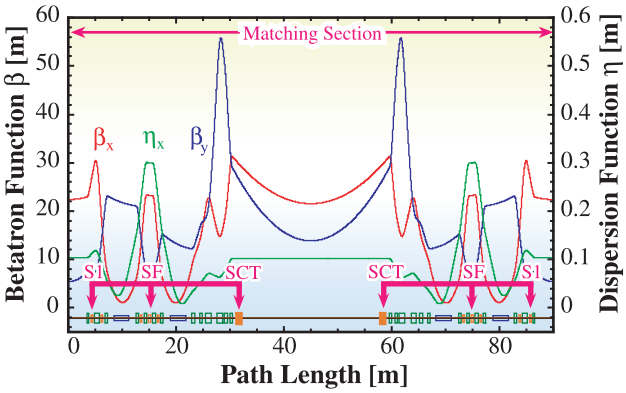

Fig. 3. Linear optics of the matching section and arrangement of the main magnets (blue: bending; green: quadrupole; orange: sextupole).

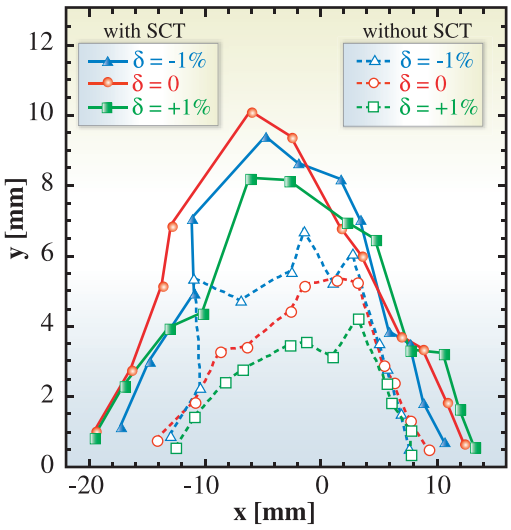

Fig. 4. Dynamic apertures at the injection point before (dashed lines) and after (solid lines) installing the counter-sextupole magnets. The momentum deviation is indicated by δ.

the dynamic aperture becomes smaller. At present, as a compromise, we excite only one family of sextupole in the matching section with a weak strength, labeled "SF" in Fig. 3, and both beam lifetime and injection efficiency are at acceptable levels for top-up operation.

To obtain longer beam lifetime and higher injection efficiency for stable top-up operation, we need to enlarge the dynamic aperture for on- and off-momentum electrons. For this purpose, we have recently developed a new scheme of local chromaticity correction. In this scheme, we use additional sextupoles which cancel nonlinear kicks due to SF in an approximate manner. These are "S1" and "SCT" in Fig. 3, and these are separated from SF by about π in the horizontal betatron phase. The magnet S1 has already been installed from the beginning, and SCT is a new one which we call counter-sextupole. The installation of counter-sextupole magnets will be completed in 2007.

After installing the counter-sextupole magnets, we can make the matching section "transparent" both for on- and off-momentum electrons. This also means that the optics will become more flexible; i.e., it will become easier to independently tune the local optics at each long straight section. This is another advantage of installing counter-sextupole magnets. In Fig. 4, we show the calculated dynamic apertures. The momentum deviation is indicated by δ. We see that the dynamic aperture is enlarged by introducing the counter-sextupole.

Renewal of BPM Electronics

The signal processing electronic circuits of the SPring-8 storage ring beam position monitors (BPM) were replaced during the summer shutdown of 2006. All of the 24 sets of circuits covering the entire ring were replaced at this time to improve the closed orbit distortion (COD) measurement performance.

The electronics are configured to measure the amplitude of the single component of 508.58 MHz, which is the RF acceleration frequency, in the signal induced on the electrodes by the electron beams (Fig. 5). The input signals from 12 electrodes of 3 BPMs are multiplexed in the switch-filter module, and processed in one common path of the circuits. One set of the circuits is composed of four of these paths. After the multiplexing stage, signals go through band-pass filters (BPF) to select the RF acceleration frequency component in the pickup signals. The selected narrow-band RF signals are amplified and down-converted to 250 kHz intermediate frequency (IF) signal, amplified with variable-gain IF amplifiers, and sampled by 16-bit 2MSPS (mega samples per second) ADCs. Finally, the signal amplitudes are calculated in digital signal processors (DSP) using the digital data sampled by ADCs. In addition, the DSP has the following three functions: calculating the beam positions, setting the gain of the IF amplifier and switching the multiplexer, and communicating with the control system of the accelerator complex.

During the usual operation for user experiments, the position data are averaged for 100 times in the DSPs to improve the position resolution. It takes about 3 seconds to process all of the BPM around the entire ring. Since the old circuits, which were used until the 2006 summer shutdown, require more than 20 seconds to measure beam positions of the entire ring, the measurement speed improved by a factor of 7.

We continuously measured the COD every four seconds in order to estimate the position resolution; the differences in the two consecutive measurements were calculated to obtain the root mean square (r.m.s.) value of over a hundred measurements for each BPM. The r.m.s. value of each BPM includes the intrinsic resolution of the measurement system and also the movement of the COD between the two consecutive measurements. Figure 6 shows the r.m.s. values against the BPM serial numbers. A characteristic pattern appears in the graph. It seems that this pattern relates to the betatron function values. The square root of the betatron function values are also plotted in the same graph. The pattern observed in the r.m.s. values agrees well with the square root of the betatron function values when scaled and shifted properly.

We can postulate a model showing that the measured r.m.s. values can be decomposed to the intrinsic resolution and the effect of beam motion whose amplitude is proportional to the square root of the betatron function values at the BPM locations. According to the decomposition model, the measured r.m.s. values are expressed as

$$\sigma_i^2 = \sigma_0^2 + \sigma_{\mathrm{COD}_i}^2 = \sigma_0^2 + \varepsilon_0 \times \beta_i ,$$

where σ_i is the measured r.m.s. value of the i-th BPM, σ_0 is the intrinsic resolution, $\sigma_{\mathrm{COD}i}$ is the r.m.s. of the effect of the COD movement at the i-th BPM, β_i is the betatron function value at i-th BPM, and ε_0 is the proportionality constant. The assumptions in the model are that the intrinsic resolution is common to all of the BPM, the amplitudes of the COD motion are proportional to the square root of the betatron function values, and there is no correlation between the intrinsic resolution and the COD motion terms.

We plotted the squares of r.m.s. against the betatron function values as in Fig. 7, and carried out regression analysis with linear model as $\sigma^2 = a + b \cdot \beta$, where σ^2 is the measured r.m.s., β is the beta function value, a and b are the fitting parameters. The parameter a interests us; the

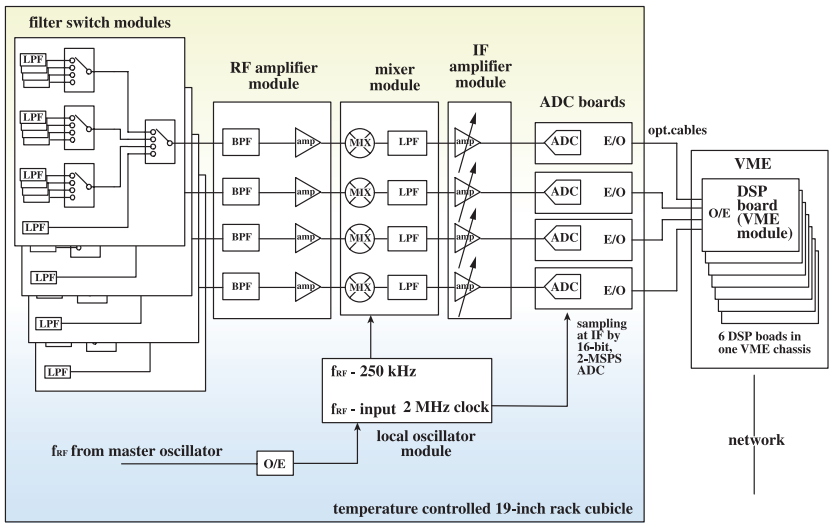

Fig. 5. Block diagram of one set of the signal processing circuits.

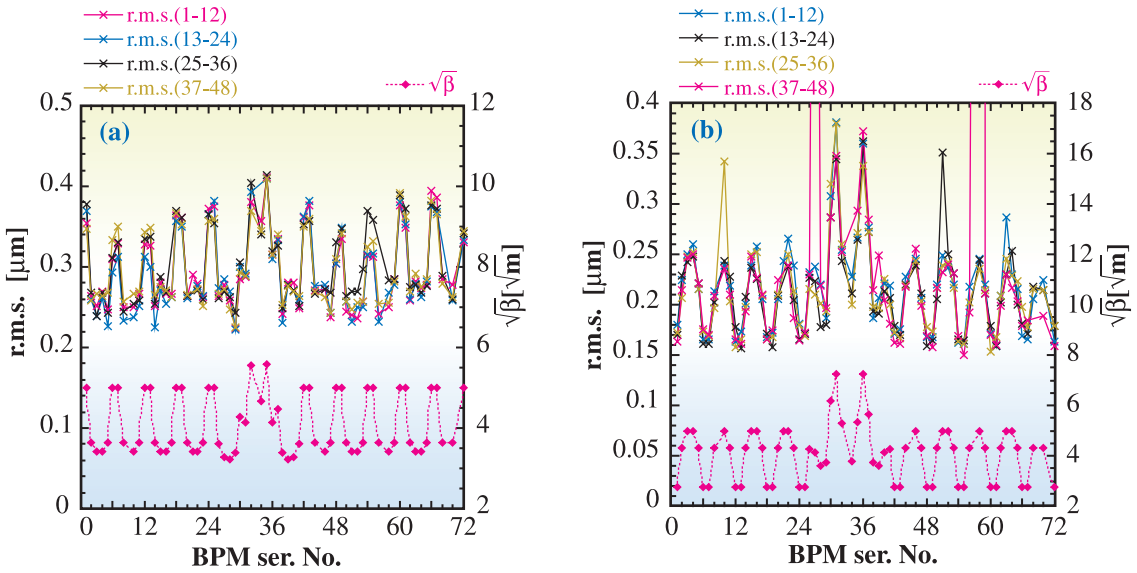

Fig. 6. The r.m.s. values of the difference in two consecutive COD measurements over 100 times against the serial number of BPMs (left axis). The plots are 4-folded, because the storage ring has a 4-fold symmetry in the lattice structure. The square root of the betatron function values are also plotted (left axis). **(a)** horizontal direction, **(b)** vertical direction.

obtained parameters are 0.017±0.002 μm^2 in the horizontal direction and 0.010±0.001 μm^2 in the vertical direction, respectively. From these values, we estimated the intrinsic resolution as 0.130±0.008 μm for horizontal and 0.100±0.005 μm for vertical directions. Rounding to one decimal place, the intrinsic resolution was found to be 0.1 μm.

For comparison, we performed a similar analysis for the data taken with the old signal processing circuits, and obtained a resolution 0.28±0.04 μm for the horizontal direction. For the vertical direction, we could not observe the distinct betatron function dependence pattern; the cause was not clear. Therefore, no values were obtained in the vertical direction by this method. By rounding to one decimal place, the resolution was found to be 0.3 μm for the old circuit. By comparing the intrinsic resolutions of the old and the new circuits, the resolution improved by a factor of three.

We observed bunch filling pattern dependence in the order of a few tens μm. The cause was attributed to the effect of the partial conduction of the diodes that were put to protect against very high voltage inputs to the multiplexer ICs; because of this, the linearity of the circuit response was degraded. The solution to this problem would be to put BPFs at the input to the multiplexer to eliminate the unnecessary components of the electrode signals, and lower the peak of the input voltage. The addition of the BPFs is expected to be carried out in a year or two. Further improvement is necessary to overcome the filling pattern dependence.

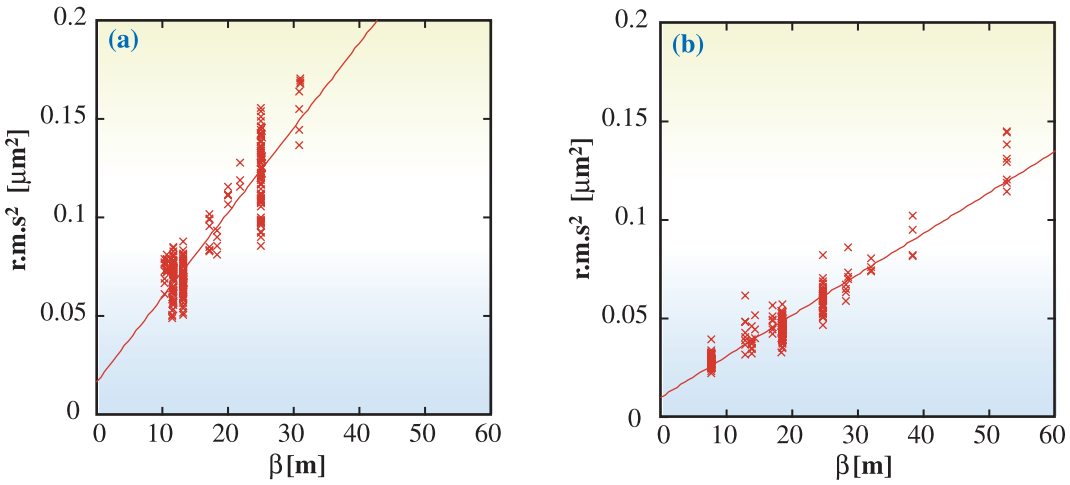

Fig. 7. The squares of measured r.m.s. values against betatron function values. The straight line is the fitting result with linear function. **(a)** horizontal direction, **(b)** vertical direction.

Development of Accelerator Diagnosis Beamlines

The accelerator diagnosis beamline I (BL38B2) has a bunch purity monitor to evaluate the purity of the main bunches of several-bunch operation modes [3] and an X-ray beam imager for beam emittance diagnosis [4]. The data acquisition system of the bunch purity monitor and the X-ray beam imager was developed for real-time beam monitoring. The bunch purity monitor is now continuously monitoring the electron beam of the user experiments under top-up injection. The continuous operation of the X-ray beam imager is suspended because of the degradation of the input photocathode of the X-ray zooming tube.

A study on the production of γ-ray photons in the energy range of 10 MeV has been performed at the diagnosis beamline I [5]. The MeV γ-rays are generated by the backward Compton scattering of optically pumped far-infrared (FIR) laser photons from 8 GeV electrons in the storage ring. Figure 8 shows the measured energy spectra under the conditions of "FIR laser on" and "FIR laser off". The MeV photons and synchrotron radiation less than 2 MeV were electrically discriminated by the detection circuits. Figure 8 also shows the net MeV γ-ray spectrum deduced by subtracting the "FIR laser off" spectrum from the "FIR laser on" spectrum. The estimated MeV photon production rate is 2×10^3 photons/sec per FIR laser output power of 1 W.

The construction of the accelerator diagnosis beamline II (BL05SS) is in progress. The front end and the radiation shielding hutches have already been completed, and now, the so-called edge radiation from the bending magnets upstream and downstream of the ID straight section of the beamline can be delivered to the optics hutch I. To study the coherent synchrotron radiation in the wavelength region comparable to the bunch length, the intensity of the microwave component of the edge radiation was measured as functions of the bunch length and the bunch current. A significant correlation between the microwave intensity and the bunch length was observed. To start the commissioning of the ID, which was installed in the summer of 2005, the steering magnets of the ID were tuned for various magnet gaps. The development of the vacuum components of the optics hutches I and II is in progress. The components of the optics hutch I, such as the movable mirror to pick off-the-edge radiation, the masks, the graphite filters, the metal filters, and the absorber, have been completed. The screen monitor and the double crystal monochromator, which is to be installed in the optics hutch II, are under development. The x- and y-slits to shape the input X-ray beam of the monochromator, which are to be added to the front end, are also under development.

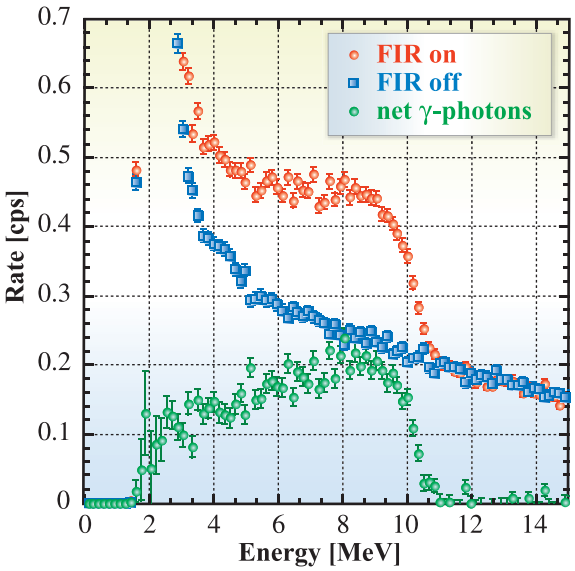

Fig. 8. Measured energy spectra of MeV γ-rays generated by backward Compton scattering.

To produce highly intense MeV γ-ray photons, an advanced plan of laser Compton scattering is in progress at the diagnosis beamline II, which has a straight section suitable for interaction between FIR laser photons and 8 GeV electrons. The expected production rate of MeV photons is more than 10^5 photons/sec. The construction of the laser clean room and the installation of the wave guide system for the transport of the FIR laser have been completed.

Development of New Gate Valve with a Comb-type RF Shield

One of the limitations of the bunch current is the increase in temperature of the finger-type RF shield of gate valves. The finger-type RF shield, which is made from BeCu, is attached for the smooth streaming of the wall current induced by the electron beam. The contact force of BeCu decrease because of the creep phenomena, if its temperature increases to 150°C. The reduction in contact force of BeCu induces more temperature increase, and finally, the finger-type RF shield will break, and the gate valve will not work. For example, the temperature of the finger-type RF shield increases to more than 80°C with the 203 bunches operation.

To realize the high-bunch current operation, it is necessary to develop a gate valve with a new type of RF shield. KEK already developed the gate valve with a comb-type RF shield, and it is used in the KEK B-Factory [6]. We tried to apply the comb-type RF shield to a new type of gate valve in collaboration of KEK (Fig. 9). A prototype of the gate valve with a comb-type RF shield will be manufactured by March 2007, and several tests will be scheduled.

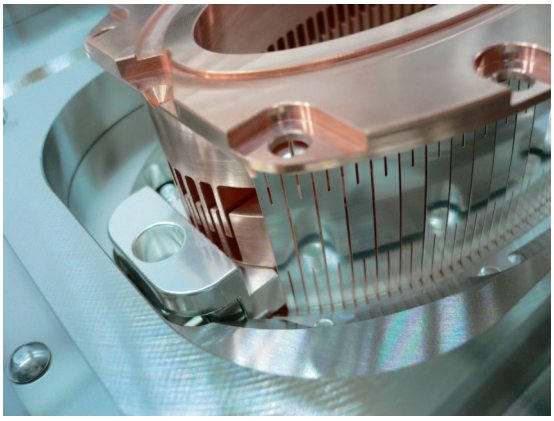

Fig. 9. Comb-type RF shield for SPring-8 gate valve.

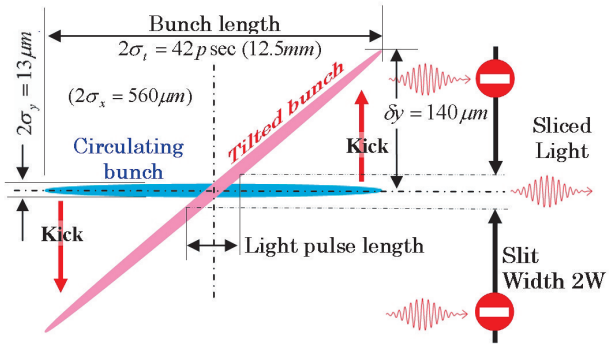

Fig. 10. Principle of FSX generation. A circulating electron bunch is kicked and tilted by RF deflectors. A portion of the emitted X-ray can pass through the slit. The bunch size and tilting are values for 8 GeV.

Development of Femtosecond Pulse X-ray Generation

The SPring-8 storage ring has a very small vertical bunch size. By using this feature, it is possible to generate a femtosecond pulse X-ray (FSX) by the bunch slicing method [7,8]. The achievable performance of the X-ray has been estimated for the operating conditions of the storage ring by installing four superconducting RF deflectors and a minipole undulator. The calculated pulse width, flux density and X-ray energy are 600 fsec in two standard deviations, 8.483×10^{15} photons/(sec • mrad^2 • 0.1%BW • 100 mA), and 10.7 keV, respectively, for 4 GeV operation.

On the other hand, problems are discussed and their countermeasures are developed to realize the FSX generation. The required phase stability among the RF deflectors was determined to be as small as 14.1 mdeg, and the mechanical vibration of cavities was considered as the main phase instability source. The phase stability of a superconducting cavity under operation at KEK was studied to confirm the analytical vibration model and to determine points of issue such as vibration sources. A high-speed and high-power phase shifter has been developed as a phase control device. Its phase control speed of 1 kHz at the 3 dB down point with a ±1-degree span has been obtained in a 300-kW power test. This year, the basic principle of FSX and a conceptual design are presented and details of the development will be reported next year.

The principle of FSX generation is shown in Fig. 10. The electrons in a bunch circulating in the storage ring have a three-dimensional Gaussian distribution. The bunch size in two standard deviations is 560 μm in the horizontal, 13 μm in the vertical, and 12.5 mm (42 psec) in the longitudinal or the traveling direction. If this bunch is tilted, as shown in Fig. 10, the X-ray emitted from each part of the bunch is vertically separated; the X-ray from the head of the bunch travels in the upper space, and that from the tail in the lower space. If we place a slit along the X-ray path, as Fig. 10, we can obtain a short pulse of X-ray emitted only at around the center of the bunch, and the other parts from the head and tail are blocked out. This method enables a storage ring to generate FSX whose pulse width is much shorter than its bunch length. In Fig. 10, the electrons do not collide with the slit if the slit is placed away from the electron orbit.

We have four 27-m magnet-free sections, called long straight sections, in the storage ring. Figure 11 shows an example of FSX generator installed in one of the long straight sections. In this figure, we configured four RF deflectors and an insertion device. The bunch enters into the FSX generator from “A” in Fig. 11; its head and tail are kicked to the opposite side by the first deflector “Def1.” The bunch then rotates in the drift space “B”, and its rotation is stopped by the second deflector “Def2.” In the insertion device, the bunch emits X-ray in a stationary tilted position, and its tilting is returned back to the initial position inversely by “Def3” and “Def4,” which are placed in a symmetric position as “Def2” and “Def1.” The bunch has neither rotation nor tilting at exit “A' ” of the FSX generator. Although a four-deflector design is shown here for easy understanding, another low-cost two-deflector design would be possible if “Def2” and “Def3” are replaced with two quadrupole magnets.

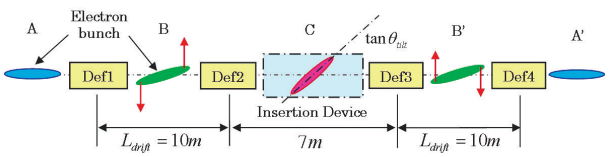

Fig. 11. Conceptual design of FSX generator. Four RF deflectors and an insertion device are installed in the 27-m-long straight section.

Developments and Upgrades of Linac

High Power RF Backup System [9]

The linac is equipped with thirteen 80 MW pulse klystrons (E3712, Toshiba Electron Tubes & Devices Co.,Ltd). All the klystrons are feeding RF power (10 pps) to the accelerating structures, and two are intermittently disabled by the trigger system in synchrony with the beam trigger signals (1 pps) to avoid beam accelerations. That is, eleven of the klystrons have usually been used to accelerate electron beams to 1 GeV, and the other two have been kept for hot spares on line.

Except for the primary and ECS's klystrons, when one of the eleven working klystrons fails and it cannot recover within a few minutes, a standby klystron is activated to accelerate the beams instead of the failed one. A serious failure of the primary klystron, however, completely stops the linac operation for a long time because it feeds RF power to the injector section of the linac and the long drive line for the other eleven klystrons.

We therefore constructed a backup system for the primary klystron to feed RF power from the second klystron to the injector, as shown in Fig. 12. The backup system is composed of waveguide circuits, a high-power waveguide switch, and its control system. The waveguide switch, the key component of this system, was developed based on the design of a commercial waveguide switch manufactured by Nihon Koshuha Co., Ltd.

High-power waveguide switches (rotary E-bend type) are widely used in accelerators but most are used in SF6 gas. In the SPring-8 linac, high-power waveguides are used in a vacuum except for the bunching section. Therefore, a vacuum-type waveguide switch is preferred for this backup system. A 10 MW waveguide switch used in a vacuum has been developed by Nihon Koshuha Co., Ltd. We improved this waveguide switch to transmit higher peak and average RF power. Relevant improvements are listed below:

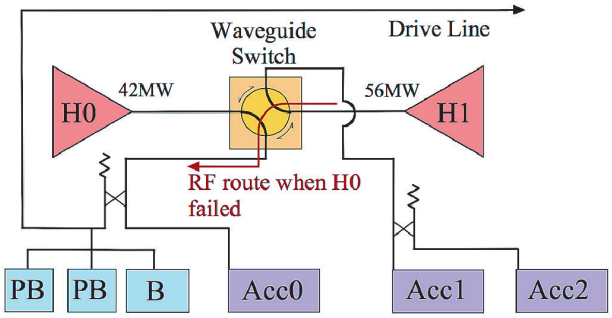

Fig. 12. New backup system for primary klystron H0.

- The bonding method for the rotor (material: OFC C1011, Hitachi Cable, Ltd.), fabricated in halves, was changed from bolt connection to diffusion bonding. This prevents air voids between bonding surfaces and contributes to UHV stability.
- The surface of the rotor was processed by an electropolishing method to remove microstructures and minimize the possibility of vacuum RF discharges in the waveguide switch.
- A rotor cooling system was fabricated as illustrated in Fig. 13. A copper rod is firmly attached to the rotor to conduct the heat due to RF power loss. The rod is detached from the rotor during rotation.
- A vacuum evacuation port was added to enhance pumping speed in the choke groove and in the thermal conductor chamber.

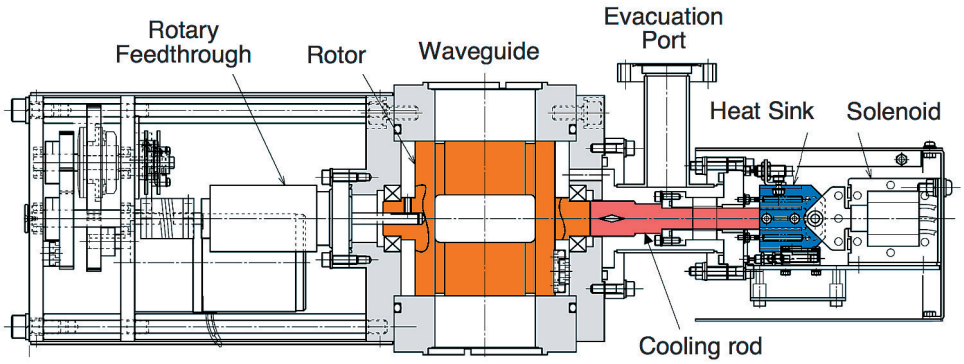

Fig. 13. Structure of waveguide switch.

After a high-power test of the waveguide switch at the RF gun test stand, in February 2006, the waveguide switch was installed between the high-power waveguide circuits of the first (H0) and second (H1) klystrons to establish the backup system.

RF conditioning was performed for seven days in the daytime with an increased repetition rate of 60 pps (normally 10 pps). After conditioning for 24 hours, the peak power of the H0 klystron reached a normal level (50 MW), and the drive power for the other klystrons became sufficient. The RF power of the second klystron reached a maximum of 74 MW after conditioning for 56 hours. Under this condition, the power loss in the rotor of the waveguide switch was estimated at 10 W, and the temperature of the heat-sink at the outer end of the thermal conductor of the waveguide switch became 42°C based on an actual measurement.

Thus, the availability and reliability of the high power RF system in the SPring-8 linac have been enhanced with the construction of this backup system. In 2007, we will install a backup electron gun to increase total reliability.

Development of Photocathode RF Gun - Laser pulse stacker forming long light pulse [10]

To minimize the beam emittance of a photocathode RF gun, the laser pulse shape should be optimized three-dimensionally. One of the candidates of reliable 3D laser pulse shape is cylindrical (spatially top-hat, and temporally rectangular pulse). In the test facility of the photocathode laser light source at SPring-8, several 3D shaping systems have been developed as a combination of spatial (transverse: x-, y-axes) and temporal (longitudinal: z-axis) pulse-shaping methods in the last 5 years. The spatial profile has been reformed with a microlens array or a deformable mirror (DM). The temporal profile has been formed with a spatial light modulator (SLM) or a light pulse stacker.

A pulse stacker forms a long light pulse by stacking short light pulses. The pulse stacker developed in SPring-8 is composed of three stages: a pulse doubler unit, which consists of a pair of polarizing beam splitters, a half-wave plate, and a movable corner reflector to adjust an optical delay. The optical system was designed to alternate s- and p-polarization in the final light pulse train in order to avoid optical interference between the adjacent light pulses, as illustrated in Fig. 14.

A pulse doubler unit works as follows: The fully s-polarization of a laser pulse is rotated to 45-degree polarization with the half-wave plate. It is divided into s- and p-polarized pulses with the first polarizing beam splitter. The p-polarized pulse is delayed with the optical delay line and then recombined with the s-polarized pulse with the second beam splitter to form a double pulse light. That is, the laser pulses of 2.5 ps were successively doubled at each stage to generate a longer pulse train. The dispersion of the downstream optical system broadens each micropulses of the pulse train and consequently results in a single rectangular shape pulse. Stacking eight micropulse in the three stages, we can obtain a 20-ps width pulse. The quality of the laser pulse stacking was verified by observing electron bunch shapes as described below.

We adjusted the optical delay lines and verified the

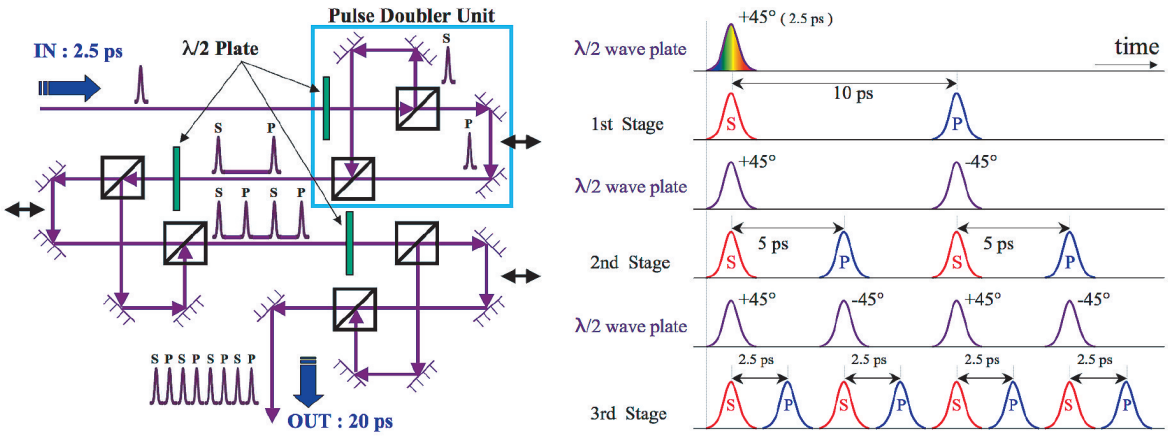

Fig. 14. Optical system (left) and timing chart (right) of UV-laser pulse stacker.

temporal profile of the stretched laser pulse, observing the projection of the temporal profile of an electron bunch as follows [11]: When the RF phase is tuned at an appropriate value to provide temporal (longitudinal) energy gradation to a bunch, the temporal distribution of the bunch is projected to the beam energy distribution which can be easily measured. Figure 15 shows examples of the beam energy distributions on a fluorescence screen downstream of a bending magnet as an energy analyzer. This method determined the absolute zeros of the optical delay lines with a good precision of about 0.5 ps, which was evaluated from the beam position jitters observed on the screen caused by the RF phase fluctuation.

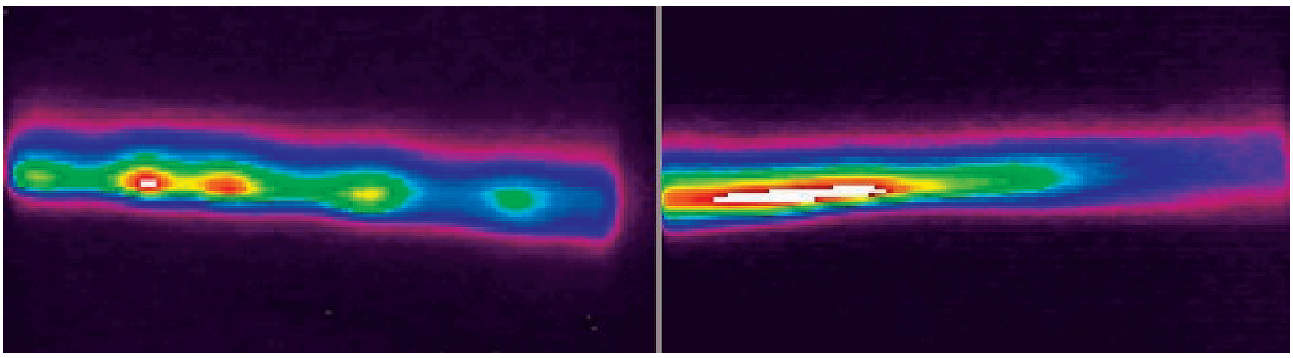

Fig. 15. Examples of the energy distributions of a 20 ps bunch on a screen monitor. The left profile in the process of optical adjustment shows discrete laser pulses, whereas the right case shows that the laser pulses were almost perfectly aligned to form a long light pulse.

Haruo Ohkuma*, Hiroto Yonehara and Hirofumi Hanaki

SPring-8/JASRI

*E-mail: ohkuma@spring8.or.jp

References

[1] T. Ohshima *et al.*: Proc EPAC2006, Edinburgh, Scotland, p.1133.
[2] H. Tanaka *et al.*: Proc. EPAC2000, Vienna, Austria, p.1086.
[3] K. Tamura *et al.*: Proc. of 1st Annual Meeting of Particle Accelerator Society of Japan and 29th Linear Accelerator Meeting in Japan, Funabashi, 2004, p.581.
[4] S. Takano *et al.*: Nucl. Instrum. Meth. A **556** (2006) 357.
[5] H. Ohkuma *et al.*: Proc. EPAC2006, Edinburgh, Scotland, p.961.
[6] Y. Suetsugu *et al.*: Proc. PAC2005, Knoxville, Tennessee, p.3203.
[7] M. Katoh: Jpn. J. Appl. Phys. **38** (1999) L547.
[8] A. Zholents *et al.*: Nucl. Instrum. Meth. A **425** (1999) 385.
[9] T. Taniuchi *et al.*: Proc. EPAC2006, Edinburgh, Scotland, p.1397.
[10] H. Tomizawa *et al.*: Russian Journal of Quantum Electronics (2007) - to be published.
[11] H. Dewa *et al.*: Proc. FEL'06, Berlin, Germany.

New Apparatus & Upgrades

Status of Engineering Research Science II Beamline BL14B2

By promoting the synchrotron radiation utilizations in the industrial field since fiscal 2000, the number of SR users increased in industrial applications using XAFS, powder diffraction, imaging, fluorescent X-ray analysis. We already have several public beamlines for XAFS (**BL1B1**), powder diffraction (**BL02B2**), and engineering research science (**BL19B2**) for industrial applications. However, the insufficiency of beam time particularly for XAFS and powder diffraction users is a serious problem. Thus, RIKEN and JASRI decided to fund and construct a new public beamline of XAFS for industrial applications at the bending magnet section **BL14B2**. We started the conceptual design of the beamline in fiscal 2005 and started construction in fiscal 2006.

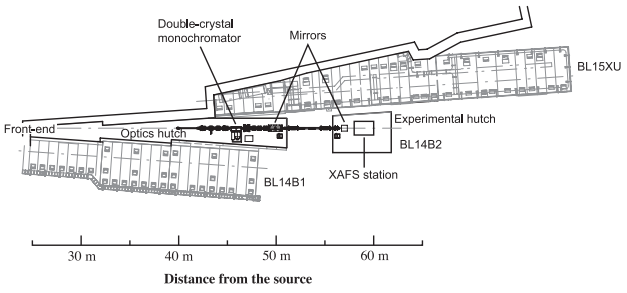

Fig. 1. Layout of beamline BL14B2.

Figure 1 shows the beamline layout including shielding hutches, optics and a transport channel, and the experimental station. The beamline component layout is similar to the layout of other SPring-8 standard bending magnet beamlines. The main optics components are the standard double-crystal monochromator and total-reflection mirrors for higher-harmonics rejection. The double-crystal monochromator and first mirror are installed in the optics hutch (Fig. 2). Silicon 111, 311 and 511 reflections cover the photon energy region from 5 to 100 keV. For higher-harmonics rejection, double-rhodium-coated mirrors can be set with glancing angles from 2 mrad up to 8 mrad depending on photon energy. They can also be taken from a direct beam path for higher energy utilization. An experimental hutch 6 m long × 4 m wide × 3.3 m high was constructed 4.7 m downstream of the optics hutch. The photon beam is guided through a lead-shielded beam duct between the hutches. The reflected beam from the first mirror is followed by the second mirror placed in the experimental hutch.

Fig. 2. Components of optics hutch. The SR beam comes from the left. The double-crystal monochromator (left), first mirror (right), and other beamline components (e.g. shutter and slit) between them can be seen.

In the experimental hutch, basic equipment for XAFS will be installed (Fig. 3). Transmission XAFS and fluorescence XAFS can be performed. Sample stages, attachments for sample environments, various detectors of germanium SSD, a silicon drift detector, and ionization chambers are installed on the table.

The beamline construction was completed in fiscal 2006. Commissioning started at the end of February 2007 and user operation will start in September 2007.

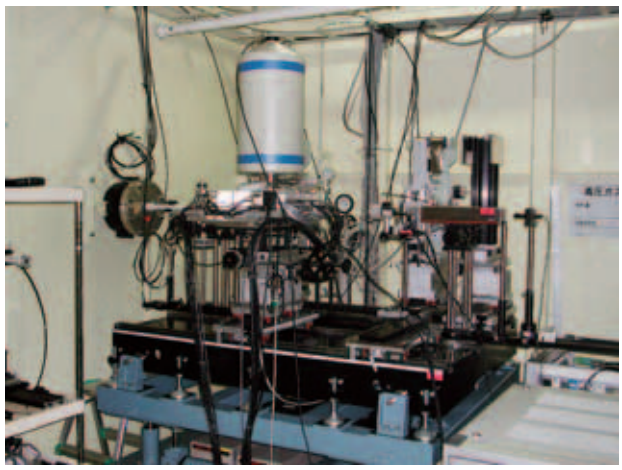

Fig. 3. Equipments of XAFS in experimental hutch (to be installed).

Shunji Goto

SPring-8 / JASRI

E-mail: sgoto@spring8.or.jp

Diamond Double-crystal Monochromator for SPring-8 Undulator Beamlines

A high-heat-load monochromator has been a key optical component for the undulator beamlines of the third-generation synchrotron facilities. In 1997, we installed silicon double-crystal monochromators for all standard the undulator beamlines of SPring-8 [1]. The first crystal with a pin-post cooling channel was directly cooled by water [2]. In 2000, we developed a closed-loop circulation system of liquid nitrogen (LN_2) with helium refrigerators [3]. This LN_2 cooling system was installed for a number of beamlines by 2005, because we can simply use a silicon block in contact with a copper block in the LN_2 temperature range (i.e., indirect cooling). However, a serious drawback is the high cost for installation, running, and maintenance.

Diamond crystal has been considered as one of the best candidates for a high-heat-load monochromator. Diamond shows a high transmissivity of X-rays and an excellent thermal property, which is evaluated using the ratio of thermal conductivity to thermal expansion. This ratio for diamond at room temperature (RT) is ~30 times better than that for silicon at the RT. Thus, diamond can manage an incident power of hundreds of watts simply by indirect cooling by water, which enables a high-performace, moderate-cost monochromator. Diamond is also promising as a monochromator of X-ray free-electron laser (XFEL), because only hard materials consisting of light elements are sustainable under strong irradiation.

We have installed diamond double-crystal monochromators to upgrade three undulator beamlines (**BL09XU**, **BL10XU**, **BL39XU**) of SPring-8 by 2006. High-quality diamond (111) crystals in type IIa, which are the results of a collaboration with Sumitomo Electric Industries Ltd. [4], have been mounted on copper crystal holders in the Bragg geometry. The typical size of the crystal is 10 × 4 × 0.4 mm^3. An edge-cooling design was adopted to reduce excess heat load from undiffracted X-rays. Special attention has been paid to crystal mounting. A thermal mounting method, which employs a heated indium sheet for glue, was developed to maintain a sufficient thermal contact with a negligible mounting stress [5].

Moreover, a new monochromator mechanism was installed to upgrade BL39XU in the spring of 2006 (Fig. 1). A notable departure from the SPring-8 standard monochromator (SSM) mechanism [1] is (i) a Bragg angle range of 4.5 to 45 degrees (3 to 27 degrees for the SSM), which corresponds to a photon energy range of 4.3 to 38.3 keV with diamond 111 diffraction. The energy range is the same as that of the SSM with silicon 111 diffraction. This modification enables us (ii) to design the translation mechanism of the first crystal to be compact and (iii) to omit an additional weight-compensation mechanism possibly resulting in instability.

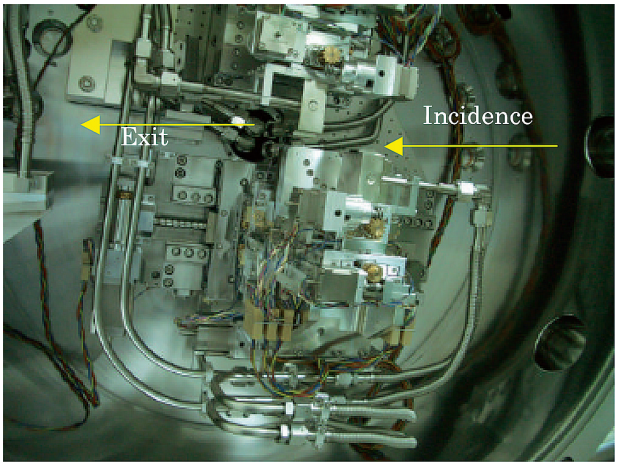

Fig. 1. Mechanism of diamond double-crystal monochromator.

Detailed performance was evaluated at BL39XU [5]. Figure 2 shows the photon flux of the monochromatic beam measured at the exit of the Be window. The size of the front-end slit was 1.0(h) × 0.7(v) mm^2 with a storage-ring emittance of ε = 3 nm·rad. The agreement between the measurement and a calculation carried out by the simulation code SPECTRA is excellent below 20 keV. For a comparison, the flux with the LN_2 cooled silicon DCM was measured at **BL29XU**. The flux of the diamond reaches 60% of that of the silicon.

Figure 3 (a) shows deconvoluted angular widths $\Delta\theta_d$ from the measured rocking curve width to the calculated width. $\Delta\theta_d$, which relates to lattice distortion, is nearly constant with the photon energy (the incident power). In particular, $\Delta\theta_d$ at E = 15 keV with the third and the first harmonic radiations is unchanged; however, the incident power of the former (370 W, a power density of 450 W/mm^2) is four times larger than that of the latter (below 100 W), as shown in Fig. 3 (b). The thermal deformation of the crystal is negligible even at a high heat load.

We investigated a long-term angular stability by repetitive measurements of the rocking curve of the first crystal. The angular shift of the first crystal, measured with a front-end slit size of 0.5 × 0.5 mm^2 (an incident power of 95 W), is kept smaller than 1 μrad after the 3 hour irradiation. This level is sufficiently acceptable for high-resolution spectroscopic experiments.

We conclude that the diamond monochromator is a reasonable alternative to the LN_2-cooled silicon monochromator, when considering the balance between the final performance and the required cost, particularly for spectroscopic and diffraction applications at the energies lower than 20 keV.

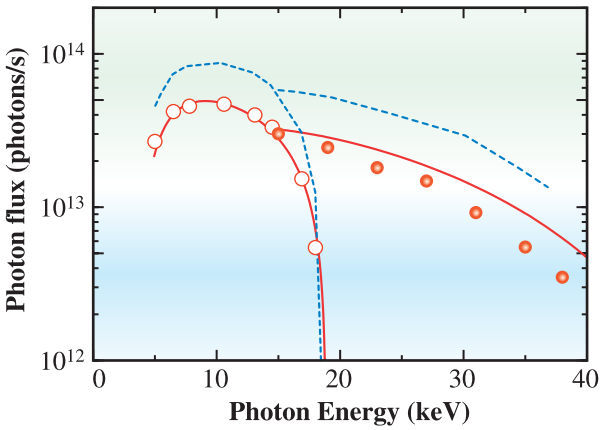

Fig. 2. Photon flux of monochromatic beam with diamond DCM. The open (solid) circles show the measured flux for the first (third) harmonic of the undulator radiation, and the red solid line shows the calculated flux. The blue dashed lines are the measured results for the LN_2-cooled silicon monochromator.

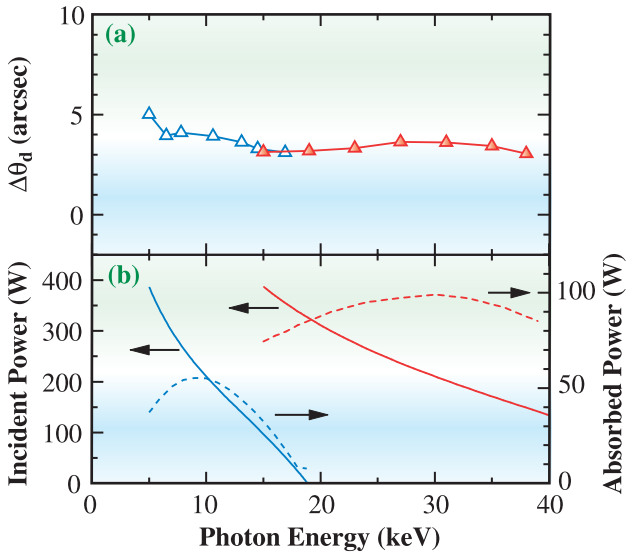

Fig. 3. **(a)** Deconvoluted rocking curve widths *vs* photon energy. The open triangles (the solid triangles) are for the first (third) harmonic radiation. **(b)** Incident power (solid line, left axis) and absorbed power (dashed line, right axis) *vs* peak photon energy. The blue (red) line shows the result for the first (third) harmonic radiation.

Makina Yabashi*, Shunji Goto and Motohiro Suzuki

SPring-8 / JASRI

*E-mail: yabashi@spring8.or.jp

References

[1] M. Yabashi *et al.*: Proc. SPIE **3773** (1999) 2.
[2] M. Kuroda *et al.*: J. Synchrotron Rad. **5** (1998) 1211.
[3] T. Mochizuki *et al.*: Nucl. Instrum. Meth. A **467-468** (2001) 647.
[4] K. Tamasaku *et al.*: J. Phys. D **38** (2005) A61.
[5] *M. Yabashi, S. Goto, Y. Shimizu, K. Tamasaku, H. Yamazaki, Y. Yoda, M. Suzuki, Y. Ohishi, M. Yamamoto and T. Ishikawa: AIP Conf. Proc.* ***879*** *(2007) 922.*

Facility Status

General

The year 2006 was characterized by a transition of the legal framework of SPring-8 and a series of important reviews that determine the direction in which SPring-8 will proceed. Therefore, it should be noted that this report will inevitably contain some inaccuracies in describing the current status of SPring-8, since the consequent reformation was still in progress at the time of writing this report.

Legal Framework Transition

The Japan Atomic Energy Research Institute (JAERI) relinquished responsibility for the operation and management of SPring-8 in 2005. Since then, RIKEN and the Japan Synchrotron Radiation Research Institute (JASRI) have been operating and managing SPring-8 in a unified manner as the owner and operator/manager of the facility after being uniquely appointed in accordance with the "Law on the Promotion of Public Utilization of the Specific Synchrotron Radiation Facilities," respectively. However, this law was amended from the viewpoint of securing fairness and transparency, limiting the affairs of JASRI to only selecting user proposals, utilizing the facility and providing support, thus excluding JASRI from operating SPring-8. This amendment was put into effect on July 1, 2006.

Under the amended law, JASRI has been positioned as one of the official candidates for selecting user proposals, facilitating the utilization, and supporting the users at SPring-8, and was appointed as the body in charge of these duties for the remaining period of FY2006 as a transitional measure. An examination will be conducted by the Ministry of Education, Culture, Sports, Science and Technology (MEXT) to appoint the appropriate body/bodies for such duties in 2007 from the registered candidates.

In addition, in the framework of the amended law, it has become RIKEN's responsibility to select an appropriate body for operating the SPring-8 facility by bidding. In the bidding, to be conducted by RIKEN in 2007, JASRI will be one of the bidders, even though JASRI has been responsible for operating the facility since 1997, before the law was amended.

Under the amended law, the Advisory Committee that had deliberated on key issues related to the management, operation, and utilization of SPring-8 was dissolved at the end of March 2007, and a new committee, namely, the Proposal Selection Committee, whose duties are limited to deliberating only those issues related to proposal selection, was created in April 2007.

Reviews Conducted

In 2002, the Government of Japan established the Council for Science and Technology Policy in the Cabinet Office to steer science and technology in Japan. Although the management system for SPring-8 was considered to become more transparent owing to the transition from trilateral to bilateral management due to the JAERI's withdrawal, the council anticipated that complications and opaqueness in allocating the budget from RIKEN to JASRI, and in managing the facility would still remain, the transparency and efficiency of the new bilateral management system.

Hence, the council, advised JASRI to organize an international advisory council and respect their recommendations, upon which JASRI could improve the transparency and efficiency of the SPring-8 management system to ensure scientific and technological productivity at the facility for full-fledged exploitation. In order to immediately and appropriately respond to the advice given by the council, JASRI organized the JASRI International Advisory Council 2006 (JIAC), which held a meeting in Himeji at the beginning of July 2006.

In its report, JIAC stated that the SPring-8 facility should be operated and managed by RIKEN and JASRI in a unified manner as it was under the amended law, acting as an international leading-edge COE with respect to its excellent accomplishments thus far achieved.

Almost immediately after the JIAC meeting, MEXT launched an official committee for the interim assessment, and initiated an intensive review process for evaluating overall SPring-8 activities. There were five meetings held by the end of 2006, and one to be held by the end of March 2007. Following the recommendation submitted by the committee, it is expected that the Minister of MEXT will issue an amended policy as well as a guideline for the promotion of the public utilization of SPring-8 by the middle of 2007.

Selecting a few of the beamlines in the order of their completion times, JASRI has been systematically

conducting a series of reviews on the public beamlines since 2002. In 2006, JASRI reviewed BL13XU (Surface and Interface Structures), BL19B2 (Engineering Science Research), BL20XU (Medical and Imaging II), and BL37XU (Trace Element Analysis), which were the last four beamlines remaining unreviewed. Completing the review of the public beamlines, JASRI will follow the recommendations made by the review committee while maintaining and upgrading the beamlines in future.

In order to expand the number of users mainly focusing on industrial applications, JASRI has been conducting a trial use program since 2001 and has been running the Program for Strategic Use of Advanced Large Scale Facilities by MEXT since 2005. During 2006, there have been 4 proposals accepted for trial use, the experiments of which were carried out at BL19B2 (Engineering Science Research), BL13XU (Surface and Interface Structures), BL46XU (R&D), and BL47XU (HXPES, MCT). In the framework of the Program for Strategic Use of Advanced Large Scale Facilities, the number of the proposals accepted amounted to more than 100 during 2006. A review committee established by JASRI has outlined all the activities and accomplishment leading to the promotion of industrial applications and determined that the program has successfully vitalized this field of SR science and technology, making a significant contribution to the cultivation of new users from the industrial domain.

New Beamline for Industrial Applications

When it became clear that the number of proposals accepted for industrial applications was exceeding the capacity of BL19B2 (Engineering Science Research), JASRI decided to donate 150 million yen to RIKEN in early 2006, for construction of a new public beamline for industrial application (BL14B2 Engineering Science Research II). The construction was initiated in late 2006, and is expected to be finished by the middle of 2007, immediately followed by public use.

New Utilization Systems

With guidance from the Government, RIKEN amended the policy relating to the public utilization of SPring-8 with respect to the social circumstances in 2005, and instituted a new policy in 2006, which involved (i) user fees, (ii) non-proprietary grant-aid proposal, and (iii) new beamtime fees for proprietary research.

User Fees

In accordance with the new policy that requires the users to share the expenditure costs, all public beamline users, including those users of contract beamlines for public use as well, have been required to pay an expenditure fee for materials such as coolants, buffer gases, and stock room reagents, parts, stationery, and so forth. The fee consists of a basic charge (10,300 yen/shift) and a variable charge determined on the basis of the expenses of the consumables actually used.

Non-Proprietary Grant-Aid Proposal

Also introduced under the new policy is a new program intended for research proposals that have been reviewed and approved for a large research grant. Under the program, the proposals are exempted from the scientific review process under the conditions that the program fee is paid and that the research results are made available to the public; only the safety and technical feasibility of the experiment, and the necessity of the use of SPring-8 are considered. Under this new program, such users can conduct their experiment by paying the program fee of 131,000 yen/shift as well as the fixed and expenditure fees.

New Beamtime Fees for Proprietary Research

Under the new policy, the beamtime fees for proprietary research, which had been kept unchanged since the introduction of the system in 1999, have been revised. The revised fees are 480,000 yen/shift for public beamlines, 720,000 yen/shift including a 50% premium for public beamlines for time-designated proposals, and 312,000 yen/shift for contract beamlines.

SPring-8 Website Renewal

The SPring-8 website has been completely reorganized from the viewpoint of user-friendliness. The new website was developed in such a way that new comers can obtain sufficient information to adequately generate their own proposals. To meet this requisite, the new website contains an advanced database made up of a wide range of information on the user experiments thus far conducted. When visiting the new website, one can obtain such information by selecting relevant words from the database.

Machine Operation

The operation statistics since, which have been collected the facility was opened to users are shown in Fig. 1. Recently, the SPring-8 storage ring has been operated on four- or five-week periods for one operation cycle. Since 2004, long-term operation cycles have also been performed. In 2006, the total operation time of the accelerator complex was 5026.2 hours. The operation time of the storage ring was 5008.5 hours, of which 75.7% (3790.1 hours) was made available to users. The downtime resulting from failure accounted for 1.1% (42.5 hours) of the operation time of the storage ring; in 2006, no great loss of user time exceeding several hours occurred. Since 2004, there has been no injection time because top-up injection was being introduced. Concerning user service operation, high availability (ratio of net user time to planned user time) was achieved, e.g., 98.7% in 2006. A total tuning and study time of 1193.6 hours was used for machine tuning, and the study of the linac, booster synchrotron and storage ring, and also used for beamline tuning and study.

Operations in three different filling modes were provided for the following user time percentages: 8.8% in the multi-bunch mode, 56.4% in the several bunch mode, such as the 203-bunch mode (203 equally spaced bunches) and 34.9% in the hybrid filling mode such as a 2/21- partially filled multi-bunch with 18-isolated bunches. In 2006, the use of the several bunch mode increase in frequency. In particular, the 203-bunch mode accounted for 36.3% of the total user time. For the hybrid filling mode, a current of 0.8 mA, 1.0 mA, 1.5 mA, or 1.8 mA is stored in each isolated bunch. An isolated bunch purity of better than 10^{-9} is routinely maintained in the top-up operation.

Table I presents a summary of useful beam parameters of the storage ring.

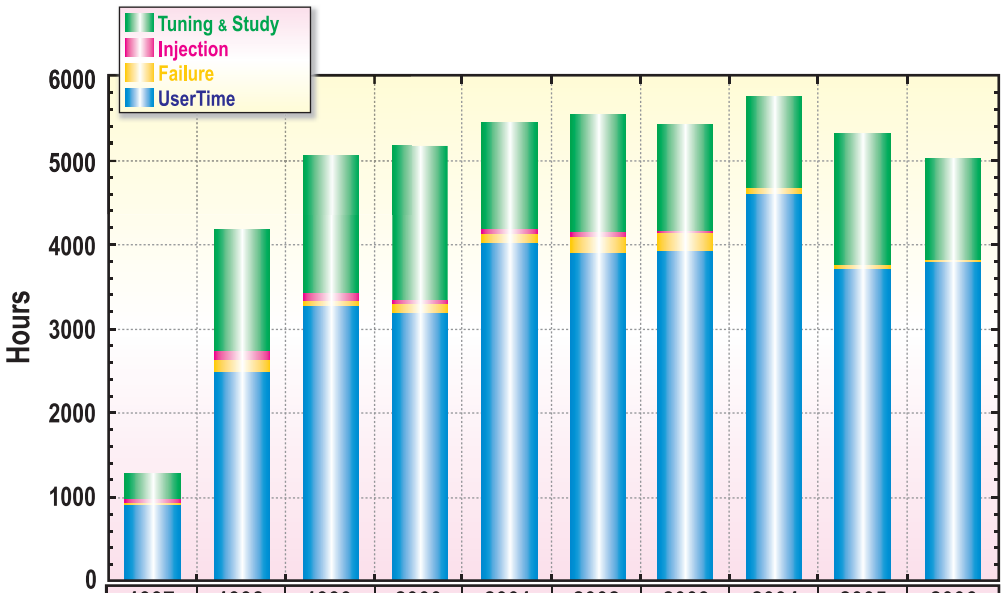

	1997	1998	1999	2000	2001	2002	2003	2004	2005	2006
Accelerator Operation Time	1286	4189.6	5051.6	5167.5	5456.1	5542.9	5419.5	5759.2	5317.1	5026.2
Storage Ring Operation Time	1270.6	4135.4	4863.9	4972.9	5340.6	5484.1	5328.5	5736.7	4781.3	5008.5
Tuning & Study (Accel. & BL)	304	1457.6	1624.2	1815	1276.5	1394.9	1245.8	1085.9	1559.2	1193.6
Injection	50	110	95.2	70.4	59.3	60.8	39.2	0	0	0
Failure	26	110	57.2	88.7	87.1	190.5	208.5	82.4	59.7	42.5
User Time	906	2512	3275	3193.4	4033.2	3896.7	3926	4590.9	3698.2	3790.1
Planned Time	984	2712	3432	3352	4176	4152	4176	4680	3762	3840
Availability (%)	97.2	96.7	98.2	97.4	98	95.3	95	98.1	98.3	98.7

Fig. 1. Operation statistics since the facility became available to users.

Table I. Beam parameters of SPring-8 storage ring

Energy [GeV]	8
Number of buckets	2436
Tunes (ν_x / ν_y)	40.15 / 18.35
Current [mA]:	
single bunch	10
multi bunch	~100
Bunch length (σ) [psec]	13
Horizontal emittance [nm·rad]	3.4 *
Vertical emittance [pm·rad]	6.8 *
Coupling [%]	0.2
RF Voltage [MV]	16
Momentum acceptance [%]	±2.5 (=±200 MeV)
Beam size [μm]: (σ_x / σ_y) [μm]	
Long ID section	294 / 10
ID section	301 / 6
BM section	107 / 13
Beam divergence [μrad]: ($\sigma_{x'}$ / $\sigma_{y'}$) [μrad]	
Long ID section	13 / 0.7
ID section	12 / 1.1
BM section	56 / 0.6
Operatinal chromaticities: (ξ_x / ξ_y)	+2 / +2 **
Lifetime [hr]:	
100 mA (multi bunch)	~ 200
1 mA (single bunch)	~ 15
Horizontal dispersion [m]:	
Long ID section	0.103
ID section	0.107
BM section	0.032
Fast orbit stability (0.1 – 200 Hz) [μm]:	
horizontal (rms)	~ 4
vertical (rms)	~1

* Assuming that 0.2% coupling for "Low Emittance Optics"
** With bunch-by-bunch feedback

Beamlines

The electron storage ring of the SPring-8 accelerator complex can potentially accommodate sixty-two beamlines (34 insertion devices, 4 long undulators, 23 bending magnets and 1 infrared). Occupying about 75% of its full capacity, there are 48 beamlines currently in operation as shown in the Beamline map (Fig. 2) and List of beamlines (Table II).

These beamlines are primarily categorized into the following four groups:
(1) Public Beamlines,
(2) Contract Beamlines,
(3) RIKEN Beamlines, and
(4) Accelerator Beam Diagnosis beamlines.

Constructed by JAEA (Japan Atomic Energy Agency)[1] and RIKEN with governmental grants, the Public Beamlines have been operated for public use. Now, there are 25 public beamlines in operation; 22 X-ray beamlines, two soft X-ray beamlines and one infrared beamline. Among them, three beamlines had been specifically used for R&D. According to the recommendation made by the R&D Beamline Review Committee, however, two of the R&D beamlines have had their status changed to general use since the period of 2005A, although one of them (BL46XU) is still solely used for R&D programs as an interim measure.

In order to accommodate the rapid increase in the number of users from the industrial domain, the construction of a new beamline has begun at the site of BL14B2.

The contract beamlines are installed, owned, operated and maintained by universities, companies, and other organizations for exclusive use by contractors. Currently, there are 14 contract beamlines in operation, including JAEA beamlines[2]. The experimental stations of BL22XU and BL23SU are located at JAEA's RI Laboratory and are dedicated to research utilizing radioactive isotopes and actinide materials. The National Synchrotron Radiation Research Center of Taiwan (NSRRC) was the first foreign organization to construct contract beamlines at SPring-8, i.e., BL12B2 and BL12XU.

There are 7 RIKEN beamlines for their exclusive use to promote RIKEN's research activities, although 20% of the beamtime is reserved for public use. RIKEN BL19LXU is the only beamline equipped with a long undulator, realizing the highest degree of brilliance. BL26B1 and BL26B2 are the beamlines used for high-throughput protein crystallography, a method used in the human genome project. BL29XU has two experimental stations, one located in the experimental hall and the other at the end of the 1 km beamline.

Dedicated to the study of the characteristics of the electron beam accumulated in the storage ring, the accelerator beam diagnosis beamlines are currently used exclusively by the JASRI accelerator group.

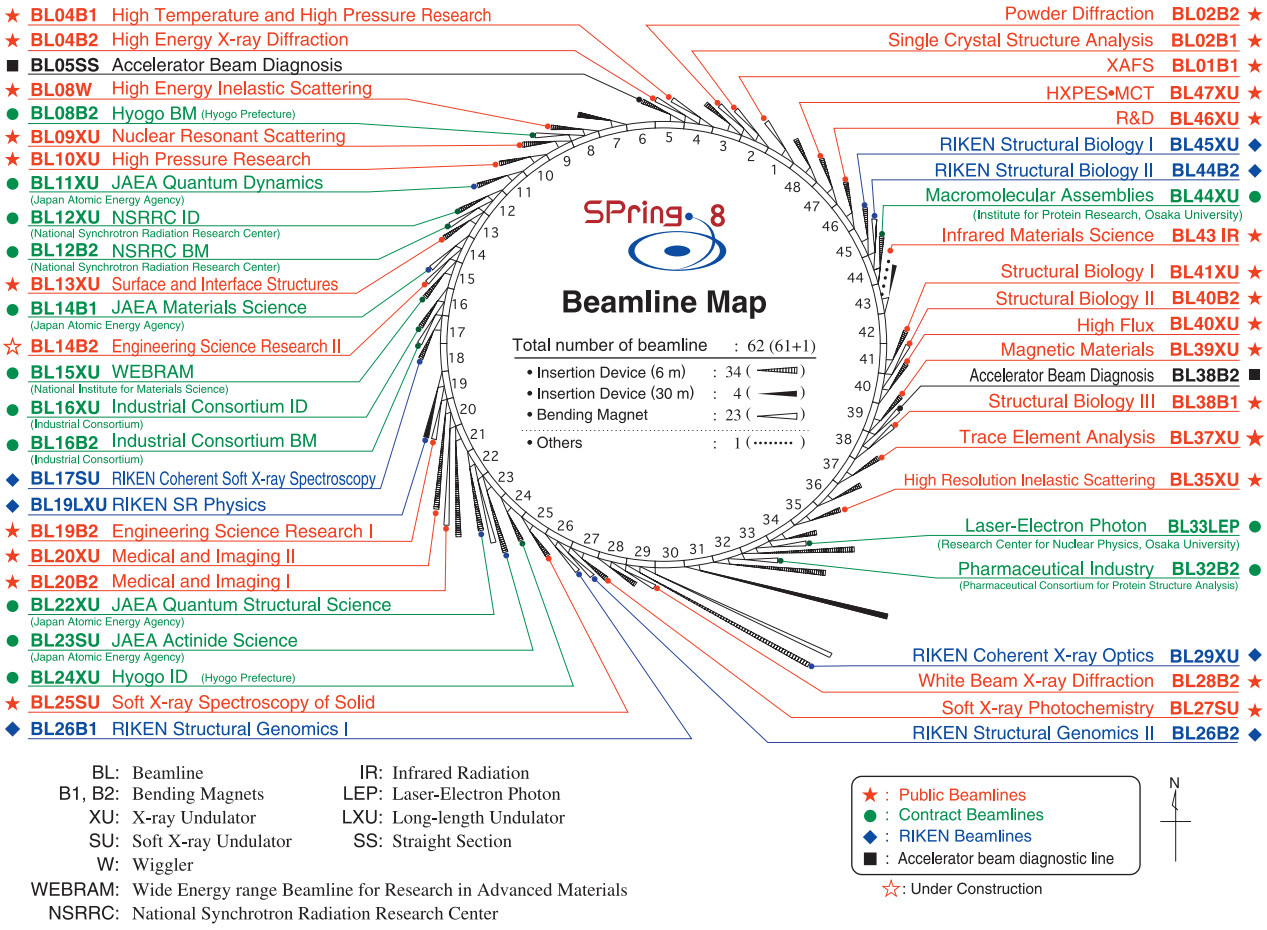

Fig. 2. Beamline map.

[1] The Japan Atomic Energy Research Institute (JAERI) was transformed into an independent administrative institution, now called Japan Atomic Energy Agency (JAEA), on October 1, 2005.

[2] Owing to the withdrawal of JAERI from the SPring-8 management on October 1, 2005, JAEA beamlines, previously called JAERI beamlines, are now categorized as contract beamlines.

Table II. List of beamlines (April, 2006)

BL #	Beamline Name	(Public Use)	Areas of Research
★ Public Beamlines			
BL01B1	XAFS	(Oct. 1997)	XAFS in wide energy region (3.8 to 113 keV). XAFS of dilute systems and thin films.
BL02B1	Single Crystal Structure Analysis	(Oct. 1997)	Structure physics using single crystal analysis. Precise structure analysis of photo-excited state.
BL02B2	Powder Diffraction	(Sep. 1999)	Accurate structure analysis of crystalline materials using powder diffraction data by Rietveld refinements and MEM (maximum entropy method).
BL04B1	High Temperature and High Pressure Research	(Oct. 1997)	Mineral physics at high temperature and high pressure. Energy-dispersive X-ray diffraction and X-ray radiography using the large-volume press.
BL04B2	High Energy X-ray Diffraction	(Sep. 1999)	Structural analysis of glass, liquid, and amorphous materials. X-ray diffraction under ultra high-pressure. Precise single crystal structure analysis
BL08W	High Energy Inelastic Scattering	(Oct. 1997)	Magnetic Compton scattering. High-resolution Compton scattering. High-energy Bragg scattering. High-energy fluorescent X-ray analysis.
BL09XU	Nuclear Resonant Scattering	(Oct. 1997)	Time domain Mössbauer spectroscopy. Lattice dynamics study using nuclear resonant scattering.
BL10XU	High Pressure Research	(Oct. 1997)	Structure physics and earth science under ultra high pressure using DAC.
BL13XU	Surface and Interface Structures	(Sep. 2001)	Atomic-scale structure analysis of an ultra-thin film, nanostructure and surface, using in-air measurements (room temperature to 500 °C) and in-vacuum measurements (20 to 1300 K).
BL19B2	Engineering Science Research	(Nov. 2001)	Industrial application using XAFS in wide energy region, residual stress measurement, structural analysis of thin film, surface and interface, powder diffraction, and X-ray imaging.
BL20XU	Medical and Imaging II	(Sep. 2001)	Medical application: Microangiography, refraction-enhanced imaging. / Microimaging: Scanning microscopy, imaging microscopy, microtomography, X-ray holography and X-ray optics. / Ultra-small angle scattering.
BL20B2	Medical and Imaging I	(Sep. 1999)	Medical application: Microradiography, micro-tomography and refraction-enhanced imaging. / Microimaging: R&D of optical elements for novel imaging techniques.
BL25SU	Soft X-ray Spectroscopy of Solid	(Apr. 1998)	High resolution photoemission spectroscopy. Photoelectron diffraction and holography. Magnetic circular dichroism (MCD). Photoelectron emission microscope (PEEM).
BL27SU	Soft X-ray Photochemistry	(May 1998)	Industrial research of functional material. Atomic and molecular spectroscopy by high resolution electron spectroscopy. Surface analysis and solid state physics.
BL28B2	White Beam X-ray Diffraction	(Sep. 1999)	White X-ray diffraction. Time-resolved energy-dispersive XAFS (DXAFS) .
BL35XU	High Resolution Inelastic Scattering	(Sep. 2001)	Material dynamics on ~ meV energy scales using inelastic X-ray scattering (IXS) and nuclear resonant scattering (NRS).
BL37XU	Trace Element Analysis	(Nov. 2002)	X-ray microbeam spectrochemical analysis. Ultra trace element analysis. High energy X-ray fluorescence analysis.
BL38B1	Structural Biology III	(Oct. 2000)	XAFS. R&D of optics and detector. Macromolecular crystallography.
BL39XU	Magnetic Materials	(Oct. 1997)	X-ray magnetic circular dichroism (XMCD) spectroscopy. Element-specific magnetometry. X-ray emission spectroscopy and its magnetic circular dichroism. Resonant or non-resonant magnetic scattering.
BL40XU	High Flux	(Apr. 2000)	Time-resolved diffraction and scattering experiments. X-ray speckle. X-ray fluorescence trace analysis.
BL40B2	Structural Biology II	(Sep. 1999)	Macromolecular crystallography. Small angle X-ray (solution) scattering.
BL41XU	Structural Biology I	(Oct. 1997)	Biological macromolecular crystallography.
BL43IR	Infrared Materials Science	(Apr. 2000)	Infrared microspectroscopy. Magneto-optical spectroscopy. Infrared surface science. Absorption and reflection spectroscopy. Time-resolved experiments with pulsed laser and SR (pump and probe).
BL46XU	R&D	(Nov. 2000)	Insertion devices R&D. Resonant and non-resonant magnetic scattering structural analysis.
BL47XU	HXPES・MCT	(Oct. 1997)	R&D of microtomography and microbeam technique. High energy photoemission spectroscopy.

(April, 2006)

BL #	Beamline Name	(First Beam)	Areas of Research
	● Contract Beamlines		
BL08B2	**Hyogo BM** (Hyogo Prefecture)	(Jun. 2005)	XAFS in a wide energy region. Small angle X-ray scattering for structural analyses of polymer and nano-composite materials. X-ray topography. Imaging. Powder diffraction with a high angular resolution.
BL12XU	**NSRRC ID** (National Synchrotron Rad. Res. Center)	(Dec. 2001)	High resolution non-resonant or resonant inelastic X-ray scattering. High resolution near-edge X-ray Raman scattering. Phase transitions under high-pressure, low and high temperatures. High-resolution X-ray absorption and emission spectroscopy. X-ray physics and optics.
BL12B2	**NSRRC BM** (National Synchrotron Rad. Res. Center)	(Oct. 2000)	X-ray absorption spectroscopy. Powder X-ray diffraction. High resolution X-ray scattering. Protein crystallography.
BL15XU	**WEBRAM** (National Institute for Materials Science)	(Jan. 2000)	High resolution X-ray photoemission microscopy. High energy excitation X-ray photoelectron spectroscopy. High resolution X-ray emission spectroscopy. Highly precise X-ray powder diffraction and ultra-small angle scattering.
BL16XU	**Industrial Consortium ID** (Industrial Consortium)	(Oct. 1998)	Characterization of thin films for ULSI and magnetic devices, catalysts, functional materials, and structural materials by X-ray diffraction, fluorescence X-ray analysis, X-ray magnetic circular dichroism, and imaging with X-ray microbeam.
BL16B2	**Industrial Consortium BM** (Industrial Consortium)	(Oct. 1998)	Characterization of industrial materials, such as metal and oxide films, semiconductor crystals by XAFS, topography and other methods.
BL24XU	**Hyogo ID** (Hyogo Prefecture)	(May 1998)	Structure analysis of small bio-crystals for industry. Surface/interface analysis for industry by fluorescent X-ray analysis, strain measurements and grazing incidence X-ray diffraction. Microbeam formation studies for materials and life sciences.
BL32B2	**Pharmaceutical Industry** (Pharmaceutical Consortium for Protein Structure Analysis)	(Apr. 2002)	Protein structure analysis for structure-based drug design: Design and optimization of new leading compounds based on pharmacodynamic action mechanism elucidated at the molecular level which obtained from a detailed interaction analysis of receptor-drug complexes.
BL33LEP	**Laser-Electron Photon** (RCNP, Osaka University)	(Jun. 1999)	Meson photoproduction from nucleon and nucleus. Photoexcitation of hyperons, nucleon resonances, and other exotic states. Photonuclear reactions. Beam diagnoses. Test and calibration of detectors with GeV photon beam.
BL44XU	**Macromolecular Assemblies** (IPR, Osaka University)	(May 1999)	Crystal structure analysis of biological macromolecular assemblies (e.g. membrane complexes, protein complexes, protein-nucleic acid complexes, and viruses).
BL11XU	**JAEA Quantum Dynamics**	(Oct. 1998)	Nuclear resonant scattering. Surface and interface structure with MBE. Inelastic scattering. XAFS.
BL14B1	**JAEA Materials Science**	(Dec. 1997)	Materials science at high pressure. Structure physics.
BL22XU	**JAEA Quantum Structural Sci.**	(May 2002)	Materials science at high pressure. Resonant X-ray scattering (activity at RI laboratory).
BL23SU	**JAEA Actinide Science**	(Feb. 1998)	Surface chemistry with supersonic molecular beam. Biophysical spectroscopy. Photoelectron spectroscopy (activity at RI laboratory). Magnetic circular dichroism (activity at RI laboratory).
	◆ RIKEN Beamlines		
BL17SU	**RIKEN Coherent Soft X-ray Spectroscopy**	(Sep. 2003)	Spectroscopy of multiply charged ions. Angle-resolved photoemission spectroscopy (ARPES). Soft X-ray emission spectroscopy.
BL19LXU	**RIKEN SR Physics**	(Oct. 2000)	Any research field requiring the highly brilliant X-ray beam.
BL26B1/B2	**RIKEN Structural Genomics I & II**	(Apr. 2002)	Structural genomics research based on single crystal X-ray diffraction.
BL29XU	**RIKEN Coherent X-ray Optics**	(Dec. 1998)	X-ray optics, especially coherent X-ray optics.
BL44B2	**RIKEN Structural Biology II**	(Feb. 1998)	Macromolecular crystallography.
BL45XU	**RIKEN Structural Biology I**	(Jul. 1997)	Macromolecular crystallography. Time-resolved structures of non-crystalline biological materials using small-angle scattering and diffraction technique.
	■ Accelerator Beam Diagnosis		
BL05SS	**Accelerator Beam Diagnosis**	(Mar. 2004)	Accelerator beam diagnostics. R&D of accelerator components.
BL38B2	**Accelerator Beam Diagnosis**	(Sep. 1999)	Accelerator beam diagnostics. R&D of accelerator components. Production of MeV γ-ray photons.

Proposal Schemes, Utilization Statistics and Research Outcome

Overview

JASRI invites General Proposals twice a year. Submitted proposals are reviewed by the SPring-8 Proposal Review Committee (PRC). In the General Proposal scheme, the PRC approved 357 of 591 proposals in 2005B and 522 of 696 in 2006A. In the Priority Field Proposal scheme, 267 proposals were adopted from 382 in 2005B and 93 were adopted from 136 in 2006A. In total, 4,020 hours of beamtime was allocated to users from 2005B through 2006A.

SPring-8 user operation statistics for the period from 1997B to 2006A are shown in Table III. This table summarizes the beamtime available to users, the number of users and the number of experiments conducted at both public and contract beamlines, which are also illustrated in Fig. 3. The number of experiments conducted in the reserved beamtime at RIKEN beamlines and the number of Priority Research Proposals are included in the number of Public BL experiments in the table and figure.

In 2005B and 2006A, SPring-8 provided users with 1,818 and 2,202 hours of beamtime in three and four operation cycles, respectively. As for 2005B, 4,032 individuals utilized the public beamlines in 619 independent experiments, while 1,379 individuals utilized the contract beamlines in 227 experiments. In 2006A, 4,809 individuals utilized the public beamlines in 722 independent experiments, while 1,831 individuals utilized the contract beamlines in 227 experiments. From October 1997, when SPring-8 was opened to the public, through 2006A, a total of 65,566 users conducted 9,780 experiments at public and contract beamlines.

Table III. SPring-8 user operation results.

Research Term	User Time (hours)	Public BL		Contract BL	
		Experiments	Users	Experiments	Users
1997B: 1997.10 - 1998.03	1,286	94	681		
1998A: 1998.04 - 1998.10	1,702	234	1,252	7	
1999A: 1998.11 - 1999.06	2,585	274	1,542	33	467
1999B: 1999.09 - 1999.12	1,371	242	1,631	65	427
2000A: 2000.02 - 2000.06	2,051	365	2,486	100	794
2000B: 2000.10 - 2001.01	1,522	382	2,370	88	620
2001A: 2001.02 - 2001.06	2,313	473	2,915	102	766
2001B: 2001.09 - 2002.02	1,867	486	3,277	114	977
2002A: 2002.02 - 2002.07	2,093	543	3,246	110	1,043
2002B: 2002.09 - 2003.02	1,867	538	3,508	142	1,046
2003A :2003.02 - 2003.07	2,246	632	3,777	164	1,347
2003B: 2003.09 - 2004.02	1,844	548	3,428	154	1,264
2004A: 2004.02 - 2004.07	2,095	568	3,756	161	1,269
2004B: 2004.09 - 2004.12	1,971	554	3,546	146	1,154
2005A: 2005.04 - 2005.08	1,880	560	3,741	146	1,185
2005B: 2005.09 - 2005.12	1,818	619	4,032	187	1,379
2006A: 2006.03 - 2006.07	2,202	722	4,809	227	1,831
TOTAL	32,713	7,834	49,997	1,946	15,569

Figures 4 and 5 indicate the number of conducted experiments along with the affiliated number of users and the research fields from 1997B to 2006A. In Fig. 5, three types of research, namely, those performed under Advanced Large-Scale Research Facilities Strategic Program, Power User Proposal, Strategy Proposal, which have their own original peer review system, are separated from the other general research fields.

The percentages of experiments conducted by foreign users were 4.5% for 2005B and 4.8% for 2006A. The number ratios of Life Science to

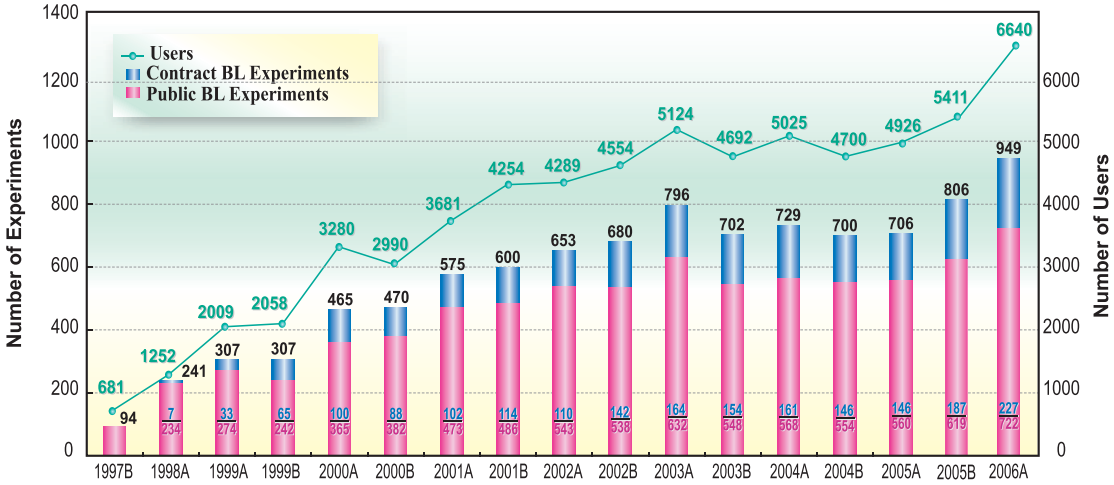

Fig. 3. Numbers of users and experiments conducted.

Diffraction & Scattering to other experiments has approximately been 1:1:1 since the inauguration of SPring-8. The number ratios of XAFS to Spectroscopy to Method & Instrumentation experiments, all of which are categorized as "others," has also approximately been 1:1:1. Recently, however, the number ratio of Diffraction & Scattering to Industry has increased.

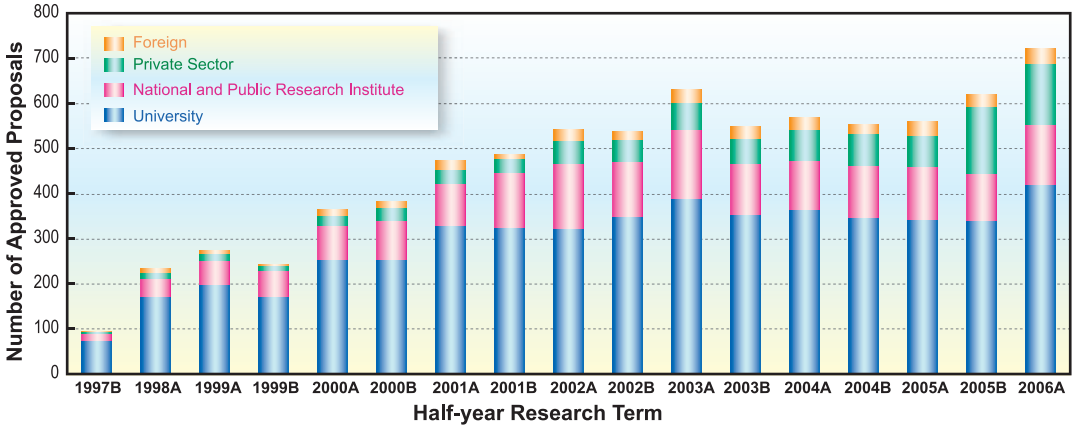

Fig. 4. Number of conducted proposals by affiliation of applicants (public beamlines).

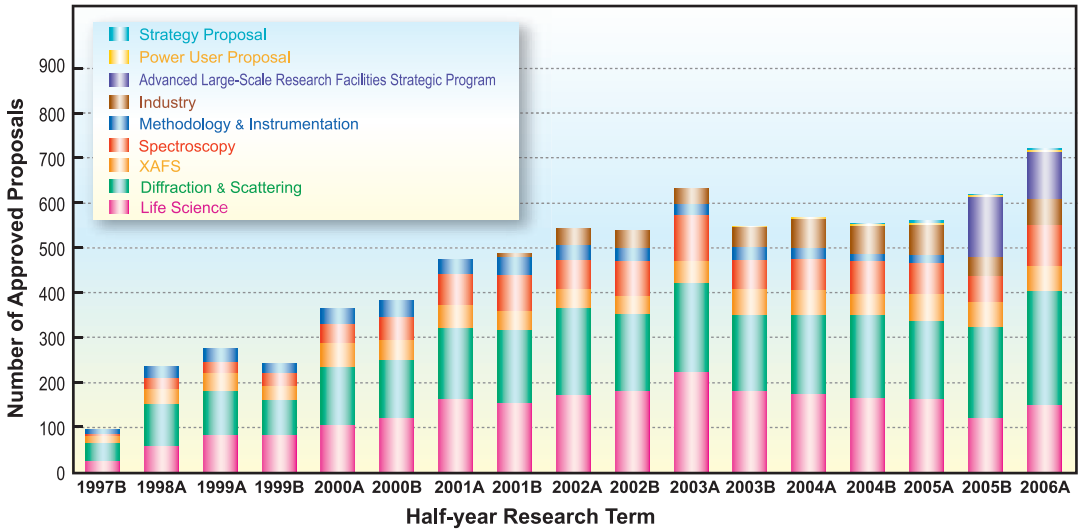

Fig. 5. Number of selected proposals by affiliation of applicants (public beamlines).

Long-term Proposal

Independent of the General Proposals, JASRI has developed a novel scheme for the long-term use of beamlines, in which beam access is guaranteed for up to three years. This system aims to further promote research that is expected to produce outstanding results in the field of science and technology to pave the way for new research areas and research methodologies and to significantly help improve the technology for the industrial base by making the best use of the characteristics of SPring-8. Three proposals were selected from 6 submitted in 2005B and 1 was submitted and selected in 2006A. Seven proposals were carried out by the end of 2006A.

Urgent Proposal

In 1999A, an Urgent Proposal scheme was established in order to adequately respond to urgent requests for conducting experiments as soon as possible. Upon receiving an Urgent Proposal of non-proprietary use, the Proposal Review Committee promptly reviews it electronically in terms of its necessity and urgency as well as on the basis of the criteria for General Proposals of non-proprietary use.

Proprietary Research Proposal

Users can conduct proprietary research by paying the beamtime fee, which was repriced from 472,000 yen/shift to 480,000 yen/shift in 2006B. Proprietary research is essential when users have commercially confidential information in their experiment or samples and do not wish to disclose their research results. In 2005B, 32 proprietary experiments were performed at public beamlines and 24 were performed at contract beamlines (21 at BL32B2, 1 at BL24XU, and 2 at BL16XU). In 2006A, 24 experiments were conducted at public beamlines and 25 experiments were conducted at contract beamlines (22 at BL32B2, 2 at BL24XU, and 1 at BL16B2). From 1999B, when the system was introduced, to 2006A, a total of 422 proprietary experiments were carried out at both public and contract beamlines. The Pharmaceutical Consortium spent most of their beamtime on proprietary research at their contract beamline BL32B2 in 2005B and 2006A.

Proprietary Time-designated Proposal

In 1999B, JASRI established a utilization scheme for those who wish to take sole possession of their results and perform experiments during a specific time period by paying a beamtime fee with an increase in price of 50% compared with that charged for public beamlines as premium, which was revised from 708,000 yen/shift to 720,000 yen/shift in 2006B. In this utilization scheme, users can specify the preferred time period in their Proprietary Time-designated Proposal, which will be promptly reviewed once submitted.

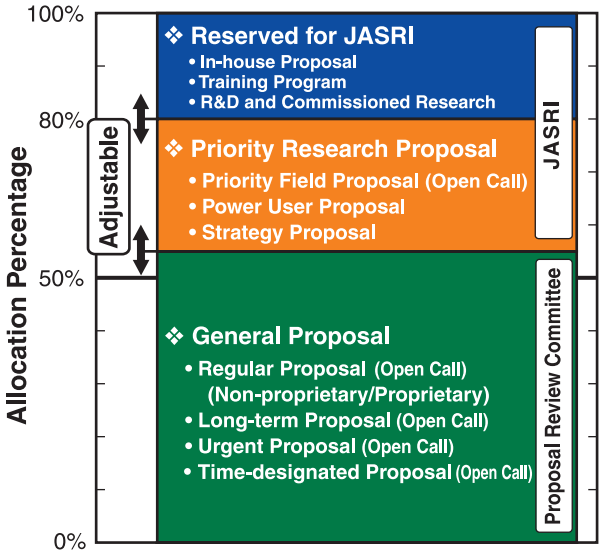

Fig. 6. Beamtime allocation scheme for public beamlines.

Priority Research Proposal

In FY2003, a new scheme for the management of public beamlines was established on the basis of a report on SPring-8 by the governmental review committee. The report called for SPring-8 to further promote the use of public beamlines to produce more research results. The most important point of the scheme was its launching of the Priority Research Program. The new scheme is shown in Fig. 6. As can be seen from the figure, beamtime not exceeding 50% is allocated to Priority Research Proposals and proposals using beamtime reserved for JASRI; thus, more than 50% of the total user beamtime is guaranteed for General and Long-term proposals. The Priority Research Program scheme is intended to make the best use of SPring-8 and to produce more research results. Priority Research Proposals are tentatively categorized into the following three groups.

- Priority Field Proposal
- Power User Proposal
- Strategy Proposal

Priority Field Proposal

In this particular proposal scheme, JASRI strategically designates research fields in order to promote excellent research results from those areas in scientific and/or industrial domains with high strategic significance. The Priority Field Proposals are further categorized into four subgroups: Nanotechnology Support, Protein 500, Industrial Use and Medical bio trial use. These proposals are reviewed before General Proposals at the review committees designated for each priority field. The outline of each priority research field is as follows.

Nanotechnology Support

This priority research field was developed to support developments in nanotechnology, using 12 beamlines at SPring-8. Nanotechnology Support at SPring-8 had already started in 2002 under the Nanotechnology Researchers Network Project (Nanonet Project) of MEXT, and was consolidated into the Priority Research Program in FY2003. In 2005B and 2006A, a total of 106 proposals were selected from 211 submitted proposals. This Project will be in effect until the end of FY2006.

Protein 500

Just as Nanotechnology Support, Protein 500 at SPring-8 started shortly after MEXT launched the Protein 3000 Project in 2002 as a post-human genome program to analyze the structure of 3,000 proteins and was taken over by the Priority Field Program in FY2003. Under the Project, three of the

SPring-8 structural biology beamlines are assigned to analyze 500 kinds of protein structure, and 30% of their beamtime is allocated every year. In 2005B and 2006A, a total of 194 proposals were selected. This Project will be in effect until the end of FY2006.

Industrial Use

In relation to industrial use, the Trial Use Program originally ran from 2001B to 2002A for the purpose of attracting new users to SPring-8 mainly from industries, and was restarted as one of the Priority Field Proposals in 2003A. In 2005B, 4 from 6 proposals were selected and the Trial Use program for industrial use was successfully completed. In the same period, the Advanced Large-Scale Research Facilities Strategic Utilization Program, which is mainly focused on enhancing industrial use, was launched as a national project. There were 194 and 148 proposals submitted, of which 134 and 103 were approved to be conducted in 2005B and 2006A, respectively.

Medical Biology

Since November 2005, JASRI has further designated Medical Biology as a priority field to expand the number of users in this field by organizing a trial use from 2006A. In 2006A, 7 from 13 proposals were selected.

Power User Proposal

The Power User Proposal category refers to proposals of user groups who have a complete understanding of beamline instrumentation, and are highly likely to produce excellent research results in the future. Such user groups are designated as Power Users (PUs) by JASRI and expected to provide support for general users. In return for their support, up to 20% of beamtime of relevant beamlines can be used by the PUs. Five groups were designated as PUs in May 2003. There have been 10 research subjects executed including five running subjects from 2005B and 2006A.

Strategy Proposal

Strategy Proposals are expected to contribute to the promotion of research at SPring-8, including the development of new technologies necessary for the operation of the facility. JASRI will conduct such research by itself or jointly with other organizations. The three following strategies research subjects were designated as follow:

- Analysis of Nanocomposite Materials (designated in May 2004)
- X-ray Pinpoint Structure Measurements (designated in January 2005)
- Observations of Biomolecular Structural Recognition Process from Highly Accurate Individual Single Molecular Movies (designated in October, 2006)

Beamtime Reserved for JASRI

Twenty percent of the total beamtime is reserved for JASRI to conduct its own research programs, to flexibly accept the Urgent Proposals mentioned above, to modify and adjust the instruments according to the users' requests, and to maintain the beamlines.

Industrial Research

In addition to the promotion of research activities in the field of basic science, the contribution to the reinforcement of the technological base in industry has been one of the main pillars of the SPring-8 Project. In 2005, JASRI established the Industrial Application Division, by promoting Industrial the Application/Utilization Support Group. In this particular year, the division had intensively carried out the Advanced Large-Scale Research Facilities Strategic Utilization Program of MEXT, and has succeeded in doubling the number of new users conducting experiments at SPring-8. The total number of proposals adopted for industrial applications accounts for more than 20% of the entire use.

The coordinator system, introduced in FY2000 to support industrial use, mainly through consultation, continues to play a crucial role in exploring and acquiring new users from industrial domains. The Trial Use Program has made a significant contribution to industries by revitalizing local industries and creating and promoting new industries. Public beamline BL19B2, Engineering Science Research Beamline, which was built to promote SR use by industries, is the primary beamline used for the Trial Use Program. There are three contract beamlines, which were constructed by the Industrial Consortium and Pharmaceutical Consortium for use by consortium members. There have been workshops and training courses organized to introduce a variety of research fields and SR instrumentation.

As mentioned at the beginning of this report, JASRI decided to donate 150 million yen to RIKEN in early 2006 for the construction of a new public beamline for industrial application (BL14B2 Engineering Science Research II), because it became clear that the number of proposals accepted for industrial applications was exceeding the capacity of BL19B2 (Engineering Science Research). The construction was initiated in late 2006, and is expected to be finished by the middle of 2007, immediately followed by public use.

Research Outcome

Under the new utilization system established in 2006, SPring-8 users are charged only the expenditure fee for non-proprietary research, provided that they submit an experiment report within sixty days after their experiments. When their results are disclosed in scientific journals or any other form of publication, the project leaders are required to report to JASRI and have their results registered with JASRI. As of March 30, 2007, the cumulative number of refereed publications (journals, proceedings and dissertations) was 4,535, of which 3,130 were attributed to public use, 679 were attributed to contract beamlines and 527 were attributed to RIKEN beamlines; here, publications related to two or more beamlines are counted separated for each beamline. Figure 7 shows the number of refereed publications annually counted.

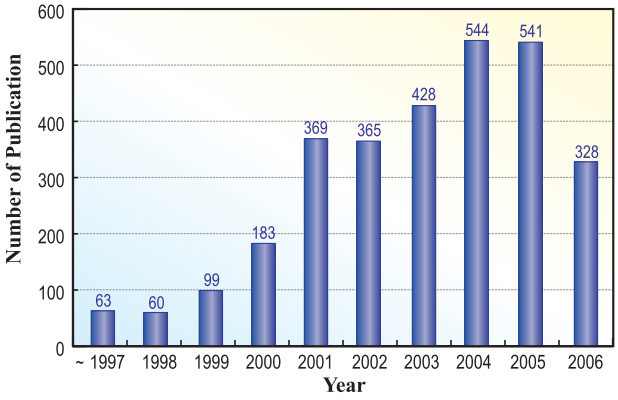

Fig. 7. Annual record of refereed publications as of September 30, 2006.

Budget and Personnel

After becoming open to public use in 1997, SPring-8 was managed by the three-party system of RIKEN, JAERI, and JASRI in a unified manner until September 30, 2005, when JAERI relinquished responsibility for SPring-8 management. Since the withdraw of JAERI, SPring-8 has been managed by the remaining two-party system of RIKEN and JASRI, although JASRI had a legal status transition during FY2006, as described at the beginning of this report. Figures 8 and 9 display the variations in the total budgets allocated to SPring-8 and the numbers of staff members on the SPring-8 campus each year from FY1997 up to the current fiscal year. The total budget allocated to SPring-8 for FY2006 is almost the same as that of FY2005, maintaining the recent trend. In FY2006, the total number of JASRI staff members was 557. The total number of SPring-8 staff members amounts to 1,200 when the numbers of staff members at the JAEA Kansai Research Establishment and the RIKEN Harima Institute are combined with the number of JASRI staff members. The numbers of staff members categorized by the types and fields of employment are illustrated in Fig. 9.

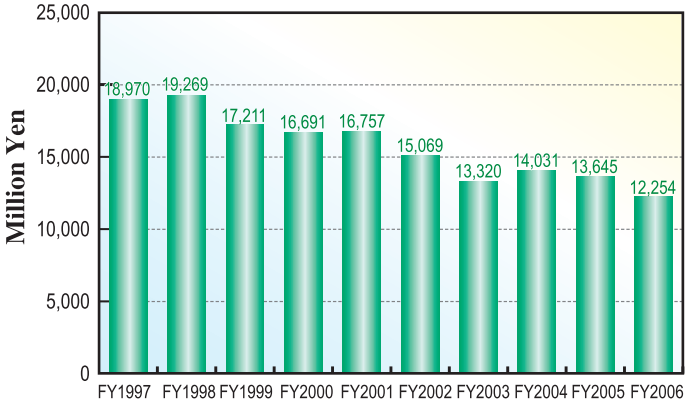

Fig. 8. Budget at SPring-8.

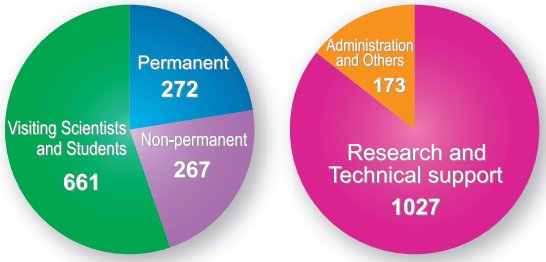

	by Type			by Field		Total
	Permanent	Non-permanent	Visiting Scientists and Students	Research and Technical Support	Administration and Others	
JASRI	212	155	190	414	143	557
RIKEN	60	109	464	606	27	633
XFEL	0	3	7	7	3	10
	272	267	661	1027	173	1200

Fig. 9. Personnel at SPring-8: JASRI, RIKEN and XFEL (FY2006).

Research Complex

As a center of excellence, SPring-8 forms a research complex for synchrotron radiation science and technology, being composed of JASRI, the RIKEN Harima Institute, and the JAEA Synchrotron Radiation Research Center together with various universities and institutes, as illustrated in Fig. 10. The two major bodies of the COE are JASRI and the RIKEN Harima Institute, the organization charts of which are shown in Fig. 11 and Fig. 12, respectively.

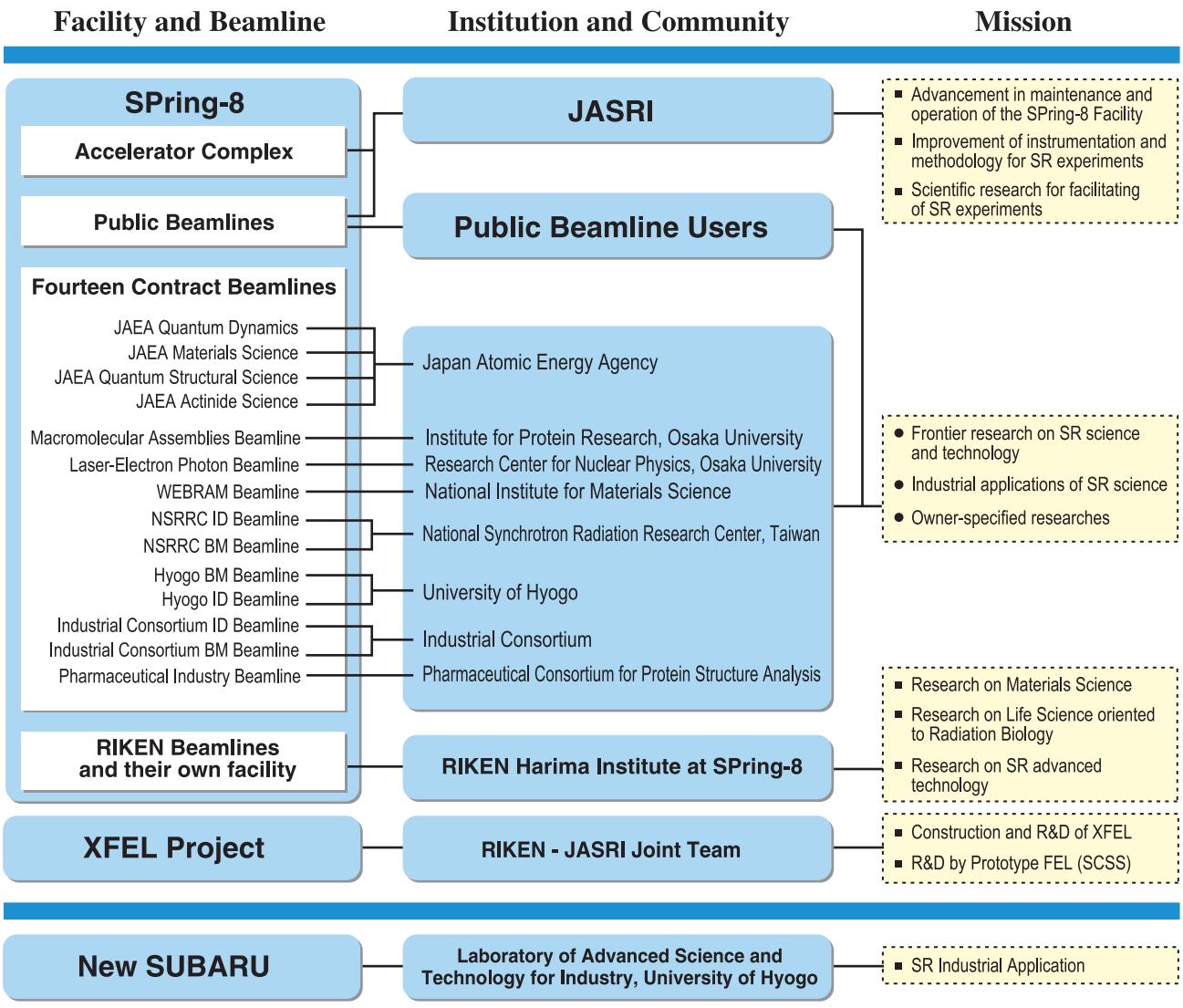

Fig. 10. SPring-8 Research Complex.

April, 2006.

Japan Synchrotron Radiation Research Institute (JASRI)

Director General A. Kira
Senior Exec. Director H. Ohno
Managing Exec. Director M. Nagata, M. Hattori

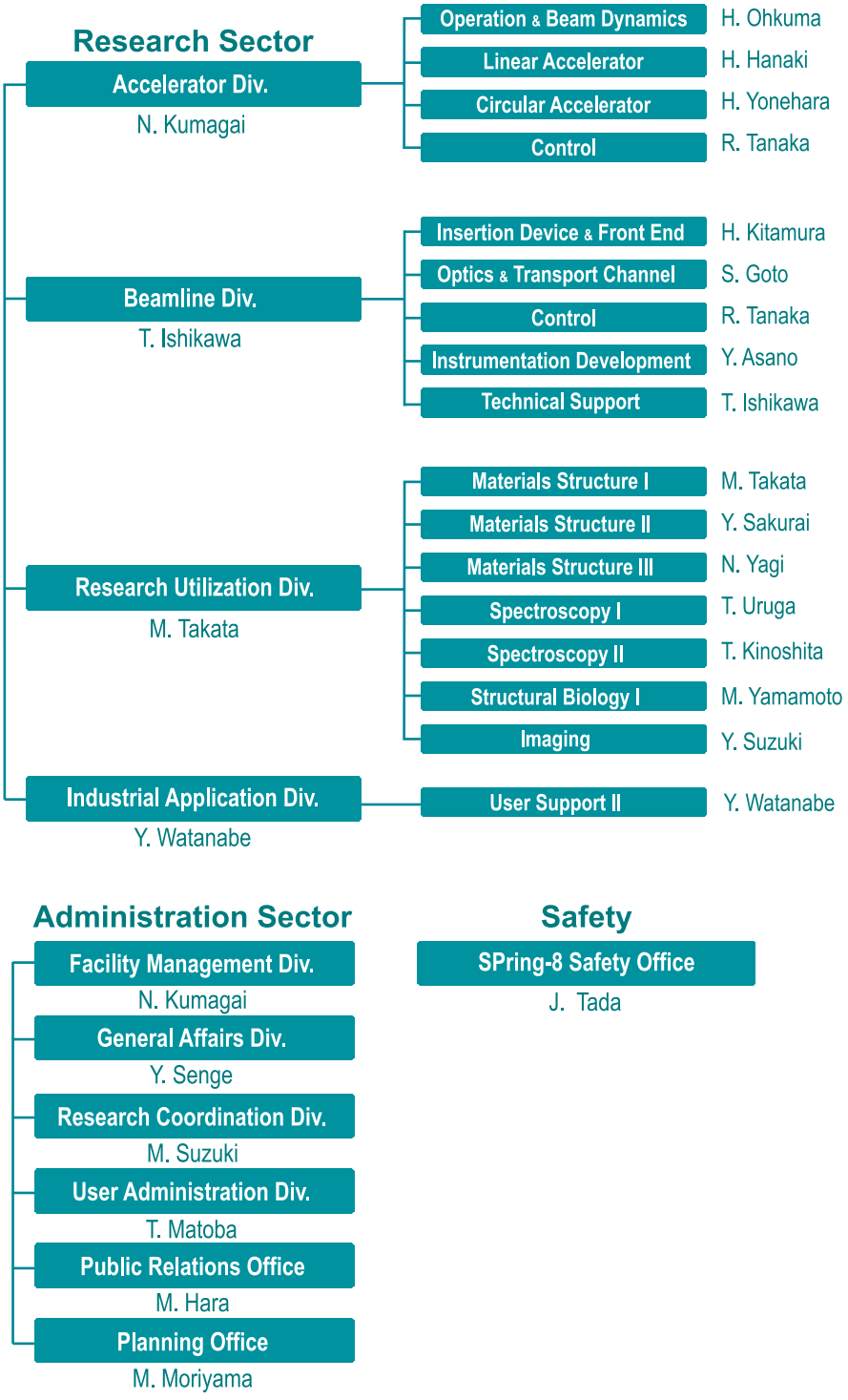

Figure 11

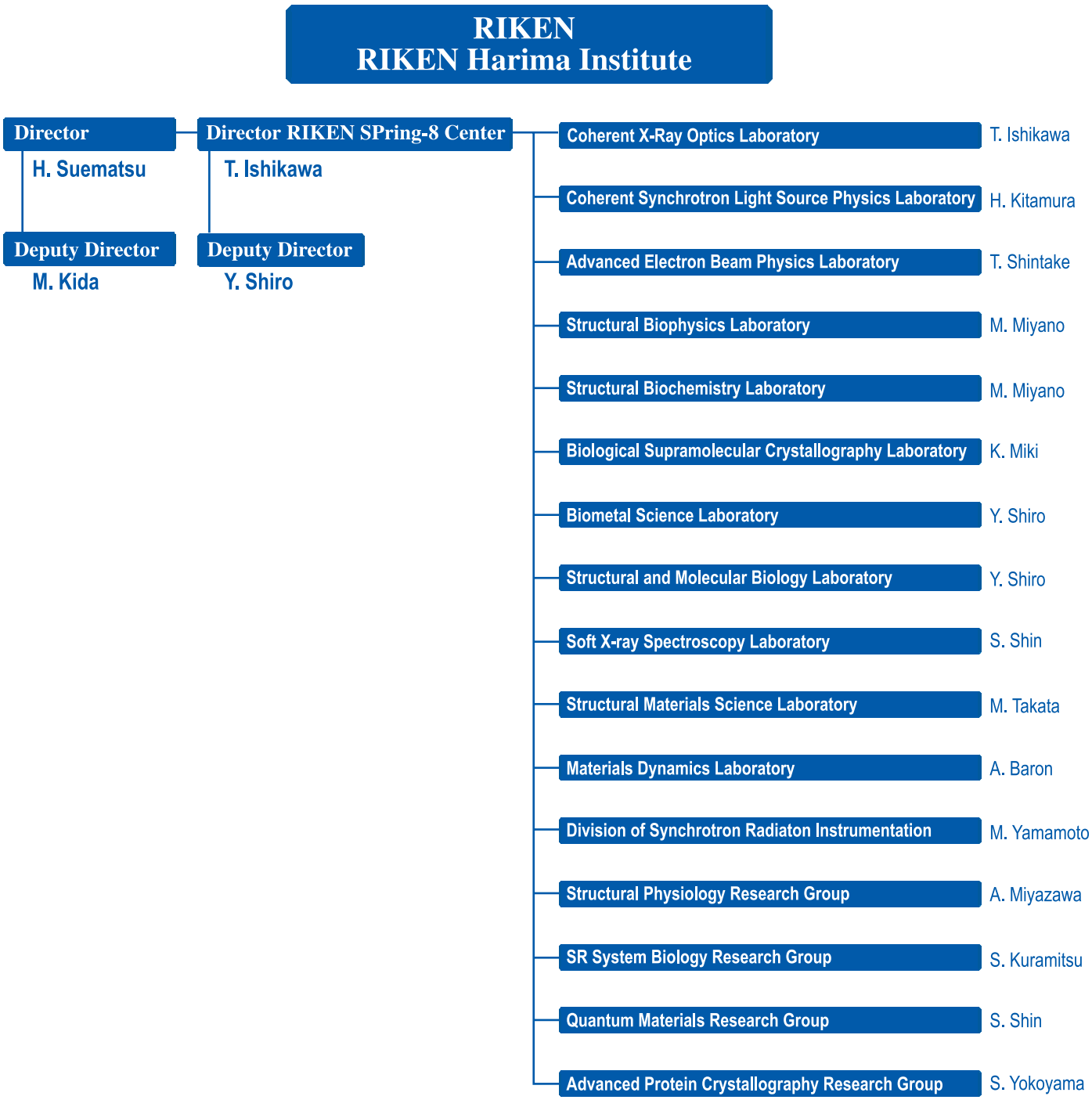
RIKEN
RIKEN Harima Institute
Director
H. Suematsu
Director RIKEN SPring-8 Center
T. Ishikawa
Deputy Director
M. Kida
Deputy Director
Y. Shiro
Coherent X-Ray Optics Laboratory
T. Ishikawa
Coherent Synchrotron Light Source Physics Laboratory
H. Kitamura
Advanced Electron Beam Physics Laboratory
T. Shintake
Structural Biophysics Laboratory
M. Miyano
Structural Biochemistry Laboratory
M. Miyano
Biological Supramolecular Crystallography Laboratory
K. Miki
Biometal Science Laboratory
Y. Shiro
Structural and Molecular Biology Laboratory
Y. Shiro
Soft X-ray Spectroscopy Laboratory
S. Shin
Structural Materials Science Laboratory
M. Takata
Materials Dynamics Laboratory
A. Baron
Division of Synchrotron Radiaton Instrumentation
M. Yamamoto
Structural Physiology Research Group
A. Miyazawa
SR System Biology Research Group
S. Kuramitsu
Quantum Materials Research Group
S. Shin
Advanced Protein Crystallography Research Group
S. Yokoyama

Figure 12

SPring-8 User Societies

In order to advance the research activities of users at SPring-8, the **SPring-8 Users Society** was established in May 1993 in such a way that the users can cooperate in the upgrading, facilitation and promotion of SPring-8 utilization, and can communicate and exchange information with each other and with the facility. At present, 34 working groups are actively making scientific contributions to develop SPring-8 activities. The number of the members in the Society reached 1500 as of April 2007.

To promote utilization by the industrial users of SPring-8, the **SPring-8 Industrial User Society** was established in September 1990, and has been investigating and deliberating the feasibility of making improvement on the SPring-8 utilization system and on SPring-8 utilization by the industry and making recommendations. Eight workshops have been organized on various utilization topics, such as practical catalysis and stress analysis. The activities of this Society have played important roles in promoting communication between industrial uses and JASRI and/or MEXT. The number of companies and corporations joining the Society reached 70 as of April 2007.

Users Meeting

The meetings for users jointly organized by JASRI and the SPring-8 User Society, and the SPring-8 Industrial User Society are listed below.

- The 10th SPring-8 Symposium
  November 1-2, 2006.

- Symposium on the Industrial Applications
  September 5-6, 2006.

International Conferences and Workshops

The International Conferences and Workshops organized/sponsored by SPring-8 (JASRI and RIKEN) in 2006 are listed below.

- SRI2006 (Ninth International Conference on Synchrotron Radiation Instrumentation)
  May 28 - June 2, 2006 – Daegu, Korea

- MEDSI2006 (International Workshop on Mechanical Engineering Design of Synchrotron Radiation Equipment and Instrumentation)
  May 24-26, 2006 – SPring-8, Japan

- Synchrotron Radiation in Polymer Science III
  July 6-8, 2006 – SPring-8, Japan

- The 5th International Conference on LEEM/PEEM
  October 15-19, 2006 – Egret, Himeji, Japan

- The 1st Asian/Oceanic Forum for Synchrotron Radiation Research
  November 24-25, 2006 – KEK, Tsukuba, Japan

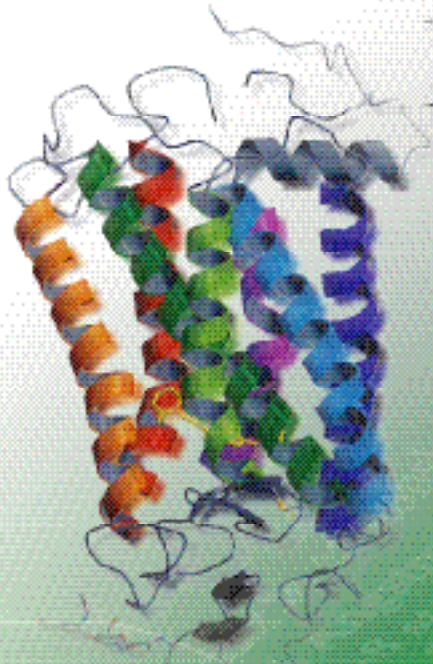

Project XFEL

SCSS

First Lasing of SCSS Test Accelerator

X-ray Free-Electron Lasers (XFEL) will enable atomic-resolution imaging with a femtosecond snapshot. Research on XFEL has competitively progressed in the United States, Europe, and Japan. In FY2006, the construction of XFEL machine was officially started by a joint project organization termed the "RIKEN-JASRI Joint Project for the SPring-8 XFEL." This five-year project (FY2006-FY2010) has been recognized as one of the key technologies of national importance in the 3rd Science and Technology Basic Plan. The Japanese XFEL aims to achieve excellent performance with a compact machine, which can drastically reduce construction cost and improve the reliability of machine operation. The novel design, which is composed of a low-emittance electron gun with a thermionic cathode, a multiple-stage bunch compression system, high-gradient normal-conducting C-band linacs, and short-period in-vacuum undulators [1], is significantly different from those seen in other FEL projects. Thus, the experimental verification of the concept prior to finalizing the XFEL design is a stringent subject.

The SCSS (SPring-8 Compact SASE Source) test accelerator was primarily designed to perform proof-of-principle experiments for FEL operation. The beam energy of the machine is E_B = 250 MeV, which is only 1/32 that of the XFEL machine, E_B = 8 GeV. However, the test accelerator includes all basic components planned for the 8-GeV machine (Fig. 1). Following the construction and the observation of the first spontaneous light in 2005, we intensively conducted machine tuning to achieve lasing condition from May to July of 2006.

FEL accelerators should generate a high-density electron beam in both space and time. The performance is characterized by a normalized slice emittance ε_n and a peak current I_p. The target values are ε_n ~ 1 π mm•mrad and I_p ~ kA, although the achievement of both criteria is a technical challenge. For this purpose, we have designed an injector system that combines a low-emittance electron gun with an adiabatic bunch compression system; the bunch length gradually decreases (i.e., peak current increases) as beam energy is boosted. This scheme is planned to suppress the space charge force, which can degrade the original emittance at the gun in the low-energy high-density electrons. The first target of the machine tuning is the verification of emittance preservation in compression.

The electron beam with a small emittance (ε_n = 0.6 π mm•mrad) is launched from a 500-kV pulsed electron gun equipped with a CeB_6 thermionic cathode (E_B ~ 500 keV, I_p ~ 1 A, pulse width τ ~ 2 microsecond) [2]. The beam is transmitted in a beam deflector (τ ~ 1 nanosecond), and is gradually compressed and accelerated with a 238-MHz pre-buncher cavity, a 476-MHz booster cavity, S-band linacs, and a magnetic chicane. At the end of this injector section,

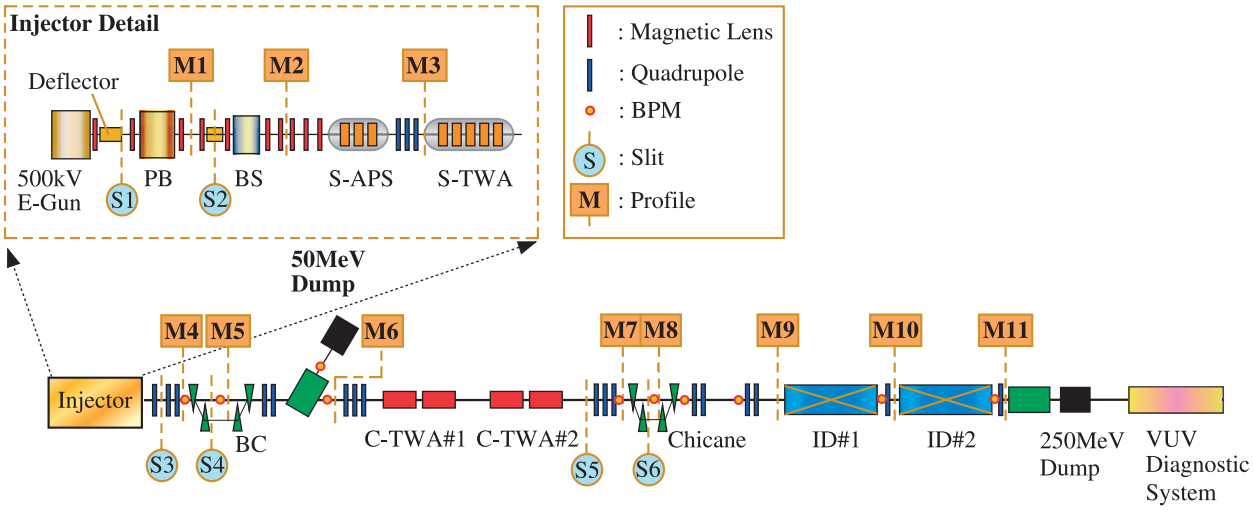

Fig. 1. Schematic layout of SCSS test accelerator.

the beam energy is boosted up to E_B ~ 40 MeV at I_p ~ 800 A and τ ~ 0.7 picoseconds. To maintain the original emittance we have to avoid over-focusing and over-bunching resulting in an emittance increase. Thus, we have carefully checked the beam property by beam profile and bunch length monitors, and optimized focusing and compression strengths.

The beam projected emittance at the exit of the injector section has been measured by a conventional Q-scan method, which monitors the response of the focusing strength of the quadropole magnet to the beam size (Fig. 2). The measured emittance of 3 π mm•mrad in the horizontal (3 π mm•mrad in the vertical) directions is in accordance with the simulated value of 2.8 π mm•mrad (2.6 π mm•mrad). We have experimentally confirmed the suppression of emittance growth in the compression scheme [3].

The electron beam is further accelerated with C-band linacs up to E_B = 250 MeV, and transported into in-vacuum undulators which modulate the trajectory of the electron beam by periodic magnets (15-mm period with a periodic number of 600) to produce short-wavelength radiation in the forward direction. When a small emittance and a large peak current of the electron beam are achieved, the power of the photon beam is dramatically enhanced owing to the efficient exchange of energies between electrons and photons. This lasing condition is characterized by diagnosing the photon beam properties.

On June 20, 2006, we observed the first lasing just after starting the commissioning of the undulator. Figure 3 shows the typical energy spectra of the laser and the usual spontaneous radiation with an electron beam charge of 0.25 nC and an undulator K-value of 1.3. A 6,000-fold amplification at a wavelength of λ = 49 nm was observed. The peak current of the electron beam is estimated to be I_p ~ 1 kA from a systematic study of the gain dependence on undulator K-values [3].

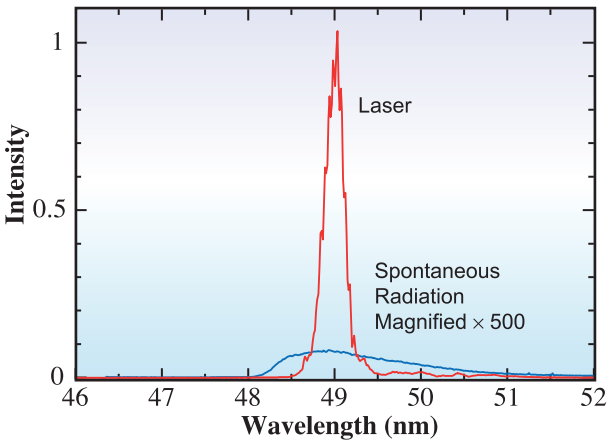

Fig. 3. Energy spectra of laser and spontaneous radiation.

The photon beam properties (a variable wavelength of $\lambda \geq$ 49 nm, a bandwidth of 0.4%, a pulse energy of a few μJ, and a pulse width smaller than 100 fs [4]) is prominent among vacuum ultraviolet (VUV) sources. We are planning to construct a VUV experimental station for public use in 2007. This machine will play crucial roles not only as a 'test' accelerator for studying FEL technologies but also as a 'practical' light source for developing novel scientific applications with intense VUV radiation.

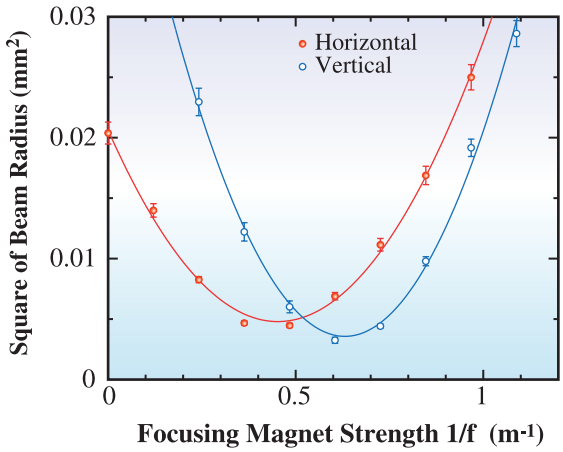

Fig. 2. Emittance measurement at exit of the injector.

Makina Yabashi [a,*], Hitoshi Tanaka [b] and Toru Hara [b]

[a] SPring-8 / JASRI
[b] SPring-8 / RIKEN

*E-mail: yabashi@spring8.or.jp

References

[1] T. Shintake *et al.*: Proc. SPIE **4500** (2001) 12.
[2] K. Togawa *et al.*: Phys. Rev. ST AB 10 (2007) 020703.
[3] *H. Tanaka, K. Togawa, H. Baba, T. Hara, A. Higashiya, T. Inagaki, H. Maesaka, H. Matsumoto, K. Onoe, Y. Otake, K. Shirasawa, T. Tanaka, T. Tanikawa, M. Yabashi and T. Shintake: Proc. FEL2006 (BESSY, Berlin, Germany, 2006) 769.*
[4] *M. Yabashi, T. Hirono, H. Kimura, H. Ohashi, S. Goto, S. Takahashi, K. Tamasaku and T. Ishikawa: Proc. FEL2006 (BESSY, Berlin, Germany, 2006) 785.*

Editor
Seishi Kikuta
SPring-8 / JASRI

Editing & Layout
Marcia M. Obuti-Daté
SPring-8 / JASRI

Printing
Xworks Co., Ltd.

J A S R I
Library and Information
Users Administration Division

1-1-1 Kouto, Sayo-cho, Sayo-gun
Hyogo 679-5198 • JAPAN
Tel. +81-(0)791 58-2797 Fax. +81-(0)791 58-1869

frontiers@spring8.or.jp
http://www.spring8.or.jp/

© **SPring-8 / JASRI**
July 2007

Japan Synchrotron Radiation Research Institute
1-1-1 Kouto, Sayo-cho, Sayo-gun, Hyogo 679-5198 JAPAN
http://www.spring8.or.jp